VOLUME 81 JUNE 30, 1977 NUMBER 13

JPCHAx

THE JOURNAL OF PHYSICAL CHEMISTRY

PUBLISHED BIWEEKLY BY THE AMERICAN CHEMICAL SOCIETY

THE JOURNAL OF PHYSICAL CHEMISTRY

BRYCE CRAWFORD, Jr., *Editor*
STEPHEN PRAGER, *Associate Editor*
ROBERT W. CARR, Jr., C. ALDEN MEAD, *Assistant Editors*

Published by the
AMERICAN CHEMICAL SOCIETY
BOOKS AND JOURNALS DIVISION
D. H. Michael Bowen, Director
Marjorie Laflin, Assistant to the Director

Editorial Department: Charles R. Bertsch, Head; Marianne C. Brogan, Associate Head; Celia B. McFarland, Joseph E. Yurvati, Assistant Editors
Magazine and Production Department: Bacil Guiley, Head
Research and Development Department: Seldon W. Terrant, Head

Advertising Office: Centcom, Ltd., 25 Sylvan Road South, Westport, Conn. 06880.

Published biweekly by the American Chemical Society at 20th and Northampton Sts., Easton, Pennsylvania 18042. Second class postage paid at Washington, D.C. and at additional mailing offices.

Editorial Information

Instructions for authors are printed in the first issue of each volume. Please conform to these instructions when submitting manuscripts.

Manuscripts for publication should be submitted to *The Journal of Physical Chemistry,* Department of Chemistry, University of Minnesota, Minneapolis, Minn. 55455. Correspondence regarding **accepted papers and proofs** should be directed to the Editorial Department at the ACS Easton address.

Page charges of $60.00 per page may be paid for papers published in this journal. Ability to pay does not affect acceptance or scheduling of papers.

Bulk reprints or photocopies of individual articles are available. For information write to Business Operations, Books and Journals Division at the ACS Washington address.

Requests for **permission to reprint** should be directed to Permissions, Books and Journals Division at the ACS Washington address. The American Chemical Society and its Editors assume no responsibility for the statements and opinions advanced by contributors.

Subscription and Business Information

1977 Subscription rates—including surface postage

	U.S.	PUAS	Canada, Foreign
Member	$24.00	$33.00	$34.00
Nonmember	96.00	105.00	106.00
Supplementary material	15.00	19.00	20.00

Air mail and air freight rates are available from Membership & Subscription Services, at the ACS Columbus address.

New and renewal subscriptions should be sent with payment to the Office of the Controller at the ACS Washington address. **Changes of address** must include both old and new addresses with ZIP code and a recent mailing label. Send all address changes to the ACS Columbus address. Please allow six weeks for change to become effective. **Claims for missing numbers** will not be allowed if loss was due to failure of notice of change of address to be received in the time specified: if claim is dated (a) North America—more than 90 days beyond issue date, (b) all other foreign—more than 1 year beyond issue date; or if the reason given is "missing from files". Hard copy claims are handled at the ACS Columbus address.

Microfiche subscriptions are available at the same rates but are mailed first class to U.S. subscribers, air mail to the rest of the world. Direct all inquiries to Special Issues Sales, at the ACS Washington address or call (202) 872-4554. **Single issues** in hard copy and/or microfiche are available from Special Issues Sales at the ACS Washington address. Current year $4.75. Back issue rates available from Special Issues Sales. **Back volumes** are available in hard copy and/or microform. Write to Special Issues Sales at the ACS Washington address for further information. **Microfilm** editions of ACS periodical publications are available from volume 1 to the present. For further information, contact Special Issues Sales at the ACS Washington address. **Supplementary material** mentioned in the journal appears in the microfilm edition. Single copies may be ordered directly from Business Operations, Books and Journals Division, at the ACS Washington address.

	U.S.	PUAS, Canada	Other Foreign
Microfiche	$2.50	$3.00	$3.50
Photocopy			
1–7 pages	4.00	5.50	7.00
8–20 pages	5.00	6.50	8.00

Orders over 20 pages are available only on microfiche, 4 × 6 in., 24X, negative, silver halide. Orders must state photocopy or microfiche if both are available. Full bibliographic citation including names of all authors and prepayment are required. Prices are subject to change.

American Chemical Society
1155 16th Street, N.W.
Washington, D.C. 20036
(202) 872-4600

Member & Subscription Services
American Chemical Society
P.O. Box 3337
Columbus, Ohio 43210
(614) 421-7230

Editorial Department
American Chemical Society
20th and Northampton Sts.
Easton, Pennsylvania 18042
(215) 258-9111

Notice to Authors last printed in the issue of January 13, 1977

THE JOURNAL OF

PHYSICAL CHEMISTRY

Volume 81, Number 13 June 30, 1977

JPCHAx 81(13) 1217–1342 (1977)

ISSN 0022-3654

■ Supplementary and/or miniprint material for this paper is available separately (consult the masthead page for ordering information); it will also appear following the paper in the microfilm edition of this journal.

* In papers with more than one author, the asterisk indicates the name of the author to whom inquiries about the paper should be addressed.

AUTHOR INDEX

THE JOURNAL OF
PHYSICAL CHEMISTRY

Registered in U. S. Patent Office

VOLUME 81, NUMBER 13 JUNE 30, 1977

Kinetics and Mechanism of Recoil Chlorine Atom Reactions with Ethylene

Don J. Stevens and Leonard D. Spicer*

Department of Chemistry, University of Utah, Salt Lake City, Utah 84112 *(Received November 19, 1976)*

Publication costs assisted by the United States Energy Research and Development Administration

Addition and abstraction are the major reactions observed between nuclear recoil generated chlorine atoms and ethylene. The addition reaction is characterized, and its relative efficiency is determined for low energy chlorine in systems containing H_2 and C_3F_6 as competitive reactants. At low pressures, the unimolecular kinetics of an addition–decomposition process yielding HCl are examined, and the relative translational energy of the chlorine atoms which initiate that reaction is estimated. Hydrogen abstraction from ethylene is also explored in this system and found to be predominantly a low energy process in competition with addition. In the limits of high pressure and high moderation, the rate ratio of addition to abstraction for low energy chlorine atoms with ethylene is found to be 15.5 ± 0.5. Results for competitive addition reactions between C_2H_4 and C_3F_6 yield a rate ratio of 16 ± 2 favoring ethylene. The only additional reaction observed in pure ethylene corresponds to carbon–carbon bond scission and accounts for less than 1% of the total yield.

Introduction

Thermal and hot reactions between halogen atoms and olefinic molecules are of considerable importance to recoil chemistry since these species are frequently utilized as scavengers.[1-15] In this capacity unsaturated molecules are used to control the thermal chemistry of the system by providing a favorably competitive reactant for atomic and radical species. As an added reactant, however, scavengers must be carefully examined to determine the extent to which they interfere with primary hot reactions of interest in recoil studies. Double bonded molecules which have been used as scavengers include hexafluoropropene,[1] 1,2-dichloroethylene,[2] and 1,3-butadiene with O_2 added,[3] and ethylene which has been used both alone and in combination with I_2,[4,9-15] HI,[6,7] and O_2.[3] The addition of small amounts of the secondary scavenger has been found in general to enhance scavenging efficiency by effectively terminating free-radical intermediates.

Ethylene was first used extensively as a primary scavenger in studies of recoil ^{18}F atom reactions.[4] The scavenging reaction was found to proceed by addition of fluorine to the double bond followed by free-radical termination with added iodine vapor

$$C_2H_4 + {}^{18}F \rightarrow C_2H_4{}^{18}F \quad (1)$$

$$C_2H_4{}^{18}F\cdot + I_2 \rightarrow C_2H_4{}^{18}FI + I \quad (2)$$

At sufficiently low pressures it was reported[4] that the excited fluoroethyl radical was also subject to competitive unimolecular decomposition through a hydrogen atom elimination to form vinyl fluoride product. In later studies HI was found to be equivalent to I_2 as a secondary scavenger in recoil fluorine systems[6,7] and, in addition, decomposition of the intermediate fluoroethyl radical through cleavage of the carbon–carbon bond was noted. Recent work[7] with ethylene and acetylene, however, has shown that the addition reaction to ethylene which is the primary scavenging reaction is approximately 20% slower than that with acetylene. In general the ethylene scavenger may not be effective for all reactant systems and must be carefully examined in each recoil fluorine study.

The high reactivity of thermal chlorine atoms with ethylene has promoted its use as a scavenger in studies of recoil chlorine atom reactions as well.[12-14] In combination

---

* Camille and Henry Dreyfus Teacher Scholar 1972–1976. Author to whom correspondence should be addressed.

with iodine vapor the scavenging reaction was found to proceed by the stepwise addition similar to eq 1 and 2 with resultant formation of $C_2H_4I^{38}Cl$ scavenger product. The high efficiency of this combination scavenger in recoil chlorine systems, however, contrasts with that found for either ethylene alone or in combination with added O_2 both of which have been shown[3] to be less efficient in controlling thermal reactions. Ethylene and I_2 have also been investigated[15] as reactants in nuclear recoil generated ^{128}I atom systems, but the observed product distribution is highly atypical of the chlorine or fluorine atom reactions. Recoil iodine systems are more complex in general and are characterized by the presence of ionic and electronically excited species in addition to translationally excited atoms.

In this study reactions of nuclear recoil generated chlorine-38 atoms with ethylene are examined in detail. Very recently, selected features of the thermal component of this reaction have been studied.[8] Here the efficiency of ethylene as a competitive reactant for thermalized chlorine atoms is determined in mixed reactant systems containing CF_2Cl_2, H_2, and $CF_2{=}CF{-}CF_3$. Addition reactions to ethylene produce both stable radicals and vibrationally excited radical intermediates which undergo $H^{38}Cl$ elimination in competition with collisional stabilization. Evidence is also presented for concerted hydrogen abstraction from ethylene and the energy dependence of both the addition and abstraction reactions is explored. Finally, evidence is presented for a minor reaction mechanism involving cleavage of the carbon–carbon bond.

Experimental Section

Translationally hot chlorine atoms were generated by the $^{37}Cl(n,\gamma)^{38}Cl$ nuclear reaction using a californium-252 source at the University of Utah Nuclear Reactor Center. Samples were irradiated 2–3 h at 300 K in a dry port with a slow neutron flux measured to be 5×10^7 n/cm^2 s, a fast neutron flux of 2×10^7 n/cm^2 s, and a γ flux estimated to be 5×10^7 photons/cm^2 s. Radiation damage from the source in this configuration was measured to be less than 0.001 eV/molecule using an acetylene-to-benzene chemical dosimeter.[16]

Reuseable sample vessels consisted of 90-mL cylindrical, high-purity quartz ampoules connected by 175 mm × 2 mm i.d. pyrex capillary tubing to high vacuum teflon stopcocks. The sample vessels were routinely heated overnight at 150 °C to ensure dryness prior to filling. Reaction mixtures were prepared in the vessels by successive piling on of gaseous sample components using standard high-vacuum techniques. Samples contained CF_2Cl_2 which served concurrently as a naturally abundant source of chlorine for the nuclear reaction and as a moderator bath gas, and ethylene which served as a reactant and a scavenger in conjunction with I_2 at its ambient temperature vapor pressure. Some samples also contained H_2 or C_3F_6 as competitive reactants. The gaseous reactants CF_2Cl_2 and H_2 from Matheson and Phillips Research Grade ethylene were used directly from lecture bottles without further purification after analysis by gas chromatography and mass spectroscopy showed purities of greater than 99.9%. Mallinckrodt Research grade iodine crystals were resublimed prior to use, and perfluoropropene from PCR Inc. was purified by vacuum distillation and degassed by repeated freeze–pumping under high vacuum prior to sample filling.

Following irradiation, samples were promptly analyzed in the following manner. $H^{38}Cl$ formed during the reaction process was separated from other products using a stripper apparatus[17] consisting of a 5.5-cm column containing 20 g of granular K_2CO_3 through which the gaseous components of the product mixture were expanded to remove hydrogen chloride. The remaining gaseous components were collected at liquid nitrogen temperature in a 20-mL pyrex cold trap sealed with Burrell connectors. In samples with H_2, the noncondensible reactant was pumped through the cold trap into the vacuum system via a teflon needle valve to minimize surging. Hydrogen chloride adsorbed on the reaction vessel walls was removed by repeated rinses with 0.1 M aqueous Na_2CO_3 solution. The absolute yields of $H^{38}Cl$ on both the stripper column and in the aqueous rinses as well as the summed yields of all other products collected in the cold trap were determined on a dual channel analyzer with a 3 in. × 3 in. NaI(Tl) scintillation detector. Details of the $H^{38}Cl$ identification procedure are presented elsewhere.[14,18]

Separation and identification of products in the cold trap was carried out by radiogas chromatography incorporating a thin-window external flow proportional counter.[13,14] Product identification was based on coincident elution with added carrier gas on two columns having different separation characteristics. In the case of $CH_2{}^{38}ClI$, for which no carrier was available, characterization was based on similar retention times and the behavior noted in previous work.[10] Chromatography columns used were 0.25-in. copper tubing and consisted of a 5 ft, 5% and a 25 ft, 20% SF-96 silicone oil column as well as a 15 ft, 20% hexamethylphosphoramide column each utilizing Chromosorb P support. All chromatographic separations were carried out at ambient temperature with flow rates of 60 cm^3/min.

Results and Discussion

Addition Reactions. The most efficient low energy reaction channel for chlorine atoms with unsaturated hydrocarbons is addition at the site of unsaturation. Such addition reactions to double bonds have been used extensively for scavenging of thermalized species in recoil halogen systems.[1-15] In the case of chlorine atom addition to ethylene, two competing processes are observed following the initial reaction. The radical formed initially may either react further and be terminated or it may decompose by HCl elimination if it is formed with enough excess energy. Chlorine atom elimination is also possible but this simply makes the chlorine atom again available for reaction at an equal or lower energy than it was initially. Each of the first two processes is examined in detail below to better characterize the addition reaction between recoil chlorine and ethylene.

In both recoil chlorine and recoil fluorine atom studies, ethylene has been used in conjunction with iodine as a scavenger.[4,9-14] The primary scavenging reaction for chlorine is the stepwise process:

$$Cl + H_2C{=}CH_2 \rightarrow ClH_2C\text{-}CH_2\cdot \qquad (3)$$

$$ClH_2C\text{-}CH_2\cdot + I_2 \rightarrow ClH_2C\text{-}CH_2I + I \qquad (4)$$

The overall efficiency of this system depends on the competition between ethylene and other components for reaction with thermalized chlorine atoms. The chlorine addition to ethylene occurs readily having little or no activation barrier and an exothermicity of 22 kcal/mol.[19] The Arrhenius rate constant for the process has been determined to be $k = 5 \times 10^{10}$ L/mol s at 298 °C.[19]

The efficiency of the chlorine addition process represented by reactions 3 and 4 was examined in competition with the chlorine atom reaction with H_2

$$^{38}Cl + H_2 \rightarrow H^{38}Cl + H \qquad (5)$$

by monitoring $H^{38}Cl$ production as a function of the

TABLE I: Relative Efficiencies of C_2H_4 and CF_3-$CF=CF_2$ as Scavengers for Near Thermal ^{38}Cl Atoms

	Sample no.			
	169	176	173	175
Reactant ratio				
Hexafluoropropene/ethylene	0.961	1.50	2.96	3.92
Absolute yields				
$C_2H_4I^{38}Cl$	93.1	89.8	80.3	79.2
$C_3F_6I^{38}Cl$	5.2	8.6	17.1	17.6
$CF_3{}^{38}Cl + CF_2Cl^{38}Cl + CFCl_2{}^{38}Cl + C_2F_3{}^{38}Cl$	1.7	1.5	2.6	3.2
Product yield ratio				
$C_2H_4I^{38}Cl/C_3F_6I^{38}Cl$	17.8	10.4	4.61	4.50
Relative scavenging efficiency[a]				
C_2H_4/C_3F_6	17.1	15.6	13.6	17.6

[a] Average relative scavenging efficiency = 16 ± 2

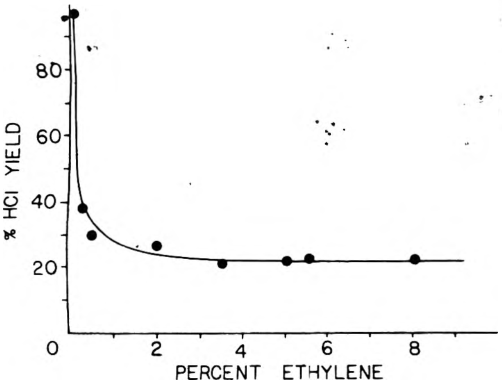

Figure 1. Dependence of the absolute yield of $H^{38}Cl$ on the concentration of ethylene in a 1:1 mixture of H_2 reactant and CF_2Cl_2 moderator at 800 Torr total pressure.

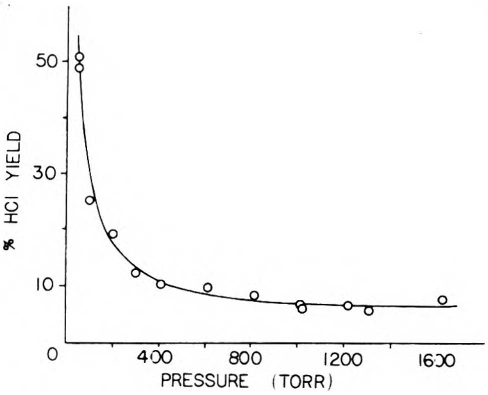

Figure 2. Pressure dependence of the absolute $H^{38}Cl$ yield from the $^{38}Cl + C_2H_4$ reaction at 95% moderation with CF_2Cl_2 bath gas.

concentration of ethylene added to the system. The ethylene concentration was varied from 0.1 to 8.0 mol % in a reactant mixture with a 1:1 ratio of H_2 reactant and CF_2Cl_2 which served as a moderator and a source of chlorine for the nuclear recoil reaction. The total pressure of the system was maintained at 800 Torr. The yield of $H^{38}Cl$ as a function of ethylene additive is shown in Figure 1 and appears to represent a classical scavenger curve. In the well scavenged region above 1% ethylene concentration, the linear data indicate the high efficiency of the ethylene scavenger. Competition with H_2 for thermal chlorine atoms is negligible since doubling the ethylene composition from 4 to 8 mol % fails to alter the HCl yield. Whereas the effective temperature of the recoil system at 50% moderation is unknown, this result is comparable to what is expected on the basis of the measured thermal rate constants where $k_H = 3.9 \times 10^6$ L/mol s at 298 K,[20] showing that addition to ethylene is about 10^4 times as efficient as reaction with H_2 at 298 K.

The efficiency of the ethylene double bond in competing for low energy chlorine atoms was also determined in relation to the olefinic halocarbon perfluoropropene. The perfluoropropene scavenging reaction proceeds in a stepwise fashion to form the chloroiodo addition product in a manner identical with the scavenging reaction of ethylene. In a mixed reactant system the relative yields of ethyl and propyl halocarbons will directly reflect differences in the competitive rate constants. The competitive addition reaction was investigated in reactant mixtures of 5% ethylene, 5–20% C_3F_6, iodine at its ambient temperature vapor pressure, and CF_2Cl_2 source gas added to a total pressure of 1000 Torr. The results of the competitive addition are shown in Table I and indicate that the rate of chlorine atom addition to ethylene is 16 ± 2 times faster than to perfluoropropene. In both the hydrogen and perfluoropropene studies, ethylene is a highly effective competitor for low energy chlorine atoms which reaffirms the fact that it is an effective scavenger for recoil chlorine atom systems in general.

The chlorine atom addition reaction may also be followed by subsequent unimolecular decomposition of the intermediate chloroethyl radical into $H^{38}Cl$ and the vinyl radical if sufficient energy is available.

$$^{38}Cl + C_2H_4 \xrightarrow{k_1} \cdot C_2H_4{}^{38}Cl^* \xrightarrow{k_2} H^{38}Cl + C_2H_3\cdot \qquad (6)$$

This net reaction is endothermic by ~5 kcal/mol and will require in addition enough energy to overcome the activation energy for the four-centered HCl elimination from the intermediate radical. The activation barrier for HCl elimination from chloroethane has been calculated to be approximately 55 kcal/mol,[21] and it is in the range 55–58 kcal/mol for HCl elimination from 1,2-dichloroethane[22] and 1,1,2-trichloroethane.[23] The chloroethyl radical is expected to be most closely approximated by the chloroethane molecule, and it is estimated that the activation barrier for elimination from the radical will be ~50 kcal/mol due to the decreased carbon–carbon bond length in the radical. The threshold energy for the overall reaction in (6) is then estimated to be 28 kcal/mol, and this excess energy must be provided in the form of translational energy by the ^{38}Cl atom for $H^{38}Cl$ elimination to occur.

The excited chloroethyl radical intermediate in reaction 3 may also be collisionally stabilized by the surrounding bath gas in competition with unimolecular decomposition.

$$\cdot C_2H_4{}^{38}Cl^* + M \xrightarrow{k_3} \cdot C_2H_4{}^{38}Cl + M^* \qquad (7)$$

The rate of stabilization is directly related to the collision frequency ω and can be investigated experimentally as a function of pressure. This addition–decomposition process was characterized by monitoring the $H^{38}Cl$ yield over the pressure range 50–1600 Torr in a reaction system of 5% ethylene, I_2 at its ambient temperature vapor pressure, and 95% CF_2Cl_2 moderator which served simultaneously as a

TABLE II: Typical Absolute Yield Data for the Recoil Chlorine Atom Reactions with Ethylene in the Presence of CF_2Cl_2 Source Gas and Moderator

% C_2H_4	Total sample pressure,[a] Torr	% absolute yields[b]			
		$H^{38}Cl$	$CH_2ICH_2{}^{38}Cl$	$CH_2I^{38}Cl$	$CF_2Cl^{38}Cl + CFCl_2{}^{38}Cl$
29.9	1000	9.1	90	0.6	0.3
18.8	1000	7.3	92	0.3	0.4
10.0	1000	6.8	92	0.4	0.4
5.0	1291	5.8	93	0.4	0.4
4.9	1006	6.2	93	0.2	0.5
5.0	1000	6.9	92	0.4	0.5
5.0	806	8.4	91	0.2	0.4
5.0	603	10.3	89	0.2	0.3
5.0	201	19.3	80	0.4	0.5

[a] Total pressure = $P_{C_2H_4} + P_{CF_2Cl_2}$. [b] Errors in the HCl yield are estimated to be ±7% based on multiple determinations. $CH_2ICH_2{}^{38}Cl$ (±3%) and $CH_2I^{38}Cl + CF_2Cl^{38}Cl + CF_2Cl^{38}Cl$ (±15%) error limits are based on counting statistics of single determinations.

TABLE III: $H^{38}Cl$ Yields as a Function of Pressure and Moderation in the $^{38}Cl + C_2H_4$ System with CF_2Cl_2 Moderator

	60% moderation			95% moderation		
	100 Torr	200 Torr	1000 Torr	100 Torr	200 Torr	1000 Torr
Total $H^{38}Cl$	29.2 ± 3.0	19.1 ± 1.5	10.0 ± 0.7	25.2 ± 2.6	18.1 ± 1.4	6.5 ± 0.5
Addition–decomposition produced $H^{38}Cl$	19.4 ± 3.1	9.3 ± 1.7	0.2 ± 0.2	18.7 ± 2.6	11.6 ± 1.5	0.2 ± 0.2
Abstraction produced $H^{38}Cl$	9.8 ± 0.9	9.8 ± 0.9	9.8 ± 0.9	6.3 ± 0.4	6.3 ± 0.4	6.3 ± 0.4

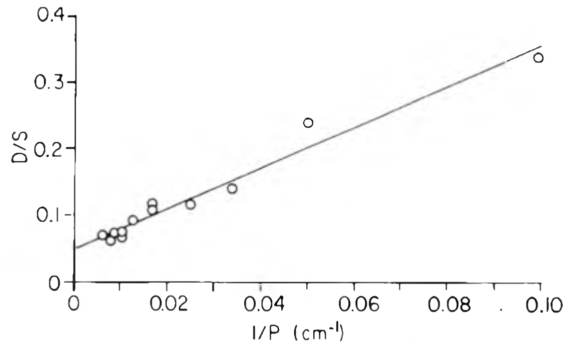

Figure 3. The uncorrected yield ratio $H^{38}Cl/CH_2{}^{38}ClCH_2I$ (D/S) as a function of $1/P$ for the $^{38}Cl + C_2H_4$ reaction.

source gas for chlorine. Complete yield distributions for typical pressure experiments are listed in Table II, and the full set of experimental results for the $H^{38}Cl$ dependence on pressure is illustrated in Figure 2. The HCl yield generated via the unimolecular process increases rapidly at pressures below 300 Torr while collisional stabilization above that pressure maintains a constant hydrogen chloride yield to pressures of at least 1600 Torr.

The high pressure rate constant for this unimolecular process can be defined as

$$k_d = \omega\beta(D/S) \tag{8}$$

where β is the relative collisional stabilization efficiency of the bath gas and ω is the collision frequency for the excited chloroethyl radical.[24] Plotting the D/S ratio as a function of reciprocal pressure then should show linear behavior with the slope of the line being directly proportional to k_d. The experimental results are plotted in Figure 3. Upon correction for the noncompetitive contribution to the yields these data give a high pressure rate constant of $k_d/\beta = 8 \pm 3 \times 10^8$ s^{-1}. The collisional energy transfer efficiency for CF_2Cl_2 is expected to be relatively high based upon results in other unimolecular systems[25] and the value of β is estimated to be approximately unity.

On the basis of classical Kassel theory, the value determined for k_d suggests that the average excitation energy of the chemically activated intermediate is very nearly equal to the decomposition threshold E_0.[24] Since E_0 is estimated to be 50 kcal/mol the amount of effective translational energy deposited on reaction is severely limited which indicates that the effective cross section for this addition mechanism extends only to the epithermal energy region. This is not surprising since the pressure dependent data were determined at 95% moderation with CF_2Cl_2 bath gas. Extrapolation to infinite pressure at the left-hand axis indicates a 6.3 ± 0.5% $H^{38}Cl$ yield at that limit. Since the addition–decomposition component of the hydrogen chloride yield must extrapolate to zero, the additional yield is felt to arise from a second reaction mechanism which is examined in detail in the following section.

The extent to which hot reaction contributes to the addition–decomposition mechanism was further investigated experimentally by lowering the mole fraction of CF_2Cl_2 moderator to increase the probability of high energy collision between ^{38}Cl and ethylene. $H^{38}Cl$ production was determined as a function of pressure in a reaction system prepared with 40% ethylene, 60% CF_2Cl_2 moderator, and I_2 at its ambient vapor pressure. The results are shown in Table III where the yields of hydrogen chloride at 95% moderation are also listed. The $H^{38}Cl$ yield attributed to the addition–decomposition pathway was calculated by subtracting the extrapolated high pressure limiting value of the hydrogen chloride yield as determined by the D/S plot from the total yields measured at each pressure.

The data exhibit similar behavior independent of moderation with suppression of the addition–decomposition pathway at high pressures followed by a rapid increase in the $H^{38}Cl$ yield at low pressures. The addition–decomposition yield at both 100 and 200 Torr are identical within experimental error at each moderation further suggesting that high energy collisions are ineffective in contributing to the addition mechanism which results in HCl elimination.

The additional contribution to the addition mechanism which might be expected leads to an excited radical which redissociates into ethylene and ^{38}Cl atoms. The ^{38}Cl atom may be recycled several times in this manner, losing energy and nearing thermalization with each encounter, and thus the process can be thought of simply as an inelastic scattering event.

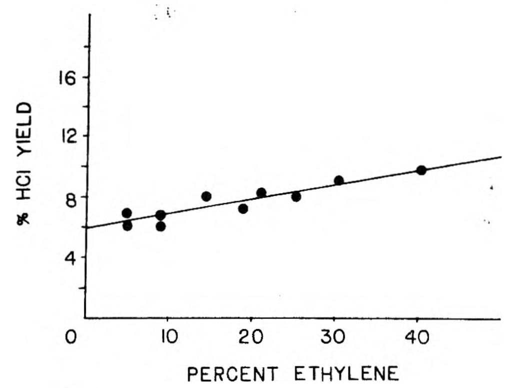

Figure 4. Dependence of the absolute yield of $H^{38}Cl$ on CF_2Cl_2 moderator concentration at 1000 Torr total pressure for the reaction $^{38}Cl + C_2H_4$.

Abstraction Reaction. The experimental results suggest that a direct abstraction mechanism also produces $H^{38}Cl$ from ethylene. This evidence is based on the observation that even at high pressures, where collisional stabilization suppresses the addition–decomposition mechanism, hydrogen chloride is a reaction product. This process is represented by

$$^{38}Cl + C_2H_4 \rightarrow H^{38}Cl + C_2H_3\cdot \quad (9)$$

Abstraction of hydrogen by chlorine atoms has been well documented in the case of various alkanes[20,26–29] and polychloroalkanes[20,29–32] but is less well understood in the case of olefinic hydrocarbons since addition to double bonds is consistently more rapid than abstraction. In the analogous case of thermal hydrogen atoms abstracting bound hydrogen, abstraction/addition ratios have been found[33] to be on the order of 0.03% for ethylene reactant and from 0.2 to 1.6% for other olefins. In addition fluorine atoms studies with acetylene have shown[7] abstraction of hydrogen to occur ~12% as frequently as addition, and abstraction is expected to be even more efficient in the case of ethylene. The extrapolated 6.3% $H^{38}Cl$ yield at the limit of infinite pressure is thus intermediate between the H· and F· reactant systems.

The nature of the direct abstraction mechanism was investigated experimentally by varying the CF_2Cl_2 moderator concentration while the pressure was maintained at 1000 Torr in order to suppress the addition–decomposition process. At high pressure, the experimentally observed $H^{38}Cl$ yield is a measure of the competitive rate of abstraction vs. the total rate of addition:

$$Y_{H^{38}Cl} = \frac{k_{\text{abstraction}}}{k_{\text{addition}} + k_{\text{abstraction}}} \quad (10)$$

since the total yield of these two processes is >99%. The rate of addition to the double bond was shown above to be predominantly a low energy process and the yield of addition product is considerably larger in magnitude than that for direct abstraction at both 60 and 95% moderation.

The abstraction reaction was examined experimentally in a system of 5 to 40% ethylene, I_2 at its ambient vapor pressure, and CF_2Cl_2 moderator added to a total pressure of 1000 Torr. Typical yield distributions are shown in Table II and data from the $H^{38}Cl$ dependence on moderation are shown in Figure 4. The data display linear behavior with a positive least-squares slope of 1% $H^{38}Cl$ yield per 10% rise in ethylene concentration and an intercept of 6.0% $H^{38}Cl$ yield. The linearity of the plot suggests that the increased yield at lower moderations is due primarily to a dilution effect on the potentially reactive high energy collisions. This behavior indicates that the cross section for abstraction reaction extends beyond that for addition to and scavenging by ethylene. Extrapolation to a nonzero intercept in the high moderation limit suggests also that the abstraction reaction cross section extends downward to near-thermal energies as might be expected and that most of the $H^{38}Cl$ yield from this mechanism is formed from low energy abstraction reactions in competition with the addition reactions discussed previously. The yield ratio of the addition product, $CH_2{}^{38}ClCH_2I$, to the abstraction product $H^{38}Cl$ at high moderation and high pressure is 15.5 ± 0.5. Since direct abstraction is endothermic by about 5 kcal/mol, this result suggests that epithermal reactions are occurring at moderator concentrations in excess of 95%. Clearly the competitive rates determined in this recoil system do not reflect relative thermal rate coefficients.

Carbon–Carbon Bond Scission Reaction. The single additional reaction[34] observed between ethylene and ^{38}Cl atoms in this recoil system induces the scission of the double bond with the radical formed being scavenged by iodine as follows:

$$^{38}Cl^* + C_2H_4 \rightarrow \cdot CH_2{}^{38}Cl^* + :CH_2 \quad (11)$$

$$CH_2{}^{38}Cl^*\cdot + I_2 \rightarrow CH_2I^{38}Cl + I \quad (12)$$

The iodochloromethane product accounts for ≤0.4% of the absolute yield in all samples. No trend in the yield of this product was observed with changing pressure or moderation, but the low yield in general precluded a detailed study of this product. Nevertheless, on the basis of the overall endothermicity of this process some 85 kcal of excess translational energy is required to generate the $CH_2{}^{38}Cl\cdot$ radical and thus the reaction may also be thought of as occurring in the epithermal energy range.

Acknowledgment. This work was supported by the U.S. Energy Research and Development Administration under Contract No. EY-76-S-02-2190. The cooperation of the staff at the University of Utah Nuclear Radiation Center is acknowledged. D.J.S. expresses appreciation for a NDEA Title IV Graduate Fellowship.

References and Notes

(1) E. R. Grant and J. W. Root, *J. Chem. Phys.*, **64**, 417 (1976).
(2) (a) C. M. Wai and F. S. Rowland, *J. Am. Chem. Soc.*, **90**, 3638 (1968); (b) *ibid.*, **91**, 1053 (1969).
(3) C. M. Wai and F. S. Rowland, *J. Phys. Chem.*, **71**, 2757 (1967).
(4) (a) N. Colebourne and R. Wolfgang, *J. Chem. Phys.*, **38**, 2782 (1963); (b) J. F. J. Todd, N. Colebourne, and R. Wolfgang, *J. Phys. Chem.*, **71**, 2875 (1967).
(5) Z. B. Alfassi and S. Amiel, *Radiochim. Acta*, **15**, 201 (1971).
(6) R. L. Williams and F. S. Rowland, *J. Phys. Chem.*, **76**, 3509 (1972).
(7) R. Milstein, R. L. Williams, and F. S. Rowland, *J. Phys. Chem.*, **78**, 857 (1974).
(8) F. S. C. Lee and F. S. Rowland, preprint.
(9) L. D. Spicer and A. Siuda, *Radiochim. Acta*, **18**, 16 (1972).
(10) L. Spicer and R. Wolfgang, *J. Chem. Phys.*, **50**, 3466 (1969).
(11) L. Spicer, J. F. J. Todd, and R. Wolfgang, *J. Am. Chem. Soc.*, **90**, 2425 (1968).
(12) L. Spicer and R. Wolfgang, *J. Am. Chem. Soc.*, **90**, 2426 (1968).
(13) L. D. Spicer, *J. Am. Chem. Soc.*, **95**, 51 (1973).
(14) D. J. Stevens and L. D. Spicer, *J. Chem. Phys.*, **64**, 4798 (1976).
(15) R. Pettijohn and E. P. Rack, *J. Phys. Chem.*, **76**, 3342 (1972).
(16) L. M. Dorfman and F. J. Shipka, *J. Am. Chem. Soc.*, **77**, 4723 (1955).
(17) N. J. Parks, K. A. Krohn, and J. W. Root, *J. Chem. Phys.*, **55**, 2690 (1971).
(18) D. J. Stevens and L. D. Spicer, *J. Phys. Chem.*, submitted for publication.
(19) J. A. Kerr and M. J. Parsonage, "Evaluation Kinetic Data on Gas Phase Addition Reactions", Camelot Press, Southampton, England, 1972.
(20) G. C. Fettis and J. H. Knox, *Prog. React. Kinet.*, **2**, 1 (1964).
(21) W. G. Clark, D. W. Setser, and K. Dees, *J. Am. Chem. Soc.*, **93**, 5328 (1971).
(22) K. Dees and D. W. Setser, *J. Chem. Phys.*, **49**, 1193 (1968).
(23) K. C. Kim and D. W. Setser, *J. Phys. Chem.*, **76**, 283 (1972).
(24) P. J. Robinson and K. A. Holbrook, "Unimolecular Reactions", Wiley-Interscience, New York, N.Y., 1972.
(25) S. C. Chan, B. S. Rabinovitch, J. T. Bryant, L. D. Spicer, T. Fujimoto, Y. N. Lin, and S. P. Pavlou, *J. Phys. Chem.*, **74**, 3160 (1970).
(26) W. H. S. Yu and M. H. J. Wignen, *J. Chem. Phys.*, **52**, 2736 (1970).

(27) P. S. Fredericks and J. M. Tedder, *J. Chem. Soc.*, 144 (1960).
(28) H. O. Pritchard, J. B. Pyke, and A. F. Trotman-Dickenson, *J. Am. Chem. Soc.*, **76**, 1201 (1954).
(29) J. H. Knox, *Trans. Faraday Soc.*, **58**, 275 (1962); J. H. Knox and R. L. Nelson, *Trans. Faraday Soc.*, **55**, 937 (1959).
(30) G. J. Martens, J. A. Franklin, M. Godfroid, M. Delvaux, and J. Verbeyst, *Int. J. Chem. Kinet.*, **5**, 539 (1973).
(31) C. Cillian, P. Goldfinger, G. Huybrechts, and G. Martens, *Trans. Faraday Soc.*, **63**, 1631 (1967).
(32) W. H. S. Yu and M. H. J. Wijnen, *J. Chem. Phys.*, **52**, 4166 (1970).
(33) W. E. Falconer and W. A. Sunder, *Int. J. Chem. Kinet.*, **4**, 315 (1972).
(34) The additional fluorinated products reported in Tables I and II derive either from ^{38}Cl reaction with the CF_2Cl_2 used as a moderator and source gas for recoil chlorine or from replacement reaction with the competitive reactant C_3F_6. No evidence for ethyl chloride or vinyl chloride products was found in these studies.

Thermal Chlorine-38 Reactions with Propene

F. S. C. Lee and F. S. Rowland*

Department of Chemistry, University of California, Irvine, California 92717 *(Received January 19, 1977)*

Publication costs assisted by the U.S. Energy Research and Development Administration

Thermal ^{38}Cl atoms react with gaseous propene at 20 °C by terminal addition to form $CH_3CHCH_2{}^{38}Cl$ and by central addition to form $CH_3CH^{38}ClCH_2$. These two processes account for $86 \pm 4\%$ of the available thermal ^{38}Cl, with the remainder presumably reacting by abstraction of the allylic hydrogen to form $H^{38}Cl$. Both radicals are able to decompose by loss of ^{38}Cl or to be stabilized by collision with $CClF_3$, with the two processes equally likely at 150 ± 50 Torr pressure. The ^{38}Cl atoms are produced by the thermal neutron induced nuclear reaction $^{37}Cl(n,\gamma)^{38}Cl$, and thermalized by multiple collisions with $CClF_3$ which is present in large excess. The addition process favors the terminal position, but the terminal/central ratio is dependent upon the scavenger HI concentration, i.e., upon the time required for scavenging of stabilized $C_3H_6{}^{38}Cl$ radicals. The terminal/central ratio varied between 6.5 to 12.3 in these experiments, and was consistently related only to HI concentration. The increasing $CH_3CHCH_2{}^{38}Cl$ concentration with lower HI concentration indicates the isomerization of $CH_2CH^{38}ClCH_2$ to $CH_3CHCH_2{}^{38}Cl$ with a rate constant of $\sim 10^7$ s^{-1}. The original terminal/central addition ratio for thermal atomic Cl is about 6.

Introduction

The selectivity of attack of chlorine atoms upon asymmetric olefins has long been of interest, and the qualitative generalization is well known that such free-radical attack occurs primarily at the less alkyl-substituted end of alkenes. The addition to a terminal olefin position (other than C_2H_4) results in the formation of either a secondary or tertiary radical, more stable than the primary radical formed by addition to the more highly substituted position. These energetic differences provide a sufficient basis for rationalization of a preference for terminal addition although other factors may also be involved.

However, quantitative measurements of such selectivity have been hampered by problems with specific chlorine atom sources.[1-9] For example, the terminal and central addition reactions with propene in reactions 1 and 2 lead

$$Cl + CH_3CH{=}CH_2 \rightarrow CH_3CHCH_2Cl^* \qquad (1)$$

$$Cl + CH_3CH{=}CH_2 \rightarrow CH_3CHClCH_2{}^* \qquad (2)$$

to the same product with Cl_2 or *tert*-butyl hypochlorite as the source, as the radicals from (1) and (2) react further with the source to form $CH_3CHClCH_2Cl$ in each case. On the other hand, with HCl as the Cl atom source the free-radical yields are complicated by the presence of polar ionic reactions leading to the same products and by the slow chain transfer step for R + HCl → RH + Cl because of the strength of the HCl bond.

Competitive photochlorination experiments have established that Cl atoms react very rapidly with propene. In studies using the photolysis of $COCl_2$ as the Cl atom source, several radical combination products were isolated which contained the CH_3CHCH_2Cl radical (*i*-ClPr) from (1), e.g., *i*-ClPr–C_3H_7; *i*-ClPr–*i*-ClPr, as well as 1,3-dichloropropane, which could be formed by disproportionation between two *i*-ClPr radicals.[10] The absence of any observed products involving nonterminally bonded chlorine was interpreted as evidence for strongly preferential terminal addition in the original reaction with the olefin. We have carried out a series of experiments involving thermal ^{38}Cl reaction with propene with the primary intention of measuring the selectivity of attack on the two olefinic positions. In addition, data were obtained on the rates of loss of Cl from the radicals of (1) and (2). The thermal ^{38}Cl technique is especially suitable for measurement of the selectivity of (1) vs. (2), since the inclusion of HI as a scavenger molecule converts the ^{38}Cl radical from (1) into n-$Pr^{38}Cl$, and that of (2) into i-$Pr^{38}Cl$, as shown in (3) and (4).[11,12]

$$CH_3CHCH_2{}^{38}Cl + HI \rightarrow CH_3CH_2CH_2{}^{38}Cl + I \qquad (3)$$

$$CH_3CH^{38}ClCH_2 + HI \rightarrow CH_3CH^{38}ClCH_3 + I \qquad (4)$$

The basic advantage involved in using radioactive ^{38}Cl is that the chlorine source and radical scavenger are totally different molecules, in contrast to Cl_2 or HCl which served both functions simultaneously in the earlier experiments. The technique of creating the ^{38}Cl atom by the thermal neutron reacton $^{37}Cl(n,\gamma)^{38}Cl$ utilizes the otherwise extremely inert molecule $CClF_3$ as the chlorine atom source.[11,12] The radical scavenging function is then carried out by a molecule that does not contain chlorine, e.g., HI or H_2S. The analytical technique of radio gas chromatography permits search for the ^{38}Cl-labeled species while ignoring any nonradioactive products originating from I or SH radicals. Furthermore, the termination of the

TABLE I: Experimental Conditions for Irradiation, Product Separation, and Radiochemical Analysis Involving Atomic ^{38}Cl Reactions with Propene

	Neutron irradiation conditions			
Sample	Reactor power, kW	Irradiation time, min	Chromatographic columns	Proportional counter
All listed in Table II, except no. 6	25	5	TTP-50-1 + PCA 24 ft	Counter at 25 °C
All listed in Table III, except no. 24	10–15	2	TTP-50-1 + PCA 24 ft	Counter heated to 100 °C
24	15	2	DMS-50-7 + PCA 24 ft	Counter heated to 100 °C
6	100	5	TTP-50-1 + PCA 24 ft	Counter at 25 °C

radicals by reaction with a hydrogen-donor scavenger such as HI provides an inherently simpler analysis than that required when radical–radical combination and disproportionation are responsible for the final stable product molecules.

Experimental Section

The techniques for producing thermal ^{38}Cl ($t_{1/2}$ = 37.3 min) from the thermal neutron irradiation of gaseous CClF$_3$ [^{37}Cl(n,γ)^{38}Cl] in mole fractions >0.9 have been described in detail elsewhere.[11] Further information about the ^{38}Cl technique has been given in studies of its application to methane and ethane,[13] acetylene,[14] and ethylene.[15] All experiments were carried out at about 20 °C.

The analysis of radioactive ^{38}Cl-labeled products was carried out with two chromatographic columns in series. The second of these columns was always a 24-ft propylene carbonate on alumina (PCA) column, while the first was normally a 50-ft tritolyl phosphate (TTP) column, both operated at room temperature. The PCA column was used to separate ^{41}Ar from C^{38}ClF$_3$, and was usually withdrawn from the sequence after the emergence of the ^{41}Ar peak. The possibility of measuring C^{38}ClF$_3$ was discarded in order to avoid reducing the accuracy of measurement of later peaks through excessive decay of the ^{38}Cl in higher boiling compounds. Little difference was observed in the analytical results obtained when the external gas flow proportional counter was heated to 100 °C to reduce peak-tailing of the less volatile ^{38}Cl-labeled products.[11]

The neutron irradiation conditions and analytical conditions for the various samples are summarized in Table I. The major observed products in all experiments, totaling as much as 79% of all ^{38}Cl formed in the system, were CH$_3$CH$_2$CH$_2{}^{38}$Cl and CH$_3$CH^{38}ClCH$_3$ with the former heavily predominant. In addition, peaks were observed from seven low-boiling radioactive organic compounds and from ^{41}Ar in minor yield. At 3000-Torr total pressure the yields from ^{38}Cl atom reactions with the source molecule (CClF$_3$) were C^{38}ClF$_3$ (0.9%), CCl^{38}ClF$_2$ (0.5%), and CH^{38}ClF$_2$ (0.6%).[11] A separate yield of CF$_3{}^{128}$I was observed when analytical conditions are optimized for determining the separate contributions of CF$_3{}^{128}$I, CH$_3{}^{38}$Cl, and CH^{38}ClF$_2$. The yields of CH$_3{}^{38}$Cl, C$_2$H$_3{}^{38}$Cl, and C$_2$H$_5{}^{38}$Cl are all negligibly small (sum <0.5%). However, when the conditions were optimized for the separation of low-boiling components, the elution times of n-C$_3$H$_7{}^{38}$Cl and i-C$_3$H$_7{}^{38}$Cl are so long in comparison with the 37-min half-life of ^{38}Cl that no useful assay could be made. The ^{128}I atoms are created by the ^{127}I(n,γ)^{128}I reaction on HI, and are not observed when HI is absent.

A typical analysis with a 50-ft TTP column is illustrated in Figure 1. For most samples in Table II, the chromatographic columns were initially in the order TTP first and PCA second, and the gases all first initially passed into the TTP column. After the ^{41}Ar and CH$_3{}^{38}$Cl peaks had passed through both TTP and PCA columns and emerged into the proportional counter, the sequence of the columns was then reversed to PCA + TTP maintaining the same direction of flow through each segment. At this time, both C^{38}ClF$_3$ and the macroscopic propene had passed through the TTP column and were now in the PCA column. All of the other molecules were then allowed to elute, including the mass peak for C$_3$H$_6$. The elution sequence from this procedure was ^{41}Ar, C^{38}ClF$_3$, (CF$_3{}^{128}$I + CH$_3{}^{38}$Cl + CH^{38}ClF$_2$), C$_2$H$_3{}^{38}$Cl, C$_3$H$_6$, i-C$_3$H$_7{}^{38}$Cl, and n-C$_3$H$_7{}^{38}$Cl. The three compounds CF$_3{}^{128}$I, CH$_3{}^{38}$Cl, and CH^{38}ClF$_2$ were not separated and showed up as one single radioactive peak. The samples in Table III were analyzed with a shorter TTP column in sequence with the PCA column and the column switching was controlled to emphasize measurement of only ^{41}Ar, i-C$_3$H$_7{}^{38}$Cl, and n-C$_3$H$_7{}^{38}$Cl.

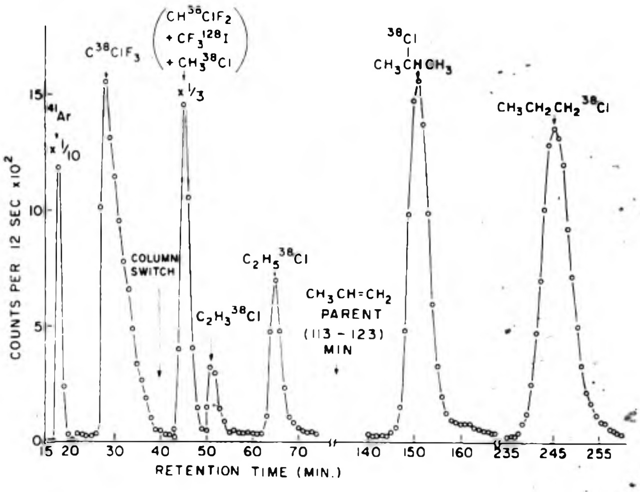

Figure 1. Radiogas chromatogram of the volatile radioactive products observed for neutron irradiated mixtures of excess CClF$_3$, propene, and HI. (Sample no. 16, Table II; analyzed with dual columns of 50-ft tritolylphosphate and 24-ft propylene carbonate-on-alumina, as described in the text.)

The yields from the sample shown in Figure 1 are typical: C^{38}ClF$_3$ (0.96%), C$_2$H$_3{}^{38}$Cl (0.06%), C$_2$H$_5{}^{38}$Cl (0.40%), n-C$_3$H$_7{}^{38}$Cl (8.2%), i-C$_3$H$_7{}^{38}$Cl (62.0%). Note that Figure 2 shows the actual number of observed counts, uncorrected for decay of the 37-min half-life of ^{38}Cl. The apparent near-equality in size of the i-C$_3$H$_7{}^{38}$Cl and n-C$_3$H$_7{}^{38}$Cl yields in Figure 1 illustrates the problems that can be incurred from such decay. Approximately 6% of the i-C$_3$H$_7{}^{38}$Cl present at injection (t = 0) still remains at its emergence at 150 min, while only 1% of the n-C$_3$H$_7{}^{38}$Cl is left 245 min after injection. Typically, about 1 to 1.5 half-lives had already passed between the end of the neutron irradiation and injection into the chromatographic column. Most of this time was allowed to permit the decay

TABLE II: Absolute Yields of Volatile ^{38}Cl-Products from the Reactions of ^{38}Cl Atoms with Propene

Sample no.	1	3	5	6	7	4	8	9	15	16	17	18	19
	Sample Composition Pressure, Torr												
$CClF_3$	2790	2890	2890	479	2960	3010	2920	2910	2980	2720	2980	2990	2990
$CH_3CH{=}CH_2$	91.0	97.0	96.3	16.0	29.5	96.1	29.2	16.4	11.1	205	4.9	9.1	1.9
HI	180	20.2	16.1	5.8	9.8	31.6	58.5	80.1	4.0	68.4	10.0	6.0	4.0
Total pressure[a]	3070	3020	3010	511	3010	3150	3010	3010	3000	3000	3000	3010	3000
HI/C_3H_6	2.0	0.2	0.17	0.37	0.33	0.33	2.0	4.9	0.36	0.33	2.0	0.66	2.1
$A_0(10^6$ DPM)[b]	3.3	11.2	9.8	5.3	11.7	8.7	6.7	3.4	11.1	8.9	6.3	10.2	7.8
Yields of ^{38}Cl product	Absolute Yield, % Total ^{38}Cl Atoms												
i-$C_3H_7{}^{38}Cl$	5.37	8.13	7.63	5.55	6.34	8.30	5.06	2.84	4.90	8.21	3.34	5.33	3.00
n-$C_3H_7{}^{38}Cl$	35.6	71.0	68.7	57.2	64.8	63.9	38.8	20.7	60.1	62.0	33.9	58.2	36.1
R[c]	6.6 ± 0.1	8.7 ± 0.1	9.0 ± 0.1	10.2 ± 0.1	10.2 ± 0.1	8.3 ± 0.1	7.7 ± 0.1	7.3 ± 0.2	12.3 ± 0.1	7.6 ± 0.1	10.2 ± 0.1	10.9 ± 0.1	12.1 ± 0.2

[a] Includes 7 to 10 Torr of Ar for neutron flux monitoring. [b] A_0 = ^{38}Cl activity of n-$C_3H_7{}^{38}Cl$, corrected to the end of the irradiation, as a measure of the relative amounts of ^{38}Cl products [pressure of $CClF_3$ × kilowatt-minutes of irradiation]. [c] R = n-$C_3H_7{}^{38}Cl$/i-$C_3H_7{}^{38}Cl$.

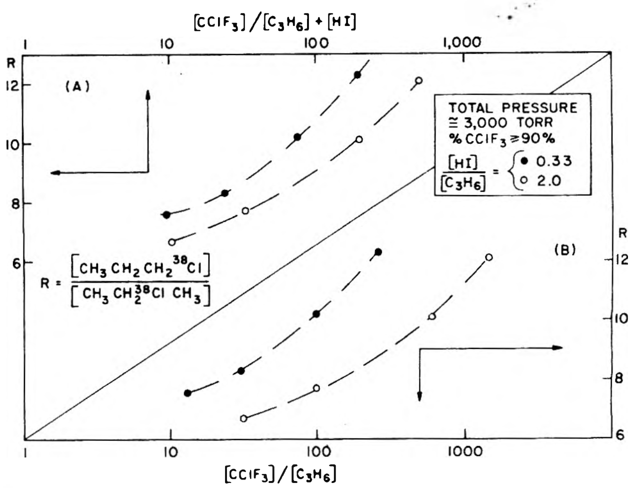

Figure 2. Moderator correlation of observed ratios of n-$C_3H_7{}^{38}Cl$ to i-$C_3H_7{}^{38}Cl$ from thermal ^{38}Cl addition to propene in HI-scavenged excess $CClF_3$: (●) $[(HI)/(C_3H_6)] = 0.33$; (○) $[(HI)/(C_3H_6)] = 2.0$. The data are plotted in the lower right in terms of relative numbers of molecules of moderator ($CClF_3$) and reactant (C_3H_6), with HI ignored. The data are plotted in the upper left with both C_3H_6 and HI considered as reactants and $CClF_3$ as the moderator. In neither case are the data fitted by a single line as would be expected for a moderator effect.

of short-lived radioactivities in the glass ampoules.

Results

The absolute yields of i-$C_3H_7{}^{38}Cl$ and n-$C_3H_7{}^{38}Cl$ are summarized in Tables II and III for a variety of experimental conditions. The important parameters being varied in these samples include total pressure, absolute HI concentration, $(HI)/(C_3H_6)$ ratio, and radiation damage (proportional to total neutron dose).

The only exothermic reactions for Cl with propene are the two addition reactions, and hydrogen abstraction from the methyl position, as in (5). The $H^{38}Cl$ expected from

$$^{38}Cl + CH_3CH{=}CH_2 \rightarrow H^{38}Cl + CH_2{\doteq}CH{\doteq}CH_2 \quad (5)$$

(5) was not directly determined, but is demonstrably not the major yield since as much as 79% of the ^{38}Cl radioactivity has been detected in the two propyl chlorides. The estimated thermochemistry of the various reactions is summarized in Table IV.

The very small yield of $C_2H_3{}^{38}Cl$ demonstrate that decomposition of $CH_3CH^{38}ClCH_2{}^*$ by CH_3 loss as in (6)

$$CH_3CH^{38}ClCH_2{}^* \rightarrow CH_3 + CH^{38}Cl{=}CH_2 \quad (6)$$

is a very minor process even at the lowest pressures. In comparable experiments with ^{18}F atom addition to $CH_3CH{=}CH_2$ decomposition to $CH_2{=}CH^{18}F$ following addition to the central carbon atom accounts for 20% of the total $CH_3CH^{18}FCH_2{}^*$ at 500 Torr pressure. However, the substitution of F for CH_3 is exothermic while that of Cl for CH_3 is endothermic, and the absence of CH_3 loss from $CH_3CH^{38}ClCH_2{}^*$ is expected on energetic grounds. The observed yields of $CH_2{=}CH^{38}Cl$ were respectively 0.01, 0.04, and 0.06% for samples 7, 4, and 16, which had propene/$CClF_3$ ratios of 0.01, 0.03, and 0.07. These data indicated that the $CH_2{=}CH^{38}Cl$ originates with energetic ^{38}Cl atoms, and would have a yield of ≪0.01% in a more completely moderated system, i.e., propene/$CClF_3$ ≤ 0.001.

The yields of $CH_3{}^{38}Cl$ and $C_2H_5{}^{38}Cl$ are always small and can be ignored here. The former is also formed by a hot ^{38}Cl reaction, while the latter is believed to be formed by reaction with C_2H_4 introduced by radiation damage to propene.

TABLE III: Absolute Yields of i-$C_3H_7{}^{38}Cl$ and n-$C_3H_7{}^{38}Cl$ from the Reactions of Thermal ^{38}Cl atoms with Propene

Sample no.	23	25	26	27	28	31	33	34	36
				Sample Composition Pressure, Torr					
$CClF_3$	4500	1000	2200	2990	3200	299	400	200	270
$CH_3CH=CH_2$	120	25.8	52.7	14.7	19.7	10.5	10.3	10.1	10.3
HI	39.7	8.6	17.5	59.3	200	40.4	60.2	30.0	40.0
Total pressure[a]	4710	1060	2290	3080	3440	361	478	248	321
$[HI]/[C_2H_4]$	0.33	0.33	0.33	4.0	10.2	3.9	6.0	3.0	3.9
$A_0(10^6$ DPM$)$[b]	3.8	0.85	1.9	0.90	0.64	0.37	0.24	0.09	0.04
				Absolute Yield, % Total ^{38}Cl Atoms					
Yield of ^{38}Cl product									
i-$C_3H_7{}^{38}Cl$	8.69	6.99	7.14	2.91	1.82	2.84	1.87	3.22	2.7
n-$C_3H_7{}^{38}Cl$	69.4	65.9	62.9	22.2	11.9	24.3	14.7	22.7	20.4
R[c]	8.0 ± 0.1	9.4 ± 0.2	8.8 ± 0.1	7.6 ± 0.1	6.5 ± 0.1	8.6 ± 0.2	7.9 ± 0.4	7.1 ± 0.2	7.6 ± 0.5

[a] Includes 8 to 18 Torr of Ar for neutron flux monitoring. [b] A_0 = ^{38}Cl activity of n-$C_3H_7{}^{38}Cl$, corrected to the end of the irradiation as a measure of the relative intensity of the neutron irradiation. [c] $R = n\text{-}C_3H_7{}^{38}Cl/i\text{-}C_3H_7{}^{38}Cl$.

TABLE IV: Estimated Heats of Reaction for Various Possible Reactions of Atomic Chlorine with Propene

Reactants	Products	ΔH, kcal/mol
$Cl + C_3H_6$	$CH_3CHClCH_2$	−23
	CH_3CHCH_2Cl	−26
	$HCl + CH_2=CH=CH_2$	−15
	$CH_3 + CHCl=CH_2$	+5.5
	$CH_3Cl + CH=CH_2$	+15
	$H + CH_2=CHCH_2Cl$	+16
Heats of formation	(Ref 16)	(Ref 17)
Cl +28.9	CH_3 +34.3	$CH_3CHClCH_3$ +11
C_3H_6 +4.9	C_3H_5 +40.6	CH_3CHCH_2Cl +8
HCl −22.0	C_2H_3 +69	
CH_3Cl −19.6	$CH_2=CHCH_2Cl$ −2	
CH_2CHCl +5.0	H 52.1	

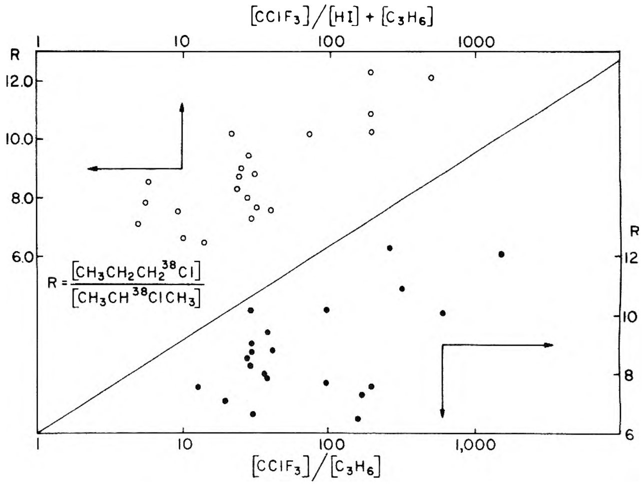

Figure 3. Moderator correlation of observed ratios of n-$C_3H_7{}^{38}Cl$ to i-$C_3H_7{}^{38}Cl$ from thermal ^{38}Cl addition to propene in HI-scavenged excess $CClF_3$. The data are plotted in the lower right in terms of relative numbers of molecules of moderator ($CClF_3$) and reactant (C_3H_6) with HI ignored. In the upper left both HI and C_3H_6 are considered to be reactants. In both cases the correlation is not very strong.

Terminal/Central Ratio for Addition

The measured ratios, R, of the yields of n-$C_3H_7{}^{38}Cl$ to i-$C_3H_7{}^{38}Cl$ vary from 6.5 to 12.3 in Tables II and III. As described below, the value of R varies regularly with the absolute concentration of HI, and does not vary systematically with the total pressure, the ratio of $(HI)/(CH_3CH=CH_2)$, or the ratio of $(CClF_3)/(CH_3CH=CH_2)$. After documenting the dependence on the absolute concentration of HI and lack of dependence on the other variables, explanations for the former will be discussed.

(a) *Variation of R with Moderation.* Since the ^{38}Cl atoms are initially very energetic, the possibility must be considered that a nonnegligible fraction of ^{38}Cl atoms might react with propene while still possessing some energy in excess of thermal. If this were so, the value of R should depend on the ratio of numbers of collisions with propene vs. the energy-moderating collisions with $CClF_3$. Experiments with C_2H_4 have shown no evidence for variations in the rate of decomposition of $C_2H_4{}^{38}Cl^*$ from ^{38}Cl atom addition to ethylene even in much lower $CClF_3$ mole fractions than the >0.9 used in these propene experiments.[12] Nevertheless, the possibility can be considered that R might be even more sensitive to moderator ratios than is the decomposition rate of $C_2H_4{}^{38}Cl^*$. A possible correlation of R with initial kinetic energy of the atom forming the radical could be very interesting since quantitative comparisons between the selectivity for hot and thermal atom additions are essentially unknown experimentally. Intuitively, the selectivity of attack on an olefin should decrease as the kinetic energy of the reacting atom increases, as has been suggested from the reported work concerning hot CH_3 radical abstraction reactions.[18]

In these mixtures of $CClF_3$, C_3H_6, and HI, energy-moderating collisions can occur with any of the three components, and the extent of moderation in each sample could readily be expressed as (a) $(CClF_3)/(C_3H_6)$, (b) $(CClF_3)/\{(C_3H_6) + (HI)\}$, or (c) $\{(CClF_3) + (HI)\}/(C_3H_6)$. In our samples expressions (b) and (c) are essentially equivalent since $CClF_3$ is always present in mole fraction >0.9, and only one of the two ratios need be evaluated.

The values of R are plotted in Figure 2 vs. $(CClF_3)/(C_3H_6)$ and $(CClF_3)/\{(C_3H_6) + (HI)\}$ ratios, respectively. All the data in the figure are for samples with total pressure of about 3000 Torr and $(HI)/(C_3H_6)$ equal to either 0.33 or 2.0. For the same $(HI)/(C_3H_6)$ ratio, R increases steadily as the moderation ratios are increased. However, when the data for the different $(HI)/(C_3H_6)$ ratios are compared in Figure 2 two different, but nearly parallel, sets of lines are obtained. Different sets of lines for different $(HI)/(C_3H_6)$ ratios are not consistent with a moderator effect on selectivity of attack on propene by the ^{38}Cl atoms.

The absence of any systematic variation of R with respect to moderation is evidenced from the plot given in Figure 3, with all of the runs at different pressures and $(HI)/(C_3H_6)$ ratios plotted as a function of the $(CClF_3)/(C_3H_6)$ ratios. The systematic increase of R with increasing moderation ratios, as shown in Figure 2, is actually caused by the decrease in the absolute concentration of HI in the more highly moderated samples. This analysis is supported by comparison of pairs of samples containing roughly the same amount of HI and with the same total pressure (~3000 Torr) but different moderation ratios, as in Table V. The good agreement between the

TABLE V: Comparison of *R* Values for Fixed HI Concentrations and Variable Moderator Ratios

Sample no.	[HI], cm	$[CClF_3]/[C_3H_6]$	$[CClF_3]/([C_3H_6] + [HI])$	R^a
7	9.8	100	75	10.2 ± 0.1
17	10.0	610	200	10.2 ± 0.1
1	180	31	10	6.6 ± 0.1
28	200	160	15	6.5 ± 0.1

[a] $R = (n\text{-}C_3H_7{}^{38}Cl)/(i\text{-}C_3H_7{}^{38}Cl)$.

TABLE VI: Comparison of *R* Values for Variable Total Pressures and Fixed HI Concentration

Sample no.	Total pressure, Torr	$[HI]/[C_3H_6]$	HI, Torr	*R*
23	4710	0.33	39.7	8.0 ± 0.1
4	3150	0.33	31.6	8.3 ± 0.1
8	3010	2.0	58.5	7.7 ± 0.1
27	3080	4.0	59.3	7.6 ± 0.1
33	478	5.8	60.2	7.9 ± 0.4
31	361	3.8	40.4	8.6 ± 0.2
36	321	3.9	40.0	7.6 ± 0.5

R values for each pair serves to confirm the assumption that *R* is not moderation dependent. The independence of moderation of *R* implies that the energies of the ^{38}Cl atoms are very well thermalized prior to reaction with propene.

(b) *Pressure.* The *R* ratio could exhibit pressure dependence if a significant fraction of either or both of the $n\text{-}C_3H_6{}^{38}Cl^*$ and $i\text{-}C_3H_6{}^{38}Cl^*$ radicals from (1) or (2) were to decompose in the pressure range studied, or if either were to isomerize to the other prior to its first collision with $CClF_3$. If, however, both radicals decomposed by ^{38}Cl loss at comparable rates then the fractional loss of each would be the same and *R* would not be affected.

The variation of *R* is not attributable to a pressure effect alone as shown in Figure 4, in which all the results in Tables II and III are plotted vs. total pressure. The points vary almost randomly with pressure, with values of *R* of 6.5 and 12.3 both observable at 3000 Torr.

In Table VI, several samples with different total sample pressures are compared. All the samples contained HI pressure in the range of 30 to 60 Torr, with the total pressure varying from 360 to 4700 Torr. It is evident that there is no obvious variation of *R* with total pressure. Actually, the observed *R* values are roughly constant, ~8.1 ± 0.5, over a 13-fold change in pressure, provided that the amount of HI present in the sample is about the same.

The lack of change in *R* with total pressure eliminates isomerization of the initially excited $CH_3CH^{38}ClCH_2{}^*$ radicals by 1,2-^{38}Cl shift as the main source of the variation in *R*. The independence of total pressure signifies also that the decomposition rates by ^{38}Cl loss are either (a) the same for $CH_3CH^{38}ClCH_2{}^*$ and $CH_3CHCH_2{}^{38}Cl^*$, or (b) very slow for both. In a later section we shall discuss the evidence which indicates that some ^{38}Cl is actually lost from each $C_3H_6{}^{38}Cl^*$ radical at the lowest pressures, requiring then that the decomposition rates for the two $C_3H_6{}^{38}Cl^*$ radicals must be quite similar. From a theoretical point of view, each $C_3H_6{}^{38}Cl^*$ radical is excited by the bond energy of the newly formed C–Cl bond plus the thermal energies of ^{38}Cl and of propene. Although the newly formed C–Cl bond energies are not the same for the two $C_3H_6{}^{38}Cl$ radicals each excited radical requires exactly the same amount of energy imparted by bond formation to reverse the initial addition of loss of ^{38}Cl. Put another way, the calculated rate of decomposition for a $C_3H_6Cl^*$ radical excited by 2 kcal/mol beyond the minimum needed for C–Cl rupture is very similar whether the minimum energy is actually 23 or 26 kcal/mol.

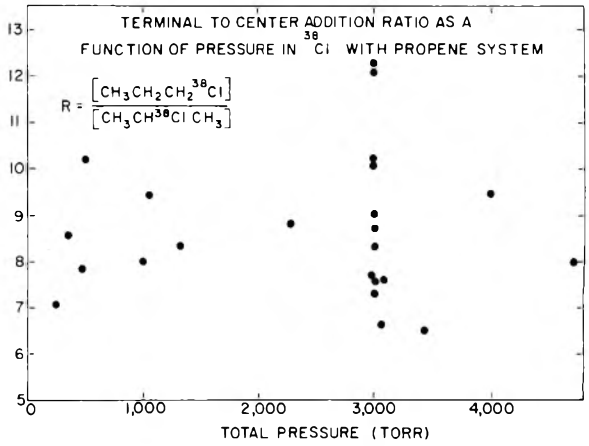

Figure 4. Correlation with total pressure of observed ratios of $n\text{-}C_3H_7{}^{38}Cl$ to $i\text{-}C_3H_7{}^{38}Cl$ from thermal ^{38}Cl addition to propene in HI-scavenged excess $CClF_3$. The correlation is very weak.

(c) *HI Concentration and* $(HI)/(C_3H_6)$. At least two possible reasons can be suggested to explain a dependence of *R* on HI concentration. If the amount of HI in the sample is insufficient to scavenge the $CH_3CH^{38}ClCH_2$ or $CH_3CHCH_2{}^{38}Cl$ radicals, then the observed *R* would vary with HI concentration.[11] On the other hand, if isomerization of one radical to the other were to occur, and this isomerization were in competition with the rates of HI-scavenging reactions, the observed *R* would also show (HI) dependence.

The most direct test to differentiate between these two possibilities is comparison of the absolute yields of the products $n\text{-}C_3H_7{}^{38}Cl$ and $i\text{-}C_3H_7{}^{38}Cl$ in samples with different H concentrations but the same $(HI)/(C_3H_6)$ ratio. In the first case above, the yields of either or both of the two products should decrease, and the sum of the two yields should then decrease as the HI concentration decreases. In the second, on the other hand, a complementary relationship between the two products should be

TABLE VII: Yields of Terminal to Center Addition Products as a Function of HI Concentration in the Reactions of ^{38}Cl with Propene

	$[HI]/[CH_3CH{=}CH_2] = 0.33$			
Parent HI, Torr	4.0	9.8	31.6	68.4
% yield $n\text{-}C_3H_7{}^{38}Cl$	60.1	64.8	63.9	62.0
% yield $i\text{-}C_3H_7{}^{38}Cl$	4.90	6.34	8.30	8.21
$n\text{-}C_3H_7{}^{38}Cl/i\text{-}C_3H_7{}^{38}Cl$	12.3 ± 0.1	10.2 ± 0.1	8.3 ± 0.1	7.6 ± 0.1
$n\text{-}C_3H_7{}^{38}Cl + i\text{-}C_3H_7{}^{38}Cl$	65.0	71.1	72.2	70.2
	$[HI]/[CH_3CH{=}CH_2] = 2.0$			
Parent HI, Torr	4.0	10.0	58.5	180
% yield $n\text{-}C_3H_7{}^{38}Cl$	36.1	33.9	38.8	35.6
% yield $i\text{-}C_3H_7{}^{38}Cl$	3.00	3.34	5.06	5.37
$n\text{-}C_3H_7{}^{38}Cl/i\text{-}C_3H_7{}^{38}Cl$	12.1 ± 0.2	10.2 ± 0.1	7.7 ± 0.1	6.6 ± 0.1
$n\text{-}C_3H_7{}^{38}Cl + i\text{-}C_3H_7{}^{38}Cl$	39.1	37.2	43.9	41.0

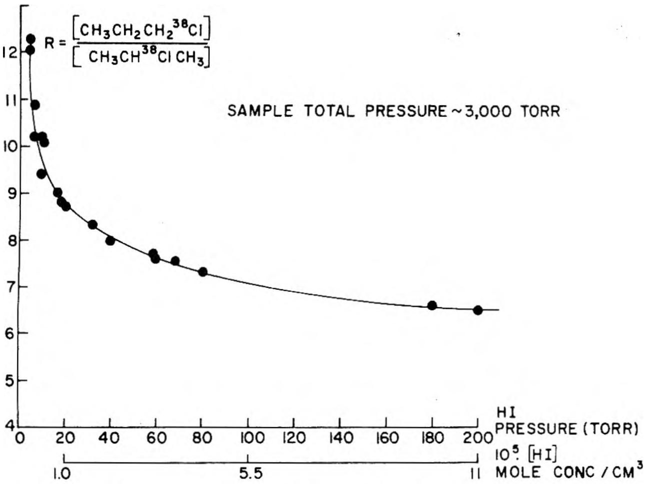

Figure 5. Correlation with absolute concentration of HI of observed ratio of n-$C_3H_7{}^{38}Cl$ to i-$C_3H_7{}^{38}Cl$ from thermal ^{38}Cl addition to propene in HI-scavenged excess $CClF_3$.

TABLE VIII: Independence of n-Pr-^{38}Cl/i-Pr-^{38}Cl Ratio, R, on Propene Concentration

	I		II		III	
HI, Torr	4.0	4.0	40.4	39.7	58.5	59.3
C_3H_6, Torr	1.9	11.1	10.5	120.0	29.2	14.7
R	12.1	12.3	8.6	8.0	7.7	7.6

observed and the sum of the two should remain constant as the HI concentration changes. A comparison of the results of two sets of runs with the same total pressure (~3000 Torr) and different (HI)/(C_3H_6) ratios (0.33 and 2.0, respectively) is given in Table VII.

Although the yield of i-$C_3H_7{}^{38}Cl$ increases regularly as the concentration of HI increases in both sets of samples, no obvious trend is observed in either the n-$C_3H_7{}^{38}Cl$ yield or the sum of the yields of the two products. Within the experimental errors either the yield of n-$C_3H_7{}^{38}Cl$ is constant or the sum of the two propyl-^{38}Cl yields is constant. The former could indicate a scavenging failure for $CH_3CH^{38}ClCH_2$ radicals only, but can be dismissed since it is the more exothermic of the two HI reactions and there is no evidence for such a failure elsewhere.

A direct plot of R vs. the absolute concentration of HI, however, gives a smooth plot as shown in Figure 5 for all the experiments at 3000 Torr total pressure. A smooth decrease in R from 9 to 6.5 is found for HI concentrations between 20 and 200 Torr as well as at lower concentrations. While radiation damage effects resulting in depletion of HI have been observed in low concentration HI samples,[11] the existence of the same trend at high HI concentrations means that the variations in R cannot be assigned solely to depletion of HI by radiation damage.

The possibility that one or the other of the radicals is lost by reaction with propene itself can be eliminated by the comparison of Table VIII in which the value of R is shown to be independent of propene concentrations for fixed concentrations of HI.

Isomerization of $CH_3CH^{38}ClCH_2$ to $CH_3CHCH_2{}^{38}Cl$. This examination of the dependence of R on various system parameters makes it clear that the only observed correlation is an increase in R with a decrease in the absolute concentration of HI. This basic observation indicates that $CH_3CH^{38}ClCH_2$ is able to convert to $CH_3CHCH_2{}^{38}Cl$ if it has sufficient time after formation before undergoing the scavenging reaction with HI. The isomerization reaction 7 is not, however, a reaction of the excited radical initially formed but is rather a reaction of a radical which has undergone many collisions with $CClF_3$. For example, the change in R observed with pressures less than 20 Torr of HI occurs for radicals which have undergone an average of more than 150 collisions with $CClF_3$, and should be thoroughly thermalized.

$$CH_3CH^{38}ClCH_2 \rightarrow CH_3CHCH_2{}^{38}Cl \qquad (7)$$

The change of R with HI concentration cannot be fitted with a simple assumption that the isomerization rate constant for reaction 7 is completely independent of the excitation energy of the $CH_3CH^{38}ClCH_2$ radical. On the other hand, the data on Figure 5 can be fitted with an assumption that k_7 varies with energy and is about 10–20 times faster on the average after 15 collisions with $CClF_3$ than it is after 150 collisions. A corollary to such an assumption must be that a radical which was originally excited by about 20–25 kcal/mol above thermal energies would still have several kilocalories per mole of excess energy after 15 collisions with $CClF_3$.

This assumption of continuing weak collisions, e.g., loss of about 10% of the excess energy per collision, seems quite acceptable when contrasted with estimates of 2 kcal/mol loss per collision (of about 50 kcal/mol excess energy) for $C_2H_4{}^{18}F$ with CF_4[19,20] and evidence for weak collision in other systems.

The overall conclusion from Figure 5 is then that the initial addition of ^{38}Cl to propene favors the terminal carbon by a factor of about 6, or perhaps somewhat less, with the remaining uncertainty dependent primarily upon the question of the rate of the isomerization reaction 7 during the time period of the first 5 or 10 collisions with $CClF_3$. This conclusion amply confirms the qualitative observation that the chlorine atoms are far more frequently observed in terminal positions of products than elsewhere. The observation of 15% initial central addition does not violate any theoretical arguments, since the strong preference for terminal addition is not indicated to be an exclusive process, but simply a preference for forming the more stable radical.

Most experiments with C_3H_6Cl radicals are quite likely to allow far more time before reaction (e.g., radical–radical reaction) than that available with HI at 200 Torr, or even with HI at 4 Torr. Thus, while the initial addition of thermal chlorine atoms favors the terminal position of propene to the extent of about 80–85%, isomerization by 1,2-Cl shift will drive this steadily toward 100% if the C_3H_6Cl radicals are not rapidly made to react with some scavenger molecule.

Since the rate constant for radical scavenging at low HI concentrations is $\sim 10^7$ s^{-1}, the value of k_7 is also in this range or slower since isomerization is far from complete even at 4 Torr pressure of HI.

Loss of ^{38}Cl from Excited $C_3H_6{}^{38}Cl^*$ Radicals. The loss of ^{38}Cl from excited $C_3H_6{}^{38}Cl^*$ radicals by (8) places these

$$C_3H_6{}^{38}Cl^* \rightarrow {}^{38}Cl + CH_3CH{=}CH_2 \qquad (8)$$

$$^{38}Cl + HI \rightarrow H^{38}Cl + I \qquad (9)$$

$$C_3H_6{}^{38}Cl^* + M \rightarrow C_3H_6{}^{38}Cl + M \qquad (10)$$

atoms back into the pool of thermal ^{38}Cl atoms, from which they can react by reaction with propene (reactions 1, 2, or 5) or by reaction with HI, as in (9). If there is no loss from (8) because of much more rapid stabilization in (10), then the competition between (1) + (2) and (9) should be pressure independent. However, if the loss in (8) is competitive with (10), then at low pressure ^{38}Cl atoms can make repeated passes through the (1) + (2) vs. (9) competition, and reaction 9 will form additional $H^{38}Cl$ molecules during the multiple tries. Experiments with ^{38}Cl atom additions to acetylene[14] and ethylene[15] have shown

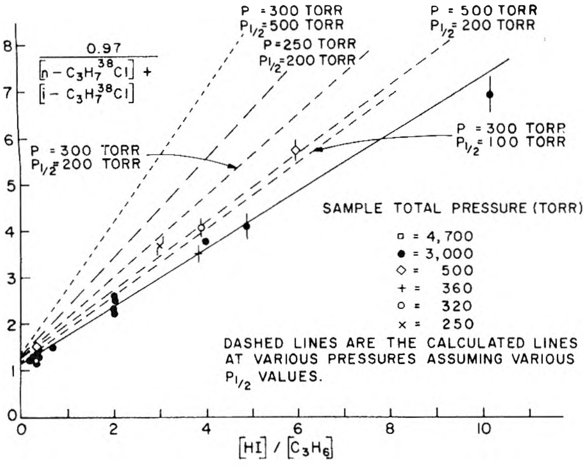

Figure 6. Ratios of n-$C_3H_7{}^{38}Cl$ to i-$C_3H_7{}^{38}Cl$ for various predicted decomposition rates of $C_3H_6{}^{38}Cl^{\bullet}$ vs. (HI)/(C_3H_6) ratios. The data are consistent with decomposition and stabilization of $C_3H_6{}^{38}Cl^{\bullet}$ being approximately equal at 150 ± 50 Torr.

that both $C_2H_2{}^{38}Cl^*$ and $C_2H_4{}^{38}Cl^*$ radicals *do* lose ^{38}Cl atoms, with stabilization and decomposition approximately equal at 800 Torr total pressure.

A similar test can be made for the propene system through a graph of the reciprocals of the summed $C_3H_7{}^{38}Cl$ yields vs. HI/C_3H_6 ratio at several pressures, as in Figure 6. The scattered low pressure data points for propene do not quite fall on the high pressure line, indicating some loss by reaction 8. The predicted slopes for several different assumed half-pressures (i.e., $P_{1/2}$ = the pressure for which $k_8 = k_{10}$) are also shown on Figure 6. The best average fit appears to be for $P_{1/2} = 150 \pm 50$ Torr, which would correspond to only 5% decomposition by (8) in samples with 3000 Torr total pressure, and about 25–40% decomposition at 300 Torr total pressure.

The absence of any marked change in R vs. total pressure (Figure 4) in the face of 25–40% decomposition of the radicals requires then that the reaction rate k_8 must be quite similar for both $CH_3CH^{38}ClCH_2^*$ and $CH_3CHCH_2{}^{38}Cl^*$ radicals. As discussed earlier, this near-equality in rates is actually an expected result.

The best fit to the 3000 Torr data in Figure 6 leads to a slope of 0.62 ± 0.04 and an intercept of 1.15 ± 0.06. The former indicates that reaction of ^{38}Cl with HI is about 1.6 times as rapid as with propene, while the latter indicates that 86 ± 4% of the thermal ^{38}Cl would react with the olefinic positions if no HI were present to compete for the ^{38}Cl. The abstraction reaction 5 can thus account for no more than 14 ± 4% of the total available thermal ^{38}Cl atoms reacting with propene. The addition reactions of ^{38}Cl to ethylene and to acetylene are also almost as rapid as the direct reaction of ^{38}Cl with HI.[14,15]

Estimated Absolute Reaction Rates. These experiments with thermal ^{38}Cl atoms do not provide any direct information about the absolute reaction rates of chlorine atoms. However, measurement of relative rates which include one known on an absolute basis can serve to normalize all of the other reactions. The abstraction of H from C_2H_6 by Cl has been shown to have an absolute reaction rate that is very rapid, about 6×10^{-11} cm^3 molecule^{-1} s^{-1}.[21,22] Since the CH_3 bonds of propene are allylic C–H bonds, and are weaker than those C_2H_6 by about 10 kcal/mol, the absolute reaction rate for H abstraction from CH_3 in propene can hardly be less than that of C_2H_6 per atom, indicating that $k_5 \geq 3 \times 10^{-11}$ cm^3 molecule^{-1} s^{-1}. Despite this very rapid abstraction rate only about 14% of the thermal ^{38}Cl atoms react by this route, and about 86% react by addition to the olefinic bond. This ratio of reactivities leads to the estimate that $(k_1 + k_2)$ is about 2×10^{-10} cm^3 molecule^{-1} s^{-1}, or essentially reaction in not more than 3 or 4 collisions.

Reactivity and Structure in 1,2-Chlorine Migration. Discussions of bromo and chloro radicals have frequently considered the possibility of "bridged" radicals, e.g.,

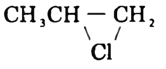
$$CH_3CH - CH_2 \text{ bridged by } Cl$$

a structure in which the halogen atom is shared between two adjacent carbon atoms. The electron spin resonance structures of several methyl-substituted β-chloroethyl radicals have been studied independently by Kochi et al.[23] and by Jackson et al.[24] On the basis of low values of hyperfine coupling constants and significantly larger "g" values than those of hydrocarbon analogues, both groups reached the same conclusion that the Cl atom is "unsymmetrically bridged" between the two neighboring carbon atoms. Furthermore, the sharp ESR lines indicate failure of interconversion of radicals on the ESR time scales. Our results with variable R values also suggest two reacting radicals, although it would also be possible to hypothesize a symmetrically-bridged radical whose branching ratio to the two products is energy dependent. However, with the close direct analogy to these ESR experiments, we consider our results to involve two reactive, isomeric $C_3H_6{}^{38}Cl$ radicals.

The 1,2 migration of atomic Cl was reported by Nesmeyanov et al. during the reaction of Br_2 with $CCl_3CH{=}CH_2$.[25] The 1,2 migration of a Cl atom was reported by Skell for the conversion of the primary radical $(CH_3)_2CClCH_2$ to its tertiary isomer $(CH_3)_2CCH_2Cl$.[26] The migration rate of Cl in this system was about 10^{10} s^{-1}. Evidence for similar isomerizations have been reported by Kochi, Jackson, and others from ESR studies, who detected only the tertiary radical even at −120 to −130°C. The reported ESR spectrum of the chloropropyl radical is discussed only in terms of CH_3CHCH_2Cl. However, since SiH_3 may well have a strong preference for abstraction of the Cl from the secondary carbon in $CH_3CHClCH_2Cl$, there is no evidence that $CH_3CHClCH_2$ radicals were ever formed in that system.

The reported rates of isomerization to tertiary radicals are considerably faster ($\sim 10^{10}$ s^{-1}) than that observed here from primary to secondary radicals ($\sim 10^7$ s^{-1}). The energetics are also much more exothermic in the former case, and the correlation of more rapid reaction with greater exothermicity of isomerization is quite plausible since the activation energies of isomerization should be lower for the more exothermic processes.

Acknowledgment. This research was supported by U.S. ERDA Contract No. E(04-3)-34, Project Agreement No. 126.

References and Notes

(1) W. A. Noyes and P. A. Leighton, "The Photochemistry of Gases", Dover Publications, New York, N.Y., 1941.
(2) E. W. R. Steacie, "Atomic and Free Radical Reactions", Reinhold, New York, N.Y., 1954.
(3) F. R. Mayo, *J. Am. Chem. Soc.*, **76**, 5392 (1954).
(4) R. J. Cvetanovic, *Adv. Photochem.*, **1**, 115 (1963).
(5) M. L. Poutsma, *Methods Free-Radical Chem.*, **1**, 79 (1970).
(6) M. L. Poutsma, *Science*, **157**, 997 (1967).
(7) M. L. Poutsma, *J. Am. Chem. Soc.*, **87**, 2161 (1965).
(8) A. K. E. Hagopian, J. H. Knox, and E. A. Thompson, *Bull. Soc. Chim. Belg.*, **71**, 764 (1962).
(9) J. H. Knox and K. C. Waugh, *Trans. Faraday Soc.*, **65**, 1585 (1969).
(10) Experiments by M. H. J. Wijnen quoted in ref 4.
(11) F. S. C. Lee and F. S. Rowland, *J. Phys. Chem.*, submitted for publication.
(12) F. S. C. Lee, Ph.D. Thesis, University of California, Irvine, Calif., 1975.
(13) F. S. C. Lee and F. S. Rowland, *J. Phys. Chem.*, **81**, 86 (1977).

(14) F. S. C. Lee and F. S. Rowland, *J. Phys. Chem.*, **81**, 684 (1977).
(15) F. S. C. Lee and F. S. Rowland, *J. Phys. Chem.*, submitted for publication.
(16) S. W. Benson, "Thermochemical Kinetics", 2nd ed, Wiley-Interscience, New York, N.Y., 1976.
(17) The heats of formation for C_3H_6Cl radicals are estimated from kinetic behavior, but are not well known.
(18) See, for example, D. J. Henderson, Ph.D. Thesis, University of Wisconsin, 1968.
(19) J. P. Frank and F. S. Rowland, *J. Phys. Chem.*, **78**, 850 (1974).
(20) F. S. Rowland, F. Rust, and J. P. Frank, American Chemical Society Symposium on Fluorine-Containing Free Radicals, in press.
(21) D. D. Davis, W. Braun, and A. M. Bass, *Int. J. Chem. Kinet.*, **2**, 101 (1970).
(22) R. G. Manning and M. J. Kurylo, *J. Phys. Chem.*, **81**, 291 (1977).
(23) K. S. Chen, I. H. Elson, and J. K. Kochi, *J. Am. Chem. Soc.*, **95**, 5341 (1973).
(24) J. Cooper, A. Hudson, and R. A. Jackson, *Tetrahedron Lett.*, **11**, 831 (1973).
(25) A. N. Nesmeyanov, R. K. Friedlina, and V. N. Kost, *Tetrahedron Lett.*, **1**, 241 (1957).
(26) P. S. Skell, *Chem. Soc., Spec. Publ.*, **No. 19** (1965).

Thermal Chlorine-38 Atom Sources. Neutron Irradiation of $CClF_3$ and CCl_2F_2

F. S. C. Lee and F. S. Rowland*

Department of Chemistry, University of California, Irvine, California 92717 *(Received January 19, 1977)*

Publication costs assisted by the United States Energy Research and Development Administration

The energetic chemical reactions of ^{38}Cl formed by the $^{37}Cl(n,\gamma)^{38}Cl$ nuclear reaction account for only 3 and 6% of the total yield in $CClF_3$ and CCl_2F_2, respectively. The remainder are thermalized by multiple nonreactive collisions with the source molecules, and can then react thermally with chosen substrate molecules. At substrate mole fractions less than 0.1 energetic ^{38}Cl reactions with the substrate represent a negligible fraction of the total ^{38}Cl. Radiation effects can be quite important in perturbing radioactive product distributions but can be kept well within tolerable experimental limits.

Introduction

The thermal neutron irradiation of compounds containing ^{37}Cl (24.5% natural abundance) produces through the $^{37}Cl(n,\gamma)^{38}Cl$ nuclear reaction energetic ^{38}Cl atoms capable of undergoing a variety of "hot" chemical reactions with substrate molecules.[1-5] In "hot atom" studies those ^{38}Cl atoms which do not react while hot are thermalized by collision with moderator molecules, and are usually removed by scavenger molecules to prevent their ^{38}Cl-labeled reaction products from mixing with the products from bona fide hot processes. The purpose of the present experiments is in marked contrast to such hot atom studies. We have sought a system in which the hot processes represent a very minor fraction of the total ^{38}Cl atoms, and which is inert toward thermal ^{38}Cl atoms. In such a system almost all of the ^{38}Cl atoms are thus available to react as thermal ^{38}Cl atoms with other molecules present in the system as minor constituents. These minor components often perform exactly the same chemical function as the scavenger molecules in a hot system, except that the main purpose of the experiment is now directed toward the *thermal* ^{38}Cl reactions with these selected molecules, and the hot reactions are simply present as a necessary background. The scavenging of essentially thermal chlorine atoms has already been demonstrated with ^{38}Cl by $CHCl{=}CHCl$[6] and with ^{39}Cl by C_2H_4.[7] The nuclear reaction $^{40}Ar(\gamma,p)^{39}Cl$ is a useful source of a different chlorine isotope for such studies.

The ideal target molecule for such thermal ^{38}Cl studies must meet several criteria. It must contain at least one Cl atom per molecule as source for the $^{37}Cl(n,\gamma)^{38}Cl$ reaction, and should (a) have a vapor pressure of at least several atmospheres at room temperature to permit gas phase studies over a wide range of pressures; (b) not react with thermal chlorine atoms; and (c) preferably be quite inert generally toward reactive chemicals so that one target compound can be used with a variety of substrate molecules.

Earlier experiments by Lee and Hower have shown that the chlorofluoromethane molecules do not give large hot yields with ^{38}Cl.[8] Furthermore, with the perhalo molecules of this series the abstraction of Cl or F by ^{38}Cl is endothermic and does not occur thermally.[9] Consequently, our choices for a universal target molecule as the main component in systems for the study of thermal ^{38}Cl atoms lay among molecules such as CCl_4, CCl_3F, CCl_2F_2, $CClF_3$, and their 2- and 3-carbon analogues. Since the room temperature vapor pressures of $CClF_3$ and CCl_2F_2 are respectively about 20 and 5 atm, these two are obviously excellent choices. While CCl_2F_2 furnishes two target Cl atoms per molecule instead of one, and therefore twice as much ^{38}Cl per unit irradiation, most of our subsequent thermal ^{38}Cl atom studies have utilized $CClF_3$ as the major component. This choice has been dictated by the greater range of pressures available with $CClF_3$, and by the greater simplicity of its hot ^{38}Cl reaction spectrum. Both molecules are excellent in their inertness toward chemical reaction with other compounds in general,[10] as well as with thermal ^{38}Cl atoms. Stevens and Spicer have recently reported the use of CCl_2F_2 as both ^{38}Cl atom source and moderator for experiments with both H_2[11] and C_2H_4.[12] In general, however, they have not used it as a *thermal* ^{38}Cl source.

The basic pattern for these ^{38}Cl atom studies has been similar to the thermal ^{18}F studies carried out in this laboratory utilizing the $^{19}F(n,2n)^{18}F$ reaction. In the ^{18}F studies the most common inert target has been SF_6 although numerous experiments have also involved CF_4, C_2F_6, and NF_3 as the fluorine source.[13-16]

Experimental Section

The standard experimental arrangement for the study of thermal ^{38}Cl reactions involves the neutron irradiation of a sample ampoule containing >90% "inert" target (e.g., $CClF_3$ or CCl_2F_2), plus small amounts of the reactant of interest, of argon, and often of a known scavenger molecule such as O_2, H_2S, or HI. Argon is present as an internal neutron flux monitor through the $^{40}Ar(n,\gamma)^{41}Ar$ reaction,[6] since ^{41}Ar can readily be determined during the same standard radio gas chromatographic techniques used for analysis of many ^{38}Cl-containing products. The known scavenger molecules usually are present to convert radical products into more readily measurable stable compounds, e.g.

$$C_2H_4{}^{38}Cl \xrightarrow{HI} C_2H_5{}^{38}Cl$$

but normally also act as competitors for the thermal ^{38}Cl atoms as well.

Reactor Irradiations. The available reactor fluxes are easily sufficient to produce readily measurable yields of ^{38}Cl, but increased-power levels or longer irradiation times simultaneously produce more radiation damage to the samples. Consequently, irradiations were usually terminated with as little ^{38}Cl formed consistent with reasonable radioactive counting statistics in the ^{41}Ar monitor and in the ^{38}Cl products. Irradiation times were usually varied from 0.5 to 5 min, and reactor power (proportional to neutron flux) from 5 to 100 kW.[17] Normally a "cooling-off" period of about 30 min was allowed after irradiation to permit the decay of radioactivities in the glass ampoule, especially ^{28}Al (half-life 2.3 min).

The sample mixtures were sealed into pyrex glass ampoules on a calibrated glass vacuum line, and were then irradiated in the TRIGA Mark I reactor at the University of California, Irvine, with thermal neutron flux of 0.7×10^{12} neutrons cm^{-2} s^{-1} at the maximum 250 kW. In a typical sample a total of 10^8 to 10^9 ^{38}Cl atoms were produced, at an average production rate of 10^6 to 10^7 ^{38}Cl atoms s^{-1}. This corresponds to ^{38}Cl activity in the microcurie range.

The irradiated samples were analyzed by conventional radiogas chromatographic techniques.[17,18] The method utilizes a standard gas chromatography unit with a thermal conductivity detector for the measurement of macroscopic amounts of volatile compounds in the sample. This is followed in series by a thin-window gas flow proportional counter for the detection of the radioactivities in each product. The percentage yield of each ^{38}Cl-labeled product was determined by comparing each product's total ^{38}Cl activity as measured by proportional counter to the total ^{38}Cl activity produced in the system. All ^{38}Cl-labeled products are assayed by the penetration through the thin counter wall of the same radioactivity from gas molecules distributed homogeneously through the same gas volume, and hence all have the same efficiency.

The absolute yield of ^{38}Cl was determined from the ^{41}Ar radioactivity produced in the ^{40}Ar monitor in the same samples, and assayed by the same procedures. Since the ^{40}Ar atoms were irradiated under identical conditions to those of the target molecules, and all radioactivities were monitored on the same counter on the same flow stream, the counting efficiency of this counter for ^{41}Ar relative to ^{38}Cl was also determined as part of the monitor calibration procedure.

Only the volatile contents of the sample products were injected and analyzed by means of the standard radiogas chromatography setup. Furthermore, some of the possible volatile inorganic ^{38}Cl products, such as $Cl^{38}Cl$, $H^{38}Cl$, etc., were not eluted from the columns used, and no attempt was made here to assay for them. Their yields were indirectly estimated from kinetic analysis. Further details are given in the Ph.D. Thesis of Lee.[17] Analysis for $H^{38}Cl$ by trapping the flow stream with granular K_2CO_3 has been described by Stevens and Spicer.[12]

Radiogas Chromatography. The sample analysis techniques were similar to those described previously from this laboratory. Whenever HI was present in a sample, a 8-cm "stripper" column packed with $K_4Fe(CN)_6 \cdot 3H_2O$ was placed between the injection loop and the analytical column. This stripper column was shown to adsorb HI irreversibly without affecting the passage of ^{38}Cl-labeled organic molecules.

The radioassay for ^{38}Cl was performed with an "external" gas flow proportional counter consisting of a middle cell through which the sample gas stream flows sandwiched between two half-cylindrical proportional counters; the cell and the counters are separated by thin windows.[19-21]

In the early stages of this investigation a 22.5-cm^3 brass cell with a 0.25-mil thick aluminized mylar window was used. However, some of the higher boiling compounds exhibited substantial broadening and tailing of the radioactive peaks. Presumably, both effects result from $CCl_2{=}CCl^{38}Cl$ molecules sticking to the walls of the counter cell. No appreciable improvements in peak tailing or background recovery were observed when the cell surface characteristics were changed by construction of cells and windows from stainless steel, teflon, etc. Accordingly, a stainless steel cell with 1-mil stainless foil windows was developed which could be internally heated to temperatures of 100 °C or higher. Both the excessive peak widths and the long-term increase in background are substantially reduced with the use of the heated counter. Most molecules studied do not stick as badly as $CCl_2{=}CCl^{38}Cl$, and no differences from the ordinary counter behavior are observed with the heated counter in the assay of volatile molecules such as $C_2H_3{}^{38}Cl$, $C_2H_5{}^{38}Cl$, n-$C_3H_7{}^{38}Cl$, etc. Heating the counter to 100 °C has negligible effects on both its plateau and its natural background counting rate.

^{41}Ar as a Neutron Flux Monitor. The wall of the thin-walled external counter is still thick enough to absorb substantial (and different) fractions of the β radiation from ^{41}Ar and ^{38}Cl. Accordingly, the relative efficiencies of the external counter for the β radiation of ^{41}Ar and ^{38}Cl were determined with samples passed in sequence through an external counter, and then, after mixing with a counting gas, through an internal counter whose efficiency for counting both is ~100% (and therefore equal). The samples each contained both ^{41}Ar and ^{38}Cl, the latter as carrier-free $C_2H_5{}^{38}Cl$ for which electron quenching was negligible. In the heated stainless steel counter, the counting efficiency for ^{38}Cl is 1.35 times greater than that for ^{41}Ar.

The internal Ar monitor technique cancels out many potential variables, but is dependent upon the relative thermal neutron cross sections of ^{37}Cl and ^{40}Ar. Since the introduction of the internal Ar monitor technique in our laboratory by Wai and Rowland in 1964,[21] the best values of the cross sections of both ^{37}Cl and ^{41}Ar have been substantially revised. The new σ values are $\sigma_{^{40}Ar} = 0.61$ b[22] (old: 0.53 b) and $\sigma_{^{37}Cl} = 0.43$ b (old: 0.56 b).[23] In addition, Wai and Rowland assumed that the relative efficiencies of their very thin-mylar-walled external counter were equal for ^{38}Cl and ^{41}Ar. However, sequential measurements on the mylar counter as described above for the stainless steel counter indicate a slight difference in efficiencies, with that for ^{38}Cl 1.1 times more sensitive than that for ^{41}Ar. The absolute yields quoted earlier for ^{38}Cl

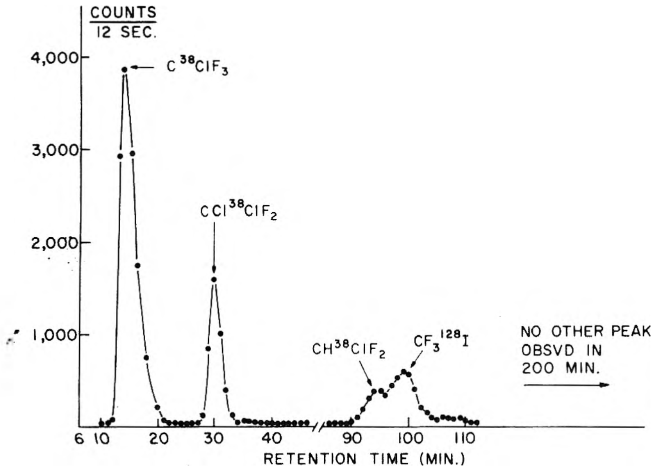

Figure 1. Radiogas chromatogram of radioactive products from neutron irradiation of $CClF_3$/HI mixtures: $CClF_3$, 3960 Torr; HI, 189 Torr. 50-ft DMS column at 25 °C and 30 mL/min flow rate.

products by Wai and Rowland should now be increased by a factor of 1.36 [(0.56/0.43)(0.61/0.53)(1/1.1)] on the basis of present knowledge of neutron cross sections. The accuracy of absolute yields is now estimated to be about ±10%, while the relative yields of major peaks (i.e., those with good counting statistics) within a particular sample can be precise to ±2%.

Charge State of ^{38}Cl at the Time of Thermal Reaction. The ^{38}Cl atom freshly formed in the (n,γ) nuclear reaction has a maximum of 527 eV kinetic energy, and reaction of ^{38}Cl in the +1 state or in an excited neutral state needs to be considered. The experiments of Wai and Rowland established parallel behavior for ^{39}Cl, ^{34m}Cl, and ^{38}Cl in comparable systems despite their origin in vastly different nuclear reactions. The ionization potentials of Cl, $CClF_3$, and CCl_2F_2 are 13.01, 12.94, and 11.7 eV, respectively. Accordingly, charge transfer converting Cl^+ to Cl is always exothermic with either $CClF_3$ or CCl_2F_2 present as the main component, and charged Cl^+ is no more likely than in the Wai-Rowland experiments.[6] There is still no evidence inconsistent with the hypothesis that essentially all of the thermalized ^{38}Cl species react in the neutral ground state.

Results

Hot Reactions of ^{38}Cl with $CClF_3$. Energetic ^{38}Cl atoms are able to react with $CClF_3$ by two substitution channels (1) and (2) resulting in the formation of $C^{38}ClF_3$ and

$$^{38}Cl + CClF_3 \rightarrow C^{38}ClF_3{}^* + Cl \quad (1)$$

$$^{38}Cl + CClF_3 \rightarrow CCl^{38}ClF_2{}^* + F \quad (2)$$

$CCl^{38}ClF_2$ in yields reported earlier as 0.74 and 0.65%, respectively, at 1 atm.[2] In both cases analogy with other such substitution reactions strongly suggests that the initial products are highly excited and frequently decompose before they can be stabilized by collision with another gas molecules.[24] The most energetically favorable decomposition paths are those involving C–Cl bond break, as in (3) and (4). Although the C–Cl bonds are weaker than

$$C^{38}ClF_3{}^* \longrightarrow CF_3 + {}^{38}Cl \quad (3)$$

$$CCl^{38}ClF_2{}^* \longrightarrow CClF_2 + {}^{38}Cl \quad (4a)$$

$$\hookrightarrow C^{38}ClF_2 + Cl \quad (4b)$$

the C–F bonds in chlorofluoromethanes, the more energetic decomposition paths of C–F bond break in (5) and (6) are

$$C^{38}ClF_3{}^* \rightarrow C^{38}ClF_2 + F \quad (5)$$

$$CCl^{38}ClF_2{}^* \rightarrow CCl^{38}ClF + F \quad (6)$$

also feasible. All of these hot reaction possibilities are confirmed by the observation of the additional labeled compounds, $CH^{38}ClF_2$ and $CHCl^{38}ClF$, in the presence of HI or H_2S, as in (7) and (8).

$$C^{38}ClF_2 + HI \rightarrow CH^{38}ClF_2 + I \quad (7)$$

$$CCl^{38}ClF + HI \rightarrow CHCl^{38}ClF + I \quad (8)$$

The radiogas chromatographic analysis of an HI-scavenged sample on a 50 ft dimethylsulfolane column is illustrated in Figure 1. About 25% of the ^{38}Cl in $C^{38}ClF_3$ decays between injection and emergence of its peak in Figure 1, while 83% of $CH^{38}ClF_2$ has decayed when its peak is detected. The peak for $CHCl^{38}ClF$ does not elute soon enough to be measured in Figure 1, but was measured from similar samples with a 50-ft silicone oil column operated at 70 °C. Calibrated retention times for these compounds on ten different chromatographic columns used for routine analysis are given in ref 17.

A non-^{38}Cl radioactivity is also shown, with the presence of $CF_3{}^{128}I$ containing ^{128}I from the $^{127}I(n,\gamma)^{128}I$ nuclear reaction on HI. As expected, the $CF_3{}^{128}I$ peak is absent from H_2S-scavenged samples. The ^{128}I impurity is not the only one which might occasionally be observed, with ^{35}S from the $^{35}Cl(n,p)^{35}S$ reaction another possibility. We could not observe any ^{35}S compound in these systems because of the weakness of its β radiation, but $OC^{35}S$ was earlier identified from similar irradiations with chlorofluorocarbon sources when analyzed with an internal proportional counter.[25]

The yield of $C^{38}ClF_3$ and $CCl^{38}ClF_2$ decrease with decreasing total pressure in the system, as illustrated in

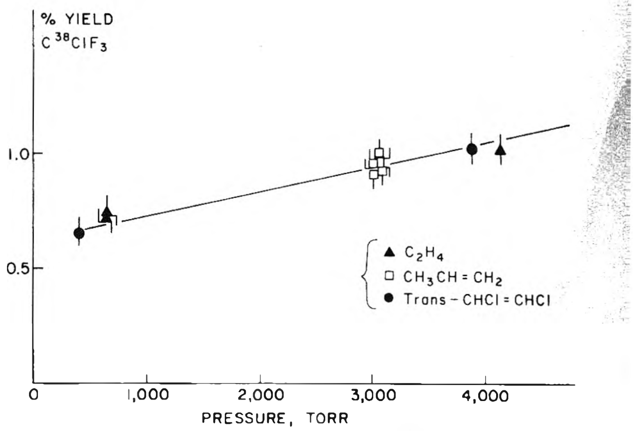

Figure 2. Pressure dependence of $C^{38}ClF_3$ yield from ^{38}Cl reactions in $CClF_3$/olefin/HI mixtures: (▲) C_2H_4; (□) $CH_3CH{=}CH_2$; (●) *trans*-CHCl=CHCl. Mole Fraction $CClF_3 \geq 0.9$.

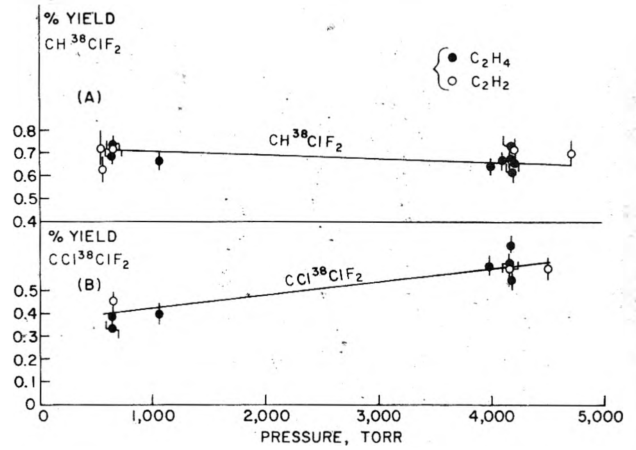

Figure 3. Pressure dependence of $CCl^{38}ClF_2$ and $CH^{38}ClF_2$ yields from ^{38}Cl reactions in $CClF_3$/unsaturate/HI mixtures: (●) C_2H_4; (O) C_2H_2.

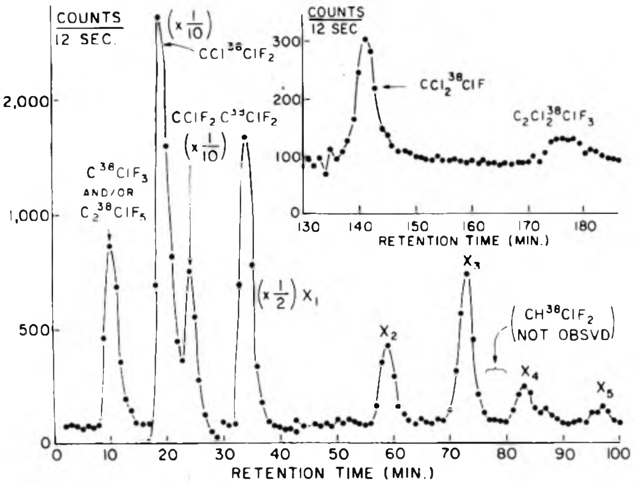

Figure 4. Radiogas chromatogram of radioactive products observed from neutron-irradiated unscavenged $CClF_3$. Five radioactive peaks have not been uniquely identified.

Figures 2 and 3. These decreases are just those expected from the decomposition reactions of eq 3–6. The expected loss of ^{38}Cl from $C^{38}ClF_3{}^*$ leaves no labeled fragment to identify the temporary existence of this molecule. With $CCl^{38}ClF_2$ statistical loss of Cl and ^{38}Cl would result in a pressure-dependent increase of $CH^{38}ClF_2$ at low pressures only half as large as the decrease in $CCl^{38}ClF_2{}^*$. The data of Figure 3 are consistent with this interpretation, but the changes are not large for either compound. Nonetheless, the total decomposition of $CCl^{38}ClF_2$ is ~50% at the higher pressures. The identification of $CHCl^{38}ClF$ in yields of 0.1–0.2% demonstrates that small amounts of C–F bond break can also occur.

At the higher pressures (~4000 Torr) the hot yields from ^{38}Cl reaction with $CClF_3$ total about 2.5%, including 1.0% $C^{38}ClF_3$, 0.6% $CCl^{38}ClF_2$, 0.7% $CH^{38}ClF_2$, and 0.16% $CHCl^{38}ClF$. The remaining 97⁺% of the ^{38}Cl is then free to react thermally with the minor components of the system. In the absence of a reactive hydrogen donor such as HI or H_2S about 1% of the total ^{38}Cl activity is present as the radicals $C^{38}ClF_2$ and $CCl^{38}ClF$ and is a possible source of minor errors if attributed to thermal ^{38}Cl atom reactions.

Hot Reactions of ^{38}Cl with CCl_2F_2. Energetic ^{38}Cl atoms substitute into CCl_2F_2, with the formation of both $CCl_2{}^{38}ClF^*$ and $CCl^{38}ClF_2{}^*$ in analogy with the $^{38}Cl/F$ and $^{38}Cl/Cl$ reactions found with $CClF_3$. In an unscavenged sample of CCl_2F_2 at 700 Torr pressure the observed absolute yields are 0.55% for $CCl^{38}ClF_2$ and 0.10% for $CCl_2{}^{38}ClF$. In addition, another eight ^{38}Cl-labeled peaks are readily separated in minor yields as shown in Figure 4. While most of these peaks have not been identified, several can be formed by $C^{38}ClF_2$ or $CCl^{38}ClF$ radicals (e.g., C_2ClF_5, $CClF_2CClF_2$, CCl_2FCClF_2). The number of ^{38}Cl-labeled compounds and their total yields are both greater with pure CCl_2F_2 than for comparably irradiated samples of $CClF_3$. One difference is that the loss of Cl from $C^{38}ClF_3$ cannot leave a ^{38}Cl-labeled radical, while the loss of Cl from $CCl^{38}ClF_2$ or $CCl_2{}^{38}ClF$ can and does. Generally, CCl_2F_2 appears to be somewhat more sensitive to radiation damage itself. When choosing a source compound for thermal ^{38}Cl studies, of course, the greater complexities of the hot ^{38}Cl spectrum from CCl_2F_2 can be avoided simply by choosing $CClF_3$ as the source.

When CCl_2F_2 scavenged by 10% H_2S is irradiated and analyzed at the same total pressure, the yields of $CCl^{38}ClF_2$ and $CCl_2{}^{38}ClF$ are unchanged within the error of the measurement, 1.8% $CH^{38}ClF_2$ and 1.4% $CHCl^{38}ClF$ are also detected, and the minor peaks of Figure 4 have all been removed. If the 1.8% yield of $C^{38}ClF_2$ radicals represents, as is likely, the decomposition of $CCl^{38}ClF_2{}^*$, then an additional 1.8% should be allowed for decomposition to $^{38}Cl + CClF_2$, and the fractional survival of $CCl^{38}ClF_2{}^*$ is about (0.55)/(0.55 + 1.8 + 1.8) or 13% at 1 atm pressure. Similarly, the 1.4% $CHCl^{38}ClF$ should be accompanied by 0.7% decay to $^{38}Cl + CCl_2F$, and the fractional survival of $CCl_2{}^{38}ClF^*$ at 1 atm pressure is (0.10)/(0.10 + 1.4 + 0.7) or 5%. The total original hot ^{38}Cl yield is then about 4.2% for $CCl^{38}ClF_2$ and 2.2% for $CCl_2{}^{38}ClF$ indicating that hot ^{38}Cl substitution for Cl is about twice as likely as for F. No comparable data can be obtained from the $CClF_3$ experiments since the $^{38}Cl/Cl$ product $C^{38}ClF_3{}^*$ normally loses its label in decomposition. At 1 atm pressure (Figure 3) the products from the $^{38}Cl/F$ process in $CClF_3$ ($CCl^{38}ClF_2$ and $CH^{38}ClF_2$) have yields of about 0.4 and 0.7%, respectively. After adding 0.7% for decay to ^{38}Cl and $CClF_2$, the survival fraction for $CCl^{38}ClF_2$ is approximately (0.4)/(0.4 + 0.7 + 0.7) or 18%, in reasonable agreement with the 13% calculated above for $^{38}Cl/F$ in CCl_2F_2. Since these estimates have ignored the loss of F from excited molecules (i.e., $CHCl^{38}ClF$ from $CClF_3$), no accurate quantitative calculations can actually be carried out. Two semiquantitative conclusions about these hot reactions seem justified, however: (a) hot substitutions of ^{38}Cl for Cl or F usually deposit very high excitation energies on the product molecules, and most such molecules are *not* collisionally stabilized at 1–5 atm pressure; (b) the hot substitution of ^{38}Cl for Cl is preferred over F, per atom, by about a factor of 2. The extensive decomposition of such excited molecules is consistent with earlier ^{38}Cl studies with a variety of substrate molecules.

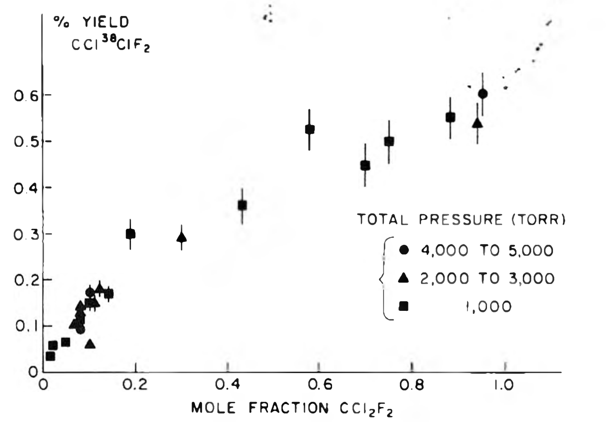

Figure 5. Observed yield vs. mole fraction of CCl_2F_2 for radioactively-labeled parent molecule ($CCl^{38}ClF_2$) from ^{38}Cl reactions with CCl_2F_2 scavenged by (C_2H_4 or C_2H_2) and (HI or H_2S).

The dependence of $CCl^{38}ClF_2$ yield from ^{38}Cl-atom reaction with CCl_2F_2 vs. mole fraction of CCl_2F_2 parent is shown in Figure 5, for dilution with C_2H_4 and C_2H_2. Within the experimental errors, a smooth curve is obtained with a yield of $CCl^{38}ClF_2$ decreasing from 0.55% at ~0.95 mole fraction CCl_2F_2 to 0.03 at a mole fraction of 0.02. Extrapolation to zero mole fraction CCl_2F_2 gives a residual yield of ≤0.01% for $CCl^{38}ClF_2$. This extrapolation represents an estimated upper limit for the failure of bond rupture after ^{38}Cl recoil, i.e., ≥99.9% of all ^{38}Cl atoms escape from the CCl_2F_2 molecule containing the ^{37}Cl target atom. A similar estimate of ≤0.01% bond rupture failure has been given for ^{38}Cl from 1,2-dichlorobutane by Wai and Rowland.[26]

The total energetic ^{38}Cl-atom substitution yields in both $CClF_3$ and CCl_2F_2 systems are both ~3–6%. While abstraction of Cl or F by ^{38}Cl is endothermic, the observation

TABLE I: Radiation Effects in Neutron Irradiated $CClF_3$ Scavenged with C_2Cl_4

	Sample Composition Pressure, Torr				
$CClF_3$	2920	2760	3000	2950	3000
C_2Cl_4	10.9	10.1	15.0	14.7	10.1
Ar	23.2	16.6	9.6	9.0	10.6
Scavenger HI				15.2	
O_2					5.3
	Irradiation				
Power, kW	1	5	25	25	25
Time, min	5	5	5	4	5
% $C_2Cl_3{}^{38}Cl$ yield	8.7	29.6	92.3	1.0	1.4

of the endothermic $^{38}Cl/F$ substitution indicates that "hot" endothermic processes must be considered. The hot reaction yields of $Cl^{38}Cl$ and ^{38}ClF were not directly studied in this research, but are believed to be negligibly small since >90% of the ^{38}Cl has been recovered in thermal ^{38}Cl processes, as discussed below. The upper limit on the total hot halogen abstraction is <5% by activity balance, and is probably <1%. No indications of the formation of either $Cl^{38}Cl$ or ^{38}ClF have appeared in any of our experiments.

Thermalization of ^{38}Cl Atoms. The ^{38}Cl atoms which fail to undergo hot reaction with pure $CClF_3$ or CCl_2F_2 are left to react with other molecular species included in the original system. A finite possibility always exists for ^{38}Cl collisions with these substrate molecules before thermalization, with a probability proportional (roughly linear) to the mole fraction of substrate. A number of systems have been investigated in which reactions known to be highly endothermic are observed,[17] as in (9) to (11), for

$$^{38}Cl + CH_3CH{=}CH_2 \rightarrow CH_2{=}CH^{38}Cl + CH_3 \tag{9}$$

$$^{38}Cl + CH_2{=}CH_2 \rightarrow CH_2{=}CH^{38}Cl + H \tag{10}$$

$$^{38}Cl + CH_2{=}CH_2 \rightarrow CH_2{}^{38}Cl + CH_2 \tag{11}$$

example. These reactions require energetic ^{38}Cl atoms to be observed.

As the mole fraction of the substrate (e.g., propene or ethylene) is reduced in mixtures with $CClF_3$ the yields of such "hot" products are also reduced, with yields extrapolating to zero at zero mole fraction of substrate. Experimentally these "hot" yields become negligible at substrate mole fractions of <0.01 (e.g., the $CH_2{=}CH^{38}Cl$ yield is 0.01% at 0.01 mole fraction propene and 0.08% for 0.01 mole fraction ethylene) and generally not important below 0.1 mole fraction.

The reactions cited above require excess energies in the 10–50 kcal/mol range, and are not sensitive to smaller excesses of energy above thermal. More sensitive tests for nonthermal atoms include the unimolecular decay of $C_2H_4{}^{38}Cl^*$ for which 1 or 2 kcal/mol represents a factor of 2 or 3 in rate of loss of ^{38}Cl. Again, with substrate mole fractions less than 0.1 there is no indication of deviations attributable to a measurable component of ^{38}Cl atoms that had not been thermalized at the time of addition to C_2H_4.[17,27]

In general then the use of substrate mole fractions less than 0.1 is sufficient to ensure that the measured reactions are overwhelmingly thermal ^{38}Cl reactions. In each case, when necessary or desired, the substrate mole fraction can be varied and the reaction yields extrapolated to zero substrate in order to ensure thermalization.

Radiation Effects in Neutron-Irradiated Chloromethanes. In experiments with C_2Cl_4 as the only scavenger molecule for bulk $CClF_3$, the sole observed ^{38}Cl-labeled product aside from the hot products with $CClF_3$ is $CCl_2{=}CCl^{38}Cl$ (Table I). However, when roughly comparable samples are irradiated at power levels of 1, 5, and 25 kW, the yield of $CCl_2{=}CCl^{38}Cl$ increased from 8.7 to 92.3%. Moreover, at the highest power level the inclusion of either O_2 or HI as a second scavenger reduced the $CCl_2{=}CCl^{38}Cl$ yield to about 1%. A more extended set of observations with *trans*-CHCl=CHCl as the scavenger gave comparable results, as given in Table II. Again, variable yields of $CHCl{=}CH^{38}Cl$ were observed, with low yields at low power and in the presence of O_2. Comparison of the two samples irradiated at 5 kW for 3 min shows yields differing by a factor of 4 despite nearly identical experimental conditions.

The difficulties with these samples arise from the presence of trace O_2 impurities, since gas handling with these compounds seldom operates much lower than a real background pressure of 10^{-3} Torr. As neutron irradiation proceeds, the radicals induced by radiation damage to the system react with and remove the O_2, and eventually the system becomes genuinely O_2-free. However, at the low power levels this O_2-free situation is not attained until late in the irradiation, if at all.

When otherwise typical samples were preirradiated with an 11 000 Ci γ-radiation source, radiation damage removes the O_2 but no ^{38}Cl is formed. Then, when neutron irradiated the low power experiments have the *highest* ^{38}Cl yields instead of the lowest. The results from a series of samples with O_2 removed by γ radiation are given in Table III. The ^{38}Cl yields from these experiments show a smooth trend of decreasing yields with increasing neutron exposure, as shown in Figure 6. Clearly, after removal of traces of O_2 which suppress reactions initially, the effect of additional radiation exposure is to reduce the yields of ^{38}Cl-labeled CHCl=CHCl molecules.

Measurements of the survival of the unlabeled *trans*-CHCl=CHCl in these experiments showed that macro-

TABLE II: Dose Dependence of the Yields of ^{38}Cl Products from ^{38}Cl-Atom Reactions in Mixtures of $CClF_3$/*trans*-CHCl=CHCl/Ar

	Sample Composition Pressure, Torr										
$CClF_3$	3000	3080	3000	2920	3020	3000	3130	3010	3000	3010	3000
trans-CHCl=CHCl	10.0	10.2	10.0	9.8	9.9	10.3	10.3	10.1	10.3	10.2	10.2
Ar	32.1	16.4	16.8	16.0	16.1	10.2	16.8	12.6	22.4	16.4	O_2, 10.3
	Irradiation										
Power, kW	1	1	5	5	5	12	50	125	100-MW pulse	100-MW pulse	125
Time, min	3	3	3	3	7	3	3	3	10-ms	10 ms	3
Total ^{38}Cl activity (10^5 counts)[a]	5.7	5.7	37	29	67	66	280	660	290	330	670
^{38}Cl product	Absolute Yield, % Total ^{38}Cl Atoms										
trans-$CHCl{=}CH^{38}Cl$	3.0	3.1	2.8	12.2	13.5	9.4	10.1	9.2	3.1	3.4	2.3
cis-$CHCl{=}CH^{36}Cl$	5.4	6.5	6.0	31.4	35.3	24.2	24.9	22.5	5.9	5.3	4.2

[a] Number of counts per minute of ^{38}Cl, calculated at time of injection to chromatographic column.

TABLE III: Dose Dependence of the Yields of ^{38}Cl Products from ^{38}Cl Reactions in ^{137}Cs-Preirradiated Samples with Mixtures of $CClF_3$/*trans*-CHCl=CHCl/Ar[a]

	Sample Composition Pressure, Torr					
$CClF_3$	2970	2980	3020	3000	3050	2890
trans-CHCl=CHCl	10.0	9.8	9.9	10.1	10.0	9.5
Ar	15.8	15.3	17.3	12.7	12.1	16.1
	Irradiation					
Power, kW	1	1	10	5	50	50
Time, min	3	3	3	15	3	3
Total ^{38}Cl activity (10^5 counts)	6.1	7.6	58	110	280	270
^{38}Cl product	Absolute Yield, % Total ^{38}Cl					
trans-CHCl=CH^{38}Cl	17.9	18.6	13.5	9.9	9.4	10.5
cis-CHCl=CH^{38}Cl	48.2	50.6	34.7	25.8	23.1	26.1

[a] All samples were preirradiated with a 11 000 Ci ^{137}Cs source for 10 min prior to reactor irradiation.

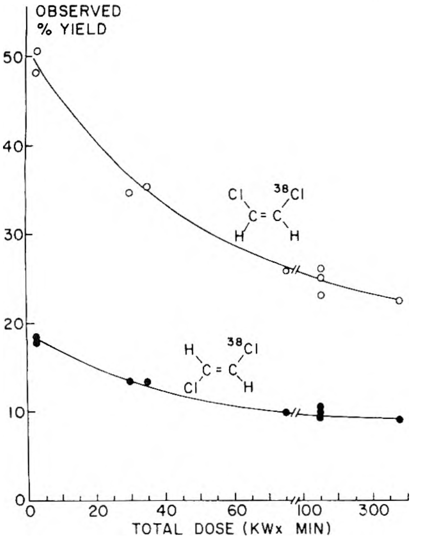

Figure 6. Observed yields vs. radiation dosage of CH^{38}Cl=CHCl (cis and trans) from ^{38}Cl reactions in $CClF_3$/*trans*-CHCl=CHCl mixtures. Radiation dose expressed in minutes of reactor operation times reactor power.

scopic damage was also observable. After 400 kW-min of neutron irradiation, about 30% of the *trans*-CHCl=CHCl molecules had been removed. After an equivalent exposure the yields of *labeled* CHCl=CH^{38}Cl molecules had fallen by more than 50%. The net yield of CHCl=CH^{38}Cl is reduced both by destruction of molecules after formation and by competitive reactions preventing formation of some of the CHCl=CH^{38}Cl in the later stages of irradiation.

The overall behavior indicates that most of the radiation damage in these systems results from free-radical reactions induced both by the natural radiation background of the nuclear reactor and by the processes induced in the glass ampoules and their contents. In typical irradiation conditions in the U.C.I. Mark I TRIGA, the total absorbed radiation dose is about 10^{17} eV s^{-1} g^{-1} at 250 kW reactor power.[17] A substantial fraction of this damage comes from the ampoule walls, and experiments at low pressures have the disadvantage that all of this radiation effect will be distributed over fewer total molecules and hence will have a larger percentage change. Experiments at 100 Torr or less would require additional assessment of radiation effects since the yields of ^{38}Cl are necessarily reduced by a factor of 40 per unit irradiation time (4000 Torr vs. 100 Torr).

In general these experiments demonstrate that radiation-induced effects can be reduced to negligible importance, but that they are sufficiently likely that consideration must be given to them in most systems if only to avoid them. When a few percent of a free-radical scavenger is deliberately introduced into the system the radiation damage effects are effectively suppressed; with substantially lower scavenger concentrations their possible depletion has to be kept in mind.

Conclusions

Both $CClF_3$ and CCl_2F_2 are excellent sources of thermal ^{38}Cl atoms when irradiated with thermal neutrons. More than 90% of the ^{38}Cl atoms are actually available for reaction with appropriate substrate molecules as thermal ^{38}Cl atoms, while most of the remaining ^{38}Cl atoms will appear in readily identifiable forms such as $C^{38}ClF_3$, $CCl^{38}ClF_2$ and $CCl_2{}^{38}ClF$. The ^{38}Cl-labeled fragments most likely to cause analytical confusion are the residues from the loss of Cl of F from the excited [^{38}Cl]-chlorofluoromethanes, present in 1–2% total yield. In most cases, these perhalo radicals can be trapped with H_2S or HI and converted to the corresponding mono-hydrogen chlorofluoromethanes.

Heavy neutron irradiation not only produces more than ample amounts of ^{38}Cl for radioassay, but also causes appreciable radiation damage in the samples, enough to be serious for reactive substrate molecules such as olefins. However, there is also a reasonable range of conditions for which enough ^{38}Cl is present for convenient assay without incurring too much radiation damage to the ^{38}Cl-labeled products, the original target molecule, or the reacting substrate molecule.

This source of thermal ^{38}Cl is most satisfactory for gas phase experiments in the pressure range of 1–5 atm. Experiments at lower pressures become progressively more difficult since the total yield of ^{38}Cl is directly proportional to the amount of material irradiated, and the source gas is by far the major component in the system by mole fraction.

Thermal ^{38}Cl atoms from such sources have been applied to the study of atomic chlorine reactions with ethylene,[12,27] acetylene,[28] propene,[29] alkynes,[17] and metallo-organic compounds.[30]

Acknowledgment. This research was supported by U.S. ERDA Contract No. AT(04-3)-34, Project Agreement 126.

References and Notes

(1) J. E. Willard, *Annu. Rev. Phys. Chem.*, **6**, 141 (1955).
(2) "Chemical Effects of Nuclear Transformations", 2 volumes, International Atomic Energy Agency, Vienna, 1961.
(3) R. Wolfgang, *Prog. React. Kinet.*, **3**, 97 (1965).
(4) F. S. Rowland, *MTP Int. Rev. Sci., Phys. Chem., Ser. One*, **9**, 109 (1972).
(5) D. Urch, *MTP Int. Rev. Sci., Inorg. Chem., Ser. One*, **8**, 149 (1972).
(6) C. M. Wai, and F. S. Rowland, *J. Am. Chem. Soc.*, **90**, 3638 (1968).
(7) L. Spicer and R. Wolfgang, *J. Am. Chem. Soc.*, **90**, 2426 (1968).
(8) F. S. C. Lee and C. O. Hower, *J. Phys. Chem.*, **75**, 2625 (1971).
(9) The abstraction of Cl from $CClF_3$ by Cl to form Cl_2 is endothermic by 28 kcal/mol and has been reported to have an activation energy

of 31 kcal/mol. J. C. Amphlett and E. Whittle, *Trans. Faraday Soc.*, **63**, 2695 (1967). The abstraction of F from $CClF_3$ by Cl to form ClF is more than 50 kcal/mol endothermic.
(10) M. Hudlicky, "Chemistry of Organic Fluorine Compounds", MacMillan, New York, N.Y., 1962, p 297 *ff*.
(11) D. J. Stevens and L. D. Spicer, *J. Chem. Phys.*, **64**, 4798 (1976).
(12) D. J. Stevens and L. D. Spicer, preprint.
(13) T. Smail, R. S. Iyer, and F. S. Rowland, *J. Am. Chem. Soc.*, **94**, 1041 (1972).
(14) R. L. Williams and F. S. Rowland, *J. Phys. Chem.*, **76**, 3509 (1972).
(15) J. P. Frank and F. S. Rowland, *J. Phys. Chem.*, **78**, 850 (1974).
(16) F. S. Rowland, F. Rust, and J. P. Frank, *ACS Symp. Ser.*, in press.
(17) Extensive details are given in the Ph.D. Thesis of F. S. C. Lee, University of California, Irvine, Calif., 1975.
(18) J. K. Lee, E. K. C. Lee, B. Musgrave, Y.-N. Tang, J. W. Root, and F. S. Rowland, *Anal. Chem.*, **34**, 741 (1962).
(19) M. J. Welch, R. Withnell, and A. P. Wolf, *Chem. Instrum.*, **2**, 177 (1969).
(20) R. S. Iyer, Ph.D. Thesis, University of California, Irvine, Calif., 1973.
(21) C. M. Wai, Ph.D. Thesis, University of California, Irvine, Calif., 1967.
(22) C. M. Lederer, J. M. Hollander, and I. Perlman, "Table of Isotopes", 6th ed., Wiley, New York, N.Y., 1967.
(23) T. B. Ryves and D. R. Perkins, *J. Nucl. Energy*, **24**, 419 (1970).
(24) Y.-N. Tang, W. S. Smith, J. L. Williams, K. Lowery, and F. S. Rowland, *J. Phys. Chem.*, **75**, 440 (1971).
(25) E. K. C. Lee, Y.-N. Tang, and F. S. Rowland, *J. Phys. Chem.*, **68**, 318 (1964).
(26) C. M. Wai and F. S. Rowland, *J. Phys. Chem.*, **74**, 434 (1970).
(27) F. S. C. Lee and F. S. Rowland, *J. Phys. Chem.*, **81**, 1235 (1977).
(28) F. S. C. Lee and F. S. Rowland, *J. Phys. Chem.*, **81**, 684 (1977).
(29) F. S. C. Lee and F. S. Rowland, *J. Phys. Chem.*, **81**, 1222 (1977).
(30) M. Kikuchi, F. S. C. Lee, and F. S. Rowland, unpublished experiments.

Thermal Chlorine-38 Atom Reactions with Ethylene

F. S. C. Lee and F. S. Rowland*

Department of Chemistry, University of California, Irvine, California 92717 *(Received January 19, 1977)*

Publication costs assisted by the U.S. Energy Research and Development Administration

The reactions of thermal chlorine atoms with ethylene have been studied using radioactive ^{38}Cl atoms from the neutron reaction $^{37}Cl(n,\gamma)^{38}Cl$ on $CClF_3$. The ^{38}Cl atoms are moderated to thermal energies by multiple collisions with $CClF_3$ (mole fraction >0.9), and then allowed to react with C_2H_4 plus HI or H_2S. The only observed product is $C_2H_5{}^{38}Cl$, representing addition to ethylene to form $C_2H_4{}^{38}Cl^*$. The decomposition rate of $C_2H_4{}^{38}Cl^*$ by loss of ^{38}Cl was measured by varying the total pressure in the system. The rates of decomposition and collisional stabilization are equal at a $CClF_3$ pressure of 800 ± 120 Torr. The rate constants for reactions 1, 10, and 15 are in the ratios $(k_{10}/k_1) = 0.60 \pm 0.05$ and $(k_{15}/k_1) = 0.45 \pm 0.05$ at 293 K: $^{38}Cl + C_2H_4 \rightarrow C_2H_4{}^{38}Cl^*$ (1); $^{38}Cl + HI \rightarrow H^{38}Cl + I$ (10); $^{38}Cl + H_2S \rightarrow H^{38}Cl + SH$ (15).

Introduction

The only exothermic reaction with gaseous ethylene available to thermal chlorine atoms is addition to form a chloroethyl radical as in

$$Cl + C_2H_4 \rightarrow CH_2CH_2Cl^* \qquad (1)$$

The hydrogen abstraction reaction 2 is endothermic by 6

$$Cl + C_2H_4 \rightarrow HCl + C_2H_3 \qquad (2)$$

kcal/mol and is an unlikely process at room temperature.[1] Almost all Cl atoms at 300 K must then either react by (1) or find some other molecule with which to react in ethylene-containing systems. The possible subsequent reactions of $C_2H_4Cl^*$ radicals include the reverse of the formation reaction, as in (3), and collisional stabilization

$$C_2H_4Cl^* \rightarrow Cl + C_2H_4 \qquad (3)$$

$$C_2H_4Cl^* + M \rightarrow C_2H_4Cl + M \qquad (4)$$

of the excited radical, reaction 4. The loss of H from $C_2H_4Cl^*$ is highly endothermic and cannot occur with radicals formed by addition of thermal chlorine atoms to ethylene.[1] Earlier studies of the atomic chlorine–ethylene reaction were concerned with the relative reactivity of ethylene and the various chloroethylenes, and showed that the rates of reaction with all except C_2Cl_4 were comparably rapid, and had low activation energies (≤2 kcal/mol).[2-4] These studies thereby confirmed that reaction 1 is quite rapid, and that an appreciable fraction of the radicals from (1) did not undergo the reverse reaction 3.

Wijnen has studied the reactions of stabilized C_2H_4Cl using the photolysis of phosgene, $COCl_2$, as the source of atomic chlorine.[5] The chief C_2H_4Cl product observed was 1,4-dichlorobutane from the combination of two such radicals, as in (5). Wijnen et al. also used ultraviolet

$$2C_2H_4Cl \rightarrow CH_2ClCH_2CH_2CH_2Cl \qquad (5)$$

Cl transfer

$$C_2H_4Cl + C_2H_4Cl \rightarrow C_2H_4 + C_2H_4Cl_2 \qquad (6)$$

H transfer

$$C_2H_4Cl + C_2H_4Cl \rightarrow C_2H_3Cl + C_2H_5Cl \qquad (7)$$

photolysis of CCl_4 as a Cl-atom source for reaction with ethylene.[6] In these experiments, disproportionation products from Cl and H transfer between C_2H_4Cl radicals were observed, as in (6) and (7). The yields of the observed two-carbon products (C_2H_3Cl, C_2H_5Cl, $C_2H_4Cl_2$) indicated that the disproportionation processes 6 and 7 were ≤0.1 as probable as combination 5. The ultraviolet photolysis of CCl_4 has recently been shown to lead in some cases to $CCl_2 + Cl_2$ rather than $CCl_3 + Cl$,[7] but the implication of this observation for the interpretation of Cl + ethylene reactions has not yet been examined. The loss of Cl from excited $C_2H_4Cl^*$ was not explicitly considered in Wijnen's work.

A further study of the $Cl + C_2H_4$ system has been made by Heicklen, again using the photolysis of $COCl_2$ as the source of atomic chlorine.[8] These data showed a much higher disproportionation/combination ratio (0.45) and indicated that the H-atom transfer of (7) was four times as probable as the Cl-atom transfer of (6). Heicklen also suggested the reaction of two C_4H_8Cl radicals with one another, as in

$$2C_4H_8Cl \rightarrow C_4H_7Cl + C_2H_5Cl + C_2H_4 \qquad (8)$$

We have utilized thermal ^{38}Cl atoms formed by thermal neutron irradiation of $CClF_3$[9] for study of the atomic chlorine–ethylene system. The initially energetic ^{38}Cl atoms are thermalized by multiple collisions with $CClF_3$ (mole fraction >0.9) prior to reaction with ethylene. In the presence of hydrogen-donor radical scavengers (e.g., HI or H_2S), the stabilized chloroethyl radicals from the ^{38}Cl analogue of (4) are converted to $C_2H_5{}^{38}Cl$ and assayed in this form, as in

$$CH_2CH_2{}^{38}Cl + HI \rightarrow CH_3CH_2{}^{38}Cl + I \tag{9}$$

However, the inclusion of HI (or H_2S) furnishes a competitor molecule for ethylene in reaction with the initial ^{38}Cl atoms, and increasing concentrations of HI (or H_2S) can be expected through reaction 10 to reduce the yield

$$^{38}Cl + HI \rightarrow H^{38}Cl + I \tag{10}$$

of $C_2H_4{}^{38}Cl^*$ from (1), and thereby of $C_2H_5{}^{38}Cl$ from (9).

Some earlier experiments with radioactive Cl atoms and ethylene were performed by Spicer and Wolfgang who used a different nuclear reaction $^{40}Ar(\gamma,p)^{39}Cl$, and chose a mixture of C_2H_4 and I_2 as a scavenger combination in argon–alkane mixtures.[10] They found more than 90% of the ^{39}Cl activity as $C_2H_4{}^{39}ClI$ in a typical sample containing 600 Torr of Ar, 150 Torr of CH_4, 20–40 Torr of C_2H_4, and traces of I_2. Obviously almost all of the ^{39}Cl atoms in this system followed the reaction route of (1), (4), and then reaction of $C_2H_4{}^{39}Cl$ with I_2 to form $C_2H_4{}^{39}ClI$, and strongly suggests that the bulk of these reactions were those of thermalized ^{39}Cl atoms. The relative nonreactivity of methane toward thermal ^{39}Cl is consistent with the measured rate constants for that abstraction reaction.[11,12] Very recently Stevens and Spicer have applied ^{38}Cl from neutron irradiation of CCl_2F_2 to the study of ^{38}Cl reactions with H_2[13] and C_2H_4.[14]

Experimental Section

The procedures for forming ^{38}Cl ($t_{1/2}$ = 37.3 min) by thermal neutron irradiation of ^{37}Cl contained in $CClF_3$ or CCl_2F_2 have been described elsewhere.[9] The difficulties encountered with radiation damage problems in such irradiations are discussed there in detail. Essentially such irradiations are most susceptible to radiation damage alteration of the observed product spectrum at high reactor power (i.e., high neutron flux), long reactor exposure times, and low absolute concentrations of reactive species, e.g., HI. Some of the low concentration HI experiments described here suffered from radiation removal of HI, and are disregarded in the quantitative evaluations.

When $CClF_3$, C_2H_4, and HI or H_2S are irradiated, the chief ^{38}Cl-labeled product is $C_2H_5{}^{38}Cl$, with lesser amounts of $CH_3{}^{38}Cl$ and $CH_2{=}CH^{38}Cl$ also being formed. However, when the mole fraction of $CClF_3$ exceeds 0.90, the yields of $CH_3{}^{38}Cl$ and $CH_2{=}CH^{38}Cl$ are negligibly small, indicating that they require nonthermal ^{38}Cl atoms for their formation. The reactions of *energetic* ^{38}Cl atoms with ethylene have also been studied through the use of $CClF_3$–C_2H_4 mixtures with the mole fraction of $CClF_3$ varying from 0.1–0.8.[15]

The analysis of the radioactive products in $CClF_3$–ethylene mixtures in highly moderated systems (mole fraction of $CClF_3$ >0.9) is carried out by radiogas chromatography using two chromatographic columns in series, 50-ft dimethylsulfolane (DMS) and 24-ft propylene carbonate on alumina (PCA). The PCA column was necessary for the separation of ^{41}Ar and $C^{38}ClF_3$, with the former serving as an internal neutron flux monitor for absolute calculation of ^{38}Cl yields through the $^{40}Ar(n,\gamma)^{41}Ar$ nuclear reaction.

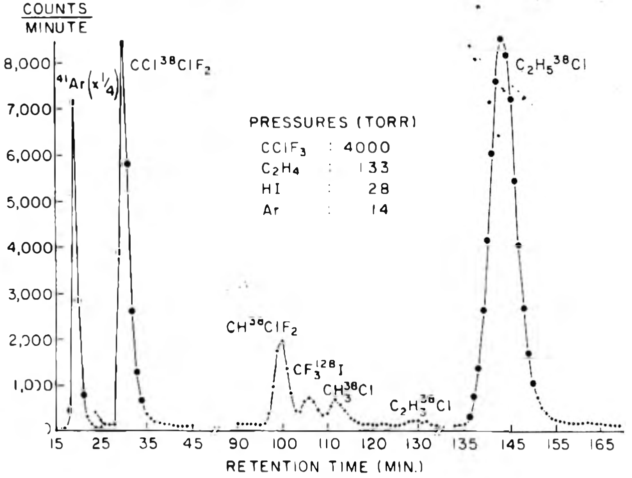

Figure 1. Radiogas chromatogram of ^{38}Cl products from ^{38}Cl-atom reactions in $CClF_3/C_2H_4$/HI/Ar mixture. Analysis with dimethylsulfolane and propylene carbonate-on-alumina columns. The PCA column is removed from the flow stream during the analysis, and the peak for $C^{38}ClF_3$ never emerges.

After injection of the irradiated sample, both ^{41}Ar and $C^{38}ClF_3$ passed rapidly through the DMS column and into the PCA column. After the entire system had been tested with a few samples, the $C^{38}ClF_3$ yields were no longer measured, and the PCA column was removed from the flow stream as soon as ^{41}Ar had emerged from the PCA column and had been assayed. The other radioactive molecules then passed directly from the DMS column into the gas proportional counter for radioassay while the $C^{38}ClF_3$ peak was usually left in the PCA column and not analyzed. A series of separate experiments had demonstrated that the yield of $C^{38}ClF_3$ was consistent, varying from about 0.5% at 500 Torr to 1.0% at 4000 Torr. Only about 7% of the ^{38}Cl radioactivity present as $C_2H_5{}^{38}Cl$ at injection is still present during assay 140 min later.

A radiogas chromatogram of the analysis of a typical $CClF_3$–C_2H_4 sample is shown in Figure 1. The small yield of $CF_3{}^{128}I$ is formed from ^{128}I atoms created by the $^{127}I(n,\gamma)^{128}I$ nuclear reaction on the HI scavenger. All of these experiments were carried out at room temperature, about 293 K in the reactor irradiation facility.

Results and Discussion

Approximately 97% of the total ^{38}Cl radioactivity formed by neutron irradiation of $CClF_3$ is available as thermal ^{38}Cl.[9] In the present experiments the only measured product from these thermal atoms is $C_2H_5{}^{38}Cl$. About 3% of the ^{38}Cl radioactivity is observed as reaction products from hot ^{38}Cl reactions with $CClF_3$, while traces are formed from hot ^{38}Cl reactions with C_2H_4. The remainder of the ^{38}Cl is presumed present as $H^{38}Cl$ from reaction 10, but was not directly assayed in these experiments. The yields of these various ^{38}Cl-labeled organic molecules are summarized in Table I for a series of experiments at a total pressure of about 4100 Torr. Similar experiments at 1000 and 640 Torr are given in Table II.

The observed yields of $C_2H_5{}^{38}Cl$ are consistent with a mechanism involving competition between reactions 1 and 10 for thermalized ^{38}Cl atoms, and between decomposition (3) and stabilization (4) for the excited $C_2H_4{}^{38}Cl^*$ radicals formed in (1). The stabilized $C_2H_4{}^{38}Cl$ radicals are all assumed to be converted to $C_2H_5{}^{38}Cl$ by reaction 9. If reaction 1 occurs only for thermal ^{38}Cl atoms, then the $C_2H_4{}^{38}Cl^*$ radicals are essentially monoenergetic and can be effectively described by an average decomposition rate, k_3. The stabilization rate is then given by a rate constant proportional to pressure, k_4M, and the rates of formation

TABLE I: ^{38}Cl Radioactive Product Yields with Ethylene and HI as Competitors in Highly Moderated $CClF_3$ Systems, Total Pressure 4100 Torr[a]

	Sample Composition Pressure, Torr						
$CClF_3$	4000	3970	4000	3960	4000	4000	4000
C_2H_4	28.1	40.0	26.3	9.9	80	133	133
HI	160	120	60.0	20.4	80	27.6	26.4
Ar	14.8	15.1	14.9	14.3	15.6	13.7	10.8
$[HI]/[C_2H_4]$	5.7	3.0	2.3	2.1	1.0	0.21	0.20
Total pressure	4200	4140	4100	4000	4180	4170	4170
	Absolute Yield, % Total ^{38}Cl						
^{38}Cl product							
$C^{38}ClF_3$	*b*	1.02 ± 0.01	*b*	*b*	*b*	*b*	*b*
$CCl^{38}ClF_2$	0.55 ± 0.01	*b*	*b*	0.61 ± 0.01	0.74 ± 0.05	0.62 ± 0.01	0.51 ± 0.02
$CH^{38}ClF_2$	0.66 ± 0.01	*b*	0.67 ± 0.01	0.64 ± 0.01	0.60 ± 0.01	0.68 ± 0.01	0.59 ± 0.02
$CH_3{}^{38}Cl$	<0.03	<0.02	0.10 ± 0.02	0.10 ± 0.02	0.04 ± 0.01	0.15 ± 0.02	0.10 ± 0.02
$C_2H_3{}^{38}Cl$	0.08 ± 0.01	<0.02	<0.02	<0.02	<0.02	<0.03	0.08 ± 0.02
$C_2H_5{}^{38}Cl$	17.7 ± 0.2	32.3 ± 0.2	33.3 ± 0.2	37.0 ± 0.3	60.8 ± 0.4	86.2 ± 0.6	69.7 ± 0.4

[a] All samples were irradiated at 10 to 25 kW reactor power for about 2 to 4 min. [b] Not measured.

TABLE II: ^{38}Cl Radioactive Product Yields with Ethylene and HI as Competitors in Highly Moderated $CClF_3$ Systems, Total Pressure 640 or 1030 Torr[a]

	Sample Composition Pressure, Torr					
$CClF_3$	504	501	501	500	1000	1000
C_2H_4	20	32	40	61	7.1	33
HI	105	96	86	61	35	7.3
$[HI]/[C_2H_4]$	5.1	3.4	2.1	1.0	4.9	0.22
Total pressure	641	643	640	636	1,060	1,050
	Absolute Yield, % Total ^{38}Cl					
^{38}Cl product						
$C^{38}ClF_3$	*b*	0.74 ± 0.02	*b*	0.72 ± 0.02	*b*	*b*
$CCl^{38}ClF_2$	0.38 ± 0.02	*b*	0.33 ± 0.02	*b*	0.39 ± 0.01	0.48 ± 0.02
$CH^{38}ClF_2$	0.74 ± 0.02	*b*	0.69 ± 0.03	*b*	0.67 ± 0.02	0.48 ± 0.02
$C_2H_3{}^{38}Cl$	<0.05	<0.05	<0.05	<0.05	<0.03	0.07 ± 0.01
$C_2H_5{}^{38}Cl$	11.2 ± 0.2	19.4 ± 0.3	24.8 ± 0.4	41.1 ± 0.5	16.6 ± 0.5	59.2 ± 0.3

[a] All the samples were irradiated at 30-kW reactor power for 3 min, and contained 10–18 Torr of Ar. [b] Not measured. $CH_3{}^{38}Cl$ yield always <0.05%.

of $H^{38}Cl$ and $C_2H_5{}^{38}Cl$ are given by

$$\frac{(H^{38}Cl)}{(C_2H_5{}^{38}Cl)} = k_{10}(HI)\Big/\left[k_1(C_2H_4)\frac{k_4M}{(k_4M + k_3)}\right] \qquad (11)$$

Any ^{38}Cl atom reacting with C_2H_4 and released by (3) simply goes through the HI vs. C_2H_4 competition again, and repeats the process until either $H^{38}Cl$ or $C_2H_5{}^{38}Cl$ is formed.

If 97% of the ^{38}Cl atoms are assumed to react to form either $H^{38}Cl$ or $C_2H_5{}^{38}Cl$, then eq 11 can be rewritten as

$$\frac{(d/dt)[(C_2H_5{}^{38}Cl) + (H^{38}Cl)]}{(d/dt)(C_2H_5{}^{38}Cl)} = \frac{0.97}{\text{yield}(C_2H_5{}^{38}Cl)}$$

$$= 1 + \left\{k_{10}(HI)\Big/\left[k_1(C_2H_4)\frac{(k_4M)}{(k_4M + k_3)}\right]\right\} \qquad (12)$$

and rearranged to

$$\frac{0.97}{Y(C_2H_5{}^{38}Cl)} = 1 + \frac{k_{10}(HI)}{k_1(C_2H_4)}\left\{1 + \frac{k_3}{k_4'\omega P}\right\} \qquad (13)$$

The concentration M has been rewritten as a collision frequency per unit pressure, ω, and k_4' now explicitly has the significance of probability of stabilization per collision, and has the value 1 under "strong" collision conditions, i.e., when every collision of (4) removes enough energy from $C_2H_4{}^{38}Cl^*$ that decay by (3) can no longer happen.

If we define $P_{1/2}$ as the pressure at which half of the $C_2H_4{}^{38}Cl^*$ radicals are stabilized (i.e., $k_3 = k_4'\omega$), then eq 13 can be rewritten once more as

$$\frac{0.97}{Y(C_2H_5{}^{38}Cl)} = 1 + \frac{k_{10}(HI)}{k_1(C_2H_4)}\left\{1 + \frac{P_{1/2}}{P}\right\} \qquad (14)$$

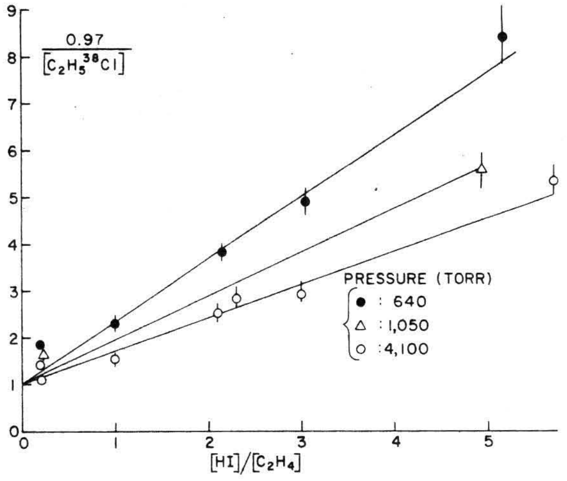

Figure 2. Reciprocal yield of $C_2H_5{}^{38}Cl$ in competition between C_2H_4 and HI for thermal ^{38}Cl atoms in highly moderated $CClF_3$ systems.

This equation indicates at each pressure a linear relationship with an intercept of 1.0 for $0.97/Y(C_2H_5{}^{38}Cl)$ vs. the ratio $(HI)/(C_2H_4)$. If the value of $P_{1/2}$ is very low (i.e., decay by (3) is unimportant at all pressures), then values of $Y(C_2H_5{}^{38}Cl)^{-1}$ at all pressures would fit on the same straight line and provide directly a measure of k_{10}/k_1. Otherwise, different straight lines are expected at each pressure, and the different slopes can be used to evaluate first $P_{1/2}$, and then k_{10}/k_1.

The data of Tables I and II are graphed in Figure 2, showing the straight lines and unit intercepts expected from eq 14. When the absolute concentrations of HI are relatively low (<10 Torr), radiation damage in the system can so seriously deplete the HI that some stabilized

TABLE III: Competition between Ethylene and Hydrogen Sulfide for ^{38}Cl Atoms in Highly Moderated CCl_2F_2

Sample Composition Pressure, Torr			
CCl_2F_2	3960	3640	3720
C_2H_4	101	99	69
H_2S	101	200	220
Total pressure	4180	3960	4020
$[H_2S]/[C_2H_4]$	1.0	2.0	3.2
Absolute Yield, % Total ^{38}Cl			
^{38}Cl product			
$CCl^{38}ClF_2$	0.60 ± 0.02	0.68 ± 0.02	0.72 ± 0.02
$CH^{38}ClF_2$	0.21 ± 0.02	0.39 ± 0.02	0.54 ± 0.02
$CH_3{}^{38}Cl$	0.05 ± 0.01	0.05 ± 0.01	0.03 ± 0.01
$C_2H_3{}^{38}Cl$	<0.02	<0.01	~ 0.01
$C_2H_5{}^{38}Cl$	60.7 ± 0.2	46.8 ± 0.2	36.5 ± 0.1

[a] All samples were irradiated at 10-15-kW reactor power for ~ 2 min, and contained 16-18 Torr of Ar.

TABLE IV: Measured and Calculated Decomposition Rates for $C_2H_4Cl^* \rightarrow C_2H_4 + Cl$

	Experimental			Calculated		
Reference	17	18	This work	4	19	19
Bath gases	Cl_2	HCl	$CClF_3$			
Assumed collision diameter, Å^2	4.2	4.0	5.5			
Assumed E_0, kcal/mol				21.3	20.6	17.7
Pressure range, Torr	<300	200-700	500-4100	0-∞	0-∞	0-∞
Temp range, K	310	290	293	308	310	310
$(k_3\ s^{-1}) \times 10^9$	2-3	~5	~10	0.15-0.4	0.5-0.9	1.3-2.1

$C_2H_4{}^{38}Cl$ radicals are not converted to $C_2H_5{}^{38}Cl$. Ignoring the low HI concentration samples, the remaining data at all three pressures are consistent with $P_{1/2} = 800 \pm 120$ Torr and $(k_{10}/k_1) = 0.60 \pm 0.05$.

Similar data with H_2S as the scavenger instead of HI (and CCl_2F_2 as the ^{38}Cl source) are given in Table III. The slope of the line for these data at 4100 Torr is 0.53 ± 0.03 vs. 0.71 ± 0.06 at 4100 Torr in Figure 2. Since the $P_{1/2}$ values for $C_2H_4{}^{38}Cl^*$ should be quite similar for CCl_2F_2 and $CClF_3$, the difference in slope indicates that reaction 15

$$^{38}Cl + H_2S \rightarrow H^{38}Cl + SH \tag{15}$$

is slower than reaction 10 by the ratio of the slopes, and (k_{15}/k_1) is thus about 0.45 ± 0.05. Our measurements do not directly give any estimates of the absolute reaction rates for k_1, k_{10}, and k_{15}. However, comparison of the relative rates with C_2H_6,[12] $CH_3CH{=}CH_2$,[16] etc., indicate that k_1, k_{10}, and k_{15} are all very fast with absolute rate constants of about 10^{-10} cm^3 molecule^{-1} s^{-1}.

The value of 800 Torr for $P_{1/2}$ corresponds to a rate constant $k_3 \sim 10 \times 10^9$ s^{-1}, and is in fair agreement with the values for k_3 measured earlier with Cl_2 and HCl as bath gases,[17,18] as summarized in Table IV. Considerably slower decomposition rates for these excited $C_2H_4Cl^*$ radicals have been calculated by two different research groups,[2,18] as recorded in Table IV.

The apparent discrepancy between calculated and experimental rates for k_3 could originate in (a) incorrect transition states in the calculated values; and/or (b) failure of the strong collision assumption for collisions of $C_2H_4{}^{38}Cl^*$ with $CClF_3$ or CCl_2F_2. Since the collisions of excited $C_2H_4{}^{18}F^*$ with CF_4 and C_2F_6 have been shown to involve very weak collisions,[20,21] the second hypothesis is quite reasonable, and could mean that the observed value of k_3 should be divided by 2 or 3 for comparison with the theoretical calculations.

TABLE V: Relative Collisional Efficiencies for Deactivation of $C_2H_4Cl^*$

Bath gas	Relative deactivation	Ref
C_2H_6	1.0	16
Cl_2	0.5	16
C_2H_4	0.5	16
CO_2	0.5	16
SF_6	0.3	16
HCl	0.3	17

The average relative energy losses per collision have been measured for $C_2H_4Cl^*$ with various bath gases as summarized in Table V.[4,19] Further consideration of the discrepancies in k_3 of Table IV does not seem worthwhile until measurements have been made of the absolute average energy losses per collision for $C_2H_4Cl^*$ radicals with some of these gases.

The present experiments have served primarily for the evaluation of the decomposition and stabilization reactions of $C_2H_4Cl^*$, with little information about the subsequent reactions of stabilized C_2H_4Cl radicals. In particular our experiments have not provided any further elucidation of the C_2H_4Cl radical combination/disproportionation experiments of Wijnen and Heicklen.[5,6,8]

In these earlier studies of C_2H_4Cl radicals, no explicit consideration was given to the loss of Cl from excited $C_2H_4Cl^*$ radicals. Such loss should not affect their experimental observations very much since the released Cl atoms would normally add to ethylene repeatedly until the $C_2H_4Cl^*$ radical is eventually stabilized by collision. Our experiments produce very low concentrations of $C_2H_4{}^{38}Cl$ radicals, and even in the absence of scavenger molecules negligible concentrations of unlabeled C_2H_4Cl radicals. These tracer experiments with thermal ^{38}Cl can be adapted to the study of radical-radical reactions, but will require the simultaneous production of some particular unlabeled radical with which the $C_2H_4{}^{38}Cl$ radical can react. In the present system no particular radical (e.g., C_2H_4F, C_2H_4Cl, C_2H_5) has been identified as the dominant unlabeled radical. Consequently, there is no simple method of identifying a particular stable product representative of stabilized $C_2H_4{}^{38}Cl$ radicals. Further experiments, however, should be able to provide information about these $C_2H_4{}^{38}Cl$ reactions.

Acknowledgment. This research was supported by U.S. ERDA Contract No. E(04-3)-34, Project Agreement No. 126.

References and Notes

(1) From the heats of formation given below, the abstraction of H is calculated as 6 ± 2 kcal/mol endothermic, and the replacement of H by Cl to form $CH_2{=}CHCl$ is 16 kcal/mol endothermic. Heats of formation in kcal/mol at 300 K, as given by S. W. Benson, "Thermochemical Kinetics", 2nd ed, Wiley-Interscience, New York, N.Y., 1976: H, 52.1; Cl, 28.9; C_2H_4, 12.5; HCl, -22.0; C_2H_3Cl, 5.0; C_2H_3, 69 ± 2. By analogy between the addition of H to $CH_2{=}CHCl$ and that of H to C_2H_4, reaction 1 is estimated to be about 22 kcal/mol exothermic.

(2) F. S. Dainton, D. A. Lomax, and W. Weston, *Trans. Faraday Soc.*, **58**, 308 (1962).

(3) J. A. Franklin, P. Goldfinger, and G. Huybrechts, *Ber. Bunsenges. Phys. Chem.*, **72**, 173 (1968).

(4) P. C. Beadle, J. H. Knox, F. Placido, and K. C. Waugh, *Trans. Faraday Soc.*, **65**, 1571 (1969).

(5) M. H. J. Wijnen, *J. Am. Chem. Soc.*, **83**, 3014 (1961).

(6) B. C. Roquitte and M. H. J. Wijnen, *J. Chem. Phys.*, **38**, 4 (1963).

(7) D. D. Davis, J. F. Schmidt, C. M. Neeley, and R. J. Hanrahan, *J. Phys. Chem.*, **79**, 11 (1975).

(8) J. Heicklen, *J. Am. Chem. Soc.*, **87**, 445 (1965).

(9) F. S. C. Lee and F. S. Rowland, *J. Phys. Chem.*, **81**, 1229 (1977).

(10) L. Spicer and R. Wolfgang, *J. Chem. Phys.*, **50**, 3466 (1969).

(11) R. T. Watson, *J. Phys. Chem. Ref. Data*, in press.

(12) F. S. C. Lee and F. S. Rowland, *J. Phys. Chem.*, **81**, 86 (1977).

(13) D. J. Stevens and L. D. Spicer, *J. Chem. Phys.*, **64**, 4798 (1976).
(14) D. J. Stevens and L. D. Spicer, preprint.
(15) F. S. C. Lee, Ph.D. Thesis, University of California, Irvine, 1975.
(16) F. S. C. Lee and F. S. Rowland, *J. Phys. Chem.*, **81**, 1222 (1977).
(17) J. H. Knox and K. C. Waugh, *Trans. Faraday Soc.*, **65**, 1585 (1969).
(18) R. A. Johnson and R. Barker, *Trans. Faraday Soc.*, **65**, 1585 (1969).
(19) L.-K. Huy, W. Forst, J. A. Franklin, and G. Huybrechts, *Chem. Phys. Lett.*, **3**, 307 (1969).
(20) J. P. Franks and F. S. Rowland, *J. Phys. Chem.*, **78**, 850 (1974).
(21) F. S. Rowland, F. Rust, and J. P. Frank, *ACS Symp. Ser.*, in press.

Reactions of Iodine with Olefins. 4. Preferential Site Attack of Electrophilic High Energy Iodine in Gaseous, High Pressure, and Liquid Butene-1[1]

Kar-Chun To, M. E. Berg, and E. P. Rack*

Department of Chemistry, University of Nebraska, Lincoln, Nebraska 68588 and General Medical Research, V.A. Hospital, Omaha, Nebraska 68105
(Received October 28, 1976; Revised Manuscript Received April 14, 1977)

Publication costs assisted by the U.S. Energy Research and Development Administration

Reactions of high energy iodine with butene-1 have been found to yield six organic products. Additive studies show that of 21.4% total organic product yield at 1 atm, the majority is the result of high energy reactions, many radical in nature. The gas to condensed phase transition shows a typical rise in all organic products except vinyl iodide. Analysis of all available data suggests that the products formed in the reactions of iodine with butene-1 arise from a diverse and complex series of product formation routes; however, greater than 70% of the organic products formed at 1 atm are the result of preferential site attack by iodine at or near the double bond.

Introduction

Iodine is a multifaceted reagent that may enter into high energy,[2] photochemical,[3,4] or ion–molecule[5] reactions. While previous studies involving tritium,[6-9] fluorine,[10-12] and chlorine[13] have been dominated by nonselective direct substitution reactions, iodine–olefinic systems can be complicated by competition among more than one of these reaction classes. Unlike photochemical addition, iodine species produced by recoil techniques exhibit electrophilic behavior in their reactions with ethylene.[5] This has also been found to be true in acetylene[14] where no hydrogen substitution products were found. High energy iodine reactions with propylene[5] and higher olefins[2,3] also demonstrate the selectivity of site attack.

Recent studies of recoil iodine with acetylene[14] and ethane[15,16] employing the gas to condensed phase transition technique have provided evidence for the formation of electronically excited reaction complexes. These studies provide information on new reaction channels unobtainable to the thermal, photochemical, or molecular beam chemist because of energy and/or molecular density restrictions. We have investigated the electrophilic character of high energy iodine species with olefins. Of all the olefins, the butenes are the most ideal to study at atmospheric, high pressure gas and condensed phase conditions. The butenes provide a π-bond site and multiple σ-bond sites where reaction can occur as distant as two carbon lengths from the double bond. Propene is less favorable because of the shorter carbon chain; whereas pentenes easily condense making it experimentally difficult to obtain high pressure gas samples.

In this paper we report on the reactions of iodine-128 activated by radiative neutron capture with the isomer butene-1. We have found that greater than 70% of the high energy organic product yield occurs as the result of the electrophilic attack of iodine at or near the π-bond system.

Experimental Section

Materials. Research-grade xenon, helium, krypton, and oxygen (stated purities 99.99 mol %) were obtained from Matheson Chemical Co. and were used without further purification; butene-1 (Matheson research grade with 99.85 mol % purity) and trifluoroiodomethane (Pierce Chemical Co.) were used after repeated degassing on the vacuum line. Iodine was sublimed from a mixture of Mallinkrodt reagent grade I_2, Baker reagent grade potassium iodide, and calcium oxide.

Preparation of Reaction System. Description of the techniques used to produce atmospheric, high pressure gas, and condensed phase samples has recently been reported.[15,17] High pressure gaseous samples were prepared by freezing 0.2 ± 0.01 Torr of iodine and 5 Torr of the iodine source into the ampoule followed by the measured quantity of 1-butene. Rare gas additives used in 1-atm samples were filled in the customary manner.[15]

Liquid samples were prepared by first freezing known quantities of iodine (5.15×10^{-5} mole fraction) into the ampoule followed by a known quantity of butene-1.

All samples were filled in a dark room, wrapped in aluminum foil, and stored in liquid nitrogen until just prior to irradiation to prevent photoinduced reactions.

Neutron Irradiation. All irradiations were performed in the Omaha, Nebraska V.A. Hospital TRIGA reactor at a thermal neutron flux of 1.1×10^{11} neutrons cm^{-2} s^{-1}, and accompanying γ ray flux of 3×10^{17} eV g^{-1} min^{-1}. The samples were irradiated from 0.5 to 30 min and extrapolated to zero irradiation time for correction of radiation damage. The liquid phase samples were irradiated at room temperature, immersed in ice water or dry ice. The density of the reaction mixture was determined by the method of Willard and Rice[19] and compared to literature values.[20,21] To minimize thermal reactions of I_2 with 1-butene, temperatures greater than room temperature were not attempted.

Extraction Procedure. Total organic product yields (TOPY)[18] were determined by breaking the irradiated samples in a separatory funnel containing 5 mL each of

---

* Address correspondence to this author at the Department of Chemistry, University of Nebraska.

$CCl_4 + I_2$ and 0.5 M Na_2SO_3 solution. The organic and inorganic phase (3 mL each) were counted in an Ortec single channel analyzer employing a 3 × 3-in. NaI(Tl) detector. All xenon samples were counted on a Harshaw 12.2% efficient Ge(Li) detector interfaced with a Nuclear Data 2400 1024-channel analyzer.

Radiogas Chromatographic Separations of Activated Mixtures. The radiogas chromatography used in this research has been previously described.[15,17] The column used was a 3-m SS coil containing 5% by weight di-(2-ethylhexyl) sebacate on 50/60 mesh firebrick. Linear temperature programming from 25 to 130 °C was used for gaseous samples together with a mixture of known carrier composition which was simultaneously injected into the helium stream. Liquid phase samples were directly injected into the chromatograph by employing the preinjection freeze, controlled thaw technique.[15]

Individual organic product yields were determined by triplicate radiogas chromatographic runs. Integration of the chromatograms produced relative yields which were first corrected for radiolytic damage and then to the total organic product yield to give the absolute individual organic product yields (IOPY).[18] A radiation dose curve was established for each sample condition by evaluating yields for 0.5-, 1.0-, 2.0-, 5.0-, 10.0-, 15.0-, 20.0- and 30.0-min irradiations. Extrapolation to zero irradiation time gave TOPY and IOPY values corrected for radiolytic contributions. Due to the rapid exchange between I_2 and HI we did not attempt to analyze the inorganic products $H^{128}I$ produced by abstraction or ^{128}I–I by thermal exchange with scavenger.

Results and Discussion

Characteristics of the Reaction System. The characteristics of recoil iodine has recently been discussed in detail.[14] Briefly, the iodine species has been characterized as possessing a range of translational energies from 0 to 194 eV.[22] In addition, Auger and secondary electron cascades caused by γ-ray radiolysis creates a spectrum of positively charged iodine ions[23] which may rapidly undergo charge transfer with bath molecules until the I^+ species exists (in the case where the molecules' ionization potential is between the first and second ionization potential of iodine). As a result, at least 50% of the ^{128}I species have been found to have positive ionic character[24] with a minimum of 25% in electronically excited states.[25] Iodine-128 has been found to combine with alkanes,[15,25,26] olefins,[2,3,5] and acetylene[14] in high energy,[25] photochemical,[3,4] and ion–molecule[5] reactions.

Butene-1 provides a low mass hydrocarbon system containing both an electron rich π-bond site and σ-bond carbon–hydrogen and carbon–carbon sites, both adjacent to and removed from the π bond, which are subject to attack by iodine species. The butene-1 system displays the additional advantage of steric influences, whereas, such factors are not present in the propene and ethene systems. Conformational analysis of butene-1[27,28] shows that the molecules exist in approximately equal proportions of the cis and skew conformers. "Free" rotation of the terminal carbon–carbon σ bond results in a negligible enthalpy difference[29,30] between these conformers. Butene-1 has an ionization potential (IP = 9.76 eV)[31] lower than that of iodine (IP = 10.454 eV)[31] suggesting the probability of exothermic charge transfer resulting in neutral iodine species.

The 1-Atm System. Extrapolation to unit mole fraction of rare gas additive produces insight into the proportion of organic products formed by high energy, $I^+(^1D_2)$, and other (thermal) reactions. Figure 1 shows the behavior of total organic product yield (TOPY) with mole fraction additive at 1 atm pressure. 21.4% of the iodine-128 produced is organically bound in the butene-1 system when no additive other then I_2 is present. In the absence of the I_2 scavenger the total organic product yield increases to 27.9%. The total organic product yields are reduced to 3.0% at unit mole fraction of helium and krypton and 0% at unit mole fraction of xenon. As we will show, the 18.4% drop observed with helium and krypton is the result of kinetic energy moderation. The 21.4% reduction in total organic product yield with xenon is caused by kinetic energy moderation and quenching of $I^+(^1D_2)$ as the result of near-adiabatic charge exchange.[25]

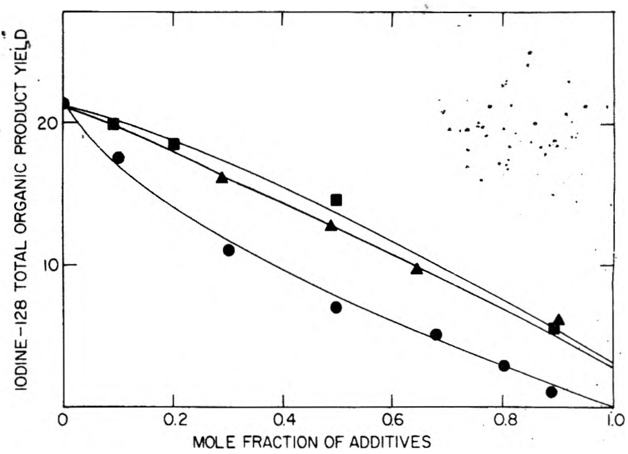

Figure 1. Effect of rare gas additives on total organic product yield at 1 atm: helium (■); krypton (▲); xenon (●).

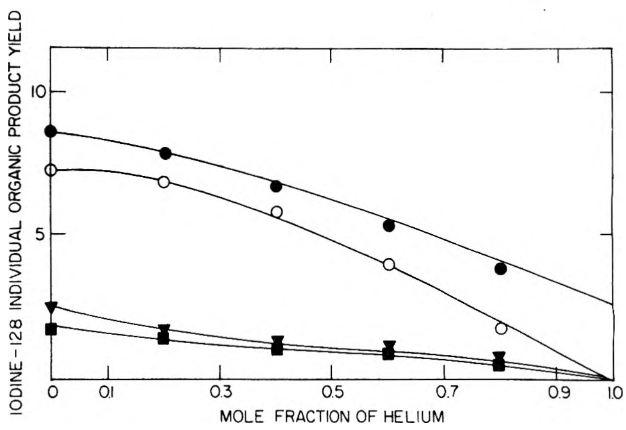

Figure 2. Effect of mole fraction helium on individual organic product yields at 1 atm: CH_3I (●), C_4H_9I (○); C_2H_3I (▼); C_4H_7I (■).

Individual organic product yield (IOPY) values were obtained from radiogas chromatographic analysis. Two major and four minor organic products were observed (contained radioiodine); viz., CH_3I (8.6%), $C_3H_7CH_2I$ (7.3%), C_2H_3I (2.7%), $CH_3CH_2CH{=}CHI$ (1.8%), C_2H_5I (0.8%), and $C_2H_5CH_2I$ (0.2%). The addition of rare gases to the reaction system provided a means to study the importance of high energy and electronic excitation to the formation of these individual organic products. Depicted in Figures 2, 3, and 4 are the effects of mole fraction He, Kr, and Xe, respectively, on the organic product yields of CH_3I, C_4H_9I, C_2H_3I, and C_4H_7I.[32] Note that all individual organic product yields extrapolate to 0% *except* that of $CH_3{}^{128}I$ in helium and krypton which extrapolates to 3.0% (thermal reaction). The additional decrease in xenon is the result of near-resonant charge exchange with $I^+(^1D_2)$. It is apparent that all observed products are solely the result of high energy reaction except CH_3I. The methyl iodide yield (8.6%) is the result of both high energy reaction (5.6%) and electronic excitation ($I^+(^1D_2)$, 3.0%).

TABLE I: Total and Individual Organic Product Yields for the Butene-1-Iodine-128 System

ρ, g cm^{-3} (state)	λ/σ	TOPY	CH_3I	C_2H_3I	C_2H_5I	C_2H_5-CH_2I	$C_2H_5CH=$ CHI	C_3H_7-CH_2I
0.002 (1 atm)	7.16	21.4 ± 0.8	8.6[a]	2.7[b]	0.8[b]	0.2[b]	1.8[b]	7.3[b]
0.007 (3 atm)	4.96	28.6 ± 2.7	12.1	1.5	2.1	0.3	4.7	7.9
0.591 (liq, 23 °C)	1.13	42.6 ± 1.6	17.3	0.3	2.2	0.7	11.0	11.1
0.619 (liq, 0 °C)	1.11	48.5 ± 2.5[c]						
0.705 (liq, −78 °C)	1.06	53.9 ± 1.7	20.9	0.3	6.1	1.3	12.4	12.9
30 mol % O_2 at 1 atm		7.5	3.0	3.0	0.3		0.4	0.8

[a] Rare gas additive studies at 1 atm ascribes the 8.6% yield of CH_3I to 5.6% the result of high energy reactions and 3.0% due to reactions of $I^+(^1D_2)$. [b] Rare gas additive studies at 1 atm suggest the entire yield observed is the result of high energy reactions. [c] Individual organic product yields could not be obtained due to the difficulty of maintaining this temperature in the reactor for the necessary irradiation time.

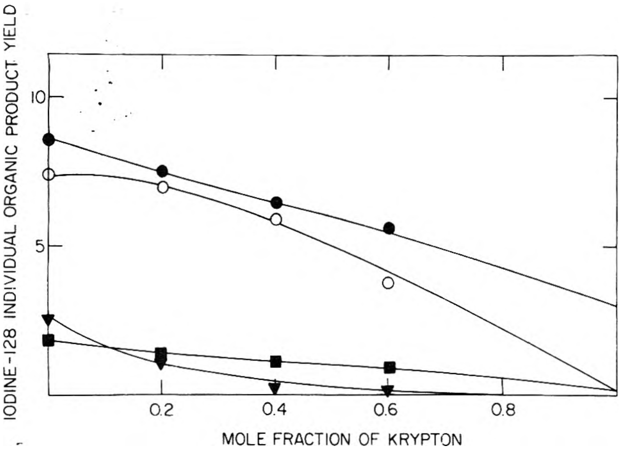

Figure 3. Effect of mole fraction krypton on individual organic product yields at 1 atm: CH_3I (●); C_4H_9I (O); C_2H_3I (▼); C_4H_7I (■).

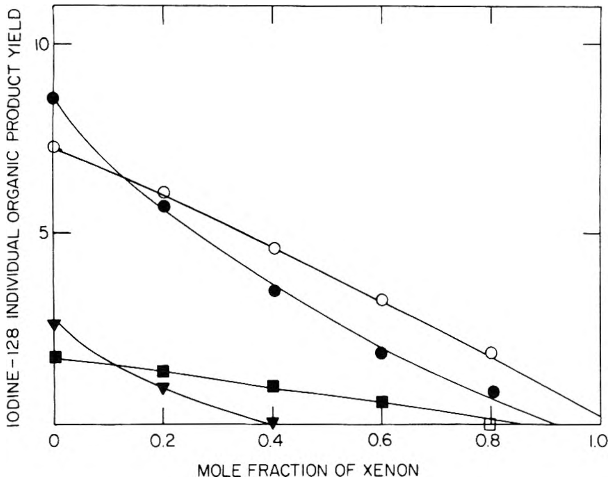

Figure 4. Effect of mole fraction xenon on individual organic product yields at 1 atm: CH_3I (●); C_4H_9I (O); C_2H_3I (▼); C_4H_7I (■).

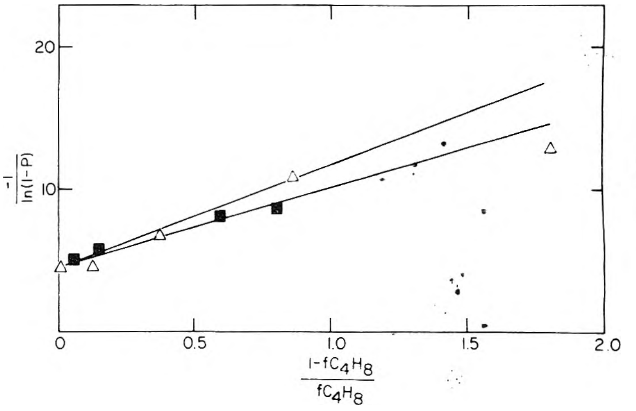

Figure 5. Kinetic theory plot of the first kind: krypton (△); helium (■).

This suggests the importance of some ion–molecule reactions in the ^{128}I-butene-1 system.

The effects of 30 mol % O_2 on the total and individual organic product yields of 1-atm ^{128}I-butene-1 systems has also been observed (Table I). The total organic product yield was observed to decrease from 21.4 (no additive) to 7.5% corresponding to a 5.6 and 6.5% decrease in the individual organic product yields of $CH_3{}^{128}I$ and $C_3H_7CH_2{}^{128}I$, respectively. This reduction in organic yields is greater than that expected from purely kinetic energy moderation arguments (kinetic theory predicts yields of 6.2 ± 1.7 and 5.8 ± 0.5%, respectively). The explanation may be that O_2 is a radical scavenger which inhibits (at least in part) the formation of these two products. (The experimental methods limits observation to products containing iodine-128 which are stable below their boiling points.) Rack and Gordus[33] have shown that the addition of O_2 has no effect on the quenching of iodine species but rather acts as a kinetic energy moderator and radical scavenger. It must be mentioned that while this is true for the methane system, other modes of O_2 competition may arise in the iodine–butene-1 system where reaction activation energies are a factor of 3 to 4 smaller. Three other products were observed to decrease in yield: ethyl iodide to 0.3%, 1-iodo-1-butene to 0.4%, and propyl iodide to 0%. Vinyl iodide appears to be unaffected by the presence of O_2. This anomalous behavior may be due to secondary (independent) product formation routes.

The corresponding system of ethene and iodine-128 was found[5] to give a total organic product yield of 18.0 ± 1.0% of which only the product $C_2H_5{}^{128}I$ (4.0%) was the result of high energy reactions. The products $CH_3{}^{128}I$ (10.0%) and $C_2H_3{}^{128}I$ (4.0%) were found to be the result of ion–molecule reactions initiated by I^+ in ground and/or excited states ($^3P_0$, $^3P_1$). The quenching of products by O_2 but not by Xe suggested that $I^+(^1D_2)$ was not directly responsible for the formation of either of these products.

Estrup and Wolfgang[34,35] have developed a kinetic theory for the reactions of high energy species based, in part, on neutron "cooling down" theory[36] and have applied it to the butene-1–tritium system activated by the $^3He(n,p)^3H$ reaction. Although the $^{127}I(n,\gamma)^{128}I$ reaction violates[22] some assumptions of the Estrup–Wolfgang kinetic theory, it can be qualitatively employed to predict the effects of additives as kinetic energy moderators. We have employed this theory, as such, as an internal consistency test of the dependence of product formation on (high) translational energy. No corrections for unimolecular and/or other secondary product formation routes were made since all products observed (with the exception of 3.0% CH_3I) were initiated by a "hot" mechanism. The correct behavior is observed for He, Kr, and Xe additives. The data for xenon were corrected for a 3.0% $CH_3{}^{128}I$ yield due to $I^+(^1D_2)$. However, the yields observed for 30 mol % O_2 is *not* consistent with kinetic theory. The lower yields must be

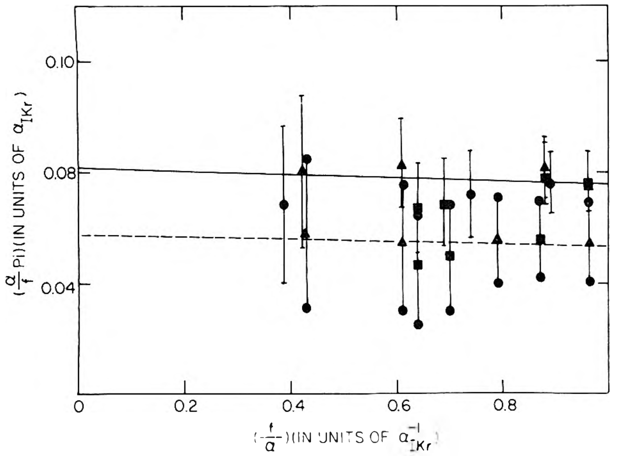

Figure 6. Kinetic theory plot of the second kind: helium (■); krypton (▲); xenon (●) for C_4H_9I (——) and CH_3I (- - -).

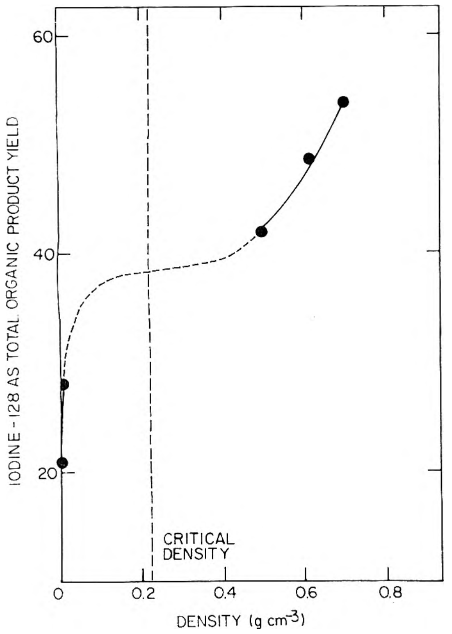

Figure 7. Variation of total organic product yield with density.

due to radical scavenging by O_2 since iodine species are unaffected by O_2.[33] The results of these calculations[37] are depicted in Figures 5 and 6. Therefore we may conclude that additive studies of rare gases suggest that 18.4% of the organic products observed are the result of high energy reactions and that 3.0% are due to $I^+(^1D_2)$.

High Pressure Gas and Liquid Phase. Figure 7 shows the variation of total organic product yield with density. The curve is of the characteristic sigmoid shape that has been previously reported by various workers[14,15,17,38-40] consisting of three regions: the first ($\rho < 0.1$ g cm^{-3}) exhibiting increased stabilization of organic products; secondly, a "leveling" region ($0.1 < \rho < 0.43$ g cm^{-3}) of approximately constant product yield; and thirdly, a region ($\rho > 0.43$ g cm^{-3}) of rapidly increasing product yield. While no quantitative assessment of contributions can be made without complete characterization of *all* products, the final region must be ascribed to a *combination* of stabilization and enhancement reactions since it has been demonstrated[14-16,40] that neither type of reaction can wholly explain the total organic product yield behavior in this region. The TOPY curve in the region $0.007 < \rho < 0.059$ g cm^{-3} was interpolated from intermolecular distance data because of condensation of butene-1 above 3 atm pressure (0.007 g cm^{-3}). No intermediate data points could be obtained as a result of experimental difficulties.

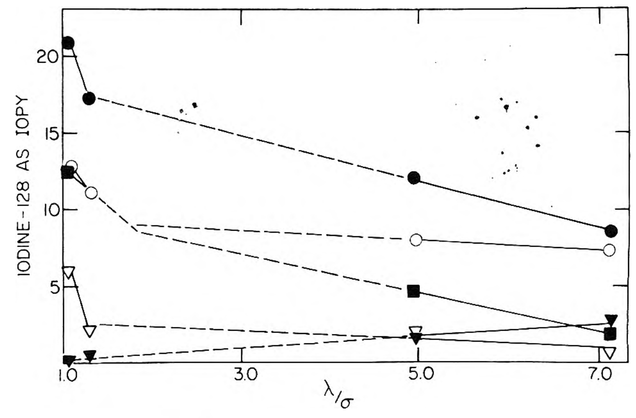

Figure 8. Variations of individual organic product yields as a function of normalized intermolecular distance: CH_3I (●); C_4H_9I (○); C_4H_7I (■); C_2H_5I (▽); C_2H_3I (▼).

Presented in Figure 8 is the behavior of the individual organic product yields (except C_3H_7I) with normalized intermolecular distance (λ/σ).[14,15,17,40] λ represents the average intermolecular distance between "point" or "center-of-mass" molecules and σ represents the molecular diameter of butene-1 along the carbon-chain axis. With the exception of the vinyl iodide yield, *which is a monotonically decreasing function of* λ/σ, the individual organic product yields consist of two approximately linear segments. The first ($\lambda/\sigma > 1.11$) is a slightly increasing function with decreasing λ/σ, while the second ($\lambda/\sigma < 1.11$) has a larger (negative) slope. The first segments are the result of increased stabilization of organic products that result from molecular reactions. It should be noted that the products CH_3I and $C_2H_5CH{=}CHI$ are more sensitive to environmental changes (stabilizing collisions) than the other organic products. By contrast, vinyl iodide appears to be *collisionally destabilized* as evidenced by the decrease in vinyl iodide yield with decreasing intermolecular distance and may be *the result of a decomposition mode of a unimolecular reaction.* The second segments are the results of enhancement reactions. Enhancement reactions are reactions in which the solvent molecules form an "envelope" around the reactants for a sufficient time to allow reaction. These multimolecular reactions are typified as "caging"[17,38,41-46] and/or stabilization of an electronically excited reaction complex.[14-16,39] Systems which are non-RRKM have been observed[47-51] and the suggestion[14,15,38] of similar behavior for electronically excited complex has been made.

It has been shown that enhancement reactions may commence with λ/σ values corresponding to high pressure gas,[17] phase change,[14] and the liquid state.[15] The ^{128}I-butene-1 system shows the last correspondence where the enhancement reactions occur after condensation has taken place. Of greater interest is the fact that enhancement commences at $\lambda/\sigma \approx 1.1$ for CH_3I and C_2H_5I whereas for C_4H_9I and $C_2H_5CH{=}CHI$ enhancement occurs at $\lambda/\sigma \approx 1.8$.

Possible Product Formation Routes. The previously discussed product yields at 1 atm (with and without additives) and at higher densities (smaller intermolecular distances) are summarized in Table I. The information presented suggests much as to the nature of the reactions of high energy iodine species (atoms and/or ions) with butene-1 molecules. To formulate a concise model for these reactions we must consider all possible reactions and reject or accept each on the basis of additive and gas to condensed phase studies.

Rare gas additive studies demonstrate the predominance of high energy reactions in the gaseous iodine-128–butene-1

TABLE II: Comparison of Product Formation Routes with Experimental Data

Product/route	Radical scavenger evidence (agreement/disagreement)	Gas to condensed phase transition evidence (agreement/disagreement)
CH_3I	Decrease	Increase
5 Substitution for $CH_3\cdot$	No	Yes
2 Cleavage of double bond	Yes	Yes
8,9 Complex formation decomposition	Yes	No
C_2H_3I	Unchanged	Decrease
4 Substitution of $CH_3CH_2\cdot$	Yes	No
8,10 Complex formation decomposition	Yes	Yes
15 Decomposition of $[C_2H_5I]_{exc}$	Yes	Yes
C_2H_5I	Decrease	Increase
3 Substitution for $CH_2{=}CH\cdot$	No	Yes
8,11 Complexation Decomposition abstraction of $H\cdot$	Yes	No
$C_2H_5CH_2I$	Decreased (to zero)	Increase
6 Substitution for $CH_3\cdot$ Abstraction of $H\cdot$	No	Yes
8,12 Complexation Elimination of (CH)	Yes	No
1 Substitution for CH_2 Abstraction of H	Yes	Yes
$C_2H_5CH{=}CHI$	Decrease	Increase
7 Substitution for vinyl H	No	Yes
8,13 Complexation Elimination of H	Yes	Yes
$C_3H_7CH_2I$	Decrease	Increase
8,14 Complexation abstraction of $H\cdot$	Yes	Yes

system. Only 3.0% of 21.4% of iodine stabilized as organic products at 1 atm was due to thermal reaction, and that was solely the reaction of $I^+(^1D_2)$ to form CH_3I. Regardless of the nature of O_2 inhibition, the O_2 additive study is of importance in that the reduction or elimination of reactions products suggests much as to the nature of product formation, viz. direct substitution or complexation.

The gas to condensed phase transition data suggest the difference between molecular and enhancement reactions. While there exists many theories of the nature of enhancement reactions,[14,17,39,40,44,52] *the effect of varying intermolecular distance on product yields provides definitive separation of molecular and cage sensitive (multimolecular) reactions.*

The following reactions[53] between iodine and butene-1 must be considered as possible routes toward the formation of the observed products:

$$CH_3CH_2CH{:}CH_2 + (I)_{exc} \rightarrow CH_3CH_2CHI + {:}CH_2 \quad (1)$$

$$\rightarrow CH_3CH_2CH + CH_2I \quad (2)$$

$$\rightarrow CH_3CH_2I + \cdot CH{=}CH_2 \quad (3)$$

$$\rightarrow CH_3CH_2 + ICH{=}CH_2 \quad (4)$$

$$\rightarrow CH_3I + CH_2CH{=}CH_2 \quad (5)$$

$$\rightarrow \cdot CH_3 + ICH_2CH{=}CH_2 \quad (6)$$

$$\rightarrow CH_3CH_2CH{=}CHI + H \quad (7)$$

$$\rightarrow [CH_3CH_2CHCH_2I]_{exc} \quad (8)$$

$$[CH_3CH_2CHCH_2I]_{exc} \rightarrow CH_3I + CH_3CH_2C \quad (9)$$

$$\rightarrow CH_2{=}CHI + CH_3CH_2 \quad (10)$$

$$\rightarrow CH_2{=}CH + CH_3CH_2I \quad (11)$$

$$\rightarrow CH_3CH_2CH_2I + (CH) \quad (12)$$

$$\rightarrow CH_3CH_2CH{=}CHI + H \quad (13)$$

$$\rightarrow CH_3CH_2CH_2CH_2I \quad (14)$$

$$[C_2H_5I]_{exc} \rightarrow C_2H_3I + (2H) \quad (15)$$

Direct substitution reactions may be favored for high energy reactions and/or certain thermal reactions, but the intermediate energies of iodine require a closer examination of all available data before a reaction scheme may be postulated. Table II summarized the O_2 additive and gas to condensed phase transition behaviors of the individual organic products and tests the validity of possible formation routes. The cleavage of the butene double bond (2) followed by abstraction of hydrogen from surrounding molecules appears to be in agreement with the radical behavior observed for CH_3I and the gas to condensed phase transition increase in yield. Abstraction of hydrogen is an endoergic process that provides an energy "sink" for the $\cdot CH_2I$ moiety allowing a decrease in internal energy. Vinyl hydrogens (on the nontarget molecules) are more acidic than the alkane hydrogens and may lower the energy barrier necessary for abstraction to occur. Yet it must be recalled that CH_3I is the only product not solely formed via high energy reaction; viz., 3.0% is the result of $I^+(^1D_2)$. Regardless of the nature of the thermal iodine species, the existence of thermal reaction product is sufficient in itself to suggest a reaction pathway other than via high energy. Complex formation (8) followed by decomposition (9) may show the correct O_2 additive behavior, but, as a decomposition which must show negative pressure dependence, cannot be consistent with gas to condensed phase transition data. The product formation route (5) (direct substitution at the terminal methyl group) concurs with these observations. We may reasonably conclude that the formation of CH_3I occurs from two independent routes.

In addition to methyl iodide three other products are present at 30 mol % O_2 additive: ethyl iodide, 1-iodobutane, and 1-iodobutene. This strongly suggests these products may be formed in part by complexation or other long term product formation routes. Yet, the large quantity of additive used did not reduce the product yield to zero, as in 1-iodopropane, suggesting the presence of direct (substitution) reactions. (1-Iodobutane is of course dependent on an external hydrogen source.) Vinyl iodide appears anomalous in that it displays negative pressure dependence while remaining unaffected by O_2.

Two product formation routes are proposed for the formation of ethyl iodide: direct substitution (3) and complexation (8) followed by decomposition (11). Neither route, of itself, is completely satisfactory. Direct substitution shows the proper phase dependence but is inconsistent with O_2 additive data. Conversely, while complexation may be subject to O_2 intervention, the decomposition would show a *negative* pressure dependence. This evidence and residual yields of 1-iodobutene-1 in the presence of O_2 suggest that *these products are most probably the result of more than one product formation route.*

Of the proposed product formation routes for vinyl iodide, direct substitution (4) must be immediately rejected. Any substitution event must show an increase in product yield with increasing density, a trend which is opposite to that observed in the gas to condensed phase transition. Decomposition of a butene–iodide complex (8,11) while consistent with the negative pressure dependence observed is not in agreement with oxygen additive data. A solution must be found elsewhere. Vinyl iodide appears to be either remotely dependent or independent of the reaction system. A suggested product formation route is that of reaction 15. In this reaction vinyl iodide is dependent on the precursor, an excited ethyl iodide molecule. The independence of vinyl iodide yield from O_2 additive further suggests that the ethyl iodide is originally formed by a direct substitution event. This excited ethyl iodide may then, independently, eliminate hydrogen to form the product vinyl iodide. This elimination/decomposition is consistent with the experimental facts.

The complete quenching of the 1-iodopropane yield by O_2 addition suggests that formation by direct substitution (6) is not a major consideration. Complexation followed by decomposition (8,12) is also, at best, of minor importance in light of the increase in product yield observed with increasing pressure. The complementary reaction to radical formation of CH_3I, reaction 1, suggests that the substitution of I for the methylene group in butene-1 would result in the proper pressure dependence and be radical in nature.

The yield of 1-iodobutene rapidly increases with pressure while being substantially reduced by the presence of O_2. Two formation routes are possible: direct substitution (7) of iodine for a vinyl hydrogen or a complexation/elimination (8,13) sequence, an equivalent path but requiring a much longer time period. The latter sequence displays the correct behavior with both gas to condensed phase and O_2 additive data, but in light of a residual yield observed in the presence of O_2, and in the absence of other data, both mechanisms must be considered.

1-Iodobutane must be the result of complexation (8) followed by the abstraction of hydrogen (14). A direct substitution reaction cannot be postulated that in one concerted step allows for both the capture of iodine and saturation of the iodobutene moiety. At first an addition reaction between the butene and the inorganic product $H^{128}I$ may be thought possible but the major product would be 2-iodobutane rather than the observed product 1-iodobutane. Also, such an addition would be thermal in nature yet the moderation (rare gas additive) studies show that no thermal reactions are involved in the formation of 1-iodobutane.

A question arises as to the ratio of C_4H_9I/C_4H_7I. The ratio decreases with increasing moderation (less energy available) but also with increasing pressure. If we seriously consider the major formation route of the unsaturated compound as via a complexation/elimination reaction (8,13) we are faced with further inconsistencies. Hydrogen abstraction (14) is a lower energy and therefore more probably process than elimination (13). This may be compensated by the higher instability of the newly formed excited olefinic molecule, resulting in the two products having approximately the same excitation energy. Although the saturated compound has six more internal degrees of freedom than the unsaturated compound, the most probable decompositions of these molecules are compensatory. The decomposition of 1-iodobutane would most likely be HI or I elimination, a process with a much lower activation energy than the C–C bond rupture most probable for the decomposition of 1-iodobutene.

In light of the conflicting evidence, close examination of the gas to condensed phase data is necessary. The saturated compound shows a more gradual increase with density than the iodobutene. *Only in the condensed phase do the two yields become approximately equal.* We feel that while in the low pressure gas region the primary formation route may be complexation the enhancement observed, particularly in the condensed phase, is the result of direct substitution reactions.

While other products may be formed by the reaction of radicals with other olefin molecules, their presence, qualitatively and quantitatively, cannot be determined as a result of experimental limitations. Thus, no statement postulating their origin or even existence can be made.

Although it would be desirable to compare the ethene and propene system with butene-1, it is not feasible to present a coherent picture at this time. The rare gas, O_2, and I_2 additive studies of ethene and propene suggested the presence of ion–molecule reactions. Opposite trends are observed in the butene-1 system where complexation and substitution reactions appear to be dominant. It is hoped that a cohesive picture of iodine reactions with olefins may be presented after the completion of our current study of all isomers of butene.

Summary

The reactions of iodine with butene-1 are very complex with contributions from direct substitution, complex formation, and possibly other mechanisms. These competing reactions, often with the same observable product, contribute in differing ways and may appear dominant under certain system conditions while recessive in others. Regardless of this, it appears that of 21.4% total organic product 15.4% of the yield is from reactions on or near the double bond. If the reaction of iodine was nonselective (random site attack) we would expect yields at the π bond to be no greater than 25–50%. We feel that preferential site attack as a result of the intermediate energies of iodine-128 activated by radiative neutron capture and the electrophilic nature of iodine makes iodine a sensitive probe of new reaction channels, viz. high energy electrophilic attack.

References and Notes

(1) This research was supported by the United States Energy Research and Development Administration Contract No. E(11-1)-1617. This is E.R.D.A. document No. COO-1617-48.

(2) R. L. Ayres, O. C. Gadeken, and E. P. Rack, *J. Phys. Chem.*, **75**, 2880 (1971).

(3) R. L. Ayres, C. J. Michejda, and E. P. Rack, *J. Am. Chem. Soc.*, **93**, 1389 (1971).

(4) A. Loventhal, M. Kim, and E. P. Rack, *Radiochim. Radioanal. Lett.*, **26**, 239 (1976).

(5) R. R. Pettijohn and E. P. Rack, *J. Phys. Chem.*, **76**, 3342 (1972).

(6) D. Urch and R. Wolfgang, *J. Am. Chem. Soc.*, **81**, 2025 (1959).

(7) J. K. Lee, B. Musgrave, and F. S. Rowland, *J. Am. Chem. Soc.*, **82**, 3545 (1960).

(8) E. K. C. Lee and F. S. Rowland, *J. Am. Chem. Soc.*, **84**, 3085 (1962).

(9) A. H. Rosenberg and R. Wolfgang, *J. Chem. Phys.*, **41**, 2159 (1964).

(10) R. L. Williams and F. S. Rowland, *J. Am. Chem. Soc.*, **94**, 1047 (1972).

(11) R. L. Williams and F. S. Rowland, *J. Phys. Chem.*, **77**, 301 (1973).

(12) R. Milstein, R. L. Williams, and F. S. Rowland, *J. Phys. Chem.*, **78**, 857 (1974).
(13) W. S. Smith, S. H. Daniel, and Y.-N. Tang, *J. Phys. Chem.*, **76**, 2711 (1972).
(14) K.-C. To, M. E. Berg, and E. P. Rack, *J. Phys. Chem.*, **80**, 1411 (1976).
(15) M. E. Berg, A. Loventhal, D. J. Adelman, W. W. Grauer, and E. P. Rack, *J. Phys. Chem.*, submitted for publication.
(16) M. D. Loberg, K. A. Krohn, and M. J. Welch, *J. Am. Chem. Soc.*, **95**, 5596 (1973).
(17) M. E. Berg, W. M. Grauer, R. W. Helton, and E. P. Rack, *J. Phys. Chem.*, **79**, 1327 (1975).
(18) The total organic product yield (TOPY) is the fraction of ^{128}I activity organically bound and is equal to OA/(OA + IA) × 100% where OA is the activity of the organic fraction and IA is the activity of the inorganic fraction of the extracted sample after corrections for isotopic decay. Individual organic product yield (IOPY) values represent the fraction of activity chemically bound with a specific organic substrate. Integration of radiogas chromatographic peaks, corrected for isotope decay and radiolytic contributions and normalized to the TOPY value, are used in the assignment of these values.
(19) W. E. Rice and J. E. Willard, *J. Am. Chem. Soc.*, **75**, 6156 (1953).
(20) R. C. Wackker, C. B. Linn, and A. V. Grosse, *Ind. Eng. Chem.*, **37**, 464 (1945).
(21) Technical Committee, National Gasoline Association of America, *Ind. Eng. Chem.*, **34**, 1240 (1942).
(22) M. Yoong, Y. C. Pao, and E. P. Rack, *J. Phys. Chem.*, **76**, 2685 (1972).
(23) T. A. Carlson and R. M. White, *J. Chem. Phys.*, **44**, 4510 (1966).
(24) S. Wexler and H. Davies, *J. Phys. Chem.*, **20**, 1688 (1952).
(25) E. P. Rack and A. A. Gordus, *J. Chem. Phys.*, **34**, 1855 (1961).
(26) A. A. Gordus and J. E. Willard, *J. Am. Chem. Soc.*, **79**, 4609 (1957).
(27) A. A. Bothner-By and C. Naer-Colin, *J. Am. Chem. Soc.*, **83**, 231 (1961).
(28) A. A. Bothner-By, C. Naer-Colin, and H. Gunther, *J. Am. Chem. Soc.*, **84**, 2748 (1962).
(29) S. Kondo, E. Hirota, and Y. Morino, *J. Mol. Spectrosc.*, **28**, 471 (1968).
(30) P. B. Woller and E. W. Garbisch, *J. Org. Chem.*, **37**, 4281 (1972).
(31) R. W. Kiser, "Tables of Ionization Potentials", U.S. Atomic Energy Commission, Office of Technical Information, No. TID-6142, 1960.
(32) The individual organic product yields of ethyl iodide and 1-iodopropane were not plotted because of the relative large errors associated with the small yields of these products.
(33) E. P. Rack and A. A. Gordus, *J. Chem. Phys.*, **36** 287 (1962).
(34) P. J. Estrup and R. Wolfgang, *J. Am. Chem. Soc.*, **82**, 2661 (1960).
(35) R. Wolfgang, *J. Chem. Phys.*, **39**, 2983 (1963).
(36) S. Glasstone, "The Elements of Nuclear Reactor Theory", Van Nostrand, New York, N.Y., 1952.
(37) The kinetic theory serves to express experimental data in terms of two parameters: (1) the reactivity integrals I_i and I which can be expressed as a function of the probability of reaction to form the particular product (I_i) or all the products (I) upon collision at energy E; (2) α values, the average logarithmic energy loss upon collision. Using the notations of Estrup and Wolfgang we have plotted $-1/\ln(1 - P)$ vs. $(1 - f_{\text{reaction}})/f_{\text{reaction}}$ (Figure 5) where P is the total probability of a high energy atom combining in any product and f_{reaction} is the relative probability of collision with 1-butene. Xe data are not plotted due to anomalous data resulting from the charge transfer process between Xe and $I^+(^1D_2)$.
Depicted in Figure 6 is a plot of $\alpha(P_i/f)$ vs. f/α where α is the weighted average of α values for each of the components and P_i is the total probability of a high energy atom combining to form a particular product i. As a result of the small yields of vinyl iodide, ethyl iodide, 1-iodopropane, and 1-iodo-1-butene only methyl iodide and 1-iodobutane are plotted. In each of the above plot corrections have been made for the 3% thermal contributions to the TOPYs and IOPYs. These two plots show that within limits of experimental error, our results are consistent with the kinetic theory. The following are the values obtained: $\alpha = 1.04 \pm 0.35$, $I = 0.21 \pm 0.03$, $I_i(CH_3I) = 0.058 \pm 0.026$, $K_i(CH_3I) = 0.0043 \pm 0.008$, $I_i(C_4H_9I) = 0.081 \pm 0.030$, and $K_i(C_4H_9I) = 0.0056 \pm 0.0010$. The parameters are expressed in units of K_{I-Kr}.
(38) A. E. Richardson and R. Wolfgang, *J. Am. Chem. Soc.*, **92**, 3480 (1970).
(39) H.-J. Machulla and G. Stöcklin, *J. Phys. Chem.*, **78**, 658 (1974).
(40) R. G. Manning and J. W. Root, *J. Phys. Chem.*, **79**, 1478 (1975).
(41) J. Franck and E. Rabinowitsch, *Trans. Faraday Soc.*, **30**, 120 (1934).
(42) R. M. Noyes, *J. Chem. Phys.*, **18**, 999 (1950).
(43) F. W. Lampe and R. M. Noyes, *J. Am. Chem. Soc.*, **76**, 2140 (1954).
(44) A. J. Cole, M. D. Mia, G. E. Miller, and P. F. D. Shaw, *Radiochim. Acta*, **9**, 194 (1968).
(45) C. Walling and A. R. Lepley, *Int. J. Chem. Kinet.*, **3**, 97 (1971).
(46) D. L. Bunker and B. S. Jacobson, *J. Am. Chem. Soc.*, **94**, 1843 (1972).
(47) C. T. Ting and F. S. Rowland, *J. Phys. Chem.*, **74**, 4080 (1970).
(48) J. D. Rynbrandt and B. S. Robinovitch, *J. Chem. Phys.*, **54**, 2275 (1971).
(49) D. L. Bunker, *J. Chem. Phys.*, **57**, 332 (1972).
(50) Y.-N. Tang and Y. Y. Su, *J. Chem. Phys.*, **57**, 4048 (1972).
(51) D. L. Bunker and W. L. Hase, *J. Chem. Phys.*, **59**, 4621 (1973).
(52) M. Milman, *Radiochem. Acta*, **1**, 15 (1963).
(53) Iodine may react as a neutral atom (initially formed or as the result of charge neutralization) or as an ion either in ground or electronically excited states. (See, for example, ref 2–5, 14–16, etc.) For reader convenience the presence or absence of charge has not been included in these reactions.

Photochemistry and Photophysics of Hexafluoroacetone Vapor at Low Pressures[†]

P. A. Hackett* and K. O. Kutschke

Division of Chemistry, National Research Council of Canada, Ottawa, Canada K1A 0R6 *(Received January 25, 1977)*

Publication costs assisted by the National Research Council of Canada

We have interpreted the low pressure phosphorescence and fluorescence yields and decay curves of hexafluoroacetone as evidence for the existence of sharp discontinuity in the hexafluoroacetone triplet state potential energy surface; triplet state molecules formed above this barrier decompose with unit efficiency, those formed below this barrier decompose as the result of a thermal decomposition. Furthermore, evidence is discussed for the transfer of the ground state thermal distribution to the excited electronic states. The mechanism leads us to conclude that the intersystem crossing rate constant for simple fluorinated ketones increases linearly as the internal energy is raised.

Introduction

The photochemistry of hexafluoroacetone subsequent to excitation of its first excited singlet state is not yet fully understood. Recently several groups have speculated on the excited state leading to the photodissociation reaction:[1]

$$CF_3COCF_3^* \rightarrow CF_3CO + CF_3 \rightarrow 2CF_3 + CO$$

Halpern and Ware[2] have investigated the variation in the rate of nonradiative processes depleting the excited singlet state at low pressures, as a function of the internal energy of the excited state. They suggest that it is possible that the sharp rise in this rate constant at internal energies greater than 6000 cm^{-1} is due to decomposition of the excited singlet state. Knecht[3] has analyzed the pressure dependence of the quantum yield of carbon monoxide production and concludes that intersystem crossing

---

[†] Issued as N.R.C.C. No. 16016.

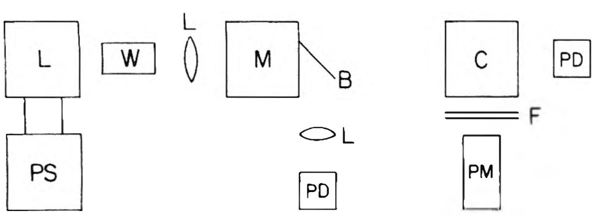

Figure 1. Apparatus used to measure quantum yields of emission: PS, Hewlett-Packard 6269B power supply; L, 1000-W xenon arc lamp; L, lens; M, Schoeffel GM250 0.25-m monochromator; B, quartz beam splitter; PD, RCA 935 photodiode; F, Corning CS 0-51 glass filter; PM, EMI 6256 photomultiplier; C, cell (phosphorimeter, Woods horn or T shaped fluorescence cell).

precedes decomposition at low internal energies, but that internal conversion increases in importance as the internal energy is raised, with the internal conversion rate being equal to the intersystem crossing rate at internal energies of 3000 cm^{-1}. Servidio and Pritchard[4] have reinvestigated the quantum yield of carbon monoxide production in the presence of vibrational relaxers and triplet quenchers at various temperatures and pressures and report an activation energy of 2000 $\mathrm{cm}^{-1}\ \mathrm{mol}^{-1}$ for the unimolecular decomposition of the upper singlet state.

In order to establish the energy dependence and nature of the nonradiative processes depleting the first excited singlet and triplet states of hexafluoroacetone we have measured the lifetime and quantum yield of emission from these excited states as a function of incident photon energy, at low pressures. The implications of these results to other studies of hexafluoroacetone photochemistry will be discussed.

Experimental Section

(a) *Materials.* Hexafluoroacetone was obtained from Matheson Co. and *cis*-butene from Phillips. All materials were completely degassed and distilled on the vacuum line, the middle portion of each being retained. Sulfur dioxide was detected as an impurity in the hexafluoroacetone used in concentrations of 1–10 ppm,[5] however, there was no measurable effect on the phosphorescence lifetime of hexafluoroacetone at hexafluoroacetone pressures of less than 10 Torr.

A mercury free vacuum system equipped with greaseless stopcocks was used to transfer gases. Pressures were measured with either of two Baratron pressure gauges, one with a range of 0–1.2 Torr, the other with a range of 0–1200 Torr. The low pressure gauge was calibrated using a precision oil manometer.

(b) *Fluoroescence Quantum Yields and Lifetimes.* Fluorescence quantum yields were measured using the apparatus illustrated in Figure 1. The first step was to determine the extinction coefficient [$\epsilon(\lambda)$] of hexafluoroacetone in the apparatus at a particular excitation wavelength [λ], from plots of optical density against pressure. Such plots yielded good straight lines at all wavelengths. The following procedure was then carried out at every excitation wavelength: the background scattered light was measured by evacuating the cell [${}^0I_E$]; the incident light intensity was measured [${}^0I_T$]; pressures [P] between 0.01 and 1.10 Torr of hexafluoroacetone and 0.2 Torr of isobutene were introduced into the cell, allowed to equilibrate, and the emitted light intensity [${}^PI_E$] was measured; the intercept [${}^0Q(\lambda)$] of plots of

$$Q(\lambda) = \frac{{}^PI_E - {}^0I_E}{{}^0I_T P} \tag{1}$$

against pressure was then determined.

The wavelength dependent sensitivity [$\gamma(\lambda)$] of the beam splitter–photodiode combination used to determine $I_T(\lambda)$ was measured by replacing the cell with rhodamine 6G and sodium salicylate quantum counters.[6] The wavelength corrected relative fluorescence efficiencies at zero pressure of hexafluoroacetone were then obtained from the relationship:

$$ {}^0R(\lambda) = {}^0Q(\lambda)\gamma(\lambda)/\epsilon(\lambda) \tag{2}$$

$Q(\lambda)$ was also determined for a sample of 0.5 Torr of hexafluoroacetone plus 0.2 Torr of isobutene plus 760 Torr of carbon dioxide [${}^\infty Q(\lambda)$]. The wavelength corrected relative fluorescence efficiencies under these conditions were then obtained from the relationship:

$$ {}^\infty R(\lambda) = {}^\infty Q(\lambda)\gamma(\lambda)/\epsilon(\lambda) \tag{3}$$

The conversion of these results to absolute quantum yields will be discussed in a later section.

At wavelengths of 352, 318, 313, and 285 nm $Q(\lambda)$ was determined for hexafluoroacetone pressures up to 40 Torr, making appropriate corrections for the geometry of the fluorescence cell at the higher pressures.[7]

Fluorescence lifetimes were measured using the time correlated single photon counting system described in detail elsewhere.[8] However, it is important to note that the excitation source was a free running 24-kV spark lamp, operated in a high pressure of nitrogen (≈4 atm) at a frequency of 20 kHz. The emission spectrum of this lamp is a continuum similar to that obtained from a high-pressure xenon arc lamp and this allowed us to measure fluorescence decay curves over the same range of excitation wavelengths as fluorescence quantum yields were measured.

(c) *Phosphorescence Quantum Yields and Lifetimes.* Phosphorescence lifetimes were measured using a small rotating can phosphorimeter fitted with a can with two 120° closed sections and two 60° open sections; the can was rotated at 3600 rpm by a Bodine synchronous motor. The incident light intensity was monitored after the phosphorimeter by an RCA 935 photodiode, the signal from this photodiode could be passed through an FET input switching circuit in order to derive a trigger signal.[9] Hexafluoroacetone was contained in a 40-mm diameter cylindrical cell made from Suprasil A placed inside the phosphorimeter. The decay of the phosphorescence was displayed in one of two ways, either in an analogue fashion on a Tektronix 7633 storage oscilloscope, or by counting photons in an Ortec 6220 multichannel analyzer, using in multichannel scaling mode. The multichannel analyzer was triggered by every other trigger pulse and was run until enough counts had been accumulated to adequately define the phosphorescence decay curve. The phosphorescence decay time was measured as 3.4 ms at all wavelengths of excitation and at all pressures in the range 0.5–10.0 Torr.

The invariance of the phosphorescence lifetime allows the above apparatus to be used to measure phosphorescence yields at low pressures. This was accomplished in the following way at every wavelength of excitation [λ]. The background scattered light intensity was measured by evacuating the cell [${}^0I_E$]; the incident light intensity [${}^0I_T$] was measured; a pressure [P] of hexafluoroacetone between 0 and 1.1 Torr was transferred to the cell and allowed to equilibrate and the emitted light intensity was measured. $S(\lambda)$ was then plotted against pressure where

$$S(\lambda) = \frac{{}^PI_E - {}^0I_E}{{}^0I_T P} \tag{4}$$

and the value ${}^0S(\lambda)$ was obtained by extrapolating the results measured at hexafluoroacetone pressures between 0.4 and 1.1 Torr to obtain the intercept at zero pressure.

The wavelength corrected relative phosphorescence efficiencies at zero pressure of hexafluoroacetone [${}^{0}T(\lambda)$] were found by determining $S(\lambda)$ for a mixture of 0.5 Torr of hexafluoroacetone and 760 Torr of carbon dioxide [${}^{\infty}S(\lambda)$]; the quantum yield of phosphorescence from this mixture should be independent of exciting wavelength,[10] thus the function

$${}^{0}T(\lambda) = {}^{0}S(\lambda)/{}^{\infty}S(\lambda) \qquad (5)$$

corrects for variation in ϵ and γ with exciting wavelength.

The conversion of these results to absolute quantum yields of phosphorescence emission will be discussed in a later section.

(d) *Experiments with Nitrogen Laser Excitation.* Several experiments were performed using the 1 MW nitrogen laser described in an earlier paper.[11] Fluorescence decay curves were measured in a single shot mode using a Tektronix 7663 storage oscilloscope. The response time of the excitation and detection system was less than 10 ns. Fluorescence decay times of 0.2 Torr of hexafluoroacetone were measured at 22, 60, and 90 °C by deconvoluting the observed excitation pulse from the observed fluorescence decay.

Phosphorescence efficiencies of low pressures of hexafluoroacetone contained in a 5-L pyrex flask were measured in single shot mode. The phosphorescence decay signal was captured by a Biomation 805 transient digitizer and plotted on a Hewlett-Packard 7044A X-Y recorder. The incident laser intensity [I_L] was captured on a Tektronix 7663 storage oscilloscope with a 7A13 differential comparator, by an RCA 935 photodiode which viewed the transmitted laser pulse through several attenuating filters. The intercept of the phosphorescence decay signal at zero time [I_P] was obtained from semilog plots. The phosphorescence efficiency (N) at pressure P was given by

$$N = I_P/(PI_L) \qquad (6)$$

A search for nonexponential phosphorescence decay of 0.3 Torr of hexafluoroacetone at room temperature was made by interfacing the transient digitizer to a Hewlett-Packard 5480A memory display. The response time of the detection system was adjusted to be less than 0.2 μs and 1024 phosphorescence decays were averaged in the memory display. The procedure was repeated with the flask evacuated. No nonexponential phosphorescence was observed in the first 200 μs of the decay.

Results

Plots of Q against pressure of hexafluoroacetone at various wavelengths of excitation are shown in Figure 2. Values of ${}^{0}Q(\lambda)$ inferred from these plots were substituted into eq 2 to derive ${}^{0}R(\lambda)$ which is plotted against λ in Figure 3. Figure 3 also shows the values of ${}^{\infty}R(\lambda)$ deduced from eq 3.

Fluorescence decay curves measured in this study showed the same pressure dependence noted by other workers.[2] At high pressures the fluorescence had a single exponential form with an exponent which was independent of pressure and wavelength of excitation. At intermediate pressures the form of the decay was multiexponential and dependent on pressure and wavelength of excitation. At low pressures the fluorescence decay was again single exponential with a pressure independent but wavelength dependent exponent. Figure 4 shows plots of the reciprocal of the fluorescence decay time against excitation wavelength for several fluorinated ketones. The fluorescence decay times were derived from fluorescence decay curves accumulated at ketone pressures within the low pressure limit described above.

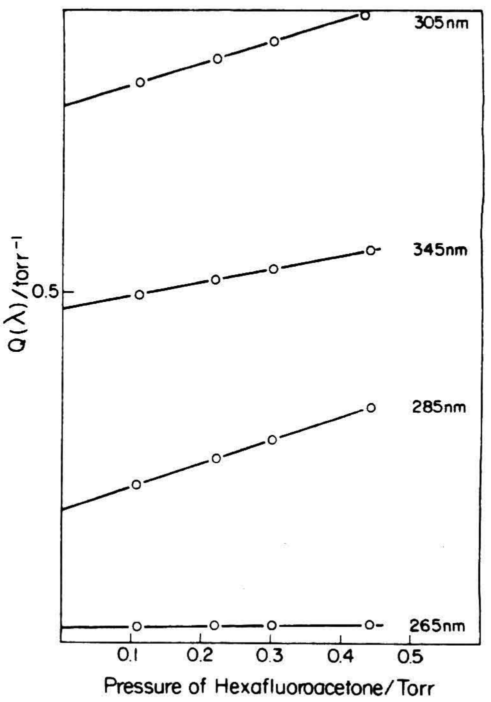

Figure 2. $Q(\lambda)$ vs. hexafluoroacetone pressure. Data obtained in Woods horn cell at 6.66-nm intervals, 22 °C, bandpass 1 nm.

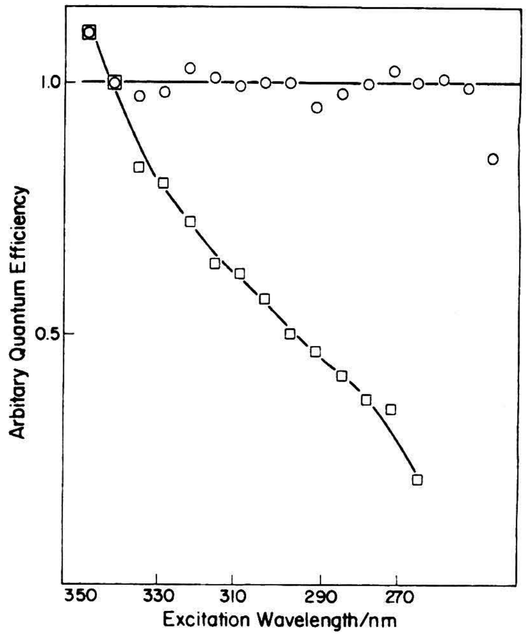

Figure 3. Values of ${}^{0}R(\lambda)$ (circles) and ${}^{\infty}R(\lambda)$ against wavelength of excitation for hexafluoroacetone at 22 °C. Values can be converted to absolute quantum yields assuming ${}^{\infty}R(\lambda) = 0.018_5$ (ref 13).

Figure 5 is a plot of $S(\lambda)$ against hexafluoroacetone pressure at various wavelengths of excitation. It can be seen that $S(\lambda)$ tends to zero at all wavelengths as the pressure decreases below 0.3 Torr. We attribute this behavior to quenching of hexafluoroacetone molecules at the walls of the cell. This is a reasonable assertion for many reasons. A calculation using the phosphorescence lifetime of hexafluoroacetone and the dimensions of the cell shows that such effects will be manifest at 0.3 Torr,[12] in the larger cell used in the nitrogen laser experiments (N vs. P) the effect only becomes apparent at 0.15 Torr;

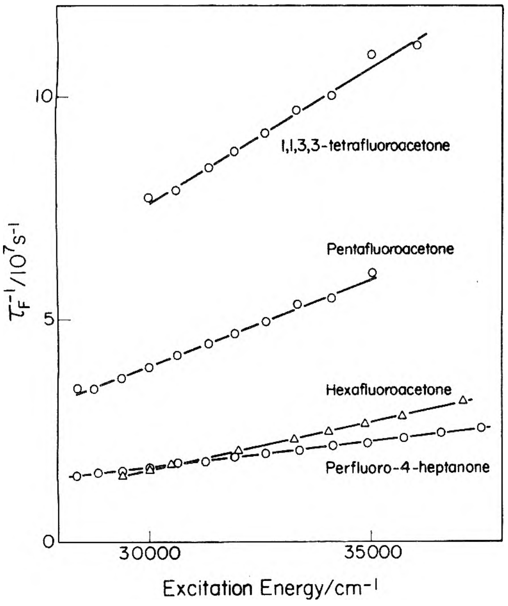

Figure 4. Values of inverse fluorescence decay time for fluorinated ketones at 22 °C. Pressures are 0.15 Torr for hexafluoroacetone and perfluoro-4-heptanone, 0.3 Torr for pentafluoroacetone, and 0.5 Torr for 1,1,3,3-tetrafluoroacetone, bandpass 1 nm.

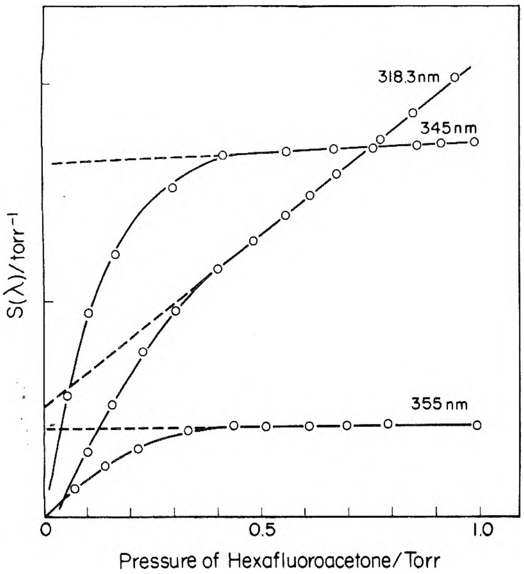

Figure 5. Phosphorescence intensity/pressure vs. hexafluoroacetone pressure: 22 °C, bandpass 1 nm. Similar curves were obtained at 3.33-nm intervals.

TABLE I: Fluorescence Lifetimes of Hexafluoroacetone, Nitrogen Laser Excitation

T, °C	P, Torr	τ_F, s × 10^{-9}
22	0.2	69
60	0.2	56
90	0.2	45

the molecule 2-furaldehyde, phosphorescence lifetime 1 ms, shows precisely similar behavior at pressures below 0.1 Torr.[11] To correct for this effect one could use larger cells or determine $S(\lambda)$ at low pressures of hexafluoroacetone in the presence of 0.3 Torr of inert gas, however, we have chosen the simpler expedient of extrapolating the values of $S(\lambda)$ determined between 0.4 and 1.2 Torr to zero pressure. Figure 6 shows a plot of $T_0(\lambda)$ derived from these intercepts against incident photon energy.

The values of fluorescence lifetimes of hexafluoroacetone determined by the nitrogen laser experiments are shown in Table I.

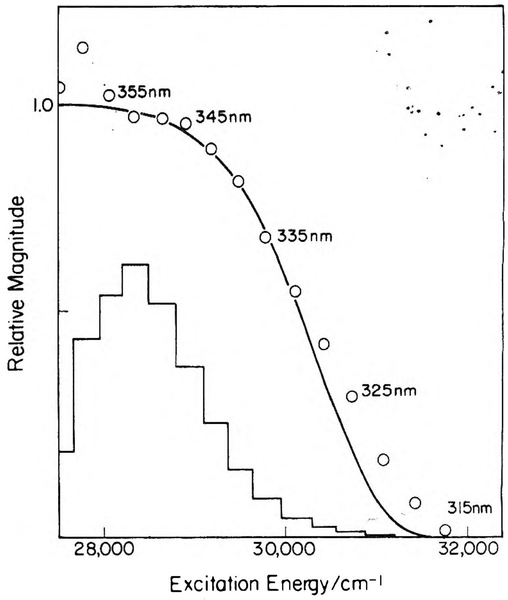

Figure 6. Values of zero pressure phosphorescence quantum efficiencies (open circles). Values are in arbitrary units and can be converted to absolute values by multiplying by 0.11_3, the high pressure phosphorescence quantum yield (ref 13). The histogram represents the ground state energy distribution, shifted by +27 500 cm^{-1}, at the experimental temperature 22 °C, used to derive the theoretical curve (solid line).

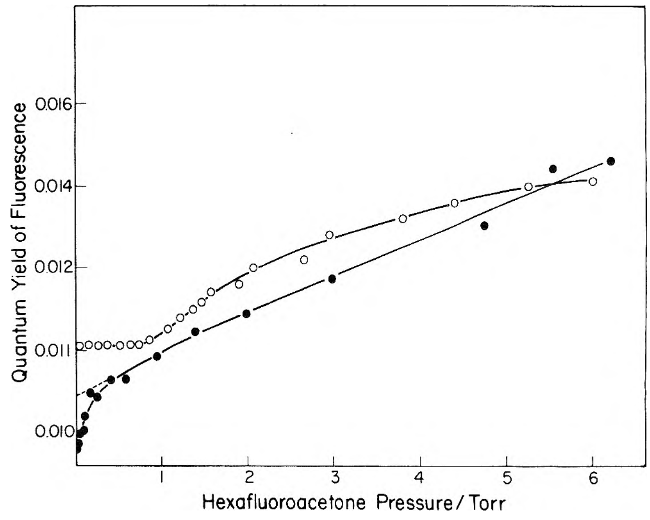

Figure 7. Quantum yield of hexafluoroacetone fluorescence excited at 313 nm vs. hexafluoroacetone pressure. Solid circles are data points from ref 13 and 14, open circles are data points from present study normalized to high pressure limit of 0.0185; temperature = 22 °C, bandpass = 1 nm, isobutene pressure = 0.2 Torr.

Before discussing the implications of these results to the photochemistry and photophysics of hexafluoroacetone we will compare them to the results from other studies. The constancy of $^{\infty}R(\lambda)$ confirms both the validity of the experimental method used in deriving $R(\lambda)$ and the observation of Gandini and Kutschke[13] that the high pressure quantum yields of fluorescence are equal (0.018_5) at 366-, 313-, and 265-nm excitation. These authors report the low pressure quantum yield of fluorescence to be 0.095 at 313 nm, 0.048 at 265 nm, and 0.014 at 254 nm.[13] However, we have reexamined the original data of Gandini and Kutschke[14] and conclude that the pressure dependence for 313-nm excitation below 0.2 Torr is erroneous. We have redetermined the values of $R(\lambda)$ in this pressure region and find a different pressure dependence. The two sets of data are shown in Figure 7. The error in the original data is almost certainly due to a mixing effect. Normalizing our data to a 313-nm value of 0.010_5 we would find values of 0.045 at 265 nm and 0.015 at 254 nm in reasonable agreement. Again, Thomas, Matuszewski, and Givens[15] find values of 0.021_4, 0.019_8, 0.011_5, and 0.006_4 following excitation at 334, 313, 302.5, and 291 nm. Normalizing our data to the 313-nm value we would find values of 0.026, 0.017, and 0.015 at 334, 302.5, and 291 nm. Clearly the zero pressure quantum yields measured by Thomas et al. vary much more rapidly with wavelength of excitation than the quantum yields measured in this and in an earlier study.[13] We cannot speculate on the source of this discrepancy, however, we note that the same workers report low pressure quantum yields of fluorescence for acetone which again vary more rapidly with excitation wavelength than do the results of a more recent determination of these parameters.[16]

The fluorescence decay times measured by Halpern and Ware[2] for 0.1 Torr of hexafluoroacetone excited at 357.7, 337, 316, and 297.7 nm agree precisely with results interpolated from Figure 4, and with that measured following nitrogen laser excitation at 337 nm. This is a gratifying result as the earlier results were obtained using a gated low pressure air spark as an excitation source. This lamp emits discrete lines from the nitrogen second positive transition and hence the spectral distribution of the exciting pulse was vastly different from the continuum source used here. However it would seem that the hexafluoroacetone molecule effectively averages the observed fluorescence decay time to that of the center frequency of the monochromator bandpass.

Previous measurements of the zero pressure quantum yield of phosphorescence[13] were made at wavelengths of excitation at which we find values of zero (265, 254 nm) or close to zero (313 nm), values of zero were reported at all three wavelengths. However, no mention was made of the wall effect on the phosphorescence yield in the earlier study. It is possible that this would account for the small discrepancy in the 313-nm results, or that the phosphorescence detected in this study was excited by longer wavelengths passed in the wings of the monochromator bandpass.

Discussion

The results reported above imply the following mechanism for low pressure hexafluoroacetone vapor:

$A_{th} + \frac{hc}{\lambda} \rightarrow A^1{}_n$	I_A
$A^1{}_n \rightarrow A + h\nu_f$	k_1
$A^1{}_n \rightarrow A$	k_2
$A^1{}_n \rightarrow A^3{}_q$	k_3
$A^3{}_q \rightarrow Y$	k_4
$A^3{}_q \xrightarrow{+A_{th}} A^3{}_{th}$	$k_5[A_{th}]$
$A^3{}_{th} \rightarrow CF_3CO + CF_3$	k_6
$A^3{}_{th} \rightarrow A + h\nu_P$	k_7
$A^3{}_{th} \rightarrow A$	k_8

where A, A^1, and A^3 refer to hexafluoroacetone molecules in the ground, excited singlet, and excited triplet states. The subscripts refer to the internal energy of the hexafluoroacetone molecule, the subscript th indicating an electronic state containing a thermally averaged distribution of excess energies. From this mechanism we obtain expressions for the quantum yield of fluorescence [$\Phi_F = k_1/(k_1 + k_2 + k_3)$], fluorescence decay time [$\tau_F = 1/(k_1 + k_2 + k_3)$], phosphorescence decay time [$\tau_P = 1/(k_6 + k_7 + k_8)$], and the quantum yield of phosphorescence [$\Phi_P = R_1R_2R_3$] where

$$R_1 = k_3/(k_1 + k_2 + k_3)$$

$$R_2 = k_5A_{th}/(k_5A_{th} + k_4)$$

$$R_3 = k_7/(k_6 + k_7 + k_8)$$

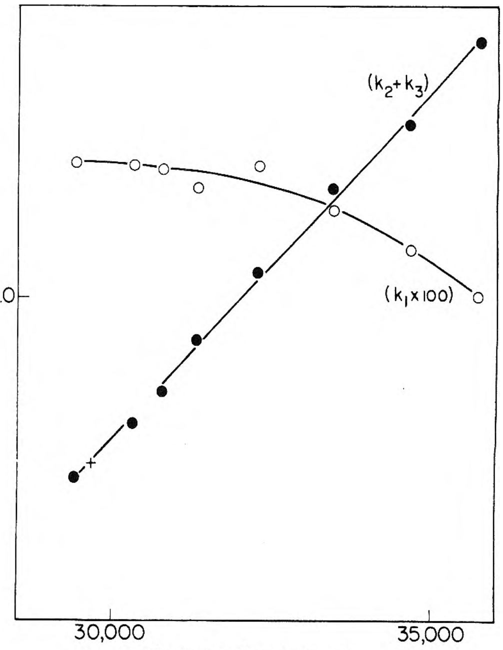

Figure 8. Energy dependence of the radiative rate constant (k_1) and the total nonradiative rate constant ($k_2 + k_3$) for hexafluoroacetone, at 22 °C: filled circles ($k_2 + k_3$); +, value of ($k_2 + k_3$) from N_2 laser excitation; open circles, k_1.

This mechanism allows us to unambiguously determine the excess energy dependence of k_1 and ($k_2 + k_3$). Plots of values of these quantities against excitation energy are shown in Figure 8.

It can be seen that the total nonradiative rate increases linearly with excess energy over the whole range of excess energies studied. We find no evidence for a sudden increase in nonradiative rate at high internal energies, as might be expected if a dissociative pathway from the excited singlet existed at internal energies accessible through light absorption. This result is in slight disagreement with a previous study[2] which found that τ_F decreased rapidly at high internal energies. However, this assertion was based upon τ_F values deduced from quantum yields of fluorescence, assuming that k_1 did not vary with excitation wavelength. We find k_1 to be wavelength dependent and hence the practice of deriving nonradiative rate constants from quantum yields[15] can lead to incorrect trends.

The internal energy dependence of the radiative rate has been reported for many other molecules. In formaldehyde[17] this rate constant is a function of the particular vibronic state, however, a general exponential decrease is noted as the internal energy increases. In other halogenated ketones[18] k_1 decreases as the energy increases. This behavior has been rationalized by Lin et al.[19] who have shown that, within the harmonic oscillator approximation for symmetry forbidden transitions, k_1 will decrease linearly if the frequency of the mode excited in the upper state is less than the ground state value. This holds for emission from single vibronic levels or from an ensemble of levels.

The trend in k_1 could originate in a fast competition in the vibrationally excited singlet state. Thus, optical ex-

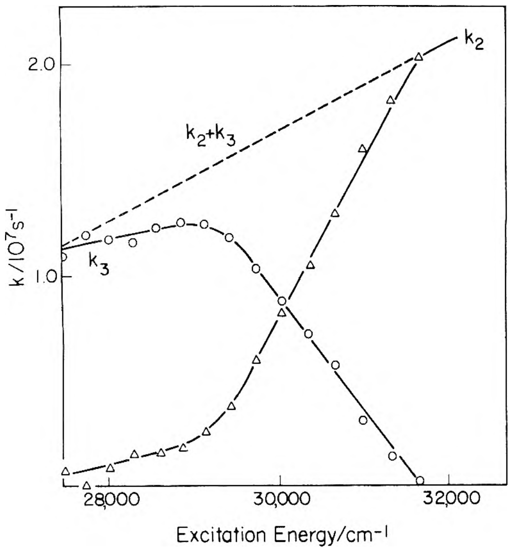

Figure 9. Values of the internal conversion rate constant (k_2) and the intersystem crossing rate constant (k_3) obtained by neglecting influence of ground state thermal population. Dashed line shows values of $k_2 + k_3$ inferred from fluorescence lifetime studies.

citation could pump a highly excited level from which predissociation could occur in competition with intramolecular vibrational redistribution to a more stable configuration of internal energies (A^1_n). Redistribution to the predissociating configuration would be an improbable event during the fluorescence decay time of A^1_n. Thus the value of Φ_F deduced for A^1_n would be too low, however, the attainment of a common value of Φ_F at moderate inert gas pressures ($^{\infty}Q(\lambda)$ = constant) at all excitation wavelengths would seem to infer that this mechanism is not operative. Such effects have been seen though in the photochemistry of benzene solutions.[20]

It is known from high pressure studies of the yield of intersystem crossing[21] that the thermal distribution of excited singlet levels crosses to the triplet with high efficiency and it is therefore tempting to set k_2 equal to zero and ascribe the trend in τ_F values to changes in the intersystem crossing rate constant. However recent calculations[22] of the energy dependence of k_2 and k_3 predict that the internal conversion rate constant will rise much faster than the intersystem crossing rate constant as the excitation energy is increased. These calculations are based on quasi-diatomic, simple harmonic oscillator Franck–Condon factor calculations.

In principle one can decide whether k_2 or k_3 contribute to the energy dependence of τ_F^{-1} by considering the low pressure phosphorescence or intersystem crossing quantum yields, however, there is then the problem of defining the properties of A^3_q, the triplet state produced by intersystem crossing from the initial singlet state. It is known from the temperature dependence of the phosphorescence lifetime that there is a triplet state barrier of 5500 cm^{-1} mol^{-1} to loss of phosphorescence.[13] Thus, it would seem reasonable to set R_2 equal to unity for triplets with energies below the barrier and equal to zero for those with energies above the barrier; the phosphorescence yield would then reflect the energy dependent factor $k_3\tau_F$ and the position of the barriers. Knowing τ_F and $k_3\tau_F$ at thermal internal energies,[2,21] one is able to solve explicitly for k_2 and k_3 at all energies. The results of such manipulations of the data are shown in Figure 9. These results are unreasonable as k_3 is predicted to decrease with increasing energy, and k_2 shows a discontinuity at 31750 cm^{-1}, furthermore k_2 does not show the simple energy dependence predicted in the model calculations.[22]

The treatment of the data can be improved considering the nature of the hexafluoroacetone absorption spectrum which is continuous rather than discrete. Thus, we are not dealing with a single vibronic level of the excited state, but rather with a distribution of excited state levels derived from the thermal distribution of ground state levels. The excited state distribution will be different from the ground state distribution in a way which is defined by the selection rules for optical transitions and the intensities of the various combination and sequence bands, however, a good case can be made that these distributions are very similar. Thus, Halpern and Ware[2] report a fluorescence lifetime of 84 ns for 0.1 Torr of hexafluoroacetone at 22 °C excited at 3577 Å which is close to the 0–0 transition. This value is equal to the high pressure value of τ_F at the same temperature, however, the high pressure value of τ_F is temperature dependent and increases to 110 ns at −77 °C.[2] Thus the emitting level at 0.1 Torr has a similar distribution to the thermalized level. Since the excited level is collision free, it would appear that this distribution must have been derived from the ground state distribution. We also note that the value of τ_F reported at 3577 Å is in agreement with a value obtained by a linear extrapolation of our results, and that extrapolation of our τ_F results to 110 ns would lead to an estimate of 27000 cm^{-1} for the 0–0 transition which is in clear disagreement with the value obtained from spectral measurements.[13] This discrepancy can only be resolved if one assumes that the photon transfers the ground state energy distribution to the excited state. Further evidence on this point is contained in Table I where it is seen directly that the low pressure fluorescence decay time depends upon the temperature of the gas, clear evidence for the transfer of some of the ground state vibrational energy to the excited state.

The Boltzmann distribution of ground state energies of hexafluoroacetone molecules at 22 °C was calculated using the direct count method.[23] The frequencies of the ground state normal modes[24] were grouped into six groups for the purposes of the calculation; the resultant Boltzmann curve was then used in the following simple scheme to fit the phosphorescence quantum yield data. It was assumed that optical excitation transferred the ground state thermal distribution to the excited singlet state; it was assumed that during the lifetime of the excited triplet state vibrational redistribution was complete, and that there existed in the excited triplet state a sharp barrier or discontinuity: triplets with internal energies above this barrier had R_2 equal to zero, those with internal energies below this barrier had R_2 equal to unity. The phosphorescence quantum yield data could be adequately fitted with an energy of 31700 cm^{-1} for the top of the barrier, by setting k_2 to equal zero at all wavelengths of excitation. The curve calculated for 22 °C is shown in Figure 6.

Several comments on this simple treatment are in order. The redistribution of internal energy in the excited triplet state can be due to intra- or intermolecular processes. There is no need to postulate intramolecular redistribution of vibrational energy, although for as large a molecule as hexafluoroacetone the large density of states near to and above the barrier (1×10^9/cm^{-1} assuming simple harmonic oscillators) makes such a process not unreasonable. A second comment concerns the value of the barrier height derived from the scheme. This energy can be compared to the activation energy for loss of phosphorescence[13] measured by other workers and the estimate of the "singlet state" activation energy.[4] The relative positions and uncertainties in these energy levels are shown in Figure 10. Parameters used to derive this figure are the energy

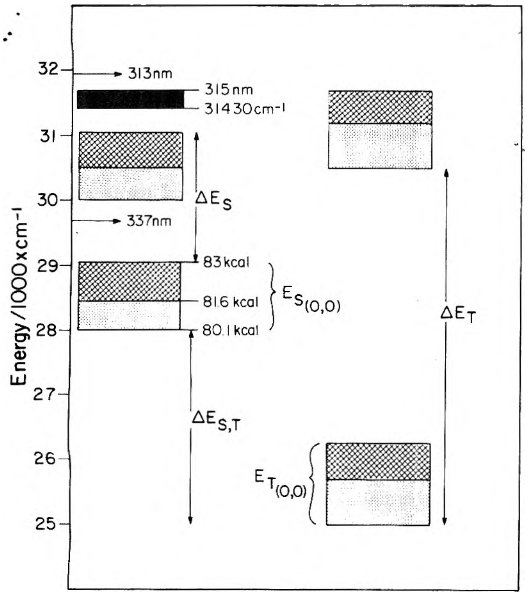

Figure 10. Energy levels relevant to the photochemistry of hexafluoroacetone. $E_{S(0,0)}$ is the energy of the vibrationless $^1n\pi^*$ state (given as 83.1 (ref 13), 81.6 (H. Okabe and E. W. R. Steacie, *Can. J. Chem.*, **36**, 137 (1958)), and 80.1 kcal mol^{-1} (ref 2)). These values were used with $\Delta E_{S,T}$, the singlet-triplet energy gap (8 kcal mol^{-1} < E_{ST} < 9 kcal mol^{-1}, ref 13), to derive the energy of the vibrationless triplet state, $E_{T(0,0)}$. ΔE_T is the activation energy for loss of phosphorescence (15.5 kcal mol^{-1}, ref 13) and ΔE_S is the estimated singlet state activation energy (6 kcal mol^{-1}, ref 3). 315 nm is the longest wavelength at which zero pressure phosphorescence is observed and 31 430 cm^{-1} is the energy of the triplet barrier used to derive the theoretical curve in Figure 6. The diagram also shows the energy of the Hg line (313 nm) and N_2 laser line (337 nm).

of the 0–0 transition of the $S_1 \leftarrow S_0$ band and the separation between the vibrationless levels of the first excited singlet and triplet. Good agreement is found between the value reported here and that derived from the phosphorescence lifetime; the value obtained from the "singlet state" activation energy would seem to yield a lower result. This latter value is based on an indirect estimate from high pressure CO quantum yield data, at temperatures at which an Arrhenius plot of high pressure fluorescence lifetime[2] shows marked curvature. It would seem therefore that this value would be subject to quite large error. Indeed the concept of "singlet state" decomposition is foreign to our interpretation, the present results would indicate that all decomposition to form CO occurs from the excited triplet potential surface. CO quantum yields measured in the presence of triplet quenchers merely measure the yield of CO formed from triplet states with energies above the triplet state barrier, thus the "singlet state" activation energy is merely another indication of the position of the barrier in the triplet. As has been pointed out before[2,18] it is difficult to distinguish between singlet state decomposition and decomposition from short-lived triplets, however, we feel the smooth decrease in fluorescence lifetime argues for the triplet state decomposition mechanism.

We should point out that the interpretation outlined above quantifies ideas expressed in earlier papers[25,26] and is in agreement with a scheme proposed by Uselman and Lee[27] to explain the fluorescence excitation spectrum of nitrogen dioxide in its first predissociation region. These authors show that the change from fluorescent NO_2* ($\tau_F \simeq 70$ μs) to predissociating NO_2* occurs within 10 cm^{-1} of internal energy; it is just such a sharp discontinuity that we propose, albeit more indirectly, for triplet hexafluoroacetone.

Yardley et al. have studied the low pressure emission from the first excited singlet[28] and triplet[29] states of biacetyl and reach conclusions which are essentially similar to ours. However, these authors consider that the low pressure yield of phosphorescence reflects the variation in the ratio R_2, that is the energy dependence of the nonradiative depletion of the triplet (k_4). The effect of the thermal distribution of ground state energies is ignored and the triplet barrier is smoothed from a discontinuity into a hump. The nonexponential low pressure phosphorescence decay implicit in this treatment has been seen for biacetyl, although an interpretation of the behavior involving reversible intersystem crossing was given.[30] However, in hexafluoroacetone such behavior was not observed in the nitrogen laser experiments. Obviously both factors contribute to the observed results, possibly results at different temperatures could ascertain the degree to which each effect contributes.

The mechanism proposed above can be used together with the derived rate constants to predict the CO quantum yield. Knecht[3] attempted to fit the CO quantum yield following 313-nm excitation as a function of pressure. He found that satisfactory agreement could only be achieved if a single step deactivation of $A^1{}_n$ was assumed, however, it is well established from fluorescence quantum yield data that vibrational deactivation of $A^1{}_n$ occurs through a multistep mechanism. Knecht therefore proposed that the internal conversion rate from $A^1{}_n$ increased as the internal energy was raised.[3] The mechanism we have proposed explains this dichotomy. Irradiation by 313-nm light produces $A^1{}_n$ states which ISC to triplet states *just* above the decomposition barrier; all such triplets decompose to yield CO with unit efficiency. Triplet states below the barrier have a much lower probability of CO production. Thus, the deactivation of the CO producing states at 313 nm may appear to be via a single step, while deactivation of fluorescing states may be via multiple steps. Many authors have attempted to fit the pressure dependence of experimental parameters to a mechanism for vibrational deactivation;[2,3,25,32,33] we find that to quantitatively fit the pressure dependence of the phosphorescence yield a vibrational relaxation rate constant twice that needed to fit the fluorescence yield data is required.[31] We are performing experiments to attempt to explain this dichotomy.

Fluorescence Decay of Other Fluorinated Ketones. We have argued above that for low pressure HFA, the decrease in fluorescence lifetime as the internal energy is raised can be attributed to an increase in the intersystem crossing rate. Tetrafluoroacetone, pentafluoroacetone, and perfluoroheptan-4-one show entirely similar behavior, as can be seen in Figure 4. It would seem that this series of molecules would make a sensitive testing ground for a statistical theory of intersystem crossing in carbonyl compounds. Several comments are appropriate. Substitution of a fluorine atom by hydrogen has the effect of increasing the absolute rate of intersystem crossing and increasing the energy dependence of the rate. The latter effect can be rationalized in terms of unimolecular decomposition, that is, reactions with higher activation energies show greater temperature dependence. Thus substitution by hydrogen has the general effect of increasing the vibrational frequencies in the molecule, increase of the frequency of the promoting mode relative to the bath of low frequency vibrations would give a similar effect. The increase in the absolute rate can be understood in terms of the effectiveness of the accepting modes, thus the C–H vibration is a more effective acceptor than the C–F vibration; such an effect has been seen before in studies of fluorinated benzenes.[34]

It has been suggested that the intersystem crossing rate constant will increase linearly if the singlet–triplet energy separation is small, if spin–orbit vibronic coupling is involved, and if there is rapid redistribution of internal energy.[35] The nπ^* states of the fluorinated ketones studied here would seem to fulfill these three criteria, i.e., the singlet–triplet energy gap is less than 3000 cm^{-1} in all cases,[18] the coupling must be vibronic since the singlet and triplet states are derived from the same electronic configuration and the need for rapid redistribution may be obviated by the distribution produced as the result of the transfer of ground state thermal energy.

Conclusions

We have seen that for ^{1}nπ^* hexafluoroacetone the radiative rate constant decreases with increasing internal energy, and that the intersystem crossing rate constant increases linearly with increasing energy. Furthermore, there is a barrier to decomposition at 31 400 cm^{-1}, in the triplet manifold. We plan to further test the role of ground state energy distribution in the photodissociation of hexafluoroacetone by measuring phosphorescence excitation spectra of low pressures of hexafluoroacetone at low temperatures.

References and Notes

(1) P. B. Ayscough and E. W. R. Steacie, *Proc. R. Soc. London, Ser. A*, **234**, 476 (1956).
(2) A. M. Halpern and W. R. Ware, *J. Chem. Phys.*, **53**, 1969 (1970).
(3) D. A. Knecht, *Chem. Phys. Lett.*, **33**, 325 (1975).
(4) F. M. Servidio and G. O. Pritchard, *Int. J. Chem. Kinet.*, **7**, 195 (1975).
(5) D. W. Grattan and M. H. Hui, private communication.
(6) Both quantum counters gave $^{\propto}R(\lambda)$ values which were constant in the range 360–250 nm.
(7) R. K. Boyd, G. B. Carter, and K. O. Kutschke, *Can. J. Chem.*, **46**, 175 (1968).
(8) D. M. Rayner, A. E. McKinnon, A. G. Szabo, and P. A. Hackett, *Can. J. Chem.*, **54**, 3246 (1976).
(9) Circuit available from authors.
(10) This follows from the fact that $^{\infty}R(\lambda)$ is independent of λ. See also ref 13.
(11) A. Gandini, P. A. Hackett, and R. A. Back, *Can. J. Chem.*, in press.
(12) S. W. Benson, "The Foundations of Chemical Kinetics", McGraw-Hill, New York, N.Y., 1960, pp 148–154.
(13) A. Gandini and K. O. Kutschke, *Proc. R. Soc. London, Ser. A*, **306**, 511 (1968).
(14) K. O. Kutschke, private communication.
(15) T. F. Thomas, B. Matuszewski, and R. S. Givens, *J. Phys. Chem.*, **78**, 2637 (1974).
(16) D. A. Hansen and E. K. C. Lee, *J, Chem. Phys.*, **62**, 183 (1975).
(17) R. G. Miller and E. K. C. Lee, *Chem. Phys. Lett.*, **33**, 104 (1975).
(18) P. A. Hackett and D. Phillips, *J. Phys. Chem.*, **78**, 671 (1974).
(19) G. R. Fleming, O. L. J. Gijzeman, and S. H. Lin, *Chem. Phys. Lett.*, **21**, 527 (1973).
(20) R. B. Cundall and L. C. Pereira, *J. Chem. Soc., Faraday Trans. 2*, **68**, 1152 (1972).
(21) A. Gandini and K. O. Kutschke, *Proc. R. Soc. London, Ser. A*, **306**, 529 (1968).
(22) G. D. Gillespie and E. C. Lim, *Chem. Phys. Lett.*, 34, 513 (1975).
(23) W. Forst, "Theory of Unimolecular Reactions", Academic Press, New York, N.Y., 1973, pp 85–104.
(24) C. V. Berney, *Spectrochim. Acta*, **21**, 1809 (1965).
(25) P. G. Bowers and G. B. Porter, *J. Phys. Chem.*, **70**, 1622 (1966).
(26) D. A. Whytock and K. O. Kutschke, *Proc. R. Soc. London, Ser. A*, **306**, 503 (1968).
(27) W. M. Uselman and E. K. C. Lee, *J. Chem. Phys.*, **64**, 3457 (1976).
(28) G. M. McClelland and J. T. Yardley, *J. Chem. Phys.*, **58**, 4368 (1973).
(29) A. Zenker Moss and J. T. Yardley, *J. Chem. Phys.*, **61**, 2883 (1974).
(30) R. van der Werf, D. Zevenhuijzen, and J. Kommandeur, *Chem. Phys. Lett.*, **27**, 325 (1974).
(31) This result is independent of the number of deactivation steps employed in the deactivation scheme.
(32) A. Gandini, D. A. Whytock, and K. O. Kutschke, *Proc. R. Soc. London, Ser. A*, **306**, 541 (1968).
(33) P. A. Hackett and D. Phillips, *J. Phys. Chem.*, **78**, 679 (1974).
(34) C. Guttman and S. A. Rice, *J. Chem. Phys.*, **61**, 661 (1974).
(35) S. Fischer, E. W. Schlag, and S. Schneider, *Chem. Phys. Lett.*, **11**, 583 (1971).

Formation of the NH($A^3\Pi$, $c^1\Pi$) Radicals by Electron Impact Near Threshold

Kiyoshi Fukui, Iwao Fujita,[†] and Keiji Kuwata*

Department of Chemistry, Faculty of Science, Osaka University, Toyonaka, Osaka, 560 Japan *(Received September 7, 1976; Revised Manuscript Received April 4, 1977)*

Emission spectra of the NH radical in the $c^1\Pi$ and $A^3\Pi$ states in electron impact of hydrogen azide, ethyleneimine, isocyanic acid, ammonia, methylamine, and hydrazine were observed, and the excitation functions for the $c^1\Pi \rightarrow a^1\Delta$ and $A^3\Pi \rightarrow X^3\Sigma^-$ transitions of the NH radicals were measured. The contribution of the triplet excited state of the parent compounds to the primary formation of the triplet NH($A^3\Pi$) radical is important near threshold. The excitation thresholds for the singlet NH($c^1\Pi$) radical formed from ammonia and hydrogen azide are slightly higher than the thermochemical values. The thresholds for the triplet NH($A^3\Pi$) radical formed from hydrogen azide, ethyleneimine, isocyanic acid, ammonia, methylamine, and hydrazine agree fairly well with the thermochemical values.

Introduction

The NH free radical is an important reaction intermediate in some flames, rocket-engine plasmas, electric discharges, and astronomical emission sources.[1] The electronic configuration for the ground state of the NH radical is $(2s\sigma)^2(2p\sigma)^2(2p\pi)^2$ which is associated with the $X^3\Sigma^-$, $a^1\Delta$, and $b^1\Sigma^+$ states, and the first excited electronic configuration of $(2s\sigma)^2(2p\sigma)(2p\pi)^3$ is associated with the $c^1\Pi$ and $A^3\Pi$ states.[2] The fluorescence due to the $A^3\Pi \rightarrow X^3\Sigma^-$ and $c^1\Pi \rightarrow a^1\Delta$ transitions has been often observed with strong intensity in almost any system which contains the nitrogen and hydrogen atoms.

The spectroscopic behavior and the collisional deactivation of the electronically excited NH radical with atoms and molecules have been investigated by many researchers. Further, mechanisms of the primary formation of the excited NH radical have been studied in vacuum-ultraviolet photolysis or in sensitization by metastable atoms for various molecules: ammonia,[3-8] hydrogen azide,[7,9,10]

[†] Present address: Osaka Electro-Communication University, Neyagawa, Osaka, 572 Japan.

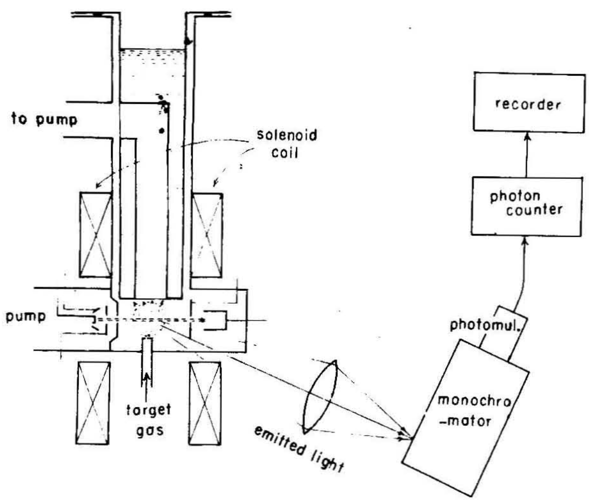

Figure 1. Schematic apparatus used in the present study.

isocyanic acid,[7,11,12] ethyleneimine,[13,14] methylamine,[15] and hydrazine.[4] The NH($c^1\Pi$) radical was formed in the primary process by vacuum-ultraviolet photolysis, while the NH($A^3\Pi$) radical appeared in the secondary process in all the molecules except hydrazine. Thus, the singlet repulsive excited state of the parent molecule has been known to be mainly responsible, on the basis of the spin conservation rule, for the primary formation of the NH($c^1\Pi$) radical in the vacuum ultraviolet photolysis of these molecules. Further, dissociation for ammonia and hydrazine by electron impact has also been studied.[16]

Though the excitation of molecule by light absorption is governed by the fairly stringent selection rule, in electron impact at low energy such a selection rule is not valid. In particular, the optically spin-forbidden transition can occur through an electron-exchange excitation. Therefore, in a reaction system involving the collisions of low velocity electrons with molecules, as in radiation chemistry and electric discharge, the excited states with different spin multiplicity from the ground state become often important. In the present system the primary formation of the NH($A^3\Pi$) radical in electron impact was examined and the triplet repulsive state of the parent molecule is found to be important in the formation of the NH($A^3\Pi$) radical near threshold.

In the present study to investigate the mechanisms of the primary formation of the NH($A^3\Pi$) and NH($c^1\Pi$) radicals, the following steps of the study were carried out: (1) the excitation functions and the threshold energies for the NH($A^3\Pi$) and the NH($c^1\Pi$) radicals from each parent molecules were examined, (2) the possible dissociation processes forming the excited NH radical and its partner were discussed, (3) the spin of the excited state of the parent molecule was assigned according to the spin-conservation rule, (4) the contribution of the triplet and singlet repulsive states of the parent molecule to the formation of the NH($A^3\Pi$) and the NH($c^1\Pi$) radicals near threshold was assessed on the basis of the features of the excitation function.

Experimental Section

Figure 1 shows a schematic diagram of a collision chamber and an optical detection system for the excited species. This apparatus was designed mainly for electron impact at lower energy. A detailed description of the apparatus has been given elsewhere.[17] The collision chamber and the chamber for the electron gun were evacuated separately. The background pressure in each chamber was measured by an ionization gauge in each chamber. The chambers were evacuated to 2×10^{-7} Torr in the absence of target gases.

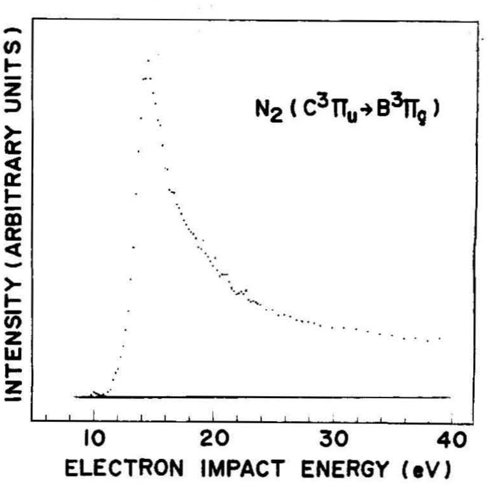

Figure 2. Excitation function for the $C^3\Pi_u \rightarrow B^3\Pi_g$ transition of N_2 (at 337.1 nm). The known energy value corresponding to the maximum intensity is used for the correction of energy of the incident electron. The background pressure in the collision chamber was 4×10^{-6} Torr.

The emitted light was focussed by a quartz lens on the inlet slit of a Nalumi RM-23 grating monochromator with a Hamamatsu R 585 photomultiplier, and its output was measured by photon counting. The observed excitation function of the nitrogen molecule in the $C^3\Pi_u$ state shown in Figure 2 is in fairly good agreement with the results of Finn et al.[18] The energy correction for the incident electron was done using the excitation function for the $C^3\Pi_u$ state of the nitrogen molecule. A typical value of the energy spread of an incident electron was 0.3 eV.

The emission spectra of the singlet and the triplet NH radicals were observed in the region 320–360 nm. The excitation functions for the NH radicals formed from hydrogen azide, ethyleneimine, isocyanic acid, ammonia, methylamine, and hydrazine were measured at a pressure of 4×10^{-6} Torr. The excitation function for the singlet NH radical was measured at 326 nm with a bandpass of 6.6 nm, and for the triplet NH radical at 336 nm with a bandpass of 3.3 nm.

Methylamine was prepared by heating at 100 °C under vacuum the mixture of $CH_3NH_2{\cdot}HCl$ and an excess amount of CaO which was dried at 450 °C under vacuum beforehand. Hydrazine was isolated by the distillation of hydrazine hydrate ($NH_2NH_2{\cdot}H_2O$) together with an excess amount of NaOH at 100 °C. Isocyanic acid (HNCO) was prepared by thermal decomposition of cyanuric acid at about 450 °C under vacuum.[11,12]

Hydrogen azide (HN_3) was prepared by heating the mixture of NaN_3 and an excess amount of stearic acid at 100 °C under vacuum.[9,10] To avoid the explosive decomposition of the azide, it was prepared and stored at pressures lower than 50 Torr. Ammonia of 99.5% purity from Matheson Co. was used without further purification. Ethyleneimine of more than 99.0% purity from Wako Inc. was used without further purification.

Results

A. *The Emission Spectra for the NH($A^3\Pi \rightarrow X^3\Sigma^-$) and the NH($c^1\Pi \rightarrow a^1\Delta$) Transitions.* In the six molecules studied the predominant emission spectrum arises from the NH($A^3\Pi \rightarrow X^3\Sigma^-$) by electron impact at electron energies up to 25 eV in the region from 300 to 600 nm as shown in Figures 3 and 4. The NH($c^1\Pi \rightarrow a^1\Delta$) emission is either weak or missing.

For ammonia the sharp (0,0) band at 336 nm and (1,1) band at 337 nm from the NH($A^3\Pi \rightarrow X^3\Sigma^-$) transition are predominant, as shown in Figure 3. The rotational P, Q,

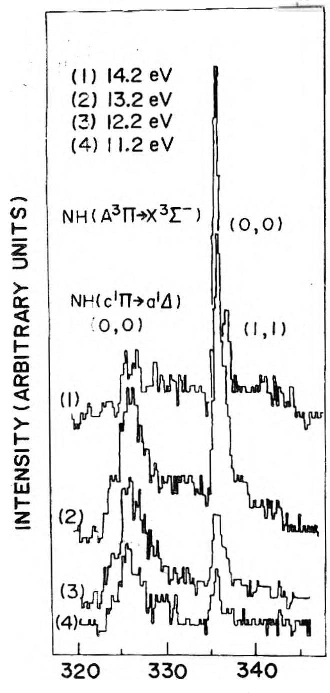

Figure 3. The NH $c^1\Pi \rightarrow a^1\Delta$ (0,0) and $A^3\Pi \rightarrow X^3\Sigma^-$ (0,0) and (1,1) emission bands formed from NH_3 under the following conditions: electron impact energy, bandpass of the monochromator, pressure in the collision chamber, and beam current: (1) 14.2 eV, 0.6 nm, 5 × 10^{-6} Torr, 20 μA; (2) 13.2 eV, 1.1 nm, 5 × 10^{-6} Torr, 20 μA; (3) 12.2 eV, 1.1 nm, 5 × 10^{-6} Torr, 20 μA; (4) 11.2 eV, 1.1 nm, 5 × 10^{-6} Torr, 20 μA.

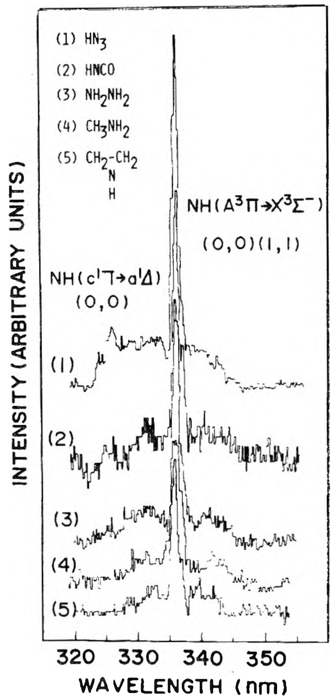

Figure 4. Emission spectra for the NH $A^3\Pi \rightarrow X^3\Sigma^-$ and the $c^1\Pi \rightarrow a^1\Delta$ transitions formed from the following parent molecules: hydrogen azide (1), isocyanic acid (2), hydrazine (3), methylamine (4), ethyleneimine (5). Bandpass of the monochromator, beam current, pressure in the collision chamber, and electron impact energy were as follows: (1) 1.0 nm, 10 μA, 4 × 10^{-6} Torr, 15 eV; (2) 1.0 nm, 7.5 μA, 1 × 10^{-5} Torr, 20 eV; (3) 1.0 nm, 10 μA, 4 × 10^{-6} Torr, 20 eV; (4) 1.65 nm, 20 μA, 5 × 10^{-6} Torr, 17 eV; (5) 1.65 nm, 20 μA, 6 × 10^{-6} Torr, 24 eV.

and R branches seem to extend to near 336 and 337 nm with weak intensity.[2] The broad (0,0) band together with the rotational structures with R head at 322 nm for the NH($c^1\Pi \rightarrow a^1\Delta$) transition is likely to extend to the 320–336-nm region.[2] Figure 3 shows the variation of the relative emission intensities of the NH($A^3\Pi \rightarrow X^3\Sigma^-$) to those of the NH($c^1\Pi \rightarrow a^1\Delta$) transition at electron energies of 14.2, 13.2, 12.2, and 11.2 eV. The relative intensity of the $A^3\Pi \rightarrow X^3\Sigma^-$ transition seems to decrease more quickly than that of the NH($c^1\Pi \rightarrow a^1\Delta$) transition as the energy of incident electron decreases. In addition, the emission spectrum from the NH_2($\tilde{A}^2A_1 \rightarrow \tilde{X}^2B_1$) transition, i.e., the α bands, could not be observed in the 400–600-nm region probably because of the weaker diffuse bands.[3] Figure 4 shows that only in hydrogen azide both the NH($A^3 \rightarrow X^3\Sigma^-$) and the NH($c^1\Pi \rightarrow a^1\Delta$) transitions are seen and for other molecules the $A^3\Pi \rightarrow X^3\Sigma^-$ transition alone is observed. The assignments of the emission spectra are just the same as for ammonia. The relative intensities for the (0,0) to the (1,1) bands and the population in the rotational levels are probably different for each parent molecule and for different electron impact energies. These quantitative examinations will be accomplished in the future.

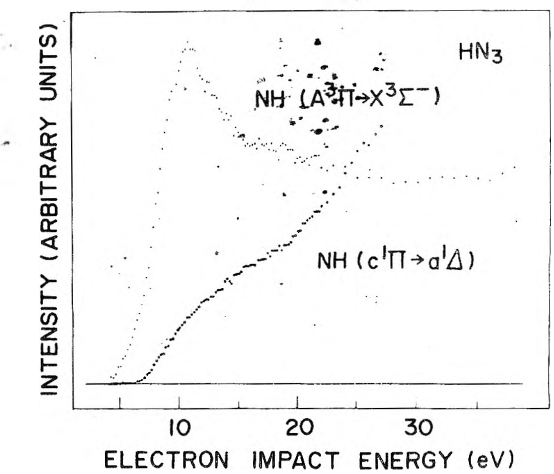

Figure 5. Excitation functions for the excited NH radicals formed in hydrogen azide; $A^3\Pi \rightarrow X^3\Sigma^-$ (●) and $c^1\Pi \rightarrow a^1\Delta$ (○). The beam current was 5.0 μA, and pressure in the collision chamber was 4 × 10^{-6} Torr.

B. *Excitation Thresholds for the NH($A^3\Pi$) and the NH($c^1\Pi$) Radicals.* Main dissociation processes leading to the formation of the NH($A^3\Pi$) and the NH($c^1\Pi$) radicals from each parent molecule near threshold energies are shown in the first column of Table I. The second column shows the threshold energies (in eV) determined in the present work, and in the third column the calculated values (in eV) of the lowest dissociation energies using the heats of formation[19] are given. The NH($A^3\Pi$) radical is formed in all of the parent molecules by electron impact near threshold energies, while the NH($c^1\Pi$) radical is formed only in ammonia and hydrogen azide, as listed in Table I.

By comparison of the excitation threshold energy with the thermochemically calculated threshold, the dissociation processes with the least energy requirement to form the NH($A^3\Pi$) radicals from each parent molecule are selected. On the other hand, excitation threshold energies of 10.1 and 6.8 eV for the NH($c^1\Pi$) radical formed in ammonia and hydrogen azide were found to be slightly higher than thermochemical values of 9.3 and 5.9 eV, respectively, within experimental error. These dissociation processes are also included in Table I.

C. *Excitation Functions for the NH($A^3\Pi$) and the NH($c^1\Pi$) Radicals.* The excitation functions of the NH($A^3\Pi$) and the NH($c^1\Pi$) radicals formed from hydrogen azide, ethyleneimine, isocyanic acid, ammonia, methylamine, and hydrazine near thresholds are shown in Figures 5–9, respectively.

TABLE I: Main Dissociation Processes for the Formation of the Excited NH Radical from Each Parent Molecule

	Dissociation processes	Threshold, eV Obsd	Threshold, eV Calcd[b]
(1)[a]	$HN_3 \rightarrow NH(A^3\Pi) + N_2(X)$	4.3	4.2
(2)	$\rightarrow NH(c^1\Pi) + N_2(X)$	6.8	5.9
(3)	$\rightarrow NH(A^3\Pi) + N_2(A^3\Sigma_u^+)$		10.3
(4)[a]	$CH_2\underset{\underset{H}{N}}{-}CH_2 \rightarrow NH(A^3\Pi) + CH_2CH_2(X)$	6.7	6.6
(5)	$\rightarrow NH(c^1\Pi) + CH_2CH_2(X)$		8.3
(6)	$\rightarrow NH(A^3\Pi) + CH_2CH_2(a^3B_{1u})$		11.2
(7)[a]	$HNCO \rightarrow NH(A^3\Pi) + CO(X)$	7.4	(7.1)[c]
(8)	$\rightarrow NH(c^1\Pi) + CO(X)$		(8.8)
(9)	$\rightarrow NH(A^3\Pi) + CO(a^3\Pi)$		(13.1)
(10)[a]	$NH_3 \rightarrow NH(A^3\Pi) + H_2(X)$		7.6
(11)	$\rightarrow NH(c^1\Pi) + H_2(X)$	10.1	9.3
(12)	$\rightarrow NH(A^3\Pi) + 2H(^2S)$	12.2	12.2
(13)[a]	$CH_3NH_2 \rightarrow NH(A^3\Pi) + CH_4(X)$		6.7
(14)	$\rightarrow NH(c^1\Pi) + CH_4(X)$		8.4
(15)	$\rightarrow NH(A^3\Pi) + CH_3(X) + H(^2S)$	11.0	11.1
(16)[a]	$NH_2NH_2 \rightarrow NH(A^3\Pi) + NH_3(X)$		5.7
(17)	$\rightarrow NH(c^1\Pi) + NH_3(X)$		7.4
(18)	$\rightarrow NH(A^3\Pi) + NH_2(X) + H(^2S)$	10.4	10.2

[a] Optically spin-forbidden reactions; (X) is the ground state of the molecule. [b] Reference 19. [c] Reference 11.

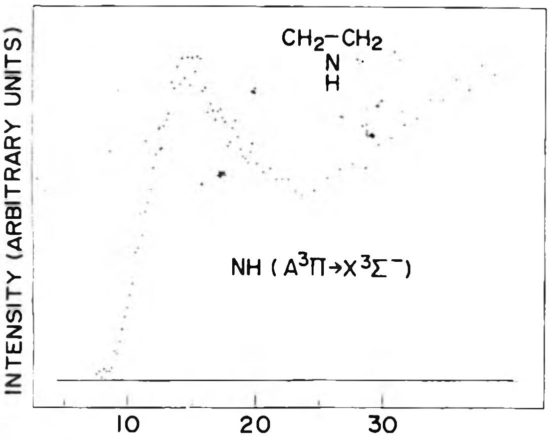

Figure 6. Excitation function for the NH radical in the $A^3\Pi$ state formed in ethyleneimine. The beam current was 5.0 μA, and the pressure in the collision chamber was 4 × 10^{-6} Torr.

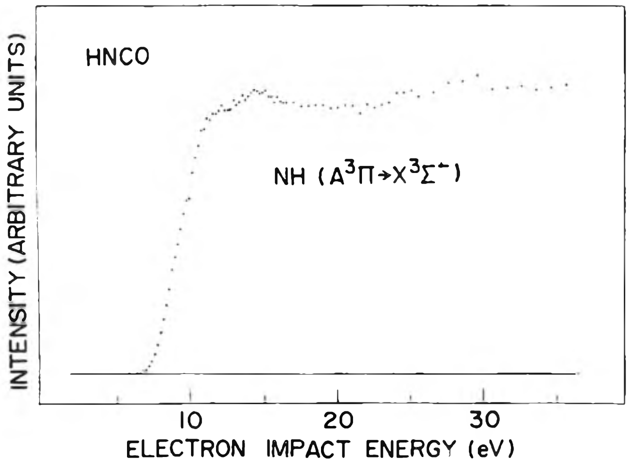

Figure 7. Excitation function for the NH radical in the $A^3\Pi$ state formed in isocyanic acid. The beam current was 5.0 μA, and pressure in the collision chamber was 4 × 10^{-6} Torr.

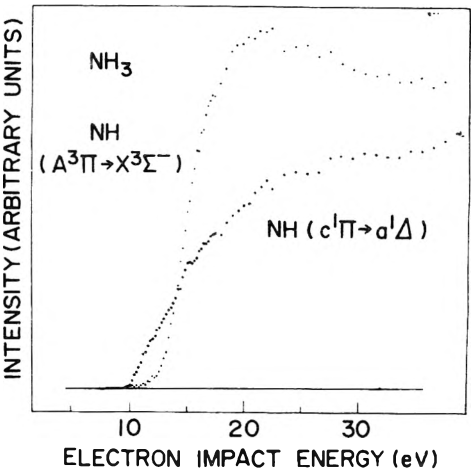

Figure 8. Excitation functions for the NH radical in the $A^3\Pi$ state (●) and the NH radical in the $c^1\Pi$ state (○) formed in ammonia. The beam current was 5.0 μA, and pressure in collision chamber was 4 × 10^{-6} Torr.

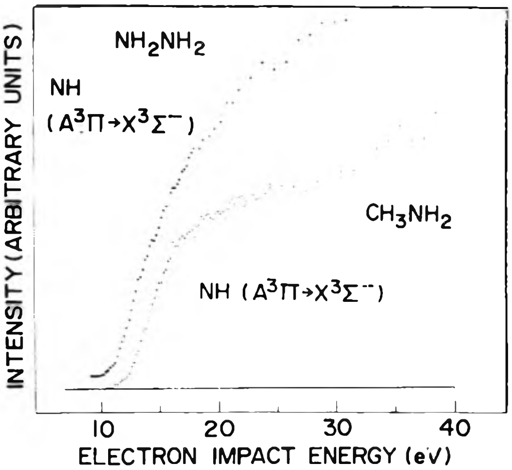

Figure 9. Excitation functions for the NH radical in the $A^3\Pi$ state formed in hydrazine (○) and methylamine (●). The beam current was 5.0 μA, and the pressure in the collision chamber was 4 × 10^{-6} Torr.

Discussion

A. *Excitation Threshold for the NH Radicals in the $A^3\Pi$ and $c^1\Pi$ states.* There are three types of dissociation process from the excited state:[20] (a) dissociation in a pure repulsive state, (b) dissociation at the repulsive wall of a bound state, and (c) predissociation. Many subcases are also included in these three dissociation processes.[21] In cases a and b, dissociation takes place in roughly half of a vibrational period, i.e., 10^{-13} s. In case c, predissociation may take 10^{-13} to 10^{-9} s depending on the interaction with a repulsive state.

In electronic excitation the Franck–Condon principle may be assumed to be valid, then, the difference between the vertical excitation threshold and the energy of dissociation limit should closely relate to such types of dissociation.

The fairly good agreement between the excitation threshold energy and the thermochemical threshold for the NH($A^3\Pi$) radical indicates that the formation of the NH($A^3\Pi$) radical may be due to dissociation at the repulsive wall of a bound excited state of each parent molecule.

On the other hand, in the case of the NH($c^1\Pi$) radical formed in hydrogen azide and ammonia the excitation thresholds were slightly higher than the thermochemical values. Okabe has measured the intensity of the fluorescence from the NH($c^1\Pi$) radical as a function of the wavelength of incident light in the region from 170 to 600 nm for hydrogen azide[10] and in the region from 105 to 165 nm for ammonia.[3] Okabe has also obtained a slightly higher excitation threshold than the thermochemical value for hydrogen azide and has concluded that the molecule is excited to a repulsive state whose potential energy surface may have a fairly steep rise near the energy of dissociation limit. In the case of ammonia, the fluorescence-yield curve has a low-lying flat part starting at 132.5 nm (9.4 eV) and then a steep rise at about 123 nm (10.0 eV). The excitation threshold of 10.1 eV obtained in the present study corresponds to the second rise at 10.0 eV in the fluorescence-yield curve.

B. *Formation of the NH($A^3\Pi$) Radical and the Excitation Function.* In electron impact at high energy (over 100 eV) the selection rules closely resemble the optical ones, and the cross sections are related to the optical absorption coefficients. Some of the selection rules, however, become invalid at lower energies. In particular, low-energy electrons (within a few tens of electron volts above the excitation threshold) can be quite effective to induce transitions between states of different spin multiplicity through electron-exchange excitation. In addition, the probability of transitions which are symmetry forbidden in optical excitation can often be drastically increased by the impact of low energy electrons.

Optical excitation by a photon is a resonance phenomena, and all of the energy of the photon is absorbed by the system and the photon is annihilated. On the other hand, in electron impact excitation the electron loses only a part of its kinetic energy for excitation and is scattered after collision, thus many excitation processes become possible by electron impact at high energy.

The excitation function shows a dependence on the energy of the incident electron of the vertical transition probability from the ground state to a repulsive state (dissociative state) of the parent molecules. The electron-exchange excitation in electron impact has been well-known to have a maximum excitation cross section just above the excitation threshold.[22-26] On the basis of this feature in the excitation function the spin state of the precursor to form the NH($A^3\Pi$) radical can be examined.

The dissociation processes of the first type as (1), (4), (7), (10), (13), and (16) in Table I include the NH radical in the $A^3\Pi$ state and a stable product in the singlet ground state. The first type may be further divided into processes involving no new bond formation (1, 4, 7) and those involving new bond formation (10, 13, 16). The latter processes have not been observed in electron impact. The second type such as (2), (5), (8), (11), (14), and (17) corresponds to the formation of the NH($c^1\Pi$) radical and two unstable radicals with a spin quantum number of $s = 1/2$, which appears in section C. Further, the third type such as (3), (6), (9), (12), (15), and (18) corresponds to the formation of the NH($A^3\Pi$) radical and a product in the stable singlet ground state.

The following dissociation processes are examples of the first type involving no new bond formation:

$$HN_3 \rightarrow NH(A^3\Pi) + N_2(X^1\Sigma_g^+)$$

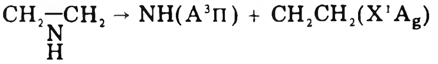

$$CH_2(NH)CH_2 \rightarrow NH(A^3\Pi) + CH_2CH_2(X^1A_g)$$

$$HNCO \rightarrow NH(A^3\Pi) + CO(X^1\Sigma^+)$$

As seen in Figures 5–7, the excitation functions for the NH($A^3\Pi$) radical formed in hydrogen azide, ethyleneimine, and isocyanic acid have a maximum just above the threshold, i.e., the feature of an electron-exchange excitation. From such electron-exchange excitation results the singlet–triplet transition of the parent molecule, that is, the triplet repulsive state of the molecule leading to the NH($A^3\Pi$) radical is formed near the threshold. This result is in agreement with the assumed spin state of the precursor of the NH($A^3\Pi$) radical on the basis of the spin conservation rule in dissociation processes (1), (4), and (7). Thus, the excitation function indicates that the contribution of the triplet repulsive state of each parent molecule to the formation of the NH($A^3\Pi$) radical is predominant near threshold.

On the other hand, it should be noted that in the case of ammonia, methylamine, and hydrazine the dissociation processes (10), (13), and (16) are not observed in the present work. That is, the excited states of ammonia, methylamine, and hydrazine have probably no relation with a favorable repulsive potential surface which leads to the formation of the NH($A^3\Pi$) radical and a stable molecule in the singlet ground state.

Further, in the higher energy region of the excitation functions of Figures 5–7, each of the dissociation processes of the third type, as (3), (6), and (9) in Table I, also contribute with each peculiar probability to the formation of the NH($A^3\Pi$) radical. Dissociation processes (3), (6), and (9) are the formation the NH($A^3\Pi$) radical and the first triplet excited state (meta stable state) of the product, i.e., $N_2(A^3\Sigma_u^+)$, $CH_2CH_2(a^3B_{1u})$, and $CO(a^3\Pi_r)$. The spin state of each repulsive state is not clear in view of the excitation functions which have no typical features of both a direct excitation and an electron-exchange excitation in the higher energy region. However, each precursor can be a singlet, triplet, and quintet state according to the spin conservation rule in each dissociation process. Because of the two electron transitions the role of the quintet state may be very minor.

Dissociation processes of the third type such as (12), (15), and (18) in Table I correspond to the formation of the NH($A^3\Pi$) radical and two unstable radicals with $s = 1/2$, as follows:

$$NH_3 \rightarrow NH(A^3\Pi) + 2H(^2S)$$

$$CH_3NH_2 \rightarrow NH(A^3\Pi) + CH_3(\tilde{X}^2A'') + H(^2S)$$

$$NH_2NH_2 \rightarrow NH(A^3\Pi) + NH_2(\tilde{X}^2B_1) + H(^2S)$$

According to the spin conservation rule, in the dissociation processes of the second type the precursor to form the NH($A^3\Pi$) radical may be in the singlet, triplet, and quintet states. The contribution of the quintet state, however, may be very minor because of the two electron transitions from the parent molecule, while the singlet and triplet states are possible. Thus, on the bases of the spin conservation rule the precursor in the singlet and the triplet states can be included in the case of ammonia, while the excitation functions show the major contribution of the triplet precursor in the formation of the $NH(A^3\Pi)$ radical near threshold. In the case of hydrazine and methylamine, however, the excitation function with no maximum near threshold shows the major contribution of the singlet repulsive state to the formation of the $NH(A^3\Pi)$ radical as compared to those in the case of ammonia. In photolysis the formation of the $NH(A^3\Pi)$ radical through the dissociation process (18) in hydrazine[4] has been known, while in the cases of ammonia and methylamine the dissociation processes (12) and (15) have not yet been observed.

C. *Formation of the $NH(c^1\Pi)$ Radical in Ammonia and Hydrogen Azide.* The processes for the formation of the $NH(c^1\Pi)$ radical from ammonia and hydrogen azide in electron impact are as follows:

$$NH_3 \rightarrow NH(c^1\Pi) + H_2(X^1\Sigma_g^+)$$

$$HN_3 \rightarrow NH(c^1\Pi) + N_2(X^1\Sigma_g^+)$$

where H_2 and N_2 molecules are in the ground state, respectively, and the repulsive states of NH_3 and HN_3 are in the singlet state according to the spin conservation rule. These processes have been observed in vacuum-ultraviolet photolysis. Thus, they proceed via a direct excitation, i.e., no electron-exchange excitation, and the excitation functions have no feature of the electron-exchange excitation, i.e., a sharp peak just above the threshold, as seen in Figures 5 and 8.

References and Notes

(1) J. M. Lents, *J. Quant. Spectrosc. Radiant. Transfer.*, **13**, 297 (1973).
(2) G. Herzberg, "Spectra of Diatomic Molecules", Van Nostrand, Princeton, N.J., 1950.
(3) H. Okabe and M. Lenzi, *J. Chem. Phys.*, **47**, 5241 (1967).
(4) K. H. Becker and K. H. Welge, *Z. Naturforsch. A*, **13**, 600 (1963).
(5) K. H. Becker and K. H. Welge, *Z. Naturforsch. A*, **19**, 1006 (1964).
(6) E. Lindholm, *Ark. Fys.*, **37**, 49 (1968).
(7) D. H. Stedman, *J. Chem. Phys.*, **52**, 3966 (1970).
(8) M. Kawasaki, Y. Hirata, and I. Tanaka, *J. Chem. Phys.*, **59**, 648 (1973).
(9) K. H. Welge, *J. Chem. Phys.*, **45**, 4373 (1966).
(10) H. Okabe, *J. Chem. Phys.*, **49**, 2726 (1968).
(11) H. Okabe, *J. Chem. Phys.*, **53**, 3507 (1970).
(12) R. N. Dixon, *Can. J. Phys.*, **37**, 1171 (1959).
(13) M. Kawasaki, Abstract No. 3F29, 26th Spring Annual Meeting of the Chemical Society of Japan, Tokyo April 1972.
(14) M. Iwasaki, N. Ibuki, and Y. Takesaki, Abstract No. 2A06. Symposium on Photochemistry (Chemical Society of Japan), Osaka, Nov. 1972.
(15) M. Kawasaki, Abstract No. 3Q39, 28th Spring Annual Meeting of the Chemical Society of Japan, Tokyo, April 1973.
(16) H. Bubert and F. W. Froben, *J. Phys. Chem.*, **75**, 769 (1971).
(17) K. Fukui, I. Fujita, and K. Kuwata, *Shitsuryo Bunseki*, **23**, 105 (1975).
(18) T. G. Finn, J. F. M. Aarts, and J. P. Doering, *J. Chem. Phys.*, **56**, 5632 (1972).
(19) J. L. Franklin, J. G. Dillard, H. M. Rosenstock, J. T. Herron, K. Draxl, and F. H. Field, *Natl. Stand. Ref. Data Ser., Natl. Bur. Stand.*, **No. 26** (1969).
(20) G. Herzberg, "Electronic Spectra and Electronic Structure of Polyatomic Molecules", Van Nostrand, Princeton, N.J., 1966.
(21) R. S. Mulliken, *J. Chem. Phys.*, **33**, 247 (1960).
(22) J. R. Oppenheimer, *Phys. Rev.*, **32**, 361 (1928).
(23) H. S. W. Massey and C. B. O. Mohr, *Proc. R. Soc. London, Ser. A*, **132**, 605 (1931).
(24) W. G. Penney, *Phys. Rev.*, **39**, 467 (1932).
(25) R. D. Bates, A. Fundaminsky, H. S. W. Massey, and J. W. Leech, *Phil. Trans. R. Soc. London, Ser. A*, **243**, 93 (1950).
(26) V. I. Ochkur, *Sov. Phys. JETP*, **18**, 503 (1964).

Measurement of the Activation Energy for the Reaction of the Hydroxyl Radical with Hydrogen in Aqueous Solution

Klaus H. Schmidt

Chemistry Division, Argonne National Laboratory, Argonne, Illinois 60439

(Received December 20, 1976)

Publication costs assisted by Argonne National Laboratory

The rate constant, k_1, for the reaction $OH + H_2 \rightarrow H_2O + H$ in aqueous solution was measured at temperatures between 15 and 90 °C. This was achieved by using a new signal averaging technique, combined with a flow system, to record the transient absorption of the OH radical during repetitive pulsing of the solution with the electron beam from a linear accelerator. From the data, the activation energy, E_a, for the above reaction was calculated. The results, with their 90% confidence limits, are k_1 (25 °C) $= 3.96 \times 10^7$ L mol^{-1} s^{-1} $\pm$ 10% and $E_a = 3.18 \pm 0.5$ kcal mol^{-1}.

Introduction

When water is irradiated with ionizing radiation, a number of transient species such as OH, H, e_{aq}^-, HO_2, and molecular products (H_2, H_2O_2, O_2) are formed,[2-4] and a multitude of reactions take place between these species. For computer model calculations of irradiated aqueous systems,[5-7] the availability of accurate values for the various rate constants is essential. Such calculations often have to be carried out for elevated temperatures, for example, if one wants to assess the production of O_2 and H_2O_2 in pressurized or boiling water reactors.[6,7]

During the last two decades, a great deal of effort, by many researchers, has been dedicated to the determination of such rate constants, and extensive compilations for reactions of e_{aq}^-,[8-11] H,[11,12] OH,[11,13] and oxygenated species[3,14] have been published. However, most rate constant values have only been measured at room temperature, in some cases with considerable discrepancies between those published by different researchers. Thus, values for $k(H + OH)$[12] vary from 7×10^9 to 3.2×10^{10} L

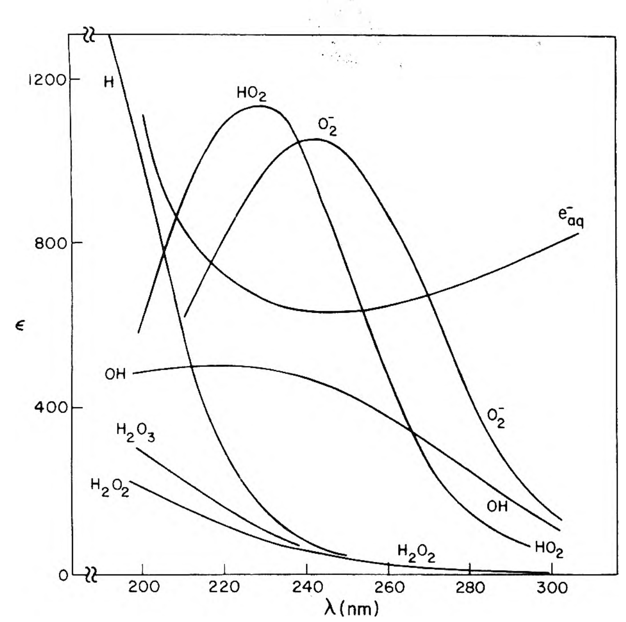

Figure 1. UV absorption spectra of water radiolysis products.

mol^{-1} s^{-1}. Activation energies are known for very few reactions, and again, considerable variations are often encountered. For example, reported values of E_a for the reaction of e_{aq}^- with H_3O^+ lie between 2.44 and 3.8 kcal mol^{-1}.[8] For most of the fast radical-radical reactions such as H + OH and OH + OH, which are assumed to be diffusion controlled, the activation energy is estimated to be between 3 and 3.5 kcal mol^{-1},[6,7] but few experimental values have been published.

One reaction whose rate strongly affects the production of O_2 and H_2O_2 in irradiated water is

$$OH + H_2 \rightarrow H + H_2O \qquad (1)$$

Whereas its rate constant at room temperature is known,[13] the only published experimental data regarding its activation energy is a difference of $\Delta E_a = 1.25$ kcal mol^{-1} [15] between reaction 1 and

$$OH + H_2O_2 \rightarrow H_2O + HO_2 \qquad (2)$$

The purpose of the present work was the determination of the activation energy for reaction 1 in liquid water for temperatures under 100 °C, with the best possible accuracy. To achieve this purpose, it was essential to keep this measurement as independent as possible from rate constants and activation energies for other reactions.

Experimental Section

General Considerations. The most promising way to minimize dependence on other reaction rates was to attempt direct observation of reaction 1 by following either the disappearance of OH or the appearance of H by pulse radiolysis techniques. Figure 1 shows the UV absorption spectra of OH,[13] H,[16] and those of the radiolysis products O_2^-,[3] HO_2,[3] H_2O_2,[17] H_2O_3,[3] and e_{aq}^-[4,16] which might possibly contribute to the measured absorption signal. After some model calculations and preliminary experiments, the following experimental conditions were decided upon: (1) species to be observed, OH; (2) wavelength, 280 nm; (3) solution, water containing about 10^{-3} mol L^{-1} N_2O, the maximum feasible amount of H_2 (see next section), and 2×10^{-5} mol L^{-1} $HClO_4$; (4) pressure, close to atmospheric; (5) radiation dose, less than 100 rad/pulse. The chosen species and wavelength gave the optimum signal-to-noise (S/N) ratio and minimum contribution to the signal by other species. The N_2O in the solution was sufficient to convert the bulk of e_{aq}^- into OH radicals, thus eliminating the contribution of e_{aq}^- to the absorption signal. The $HClO_4$ was added to shift the pH to 4.7 where the decay rate of the HO_2-O_2^- system has its maximum value.[3]

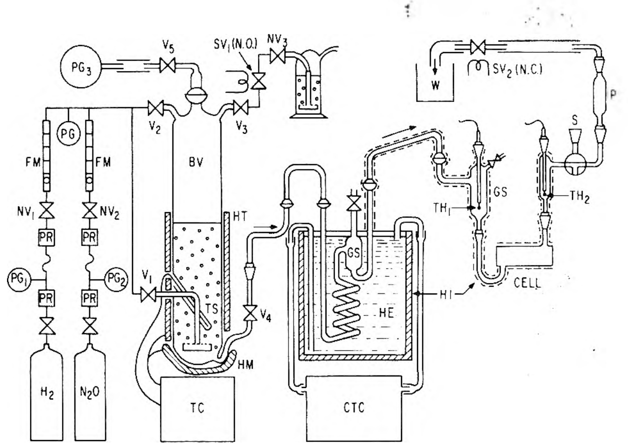

Figure 2. Schematic diagram of flow system: BV, bubbling vessel; CTC, constant temperature circulator; FM, flow meter; GS, gas separator; HE, heat exchanger; HI, heat insulation; HM, heating mantle; HT, heating tape; NC, normally closed; NO, normally open; NV, needle valve; P, pipet for collecting samples; PG, pressure gauge; PR, pressure regulator; S, sampling point; SV, solenoid valve; TC, temperature controller; TH, thermistor; TS, temperature sensor; V, valve or stopcock; W, waste container.

At atmospheric pressure, the dose had to be kept low to assure that the OH radicals decay predominantly via reaction 1. As an alternative, we had considered the use of H_2 at high pressure and a correspondingly larger dose, but calculations showed that this would not increase the S/N ratio.

Because of the low pulse dose and low absorptivity of OH, a large number of transient signals had to be averaged to obtain a satisfactory S/N ratio. The ensuing consumption of H_2 and the production of N_2 and possibly other products, in turn, made the use of a flow system mandatory.

The experimental arrangement is described in detail in the following sections.

Gas Equilibration and Flow System. Figure 2 shows a schematic diagram of the entire flow system. The gases used were hydrogen (Matheson, prepurified, 99.95%) and nitrous oxide (Liquid Carbonic, 99.9%). The gas flow rates were controlled by two needle valves, NV1 and NV2. The pressure before the needle valves was kept constant at 10 psig (ca. 1.7 atm). Two calibrated flow meters (Rotameter type, Matheson) monitored the flow rates. The ratio of the flow rate of N_2O to that of H_2 varied from 1:19 to 1:3 for water temperatures of 15 and 90 °C, respectively.

The water, distilled 5 times,[18] was placed in a 2-L bubbling vessel, and $HClO_4$ (G. F. Smith Chemical Co., reagent grade) was added to give a concentration of 2×10^{-5} mol L^{-1}. The vessel was then heated to 1-2 °C above the intended measuring temperature. During this time, the water was purged with H_2 (V1 and V5 open, V2 and V3 closed, gauge PG3 disconnected). After the preset temperature was reached, PG3 was connected, V3 opened, and the solution equilibrated with the desired mixture of H_2 and N_2O for at least 20 min. The pressure above the solution was adjusted with needle valve NV3 to such a value (about 875 Torr) that it would not change when, later, the gas outlet would be closed and the solution pumped through the cell. After equilibration, the bubbling was discontinued by closing V1 and opening V2. The flow rates were readjusted so that the gas pressure above the solution did not change.

To start the flow of the solution, SV1 was closed and SV2 opened by remote control. The water was then

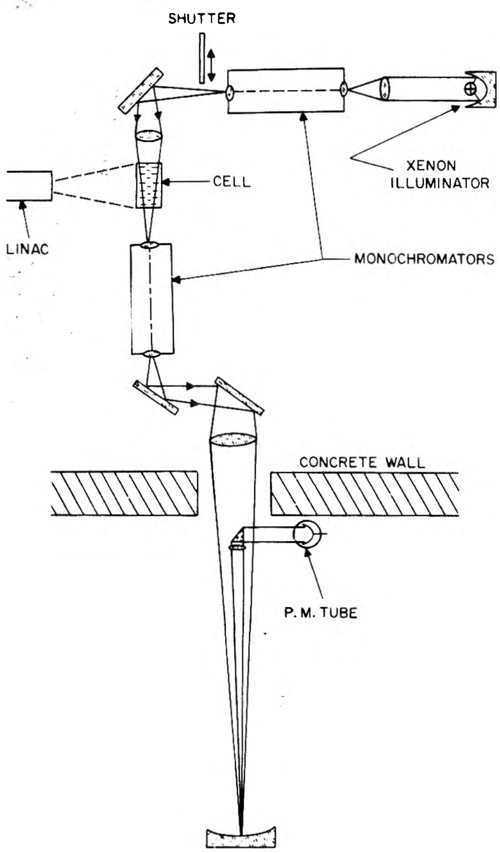

Figure 3. Optical arrangement for transient absorption measurements.

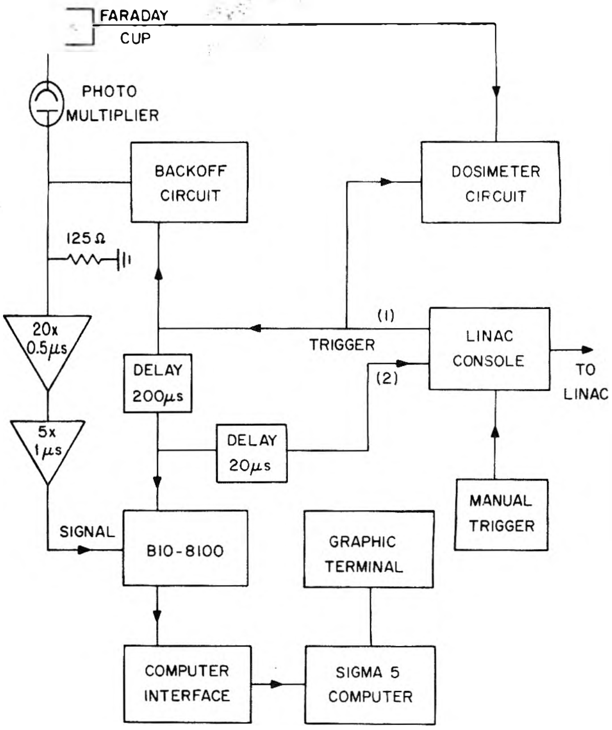

Figure 4. Block diagram of the electronic circuitry for averaging transient absorption signals.

pumped to the cell through a heat exchanger (a thin-walled glass coil) which adjusted its temperature to the desired value. Since the pressure in the bubbling vessel was constant, the water flow rate was equal to the total gas flow rate (ca. 2 mL/s). The water temperature was measured with two calibrated thermistors, TH1 and TH2, and the cell temperature assumed to be the average of the two readings. The maximum difference between the readings, at 90 °C cell temperature, was 1 °C, and was presumably caused by heat loss through the cell windows. The irradiation experiment was started when the cell temperature had reached its equilibrium value (after about 3 min).

Unirradiated samples of the solution, for H_2 analysis, were taken at the point S. Samples irradiated under steady state conditions, for H_2O_2 analysis, were taken by simultaneously stopping irradiation and flow and then removing pipet P.

Optical Arrangement. The optical apparatus for the transient absorption measurements is shown in Figure 3. An existing arrangement, originally designed for measurements in the far UV, was used after minor modifications. The light source is a Varian Type VIX 300 high-intensity illuminator (xenon) with an aluminized parabolic reflector and a sapphire window. Two Bausch and Lomb high intensity monochromators, with 200–400-nm gratings, are used to minimize scattered light. They are oriented "face to face", with their entrance slits (small aperture ends) pointing toward the cell, and all external optical elements are dimensioned in such a way that, apart from reflection losses, the photomultiplier tube receives all the light passing through the first monochromator (EMI 9783 B), and at the same time the minimum possible amount of Čerenkov light from the cell. The photomultiplier tube, and all electronic circuitry, are located outside the linac pit to avoid interference from the strong electric and magnetic fields generated by the linac system.

Electronic Circuitry and Signal Averaging System. A block diagram of the entire electronic circuitry is shown in Figure 4. The output signal from the photomultiplier tube is amplified 100 times and applied to the input of a Biomation Type 8100 transient recorder (Bio-8100). An automatic dc-backoff circuit of a design similar to one developed by Keene and Bell[19] forces the dc level at the beginning of a transient signal to zero. The Bio-8100 is interfaced with a Sigma 5 (Xerox Corp.) computer. Before starting a signal-averaging experiment, the desired number of pulses and the pulse rate is preset at the linac console, and corresponding instructions entered into the computer through a Tektronix 4010 graphic terminal. All settings of the Bio-8100 are controlled by the computer. After the irradiation sequence is initiated by a manual trigger command to the linac console, the latter transmits the preset number of trigger pulses through line 1 to our apparatus, where they are used to trigger the dc-backoff circuit, the Bio-8100, and a gated dosimeter circuit. The pulses are then returned, through line 2, to the linac console where each pulse triggers a beam pulse.

The signals from the photomultiplier are digitized in the Bio-8100, and the data transmitted to the computer. There, successive values from each channel of the Bio-8100 are added on-line to produce a histogram. At the end of the experiment, this histogram, together with the number of pulses and all settings of the Bio-8100, is automatically stored on the computer disk for further processing, and the raw data are displayed in graphic form on the terminal. Also stored are the DVM reading (I_0) and the dosimeter reading, after being entered through the graphic terminal. In our experiments, we used 512 channels of the Bio-8100, and a pulse rate of 15/s. The total number of pulses averaged for one measurement varied between about 700 and 1000.

After each irradiation experiment, a blank run without irradiation is carried out and the baseline thus obtained is subtracted from the signal. This eliminates a small 60-Hz component in the signal.

Dosimetry. The mechanical arrangement for beam collimation and monitoring is similar to one previously

TABLE I: Reactions, Rate Constants, and Activation Energies Used for Model Calculations

	Reactions	k (25 °C), L mol^{-1} s^{-1}	E_a, kcal mol^{-1}
1	$OH + H_2 \rightarrow H + H_2O$	$4 \times 10^{7\,a}$	3.2^a
2	$OH + H_2O_2 \rightarrow HO_2 + H_2O$	$2.25 \times 10^{7\,b}$	1.95^i
3	$H + H \rightarrow H_2$	$1 \times 10^{10\,c}$	3.25^j
4	$H + OH \rightarrow H_2O$	$1.5 \times 10^{10\,c}$	3.25^j
5	$H + H_2O_2 \rightarrow OH + H_2O$	$9 \times 10^{7\,c}$	3.25^k
6	$OH + OH \rightarrow H_2O_2$	$5.0 \times 10^{9\,b}$	3.25^j
7	$e_{aq}^- + N_2O \rightarrow N_2 + OH + OH^-$	$9.1 \times 10^{9\,d}$	3.5^l
8	$e_{aq}^- + H_2O_2 \rightarrow OH + OH^-$	$1.3 \times 10^{10\,e}$	3.5^l
9	$e_{aq}^- + OH \rightarrow OH^-$	$3 \times 10^{10\,e}$	3.5^l
10	$e_{aq}^- + H \rightarrow H_2 + OH^-$	$2.5 \times 10^{10\,e}$	3.5^l
11	$e_{aq}^- + e_{aq}^- \rightarrow H_2 + 2OH^-$	$5 \times 10^{9\,e}$	5.2^m
12	$e_{aq}^- + O_2 \rightarrow O_2^-$ $(+ H^+ \rightarrow HO_2)$	$1.3 \times 10^{10\,e}$	3.5^l
13	$H + O_2 \rightarrow HO_2$	$1.9 \times 10^{10\,c}$	3.25^j
14	$H + HO_2 \rightarrow H_2O_2$	$2 \times 10^{10\,c}$	3.25^j
15	$OH + HO_2 \rightarrow H_2O_3$	$1 \times 10^{10\,f}$	3.25^j
16	$HO_2 + HO_2 \rightarrow H_2O_2 + O_2$	$1.45 \times 10^{7\,g}$	2.1^n
17	$H_2O_3 \rightarrow H_2O + O_2$	20^h	20^o
18	$e_{aq}^- + H^+ \rightarrow H$	$2.3 \times 10^{10\,e}$	2.8^e

[a] Final values from our own measurements. [b] Mean, or presumably best, value from ref 13. [c] Mean, or presumably best, value from ref 12. [d] Reference 26. [e] Mean, or presumably best, value from ref 8. [f] Reported in ref 3. [g] Rate constant for the mixed reaction HO_2 (O_2^-) + HO_2, ref 3. [h] First-order rate constant (s^{-1}), ref 3. [i] From our value for reaction 1 and the E_a difference between reactions 1 and 2.[15] [j] This value used for all diffusion-controlled reactions of uncharged species. [k] No literature value known, value not critical. [l] Used for all diffusion-controlled reactions of e_{aq}^-,[18] except $e_{aq}^- + e_{aq}^-$. [m] Reference 10. [n] Reference 3. [o] Rough extrapolation from data in ref 3.

used.[20] In our newly developed integrating circuit, the beam current pulse, collected by the Faraday cup, is spread to about 10 ms width, amplified by a current-to-voltage amplifier, and fed to a voltage-to-frequency converter. A gated counting circuit then produces a direct reading of the collected charge. The dose calibration factor (dose per unit charge) was determined by measuring the e_{aq}^- absorption at 600 nm in an H_2-saturated NaOH solution at pH 11, using $G_{e_{aq}^-}\epsilon_{e_{aq}^-}{}^{600} = 34500$.[20]

Results and Evaluation

Figure 5 shows a typical computer plot of absorbance vs. time calculated from the data obtained in our experiment. The figure also shows, for comparison, the result of a computer model calculation which will be discussed later.

Measurements at 250, 260, 300, and 320 nm yielded decay curves of practically identical shape, although with a lower S/N ratio, the relative amplitudes corresponding to the OH spectrum depicted in Figure 1. When irradiation with repetitive pulses was continued after the water flow was stopped, the decay rate of the signal became increasingly slower, due to the consumption of H_2, and finally reached a value consistent with reaction 6, Table I. Also, irradiation of a fresh solution with single pulses of higher doses (ca. 10 krad) produced a predominantly second-order decay, in agreement with the known rates of reactions 1 and 6. These three tests confirm our assumption that we were indeed observing the OH radical.

For evaluating our measurements of k_1, we followed the procedure outlined below and described in more detail in the following sections.

(1) Pseudo-first-order rate constants for the OH decay were calculated from the measured decay curves, using a nonlinear least-squares fitting method.

(2) H_2 and N_2O concentrations were determined for each individual run.

(3) Uncorrected values for k_1 were calculated and used to obtain a first approximate value for E_a.

(4) A number of representative experiments were computer-modeled, using these values of k_1 and E_a, and first correction factors for other OH reactions and other absorbing species were determined.

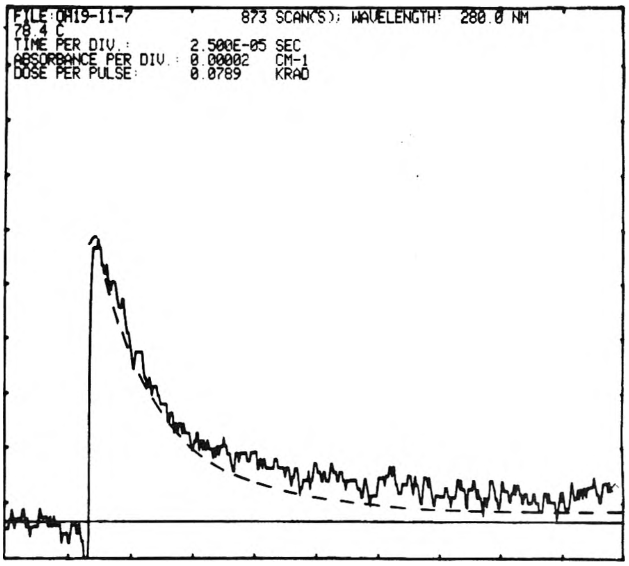

Figure 5. Computer plot of absorbance vs. time, calculated from experimental data: dashed line, result of model calculation; time range, 0–250 μs; absorbance range, 0–2 × 10^{-4} cm^{-1}.

(5) New model calculations, based on the improved values of k_1 and E_a, were carried out, and new correction factors determined.

(6) Step 5 was repeated once more to arrive at the final values for k_1 and E_a. The adjustments made in the last step were small in comparison to the overall error limits.

To obtain the pseudo-first-order rate constants we adapted a computer program developed by Jonah and Hamilton,[21] to the data format obtained from our experiments. The program performs a non-linear least-squares fit, yielding the three parameters A_0, A_{inf}, and K_1 of a first-order decay curve with final absorption:

$$A = A_{inf} + (A_0 - A_{inf})e^{-K_1 t}$$
$$= A_{inf}(1 - e^{-K_1 t}) + A_0 e^{-K_1 t} \quad (3)$$

Figure 6 shows the computer fit for the data from Figure 5.

The equivalence of the two functions in eq 3 shows that a "tail" of the decay curve (A_{inf}) does not affect the measured K_1, if it is due to a product appearing imme-

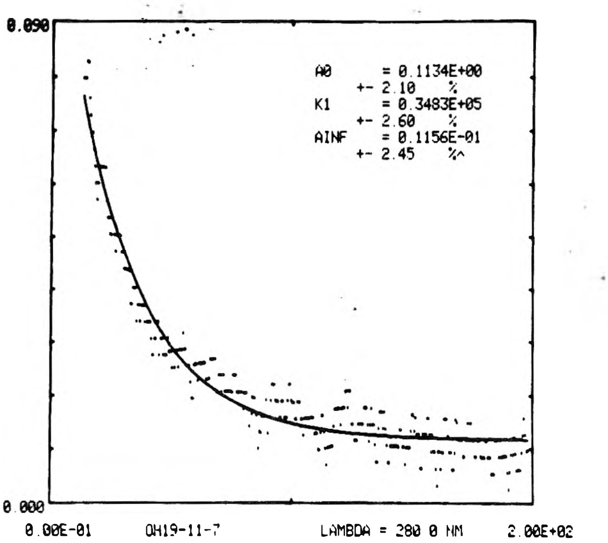

Figure 6. Example of nonlinear least-squares fit to determine pseudo-first-order rate constant: time range, 0–200 μs, absorbance range, 0–9 × 10^{-5} cm^{-1}. (The printed ordinate values, A_0 and A_{inf}, contain a scale factor of 1000.)

diately (e.g., from a rapid reaction of OH with an impurity), or to a product with a buildup time constant K_1 (e.g., from a rapid reaction of H with an impurity).

Determination of H_2 and N_2O Concentrations. Attempts to determine $[\mathrm{H_2}]$ by means of a Van Slyke manometric apparatus attached to a gas chromatograph revealed a significantly nonlinear response of the gas chromatograph with respect to $[\mathrm{H_2}]$ in the presence of $\mathrm{N_2O}$. We therefore calculated the molar $\mathrm{H_2}$ concentration from the known values of temperature, pressure, and gas flow ratio, relying on published data on gas solubility,[22] water vapor pressure,[23] and density of water.[24]

At high equilibration temperatures, the water vapor pressure approaches atmospheric pressure, and $[\mathrm{H_2}]$ depends strongly on the total pressure (850–900 Torr) which is composed of gas pressure, water vapor pressure, and hydrostatic pressure. Since the water outlet of the bubbling vessel (Figure 2) was at the bottom of a 40-cm water column, and the degree of mixing in the vessel was unknown, an uncertainty of 30 Torr existed with regard to the hydrostatic pressure. At the highest equilibration temperature used (94 °C), and 870 Torr (gas + vapor) pressure, this would be equivalent to an uncertainty of 11% for $[\mathrm{H_2}]$. To reduce this uncertainty and to test our method of $[\mathrm{H_2}]$ determination, solutions were equilibrated with $\mathrm{H_2}$ alone, one group at 99 °C, one at 89 °C, with total gas pressures between 843 and 880 Torr, and the calculated $\mathrm{H_2}$ concentrations compared with those determined by taking samples both at the outlet of the bubbling vessel and at point S of the flow system (Figure 2), and then extracting and analyzing the hydrogen in the Van Slyke apparatus.[25] No systematic differences in $[\mathrm{H_2}]$ were found between samples taken at the two different points, and the measured and calculated $\mathrm{H_2}$ concentrations agreed within 2% at both temperatures if a hydrostatic pressure of 39 cm of water (essentially the full height of the water column) was assumed.

When attempting to calculate $\mathrm{N_2O}$ concentrations, we found no reliable solubility data in the literature for temperatures above 50 °C. We therefore measured the solubility of $\mathrm{N_2O}$ between 50 and 95 °C by equilibrating water with $\mathrm{N_2O}$ at atmospheric pressure and extracting the dissolved $\mathrm{N_2O}$ in the Van Slyke apparatus by repeated equilibration. Figure 7 shows our values of β (standard 1 mL of gas dissolved in 1 g of $\mathrm{H_2O}$ at 1 atm) as a function of temperature together with literature values[22] between 0 and 50 °C. Although there is a slight discontinuity at 50 °C, the accuracy of the data was sufficient for our purposes.

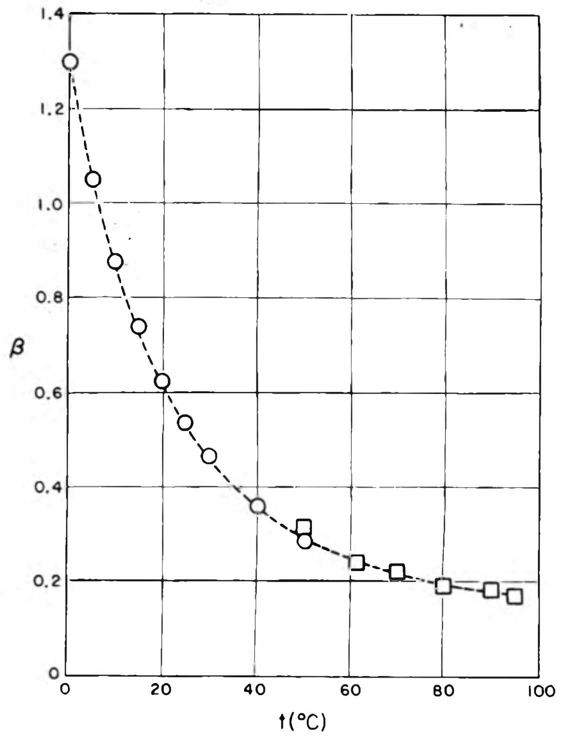

Figure 7. Solubility of $\mathrm{N_2O}$ in water: our own measurements ($t \geq$ 50 °C), and literature data[22] ($t \leq$ 50 °C). Ordinate β: standard 1 mL of $\mathrm{N_2O}$ dissolved in 1 g of $\mathrm{H_2O}$ at 760 Torr partial pressure.

Calculation of Uncorrected Second-Order Rate Constants and Activation Energy. Uncorrected values of k_1 were calculated from the values of K_1 obtained in step 1, and the molar $\mathrm{H_2}$ concentrations determined in step 2, after correcting the latter for the consumption of $\mathrm{H_2}$ during the flow of the solution through the irradiated cell. For this, we used the relation

$$G(-\mathrm{H_2}) = G_{e_{\mathrm{aq}}^-} - G(\mathrm{H_2O_2}) \tag{4}$$

dictated by the requirement of material balance (each e_{aq}^- liberates $^1/_2\mathrm{O_2}$ from $\mathrm{N_2O}$). $G(\mathrm{H_2O_2})$ was determined analytically and from model calculations (see below). One-half of the $\mathrm{H_2}$ loss in the cell thus determined (1–4%) was subtracted from the $\mathrm{H_2}$ concentrations. E_a was then calculated by performing a linear least-squares fit for the points $(1/T, \ln k_1)$, assuming equal relative error limits for all values of k_1. We obtained k_1 (25 °C)$_{\mathrm{uncorr}}$ = 4.5 × 10^7 L mol^{-1} s^{-1}, and $E_{\mathrm{a(uncorr)}}$ = 3.85 ± 0.15 (std dev) kcal mol^{-1}.

Model Calculations. All model calculations were carried out with the computer program described in ref 5. Table I lists the reactions, rate constants (for 25 °C), and activation energies used for the calculations. The species absorbing at 280 nm and those with a nonvanishing G value are listed in Table II. In the calculations, $\mathrm{HO_2}$ and $\mathrm{O_2}^-$ are treated as one species ("$\mathrm{HO_2}$"), using as rate constant for reaction 16 and for the absorptivity of "$\mathrm{HO_2}$", average values calculated for pH 4.7.

The first set of calculations was done to determine steady state concentrations of $\mathrm{H_2O_2}$, $\mathrm{O_2}$, "$\mathrm{HO_2}$", and $\mathrm{H_2O_3}$ after repetitive pulsing. The results (for 25 °C) can be summarized as follows:

(1) No buildup of $\mathrm{O_2}$, "$\mathrm{HO_2}$", and $\mathrm{H_2O_3}$ takes place regardless of an assumed small initial $\mathrm{O_2}$ contamination, which rapidly disappears.

(2) $\mathrm{H_2O_2}$ builds up to a steady state concentration of about 2 × 10^{-6} mol L^{-1}, plus twice the initial $\mathrm{O_2}$ concen-

TABLE II: Species Absorbing at 280 nm with Yields and Absorptivities

Species	G value[a] particles/ 100 eV	ϵ,[b] cm^{-1} L mol^{-1}
OH	2.7	245
H	0.45	10[c]
H_2	0.45	
H_2O_2	0.7	15
HO_2	0.02	270
H_2O_3		12
e_{aq}^-	2.81	715

[a] A consistent set of G values was derived from data in ref 2, p 64, and ref 4, p 140. [b] From ref 3, 4, 13, 16, and 17. [c] Estimated by extrapolation.

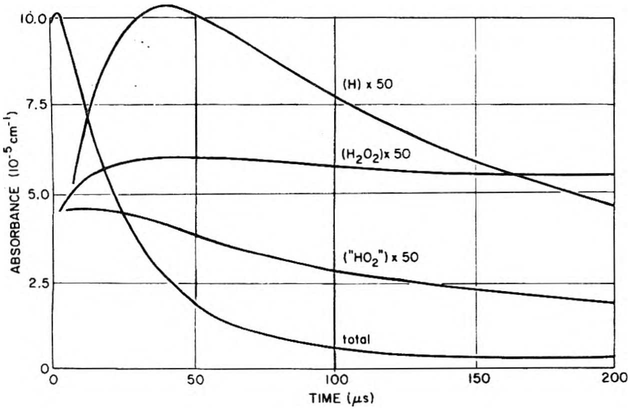

Figure 8. Calculated contributions of H, H_2O_2, and "HO_2" (pH 4.7) to total absorbance signal.

tration (in our case less than 10^{-7} mol L^{-1}). This result was confirmed by chemical analysis, using the KI method:[15] all samples analyzed contained 1-3 × 10^{-6} L mol^{-1} of H_2O_2, with no detectable effect of temperature.

(3) Equation 4 was confirmed.

In the subsequent calculations, modeling the effect of single pulses under steady-state conditions, we therefore assumed initial concentrations of 2 × 10^{-6} mol L^{-1} for H_2O_2, and zero for "HO_2", O_2, and H_2O_3. The purpose of these calculations was to determine the errors in the values of k_1 and E_a due to reactions other than reaction 1, and to absorbing species other than OH. For a number of representative experiments, the transient absorbance signal was calculated for the actual experimental conditions. A nonlinear least-squares fit, analogous to the one illustrated in Figure 6, was then performed on the calculated decay curve, and the first-order rate constant, K_1', thus determined, was divided by $K = k_1[H]$ to obtain a correction factor f_c. For the experiments not actually modeled, f_c was interpolated using the observed dependence of f_c on temperature and dose. By multiplying all "old" values of k_1 by the corresponding factors f_c, a new set of rate constants k_1 was obtained.

This procedure was repeated twice to obtain the final corrections. Table III lists all experimental data points with the original values of k_1, the final correction factors f_c, and the final values of k_1.

To illustrate the relative contribution of species other than OH to the absorbance, Figure 8 plots, for a typical experiment (84.2 °C), the contributions from H, H_2O_2, and "HO_2", together with the calculated total absorbance signal. The contribution from "HO_2" is possibly higher, since Czapski[14] now considers $\epsilon_{O_2^-}{}^{240}$ = 1950 ± 50 L mol^{-1} cm^{-1} the "best" value for the peak absorptivity, which is about twice the value plotted in Figure 1. The negligible contribution from H_2O_3 was omitted. It is evident that the three species cause a small distortion of the OH absorbance signal, in particular a "tail" of about 3% of the peak. A comparison between the calculated and the measured signal is made in Figure 5. In view of the fact that k_1 was the only adjusted parameter, the agreement is quite satisfactory. The tails (A_{inf}) of the experimental curves are generally higher than calculated, varying between 5 and 12% of the peak. We have no certain explanation for this discrepancy. However, the results from H_2O_2 analyses and from calculations rule out O_2 con-

TABLE III: Values of Uncorrected and Final Rate Constant k_1 for All Experiments, with Correction Factors f_c

Temp, °C	k_1, 10^8 L mol^{-1} s^{-1}	f_c	Model calculation	k_1(final), 10^8 L mol^{-1} s^{-1}
30.2	0.545	0.871		0.475
30.9	0.482	0.871		0.420
30.0	0.522	0.871		0.455
40.1	0.630	0.865		0.545
39.9	0.562	0.865	x	0.486
39.4	0.679	0.865		0.587
39.3	0.616	0.865		0.533
51.2	0.877	0.831		0.729
51.1	0.699	0.831		0.556
50.9	0.685	0.831		0.569
58.6	0.881	0.811		0.714
60.3	0.891	0.806	x	0.718
60.6	1.059	0.806		0.854
60.3	0.796	0.806		0.642
66.5	0.926	0.797		0.738
70.3	0.980	0.971	x	0.775
69.6	1.066	0.791		0.843
80.2	0.994	0.770		0.765
78.8	1.076	0.778	x	0.830
78.4	1.292	0.778		1.018
32.1	0.566	0.870		0.492
21.5	0.396	0.877		0.346
20.8	0.372	0.877	x	0.326
20.9	0.419	0.877		0.367
15.2	0.418	0.881		0.368
15.2	0.319	0.881		0.281
15.0	0.369	0.881		0.325
14.8	0.348	0.881		0.307
90.7	1.792	0.603		1.081
90.3	1.780	0.603	x	1.073
90.3	1.439	0.617		0.888
90.3	1.668	0.686	x	1.144
83.5	1.216	0.740		0.900
83.3	1.274	0.740		0.943

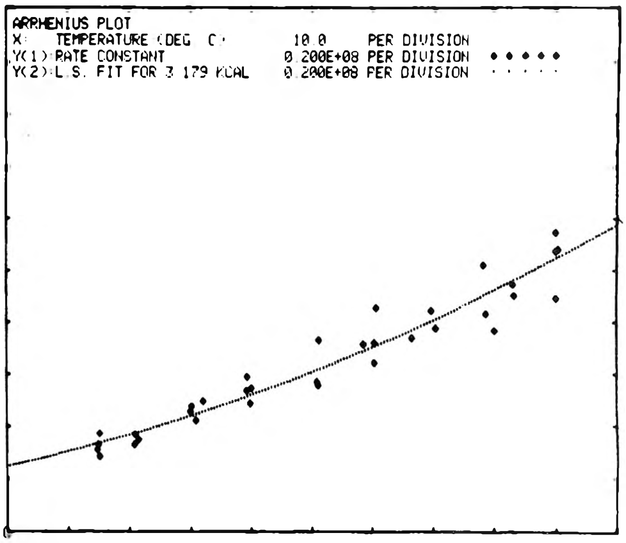

Figure 9. Plot of measured rate constant k_1 vs. temperature, with best-fitting Arrhenius function: temperature range, 0–100 °C; ordinate, k_1 (0–2 × 10^8 L mol^{-1} s^{-1}).

TABLE IV: Contribution of Various Factors to the Error Limits of $k_1(OH + H_2) = 3.96 \times 10^7$ L mol^{-1} s^{-1} and Its Activation Energy E_a = 3.2 kcal mol^{-1} (all Values are 90% Errors)

Error source	Contribution to k_1 (25 °C), %	Contribution to ΔE_a, kcal mol^{-1}
Random errors	±5	±0.28
H_2 determination	±3	±0.09
Uncertainty of k_4(H + OH)	±7	±0.3
Uncertainty of k_6(OH + OH)	±1	±0.09
Temperature errors (±0.5 °C)	Negligible	Negligible
Composite error	±9.2	±0.43

tamination. One possible explanation is a fast initial reaction of OH with a trace impurity, resulting in an absorbing product. Part of the discrepancy may also be due to the uncertainty of the values for ϵ_H, $\epsilon_{O_2^-}$, and $\epsilon_{H_2O_2}$.

The results of a detailed error analysis, carried out with the aid of model calculations, are compiled in Table IV. A conservative estimate of the total 90% confidence error of E_a is ±0.5 kcal mol^{-1}, for that of k_1 (25 °C), ±10%.

The error analysis reveals that the uncertainty of k_4 and its activation energy represents a significant contribution to the total error limits for k_1 and E_a. Thus, a new and more accurate experimental determination of k_4 and its temperature dependence would improve the accuracy of k_1 and E_a.

Comparison with Gas Phase Data

Gardiner et al.[27] have plotted all available values of k_1 measured in the gas phase between 250 and 1600 K on a log k_1 vs. $1/T$ scale and performed a least-squares fit to the function: $\log k_1 = A + B \log T + C/T$. Their resulting expression for the activation energy is

$$E_{a,gas} = 3.04 \text{ kcal mol}^{-1} + 1.77RT \qquad (5)$$

For T = 325 K, the average temperature of our measurements, eq 5 yields $E_{a,gas}$ = 4.18 kcal mol^{-1}. Smith and Zellner[28] made calculations based on the activated complex theory,[29] to predict the H/D isotope effect on k_1 in the gas phase. Although they achieved good agreement with the experimentally determined isotope effect, their chosen potential V^* (height of classical energy barrier) leads to a slightly negative temperature dependence of the activation energy:

$$E_{a,gas} = V^* + \theta RT$$

with $\theta \approx -0.5$, in strong disagreement with the experimental dependence.[30] No calculations, on a molecular basis, of E_a and its temperature dependence have been made for the condensed phase. Also, our measurements are not sufficiently sensitive to determine θ. We, therefore, tentatively compare our value ($E_{a,aq}$) with $E_{a,gas}$ on the basis of the thermodynamic relations (ref 29, p 108)

$$E_{a,aq} = \Delta H^{\circ\ddagger}_{aq} + RT \qquad (6a)$$

for the condensed phase (at constant pressure), and

$$E_{a,gas} = \Delta H^{\circ\ddagger}_{gas} + 2RT \qquad (6b)$$

for a bimolecular reaction in a perfect gas mixture at constant volume, with $\Delta H^{\circ\ddagger}$ being the enthalphy of activation. Using the experimental values for 325 K, one obtains from eq 6a and 6b: $\Delta H^{\circ\ddagger}_{gas} - \Delta H^{\circ\ddagger}_{aq}$ = 0.36 kcal mol^{-1}. This difference is much smaller than the combined error limits of the two experimental values, i.e., our value of E_a in aqueous solution is consistent with the gas phase value.

Acknowledgment. I am greatly indebted to Edwin J. Hart for giving the first impetus to this investigation, and for many fruitful discussions. An essential contribution to this work was made by Ronald E. Vanbuskirk and Paul P. Day, who developed the computer programs for the signal averaging system. I furthermore thank Charles D. Jonah and Edwin J. Hamilton, Jr., for their assistance with the nonlinear least-squares fitting program; Steve G. Petrek for building part of the electronic circuitry; and Patricia D. Walsh for helping with the chemical analyses.

References and Notes

(1) Work performed under the auspices of the U.S. Energy Research and Development Administration.
(2) L. M. Dorfman and M. S. Matheson, "Pulse Radiolysis", R. F. Gould, Ed., MIT Press, Cambridge, Mass., 1969.
(3) B. H. J. Bielski and J. M. Gebicki, *Adv. Radiat. Chem.*, **2**, 177 (1970).
(4) I. G. Draganic and Z. D. Draganic, "The Radiation Chemistry of Water", E. M. Loebl, Ed., Academic Press, New York, N.Y., 1971.
(5) K. H. Schmidt, Argonne National Laboratory Reports ANL-7199 (April 1966) and ANL-7693 (March 1970).
(6) G. H. Jenks, Oak Ridge National Laboratory Report ORNL-3848 (October 1965).
(7) G. H. Jenks and J. C. Griess, Oak Ridge National Laboratory Report ORNL-4173 (November 1967).
(8) M. Anbar, M. Bambenek, and A. B. Ross, *Natl. Stand. Ref. Data Ser., Natl. Bur. Stand.*, **No. 43** (1973).
(9) M. S. Matheson, "Reactions of Solvated Electrons", Chapter 10 in "Reactions in Condensed Phases", Physical Chemistry, Vol. VII, Academic Press, New York, N.Y., 1975, p 533.
(10) E. J. Hart and M. Anbar, "The Hydrated Electron", Wiley-Interscience, New York, N.Y., 1970.
(11) M. Anbar and P. Neta, *Int. J. Appl. Radiat. Isotopes*, **18**, 493 (1967).
(12) M. Anbar, Farhataziz, and A. B. Ross, *Natl. Stand. Ref. Data Ser., Natl. Bur. Stand.*, **No. 51** (1975).
(13) L. M. Dorfman and G. E. Adams, *Natl. Stand. Ref. Data Ser., Natl. Bur. Stand.*, **No. 46** (1973).
(14) G. Czapski, *Annu. Rev. Phys. Chem.*, **22**, 171 (1971).
(15) C. J. Hochanadel, *J. Phys. Chem.*, **56**, 587 (1952).
(16) B. D. Michael and E. J. Hart, private communication.
(17) From measurements performed at ANL by E. J. Hart, P. Walsh, and K. H. Schmidt. Compare the somewhat different values in ref 3.
(18) K. H. Schmidt and S. M. Ander, *J. Phys. Chem.*, **73**, 2846 (1969).
(19) J. P. Keene and C. Bell, *Int. J. Radiat. Phys. Chem.*, **5**, 463 (1973).
(20) B. D. Michael, E. J. Hart, and K. H. Schmidt, *J. Phys. Chem.*, **75**, 2798 (1971).
(21) C. D. Jonah and E. J. Hamilton, private communication.
(22) J. D'Ans and E. Lax, "Taschenbuch für Physiker und Chemiker", 3rd ed, Vol. I, E. Lax and C. Synowietz, Ed., Springer-Verlag, Berlin, 1964, pp 1203–1205.
(23) Reference 22, p 608.
(24) Reference 22, p 602.
(25) E. J. Hart and J. K. Thomas, Argonne National Laboratory Report ANL-7856 (September 1971).
(26) B. Hickel and K. H. Schmidt, *J. Phys. Chem.*, **74**, 2470 (1970).
(27) W. C. Gardiner, Jr., W. G. Mallard, and J. H. Owen, *J. Chem. Phys.*, **60**, 2290 (1974).
(28) I. W. M. Smith and R. Zellner, *J. Chem. Soc., Faraday Trans. 2*, **70**, 1045 (1974).
(29) R. E. Weston, Jr., and H. A. Schwarz, "Chemical Kinetics", Prentice Hall, Englewood Cliffs, N.J., p 95.
(30) A classical estimate of the temperature dependence of $E_{a,gas}$ (ref 29, p 103) yields θ = +2, which agrees fairly well with eq 5.

Evidence for Spur Overlap in the Pulse Radiolysis of Water

James E. Fanning, Jr., Conrad N. Trumbore,* P. Glenn Barkley, and Jon H. Olson†

Department of Chemistry and Department of Chemical Engineering, University of Delaware, Newark, Delaware 19711 *(Received December 16, 1974; Revised Manuscript Received April 18, 1977)*

The kinetics of the decay of hydrated electron absorbance in pure water has been studied as a function of time and radiation dose delivered by 20-ns pulses of 15-MeV electrons. In order to identify intraspur reactions of the hydrated electron, values of the function $\{[-d(e_{aq}^-)/(e_{aq}^-)]/dt\}_t$ ($\equiv Q_t$) were investigated as a function of pulse dose and time. Q_t represents the fraction of hydrated electrons disappearing at any given time, t, following the pulse. Whereas Q has the same functional form as a first-order rate constant, it is not a constant, but decreases with increasing time following the pulse. However, the *functional form of Q_t vs. time* remains the same at low pulse doses (37–380 rads) for relatively long periods of time (up to 1 μs). The dose independence of Q is interpreted as evidence for predominantly intraspur hydrated electron decay. A plot of Q_t vs. the function $[(\text{time})^{1/2}(\text{dose})^{1/3}]$ yields a relatively sharp transition from dose independent hydrated electron decay (interpreted as arising predominantly from intraspur reactions) to dose dependent decay (both interspur and intraspur decay). This transition region is interpreted as the onset of significant spur overlap. In the range 0–8000 rads per 20-ns pulse, an empirical constant: (approximate time of detectable overlap)$^{1/2}$(dose)$^{1/3}$ = 110 ± 10 ns$^{1/2}$ rads$^{1/3}$ is obtained which correlates the onset of experimentally observable spur overlap. Based upon these results, implications regarding spur sizes and spatial distributions of spurs and the need to include spur overlap considerations in modeling studies are developed.

Introduction

Much of the experimental evidence in support of the spur model in aqueous radiation chemistry has been indirect.[1-3] Despite difficulties with the spur model, experimental evidence which has appeared to conflict with the model has been accommodated by some small, but significant, modifications in initial parameters. Experiments utilizing ultrashort radiation pulses and time resolution have provided new challenges to the spur model. While certain of these challenges, most notably the results of Hunt and co-workers,[4] have been answered by Schwarz,[5] the results of Jonah et al.[6] appear to require modifications of certain spur model parameters.

What is needed to test any modified spur model is an experimental indication of the distributions of the hydrated electron and of other reactive intermediates as a function of space and time following the pulse. Toward this end, we have investigated the hydrated electron decay in pure water as a function of time and of dose delivered by 20-ns pulses of 15-MeV electrons.

We assume that the distribution function for nearest-neighbor interspur distances at the time of spur formation contains a relatively small fraction of near-zero distances. If such is the case, at low doses, the bulk of the newly formed spurs will be far enough apart that electron decay which arises predominantly from intraspur reactions can be observed. Thus, at low enough pulse doses, the measured electron decay rate for the "average" spur should be independent of pulse dose; that is, a rate which is directly proportional only to the number of spurs present. At higher pulse doses (and for longer times at lower pulse doses), it is presumed that spurs begin to overlap in large enough numbers to detect deviations from the independent, intraspur electron decay established at lower doses and thus provide rough experimental criteria for the average "size" of spurs at different times. At large enough pulse doses and at long enough times, homogeneity of all species is approached, and homogeneous treatment of the kinetics then can be compared and contrasted with the nonhomogeneous kinetics of the spur.

Experimental Section

The experimental work reported here was performed at the Chemistry Division of the Argonne National Laboratory, Argonne, Ill. Most of the techniques employed in this work are described elsewhere.[7,8] Water, which was at least triply distilled, was obtained from three different stills at three different laboratories with no variation in results. Three gases were used for saturating water. The minimum gas purities were 99.95% for hydrogen and 99.995% for helium and argon. During bulk saturation of samples helium and hydrogen were passed through a liquid nitrogen trap for further purification. The syringe technique[7,8] was used to exchange the desired gas for the air initially present. Random checks on the oxygen concentration in these solutions showed values less than 2 μM, usually between 0.2 and 1.0 μM. (See supplementary material for additional details.)

The absorbance of the hydrated electron was followed as a function of time at 633 nm in most experiments. In a number of experiments, the wavelength employed was 560 nm and after correction for the differences in extinction coefficient,[11] the kinetic data were in very good agreement with those taken at 633 nm. Silica cells of 2.0 and 4.0 cm length and 2.0 cm diameter with Suprasil end windows were used for sample irradiation.

The percent absorption and time values were obtained from oscilloscope traces. The center of the trace line was used for this measurement, and in areas where random noise produced fluctuations of the line a smooth line was drawn through the noise. At the beginning of the scan the trace changed most rapidly with time, and the noise was largest. Thus the errors are greatest in the first few points of each trace.

The data from each experiment were recorded from the oscilloscope trace and are available.[12] Three typical traces are shown in Figure 1 for doses of 140, 700, and 970 rads. As expected, the figure shows that the data do not correlate with either a conventional first- or second-order empirical rate function in the time range of the experiments. Ac-

---

* Address correspondence to this author at the Department of Chemistry.

† Department of Chemical Engineering.

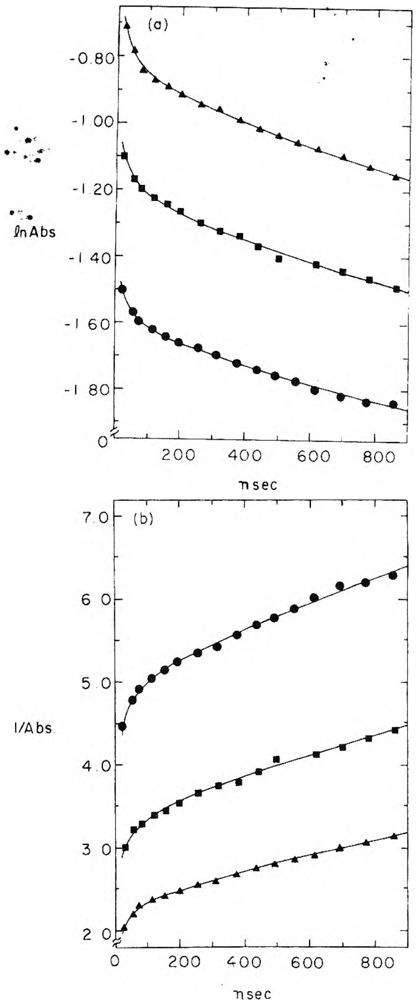

Figure 1. Typical hydrated electron decay kinetic plots. (a) ln absorbance as a function of time of gas-saturated, pure water, pH 7.0, irradiated with a 20-ns, 15-MeV electron pulse. The light intensity was monitored at 560 or 633 nm. The pulse doses were as follows; (●) 140 rads ($\epsilon l = 5.00 \times 10^5$ L mol^{-1}); (■) 700 rads ($\epsilon l = 1.276 \times 10^5$ L mol^{-1}); (▲) 970 rads ($\epsilon l = 1.276 \times 10^5$ L mol^{-1}); (b) reciprocal absorbance vs. time following pulse for same solutions as in (a). Curves in (a) and (b) are least-squares fits to data points. Parameters derived from these fitted curves were used to obtain data for Figures 3–5.

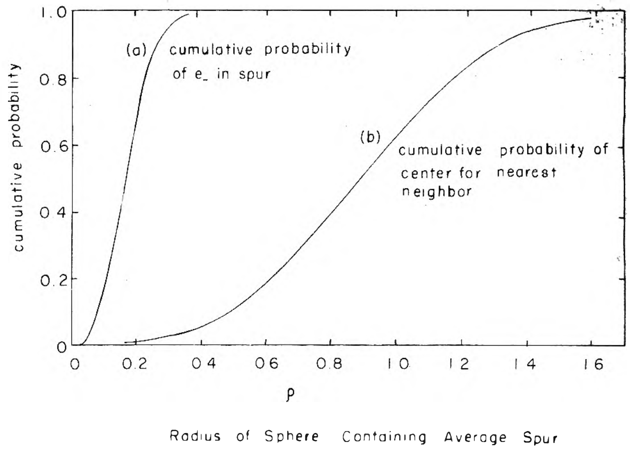

Figure 2. Comparison of cumulative radial probabilities of (a) finding electrons in a given spur and (b) of finding a randomly distributed nearest-neighbor spur center. Calculations based upon formula derived in the Appendix and on an assumed hydrated electron distribution function (see text) with a maximum at 4 nm from the spur center ($\rho = 0$), a pulse dose or 2000 rads, and 100 eV/spur. ρ is the dimensionless radius of a sphere enclosing a given spur. $\rho = r/r_0$ where r is the radius and $r_0 = (3/4\pi N)^{1/3}$, N being the number of spurs per unit volume. Curve a represents the accumulated probability of finding (immediately following an irradiation pulse) all the hydrated electrons belonging to a given spur within the volume of a sphere of radius ρ. Curve b represents the accumulated probability of finding the center of another (nearest neighbor) spur within the sphere of radius ρ. This curve is interpreted to mean that there are relatively few spurs which overlap immediately following the pulse and that the earliest hydrated electron decay is predominantly intraspur.

cordingly, an alternative interpretation of these data is needed to bring the data set into a common framework.

The concentration history of the solvated electron was converted into point rate data for the bulk of the runs by differentiation of an empirical function fit to the data by a Marquardt non-linear least-squares computation routine (typical estimated error in the derivative is 3%). At early times during very high pulse dose experiments (a minority of cases), graphical differentiation was used (typical estimated error of 5%). Fits to the data using the empirical function are shown in Figure 1. We believe the error estimates for differentiation are conservative. The details of the data reduction are given in ref 12.

Results

In treating our data, we assume that radiation energy is initially deposited in such a manner that randomly distributed, nonhomogeneous groups of radicals, called "spurs",[1,2] are formed in the pulse radiolyzed water. Among the species ultimately populating these spurs are the hydrated electron, the hydroxyl radical, the hydrogen ion, and the hydrogen atom. At low pulse dose levels and early times following the pulse, we postulate (see the Appendix for detailed reasoning) that the *average* interspur distance is large when compared with the size of the individual spur regions so that the probability for very early interspur interaction (overlap) is finite, but low, and consequently the overall kinetics *initially* are dominated by intraspur reactions. Diffusion causes the spurs to mix, and ultimately homogeneous kinetics are observed. The following is an effort to demonstrate experimentally and quantify certain aspects of these transformations from predominantly intraspur hydrated electron decay to homogeneous hydrated electron reaction. The analysis shows the importance of gathering statistically meaningful data in the nanosecond range using a wide variation of pulse dose to extend our understanding of the transition to homogeneous kinetics.

Figure 2 shows two cumulative distributions which illustrate our basic ideas regarding spur overlap. The cumulative probability distribution for the electron is based on a skewed Gaussian distribution (see later discussion) with a probability maximum at 4 nm from the spur center. The cumulative distribution function for the center of the nearest-neighbor spur is based upon the development found in the Appendix using a 2000-rad dose with 100 eV/spur average energy deposition. The curves imply that a small fraction of the spurs do overlap initially, but that most of the hydrated electron reactions occur within isolated spurs initially. The majority of radicals in individual spurs mix by diffusion before reactions with species in other spurs can occur.

The detailed kinetics of decay of the hydrated electron in the period from 60 to 900 ns after the pulse is quite complex and is not the major topic of this paper. However, the hydrated electron decay data obtained in our experiments can be arranged to yield a simple test of the above postulates. If the decay of the hydrated electron initially is controlled by intraspur reactions, the fraction of electrons decaying at any specific time, $\{[-d(e_{aq}^-)/(e_{aq}^-)]/dt\}_t \equiv Q_t$, should be independent of pulse dose *for a given time*, t, following the radiation pulse. The value of Q_t decreases with increasing time following the pulse, indicating that

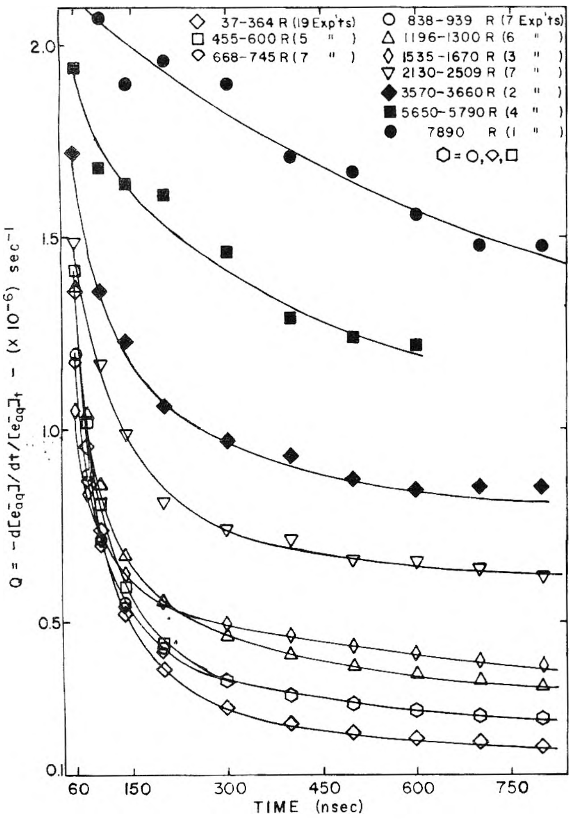

Figure 3. Time-pulse dose dependence of Q_t, the instantaneous (fractional) hydrated electron decay rate ($Q_t \equiv [-d(e_{aq}^-)/(e_{aq}^-)]/dt$). Curve fitted data from absorbance measurements similar to those represented in Figure 1 are differentiated to yield Q_t data. The points represent mean values of Q_t over the pulse dose ranges indicated on the figure. The numbers in parentheses represent the total number of experiments performed in the dose range indicated. Data in the 37–364-rad dose range showed no statistically observable trends and are shown as a single curve.

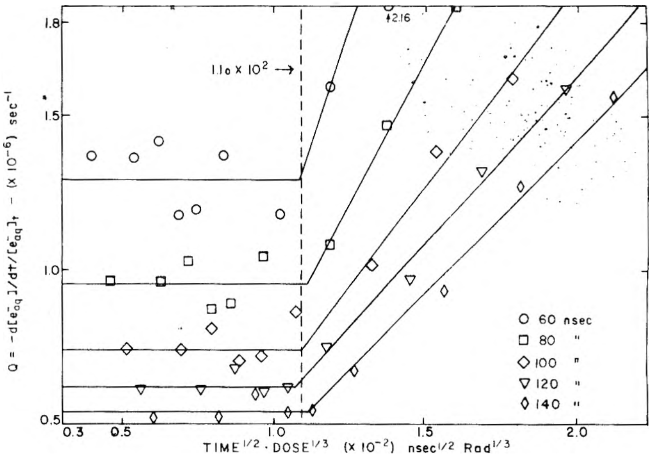

Figure 4. Test of spur model parameters Q_t and the product (time of spur overlap)$^{1/2}$(pulse dose)$^{1/3}$ according to the model of Kenney and Walker[12] in the pulse radiolysis of pure water. Breaks in curve at a value of $t^{1/2}$(dose)$^{1/3} \simeq 110 \pm 10$ ns$^{1/2}$ rad$^{1/3}$ yield a useful indicator for a given dose of the time at which experimentally detectable spur overlap is most significant. Before this time, hydrated electron decay is shown to be predominantly intraspur by the nearly horizontal lines for each of the times listed. Lines in the positive slope region are regression fits.

the intraspur kinetics are not first order.

Accordingly, a plot of Q_t vs. pulse dose with time as a fixed parameter should have two regions. At low pulse dose the value of Q_t should be independent (constant) of pulse dose. Behavior of this type suggests that the bulk of the hydrated electrons in spurs are reacting independently in isolated spurs. At still larger pulse doses, for a fixed time following the pulse, the spurs begin to interact (overlap) at the time value chosen; the relative decay rate (vs. no spur overlap) increases.

Figure 3 is a plot of Q_t, the kinetic test parameter for intraspur hydrated electron decay, vs. time for a range of doses. There is substantial scatter in these sets of curves. However, the general features of the curves clearly are: (a) an asymptotic region for times >500 ns in which the curves approach a nearly constant value; (b) the asymptotic value of Q for times >500 ns increases with dose; and (c) for times in the range 60–150 ns an asymptote with a large, negative slope from which the curves depart more readily with increasing dose. The existence of two types of asymptotes requires clarification.

The relationship between the dose and corresponding time at which the decay mode changes is expected by diffusional kinetic arguments[13] to be directly related to the functional form (time)$^{1/2}$(dose)$^{1/3}$. This form is based upon the treatment of Kenney and Walker,[14] who considered the time needed for spherical spurs, spaced evenly throughout the solution, to reach homogeneity. The factor (time)$^{1/2}$ arises from the diffusion equation where the characteristic diffusion length is proportional to $(Dt)^{1/2}$ (t is the time, D, the diffusion coefficient). The factor (dose)$^{1/3}$ relates, through the number of spurs formed, to the average distance between them. Kenney and Walker[14] proposed that the product of (time)$^{1/2}$(dose)$^{1/3}$ should be a constant. Accordingly, values of Q_t in Figure 3 are plotted vs. (time)$^{1/2}$(dose)$^{1/3}$ on Figure 4 for each of five times following the pulse, from 60–140 ns (beyond 140 ns there are insufficient data to define adequately the zero slope region value). On Figure 4 the lines are averages of the points along the zero slope region and regression fits along the positive slope region (including data at 5700 rads, but not including the more limited data at 1600 rads). The intersection of the two lines for each time yields a constant that relates the time–dose values at which the decay mode apparently changes. The average value of this constant is 110 ns$^{1/2}$ rad$^{1/3}$ with an approximate error of 10%. This constant specifically applies to 20-ns pulses of 15-MeV electrons of less than 8000 rads total dose. However, given the relatively small changes in LET with energy for high energy electrons,[15] this constant should have order-of-magnitude applicability over a relatively broad range of electron energies.

The spherical spur model can also be used to estimate the time required for spurs to mix by diffusion sufficiently to yield homogeneous kinetics. Qualitatively, spurs can be viewed as a set of points in random array for which the least sophisticated model is a cubic lattice scaled by the average spur separation distance. The time required to achieve homogeneous kinetics in the model can be estimated from simple diffusional relaxation. The time required to obtain homogeneous kinetics of the spurs should be roughly proportional to the diffusion time.

Discussion and Conclusions

The above data for solute-free water provide valuable experimental information about the timing of events in aqueous radiation chemistry. The data in Figure 4 demonstrate the importance of both the pulse dose and the time following the pulse in determining the degree to which interspur reactions are important in causing the disappearance of hydrated electrons. These findings offer research workers a method of determining quantitatively the limited amount of time available to observe predominantly intraspur hydrated electron decay processes, a time which is strongly dependent upon pulse dose. The use of the Q_t parameter at very early times in pulse radiolysis studied at higher LET's for pulses of fast electrons and other accelerated particles offers a tool for studying the hypotheses of overlapping spurs forming cylindrical tracks, blobs, and short tracks.[16]

The aqueous, electron-pulsed system can be viewed as the interaction of spurs of differing sizes which have a distribution of distances from their nearest-neighbor spurs. The time required for experimentally detectable overlap interrelates the spur size and separation distribution function, though it does not reveal the mathematical nature of either. The experimental determination of constraints on these two functions is a major contribution of this work.

Kenney and Walker[14] report observing the attainment of homogeneity in electron pulse irradiated water. A direct comparison of their results is not possible since they worked with much lower energy and therefore higher LET-electron pulses and at doses of 39, 57, and 68 krads, whereas the data here are for <8 krads. The earliest data of Kenney and Walker are at 10 ns, and from the empirical constant found above (assuming its applicability at their much higher doses), values of 10, 8, and 7 ns, respectively, are expected for onset of detectable spur overlap.

The results of this study are consistent with a nonhomogeneous distribution of primary transient species. Since the goal of spur modeling is to be able to predict both the course of the reaction at any time and the final product concentrations, the results of the present work should be taken into account in future spur modeling. Specifically, provision for overlap of spurs is necessary since, depending upon dose, a significant fraction of the initial hydrated electron concentration is still present when interspur reactions begin. The results described here provide useful benchmarks for the diffusional process. They relate times and doses necessary to experimentally detect interspur reactions and subsequently to observe homogeneous or nearly homogeneous behavior in the system.

The results reported in this paper have dealt exclusively with the pulse radiolysis of pure water. It may be argued that the presence of solutes which scavenge reactive intermediates from water radiolysis will decrease the importance of or even eliminate spur overlap. This will be true only if such solutes react with the transient intermediates of one spur before those intermediates have a chance to react with intermediates in a neighboring spur. Two situations will decrease the likelihood of the solute, even at relatively high concentrations, eliminating reactive spur–spur overlap. The first is likely at relatively large pulse doses where average interspur distances are on the same order of magnitude as the average distance between individual solute species. The second is the presence of tracks or blobs[16] in irradiations using (or producing) electrons with larger LET values than those used in this study, e.g., ^{60}Co γ radiation, 1–2 MeV Van de Graaf electrons, etc. With these sources, spur overlap along the track leading to interspur reactions may take place in competition with solute reaction with reactive intermediates of a single spur. The ubiquitous increase in G_{OH} and $G_{e_{\mathrm{aq}}^-}$ with increasing scavenger concentration in γ radiolysis may be due to solute competition with *inter*spur reactions along electron tracks as well as with intraspur reactions.

Results are reported elsewhere[12] utilizing techniques similar to those reported in this paper involving the study of various reactive scavengers such as O_2, Br^-, and 2-propanol on the decay of hydrated electron concentration following short (20 ns) pulses in the nanosecond time domain. Also reported elsewhere[17] are the preliminary results of a computer modeling study based in part on the experimental results in this paper. The model employs both a novel initial hydrated electron distribution function within the spur and includes a first-order approximation to spur overlap which provides qualitative agreement with results reported in this paper.

Acknowledgment. This work was supported in part by the U.S. Atomic Energy Commission. We wish to thank the members of the Argonne National Laboratory Accelerator Division and Drs. M. Matheson, E. J. Hart, and C. Jonah for their invaluable help during the experimental phase of this project. We have had stimulating discussions on various aspects of the theoretical interpretation of our data with Drs. J. L. Magee, H. N. Blount, III, E. Kerner, and S. Wolfe. We thank also S. A. Trumbore for some valuable help in data reduction. P.G.B. (Wake Forest University) was a participant in the summer, 1975 NSF Undergraduate Research Participation Program.

Appendix

Assume N spurs (a large number) are randomly distributed in three-dimensional space, and a spherical region is imagined around a spur located at the center of the region with unit volume. The center of the spur which is the nearest neighbor of the central spur will be located in a spherical shell of volume $4\pi r^2$ dr, r being the radius of the shell. The probability of finding the nearest-neighbor spur center at r will depend upon the probability of all spurs *other than* the two under consideration, i.e., $N - 2$ spurs, being found in the volume *outside* the volume occupied by the sphere whose center is also the center of the region and whose volume is $(4/3)\pi r^3$. Thus, each of the $N - 2$ spurs will be contained in a volume $(V - [4/3]\pi r^3)$. The probability, P, of finding the nearest-neighbor spurs a distance between r and $r + \mathrm{d}r$ apart is thus:

$$\frac{\mathrm{d}P}{\mathrm{d}r} = A\left(\frac{4\pi r^2}{V}\right)\left(\frac{V - {}^4/_3\pi r^3}{V}\right)^{N-2}$$

A is a normalization factor assuring unit probability of finding the two nearest-neighbor spur centers somewhere within the spherical region. We then assume the above distribution function to be identical with that for all spurs since there is nothing unique about the center spur.

Using $R = (3/4\pi N)^{1/3}$, the radius of the average sphere of volume to contain one spur as a scaling factor, the probability distribution has the simple dimensionless form

$$\mathrm{d}P/\mathrm{d}\rho \cong 3\rho^2 e^{-\rho^3}$$

where $\rho = r/R$, the dimensionless radius in the spur and $\mathrm{d}P/\mathrm{d}\rho$ is the dimensionless probability density function Accordingly, the most probable nearest neighbor is at $\rho_N = 0.874$.

It is also interesting to note that if $Z = \rho^3$, then $\mathrm{d}P/\mathrm{d}2 = e^{-Z}$. This formula transforms the volume of a sphere to a line on which the nearest-neighbor distance has a Poisson distribution.

Supplementary Material Available: Additional experimental details of the apparatus and techniques used (3 pages). Ordering information is available on any current masthead page.

References and Notes

(1) J. K. Thomas, *Adv. Radiat. Chem.*, **1**, 117–122 (1969).
(2) H. A. Schwarz, *J. Phys. Chem.*, **73**, 1928 (1969).
(3) A. Mozumder and J. L. Magee, *Radiat. Res.*, **28**, 203 (1966).

(4) M. J. Bronskill, R. K. Wolff, and J. W. Hunt, *J. Chem. Phys.*, **53**, 4201 (1970).
(5) H. A. Schwarz, *J. Chem. Phys.*, **55**, 3647 (1971).
(6) C. D. Jonah, M. S. Matheson, J. R. Miller, and E. J. Hart, *J. Phys. Chem.*, **80**, 1267 (1976).
(7) E. J. Hart and J. K. Thomas, Report No. ANL-7856, Argonne, Ill., Sept 1971.
(8) E. J. Hart and E. M. Fielden, *Adv. Chem. Ser.*, **No. 50**, 253 (1965).
(9) B. D. Michael, E. J. Hart, and K. H. Schmidt, *J. Phys. Chem.*, **75**, 2798 (1971).
(10) K. Sehested, E. Bjergbakke, O. L. Rasmussen, and H. Fricke, *J. Chem. Phys.*, **51**, 3159 (1969).
(11) E. J. Hart and M. Anbar, "The Hydrated Electron", Wiley-Interscience, New York, N.Y., 1970, Chapters IX and X.
(12) J. E. Fanning, Ph.D. Dissertation, University of Delaware, Newark, Del., 1975; available from University Microfilms, Ann Arbor, Michigan.
(13) T. K. Sherwood, R. L. Pigford, and C. R. Wilkie, "Mass Transfer Operations", McGraw-Hill, New York, N.Y., 1975, p 313.
(14) G. A. Kenney and D. C. Walker, *J. Chem. Phys.*, **50**, 4047 (1969).
(15) A. O. Allen, "The Radiation Chemistry of Aqueous Solutions", Van Nostrand, Princeton, N.J., 1969, pp 5–6.
(16) A. Mozumder, *Adv. Radiat. Chem.*, **1**, 69 (1969).
(17) J. E. Fanning, C. N. Trumbore, P. G. Barkley, D. R. Short, and J. Olson, *J. Phys. Chem.*, **81**, 1026 (1977).

The Structure of Aqueous Croconic Acid

Robert I. Gelb, Lowell M. Schwartz,* Daniel A. Laufer, and Janet O. Yardley

Department of Chemistry, University of Massachusetts at Boston, Boston, Massachusetts 02125

(Received January 24, 1977)

The anomalously positive standard entropy of the primary acidic dissociation of croconic acid, $\Delta S_1° = +9.5$ cal mol^{-1} K^{-1}, has been confirmed by colorimetric determination of the temperature dependence of the corresponding dissociation constant. A ^{13}C NMR study of aqueous croconic acid solutions revealed that the undissociated acid exists as two distinct equilibrating species with the exchange rate of the order of 1 s. One species is the expected $H_2C_5O_5$ structure and the other is hypothesized to be a hydrated form with a gem-diol moiety at one carbonyl. A determination of the hydration equilibrium constant shows that at 30 °C the undissociated acid is about 90% hydrated. The anomalously positive entropy of dissociation is explained as due to a highly positive entropy of dehydration, as in other carbonyl dehydration reactions, preceding the acidic dissociation.

Introduction

1,2-Dihydroxycyclopentenetrione (I) commonly known

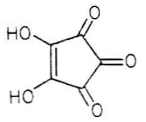

I

as "croconic acid", $H_2C_5O_5$, is a member of the oxocarbon ring systems which have been studied extensively in this laboratory and by West and co-workers.[1] Both croconic acid and squaric acid, $H_2C_4O_4$, are fairly strong in aqueous solution having pK_1 values of 0.80[2] and 0.54,[3,4] respectively. In both cases the high acid strengths have been shown to be attributable to entropy rather than energy contributions to the Gibbs free energy of dissociation. This phenomenon has been shown by Kurz and Farrar[5] to also account for the strengths of other moderately strong organic acids such as haloacetic acids. Whereas typical weak uncharged carboxylic acids have standard molar entropy changes $\Delta S°$ values in the range −20 to −30 cal mol^{-1} K^{-1}, and squaric acid[3] and other moderately strong acids[5] have $\Delta S°$ values between −1 and −13 cal mol^{-1} K^{-1}, we have found that croconic acid has $\Delta S_1° = +9.5$ cal mol^{-1} K^{-1},[2] a value much more positive than any ionic dissociation of an uncharged species of which we are aware. This result has led us to further study the aqueous croconic acid system. First we confirm the anomalous croconic acid $\Delta S_1°$ value by an independent method. In ref 2 this quantity is determined by measuring the temperature variation of pK_1 found by UV spectrophotometry; in this work we measure pK_1 by colorimetry using an acid–base indicator species. Secondly we seek some evidence of structural abnormality by observing the ^{13}C NMR spectral behavior of croconic acid as a function of pH. The NMR studies provide strong evidence for the existence of two distinct structures of undissociated croconic acid and we have been able to estimate the equilibrium constant at 30 °C for the partition between these.

Colorimetric Method

We have selected the cresol red acid–base indicator system which is sensitive to pH in the range near pK_1 of croconic acid. Cresol red changes from yellow to orange as the pH changes from 3 to 0.5 and this is due to increased absorbance of a peak centered at 518 nm and presumably attributable to the protonated indicator (HIn) and a corresponding decreased absorbance of a peak at 435 nm attributable to the unprotonated In$^-$ species. As in an early work,[6] we have chosen to measure pH by monitoring absorption of the HIn species at the fixed wavelength of 518 nm. For this we assume the validity of Beer's law for all absorbing species and a simple monobasic dissociation of the indicator acid. The dissociation equilibrium is

$$K_{\mathrm{In}} = a_{\mathrm{H}}\gamma_{-}[\mathrm{In}^-]/[\mathrm{HIn}] \quad (1)$$

where a_{H} ($\equiv 10^{-\mathrm{pH}}$) is the hydrogen ion activity, [HIn] and [In$^-$] are the molar concentration of protonated and unprotonated indicator, respectively, and γ_- is the indicator ion activity coefficient. The absorbance at a fixed wavelength in a pure indicator solution is

$$A = \epsilon_0 b[\mathrm{HIn}] + \epsilon_1 b[\mathrm{In}^-] \quad (2)$$

where ϵ_0 and ϵ_1 are the molar absorptivities of HIn and In$^-$, respectively, and b is the absorption path length. The analytical concentration of indicator is

$$C^0 = [\mathrm{HIn}] + [\mathrm{In}^-] \quad (3)$$

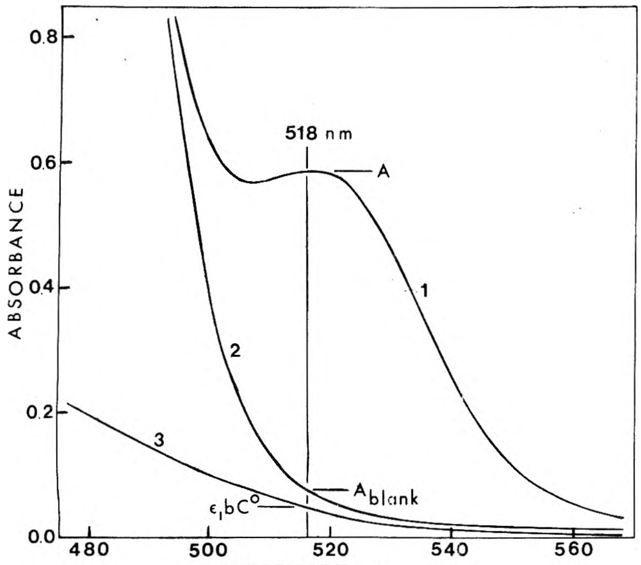

Figure 1. Curve 1 is the spectrum of 0.07 M $K_2C_5O_5$ and cresol red in 0.14 M HCl. Curve 2 is the spectrum of the same solution omitting cresol red. Curve 3 is the spectrum of cresol red in pH 4 buffer. The absorbances of curves 2 and 3 at 518 nm, A_{blank} and $\epsilon_1 bC^0$, respectively, are subtracted from the absorbance A on curve 1 to obtain absorbance A_{corr}.

and with this, eq 2 becomes

$$A_{corr} \equiv A - \epsilon_1 bC^0 = \epsilon b[\mathrm{HIn}] \qquad (4)$$

where $\epsilon \equiv \epsilon_0 - \epsilon_1$. If all solutions are made up with identical C^0 formality, then $(\epsilon_1 bC^0)$ is a constant correction to be subtracted from all measured A values to yield A_{corr} which are directly proportional to [HIn]. $(\epsilon_1 bC^0)$ is the absorbance of a totally unprotonated indicator solution which for cresol red is realized at pH 4. (See Figure 1.) Combining eq 1, 3, and 4 yields

$$\frac{1}{A_{corr}} = \frac{K_{In}}{C_{In}}\left(\frac{1}{a_H \gamma_-}\right) + \frac{1}{C_{In}} \qquad (5)$$

where $C_{In} \equiv \epsilon bC^0$, and which equation should plot as a straight line on $(1/A_{corr})$ vs. $(1/a_H\gamma_-)$ coordinates if the assumptions made above are valid and if the proper activity coefficient correlations are used. The slope K_{In}/C_{In} and intercept $1/C_{In}$ of this line determine the indicator dissociation constant K_{In} and the unknown parameter C_{In}. Equation 5, with K_{In} and C_{In} known at various temperatures, is in effect an absorbance vs. pH working curve from which pH values of croconic acid solutions will be determined by measuring A_{corr} of the indicator cresol red at 518 nm.

Absorbance measurements are made on a series of HCl–KCl–cresol red standard solutions made up with varying HCl, KCl concentration, with HCl:KCl mole ratio about 1:2, and each with identical cresol red concentration C^0. The KCl is added to adjust the ionic strength in the standards to about the same value as in the croconic acid solutions to be analyzed. Similarly the absorbance of a single cresol red solution at concentration C^0 in pH 4.0 buffer is measured to determine the correction term $(\epsilon_1 bC^0)$. In each of these solutions, $[H^+Cl^-]$ and $[K^+Cl^-]$ is known, A_{corr} is measured at 518 nm and at a number of temperatures, and a_H is $\gamma_H[H^+Cl^-]$. Ionic activity coefficients are assumed to follow the Debye–Hückel equation

$$\log \gamma = \frac{-Az^2I^{1/2}}{1 + Ba_iI^{1/2}} \qquad (6)$$

where I is ionic strength and in this equation A and B are temperature dependent parameters taken from Robinson and Stokes.[7] For the hydrogen ion activity coefficient γ_H the ion-size parameter a_i = 0.9 nm, and for the indicator γ_-, a_i = 1.2 nm.[6] In these solutions, $I = [H^+Cl^-] + [K^+Cl^-]$ since the indicator C^0 is less than these by a factor of $\sim 10^4$.

Croconic acid–indicator solutions are made up by acidifying dipotassium croconate salt with hydrochloric acid in a 1:2 mole ratio and adding the same concentration C^0 of cresol red as in the standards. Also croconic acid blank solutions of comparable concentration but with no indicator are required to measure the absorbance at 518 nm due to croconic acid–croconate absorption. Although these absorptions peak in the UV, 320–365 nm, they tail into the visible and interfere with the indicator absorption as shown in Figure 1. The croconic acid blank absorbance at 518 nm, corrected for concentration, is subtracted from each croconic acid–indicator absorption measurement to yield the indicator absorbance. Then the correction term $(\epsilon_1 bC^0)$ is subtracted from each to yield A_{corr}, from which a_H in the croconic acid solution is determined utilizing a rearranged form of eq 5. Knowing a_H, the analytical concentrations in each solution, and the secondary dissociation constant of croconic acid K_2,[2] the primary dissociation constant K_1 is determined from the set of equations

$$K_1 = a_H\gamma_1[HC_5O_5^-]/[H_2C_5O_5] \qquad (7a)$$

$$K_2 = a_H\gamma_2[C_5O_5^{2-}]/\gamma_1[HC_5O_5^-] \qquad (7b)$$

$$F_{cr} = [H_2C_5O_5] + [HC_5O_5^-] + [C_5O_5^{2-}] \qquad (7c)$$

$$2F_{cr} + [H^+] = [HC_5O_5^-] + 2[C_5O_5^{2-}] + F_{HCl} \qquad (7d)$$

$$[H^+] = a_H/\gamma_H \qquad (7e)$$

together with eq 6 for the activity coefficients, γ_H, γ_1, and γ_2. The latter two symbols refer to $HC_5O_5^-$ and $C_5O_5^{2-}$, respectively, and a_i = 0.45 nm is assumed for both. F_{cr} and F_{HCl} are the analytical concentrations of $K_2C_5O_5$ and HCl, respectively. This set of coupled equations cannot be solved directly for K_1 and so an iterative procedure is used which begins by estimating an ionic strength, solving eq 6 for activity coefficients, solving the conservation relationships for ionic species concentrations, and from these calculating a new estimate of ionic strength. The method converges rapidly.

Results

The absorbances of the standard solutions were measured at 5° intervals from 10 to 40 °C and the results fitted by least-squares lines in the form of eq 5. The rms deviations of data from the fitted lines were typically 0.006 for average $(1/A_{corr})$ ordinate values of 2, which confirms the linearity of the data with respect to eq 5 and thus the validity of the assumptions inherent in that equation. The K_{In} and C_{In} parameters from these lines were plotted vs. temperature and these were well-represented by straight lines with rms deviations of 0.6 and 0.3% of the average K_{In} and C_{In}, respectively. K_{In} and C_{In} values read from these straight lines were used in calculating croconic acid pK_1 from indicator absorbance values in the croconic acid solutions. These results are given in Table I. We note that the five 25 °C entries average to pK_1 = 0.75 (±0.02 standard deviation) and that this value agrees with the previous spectrophotometric determination of pK_1 = 0.80 ± 0.08.[2] It is also interesting to note that whereas this same colorimetric method failed to determine pK_1 of squaric acid because of the formation of a complex between cresol red and the undissociated squaric acid molecule,[6] the agreement found in the case of croconic acid means that a

TABLE I: Colorimetric Determination of $\mathrm{p}K_1$ of Croconic Acid

Temp, °C	$[H_2C_5O_5]$, M	$\mathrm{p}K_1$
25	0.09122	0.777
25	0.07388	0.722
25	0.06150	0.751
25	0.05233	0.777
12	0.07321	0.878
15	0.07321	0.837
20	0.07321	0.813
25	0.07321	0.743
30	0.07321	0.725
35	0.07321	0.665
40	0.07321	0.592

TABLE II: Propagation of Error Estimates into $\mathrm{p}K_1$ Values at 12 and 40 °C

Sources of error		Effect on $\mathrm{p}K_1$ at 12 °C	Effect on $\mathrm{p}K_1$ at 40 °C
Determinate errors			
$H_2C_5O_5$ formality	2%	0.038	0.058
HCl formality	0.1%	0.003	0.005
γ_1 and γ_2 as reflected in a_i	0.1 nm	0.049	0.058
	Total effect	0.090	0.121
Random errors			
Absorbance readings	0.003	0.036	0.060
HCl formality	0.2%	0.006	0.010
K_{In}	0.6%	0.029	0.019
C_{In}	0.3%	0.024	0.016
$\mathrm{p}K_2$	0.01	0.011	0.011
	Total effect	0.106	0.116

similar complex does not form with the indicator.

The final seven entries in Table I give the temperature dependence of $\mathrm{p}K_1$ and are plotted in Figure 2 (open circles) together with spectrophotometric $\mathrm{p}K_1$ values[2] (solid circles). The dashed lines are the locus of the ±0.08 estimated maximum error bounds on the spectrophotometric measurements and the solid line is a plot of the empirical equation

$$\mathrm{p}K_1 = -2.14(\pm 0.16) + \frac{861(\pm 47)}{T\,\mathrm{K}} \tag{8}$$

which has been obtained by a least-squares fit of the colorimetric $\mathrm{p}K_1$ values. The standard error estimates of the least-squares parameters are given in parentheses. The least-squares fit to the spectrophotometric values was previously found to be[2]

$$\mathrm{p}K_1 = -2.08(\pm 0.15) + \frac{845(\pm 45)}{T\,\mathrm{K}} \tag{9}$$

The essential agreement between eq 8 and 9 confirms our earlier measurement of the temperature dependence. To find $\Delta S_1°$, we multiply eq 8 by $-2.303RT$ to obtain $\Delta G_1°$ and then differentiate by T. At 25 °C the standard entropy change of the primary dissociation is +9.78 (±0.72 standard deviation) cal mol^{-1} K^{-1}. This value confirms our previous determination. The quoted ±0.72 cal mol^{-1} K^{-1} uncertainty in $\Delta S_1°$ reflects the scatter of the $\mathrm{p}K_1$ data point about the correlation line given by eq 8. An estimate of the maximum probable error was also obtained. To do this we estimated error bounds in the data and parameters which are used in the $\mathrm{p}K_1$ calculations and propagate these into $\mathrm{p}K_1$ maximum error bounds for the extreme temperature points at 12 and 40 °C. The extreme slopes through these bounds provide an estimate of a maximum probable error of $\Delta S_1°$. A summary of these calculations is shown in Table II. The sources of error are classified as either "determinate" or "random". A particular determinate error here propagates to both 12 and 40 °C $\mathrm{p}K_1$ values in the same direction while a particular random error may propagate in either direction. From the totals of each we see that if at 12 °C the maximum error in one direction is +0.090 + 0.106 = +0.196, then at 40 °C the maximum error in the opposite direction is +0.121 − 0.116 = +0.005. These extreme perturbations result in a maximum possible uncertainty in $\Delta S_1°$ of ±8.2 cal mol^{-1} K^{-1}.

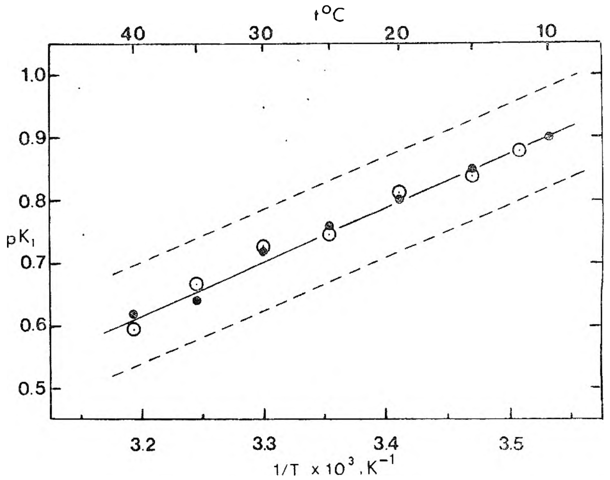

Figure 2. $\mathrm{p}K_1$ vs. temperature. The open circles are the last seven entries of Table I. The closed circles are from ref 2 and the dashed lines are approximate ±0.08 maximum uncertainties of these points. The solid line is a plot of eq 8.

^{13}C NMR Investigation

Suspecting that the anomalously positive entropy change of the primary dissociation might be reflecting some unusual structural property of one of the aqueous croconate species, we have measured ^{13}C NMR spectra of a

TABLE III: ^{13}C NMR Spectral Peaks Measured for Croconate Solutions at Various pH

pH[a]	F_{cr}[b]	Croconate solutions ^{13}C NMR peaks,[c] obsd				Dioxane ^{13}C NMR peaks[c]	Croconate solutions ^{13}C NMR peaks,[c] corr				w_i[d]
1	2	3	4	5	6	7	8	9	10	11	12
−0.422	0.1893	192.66	180.41	150.00	87.59	66.75	193.42	181.17	150.76	88.35	0.22
−0.219	0.1740	192.86	181.26	150.18	87.75	67.00	193.43	181.83	150.75	88.32	0.49
−0.017	0.1018	193.04	182.15	150.33	87.87	67.11	193.41	182.52	150.70	88.14	1.02
0.418	0.2027	193.24	183.21	150.50	88.00	67.37	193.47	183.44	150.73	88.23	1.52
0.771	0.1835	193.34	183.83	150.61	88.06	67.33	193.48	183.97	150.75	88.20	2.22
1.489	0.09789		185.29			67.60		185.33			1.38
1.963	0.09183		186.63			67.42		186.65			0.89
2.357	0.08667		187.80					187.80			0.25
>7	0.08		189.32			67.50		189.32			

[a] pH calculated as $-\log \gamma_1[\mathrm{H}^+]$. [b] Formal concentration of croconate. [c] Chemical shift in ppm from TMS. [d] Least-squares weighting factors normalized to an average of unity.

series of croconate solutions over a range of pH values. Table III shows the observed spectra at 30 °C. Considering that the croconic acid dissociation constants are approximately $pK_1 = 0.7$ and $pK_2 = 2.3$, we observe only a single peak at pH >> pK_1 and four peaks at pH near or less than pK_1. This implies that when only $HC_5O_5^-$ and $C_5O_5^{2-}$ are present, all croconate species equilibrate rapidly relative to the NMR relaxation time thus producing a single resonance, but at low pH, when $H_2C_5O_5$ also is present in significant concentration, the equilibration time is sufficiently slowed to allow the resolution of three additional widely spaced peaks. In order to draw further conclusions from these results, numerical corrections must be applied which compensate for the changing chemical environment as the pH changes. The NMR spectrometer requires the presence of deuterium in the sample for an internal reference lock signal. This was supplied by using solvents made by mixing HCl, H_2O, and D_2O such that the H:D ratio was 2:1. However, since the average magnetic environment of deuterium changes as the proportion of HCl changes, the deuterium reference shifts and this causes a spurious displacement in all the observed peaks. In order to compensate for this effect we employed a double section coaxial tube to measure the chemical shift of the equivalent carbons of dioxane in one section relative to $HCl-H_2O-D_2O$ solvents in the other. As shown in column 7 of Table III, the dioxane peak is displaced a maximum of 0.75 ppm due to shifting of the deuterium lock with changing pH. Rather than applying the corrections directly solution by solution, we first smoothed out the scatter in the correction term. Noting that the dioxane shift appeared to vary linearly with HCl concentration, we used the least-squares regression

$$\delta_{\text{dioxane}} = 67.53(\pm 0.047) - 0.2804(\pm 0.033)C_{\text{HCl}}$$

as a smoothing function. Each observed NMR peak in the croconate system was corrected to the same deuterium lock reference as in the pH >7 solution, and the corrected spectra are shown in columns 8 through 11 in Table III. After the correction is applied, the three peaks which appear only in the most acidic solutions have become virtually invariant with changing pH while the peak (column 9) which is present in all solutions continues to shift through the entire range of pH. This leads us to the conclusion that the column 9 peak reflects the weighted average magnetic environment of all five carbons on all croconate species $C_5O_5^{2-}$, $HC_5O_5^-$, and $H_2C_5O_5$ all in rapid dynamic equilibrium. The continual shifting of this peak with pH is due to the changing proportions among these three species. On the other hand, the three invariant peaks stem from a fourth species which is not in sufficiently rapid equilibrium with the others to be merged over the NMR time scale. We notice that the magnetic environments of three carbons on this fourth species are nonequivalent which implies C_{2v} symmetry for a five-membered ring. Furthermore since this species is detectable only in highly acidic solution, we hypothesize that it is a diprotonated species having structure II. We considered one other possible structure, $H_3C_5O_5^+$, but rejected this as less plausible because (1) $C_5O_5^{2-}$, $HC_5O_5^-$, and $H_2C_5O_5$ all exchanged protons rapidly in aqueous solution, and resolution of $H_3C_5O_5^+$ into a multiple-peak spectrum would seem to require an abnormally slow proton exchange reaction and (2) spectrophotometric and pH potentiometric measurements gave no indication of a protonation reaction yielding $H_3C_5O_5^+$ even with solutions having pH $\simeq 0$. The data could be fit by consideration of only three croconate species, $C_5O_5^{2-}$, $HC_5O_5^-$, and $H_2C_5O_5$. Any further protonation would have precluded these results. The proposed hydrated structure II is similar to a hydrated form of rhodizonic acid, $H_2C_6O_6$, suggested by Patton and West.[8] It is similar as well to the structure of ninhydrin, III. We measured the ^{13}C NMR spectrum of III in 2:1 H_2O-D_2O solvent and observed resonances at 198.18, 139.39, 138.96, 125.53, and 88.19 ppm from TMS. The peak at 88.19 ppm has a chemical shift in the region characteristic of sp^3 carbons, and the near identity of this to the croconic acid peak shown in column 11 of Table III convinces us of the existence of a gem-diol moiety in one croconic acid species. The chemical shift of the carbonyl carbons in ninhydrin and croconic acid is in agreement as also expected. Since the equilibrium between croconic acid and its anions is a reversible one, the hydration reaction of I to II must be in equilibrium. Yet the observation of ^{13}C NMR lines for each implies that the exchange is slow. The line widths of the NMR peaks are about 2–3 Hz so the time scale for the chemical exchange may be of the order of 0.5 s. Furthermore, we could not detect a change in the UV spectrum of aqueous $K_2C_5O_5$ after treatment with HCl (pH $\simeq 0$). Since we would expect some measurable difference in UV absorption between species I and II, this result implies that the time scale of exchange is significantly less then 10 s.

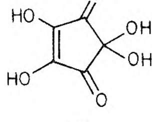

II

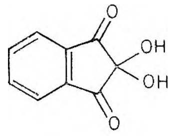

III

Croconic Acid Hydration Equilibrium

Hypothesizing the concurrent existence of both $H_2C_5O_5$ and $H_2C_5O_5 \cdot H_2O$ species in highly acidic solution, the equilibrium expression for the overall primary dissociation should be written

$$K_1' = \frac{\gamma_1^2[H^+][HC_5O_5^-]}{[H_2C_5O_5] + [H_2C_5O_5 \cdot H_2O]} \tag{10}$$

It is this pK_1' value which was measured by our previous spectrophotometric determination[2] and by the colorimetric method reported above. Neither of these methods could distinguish between the two diprotonated species appearing in the denominator. We are now interested in finding the primary dissociation constant of "unhydrated" croconic acid

$$K_1 = \gamma_1^2[H^+][HC_5O_5^-]/[H_2C_5O_5] \tag{11}$$

Writing the hydration equilibrium as

$$H_2C_5O_5(aq) + H_2O \overset{K_{\text{hyd}}}{=} H_2C_5O_5 \cdot H_2O(aq)$$

and substituting for $[H_2C_5O_5 \cdot H_2O]$ in eq 10, there results

$$K_1' = \frac{\gamma_1^2[H^+][HC_5O_5^-]}{[H_2C_5O_5] + K_{\text{hyd}}[H_2C_5O_5]} = \frac{K_1}{1 + K_{\text{hyd}}} \tag{12}$$

Equation 12 shows how the hydration equilibrium constant K_{hyd} can be found from K_1' and K_1.

K_1 can be determined from information already obtained in the ^{13}C NMR experiments. The chemical shift of the

NMR peak shown in column 9 of Table III is the weighted average of the chemical shifts of the three species $H_2C_5O_5$, HC_5O_5, and $C_5O_5^{2-}$. This averaging can be written

$$\delta = \frac{\delta_0[H_2C_5O_5] + \delta_1[HC_5O_5^-] + \delta_2[C_5O_5^{2-}]}{[H_2C_5O_5] + [HC_5O_5^-] + [C_5O_5^{2-}]} \qquad (13)$$

where the δ, δ_0, δ_1, and δ_2 represent the average and the individual species chemical shifts, respectively. Rearrangement and division by $[HC_5O_5^-]$ yields

$$\delta\left(\frac{[H_2C_5O_5]}{[HC_5O_5^-]} + 1\right) + (\delta - \delta_2)\frac{[C_5O_5^{2-}]}{[HC_5O_5^-]} = \delta_0\left(\frac{[H_2C_5O_5]}{[HC_5O_5^-]}\right) + \delta_1$$

and substituting for the concentration ratios with equilibrium expressions further yields

$$y \equiv \delta\left(\frac{\gamma_1^2[H^+]}{K_1} + 1\right) + (\delta - \delta_2)\frac{K_2}{\gamma_2[H^+]} = \delta_0\left(\frac{\gamma_1^2[H^+]}{K_1}\right) + \delta_1 \qquad (14)$$

Equation 14 predicts that if the proper value of K_1 were known a plot of y vs. $x \equiv \gamma_1^2[H^+]/K_1$ would be linear with slope δ_0 and intercept δ_1. The computational strategy will be to scan K_1 values seeking the optimum linearity of the plot of eq 14, and a weighted least-squares technique will be employed. In order to do this, weighting factors w_i and y_i and x_i for each of the i solutions must be calculated from chemical shift data δ_i, from $[H^+]_i$ and from activity coefficients γ_{1i} and γ_{2i}. The estimation of $[H^+]_i$ involves an elaborate calculation since the set of equations describing the stoichiometry and equilibria cannot be made explicit in $[H^+]$. These equations are essentially the same as the set of eq 7. Eliminating all croconate species concentrations leaves a cubic in $[H^+]$:

$$a_3[H^+]^3 + a_2[H^+]^2 + a_1[H^+] + a_0 = 0 \qquad (15)$$

where

$$a_3 = \gamma_1^2/K_1'$$

$$a_2 = 1 - a_3(F_{HCl} - 2F_{cr})$$

$$a_1 = K_2/\gamma_2 - F_{HCl} + F_{cr}$$

and

$$a_0 = -F_{HCl}K_2/\gamma_2$$

Since the ionic strength in some solutions far exceeds the region of validity of eq 6 and since the principal ionic species in the more acidic solutions is HCl, we have estimated the ionic activity coefficient γ_1 and $\gamma_2 = \gamma_1^4$ from the empirical correlation of Harned and Ehlers[9] developed for HCl solutions. However this correlation depends on the ionic strength which will not be known until eq 15 is solved for $[H^+]$ and from this, the charged croconate species concentrations found. This system of equations is solved by a double iteration procedure beginning with rough estimates of γ_1, then solving eq 15 for $[H^+]$ by Newton–Raphson iteration, calculating the concentrations of all species, and finally finding ionic strengths which in turn allow calculation of refined γ_1 estimates. We had no trouble with convergence of these iterations.

As mentioned above a weighted least-squares procedure is required for analysis of eq 14. The problem of weighting factors here is similar to that in ref 2. The y_i values as well as the x_i values are functions of $[H^+]_i$, which is one of several sources of random variability in the data. Consequently, we cannot assume that the y_i are homoscedastic, i.e., scattered equally. Weighting factors must be calculated inversely proportional to a priori variance estimates for each solution y_i value. Significant random variability enters the left-hand side of eq 14 through δ_i, δ_2, K_2 and $[H^+]_i$.

δ_i is uncertain to an estimated standard deviation $\Delta\delta_i \simeq \pm 0.06$ ppm due to an uncertainty of ±0.01 ppm in the measured value and an additional ±0.05 ppm in the correction term.

$\delta_2 \pm \Delta\delta_2 = 189.32 \pm 0.01$ ppm observed from the pH >7 solution in which all croconate is in the form $C_5O_5^{2-}$.

The statistical uncertainty of K_2 is derived from scatter of the data points about line D in Figure 1 of ref 2, i.e., $K_2 \pm \Delta K_2 = 0.00400 \pm 0.00009$.

The random variability of $[H^+]_i$ depend on the estimated statistical uncertainties of data used in their determination and these we estimate as follows: $\Delta K_1' = \pm 0.003$ based on the statistical scatter of data points from line A in Figure 1 of ref 2; $\Delta K_2 = \pm 0.00009$ as explained above; $\Delta F_{HCl} = \pm 0.003F_{HCl}$ and $\Delta F_{cr} = \pm 0.003F_{cr}$ as estimated from precision estimates of the gravimetric and volumetric procedures in preparing the solutions. The statistical uncertainties in $[H^+]_i$ are found by a Monte Carlo procedure[10] involving repeated solution of eq 15. At each repetition K_1', K_2, F_{HCl}, and F_{cr} were scattered random normally according to their estimated standard deviation. Finally $\Delta[H^+]$, $\Delta\delta_i$, $\Delta\delta_2$, and ΔK_2 are propagated into Δy_i via the left-hand side of eq 14 using the same Monte Carlo technique. The result of this is a population of statistically scattered y_i values from which the weighting factors $w_i \propto (\Delta y_i^2)^{-1}$ are calculated. These varied at most by a factor of 10 as shown in column 12 of Table III.

Having $[H^+]_i$ and w_i values for the least-squares calculations of eq 14, we scanned K_1 values to find the optimum linearity as defined as the minimum sum of squares $\sum_i w_i (y_i - \hat{y}_i)^2$, where $\hat{y}_i$ are y values predicted by the least-squares line at a particular x_i. This optimum line was found at $K_1 = 1.14$ for which the slope and intercept parameters were $\delta_0 = 180.05$ ppm, the chemical shift of $H_2C_5O_5$, and $\delta_1 = 184.22$ ppm the chemical shift of $HC_5O_5^-$.

Before discussing these results, we mention the fact that values of the dissociation constants K_1' and K_2 were not taken as the values already measured at 30 °C by either the spectrophotometric or colorimetric method because in those determinations the solvent was pure H_2O while eq 14 is applied to experiments in H_2O–D_2O. Since we could not assume that these equilibrium constants were independent of solvent, we redetermined them by the spectrophotometric method[2] but in 2:1 H_2O–D_2O and found $K_1' = 0.118$ ($pK_1' = 0.93$) and $K_2 = 0.0400$ ($pK_2 = 2.40$) in this solvent. (These compare with $pK_1' = 0.72$ and $pK_2 = 2.27$ in H_2O at 30 °C.)

The optimum K_1 value of 1.14 ($pK_1 = 0.072$), when introduced into eq 12 along with $K_1' = 0.118$, yields $K_{hyd} \simeq 9$ which means that about 90% of the undissociated croconic acid is in the form $H_2C_5O_5 \cdot H_2O$ at 30 °C. However, a rough statistical test of the significance of the K_1 determination shows that this K_{hyd} value has a fairly high level of uncertainty. The Monte Carlo simulation procedure described above provided a priori variance estimates for each y_i based on statistical uncertainties in the input data. The average y_i variance was 0.017 which for eight solutions predicted a sum of squared residuals of 0.14 and so this number is an estimate of the sum of squared deviations of y_i from $\hat{y}_i$ to be expected from statistical scatter alone. The weighted sum actually found for the $K_1 = 1.14$ line was 0.05. If we assume that significant systematic error (i.e., line curvature) is reflected by a sum of squared deviations greater than 0.14, we find that any $0.84 < K_1 < 1.80$ ($0.016 < \mathrm{p}K_1 < 0.14$) yields a line straight enough to account for statistical uncertainty. This range of uncertainty in K_1 translates to the range $6 < K_{\mathrm{hyd}} < 14$ for the hydration constant.

Discussion

We note that these results imply that unhydrated croconic acid I is extremely strong, i.e., $K_1 \simeq 1$ or $\mathrm{p}K_1 \simeq 0$. However, the anomalously positive entropy change mentioned in the Introduction does not refer to a simple acid dissociation reaction. Instead it refers to the more complicated equilibrium corresponding to K_1' and eq 12. Applying well-known thermodynamic relationships to this equation we find that the standard entropy change $\Delta S_1{}^{\circ\prime}$ is given by

$$\Delta S_1{}^{\circ\prime} = R \ln K_1' + RT\frac{\mathrm{d} \ln K_1}{\mathrm{d}T} - RT\frac{\mathrm{d} \ln (1 + K_{\mathrm{hyd}})}{\mathrm{d}T} \qquad (16)$$

A specific explanation for the positive sign of $\Delta S_1{}^{\circ\prime}$ depends on finding a positive value for the slope $\mathrm{d} \ln K_1/\mathrm{d}T$ and/or negative value for $\mathrm{d} \ln (1 + K_{\mathrm{hyd}})/\mathrm{d}T$. We would have liked to measure the temperature variation of K_1' and, hence of K_1 and K_{hyd} but the NMR spectrometer available to us did not have temperature dependent capabilities suitable to the requirements of the experiment. Without these data a further interpretation of $\Delta S_1{}^{\circ\prime}$ is not possible. However, comparable data are available for similar systems. There have been extensive studies of hydration equilibria in aqueous solution of carbonyl compounds and these have been reviewed by Bell.[11] Table I of ref 11 is a list of aldehydes and ketones whose hydration dissociation constants had been measured as of 1966. Although these constants vary over eight orders of magnitude, we will speculate that K_{hyd} of croconic acid varies with temperature similarly to those compounds whose $K_{\mathrm{hyd}} = K_{\mathrm{d}}^{-1}$ are within an order of magnitude of $K_{\mathrm{hyd}} \sim 9$. Noticing that all such compounds have ΔH_{hyd} approximately -5 kcal mol^{-1}, we select 1,3-dichloro-2-propanone (for which K_{hyd} matches croconic acid's almost exactly) as typical of these with $\Delta H_{\mathrm{hyd}} = -5.7$ kcal mol^{-1}. Writing the third term of eq 16

$$RT\frac{\mathrm{d} \ln (1 + K_{\mathrm{hyd}})}{\mathrm{d}T} = \left(\frac{K_{\mathrm{hyd}}}{1 + K_{\mathrm{hyd}}}\right)RT\frac{\mathrm{d} \ln K_{\mathrm{hyd}}}{\mathrm{d}T} = \left(\frac{K_{\mathrm{hyd}}}{1 + K_{\mathrm{hyd}}}\right)\frac{\Delta H_{\mathrm{hyd}}}{T}$$

and assuming that croconic acid ΔH_{hyd} is the same as that of $(\mathrm{CH_2Cl})_2\mathrm{CO}$, and that K_{hyd} in $\mathrm{H_2O}$ is the same as in 2:1 $\mathrm{H_2O}$–$\mathrm{D_2O}$, we estimate this term to be -17.1 cal mol^{-1} K^{-1} at 298 K. Substitution into eq 16 along with known $\Delta S_1{}^{\circ\prime} = 9.6$ and $\mathrm{p}K_1' = 0.80$ in $\mathrm{H_2O}$ at 298 K,[2] we find $RT\,\mathrm{d} \ln K_1/\mathrm{d}T = -3.8$ and so estimate $\Delta H_1{}^{\circ} \simeq -1$ kcal mol^{-1} and $\Delta S_1{}^{\circ} \simeq -4$ cal mol^{-1} K^{-1} for the primary dissociation of unhydrated croconic acid. These estimates are not much different from $\Delta H_1{}^{\circ} = -1.5$ kcal mol^{-1} and $\Delta S_1{}^{\circ} = -7.5$ cal mol^{-1} K^{-1} for squaric acid.[3] Undissociated squaric acid is unhydrated as our measurement of the ^{13}C NMR spectrum in highly acidic aqueous solution reveals only a single peak at about 196 ppm from TMS.

Our interpretation of the anomalously positive standard entropy $\Delta S_1{}^{\circ\prime}$ is that since 90% of diprotonated croconic acid is hydrated, the overall dissociation is essentially a two step process, a dehydration with $\Delta S^{\circ} \simeq +14$ cal mol^{-1} K^{-1}, as in $(\mathrm{CH_2Cl})_2\mathrm{CO}$, followed by acidic dissociation with $\Delta S^{\circ} \simeq -4$ cal mol^{-1} K^{-1}.

Experimental Section

Dipotassium croconate was synthesized by $\mathrm{H_2O_2}$ oxidation of dipotassium rhodizonate and analyzed for purity by reaction with Ce(IV); both procedures are described elsewhere.[2] Cresol red purchased from Fisher Scientific Co. and used without further purification was dissolved in water. Absorbance measurements were made with a Beckman Acta III spectrophotometer with thermostatted (±0.1°) samples.

Spectrophotometric pK values were obtained from measurements with croconate solutions containing 33% v/v $\mathrm{D_2O}$ and various HCl concentrations between 0.002 and 1.2 M. The spectral region between 250 and 400 nm was recorded. The rms deviation of the spectra calculated from estimated values of $\mathrm{p}K_1$, $\mathrm{p}K_2$, and ϵ values of diprotonated, monoprotonated, and aprotic croconate species was less than 0.005 absorbance units (about 0.5%) in all cases. Further, the calculated spectra never deviated from the observed spectra by more than 0.015 absorbance units.

Colorimetric $\mathrm{p}K_1$ measurements were made at 518 nm where the cresol red absorbance was always between 0.4 and 0.6. Croconate solutions were prepared from weighed samples of the analyzed dipotassium salt and a stoichiometric amount of HCl to convert the salt to the diprotic acid. These solutions contained 0.05 to 0.09 M croconic acid and, as a consequence of the method of preparation, 0.1 to 0.18 M KCl. In an attempt in minimize systematic errors in the activity coefficient correlation, the standard acid solutions were prepared in a similar way. Namely, HCl solutions between 0.05 and 0.09 M containing 0.1 to 0.18 M KCl and cresol red were prepared and their absorbances were measured from 10 to 40 °C. In one series croconic acid solutions of various concentrations were measured at 25 °C and in a second series a single 0.07 M croconic acid solution was measured from 12 to 40 °C. All standard and croconate solutions (except the croconate blanks) contained identical cresol red concentrations, about 10^{-5} M. The croconate blanks were prepared in the same way as the other croconic acid solutions and their absorbances were less than 0.1 at 518 nm.

^{13}C NMR measurements employed a Varian CFT-20 instrument which acquired 8192 data points over a 5000-Hz sweep. Weighed samples of potassium croconate were added to 1:2 mixtures of $\mathrm{D_2O}$ and aqueous HCl so that the resultant solution was 0.1 to 0.2 M croconate. A portion of the solution was sealed in a 10-mm NMR tube and the spectrum was recorded at 30 ± 2 °C. A typical spectrum employed 6-μs pulse width (approximately 30° tip angle); 0.8-s acquisition time; 2-s delay time between pulses; and a total of about 10 000 pulses No sample decomposition was noted during data acquisition and spectra could be duplicated to ±0.01 ppm by repeated measurements with the same sample.

Acknowledgment. We are indebted to Professor Elkan R. Blout of the Department of Biological Chemistry, Harvard Medical School for generously providing access to the CFT-20 spectrometer and to the University of Massachusetts/Boston for a faculty research grant which partially supported this work.

References and Notes

(1) D. Eggerding and R. West, *J. Am. Chem. Soc.*, **98**, 3641 (1976), and previous papers in this series.

(2) L. M. Schwartz, R. I. Gelb, and J. O. Yardley, *J. Phys. Chem.*, **79**, 2246 (1975).
(3) L. M. Schwartz and L. O. Howard, *J. Phys. Chem.*, **75**, 1798 (1971).
(4) R. I. Gelb, *Anal. Chem.*, **43**, 1110 (1971).
(5) J. L. Kurz and J. M. Farrar, *J. Am. Chem. Soc.*, **91**, 6057 (1969).
(6) R. I. Gelb and L. M. Schwartz, *Anal. Chem.*, **44**, 554 (1972).
(7) R. A. Robinson and R. H. Stokes, "Electrolyte Solutions", 2nd ed, revised, Butterworths, London, 1965.
(8) E. Patton and R. West, *J. Phys. Chem.*, **74**, 2512 (1970).
(9) H. S. Harned and R. W. Ehlers, *J. Am. Chem. Soc.*, **55**, 2179 (1933).
(10) L. M. Schwartz, *Anal. Chem.*, **47**, 963 (1975).
(11) R. P. Bell, *Adv. Phys. Org. Chem.*, **4**, 1 (1966).

Kinetics of Radical Decay. 4. Polycrystalline *p*-Azoxyanisole

John J. Tria and Russell H. Johnsen*

Department of Chemistry, Florida State University, Tallahassee, Florida 32306 *(Received February 25, 1977)*

Publication costs assisted by the U.S. Energy Research and Development Administration

Free radical decay in x-irradiated powder samples of *p*-azoxyanisole (PAA) studied between 60 °C and the liquid crystal phase transition at 118 °C was observed to occur in a "stepwise" manner with no evidence of radical conversion. Of several models tested the data were best fit by a kinetic equation due to Waite which involves a random initial spatial distribution of radicals, an activation energy for radical combination, E_{comb}, which dominates at early time, and an activation energy for diffusion, E_{diff}, which dominates at late times. Application of the model to the data yields $E_{\text{comb}} = 9.6$ and $E_{\text{diff}} = 19.3$ kcal/mol. The activation energies correspond well to those reported by other workers from NMR measurements of rotational and diffusional motion in PAA. The model also allows estimation of the diffusion coefficient provided r_0 in the kinetic equation can be approximated. Taking r_0 as the largest lattice dimension (20.5 Å) one obtains a value of $D \approx 1 \times 10^{-16}$ cm^2/s at 0.96 of the phase transition temperature. Such considerations lead to the assignment of E_{diff} to an extrinsic, defect controlled diffusion process and E_{comb} to a rotation of the radical about the long molecular axis necessary to reach a favorable orientation for combination with another radical. The general role of radical shape and ease of rotation in influencing the decay kinetics is discussed.

Introduction

The decay kinetics of free radicals produced in organic solids by ionizing radiation has been reported previously by this laboratory and by many other groups[1-10] with little consensus on the important mechanisms in the decay process. These experiments have illustrated that such factors as the crystalline or glassy nature of the matrix and its thermal history, the initial spatial distribution of radicals, and the nature of the radicals themselves can lead to profound differences in the observed decay kinetics. Generalizations are difficult but in many cases[2,6-10] a significant part of the decay occurs by a process second order in radical concentration, although other orders have been reported.[11] Second-order kinetics have been observed to govern the latter part of the decay in such systems as single crystals of irradiated anthracene,[7] imidazole,[8] and in certain amino acids[10] where the radicals formed are similar in size and shape to the parent molecule and the good agreement between activation energy for radical decay and that for bulk self-diffusion E_{diff} indicated a diffusion-controlled decay mechanism. The early part of the decay frequently does not appear to fit the same kinetic plot which describes the later data and has not been as well understood, although in some experiments it is clear that a change in radical distribution is an important factor. Unfortunately, the early radical decay is the most difficult to study because much of it can occur during the time necessary for thermal equilibration of the sample and spectrometer adjustment.

Organic solids exposed to ionizing radiation typically develop a concentration of free radicals which decay slowly at the irradiation temperature. Raising the temperature of the solid sufficiently results in a more rapid decay of at least part of the free radicals. Those systems in which decay essentially stops with a significant fraction of radicals remaining at a given temperature[2-5,9,10] but which decay by a further increment with each additional temperature increase have been particularly difficult to understand. Several groups have pointed out that this "stepwise" decay may be explained by assuming a sufficient range of activation energies corresponding to microscopic regions of varying crystal "stabilization energy"[3-5] or by developing a thermal chain reaction model[5] with an effective recombination rate dependent on concentration and an initial nonuniform distribution. While some of these approaches are useful in certain cases, their application typically yields little useful information about the system, e.g., a range of necessary activation energies or a limiting pair volume.

In a systematic approach to the problem of diffusion-limited kinetics Waite[12,13] solved the kinetic equations for several assumptions concerning initial distribution of reactants and the nature of the intermolecular reaction potential (boundary condition on the differential equations to be solved). Two of these models can lead to the prediction of a stepwise decay process under certain conditions. Both of these involve a boundary condition which describes the presence of a significant activation energy for the radical combination step E_{comb} in the kinetic process. This is in contrast to the assumption of negligible E_{act} for recombination which has been made explicitly or implicitly in some analyses.

In certain systems, e.g., hexamethylbenzene,[1] a portion of the radicals produced by irradiation at low temperatures has been observed to decay at or near temperatures at which certain molecular motions become possible. In particular for 1,4-dicyclohexylcyclohexane and 1,4-dicyclohexylbenzene, molecules of a size and shape similar to PAA, Ero, Gruner, Tompa, and Toth[14] found that a decrease in radical concentration as determined by ESR

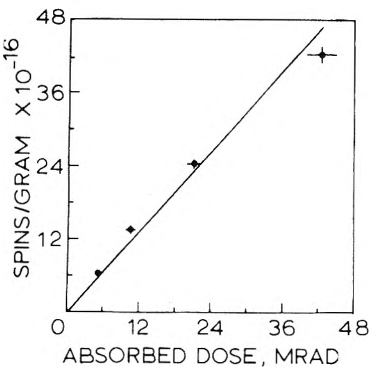

Figure 1. Yield of free radicals in polycrystalline PAA vs. absorbed dose of 3-Mev x rays at room temperature. $G(R\cdot) = 0.018$.

occurred at temperatures corresponding to the appearance of a torsional movement around the major axis of the molecules detected by NMR. Such comparison of ESR radical decay data with the NMR measurements provides a useful approach to the understanding of radical decay mechanisms in condensed media.

In the present work radicals produced in *p*-azoxyanisole (PAA) powder samples by x-irradiation at room temperature were observed to decay in a stepwise manner. The data were examined for agreement with the usual simple kinetic schemes and with Waite's kinetic equations appropriate to different models of the decay process. One of Waite's models successfully describes the stepwise nature of the decay and allows calculation of activation energy and diffusion parameters which compare favorably with literature data available from NMR molecular dynamics experiments and self-diffusion studies. In particular the origin and importance of E_{comb} in affecting the decay kinetics of radicals in solids is stressed by this work.

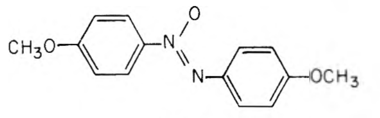

PAA

Experimental Section

p,p'-Azoxyanisole (PAA) obtained from Aldrich Chemical Co. was recrystallized from absolute ethanol to constant transition temperatures of 118.1–118.8 °C (solid to nematic phase) and 135.6–136.0 °C (nematic phase to isotropic liquid) as measured by the capillary melting tube method. Powdered samples of 0.1 g were placed in 4-mm o.d. by 3-mm i.d. Suprasil quartz tubes and were evacuated to 10^{-5} to 10^{-6} Torr, then filled to 0.5 atm with argon. The argon was included to ensure good thermal equilibration of the sample.

The Florida State University 3-MeV Van de Graaff accelerator was used to irradiate the samples at room temperature with 3-MeV x rays at a dose rate of 5.3 Mrad/h. Most kinetic data were obtained using samples irradiated to doses of 5–6 Mrad, but larger and smaller doses were used to test kinetic models. The yield of radicals per 100 eV energy absorbed (G value) was $G(R\cdot) = 0.018$ at room temperature. All samples were on the linear portion of the $G(R\cdot)$ vs. dose curve, Figure 1. The ESR signal produced in the quartz tubes was annealed out before measurements.

ESR spectra were recorded using either a Varian E-3 or E-12 spectrometer operated at X band (~9.5 GHz). A Varian Data Machines 620/i-16k minicomputer interfaced to the spectrometer was used with Varian EPR/TTY system 994002-00A software for double integration of the first derivative spectra in order to obtain spin concentrations by comparison to a calibrated pitch sample. Spin concentration measurements were made at room temperature. Microwave power saturation curves were prepared to ensure that power levels used were on the linear portion of the signal vs. $P^{1/2}$ plot, typically ~0.15 mW, for absolute spin concentration measurements.

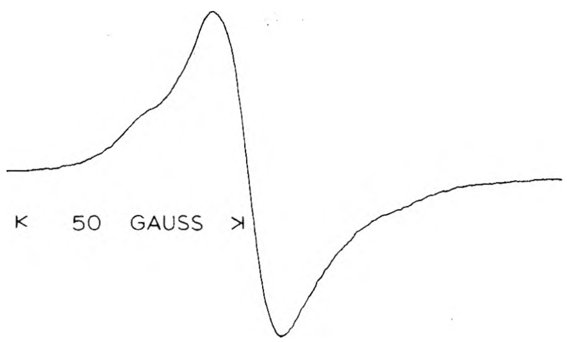

Figure 2. ESR first derivative spectrum of irradiated PAA powder sample at room temperature.

Temperature control during radical decay was maintained to ±0.5 °C with a flow of heated nitrogen gas using the Varian variable temperature accessory and cavity insert dewar. With the dewar at the control temperature, 1–2 min was required for the sample to reach the desired decay temperature as measured in a separate experiment with a thermocouple probe inserted into the sample. Radical decay was slow enough over the range studied, 60–115 °C, that loss of this earliest data was not a serious problem.

Results and Discussion

The ESR spectrum of PAA powder samples irradiated and studied at room temperature[15] is seen to consist of a broad single line with poorly resolved features as shown in Figure 2. Such a poorly resolved singlet is typical of phenyl radicals observed in the solid state, and is consistent with the single weakly resolved line attributed to phenyl radicals in irradiated azobenzene.[16,17] Another similarity to the azobenzene spectrum is the absence of evidence for the cyclohexadienyl radical (a 1:2:1 triplet with $\Delta H \sim 50$ G) which is also frequently observed in irradiated alkylbenzenes.[18,19] The presence of small amounts of radicals of the R-OCH$_2\cdot$ type, or radicals associated with the azoxy group can neither be confirmed nor denied on the basis of the spectrum as the expected hyperfine splittings would be partly overlapped by the broad singlet signal. However a significant fraction of such radicals would be expected to contribute more observable structure than is seen. The characteristic asymmetric ESR signal observed for alkoxy radicals[28,29] RO· at 77 K was not seen in samples cooled to 77 K after irradiation at 300 K. Since large fragments seldom are removed from compounds irradiated in the solid phase due to the cage effect, the majority of radicals present at room temperature in PAA are most probably phenyl type radicals derived by loss of a ring hydrogen from the parent molecule. As there are eight nonequivalent ring protons, a mixture of phenyl radicals of slightly different character would be expected and would contribute to loss of spectral resolution. At elevated temperatures the spectrum decays essentially uniformly with no radical conversions, Figure 3. The uniform decay would appear to indicate all radicals behave similarly with respect to diffusion rates and recombination probabilities, and so in the kinetic treatments a single type of radical has been assumed.

Typical free radical decay data are shown in Figure 4 which illustrates the practical cessation of decay with

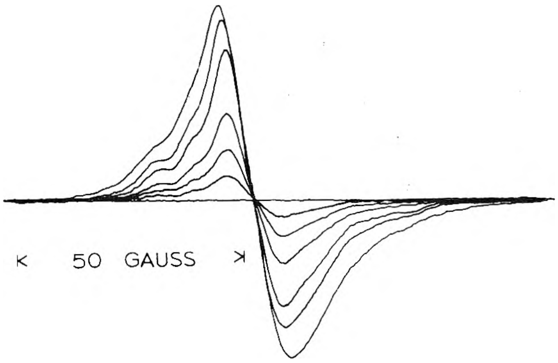

Figure 3. Thermal decay of free radicals in PAA. Spectra obtained by raising sample to successively increasing temperatures and cooling to room temperature for measurement.

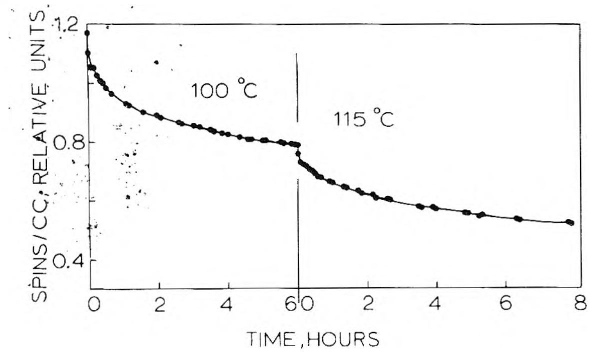

Figure 4. Radical decay at 100 °C followed by decay at 115 °C in same sample.

significant spin concentration remaining which is characteristic of "stepwise" decay. Raising the decay temperature creates another "step", the level of which depends on the temperature. This behavior persists up to the solid–nematic phase transition temperature, where the sample becomes fluid and all radicals disappear rapidly. The data do not fit simple zero or first-order decay laws. In certain irradiated systems decay has been observed to depend on "correlated recombination" of geminate pairs of radicals produced in proximity to each other. The pairs have a spectrum of activation energies for recombination and the resulting kinetics have been called "first order in dose". French and Willard[20] have noted that for such systems plots of fractional decay vs. time for samples irradiated to different total doses ought to superimpose. When applied to irradiated PAA this test does not indicate a pairwise recombination process but rather a concentration dependent one, as seen by the different fractional decay curves for different doses in Figure 5. Since a radical can only disappear by combining with another radical, second-order processes are intrinsically attractive as models and have been used successfully in some cases. However when stepwise decay occurs the data, over the entire range, cannot be fitted to a single second-order kinetic plot as shown in Figure 6. In fact the second-order plot shown exhibits two linear regions corresponding to early and late parts of the decay experiment. If one adopts a naive view and relates these two linear regions to two distinct second-order decay processes with different rates, activation energies for the processes may be calculated from Arrhenius plots. One would expect the slow process to correspond to a diffusion mechanism, as is frequently observed in solid systems, while the faster process may be associated with an activation energy for the radical combination step, due possibly to steric restrictions placed on the radical pair by the lattice which make it difficult for the radical pair to achieve a favorable relative orientation for combination. In fact, the values obtained from this naive model of $E_{\mathrm{diff}} \sim 19$ kcal/mol and $E_{\mathrm{comb}} \sim 10$ kcal/mol agree remarkably well with values of $E_{\mathrm{diff}} = 21 \pm 2$ and $E_{\mathrm{reorient}} = 10 \pm 2$ reported by Thompson, Kydon, and Pintar[21] for NMR measurements on PAA. The value quoted for E_{reorient} is believed by them to correspond to a rotational reorientation of the molecule about its long axis.

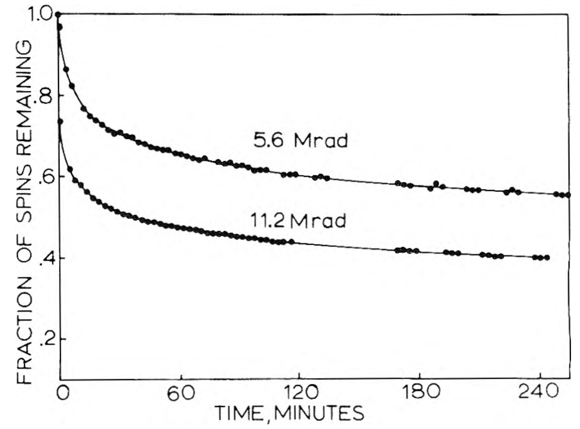

Figure 5. Fractional decay at 113 °C for samples irradiated to different doses.

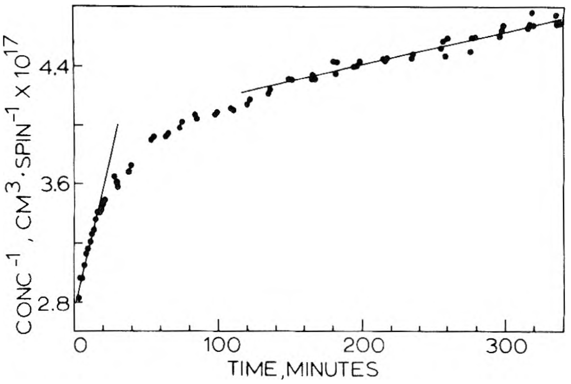

Figure 6. Second-order kinetic plot of radical decay at 115 °C.

Application of Waite's more sophisticated models of diffusion controlled kinetics to the PAA data provides both a theoretical basis for the shape of the decay curve and additional insights into the decay process which seem to support the general features of the naive model discussed above. Since the fractional decay curves at different doses indicated that a pairwise process was not involved, we omit discussion of Waite's equations for pairwise initial distributions of reactants. We consider here the application of Waite's equations for systems with a random initial reactant distribution and one of two "boundary conditions" related to the nature of the intermolecular reaction potential. The "Smoluchowski boundary condition" assumes there is a "reaction radius" r_0 within which reaction is 100% probable and outside of which it is 0% probable. This is equivalent to the assumption that $E_{\mathrm{comb}} = 0$ for the radical recombination step in the decay process, once the reactants have diffused to within r_0 of each other. If however the reaction rate depends partly on steric (or other) factors at the moment of "collision" an appropriate boundary condition may be derived by defining a pair separation $r_0 - \Delta r_0$ to r_0 within which the reaction rate proceeds via first-order kinetics. This constitutes a mathematical device which allows the "colliding" pair of radicals to have less than unit probability of immediate reaction on any given collision, and is called the "radiation boundary condition" (so named from resemblance to a problem in heat transport).

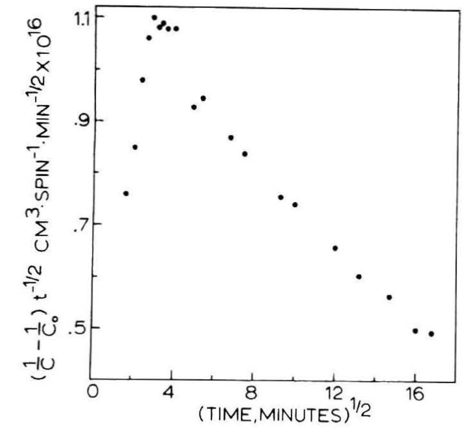

Figure 7. Kinetic plot to test data for fit to Waite's equation assuming Smoluchowski boundary condition and random initial radical distribution. Data for decay at 98 °C.

For the case of a diffusion controlled reaction with a random initial reactant distribution and the Smoluchowski boundary condition, Waite shows that after an initial transition period

$$\left(\frac{1}{C}-\frac{1}{C_0}\right)=\kappa\left[1+\frac{2r_0}{(\pi D t)^{1/2}}\right]t \tag{1}$$

where C is the concentration, C_0 is the concentration at time zero, κ is $4\pi r_0 D$ where D is the diffusion coefficient of the reactant species. As shown by Wen, Johnson, and Dole[6] this equation can be cast in the form

$$\left(\frac{1}{C}-\frac{1}{C_0}\right)\frac{1}{t^{1/2}}=\kappa t^{1/2}+\frac{2r_0\kappa}{(\pi D)^{1/2}} \tag{2}$$

whereas the usual second-order equation becomes

$$\left(\frac{1}{C}-\frac{1}{C_0}\right)\frac{1}{t^{1/2}}=k_2 t^{1/2} \tag{3}$$

Thus a plot of $(1/C - 1/C_0)t^{-1/2}$ vs. $t^{1/2}$ yields a straight line with slopes of κ or k_2 and intercept at $t = 0$ of $2r_0\kappa/(\pi D)^{1/2}$ for a diffusion-controlled second-order reaction with Smoluchowski boundary condition and random reactant distribution, or an intercept of zero for a simple second-order nondiffusion controlled reaction. For the diffusion-controlled case a deviation from the line occurs at times sufficiently small such that $t \not\gg r_0^2/D$. The intercept at $t = 0$ is then determined by extrapolation of the long-time straight line. Figure 7 presents typical results for the PAA data tested against this model. A complex curve shape similar to that shown is obtained for decay at all temperatures. While details of the curve shape vary in a regular manner with temperature, in all cases the curve is bimodal with negative slope at long time, whereas the model predicts a monotonically increasing function which approaches a straight line of positive slope at long time. Clearly the Smoluchowski boundary-random distribution case does not apply here. We have also tried the sensitive plot devised by Dole et al.[22] to test for diffusion control under the Smoluchowski boundary condition-random initial distribution model. The plot had a concave shape, atypical for such plots, with the "Q function", $t/(1/C - 1/C_0)$, extrapolating to negative values as $t^{1/2}$ goes to zero. As the theory admits only two possibilities, i.e., extrapolation to zero for diffusion control or to positive values in the absence of diffusion control, this test also ruled against the Smoluchowski boundary-random distribution model.

For the case of the radiation boundary condition and a random initial distribution of reactants, the rate expression has a complicated form which as Waite shows takes on the limiting form

$$-\mathrm{d}C/\mathrm{d}t = 4\pi r_0^2\Delta r_0 k C^2 \tag{4}$$

at very short times such that

$$D\left[\left(\frac{r_0 k\Delta r_0}{D}+1\right)/r_0\right]^2 t \simeq 0 \tag{5}$$

and the limiting form

$$-\frac{\mathrm{d}C}{\mathrm{d}t}=4\pi r_0^2 D\left[\frac{k\Delta r_0/D}{(r_0 k\Delta r_0/D)+1}\right]C^2 \tag{6}$$

for very long times such that

$$D\left[\frac{(r_0 k\Delta r_0/D)+1}{r_0}\right]^2 t\rightarrow\infty \tag{7}$$

Since both of these limiting forms are second order, the model predicts that the usual second-order plot of $1/C$ vs. time will show *two* linear regions (for early and late times) connected by a nonlinear transition region, provided $r_0 k\Delta r_0/D \not\ll 1$ in which case the reaction is not diffusion limited and the rate expressions become identical. This curve shape is in fact just what is observed for irradiated PAA, e.g., Figure 5. The "stepwise" decay behavior of the samples is seen to arise from a large difference in rates for the early and late parts of the decay curve which arises from the influence of D on the decay rate at long times. The decay rate measured at early times is largely influenced by recombination of radicals formed in close proximity to each other and the activation energy from an Arrhenius plot of the slopes of the decay curves at early times applies to factors controlling the actual radical combination step, such as lattice hindrance to molecular reorientation. At long times the decay rate is controlled by the rate of diffusion of radicals toward each other. One can easily show from (4) and (6) that

$$D=\frac{1}{4\pi r_0}\,\frac{K_{\mathrm{I}}K_{\mathrm{II}}}{K_{\mathrm{I}}-K_{\mathrm{II}}} \tag{8}$$

where

$$K_{\mathrm{I}} \equiv 4\pi r_0^2\Delta r_0 k$$

(i.e., the early slope in a $1/C$ plot) and

$$K_{\mathrm{II}} \equiv 4\pi r_0^2 D\left[\frac{k\Delta r_0/D}{(r_0 k\Delta r_0/D)+1}\right]$$

(i.e., the late slope). Thus D is known to within a multiple of r_0 and assuming the form $D = D_0 e^{-E_{\mathrm{diff}}/RT}$ an Arrhenius plot of $K_{\mathrm{I}}K_{\mathrm{II}}/(K_{\mathrm{I}} - K_{\mathrm{II}})$ yields E_{diff}. Application of this analysis to the PAA data yields $E_{\mathrm{comb}} = 9.6$ and $E_{\mathrm{diff}} = 19.3$ kcal/mol in good agreement with the previously mentioned values of $E_{\mathrm{rotation}} = 10 \pm 2$ and $E_{\mathrm{diff}} = 21 \pm 2$ from NMR experiments. Furthermore, if one makes a reasonable estimate of r_0 (say on the order of the largest lattice dimension, 20.5 Å),[23,24] then one can obtain an approximate value for D_0 of 1.8×10^{-5} cm^2/s which gives an overall $D = 1.8 \times 10^{-5} \exp[-19.3\ \mathrm{kcal/mol}^{-1}/RT]$ cm^2/s. We should emphasize that since the PAA samples studied here were polycrystalline, the dominant diffusion processes are expected to involve diffusion along dislocations and subboundaries of the crystals,[25,27] and therefore the E_{diff} and D_0 obtained pertain to such extrinsic defect processes, rather than to the intrinsic lattice self-diffusion process expected to dominate in good quality single crystals. The following paper, part 5 in this series, examines radical recombination processes in single crystals of PAA and two other members of the homologous series of *n*-alkoxyazoxybenzenes.

Conclusions

The radical decay data fit well a model which assumes a random initial distribution, diffusion control of the reaction rate at long times, and a significant activation energy for the radical combination step. The correspondence of the E_{comb} measured here with the E_{act} for molecular reorientation along the long axis from the NMR data is particularly interesting. Previous experimental studies of radical recombination in solids have often overlooked the possibility of a significant E_{act} for the combination step or have assumed it to be at most a few tenths of a kilocalorie per mole based on liquid phase kinetic studies. While the liquid phase studies can provide a limit for the activation energy (if any) intrinsic to bond formation between two radicals, it must be emphasized that motional restrictions in solid phases are much greater than in liquids and would be expected to dominate E_{comb}. The relative importance of molecular reorientation activation energies in determining radical decay kinetics may depend in general upon several factors including the shape of the radical involved, the nature of the intermolecular forces and the molecular arrangement in the crystal lattice. "Spherical" molecules in the materials known as "plastic crystals" exhibit relatively free rotation at fairly low temperature. Resing[27] has reported a comparative study of NMR relaxation phenomena in the plastic crystal adamantane (ADA) and the brittle crystal hexamethylenetetramine (HMT), both molecules having tetrahedral molecular symmetry, highly symmetric lattices (fccub for ADA and bccub for HMT) and similar molecular weights and melting points. The activation energies for rotational motion were found to be 19.3 kcal/mol for HMT, 3.08 kcal/mol for ADA in the plastic phase, and 6.5 kcal/mol in the brittle phase. The difference between rotational activation energies in this case would appear due more to the intermolecular forces than to molecular shape or lattice type. Disk shaped molecules such as imidazole and anthracene would be expected to have a rotational motion in the plane of the disk with a lower energy barrier than for the "flipping" motion out of the disk plane. Lath-shaped molecules such as PAA should be even more restricted with rotation about the long axis being the motion with lowest energy barrier. One would expect then that the molecular reorientations necessary for two "colliding" radicals to achieve a favorable relative orientation for combination might be more difficult for PAA than for molecules with discoid or spherical shapes, and the effect of the activation energy for reorientation on the decay kinetics would be more pronounced. As it seems apparent that several factors may contribute to E_{act} for reorientation, a careful study of its effect on free radical decay in solids would require examination of sets of compounds carefully chosen to vary one or more of these factors in a systematic way.

Acknowledgment. The authors wish to thank Dr. B. B. Garrett for helpful discussions, and Mr. D. E. Lott for performing the irradiations. We also acknowledge the support of the E.R.D.A. This is ORO document 2001-37.

References and Notes

(1) V. K. Ermolaev, Yu. N. Molin, and N. Ya. Buben, *Kinet. Katal.*, **3**, 58 (1962).

(2) V. K. Ermolaev, Yu. N. Molin, and N. Ya. Buben, *Kinet. Katal.*, **3**, 314 (1962).

(3) R. Bensasson, M. Durup, A. Dworkin, M. Magat, R. Marx, and H. Szwarc, *Discuss. Faraday Soc.*, **36**, 177 (1964).

(4) A. I. Mikhailov, Ya. S. Lebedev, and N. Ya. Buben, *Kinet. Katal.*, **5**, 1020 (1964).

(5) A. I. Mikhailov, Ya. S. Lebedev, and N. Ya. Buben, *Kinet. Katal.*, **6**, 48 (1965).

(6) W. Y. Wen, D. R. Johnson, and M. Dole, *J. Phys. Chem.*, **78**, 1798 (1974).

(7) A. R. McGhie, H. Blum, and M. M. Labes, *Mol. Cryst.*, **5**, 245 (1969).

(8) A. R. McGhie, H. Blum, and M. M. Labes, *J. Chem. Phys.*, **52**, 6141 (1970).

(9) F. B. Stentz, E. D. Taylor, and R. H. Johnsen, *Radiat. Res.*, **49**, 124 (1972).

(10) A. Joshi and R. H. Johnsen, *J. Phys. Chem.*, **80**, 46 (1976).

(11) P. K. Horan, W. D. Taylor, G. K. Strother, and W. Snipes, *Biophys. J.*, **8**, 164 (1968).

(12) T. R. Waite, *Phys. Rev.*, **107**, 463 (1957).

(13) T. R. Waite, **107**, 471 (1957).

(14) J. Ero, G. Gruner, K. Tompa, and F. Toth, *KFKI Kozl.*, **15**, (6), 345 (1967).

(15) The radical population stable at room temperature is different from that formed by irradiation at 77 K and examined at that temperature. The ESR spectrum at 77 K consists of the room temperature signal plus additional lines which can be interpreted as arising from closely spaced radical pairs. As the sample is warmed, the additional lines decay with a significant decrease in total spin concentration, until at about −60 °C the remaining spectrum is identical with the one obtained by room temperature irradiation. Details of the low temperature formation and decay of radicals in PAA and homologues will be the subject of a future report from this laboratory.

(16) V. I. Trofimov, I. I. Chkheidze, and N. Ya. Buben, *Zh. Strukt. Khim.*, **5**, (4), 624 (1964).

(17) I. I. Chkheidze, V. I. Trofimov, and A. T. Koritskii, *Kinet. Katal.*, **8** (2), 453 (1967).

(18) A. Zeman and H. Heusinger, *Radiochim. Acta*, **8**, (3), 149 (1967).

(19) J. Ero., *KFKI Kozl.*, **15** (4), 207 (1967).

(20) W. G. French and J. E. Willard, *J. Phys. Chem.*, **72**, 4604 (1968).

(21) R. T. Thompson, D. W. Kydon, and M. M. Pintar, *J. Chem. Phys.*, **61**, 4646 (1974).

(22) M. Dole, C. S. Hsu, V. M. Patel, and G. N. Patel, *J. Phys. Chem.*, **79**, 2473 (1975).

(23) F. Wurstlin, *Z. Kristallogr.*, **88**, 185 (1934).

(24) P. Chatelain, *C. R.*, **203**, 1169 (1936).

(25) J. N. Sherwood and D. J. White, *Phil. Mag.*, **16**, 975 (1967).

(26) H. A. Resing, *Mol. Cryst. Liquid Cryst.*, **9**, 102 (1969).

(27) J. N. Sherwood and D. J. White, *Phil. Mag.*, **15**, 745 (1967).

(28) P. J. Sullivan and W. S. Koski, *J. Am. Chem. Soc.*, **85**, 384 (1963); **86**, 159 (1964).

(29) C. Chacaty and A. Forchioni, *C. R. Acad. Sci., Ser. C*, **268**, 300 (1969).

Kinetics of Radical Decay. 5. Single Crystal *n*-Alkoxyazoxybenzenes

John J. Tria and Russell H. Johnsen*

Department of Chemistry, Florida State University, Tallahassee, Florida 32306

(Received February 25, 1977)

Publication costs assisted by the U.S. Energy Research and Development Administration

Decay kinetics of free radicals produced by x-radiolysis of single crystal samples of three members of the homologous series of *n*-dialkoxyazoxybenzenes has been studied in the range between room temperature and the solid-to-liquid crystal phase transition temperature. Radical decay was analyzed using a model due to Waite which assumes a random initial spatial distribution of radicals and separate activation energies for radical diffusion and recombination. In single crystal samples the activation energies (in kcal/mol) were 23 and 34 for *p,p'*-azoxyanisole (PAA), 17 and 40 in *p,p'*-azoxyphenetole (PAP), and 19 and 31 in heptyloxyazoxybenzene (HAB) for combination and diffusion, respectively. The activation energy for combination is attributed to a rotational reorientation of the radicals. The activation energy for diffusion is attributed to an intrinsic bulk self-diffusion process, in contrast to the grain boundary diffusion process previously reported for radical decay in polycrystalline PAA. The effect of changing length of the alkoxy group on the activation energies is discussed. A solid–solid phase transition was discovered at 91 °C in PAP. Radicals in solvent-grown crystals decayed rapidly at the transition temperature, while radicals in samples which had been annealed above the transition temperature before irradiation showed normal decay behavior.

Introduction

The decay kinetics of free radicals produced by the action of ionizing radiation on organic compounds in rigid phases has previously been studied in this laboratory and by other groups[1-11] in order to elucidate the molecular processes involved. In many cases the observations do not fit simple kinetic laws. This is true in particular for systems exhibiting so-called "stepwise decay" in which there is a dramatic slowing down of the initial rate to yield a plateau region where decay is almost negligibly slow on the original time scale. We have demonstrated in a previous study[12] that "stepwise" decay kinetics in polycrystalline *p,p'*-azoxyanisole (PAA) irradiated and studied between room temperature and the liquid crystal phase transition could best be explained by a model due to Waite[13] which involves an activation energy for diffusion of the radicals together, E_{diff}, an activation energy for the combination of two radicals, E_{comb}, and a random initial spatial distribution of radicals. It was concluded that E_{comb} arose from steric hindrance of the lattice on molecular motion as the radicals orient themselves in a configuration amenable to combination, and that E_{diff} arose from an extrinsic, defect-controlled diffusion process such as grain boundary diffusion.

The present study of single crystal samples was undertaken in order to ascertain more clearly the importance of two factors in determining the radical decay kinetics: first, the crystalline nature of the matrix and second the size and shape of the radicals involved. We report here the results of radical decay experiments in single crystals of three members of the homologous series of *p,p'*-dialkoxyazoxybenzenes, those with one, two, and seven carbon atoms respectively in the alkoxy group: PAA, *p,p'*-azoxydiphenetole (PAP) and 4,4'-bis(heptyloxy)azoxybenzene (HAB). The PAA single crystal data allow comparison with the previously reported powder sample data for this compound in order to determine the influence of degree of crystallinity on the diffusion process in radical recombination. Furthermore, since the three compounds reported here differ only in the length of the alkyl chain (and necessarily in molecular weight), the influence of this structural characteristic on E_{comb} can be studied.

Radical decay in all systems studied here was qualitatively similar to the previous report. The "two process" model and the limiting forms of the appropriate Waite equations have again been used to obtain activation energies for the radical diffusion and combination steps. Results obtained here tend to support the model of the decay process proposed in the previous study.

Experimental Section

PAA obtained from Aldrich Chemical Co. was purified by recrystallization from absolute ethanol. PAP and HAB obtained from Eastman Kodak Co. were recrystallized from toluene. Single crystals of all three materials were grown by slow evaporation from toluene solution. Samples of 0.05–0.1 g were placed in 4-mm Suprasil quartz EPR tubes, evacuated to 10^{-5} Torr, and sealed under 0.5 atm of nitrogen or argon for thermal conduction.

Samples were irradiated with 3-MeV x rays at a dose rate of ~5.3 Mrad/h using the Florida State University 3-MeV Van de Graaff accelerator. Doses used for kinetic studies were half or less of the maximum values shown in Figure 1. The yields of radicals per 100 eV of energy absorbed (*G* value) at room temperature were as follows: PAA, $G(\mathrm{R}\cdot) = 0.019$; PAP, $G(\mathrm{R}\cdot) = 0.046$; HAB, $G(\mathrm{R}\cdot) = 0.14$. The signal produced in the quartz tubes was annealed out before measurements.

For the fastest cases studied, the early part of the decay was followed in the ESR cavity as described previously.[12] For most cases the slower portion of the decay was followed for several hundreds of hours by placing the samples in gas chromatograph ovens with a temperature control capability of ±0.3 °C or better and removing them periodically for spin concentration measurements at room temperature. Thermocouple probes at the sample positions in the ovens were used to monitor temperature stability.

In order to ensure reproducible positioning of these sample tubes in the ESR cavity necessary for good quantitative measurements, the device pictured in Figure 2 was constructed of Plexiglass. A Lexan disk with a hole drilled to accommodate the sample tube was glued to the tube at an appropriate position to allow centering of the sample in the cavity. The bottom of the disk provided a vertical stop for positioning the sample, while a scribe mark on the disk could be aligned with one on the Plexiglass device for rotational repositioning of the tube. Spin

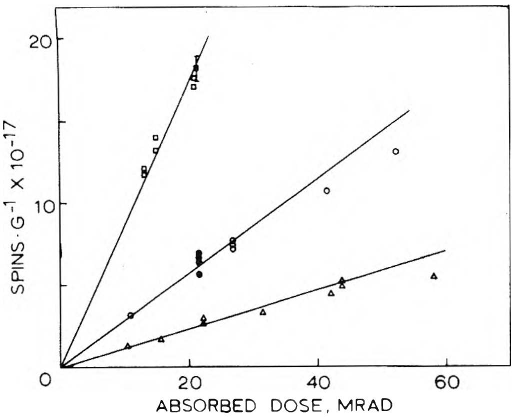

Figure 1. Radical yield at room temperature vs. absorbed dose for *n*-alkoxyazoxybenzenes irradiated with 3-MeV x rays: (△) PAA, $G(R\cdot) = 0.019$; (○) PAP not preannealed, (●) PAP preannealed, $G(R\cdot) = 0.046$; (□) HAB, $G(R\cdot) = 0.14$.

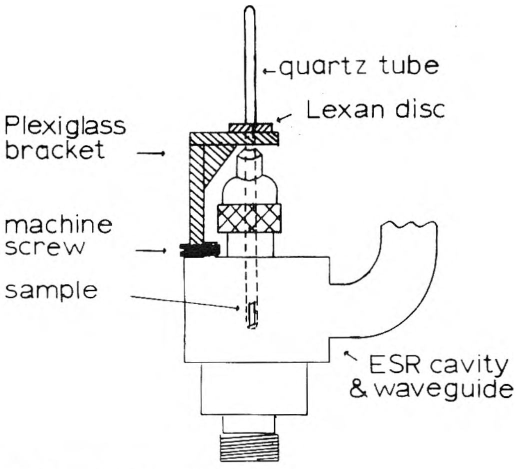

Figure 2. Sample positioning device.

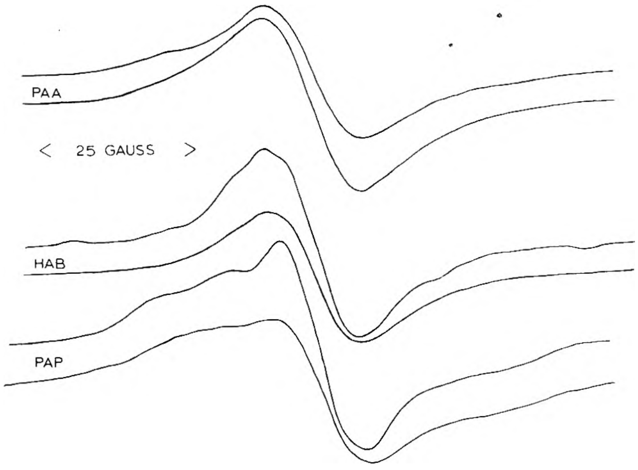

Figure 3. Power saturation effect on ESR spectra of powder samples: PAA upper curve 2 mW, lower 196 mW; HAB upper curve 4 mW, lower 196 mW; PAP upper curve 4 mW, lower 196 mW. Both spectra of each pair at same gain; pairs at different gains.

concentration measurements were performed with a Varian E-12 EPR spectrometer at ~9.5 GHz and 100-kHz modulation frequency with an on-line computer for double integration of the first derivative spectra as previously described. Plots of ESR signal vs. $P^{1/2}$ were prepared to determine microwave power levels appropriate for measurement without power saturation. For absolute spin concentration measurements, 0.15 mW was used.

Thermal analyses of PAP samples were performed using a DuPont 900 differential thermal analyzer with 20 °C/min heating rate and a nitrogen atmosphere with glass microbeads as reference and using a DuPont 950 thermogravimetric analyzer with ~17 mg sample and a nitrogen atmosphere.

Densities of single crystals were determined by the buoyancy method using glycerol–water solutions of variable composition and confirmed by Archimedes' principle measurements on two of the largest crystals. These techniques gave 1.35 g/cm^3 for PAA and 1.25 g/cm^3 for PAP in good agreement with the literature[14,15] and 1.12 g/cm^3 for HAB, previously unreported.

Results and Discussion

Radical yields at room temperature vs. absorbed dose appear in Figure 1. The radical yields are linear with dose except for a possible small falloff at the highest doses studied for each material. Kinetic data were obtained mostly on samples irradiated to approximately half the maximum doses shown in Figure 1, so that in all cases samples were still clearly on the initial linear part of the yield vs. dose curve. As the alkyl chain length increases the radical yield increases significantly, as has been observed previously in studies of irradiated alkylbenzenes.[16-18] We cannot immediately assume that all of the additional radical production is associated with the alkyl chain, as the following comments will point out.

Examination of spectra for *powder samples* of the compounds studied shows that as the alkyl chain length and $G(R\cdot)$ increase, there is some increase in structure away from the central part of the spectrum as seen in Figure 3. Similar results have been observed in *n*-alkylbenzenes by Zeman and Heusinger in a study of intramolecular energy transfer.[16] They reported that lower members of the homologous series showed only radicals associated with the aromatic ring, while higher members, starting at about seven alkyl carbons, showed increasingly great alkyl radical concentrations. Their determination of the yield of alkyl H_2 vs. number of alkyl carbons showed a smooth rise from $G \approx 0.33$ for $n = 1$ to ~0.42 for $n = 7$ and a sharp rise to ~0.62 at $n = 9$, indicating an abrupt breakdown in intramolecular protection and an expected sharp increase in alkyl radical production. While the ratios they found for radical production in compounds with one, two, and seven alkyl carbons were ~1:1:2, our results for PAA:PAP:HAB are ~1:2.4:7.4 indicating a smaller degree of protection and corresponding larger fraction of radicals in the alkyl chain. In fact, our figures are nearly linear with increasing number of alkyl carbons, implying that much of the increased radical yield may indeed be located in the alkyl chain. Since in the radiolysis of solid ethers[19,20] it is found that radicals are formed almost exclusively by loss of a hydrogen from the α-carbon atom, this probably occurs in the alkoxyazoxybenzenes also. The anticipated ESR spectra would be a triplet of ~18 G splitting for PAA and a five-line spectrum of 20–22-G splitting with approximately binomial intensity distribution for PAP and HAB (the α and β hydrogen couplings are nearly equal and the γ splitting is so small it only contributes line broadening in the solid). These spectra are much narrower overall than those expected from radicals at other sites in the alkyl chain[21] (e.g., the seven-line spectrum spanning ~150 G reported for the almost exclusive $CH_3\cdot CH(CH_2)_nCH_3$ radical reported for the radiolysis of solid alkanes) and thus agree better with the spectra of Figure 3. Two additional techniques were used to help identify the radicals involved. Power saturation studies of PAA and PAP showed only some loss of the poorly resolved structure at the highest microwave power (~196 mW) used, while HAB showed significant loss of the outermost structure and approached the spectrum observed for PAA. Similarly, during the

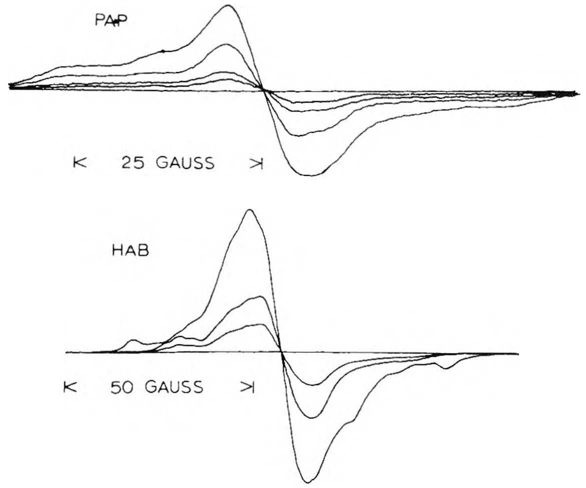

Figure 4. Thermal decay of radicals in PAP and HAB. Spectra obtained by raising sample temperature in steps; all spectra recorded at room temperature.

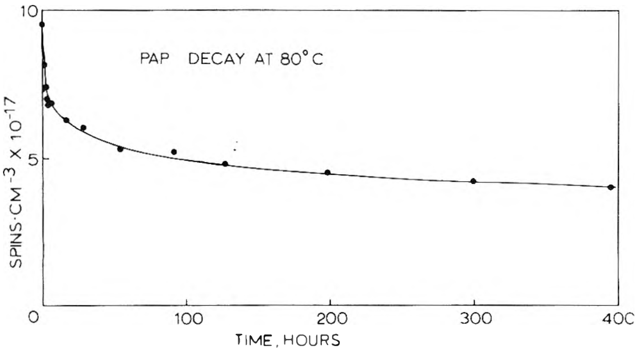

Figure 5. Radical decay in PAP single crystal at 80 °C.

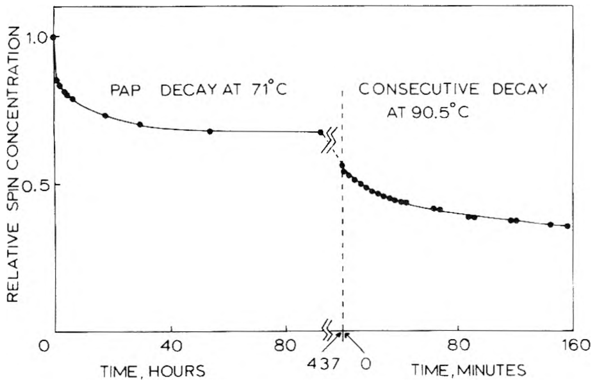

Figure 6. "Stepwise" decay in PAP: decay at 71 °C (note discontinuity in time axis) followed by decay of same sample at 90.5 °C.

course of thermal decay PAA and PAP showed some line narrowing and slight changes in the poorly resolved spectral structure, while HAB showed a significant early loss of the outermost spectral features as shown in Figure 4. None of the samples studied showed gross changes in spectra during decay nor gave evidence for any radical transformations. Overall the evidence seems to indicate that the radicals present at room temperature consist mostly of phenyl type radicals (as discussed previously[12]) for PAA, and an increasing proportion of mostly α-type radicals in PAP and HAB. Minor amounts of other radicals, particularly other alkyl types, are also likely. As in the previous paper, there was no evidence for alkoxy radicals. For all three samples it thus seems that the most probably radicals present differ only from the parent molecule by a hydrogen atom, as expected from the strong cage effect in solids. As the alkyl chain length increases,

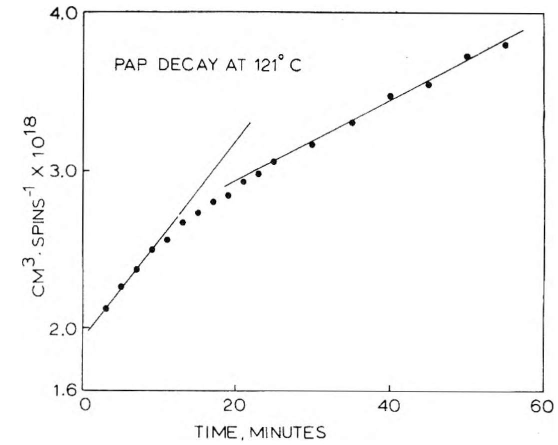

Figure 7. Second-order decay plot for preannealed PAP at 121 °C showing slopes for determining rate constants of fast and slow processes.

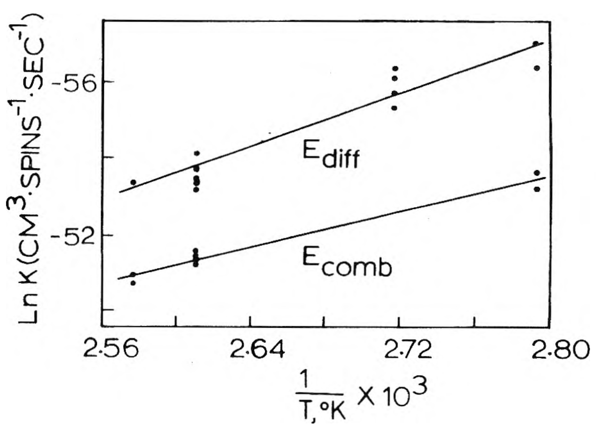

Figure 8. Arrhenius plot for activation energies for diffusion and combination of radicals in PAA.

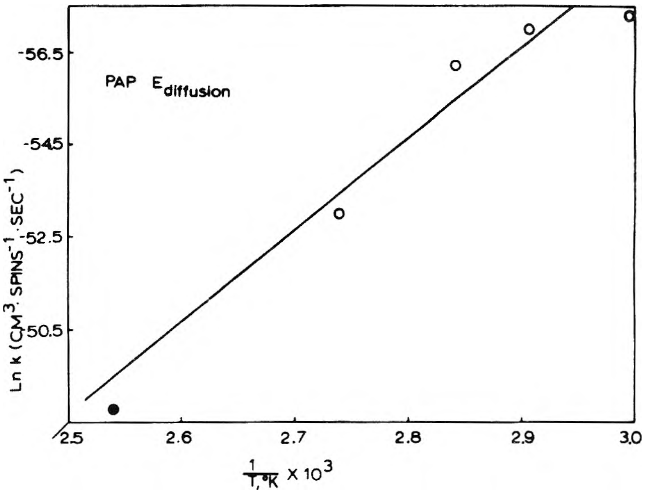

Figure 9. Arrhenius plot for diffusion activation energy in PAP: (●) preannealed sample; (O) not preannealed.

the distribution of radicals shifts more toward the ends of the molecule.

Typical radical decay vs. time data are given in Figures 5 and 6 and in all cases decay in single crystals exhibits the "stepwise" character already reported for polycrystalline PAA. Following the previously established approach[12] (concentration)$^{-1}$ was plotted against time as in Figure 7 and second-order rate constants were obtained for the early and late parts of the decay. Activation energies for the recombination and diffusion processes were obtained from Arrhenius plots such as Figures 8, 9, and 10. Results of applying the "two process" model and

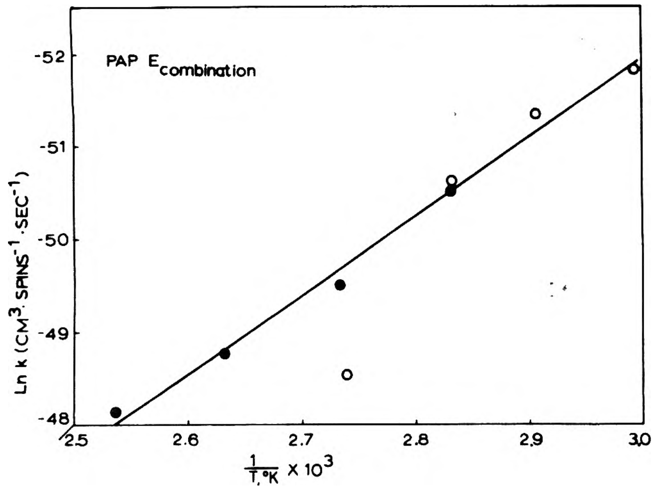

Figure 10. Arrhenius plot for combination activation energy in PAP: (●) preannealed sample; (O) not preannealed.

TABLE I: Diffusion Data for Single Crystals

Compound	E_{comb}, kcal/mol	E_{diff}, kcal/mol	Lattice energy × 2	D,[a] cm²/s
PAA[b]	23	34	~ 33–35 est	~ 2.2×10^{-18}
PAP[b]	17	40	~ 33–35 est	~ 1.2×10^{-16}
HAB[b]	19	31	~ 39–41 est	~ 1.0×10^{-19}
Anthracene[c]	f	50 ± 2; 56		2×10^{-13}
Naphthalene[d]	f	42.7		8.1×10^{-13}
Benzoic acid[e]	f	44.4	43.8 measd	5.6×10^{-14}

[a] Diffusion coefficient calculated at $0.96T_{pt}$. [b] This work. [c] References 7 and 33. [d] Reference 22. [e] Reference 37. [f] Not applicable. Values for n-alkoxyazoxybenzenes calculated from the data, lattice energies estimated as described in text. Anthracene, naphthalene, and benzoic acid data taken from references cited in text and supplied reference. Diffusion coefficients calculated at 0.96 of melting point for normal samples, and at 0.96 of first liquid crystal phase transition for PAA, PAP, and HAB.

Waite's equations (limiting form) for the case of uniform initial distribution of radicals and significant E_{act} for radical combination appear in Table I.

Both activation energies found for PAA single crystals are larger than the corresponding values of 10 and 19 kcal/mol reported elsewhere[12] for the powder samples. The lower value of E_{diff} for the powder samples can be attributed to enhanced rates of diffusion due to excess point and line defects in the material.[22] Studies by Sherwood and White of diffusion in naphthalene polycrystalline[23] and single crystal[22] samples have shown activation energies of 21 kcal/mol for diffusion along grain boundaries, the dominant process in polycrystalline naphthalene, and 43 kcal/mol for bulk self-diffusion in single crystals. For single crystals of identical high purity they found a variation of 3.1 kcal/mol depending on the extent of annealing to "heal" defects before measurement. While the greater value of E_{diff} for PAA single crystals than for powders is thus as expected, the greater value for E_{comb} in single crystals is not so easily accounted for. If one assumes the lower E_{comb} in powders is a result of radical recombination occurring predominantly in proximity to lattice defects where rotation is facilitated, then the defects must be preexisting and not radiation induced since the available NMR data agree with the radical data for powder samples as discussed in the preceding report. It is then necessary either that the radicals are preferentially formed at defects or migrate to them, where reaction occurs much more quickly than in the bulk of the lattice (assumed perfect). The role of preexisting vs. radiation-formed defects in the accumulation and decay of radicals has been discussed in detail in a previous report by Hoel and Johnsen.[35] If one assumes that the bulk of the lattice in powder samples is essentially perfect, then the NMR rotational E_{act} should be different from the radical kinetic data, not the same as is found. However, if one assumes instead that the bulk of the "lattice" in powders is so riddled with defects that essentially every lattice site is adjacent to one, then all radicals formed will effectively be formed at defects. Under this condition, both diffusion and rotation would be extrinsic, defect-controlled processes. For structurally weak, covalently bonded crystals this might not be a difficult situation to achieve by the vigorous grinding used to prepare powders. Pintar and co-workers[24] in their NMR experiment note that T_1 and $T_{1\rho}$ for PAA "may only be explained by a considerable degree of amorphousness of our sample." Additionally, Sherwood and White found that their diffusion data for polycrystalline naphthalene were well described by assuming a grain boundary width of ~10 Å, sufficiently small so that essentially every molecule is within an intermolecular distance or two of a defect.

Comparison of the single crystal data for PAA and PAP is especially interesting because they have similar crystal structures[14,15] and similar densities, 1.35 and 1.25 g/cm³, respectively. As one might expect, the E_{diff} for PAP is somewhat larger than for PAA, but the E_{comb} is smaller. This can be rationalized if the longer, more flexible alkoxy chain of the PAP molecule facilitates achievement of an orientation favorable for recombination of some radicals. However, previous magnetic resonance studies[25,26] have concluded that only the CH_2 group nearest the end of the chain in such molecules is free to rotate while the others can only move through a restricted angle. Another possibility for the lower E_{comb} in PAP is that the activation energy for rotation of the molecule is indeed lower. For $E_{rotation}$ in the homologous series of n-alkoxybenzoic acids values of 3.4 ± 1.0, 4.5 ± 1.0, and 3 ± 1 kcal/mol for compounds with alkoxy chains having one, five, and eight carbon atoms, respectively, have been determined.[26] This would tend to indicate that it may be naive to expect a simple variation of E_{comb} with increasing alkoxy chain length.

An interesting aspect of the PAP investigation is the unexpected discovery of a solid–solid phase transition at 91 °C. Single crystals grown from toluene solution showed an abrupt increase in rate of disappearance of free radicals in the neighborhood of 90 °C, and essentially complete decay occurred rapidly when samples were heated past this point, even though the solid to nematic phase transition is at 136 °C. Differential thermal analysis (DTA) showed an endothermic transition at 91 °C which did not reverse on cooling even when the sample was held at ~100 °C for several hours and then slowly recooled, see Figure 11. Thermogravimetric analysis (TGA) showed no apparent weight loss down to a sensitivity of 0.1% so that loss of crystallization solvent could be excluded. Subsequently, single crystal samples were slowly preheated past the transition at 91 °C, held for several days at ~100 °C, and slowly cooled to room temperature. Samples treated this way developed significant numbers of cracks visible to the unaided eye whereas they were previously unflawed. However, when these samples were irradiated and the radical decay studied at temperatures up to 121 °C, rate constants obtained for the fast and slow processes fall on the same line on an Arrhenius plot as rate constants

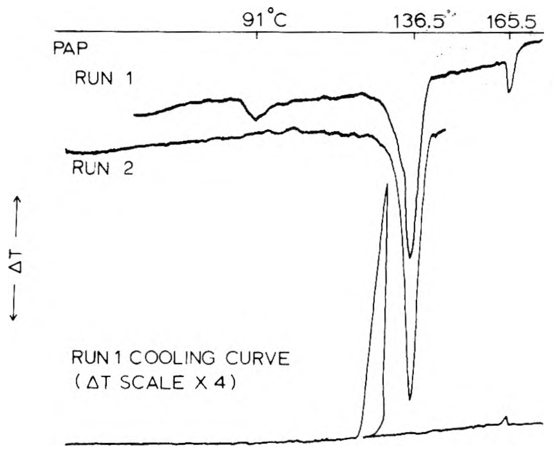

Figure 11. Differential thermal analysis thermogram of PAP: run 1, crystalline material grown from toluene; run 2, same sample after cooling to room temperature and repeating analysis.

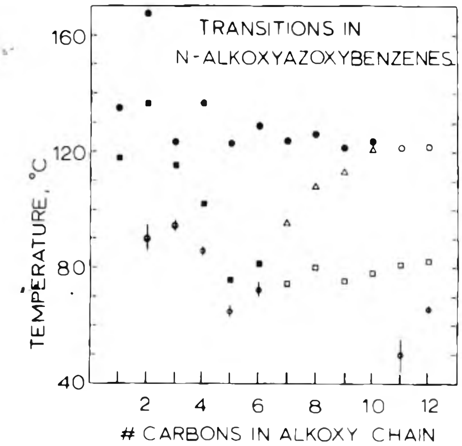

Figure 12. Transition temperatures in *n*-alkoxyazoxybenzenes: (●) nematic–isotropic liquid; (○) smectic–isotropic liquid; (■) solid–nematic; (□) solid–smectic; (△) smectic–nematic; (ϕ) solid I–solid II. Some transitions given are monotropic. The sources are ref 27–30, 34, and this paper.

obtained from decay experiments on nonpreheated samples below 91 °C, as seen in Figures 9 and 10. Solid–solid phase transitions have previously been reported for some other members of this homologous series[27-30] but not for PAP. Barrall, Porter, and Johnson[31,32] have reported the existence in some cholesteryl esters of various solid phases which when studied by DTA and differential scanning calorimetry (DSC) show behavior similar to that reported here for PAP. They attribute the behavior to existence of two different crystalline forms, one arising from the melt and one from solution. The existence of a solid–solid phase transition in PAP at 91 °C accounts for the rapid decay of radicals at that temperature in samples which had not been preannealed. Similar rapid disappearance of radicals at the temperatures of both first-order transitions (cyclohexane) and second-order transitions (neopentane) has been attributed[3] to density fluctuations accompanying reorganization of the crystal lattice.

Analysis of radical decay data for HAB crystals yields values of E_{diff} and E_{comb} intermediate between PAA and PAP although it is the largest and heaviest molecule of the three. The hypothesis that motion of the alkyl chain facilitates recombination of some radicals would explain why E_{comb} is lower than for PAA, while the increased size and mass of the molecules would be expected to contribute an offsetting effect. Having radical decay data for a few more members of the series would be necessary to determine if there is a consistent pattern or whether as in the case of rotational activation energy of the alkoxybenzoic acids there is no trend. The E_{diff} for HAB is more difficult to interpret. The molecular size is sufficiently greater than PAP that one would expect a larger E_{diff} since in the series of alkoxybenzoic acids studied by NMR[26] the E_{diff} increased from 21 ± 2 for one carbon to 24 ± 3 for three carbons in the alkoxy chain. It may be that the strict comparison of HAB with PAA and PAP is unjustified, however. Although the density 1.12 g/cm^3 follows the trend set by the other compounds, the crystal structure has not been reported. A significant difference in structure could make direct comparisons with the other compounds less meaningful. Another problem is the quality of the crystals used in the study. It was much more difficult to grow HAB crystals, and those obtained were of noticeably poorer quality than those obtained from PAA and PAP, although no quantitative measurements of defect concentration were attempted. According to the studies of Sherwood and White mentioned above, higher defect concentrations would be expected to lower the observed activation energies. Finally, because the crystal to smectic phase transition occurs at 75 °C in HAB, there is greater uncertainty in the activation energies obtained due to the reduced temperature interval over which data were taken.

Studies of bulk self-diffusion in organic solids generally yield values of E_{diff} which are double the lattice energy of the solid.[36] By using the enthalpies of phase transitions for alkoxyazoxybenzenes determined by Arnold[27] and estimating the enthalpy of vaporization from Trouton's rule, the lattice energies may be estimated. It can be seen in Table I that the measured values of E_{diff} compare well with twice the lattice energies so estimated. In addition, if one uses the largest lattice dimension of PAA, 20.5 Å, as an approximation to r_0 as done for the PAA powder data, the factor D_0 may be estimated and approximate values of D determined as done previously.[12] Table I shows values of D calculated at ~0.96 of the first liquid crystal phase transition temperature. It can be seen that diffusion coefficients are somewhat smaller than for the somewhat smaller organic molecules taken from the literature and calculated at 0.96 of the melting point, as might be expected. It thus seems reasonable to interpret our single crystal data as arising from bulk self-diffusion by a vacancy mechanism.

Conclusions

Application of the two process decay model to the single crystal data indicates that E_{comb} is generally less for molecules with a longer alkoxy chain than for PAA although the order of the HAB and PAP data is not consistent based only on chain length, and some other effects may also be involved. E_{diff} for the single crystals fall in the range reported for organic compounds of similar size, e.g., 43 ± 2 for naphthalene,[22] 50 ± 2[7] and 56[33] for anthracene, although again the HAB value seems somewhat out of order. While comparisons between the PAA and PAP data seem justified by their similar masses, densities, and crystal structures the usefulness of comparisons with HAB is uncertain due to its unknown crystal structure and the possibility of significant error due to poorer quality crystals being used. Experiments with several more members of the homologous series would be necessary to determine whether a simple trend in E_{comb} and E_{diff} exists. Examination of the transition temperatures for the series, Figure 12, indicates that in fact one might not expect a simple trend in any quantity related to lattice parameters. The results obtained by us so far for the members of the homologous series studied seem consistent enough both internally and with data from other sources to justify the continued use of the decay process model involving significant E_{comb} and E_{diff} and a random initial reactant distribution.

Acknowledgment. The authors acknowledge the support of the E.R.D.A. This is ORO document No. 2001-38.

References and Notes

(1) V. K. Ermolaev, Yu. N. Molin, and N. Ya. Buben, *Kinet. Katal.*, **3**, 58 (1962).
(2) V. K. Ermolaev, Yu. N. Molin, and N. Ya. Buben, *Kinet. Katal.*, **3**, 314 (1962).
(3) R. Bensasson, M. Durup, A. Dworkin, M. Magat, R. Marx, and H. Szwarc, *Discuss. Faraday Soc.*, **36**, 177 (1964).
(4) A. I. Mikhailov, Ya. S. Lebedev, and N. Ya. Buben, *Kinet. Katal.*, **5**, 1020 (1964).
(5) A. I. Mikhailov, Ya. S. Lebedev, and N. Ya. Buben, *Kinet. Katal.*, **6**, 48 (1965).
(6) W. Y. Wen, D. R. Johnson, and M. Dole, *J. Phys. Chem.*, **78**, 1798 (1974).
(7) A. R. McGhie, H. Blum, and M. M. Labes, *Mol. Cryst.*, **5**, 245 (1969).
(8) A. R. McGhie, H. Blum, and M. M. Labes, *J. Chem. Phys.*, **52**, 6141 (1970).
(9) F. B. Stentz, E. D. Taylor, and R. H. Johnsen, *Radiat. Res.*, **49**, 124 (1972).
(10) A. Joshi and R. H. Johnsen, *J. Phys. Chem.*, **80**, 46 (1976).
(11) P. K. Horan, W. D. Taylor, G. K. Strother, and W. Snipes, *Biophys. J.*, 8, 164 (1968).
(12) J. J. Tria and R. H. Johnsen, *J. Phys. Chem.*, preceding paper in this issue.
(13) T. R. Waite, *Phys. Rev.*, **107**, 463 (1957).
(14) (a) F. Wurstlin, *Z. Kristallogr.*, **88**, 185 (1934): $d = 1.348$ measured, 1.346 calculated; (b) J. D. Bernal and D. Crowfoot, *Trans. Faraday Soc.*, **29**, 1032 (1933): $d = 1.35$ calculated from their data.
(15) P. Chatelain, *C. R.*, **203**, 266 (1936): $d = 1.253$ measured; *Bull. Soc. Fr. Min. Crist.*, **60**, 280 (1937): $d = 1.270$ calculated; Bernal and Crowfoot, loc. cit.: $d = 1.300$ calculated from their data.
(16) A. Zeman and H. Heusinger, *Radiochim. Acta*, **8**, 149 (1967).
(17) J. Ero, *KFKI Kozl.*, **15** (4), 207 (1967).
(18) I. Kules and M. Ero-Gecs, *Acta Chim. Acad. Sci. Hung.*, **58** (4), 389 (1968).
(19) C. Chacaty, *J. Chim. Phys.*, **64**, 514 (1967).
(20) V. S. Chervonenko, V. A. Roginskii, and S. Ya. Pshezhetskii, *Khim. Vys. Energ.*, **4**, 450 (1970).
(21) B. Smaller and M. Matheson, *J. Chem. Phys.*, **28**, 1169 (1958).
(22) J. N. Sherwood and D. J. White, *Phil. Mag.*, **15**, 745 (1967).
(23) J. N. Sherwood and D. J. White, *Phil. Mag.*, **16**, 975 (1967).
(24) R. T. Thompson, D. W. Kydon, and M. M. Pintar, *J. Chem Phys.*, **61**, 4646 (1974).
(25) J. C. Rowell, W. D. Phillips, L. R. Melby, and M. Panar, *J. Chem. Phys.*, **43**, 3442 (1965).
(26) R. T. Thompson and M. M. Pintar, *J. Chem. Phys.*, **65**, 1787 (1976).
(27) H. Arnold, *Z. Phys. Chem.* (*Leipzig*), **225**, 146 (1964).
(28) H. Arnold and H. Sackmann, *Z. Phys. Chem.* (*Leipzig*), **213**, 145 (1960).
(29) H. Lippmann and K.-H. Weber, *Ann. Phys.*, **6**, 265 (1957).
(30) R. Kohler, *Ann. Phys.*, **7**, 241 (1960).
(31) E. M. Barrall, II, R. S. Porter, and J. F. Johnson, *J. Phys. Chem.*, **70**, 385 (1966).
(32) E. M. Barrall, II, R. S. Porter, and J. F. Johnson, *J. Phys. Chem.*, **71**, 1224 (1967).
(33) J. N. Sherwood, *Mol. Cryst. Liquid Cryst.*, **9**, 37 (1969).
(34) C. Weygand and R. Gabier, *J. Prakt. Chem.* (*Frankfurt am Main*), **155**, 332 (1940).
(35) D. Hoel and R. H. Johnsen, *J. Phys. Chem*, submitted for publication.
(36) A. V. Chadwick and J. N. Sherwood in "Diffusion Processes", J. N. Sherwood, A. V. Chadwick, W. Muir, and F. L. Swinton, Ed., Gordon and Breach Co., New York, N.Y., 1971, p 475.
(37) A. R. McGhie and J. N. Sherwood, *J. Chem. Soc.*, *Faraday Trans. 1*, **63** (3), 533 (1972).

Sublimation of Bis(η^8-1,3,5,7-cyclooctatetraene)uranium

R. G. Bedford

Lawrence Livermore Laboratory, University of California, Livermore, California 94550 *(Received February 24, 1977)*

Publication costs assisted by the Lawrence Livermore Laboratory

The sublimation of uranocene, $U(C_8H_8)_2$, has been investigated in the temperature range from 400 to 540 K by Knudsen effusion in a vacuum thermobalance and with a mass spectrometer. Results show that $U(C_8H_8)_2$ sublimes to monomeric gaseous molecules and also dissociates to $UC_8H_8(g) + C_8H_8(g)$. The following equations and thermochemical functions were derived for sublimation and dissociation. For $U(C_8H_8)_2(s) = U(C_8H_8)_2(g)$: $\ln P(\mathrm{Pa}) = -(13006 \pm 400)/T + (26.71 \pm 1.1)$, $\Delta H = 108.1 \pm 3.3$ kJ mol^{-1}, $\Delta S = 126.2 \pm 9.1$ J K^{-1} mol^{-1}, and for $U(C_8H_8)_2(g) = UC_8H_8(g) + C_8H_8(g)$: $\ln K(\mathrm{Pa}) = -(22840 \pm 3200)/T + (44.27 \pm 7)$, $\Delta H = 190 \pm 27$ kJ mol^{-1}, $\Delta S = 272 \pm 58$ J K^{-1} mol^{-1}. Dissociation to $U(s) + 2C_8H_8(g)$ is not important at the temperatures of this study. Appearance potentials of $UC_8H_8^+$ and $U(C_8H_8)_2^+$ ions were found to be 14.1 ± 0.5 and 8.7 ± 0.5 eV.

Introduction

There is current interest in volatile uranium compounds for their potential use, directly and indirectly, in isotope separation and other processing of uranium for use as reactor fuel. The synthesis of uranocene, $U(C_8H_8)_2$, has been reported recently with discussions of its structure, bonding, and many of its properties.[1-10] It was reported to have a relatively high vapor pressure and was purified by vacuum sublimation at moderate temperatures.[1,2,8]

An important property of any substance from both a theoretical and practical point of view is its vapor pressure, which has only been estimated for uranocene.[1,2] We studied the sublimation of uranocene by the Knudsen effusion method with a mass spectrometer as well as in a vacuum thermobalance to establish the mechanism of vaporization and to determine the vapor pressure as a function of temperature.

Previous workers believed that $U(C_8H_8)_2$ sublimes congruently without decomposition.[1,2,8,9] We found that at temperatures below 500 K uranocene sublimes primarily to monomeric gaseous $U(C_8H_8)_2$, but mass spectrometric evidence showed that dissociation also occurs. $UC_8H_8(g)$ becomes a more important vapor species as temperature increases. Our results also showed that dissociation to U(s) + $2(C_8H_8(g)$ is not important at temperatures below 540 K, in agreement with previous observations.

Experimental Section

Material. Uranocene was obtained from two sources. Dr. R. N. Zare, Columbia University, supplied the material used for mass effusion experiments and Dr. A. Streitweiser, Jr., and C. B. Grant, University of California, Berkeley, supplied the material used for the mass spectrometric study. Both samples were synthesized and purified by procedures described by Streitweiser et al.[1] and shipped under vacuum or inert gas in sealed containers. They were stored under high purity argon in an inert atmosphère glove box. Knudsen cells were loaded, weighed, and sealed in transfer jars in the box. About 0.5 g was used for mass effusion, and 0.1 g for mass spectrometry. Plastic glove bags were taped around the thermogravimetric vacuum furnace and mass spectrometer and were flushed with high purity nitrogen to minimize exposure of samples to air while loading. These precautions are necessary because of the sensitivity of uranocene to oxidation in air.[1]

Both in the mass spectrometric and mass effusion experiments, a large amount of material volatilized when samples were first heated. This was identified as cyclooctatetraene in the mass spectrometer and results from unavoidable oxidation of the samples. In both experiments, samples were sublimed until no volatile material remained. The residues, approximately 7 to 10% of the original samples, in the cells, were identified as UO_2 by x-ray powder diffraction analysis. Green condensate, identical in appearance with unoxidized uranocene, was found on cool parts surrounding the furnace of each apparatus after the experiments. This rapidly decomposed when exposed to air, evolving a strong odor of cyclooctatetraene.

Apparatus and Methods. Mass Spectrometer. The mass spectrometer used for these measurements was a 60° magnetic sector instrument with a radius of 30 cm. It was equipped with a Nier-type electron impact ion source and a Knudsen cell molecular beam source arranged so the molecular beam, electron beam, and ion beam were mutually orthogonal.

The measurements reported here were made with an ion accelerating potential of 14.5 kV. Most spectra were taken with an electron impact energy of 35 eV and bombarding currents of 4 to 25 μA. Ion intensities under these conditions were directly proportional to bombarding current. Slits were set to give trapezoidal peaks with sufficient resolution to separate masses at m/e about 500 amu with a 10% valley.

The Knudsen cell was heated by radiation from a tungsten mesh resistance element surrounded by radiation shields. Temperature was controlled by a power controller and measured with a Pt–Pt/10%Rh thermocouple on the bottom of the cell. Temperature was controlled to ±1 K but rarely changed more than 0.2 to 0.3 K during a run. The temperature of the run was taken as the average of several measurements made during the run. The overall accuracy was ±0.4 K with a possible relative error of ±0.2 K between 400 and 500 K.

A stainless steel cell with an orifice, 0.50 mm in diameter, 2 mm long, was used. It was placed in a heavy walled aluminum oxide holder on a tungsten pedestal.

The furnace chamber was separated from the ion source manifold by a water-cooled shield with a 6-mm diameter hole for the molecular beam. A shutter with 0.2- and 0.7-mm slits could be moved across the opening to examine beam profiles or to stop the beam for background measurements. Data were taken with the 0.7-mm slit in the position giving maximum intensity for material effusing from the cell.

Ion pumps maintained vacuums of about 10^{-6} Pa (10^{-8} Torr) in the furnace and source chambers, and about 10^{-7} Pa (10^{-9} Torr) in the analyzer tube and detector chamber.

Ion intensities were measured by counting amplified pulses from a 14-dynode electron multiplier used as a particle counter. Magnet field and data accumulation were controlled via a minicomputer. For these experiments the field was swept from low mass to high, and then reset to low for the next sweep. Sweeps could be divided into a number of segments, stepping between field settings with only enough delay at the beginning of each segment to permit a linear field sweep.

Initial mass, mass range, sweep rate, counting time per channel, and delay were selected for each segment by the operator. Spectra were accumulated in the computer memory and could then be displayed on an oscilloscope and processed. Data could be accumulated for any number of sweeps, allowing the operator to pick optimum data acquisition time. This multichannel analysis technique minimized effects of low frequency noise, such as sample temperature drift, on intensity ratios.

The m/e for each peak was determined from the magnet field at the center of the peak (found from the computer address). When the mass scale was normalized by calculating the radius for low masses, using residual gas in the spectrometer, the uncertainty was about ±3 amu at mass 500. After higher masses were identified a mass scale accurate to ±0.3 amu up to mass 500 was obtained by applying a radius correction that was proportional to the magnet field.

Net intensity was the average counting rate over the flat part of the peak corrected for coincidence and background. Background was measured under identical conditions with the shutter closed. Backgrounds for m/e 342 ($UC_8H_8^+$) and m/e 446 ($U(C_8H_8)_2^+$) were never more than a few tenths of a percent of measured intensities.

For example, measurements of intensity vs. temperature were taken with a sweep that accumulated data for m/e = 339 to 343 and 442 to 447. The sweep scanned 2 G per channel at 20 G/s; it covered each segment in about 5 s with delays of 4 s before the first, and 2 s before the second part. Data were accumulated for 5 to 500 sweeps, depending on ion intensities.

Ionization efficiency data were taken by controlling the magnet at the field corresponding to peak maximum and measuring intensities at various electron impact energies. The sample temperature was 430 K. The electron energy scale was normalized by measuring an ionization efficiency curve for argon.

Thermobalance. Mass effusion rates were measured from a pyrex[11] cell suspended in the center of a tungsten resistance furnace from an Ainsworth automatically recording semimicrobalance. The balance-vacuum system has been described before.[12]

The system was adapted for work at lower temperatures by replacing the pyrometer window under the furnance with a flange having two sheathed type-K thermocouples to measure and control the temperature just beneath the cell. Thermocouples were calibrated against a standard certified by the National Bureau of Standards to the International Practical Temperature Scale of 1968. Furnace temperature was controlled to ±0.4 K and measured to ±0.1. Temperatures were taken as averages of values recorded during a run. Sample temperatures were obtained from a calibration curve relating cell temperature to furnace temperature found by comparing readings of a thermocouple in a cell to those under the cell. The accuracy of corrected sample temperatures was ±0.6 K with a possible relative error from 450 to 550 K of ±0.3. The major contribution to these uncertainties was that in calibration of sample temperature vs. furnace temperature

TABLE I: Mass Spectrum of Uranocene Vapor in Equilibrium with $U(C_8H_8)_2(s)$ at 470 K[a]

Mass-to-charge ratio (m/e)	Ion	Type[b]	Rel int for an ionizing energy = 35 eV
104	C_8H_8	P(3) + f(1) + f(2)	~100
105	C_8H_8	i	~10
223	$U(C_8H_8)_2$	d	*c*
238	U		0.8
264	UC_2H_2		2
303	UC_5H_5		5
304	UC_5H_5	i	0.3
314	UC_6H_4		10
315	$UC_6H_4 + UC_6H_5$	i + f	1.3
316	UC_6H_6		18
317	UC_6H_6	i	1.1
340	UC_8H_6		17
341	$UC_8H_6 + UC_8H_7$	i + f	2.5
342	UC_8H_8	P(1) + f(2)	100
343	UC_8H_8	i	8.8
344	UC_8H_8	i	0.4
368	$U(C_8H_8)(C_2H_2)$		*c*
446	$U(C_8H_8)_2$	P(2)	94
447	$U(C_8H_8)_2$	i	14
448	$U(C_8H_8)_2$	i	1.2

[a] Vapor composition is ~60% $U(C_8H_8)_2$ and ~20% each $U(C_8H_8)$ and C_8H_8. Ions other than U^+ are not listed unless intensity exceeded 2% of the major peak. [b] p = parent peak, i = isotope peak, f = fragment, d = doubly charged ion. (1) designates $U(C_8H_8)$, (2) designates $U(C_8H_8)_2$, and (3) designates C_8H_8. [c] Intensities relative to the rest of the spectrum were not measured for the m/e ranges 107-229 and 359-425.

because of a temperature gradient in the furnace and cell. Sample temperature was thus a sensitive function of position, which could not be accurately reproduced.

The pyrex cell was made from a weighing bottle 3 cm high by 2 cm in diameter; the cover was hand-lapped to the lower part and the top ground flat. A cylindrical orifice was bored with a diamond drill. Effective orifice area was determined from geometrical measurements and by measuring the effusion rate of anthracene.[13] The effective area calculated from geometry was 0.056 ± 0.004 mm^2 and from anthracene calibration was 0.061 ± 0.004 mm^2. (Unless stated otherwise the interval of uncertainty of a value represents its precision and will be twice the standard deviation.)

Data were rejected until results at a given temperature could be reproduced after runs at higher temperatures. About 15% of the sample effused before this condition was reached. From that time until about 90% of the material had vaporized, rates of weight loss at constant temperature were constant and could be reproduced after runs at other temperatures. Cell weights could be measured to ±50 μg. Precision of weight loss rates ranged from ±0.1 to ±3.5%, depending on the time the data were recorded after steady state was reached and on the recorder chart speed.

Measured weight loss rates were corrected for contributions from UC_8H_8 and C_8H_8 by using mass spectrometric data to determine vapor composition as a function of temperature.

Results and Discussion

Mass Spectrometric Results. A mass spectrum for uranocene vapor at 470 K is shown in Table I. The prominent peaks correspond to those reported by Streitweiser.[2,9] There is a large uncertainty in relative intensities because the entire spectrum was not scanned at one time. The data had to be assembled from a number of short scans taken at different times and normalized to a common set of conditions. The spectrum below m/e 105 amu corresponded to that reported for cyclooctatetraene.[14] We believe these low-mass peaks come partly from fragmentation of organometallic precursors and partly from $C_8H_8(g)$.

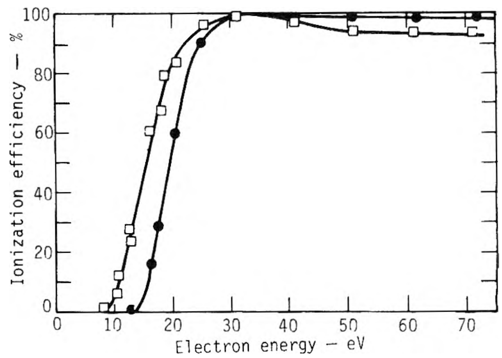

Figure 1. Relative ionization efficiency vs. electron energy for $U(C_8H_8)_2^+$ (□) and $UC_8H_8^+$ (●).

When the sample was first heated, intense cyclooctatetraene spectra were observed at temperatures too low to vaporize $U(C_8H_8)_2$. However even after the initial low temperature evolution of C_8H_8 had subsided, shutter profiles of peaks at m/e 104 and below taken at about 490 K were broader than those of heavier ions; these peaks were not completely eliminated by closing the shutter. This is characteristic of spectra from noncondensible vapors and shows that C_8H_8 is a major precursor of these peaks; they do not come entirely from fragmentation of $U(C_8H_8)_2$. Shutter-open, shutter-closed, and net spectra in the mass range 70 to 105 all corresponded to cyclooctatetraene. This suggests that some dissociation of $U(C_8H_8)_2$ occurs at temperatures above 490 K.

It is not practical to relate partial pressures of noncondensible to condensible species through their relative ion intensities because of differences in geometrical factors. Therefore, the lower mass region was not routinely scanned.

Ionization efficiency curves for $U(C_8H_8)_2^+$ and $UC_8H_8^+$ are shown in Figure 1. Appearance potentials for these ions are 8.7 ± 0.5 and 14.1 ± 0.5 eV. Error limits are estimates of accuracy and are determined primarily by uncertainties in extrapolating ionization efficiency curves to zero intensity.

Pressure is related to ion intensity by

$$P = \frac{k}{\sigma} T \Sigma I^+ = \frac{k}{\sigma} C_i I_i^+ T \qquad (1)$$

where k is an instrumental constant incorporating the gas constant, geometrical factors of cell orifice, molecular beam and ion source, ion extraction efficiency, ion transmission, and detector efficiency; σ is the total ionization cross section for the neutral species; T is the absolute temperature; $\sum I^+$ is the total ion yield from the neutral species; C_i is the ratio of total ion production to production from neutral species at mass i; and I_i^+ is the ion intensity at m/e i corrected for contributions from other precursors. C includes both isotope ratio and fragmentation effects. This assumes all contributions to sensitivity factor, k, are independent of mass, chemical effects, and temperature. The pressure ratio between two species is

$$\frac{P_1}{P_2} = \frac{\sigma_2 \Sigma I_1^+}{\sigma_1 \Sigma I_2^+} = \frac{\sigma_2 C_{1,a} I_a^+}{\sigma_1 C_{2,b} I_b^+} \qquad (2)$$

where $C_{1,a}$ is the ratio of total ion production from neutral species 1 to ion production from 1 at mass a, and so forth.

TABLE II: Summary of Intensity vs. Temperature Results of Mass Spectrometric Measurements

		$U(C_8H_8)_2^+$, m/e = 446		$UC_8H_8^+$, m/e = 342	
Run[a]	Temp, K	Intensity	Precision[b] 2σ in %	Intensity	Precision[b] 2σ in %
272-858	403.1	29.8	3.6	28.7	3.7
246-1641	409.7	56.6	3.7	49.9	4.0
248-1442	414.3	67.1	3.4	62.3	3.6
247-1115	418.4	109.8	4.2	101.7	4.4
248-1314	423.0	136.1	3.8	127.7	4.0
247-1317	438.7	441.2	2.1	397.1	2.2
269-1702	446.6	671.5	1.5	656.6	1.6
248-1120	453.7	1069.1	2.0	1115.2	2.0
247-1409	463.8	2036.1	1.4	2151.6	1.4
247-1429	466.4	2501.8	1.2	2670.0	1.2
272-1315	477.1	3705.2	1.0	4265.7	1.0
272-1134	478.3	4215.4	1.4	4933.5	1.3
272-1157	490.4	7633.0	0.7	9100.4	0.6
269-1546	501.1	12015	0.8	14108	0.7
272-1423[c]	510.5	(3820)	1.4	(5960)	1.2
272-1443[c]	512.2	(5637)	2.0	(7028)	1.7

[a] Runs are numbered in chronological order. [b] Precision determined by counting statistics alone. [c] Sample depleted during last runs but ratios are useful.

Intensities for m/e 446 amu vs. temperature are listed in Table II. Data from 403 to 501 are represented by the equation

$$\ln (I^+_{446}T) = -(12874 \pm 306)/T + (41.43 \pm 0.6)$$

The equation for $U(C_8H_8)_2$ pressure is

$$\ln P_2 = -(12874 \pm 750)/T + (41.43 \pm 0.7) + \ln \frac{C_{2,446}}{\sigma_2} + \ln k \tag{3}$$

where the error limits represent overall uncertainties, including systematic errors in temperature measurement and estimated contribution from temperature-dependent sensitivity. Subscripts 1 and 2 refer to UC_8H_8 and $U(C_8H_8)_2$, respectively, here and in the following expressions. We will use $U(C_8H_8)_2$ pressures derived from mass effusion measurements to evaluate the instrumental sensitivity factor.

Intensities for m/e 342 amu are listed in column 5 of Table II and intensity ratios of 342 to 446 peaks are shown in Figure 2. Ratio data extend to higher temperatures than absolute intensities because during the run at 510 K the amount of sample remaining in the cell began to deplete. Absolute intensities for the last runs were too low because there was insufficient sample surface to maintain saturation pressures in the cell, but intensity ratios should be close to correct values.

The temperature trend in 342–446 intensity ratios above 440 K indicates that the 342 peak has a precursor other than $U(C_8H_8)_2$. Part of the 342 peak results from fragmentation of $U(C_8H_8)_2$ and presumably part comes from ionization of UC_8H_8(g). Uranocene sublimes to monomeric molecules and also dissociates to UC_8H_8(g) + C_8H_8(g). This is consistent with the observation of cyclooctatetrene gas as one of the vapor species described above.

Data in Figure 2 were fit by least squares to the equation

$$\ln \frac{I^+_{1,342}}{I^+_{2,446}} = \ln \frac{I(342)}{I(446)} - (0.83 \pm 0.1) = -(4983 \pm 1500)/T + 9.17 \pm 3 \tag{4}$$

where $I^+_{1,342}$ is the intensity of m/e 342 amu from ionization of UC_8H_8 and $I(342)$ is the total ion intensity of 342 corrected for coincidence and background. Background corrections were very small, being negligible except for the lowest intensities. From this data the best estimate of the contribution to the 342 peak from fragmentation of $U(C_8H_8)_2$ was 83 ± 10% of the 446 peak. Equation 4 is shown as the solid line in Figure 2.

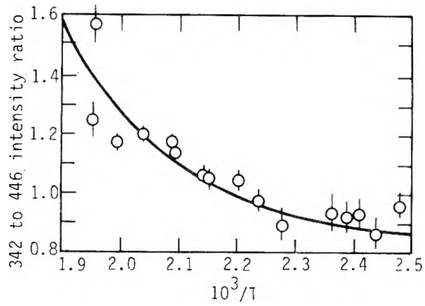

Figure 2. Ion intensity ratio vs. reciprocal temperature for $UC_8H_8^+$ to $U(C_8H_8)_2^+$. Bars represent 2 standard deviations. Equation 4 is shown as a solid line.

The relative total ionization cross sections of UC_8H_8 and $U(C_8H_8)_2$, σ_1/σ_2, was estimated to be 0.636 ± 0.3 from atomic cross sections of Mann, assuming additivity.[15] Ratios of total ion production from UC_8H_8 to net production at 342 amu and total ions from $U(C_8H_8)_2$ to net at 446 amu were estimated from our mass spectral data, assuming only a small fraction of the peaks lighter than 105 amu came from fragmentation of the organometallic molecules and that contributions to fragments lighter than 344 amu from $U(C_8H_8)_2$ and UC_8H_8 were in the same proportion as the 342 peak. Although uncertainties in $C_{1,342}$ and $C_{2,446}$ are about ±20%, many of the possible errors contribute in a similar way to both factors and thus the uncertainty interval for the ratio is only about ±10%. We found $C_{1,342}$ = 1.8 and $C_{2,446}$ = 2.7.

$$C_{1,342}/C_{2,446} = 0.67 \pm 0.07$$

With the above values for ionization cross section and ion production ratios, we find by eq 2 that

$$P_1/P_2 = (1.05 \pm 0.3)I^+_{1,342}/I^+_{2,446} \tag{5}$$

This was used with eq 4 to calculate weight fractions of $U(C_8H_8)_2$ in the vapor when the mass effusion data was treated.

Dissociation of $U(C_8H_8)_2$(s) to U(s) + $2C_8H_8$(g) is negligible under conditions of this study. This was shown by the absence of U(s) in residues after complete sublimation of $U(C_8H_8)_2$ samples found in this study and by earlier workers.[1,8] Since the only source of C_8H_8 is dissociative sublimation

$$U(C_8H_8)_2(s) = UC_8H_8(g) + C_8H_8(g)$$

the number of moles of C_8H_8 effused from the cell must equal the number of moles of UC_8H_8 effused. The range of stoichiometry of $U(C_8H_8)_2$ is very narrow, and we can assume the condensed phase remains at this congruently subliming composition at all temperatures. At each temperature steady state is established for which

$$P_A/P_B = \frac{Z_A}{Z_B}\left(\frac{M_A}{M_B}\right)^{1/2}$$

where Z is the effusion rate in moles per second, and M is the molecular weight. For equal effusion rates of C_8H_8 and UC_8H_8

$$P(C_8H_8)/P(UC_8H_8) = 0.552$$

TABLE III: Summary of Mass Effusion Results[a]

Run[b]	Temp, K	Rate of wt loss, μg/s	Precision[c] 2σ in %	Wt fraction of $U(C_8H_8)_2$	$P(U(C_8H_8)_2)$, Pa
129-1703	445.1	0.0222	3.5	0.864	0.0717
130-1450	461.5	0.0855	1.8	0.810	0.263
131-0030	461.5	0.0688	2.2	0.810	0.212
133-1800	463.2	0.0695	1.5	0.803	0.213
132-0010	475.4	0.1748	1.0	0.756	0.510
129-1200	484.7	0.386	1.8	0.717	1.080
135-1200	485.9	0.295	1.3	0.712	0.820
132-1700	490.1	0.371	0.9	0.694	1.008
132-2130	490.2	0.396	0.5	0.693	1.077
133-1500	492.4	0.479	2.1	0.683	1.286
132-1000	494.5	0.558	1.0	0.674	1.480
133-1300	502.3	0.873	1.8	0.639	2.213
132-1500	506.5	1.145	0.8	0.620	2.826
134-1200	509.1	1.370	1.4	0.608	3.327
134-1900	514.4	1.664	0.1	0.583	3.899
133-1000	517.4	2.089	0.4	0.570	4.793
132-1330	517.7	2.283	0.7	0.568	5.226
134-1000	524.2	3.169	0.4	0.539	6.922
134-1400	528.2	4.052	0.2	0.521	8.590
134-1700	536.7	6.878	0.3	0.484	13.64

[a] Effective orifice area = 0.0611 ± 0.004 mm². [b] Runs are numbered in chronological order. [c] Precision determined by weight loss and time measurement.

The equilibrium constant for dissociation of $U(C_8H_8)_2$ can now be expressed in terms of equations for $U(C_8H_8)_2^+$ ion intensity and $UC_8H_8^+$ to $U(C_8H_8)_2^+$ intensity ratios.

$$K = \frac{P(C_8H_8)P(UC_8H_8)}{P[U(C_8H_8)_2]} = 0.552(P_1/P_2)^2P_2 \qquad (6)$$

Combining eq 3 through 6, we obtain

$$\ln K = -(22840 \pm 3200)/T + (59.27 \pm 7) + \ln \frac{C_{2,446}}{\sigma_2} + \ln k \qquad (7)$$

Knudsen Effusion Results. The mass effusion results are listed in Table III. Data were fit by the equation

$$\ln [(\mathrm{d}W/\mathrm{d}t)T^{1/2}] = -(14940 \pm 470)/T + (25.86 \pm 0.94) \qquad (8)$$

where $\mathrm{d}W/\mathrm{d}t$ is the total rate of mass loss in mg/s. The temperature dependence of uncorrected mass effusion results is greater than that of mass spectrometric results for $U(C_8H_8)_2^+$ ions (eq 3). This is consistent with the existence of an additional process besides simple sublimation that has a larger enthalpy, such as dissociative sublimation. The discrepancy between the temperature dependencies exceeds the combined uncertainties associated with the measurements with 99% confidence. Also, the residual gas pressure in the thermobalance vacuum system was unusually high for runs at higher temperatures. This might have resulted from cyclooctatetraene produced by partial dissociation of the sample.

The weight fraction of $U(C_8H_8)_2$ in the effusing vapor can be calculated from vapor composition derived from mass spectrometric data.

$$W_2 = \frac{P_2M^{1/2}}{P_2M_2^{1/2} + P_1M_1^{1/2} + P(C_8H_8)M^{1/2}(C_8H_8)}$$

When molecular weights, the C_8H_8 to UC_8H_8 pressure ratio, and the UC_8H_8 to $U(C_8H_8)_2$ pressure ratio from eq 4 and 5 are inserted

$$W_2 = 1/[1 + \exp(-4983/T + 9.35)]$$

This equation is used to calculate weight fractions of $U(C_8H_8)_2$ in the vapor, listed in column 4, Table III.

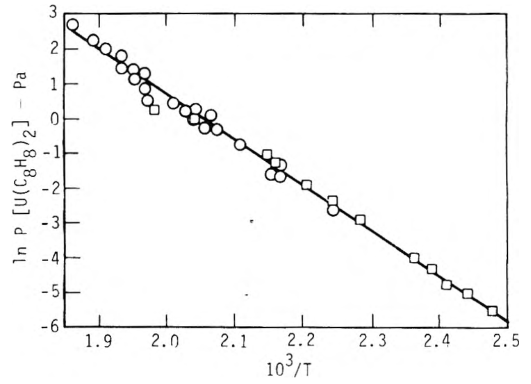

Figure 3. Vapor pressures of $U(C_8H_8)_2$ calculated from Knudsen mass effusion data (○) and from mass spectrometric data (□). Line is least-squares fit.

The equation for $U(C_8H_8)_2$ pressure vs. temperature derived from corrected mass effusion results is

$$\ln P_2(\mathrm{Pa}) = -(13410 \pm 417)/T + (27.52 \pm 0.84)$$

The equation with overall uncertainties including possible systematic temperature errors and uncertainties in vapor composition is

$$\ln P_2(\mathrm{Pa}) = -(13410 \pm 900)/T + (27.52 \pm 1) \qquad (9)$$

The coefficient of $1/T$ in eq 3 from the mass spectrometric results agrees much better with the coefficient of $1/T$ in eq 9 than that in eq 8. These coefficients in eq 3 and 8 would agree if sublimation to $U(C_8H_8)_2$ gas molecules were the only important reaction. The discrepancy in temperature dependence between eq 3 and 9 is within the combined uncertainties.

Combined Results. Since the coefficients of $1/T$ in eq 3 and 9 do not agree exactly, we chose to normalize the mass spectrometric data to the pressure data at 490 K, a mid-range temperature of the mass effusion data and within the mass spectrometric data range. This gives $(\ln (C_{2,446}/\sigma_2) + \ln k) = -15.0 \pm 1.3$.

Corrected mass effusion pressures and pressures calculated from $U(C_8H_8)_2^+$ ion intensities, using the sensitivity factor above, are shown in Figure 3, plotted as $\ln P(\mathrm{Pa})$ vs. $10^3/T$. The line is the least-squares fit for all data equally weighted:

$$\ln P_2(\mathrm{Pa}) = -(13006 \pm 205)/T + (26.71 \pm 0.4)$$

The equation for $U(C_8H_8)_2$ vapor pressure with overall uncertainties is

$$\ln P_2(\mathrm{Pa}) = -(13006 \pm 400)/T + (26.71 \pm 1.1) \quad (10)$$

Substituting for the ionization cross section, ion production, and sensitivity terms in eq 7 gives the equation for the equilibrium constant for $U(C_8H_8)_2$ dissociation.

$$\ln K(\mathrm{Pa}) = -(22840 \pm 3200)/T + (44.27 \pm 7) \quad (11)$$

The enthalpy and entropy of sublimation derived from eq 10 are $\Delta H = 108.1 \pm 3.3$ kJ mol^{-1} and $\Delta S = 126.2 \pm 9.1$ J K^{-1} mol^{-1}. The entropy of sublimation is to the vapor standard state of 1 atm fugacity.

The enthalphy and entropy of dissociation of $U(C_8H_8)_2(g)$ from eq 11 are $\Delta H = 190 \pm 27$ kJ mol^{-1} and $\Delta S = 272 \pm 58$ J K^{-1} mol^{-1}.

Since entropies or free energy functions for the species in this system are not available, calculations of "third law" enthalpies have not been attempted.

Conclusions

Previous workers have reported observations that are in apparent contradiction with our findings of the partial dissociation of $U(C_8H_8)_2$ and evidence for the existence of $UC_8H_8(g)$. Streitweiser et al. recovered only about 35% of material sublimed at about 150 °C, but obtained nearly quantitative yields with flash vacuum sublimation at 210 °C.[1] We would predict vapor compositions of about 90% $U(C_8H_8)_2$ at 150 °C and about 70% at 210 °C and expect the yield to decrease with increasing distillation temperature. Of course, conditions affecting recombination between UC_8H_8 and C_8H_8 are also important to recovery and may have been different for the two procedures.

Vapor pressures measured here are somewhat lower than estimates made by Streitweiser, et al. of 4 Pa (0.03 Torr) at 180 °C and 0.1 Pa (10^{-3} Torr) at 150 °C.[1,2] We found 0.15 Pa at 180 °C and 0.019 at 150 °C. However, this is not in bad agreement when one considers the difficulties of estimating pressures and sample temperatures under Streitweiser's conditions.

We found the following evidence for dissociation of $U(C_8H_8)_2$ on sublimation and the existence of $UC_8H_8(g)$ molecules: (1) presence of cyclooctatetraene in the vapor of subliming $U(C_8H_8)_2$; (2) greater temperature dependence for $UC_8H_8^+$ ion intensity than for $U(C_8H_8)_2^+$; (3) reconciliation of mass spectrometric data for $U(C_8H_8)_2^+$ with mass effusion by assuming dissociation to $UC_8H_8 + C_8H_8$.

An upper limit for the binding energy of the molecular ion, $(UC_8H_8^+ - C_8H_8)$, can be obtained from the difference between the appearance potential for $UC_8H_8^+$ and the ionization potential of $U(C_8H_8)_2$. Our data gave $D_0^\circ(UC_8H_8^+ - C_8H_8) < 5.2$ eV (502 kJ mol^{-1}). This seems to be very high compared to our values of 190 kJ mol^{-1} for the enthalpy of dissociation of $UC_8H_8 - C_8H_8$. The ionization efficiency measurements were made at 480 K where about 90% of the $UC_8H_8^+$ ions came from fragmentation of $U(C_8H_8)_2$ at energies above 30 eV, so ionization of UC_8H_8 would not cause an overestimate of the threshold for fragmentation. The excess energy is too high to be accounted for by excitation and translational energy of simple fragments, so most of the fragmentation reactions probably involve dissociation of the C_8H_8 into smaller pieces.

Acknowledgment. This work was performed under the auspices of the U.S. Energy Research and Development Administration, under Contract No. W-7405-Eng-48.

References and Notes

(1) A. Streitweiser, Jr., U. Müller-Westerhoff, G. Sonnichsen, F. Mares, D. G. Morrell, K. O. Hodgson, and C. A. Harmon, *J. Am. Chem. Soc.*, **95**, 8644 (1973).
(2) A. Streitweiser, Jr., and U. Müller-Westerhoff, *J. Am. Chem. Soc.*, **90**, 7364 (1968).
(3) A. Zalkin and K N. Raymond, *J. Am. Chem. Soc.*, **91**, 5667 (1969).
(4) N. Edelstein, G. N. LaMar, F. Mares, and A. Streitweiser, Jr., *Chem. Phys. Lett.*, **8**, 399 (1971).
(5) A. Streitweiser, Sr., D. Dempf, G. N. LaMar, D. G. Karraker, and N. Edelstein, *J. Am. Chem. Soc.*, **93**, 7343 (1971).
(6) D. G. Karraker, S. A. Stone, E. R. Jones, Jr., and N. Edelstein, *J. Am. Chem. Soc.*, **92**, 4841 (1970).
(7) R. G. Hayes and T. L. Thomas, *Organometal. Chem. Rev. A*, **7**, 1 (1971).
(8) D. F. Starks and A. Streitweiser, Jr., *J. Am. Chem. Soc.*, **95**, 3423 (1973).
(9) A. Streitweiser, Jr., and C. A. Harmon, *Inorg. Chem.*, **12**, 1102 (1973).
(10) R. G. Hayes and N. Edelstein, *J. Am. Chem. Soc.*, **94**, 8688 (1972).
(11) Reference to a company or product name does not imply approval or recommendation of the product by the University of California or the U.S. Energy Research and Development Administration to the exclusion of others that may be suitable.
(12) C. L. Hoenig, *J. Am. Ceram. Soc.*, **54**, 391 (1971).
(13) R. S. Bradley and T. G. Cleasby, *J. Chem. Soc.*, 1690 (1953).
(14) American Petroleum Institute Research Project **44**, "Selected Mass Spectral Data", Vol. 2, Serial No. 690 (1951), Thermodynamics Research Center, Texas Engineering Experimental Station, Texas A & M University, College Station, Tex. 1975.
(15) J. B. Mann, *J. Chem. Phys.*, **46**, 1646 (1967).

Partial Specific Volumes in Highly Concentrated Protein Solutions. 2. Mixtures of Water, Bovine Hemoglobin, and Sodium Chloride

J. Bernhardt* and **H. Pauly**

Institut für Physikalische und Medizinische Strahlenkunde der Universität Erlangen-Nürnberg, 8520 Erlangen, West Germany

(Received November 12, 1976)

Measurements of the specific volume v of water–bovine oxyhemoglobin (Hb)–sodium chloride mixtures at 25 °C were carried out using a digital densimeter with an instrumental precision of about 2×10^{-6} g cm^{-3}. Hb mass fractions extended to high values of 0.45 g of Hb/g of mixture. The mass ratio of NaCl to Hb was kept constant in each of three series of measurements, varying only the mass fraction of water. In the three series of measurements the molality of NaCl was 75, 100, and 200 mmol kg^{-1} in a mixture with 350 g of Hb per kilogram of mixture. The data for v vs. the mass fraction w for the solid component (Hb + NaCl) were approximated by a power series. In salt-free pure Hb solutions with Hb mass fractions $w > 0.2$ the partial specific volume of Hb was not anymore independent of w. Protein–protein interaction becomes visible. We found for Hb at 25 °C a partial specific volume at infinitive dilution of 0.75305 cm^3 g^{-1} with an uncertainty of 5×10^{-5} cm^3 g^{-1}. For bovine methemoglobin a value of 0.7541 cm^3 g^{-1} was found. In the linear range of the function $v(w)$, the partial specific volume of the solid component (Hb + NaCl) was found to be larger by about 1‰, than the value calculated from binary H_2O–Hb and H_2O–NaCl mixtures. The difference can be explained by assuming binding of chloride ions to Hb.

I. Introduction

In a previous paper[1] we had described measurements of the specific volume of highly concentrated and salt-free solutions of bovine serum albumin and bovine hemoglobin. The mass fraction of the protein extended to about 0.4 g of protein per gram of mixture. In the high concentration range the partial specific volumes of the protein and therefore of the water were not anymore independent of the protein mass fraction probably due to interaction of the hydrated protein molecules.

In order to understand better the physicochemical state of water in the living cell we used then, as the next step, water–protein mixtures with different contents of salt and measured the specific volume of these mixtures. We restricted ourselves to measurements of the specific volume of hemoglobin solutions with sodium chloride. As we concentrate our interest on the partial specific volume of water in these ternary mixtures, we used constant ratios between sodium chloride and hemoglobin varying only the water contents of the mixture. The results show that the specific volume of hemoglobin–salt mixtures cannot be explained quantitatively by superposition of the volume properties of pure salt and pure protein mixtures, although the v vs. w plot exhibits the characteristic features of pure NaCl solution and pure Hb solution.

II. Experimental Section

Hemoglobin. The preparation of bovine hemoglobin (Hb) was described in detail in the previous paper.[1] For the calculation of the protein molality a molecular weight of 64500 was used.[2] The purity of the Hb preparation was investigated by a gel chromatography (using Sephadex G 100 and G 150). The result of measuring the optical density at a wavelength of 280 nm vs. the different fractions was a single peak without other peaks indicating the absence of other proteins. The relation of the optical density at wavelengths 415 and 280 nm was constant in the Hb peak and characteristic for oxyhemoglobin. A quantitative estimation showed that the weight fraction of foreign proteins was certainly less than 1% and probably less than 0.4%. The H_2O–Hb–NaCl mixtures were prepared by adding step by step small amounts of a defined mass of salt to the Hb solutions. Before this the hemoglobin content was determined by measuring the dry mass fraction. The pH was between 7.10 and 7.28 (uncertainty ±0.05 units), depending on salt and protein concentrations.

Bovine methemoglobin (Mb) was prepared by oxidizing Hb into Mb, using $K_3[Fe(CN)_6]$ and deionizing the Mb solution.[3]

Sodium Chloride. The salt used was NaCl Suprapur of Merck and dried at 150 °C. All the solutions were made by weight (corrected to vacuum), using water which had been deionized and doubly distilled. This water was also used in order to calibrate the densimeter. Prior to making up the solutions, the water was degassed, then the salt solutions were degassed once more and finally the water contents were determined by weight. We found out that this was the best way in order to minimize errors caused by evaporation and by dissolved gases.

Measurements of the Specific Volumes. The determination of the specific volume by the undamped proper frequency of an oscillating glass tube, the essential part in the digital densimeter DMA 02 C of Heraeus/Paar, developed by Kratky et al.,[4] presupposes that losses due to elastic and viscous properties of the sample solution do not influence the proper frequency even with very viscous solutions. Appendix 1 (supplementary material, see paragraph at end of text regarding supplementary material) shows that this is the case within the experimental uncertainties of the measurements. The experimental procedures for the density determination were described in the previous paper.[1] The samples were kept at a temperature of 25.00 ± 0.01 °C. The densimeter was calibrated with deionized and doubly quartz distilled water, using for the specific volume the value 1.002964 cm^3 g^{-1} at 25 °C.[5]

The experimental uncertainties in the values of the specific volumes were caused practically exclusively by the uncertainties in the dry mass fractions [see Appendix 2, eq 16 and Figure 8 (supplementary material)]. In this way we obtained values for the uncertainties, σ_i, ranging from about 5×10^{-6} cm^3 g^{-1} for dilute solutions up to about 1×10^{-4} cm^3 g^{-1} for the highest protein concentrations used.

Dry Mass Determination. The procedures in determining the dry mass fraction were described in the previous paper.[1] Two modifications were made in order to improve the accuracy in determining the dry masses. First, the special glove box which contained vessels with phosphorus pentoxide (P_2O_5) and the weighing assembly of the Cahn gram electrobalance was flushed with dried nitrogen during the weighing procedure. A small excess pressure should prevent the access of moist air from the outside of the box during the weighing procedure. Furthermore, the second drying process was modified.

In order to prevent an "explosion" of the P_2O_5 in the vacuum oven which formerly occurred now and then, we allowed the P_2O_5 to react with moist air for some time. Then the vessels with P_2O_5 were covered and heated to 170 °C in a vacuum oven for 12 h. This procedure was followed by a second drying process of the protein samples in the presence of P_2O_5. The drying time at 110 to 112 °C was extended to 90 h. The instrumental uncertainties of the dry mass determination determined practically the uncertainties of the density measurement. Therefore, we determined the standard deviations of the dry mass fraction determinations, using samples with different protein concentrations. The result was used for the fitting procedure of the data points (see Appendix 2).

III. Theoretical Section

Equation of the Pseudobinary Mixture. In the theory of mixtures[6] the volume V of a ternary system with the mass m_1 of water (index 1), m_2 of hemoglobin (index 2), and m_3 of sodium chloride (index 3) as function of the partial specific volumes v_1, v_2, and v_3 of the three components mentioned yields the relation

$$V = v_1 m_1 + v_2 m_2 + v_3 m_3 \tag{1}$$

With the specific volume $v = V/(m_1 + m_2 + m_3)$, the dry weight mass fraction w

$$w = (m_2 + m_3)/(m_1 + m_2 + m_3) \tag{2}$$

and the mass fraction α of the salt in the solid (dry) mass which is kept constant in each of the five sets of measurements

$$\alpha = m_3/(m_2 + m_3) \tag{3}$$

one obtains from eq 1 for the pseudobinary mixture (α = constant)

$$v = v_1(1 - w) + v_{23} w \tag{4}$$

where

$$v_{23} = (1 - \alpha)v_2 + \alpha v_3 \tag{5}$$

The Specific Volume as Function of the Dry Mass Fraction. The data points were fitted by the power series

$$v = \beta_0 + \beta_1 w + \beta_p w^p + \beta_q w^q \tag{6}$$

trying different values of p and q and comparing different fits by using statistical methods.[7,8] The values of the powers p and q were limited to the numbers 0, 1.5, 2, 3, 4, 5, 6, 7, but $p \neq q$. The residual errors given for values of the specific volume and of the partial specific volume are related to the number and scattering of the data points as well as to the choice of the power series (goodness of fit). The procedure of finding the "best" powers and the calculation of residual errors is outlined in Appendix 2. The result was that in eq 6 a minimum of four terms was necessary for the H_2O–Hb–NaCl mixtures and a minimum number of three terms for the pure H_2O–Hb and the pure H_2O–NaCl mixtures. The powers used and the values of the coefficients β_i are given in Table I. In order to show in the graphs the rather small protein–protein interaction terms β_p and β_q becoming effective and visible at high protein mass fractions, the function Δv

$$\Delta v = v - \beta_0 - \beta_1 w \tag{7}$$

or with eq 6

$$\Delta v = \beta_p w^p + \beta_q w^q \tag{8}$$

are plotted vs. w in the Figures 1–3.

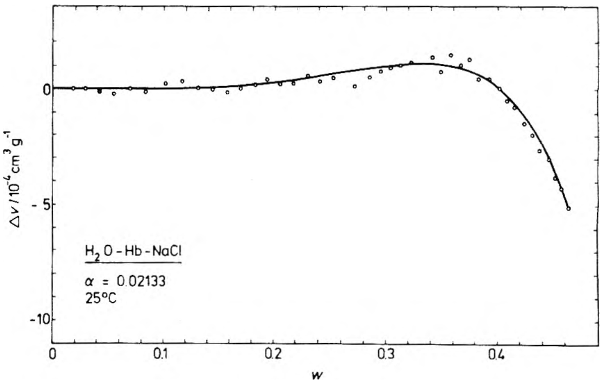

Figure 1. Experimental deviation Δv_i of the data points v_i from the linear part of eq 6 vs. the mass fraction w of the "dry" component Hb–NaCl; $w = (m_2 + m_3)/(m_1 + m_2 + m_3)$, eq 2; α = 0.021 33 or 0.021 79 g of NaCl per gram of Hb. The smooth curve represents eq 8 with p = 4 and q = 7 (Table I).

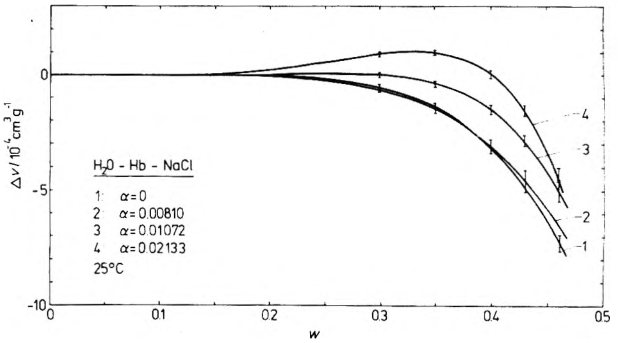

Figure 2. Deviation Δv of the specific volume from the linear part of eq 6 vs. the dry mass fraction w for the four values of α. The four curves correspond to eq 8 with values for the coefficient β_i shown in Table I. The error bars indicate residual errors (see Appendix 2).

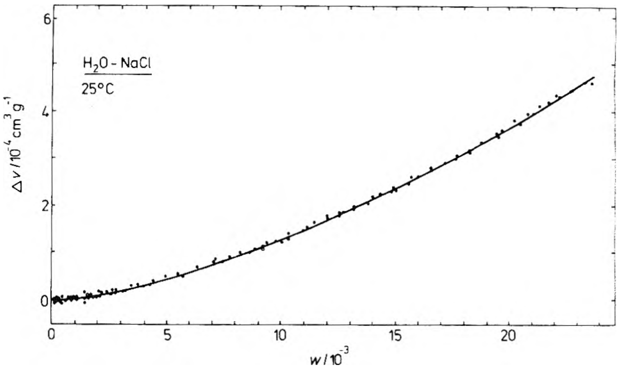

Figure 3. Experimental deviation Δv_i of the data points v_i of the specific volume from the linear part of eq 6, $\Delta v_i = v_i - \beta_0 - \beta_1 w_i$, vs. the mass fraction w of sodium chloride in water, $w = m_3/(m_1 + m_3)$. The smooth curve represents eq 8 with p = 1.5 and β_q = 0 (Table I). The mass fraction w = 0.02 corresponds to a solution of 0.349 mol of sodium chloride per kilogram of water.

The Partial Specific Volumes v_1 and v_{23} were obtained using the equations[6]

$$v_1 = v - w(\partial v/\partial w)_{T,P} \tag{9}$$

$$v_{23} = v + (1 - w)(\partial v/\partial w)_{T,P} \tag{10}$$

With eq 6 one obtains for the partial specific volume of

TABLE I: Coefficients β_i of the Power Series of Eq 6 for the Specific Volume, Mass Ratio $\alpha = m_3/(m_2 + m_3)$, Number of Experimental Data Points N, Minimum Function M (Eq 15), and the Maximum Values for the Dry Mass Fraction $w_{\max}$[a]

α	β_0, cm^3 g^{-1}	β_1, cm^3 g^{-1}	$\beta_{3/2}$, cm^3 g^{-1}	β_4, cm^3 g^{-1}	β_5, cm^3 g^{-1}	β_6, cm^3 g^{-1}	β_7, cm^3 g^{-1}	N	M	$w_{\max}$
0	+1.002982	−0.249832	0	0	0	−0.0765	0	80	221	0.466
	7	45				41				
0.00810	+1.002970	−0.253361	0	0	−0.022	0	−0.049	36	76.3	0.446
1	9	75			16		89			
0.01072	+1.002953	−0.254361	0	+0.0044	0	0	−0.160	42	31.7	0.468
1	5	50		25			29			
0.02133	+1.002959	−0.259022	0	+0.0202	0	0	−0.311	42	44.4	0.464
1	6	56		26			30			
1	+1.002963	−0.71625	+0.1274	0	0	0	0	123	135	0.024
	1	40	27							

[a] The numbers below the last digits are values for the uncertainties in the coefficients (see Appendix 2).

water $v_1{}^0$ extrapolated to infinite dilution

$$v_1{}^0 = \beta_0 \tag{11}$$

and for the partial specific volume $v_{23}{}^\infty$ for the solid (dry mass) component extrapolated to infinite dilution

$$v_{23}{}^\infty = \beta_0 + \beta_1 \tag{12}$$

IV. Results

Water-Hemoglobin-Sodium Chloride Mixtures. We measured the specific volume of salt free hemoglobin mixtures and mixtures of three mass fractions α of sodium chloride. The values of α correspond to NaCl concentrations of about 75, 100, and 200 mmol/kg of water in a mixture containing 350 g of Hb/kg of mixture. These values cover the physiological range of the H_2O–Hb–NaCl mixtures in bovine erythrocytes. The data points for α = 0.021 33 are shown in Figure 1, using the plot of Δv (eq 7) vs. w. The coefficients β_i obtained by least-squares fit (see Appendix 2) are shown in Table I. The smooth curve in Figure 1 correspond to eq 8. Figure 2 shows the best fit functions Δv vs. w for the four sets of measurements. In this graph the residual errors in Δv that is in v for some arbitrary selected values for w are shown (see Appendix 2 for residual errors).

Sodium Chloride Solution. Figure 3 shows the values Δv_i vs. w_i obtained by 123 measurements of solutions of small and physiological NaCl concentrations. The values of the coefficients of the best fit are shown in Table I (α = 1); the smooth curve in Figure 3 corresponds to this fit.

Evaluation of Partial Specific Volumes. The partial specific volumes were calculated by using eq 9 and 10 and the coefficients from Table I. As can be seen from the values β_0 in Table I, there are small systematic deviations of β_0 from the value $v_1{}^0$ of the pure water, $v_1{}^0$ = 1.002 964 cm^3 g^{-1}. This systematic displacement was taken into consideration for the calculation of the partial specific volumes. In Figure 4 the partial specific volume v_1 of water vs. w is shown for the four series of measurements. Furthermore, for some values of w the residual errors are given.

In Figure 5 the partial specific volume v_{23} of the dry mass vs. w is shown, together with the residual error bars for some values of w.

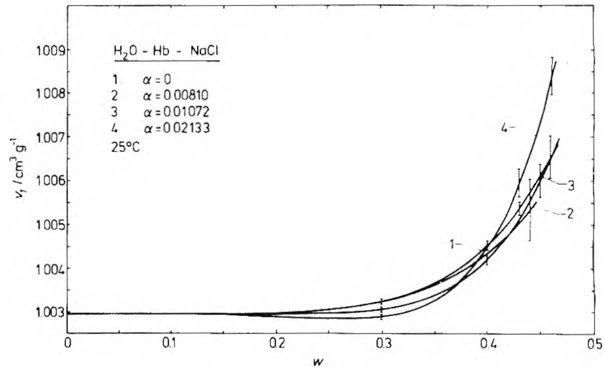

Figure 4. Partial specific volume of water v_1 vs. w for different values α. The bars indicate the residual errors in v_1.

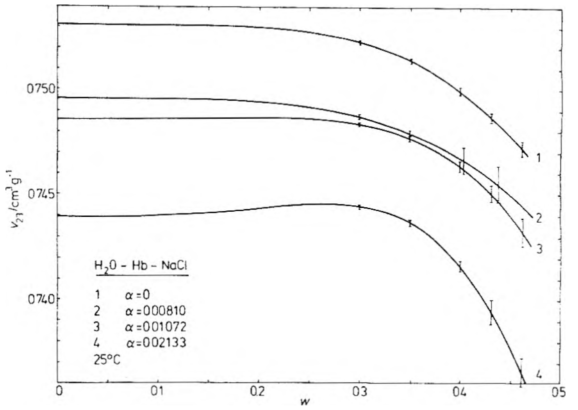

Figure 5. Partial specific volume v_{23} of the dry component vs. the dry mass (Hb + NaCl) fraction for the four sets of measurements. The bars indicate the residual errors in v_{23}.

V. Discussion

Water-Hemoglobin-Sodium Chloride Mixtures. In a previous paper[1] we described a small dependence of the partial specific volume of bovine hemoglobin on the mass fraction of the protein in water. The partial specific volume was found to be only about 1‰ smaller in a solution of 30 wt % hemoglobin than when extrapolated to infinite dilution. In case of bovine serum albumin solution, the concentration dependence is about 10 times larger than in hemoglobin solution, but still small even for very viscous protein–water mixtures.

The main influence of the salt is the very significant change in the value of the coefficient β_1 (see Table I) and hence the change of the partial specific volume for infinitely diluted solutions, $v_{23}{}^\infty$, of the "dry" component in the mixture. Looking at the linear part of v_{23} (see Figure 5), from eq 12, $v_{23}{}^\infty = \beta_0 + \beta_1$, and eq 5 results

$$\beta_1 = (1 - \alpha)v_2 + \alpha v_3 - v_1{}^0 \tag{13}$$

where $v_1{}^0$ is the specific volume of pure water. Since in Figures 1–4 the function $\Delta v = v - \beta_0 - \beta_1 w = \beta_p w^p + \beta_q w^q$ (eq 7 and 8) is plotted vs. the mass fraction w, this salt effect on β_1 is not shown. Only the effect of the salt on the high power interaction terms are shown. Δv as function of w shows characteristic features of the pure Hb solution as well as the pure NaCl solution (Figure 3), leading to a "biphasic curve" at the two higher α values (see Figure 2). The superposition principle in the strict sense cannot be applied because of the nonlinearity of the function $v(w)$.

In the previous paper[1] we explained the negative values of Δv at $w > 0.3$ by the interaction of hydrated protein molecules. Due to Brownian movement, there exists for every concentration a certain probability that the hydrated protein molecules build dimers and aggregates of higher order for a short time. During this process there occurs an interaction between the hydration shells themselves and with the surrounding "free water", containing salt. A change of the properties, e.g., the specific volume, of a certain small water region in the shell may follow. The existence of high powers in eq 6 of the order of 5, 6, or 7 (see Table I) points to such an interaction. By numerical calculations using the radii of Hb molecules we obtained curves of Δv versus w which were amazingly similar to the curves experimentally found. For this kind of interaction there are two different models imaginable.

First, during the process of "collision" of two or more hydrated protein molecules a part of water in the overlapping hydration shells may become "free" water and so change its properties (overlapping model). In order to understand the negative deviation from linearity of the specific volume of the protein solution with an increase of protein concentration, one has to assume that the specific volume of hydrated water is *larger* than that of free water.

The other model assumes that a cooperative action of the protein molecules on a certain surrounding of the "free" water, outside the hydration shells (cooperative model) may take place during the collision process. This process may lead to bridges[9] with a change of the specific volume of the "free" water in the cooperative region. In this model one has to assume that the specific volume of the water in the cooperative region is *smaller* than that of free water. Although it is not possible to say anything about the specific volume of the water in the hydration shell, one expects the same for the hydration shell, i.e., that the water, "bound" to protein, is more dense than the free water. Similar conclusions using other models has been drawn by Kauzmann et al.[10] and by Millero et al.[11]

A negative value for Δv at high mass fraction of protein could be the result of proton dissociation from imidazole groups or other groups in the region of the pronounced deviation. The partial specific volume of the hemoglobin at $w = 0.45$ is about 5×10^{-3} cm^3 g^{-1} lower than v_{23}^{∞} (see Figure 5). In order to explain this difference, using the data of Kauzmann[12,13] for the change of the partial molar volumes as a result of the dissociation of imidazole-H$^+$ in proteins, one has to assume, that 15 to 20 protons must dissociate from each hemoglobin molecule. Such an extensive dissociation can be excluded, because it would be connected with a drastic change in the pH value of the solution. This is not the case, because the pH value of an isoionic salt-free Hb solution does not change with protein concentration and for the pH values of very concentrated Hb were measured a change on addition of sodium chloride only from 7.10 to 7.28. One calculates an average net charge due to the acidic and basic groups of the Hb molecule of 10^{-4} or less elementary charges per Hb molecule in all mixtures used in this investigation. Hence the average net charge is practically zero. We are therefore convinced that the negative value of Δv is due to a protein-protein interaction which must take place in such highly concentrated protein solution.

Partial Specific Volume of Bovine Hemoglobin and Methemoglobin. From the salt-free hemoglobin solution we obtained for the partial specific volume of Hb extrapolated to infinitely diluted solution a value of $v_2^{\infty} = 0.753\,13$ cm^3 g^{-1} at 25 °C with a residual error of 4×10^{-5} cm^3 g^{-1}. This value is 2‰ lower than the value of $v_2^{\infty} = 0.754\,60$ cm^3 g^{-1} reported in the previous paper.[1] The significant difference is mainly due to the improved method for the determination of the dry mass fraction w, resulting in a further removal of about 8‰ water from the "dry mass" used in the first paper. The problem of the rather tightly bound water on and in protein molecules and the problem of the "true" water content of dried proteins have been discussed previously.[1] Therefore we cannot exclude the possibility that other authors will find better methods of drying, obtaining even somewhat smaller values for v_2^{∞}. Our values are reproducible within the small uncertainty given above.

The partial specific volume of bovine methemoglobin (Mb) in infinitely dilute solution was found to be $v_{\mathrm{Mb}}^{\infty} = 0.7541$ cm^3 g^{-1} at 25 °C within a residual error of 2×10^{-4} cm^3 g^{-1}. This value is between that of $v_{\mathrm{Mb}}^{\infty} = 0.7583$ cm^3 g^{-1} found by Bull and Breese[14] and that of $v_{\mathrm{Mb}}^{\infty} = 0.7503$ cm^3 g^{-1} found by Behlke and Wandt.[15] The hemoglobin, used in this investigation, contained between 6 and 10% methemoglobin. Using our value v_{Mb}^{∞} for methemoglobin, we obtained finally for pure bovine oxyhemoglobin a value of $v_{\mathrm{Hb}}^{\infty} = 0.753\,05$ cm^3 g^{-1} at 25 °C with a residual error of 5×10^{-5} cm^3 g^{-1}.

Sodium Chloride Solutions. From the density measurements on pure sodium chloride solutions (Figure 3, Table I) we obtained a value for the partial specific volume of NaCl extrapolated to infinite dilution v_3^{∞} of 0.2865 cm^3 g^{-1} at 25 °C with an uncertainty of 3×10^{-4} cm^3 g^{-1} or 1‰, or a partial molar volume V_3^{∞} of 16.74 cm^3 mol^{-1}. Here we used Merck Suprapur sodium chloride, the highest purity commercially available.

The published values for the partial molar volume of NaCl in infinitely dilute solution (Wirth and Bangert,[16] Millero,[17] and references in ref 17) range between 16.61 and 16.67 cm^3 mol^{-1} at 25 °C. Our value is 6‰ larger than the mean of the published values. This statistically significant difference is probably due to our simple extrapolation procedure using only the coefficients β_1 and $\beta_{3/2}$ for the fit in the range up to $w = 0.024$, corresponding to a sodium chloride solution of 0.421 mol of sodium chloride per kilogram of water. Since the salt contribution to the partial specific volume v_{23}^{∞} for the "dry" component is according to eq 5 small, the difference of 6‰ in the values for v_3^{∞} corresponds to a systematic deviation in v_{23}^{∞} of 4×10^{-6} cm^3 g^{-1} at $\alpha = 0.021\,33$. Hence the difference between the values of various authors are too small to have any influence on the conclusion, drawn from the results of our density measurements on salt-hemoglobin solutions.

NaCl-Hb Interaction in Dilute Solutions. Inspection of Figure 5 shows that for all salt concentrations used v_{23} does not deviate from v_{23}^{∞} by more than 10^{-4} cm^3 g^{-1} up to a dry mass fraction w of 0.1 corresponding to a hemoglobin concentration of about 10 wt % or 1.72 mmol of Hb per kilogram of water. Up to $w = 0.3$ the deviation of v_{23} from v_{23}^{∞} is still less than 10^{-3} cm^3 g^{-1}. So the range of the "limiting" law, $w \to 0$, extends practically to rather high Hb-NaCl concentrations. It would be better to use the term "linear range".

From eq 5 and 12 it follows that v_{23}^{∞} should be a linear function of α, $v_{23}^{\infty} = v_2 + (v_3 - v_2)\alpha$, because it can be expected that v_2 and v_3 are constant in the limiting case $w \to 0$. Figure 6 shows that the experimental values v_{23}^{∞} are a linear function of α. The value of v_{23}^{∞} obtained by extrapolation to infinitely diluted solution should, according to eq 5, be identical with the calculated value of

$$v_{23}^{\infty t} = (1-\alpha)v_2^{\infty} + \alpha v_3^{\infty} \qquad (14)$$

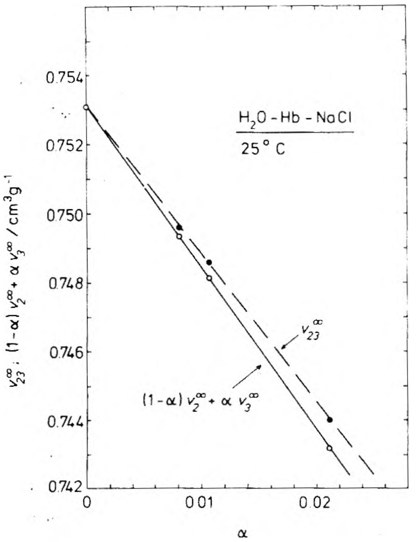

Figure 6. The experimental limiting value of v_{23}^{∞} for the "dry" component in the H_2O–Hb–NaCl mixture and the calculated limiting value of $[(1-\alpha)v_2^{\infty} + \alpha v_3^{\infty}]$ vs. α. The errors are smaller than 7×10^{-5} $cm^3\,g^{-1}$ (see Table II) and not larger than the symbols of the data points in the graph.

TABLE II: Experimental Limiting Value v_{23}^{∞} of the "Dry" Component in the H_2O–Hb–NaCl Mixture and the Calculated Limiting Value $v_{23}^{\infty t}$ for the Different Values of α[a]

α	v_{23}^{∞}, $cm^3\,g^{-1}$	$v_{23}^{\infty t}$, $cm^3\,g^{-1}$	$v_{23}^{\infty} - v_{23}^{\infty t}$, 10^{-4} $cm^3\,g^{-1}$
0	0.75313	0.75313	0
	4	4	
0.00810	0.74960	0.74935	2.5
1	7	4	8
0.01072	0.74860	0.74813	4.7
1	5	4	7
0.02133	0.74394	0.74318	7.6
1	5	4	7

[a] The numbers below the last digit of the value are residual errors (see Appendix 2).

where v_2^{∞} is the partial specific volume of Hb in the pure Hb solution ($\alpha = 0$, Table I), extrapolated to infinite dilutions, and v_3^{∞} is the partial specific volume of NaCl in the pure NaCl solution ($\alpha = 1$, Figure 3, Table I), extrapolated to infinite dilutions, if there is no interaction between Hb and the salt ions in the range $0 \leq w \leq 0.1$ considered. The result of this calculation is shown in Figure 6 and in Table II, second and third column. For $\alpha \neq 0$ the measured values v_{23}^{∞} are significantly larger than the calculated values $v_{23}^{\infty t}$. The difference is about 10 times larger than the experimental errors, given in Table II. The difference between v_{23}^{∞} and $v_{23}^{\infty t}$ increases with α, indicating a salt–protein interaction.

The salt–protein interaction leading to a larger value for v_{23}^{∞} compared to $v_{23}^{\infty t}$ could be of the following type:

(1) *Binding of Protons, e.g., by Ionized Imidazole Groups.* Using the data of Kauzmann[10,13] for the change of the partial molar volume of a protein by about 16 to 18 cm^3 per mol as a result of binding one proton by an imidazole group, one calculates a change of partial specific volume of the protein of $+2.7 \times 10^{-4}$ $cm^3\,g^{-1}$ or an increase of 0.36‰. The increase in the partial volume is largely due to the disappearance of the electrostriction of the water on the neutralization reaction. In order to explain a difference $v_{23}^{\infty} - v_{23}^{\infty t}$ (Table II) of 7.6×10^{-4} $cm^3\,g^{-1}$ at $\alpha = 0.021\,33$ one has to assume that about three more protons are bound by a Hb molecule in the presence of sodium chloride compared to a Hb molecule in salt-free solution. Because the pH value of all mixtures used is between 7.05 and 7.28, one calculates an average net charge on a Hb molecule due to proton dissociation or association of 10^{-4} or less elementary charges per Hb molecule. Therefore by the same reasoning as before salt induced binding of protons of imidazole or other groups can be excluded as an explanation for the difference $v_{23}^{\infty} - v_{23}^{\infty t}$.

(2) *Binding of Anions.* Generally the binding of a positive or negative ion to a protein will result in a volume change of the solution. A positive contribution (expansion) to the volume change will result from the removal of the ion out of the cavity surrounded by electrostrictively compressed water which will expand due to the removal of the electrical field of the ion. The second contribution to the volume change will occur on the attachment of the ion on the binding site of the protein molecule. If on binding itself the ion leads to an electrostrictive compression of the water in the immediate neighbourhood of the ion within the "bound water shell" of nearly the same degree as in pure water, both volume contributions nearly cancel and the measured net volume change will be nearly zero. Another contribution to the total volume change could arise from an allosteric volume change of the protein molecule due to the ion bound. Generally the net volume change can be positive or negative, depending on the magnitude of the three different contributions.

Rasper and Kauzmann[12] have shown that in several proteins the binding of a proton to a charged carboxyl group is accompanied by an increase in volume of about +11 cm^3 per mol of protons reacting. The neutralization reaction of a charged imidazole or amino group gives an increase in volume of +16 to +18 cm^3 per mol of hydroxyl reacting. The volume changes are positive and rather large, since two electrostrictively compressed water domains expand on the neutralization of the two charges. The other contributions mentioned are in this case obviously less important.

Volume effects attributable to the interaction of other ions than protons with proteins are not so extensively investigated and probably more complicated. Katz et al.[18] found that binding of trichloroacetate ions with bovine serum albumin is accompanied by a volume increase, while binding of thiocyanate ions can be accompanied by a volume decrease as well as by a volume increase depending on the concentration of the ion used.

Binding of sodium or chloride ions to isoionic hemoglobin could be the cause for a positive value of the difference $v_{23}^{\infty} - v_{23}^{\infty t}$. Binding of sodium can be excluded since experimentally no indication of any binding to bovine, human, horse, and dog hemoglobin in the isoionic state was found.[19] Even serum albumin known to bind anions exceptionally does not bind potassium or sodium ions.[20]

It is known that proteins do bind univalent anions. The number of binding sites and the values of the binding constants depend on the ion species and the type of protein.[21-23] Especially binding of anions to serum albumin have been investigated rather extensively.[20,22,23] However Carr[21] did find no detectable binding to hemoglobin at its isoelectric point pH 6.8 in a solution with 3.6 wt % Hb and 17 mmol of chloride per litre of solution. Recent potentiometric determination[24] of the mean activity coefficient of NaCl up to 0.5 mol of NaCl per kilogram of water and 575 g of bovine hemoglobin per kilogram of water and the analysis of the pH shift in this highly concentrated Hb solution by addition of NaCl to the isoionic Hb solution from pH 7.10 to 7.35, using Scatchard's[25] relation between the pH shift and the number of ions bound, did indicate a weak binding of chloride ions.[26] There seems to be about 30 to 40 binding sites with a rather small intrinsic association constant K_{intr} of about 5 mol^{-1} kg. Therefore in our mixtures up to four chloride ions should be bound to one Hb molecule, resulting in an increase of the partial specific volume of the "dry" component v_{23}^{∞} and hence to a positive value for the difference $v_{23}^{\infty} - v_{23}^{\infty t}$. A first rough calculation gave the right magnitude for $v_{23}^{\infty} - v_{23}^{\infty t}$.

Supplementary Material Available: Appendix 1, the influence of the viscosity of a solution on the determination of the density by the method of the undamped bending oscillation of a glass tube, and Appendix 2, determination of the coefficients β_i and residual errors (12 pages). Ordering information is available on any current masthead page.

References and Notes

(1) J. Bernhardt and H. Pauly, *J. Phys. Chem.*, **79**, 584 (1975).
(2) P. Andrews, *Biochem. J.*, **91**, 222 (1964).
(3) W. Pilz, I. Johann, and A. T. Boo, *Int. J. Environ. Anal. Chem.*, **2**, 179 (1973).
(4) O. Kratky, H. Leopold, and H. Stabinger, *Z. Angew. Phys.*, **27**, 273 (1969).
(5) P. H. Bigg, *Brit. J. Appl. Phys.*, **18**, 521 (1967).
(6) E. A. Guggenheim, "Thermodynamics", 5th ed, North-Holland Publishing Co., Amsterdam, 1967.
(7) P. R. Bevington, "Data Reduction and Error Analysis for the Physical Sciences", McGraw-Hill, New York, N.Y., 1967.
(8) S. Brandt, "Statistical and Computational Methods in Data Analysis", 2nd ed, North-Holland Publishing Co., Amsterdam, 1976.
(9) I. Oakes, *J. Chem. Soc., Faraday Trans. 1*, **72**, 216 (1976).
(10) W. Kauzmann, K. Moore, and D. Schultz, *Nature (London)*, **248**, 447 (1974).
(11) F. J. Millero, G. K. Ward, and P. Chetirkin, *J. Biol. Chem.*, **251**, 4001 (1976).
(12) J. Rasper and W. Kauzmann, *J. Am. Chem. Soc.*, **84**, 1771 (1962).
(13) W. Kauzmann, A. Bodanszky, and J. Rasper, *J. Am. Chem. Soc.*, **84**, 1777 (1962).
(14) H. B. Bull and K. Breese, *J. Phys. Chem.*, **72**, 1817 (1968).
(15) J. Behlke and I. Wandt, *Acta Biol. Med. Ger.*, **31**, 383 (1973).
(16) H. E. Wirth and F. K. Bangert, *J. Phys. Chem.*, **76**, 3488 (1972).
(17) F. J. Millero, *J. Phys. Chem.*, **74**, 356 (1970).
(18) S. Katz, J. K. Crissman, and L. C. Roberson, *J. Biol. Chem.*, **249**, 7892 (1974).
(19) C. W. Carr, *Arch. Biochem. Biophys.*, **62**, 476 (1956).
(20) G. Scatchard, I. H. Scheinberg, and S. H. Armstrong, *J. Am. Chem. Soc.*, **72**, 535 (1950).
(21) C. W. Carr, *Arch. Biochem. Biophys.*, **46**, 417 (1953).
(22) G. Scatchard, J. S. Coleman, and A. L. Shen, *J. Am. Chem. Soc.*, **79**, 12 (1957).
(23) G. Scatchard, Y. V. Wu, and A. L. Shen, *J. Am. Chem. Soc.*, **81**, 6104 (1959).
(24) H. Pfister and H. Pauly, *J. Polym. Sci., Part C*, **No. 39**, 179 (1972).
(25) G. Scatchard and E. S. Black, *J. Phys. Colloid Chem.*, **53**, 88 (1949).
(26) N. Tretter, Dissertation, Fachbereich Medizin der Universität Erlangen-Nürnberg, 1975.

Alcohol Association Studies. 3. Vapor Pressure Measurements for the Ethanol–*n*-Hexadecane System

Edwin E. Tucker* and Sherril D. Christian

Department of Chemistry, University of Oklahoma, Norman, Oklahoma 73019 *(Received January 20, 1977)*

Publication costs assisted by the National Science Foundation

The association of ethanol in *n*-$C_{16}H_{34}$ has been studied by vapor pressure measurements at 25, 35, and 45 °C. Numerical integration of the vapor pressure data has made possible the calculation of molecular weight for ethanol polymers as a function of concentration. These results clearly show that no specific polymer is the predominant associated species in any concentration range. The commonly used one parameter infinite series model for alcohol association has been shown to be invalid for dilute alcohol solutions. A number of alcohol association models, including the model recently proposed by Stokes, have been tested. The simplest model which adequately represents the vapor pressure data contains two equilibrium constants: a constant for trimer formation and a constant for sequential addition of a monomer.

Introduction

Virtually all studies of hydrogen bonding in dilute solution are interpreted with the aid of one fundamental assumption: the individual solute species (monomers and polymers) obey the ideal dilute solution laws. That is, in restricted concentration ranges, it is assumed that the activity coefficients of monomers and complexes are independent of concentration. Therefore, considering the fact that the same fundamental solution laws are invoked, it is quite surprising that so many different (and often mutually exclusive) solution models have been proposed to explain the behavior of alcohol systems.[1]

One reason for this diversity of opinion is that many investigators have attempted to extract more information from their experimental results than is justified. In most experimental studies of alcohol association two basic types of information are needed for correlating data. These are (a) the thermodynamic equilibrium constants (K) for formation of specific aggregates; and (b) technique-related intensity factors such as extinction coefficients, chemical shifts, dipole moments, and formation enthalpies of the complex species. Thus, if there are assumed to be N distinguishable alcohol complexes, it is necessary (in most experiments) to obtain at least $2N$ parameters to fit data to the chosen association model. Unfortunately, the pairs of parameters (K and the technique-related parameter) are usually highly coupled, making it difficult or impossible to obtain reliable values of these constants from a least-squares analysis of data. Consequently, we doubt that it is presently possible to obtain a reliable picture of alcohol association in dilute solution from any one type of measurement such as nuclear magnetic resonance, calorimetry, or dielectric constant.

There are experiments which can yield information about the various solute association constants, without requiring the determination of technique-related parameters. These include the thermodynamic activity methods (e.g., vapor pressure measurement) and certain infrared experiments in which it is possible to measure the absorbance of a band which may be attributable solely to the alcohol monomer. Basically, both activity and infrared measurements can be processed to yield values of the alcohol monomer concentration (C_A) and by difference the total concentration of alcohol molecules involved in polymeric species.[1,2]

Simple monomer-n-mer models (e.g., monomer–dimer, monomer–trimer, or monomer–tetramer) have quite often been proposed to explain solution data for alcohols. Unfortunately, it has not been generally realized that these models are inconsistent with available activity data for alcohol systems. In the case of phenol association, Tucker et al.[3] were able to show that monomer concentrations derived from phenol activity data are consistent with those derived from infrared absorbance data. However, the simple monomer–n-mer models which have been used to correlate calorimetric and NMR results do not yield phenol monomer concentrations which are proportional to the thermodynamic activity.[3] It has also been shown that for *tert*-butyl alcohol association, when results from three types of measurement (vapor pressure, infrared, and NMR) are fitted individually by a 1–4 model, the resulting K_4 values vary widely from one data type to another at the same temperature.[4] The three data sets can only be brought into agreement by using an activity based model which includes associated species both larger and smaller than the tetramer.[1]

Fundamentally, we can state that a primary requirement for any physically realistic association model is that the monomer concentration inferred from that model be directly proportional to the monomer activity determined by a thermodynamic technique. In cases where there is no significant interference by polymeric species at the monomer absorption band infrared measurements of monomer absorbance should also be directly related to monomer activity.

The present vapor pressure study of ethanol–n-hexadecane solutions was undertaken to provide reliable activity data for ethanol solutions. Additionally, by model-independent analysis of these data we hope to provide convincing evidence that a number of alcohol association models in present use are physically unrealistic.

Experimental Section

The ethanol used was absolute reagent grade obtained from U.S. Industrial Chemicals Co. Ethanol was further purified by fractional distillation from CaH_2 in a 20-plate still. n-Hexadecane (99%) was obtained from Aldrich Chemical Co. and purified by Al_2O_3 filtration, vacuum distillation, and fractional freezing. Vapor pressure measurements were made with a Mensor Co. quartz manometer (minimum resolution of ±0.001 Torr absolute). The thermostat bath temperature at 25, 35, and 45 °C was maintained to within ±0.003 °C. The vapor pressure data for EtOH–Hx solutions are given in Table I (supplementary material, see paragraph at end of text regarding supplementary material) along with additional experimental details.

Results and Data Treatment

Figure 1 displays the vapor pressure of EtOH–Hx solutions as a function of temperature and EtOH concentration. The fundamental assumption used in interpreting these data is that Henry's law is obeyed by the alcohol monomer (and complexes). Consequently, the partition of monomeric alcohol between vapor and solution phases can be characterized by a distribution coefficient

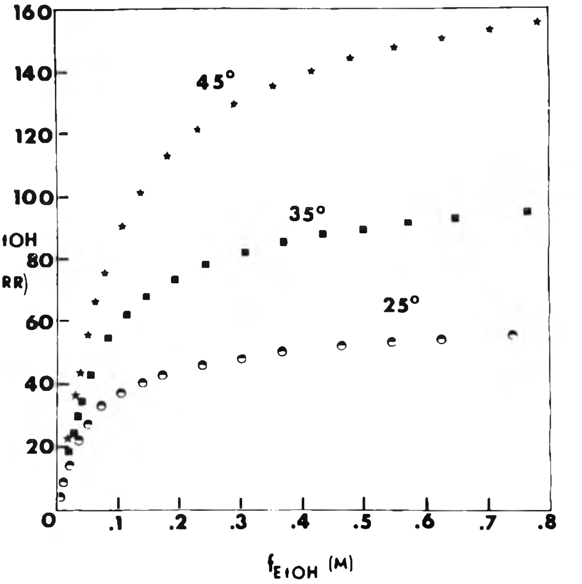

Figure 1. Vapor pressure of ethanol as a function of molar concentration in n-hexadecane at three temperatures. Only a fraction of the available data appears.

TABLE II: Infinite Dilution Distribution Coefficients (K_D) for Alcohols between Vapor and n-Hexadecane[a]

T, °C	25	30	35	40	45	50
Methanol[b]	8.25		7.07		6.06	
Methanol[c]	8.22		7.01		6.00	
Ethanol[d]	24.90		19.7		16.0	
tert-Butyl alcohol[e]		77.1	66.7	58.2	51.0	44.5

[a] K_D is for the transfer ROH(vapor) → ROH(solution) with standard states of unit molarity ideal dilute solution. [b] Data from ref 2. [c] Derived from deposited data in ref 5. [d] This work. [e] Data from ref 1. Estimated precision limits on these K's are ±0.5%.

TABLE III: Transfer Energies for Alcohols between Vapor Phase and n-Hexadecane at 298 K[a]

Methanol[b]	$-\Delta E° = 2.74 \pm 0.05$ kcal/mol
Ethanol[c]	$-\Delta E° = 4.00 \pm 0.05$ kcal/mol
tert-Butyl alcohol[d]	$-\Delta E° = 5.09 \pm 0.08$ kcal/mol

[a] Unit molarity ideal dilute solution standard state. [b] Value from ref 2 corrected for thermal expansion of solvent. [c] This work. [d] Value from ref 1 corrected for thermal expansion of solvent.

$$K_D = C_A{}^s/C_A{}^v = C_A{}^sRT/P_A \qquad (1)$$

where $C_A{}^s$ and $C_A{}^v$ are monomer EtOH molarities in solution and vapor, respectively, and P_A is the monomer pressure of EtOH (total pressure corrected for a small degree of vapor nonideality). K_D can be determined with rather high precision from the limiting behavior at infinite dilution of pressure vs. concentration data. Table II gives K_D values for EtOH–Hx solutions from this work and, for comparison, K_D values for methanol and *tert*-butyl alcohol solutions in n-hexadecane. Table III lists transfer energies for the three alcohols from vapor phase to solution in n-hexadecane.

Initially, we wish to utilize a quantitative model-independent method of analyzing association data for the purpose of severely limiting the number of models which can be used to fit data in a rational manner. It has been previously indicated by Hoffmann[6] that molecular weight data for alcohol solutions can be obtained by numerical integration of an appropriate function involving only monomer concentration and formal concentration. In

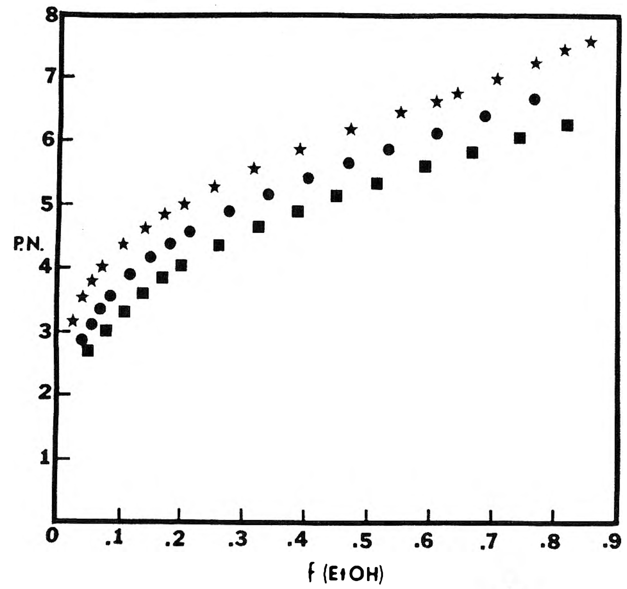

Figure 2. Average size of ethanol polymers as a function of ethanol molarity in *n*-hexadecane at three temperatures: (★) 25 °C; (●) 35 °C; (■) 45 °C.

general terms, formal alcohol concentration (f_A) and apparent alcohol concentration (e_A) are defined by

$$f_A = C_A + 2K_2C_A{}^2 + 3K_3C_A + \ldots + nK_nC_A{}^n \quad (2)$$

$$e_A = C_A + K_2C_A{}^2 + K_3C_A{}^3 + \ldots + K_nC_A{}^n \quad (3)$$

By inspection it is obvious that the following relationship is exact.

$$C_A(\mathrm{d}e_A/\mathrm{d}C_A) = f_A \quad \text{and} \quad \mathrm{d}e_A = (f_A/C_A)\,\mathrm{d}C_A \quad (4)$$

The apparent or colligative alcohol concentration (e_A) can then be obtained (from the integrated form of eq 4), without reference to any particular association model, by numerical integration of the curve f_A/C_A vs. C_A.[7]

$$e_A = \int_0^{C_A}(f_A/C_A)\,\mathrm{d}C_A \quad (5)$$

Having obtained e_A values we can define the average size of alcohol polymer (pn) by

$$\mathrm{pn} = (f_A - C_A)/(e_A - C_A) \quad (6)$$

Equation 6 has been previously used by Mukerjee and Ghosh[8] in an investigation of dye association in aqueous solution. With reference to eq 2 and 3 it is evident that, if only a single polymer of order n is formed, pn should be a concentration independent value within experimental error.

Figure 2 displays pn values obtained from our data as a function of ethanol concentration. It is obvious that no model containing a single associated species can explain these data over any reasonable concentration range. It is also obvious that fairly large alcohol polymers are present even at quite low concentration. For example, the *average* polymer size becomes larger than 4 at a formal ethanol concentration of only 0.075 M at 25 °C. We may point out that authors of recent articles assume or support the use of a 1–4 model to treat association data,[9,10] even to the extent of claiming 1–4 validity for neat alcohol solutions.[11]

The present results confirm the previous indications that the 1–4 model cannot be consistent with activity data for alcohol–hydrocarbon solutions.[1,2] Moreover, Figure 2 provides direct evidence that no 1–n model is a valid approximation for treating association data for ethanol.

Our further discussion will concentrate on models which assume series of sequential reactions for alcohol association. Historically, the first such model is one in which a single equilibrium constant is assumed for addition of a monomer unit to any alcohol species.[12,13] The formal alcohol concentration is then given by

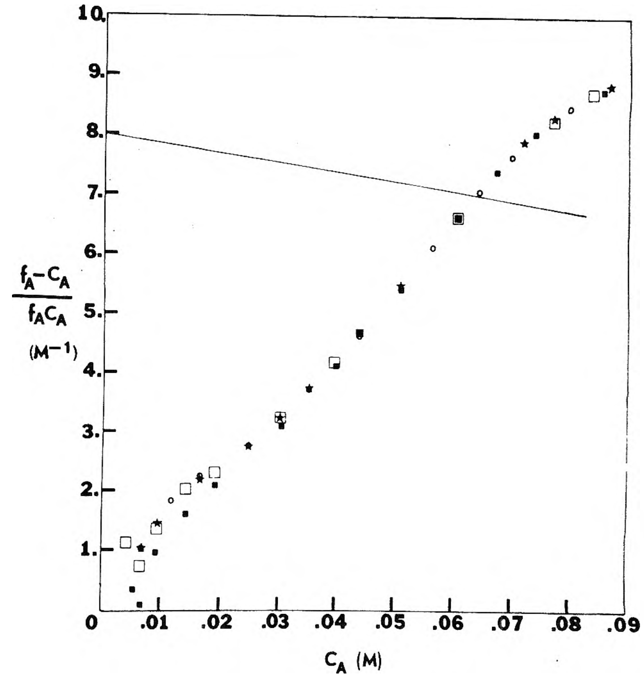

Figure 3. Plot of 35 °C vapor pressure data according to eq 8. Different symbols refer to replicate vapor pressure measurements for EtOH–Hx solutions at 35 °C. Solid line is for hypothetical data, with $K_\infty = 4.0$ M^{-1}, obeying eq 8.

$$f_A = C_A/(1 - K_\infty C_A)^2 \quad (7)$$

Rearrangement of eq 7 allows a simple test of this model with vapor pressure data.

$$(f_A - C_A)/f_AC_A = 2K_\infty - K_\infty{}^2C_A \quad (8)$$

A plot of the left-hand side of eq 8 vs. C_A should give a straight line with intercept $2K_\infty$ and slope $K_\infty{}^2$. Figure 3 gives a plot of EtOH–Hx vapor pressure data at 35 °C according to this model. For comparison, synthetic data with $K_\infty = 4$ M^{-1} are also plotted. The 1–∞ model (7) is seen to be inadequate because the experimental data do not form a straight line but, more importantly, the slope is of opposite sign to the expected slope. Thus the experimental data predict a physically impossible negative value of $K_\infty{}^2$. Previously reported vapor pressure data for methanol–Hx and *tert*-butyl alcohol–Hx solutions also give curves analogous to the experimental EtOH–Hx data. Hoffmann commented on the inadequacy of this single constant model many years ago[6] but the model is, unfortunately, still used in recent articles.[14-16] As stated by Scott and Fenby[17] most treatments of the excess thermodynamic properties of alcohol–solvent mixtures utilize the above one constant association model. Our present work shows the fundamental inability of the one constant model to even qualitatively fit the behavior of dilute alcohol–hydrocarbon solutions.

The apparent intercept as C_A approaches zero in Figure 3 is also of interest. The limiting value should closely approximate twice the dimer constant for ethanol. Although the exact value of the intercept is uncertain there can be little doubt that K_2 for EtOH is a small number, certainly much less than 1.0 M^{-1}.

The next level of model complexity is to assume a unique dimerization constant and a K for subsequent addition of a monomer to dimer or higher polymer.[18] The

TABLE IV: Root Mean Square Deviations and Equilibrium Constants for Various Fits of Ethanol-*n*-Hexadecane Vapor Pressure Data

Model	T, °C	rmsd ($M \times 10^4$)[a]	K_2, M^{-1}	K_3, M^{-2}	K_4, M^{-3}	K_∞, M^{-1}
1-2-∞	24	40.6	3.25 ± 0.02			11.23 ± 0.01
eq 9	35	33.7	2.11 ± 0.01			8.43 ± 0.01
	45	28.9	1.45 ± 0.01			6.42 ± 0.01
1-3-∞	25	21.2		47.5 ± 0.2		10.887 ± 0.008
eq 10	35	18.7		23.2 ± 0.1		8.167 ± 0.005
	45	20.7		12.49 ± 0.05		6.185 ± 0.005
1-3-∞	25	26.4		61.9 ± 0.2		12.121 ± 0.008
eq 11	35	18.7		30.0 ± 0.1		9.111 ± 0.004
	45	9.9		15.76 ± 0.03		9.939 ± 0.002
Stokes	25	49.6	6.2 ± 0.3	0.54 ± 0.06		78.0 ± 1.3
eq 12	35	46.5	4.4 ± 0.2	0.22 ± 0.02		60.0 ± 0.9
	45	40.8	2.9 ± 0.1	0.16 ± 0.02		43.4 ± 0.7
1-2-3-∞[b]	25	21.0	0.30 ± 0.14	46.4 ± 0.5		10.92 ± 0.02
	35	13.8	0.54 ± 0.06	21.8 ± 0.2		8.23 ± 0.01
	45	10.6	0.60 ± 0.03	11.1 ± 0.1		6.28 ± 0.01
1-2-3-4-∞[c]	25	17.6	−3.9 ± 0.5	120.4 ± 8.2	405.0 ± 11.0	11.17 ± 0.03
	35	12.2	−1.4 ± 0.2	47.9 ± 2.8	151.2 ± 2.8	8.38 ± 0.02
	45	8.5	−0.31 ± 0.1	20.6 ± 1.1	61.6 ± 0.9	6.37 ± 0.01

[a] rmsd is the square root of the summed squares of deviations between f_A(obsd) and f_A(calcd) divided by the degrees of freedom (i.e., number data points minus number of parameters) in the system. [b] A specific K_2 is added to eq 10. [c] Fitting equation is $f_A = C_A + 2K_2C_A^2 + 3K_3C_A^3 + (K_4C_A^4(4 - 3K_\infty C_A)/(1 - K_\infty C_A)^2)$.

formal alcohol concentration by this model (1–2–∞) then becomes

$$f_A = C_A + \frac{K_2C_A^2(2 - K_\infty C_A)}{(1 - K_\infty C_A)^2} \tag{9}$$

This two constant model is somewhat better than the 1–∞ model but, generally speaking, gives a rather poor representation of vapor pressure data for dilute alcohol–hydrocarbon solutions.[1] Additionally, Stokes has shown that the 1–2–∞ model is not even qualitatively correct for representing activity data for EtOH–cyclohexane solutions derived from freezing point measurements.[19]

Utilizing a variety of physical measurements, Tucker et al.[1,2] have found that the equilibrium constant for alcohol dimer formation must be quite small; certainly in the range from 0 to 1 M^{-1}. It has not been generally recognized that no experiment of sufficient precision has ever been performed to determine the value of K_2 (within ±100%) for alcohol systems in which higher polymers form readily. Two-parameter models which have been found to fit alcohol–hexadecane vapor pressure data to a high degree of precision have omitted a dimer constant and used a trimer and higher polymer constants.[1,2] Two models discussed previously are given:

$$f_A = C_A + K_3C_A^3\frac{(3 - 2K_\infty C_A)}{(1 - K_\infty C_A)^2} \tag{10}$$

$$f_A = C_A + \frac{3K_3C_A^3}{1 - K_\infty C_A} \tag{11}$$

The model of eq 10 is analogous to the 1–2–∞ model (eq 9) with consideration of trimer as the first significant polymer. The model of eq 11 assumes a recursion relationship which allows sequential equilibrium constants to increase slightly as a function of polymer size.

Stokes[19] has recently formulated another model for alcohol association which is given as

$$f_A = C_A + 2K_2C_A^2 + K_3C_A^3(3 + K_\infty C_A)e^{K_\infty C_A} \tag{12}$$

where the successive K for addition of a monomer to trimer or larger polymer has the definition

$$\frac{K_\infty}{n - 3} = \frac{C_{A_n}}{(C_{A_{n-1}})(C_A)} \quad \text{for } n \geq 4 \tag{13}$$

K_3 is for the reaction $3A = A_3$ (as opposed to the stepwise K_{23} used by Stokes). As compared with eq 10 and 11 the Stokes model assumes that successive K's for monomer addition decrease rapidly with polymer size due to an entropic effect.[19]

Table IV gives the results of fits of our vapor pressure data for EtOH–Hx with various association models. The 1–2–∞ model gives a relatively poor fit of the data with unreasonably large dimer constants (e.g., the predicted intercept in Figure 3 would be 4.2 according to this model). The 1–3–∞ models give satisfactory fits of the EtOH–Hx vapor pressure data. For illustrative purposes the 1–3–∞ model from eq 10 has been extended to three (1–2–3–∞) and four (1–2–3–4–∞) parameters. In the three parameter case the calculated K_2's are quite small and have unexpected temperature dependence, K_3 and K_∞ for this fit are only marginally changed from their values in the fit of the unmodified 1–3–∞ model. The four parameter fit (1–2–3–4–∞) results in uniformly negative dimerization constants.

The fit of the Stokes model in Table IV is somewhat unusual since the rmsd's are substantially larger than those for the 1–3–∞ models from eq 10 and 11 although the Stokes model contains an additional parameter. In addition to giving a poor quantitative representation of the EtOH–Hx vapor pressure data the Stokes model results in parameter values which are unreasonable. It may be expected that, if there is cooperativity in formation of alcohol complexes, the K for trimer formation should be substantially larger than $(K_2)^2$.[1] Yet, the Stokes model predicts a K_3 value which is vanishingly small in comparison with $(K_2)^2$ for the fit of eq 12 to the present data. In previous work on freezing point depressions of EtOH–C_6H_{12} solutions[19] values of K_2K_{23} (M^{-2}) were calculated which were also significantly smaller than $(K_2)^2$. An additional problem is that the K_2 value from the Stokes model is far too large to be realistic. Consequently, we feel that this model does not provide a plausible picture of EtOH self-association.

Summary and Conclusions

By use of the method of integration of experimental vapor pressure data to obtain information about alcohol polymer size we have demonstrated that no monomer–*n*-mer model is appropriate for representing the state of ethanol aggregation in a hydrocarbon solvent. More complex models for alcohol association such as the 1–∞ and 1–2–∞ are also inadequate for treating alcohol association in dilute solution. The three parameter model due to Stokes[19] has also been shown to be inappropriate. The least complex model which appears to adequately correlate alcohol association in hydrocarbon solutions utilizes two equilibrium constants: one for trimer formation and one for sequential addition of a monomer. Alcohol dimer formation appears to be of marginal significance in hydrocarbon solutions of relatively unhindered alcohols; the value of K_2 probably lies between 0 and 1.0 m^{-1} and is indeterminate within the precision of all reported data for alcohol association in hydrocarbon solvents.

In this work and in previous articles[1-3] we have shown the unique power of vapor pressure and related activity methods to eliminate a number of proposed alcohol association models. The fact that monomer alcohol concentration is rather directly obtained from vapor pressure and related activity measurements allows us to reject a number of models which might appear to be reasonable when used only to correlate data from less discriminatory types of measurements such as nuclear magnetic resonance and calorimetry.

Analysis of the EtOH–Hx vapor pressure data allows us to postulate a reasonably plausible mass action model for ethanol association. Structural questions such as the relative proportions of cyclic and acyclic alcohol complexes cannot be resolved by use of a single type of experimental data. Previous work has indicated possible approaches for combining vapor pressure data with spectroscopic data in order to suggest plausible alcohol complex structures.[1] Our ability to derive unambiguous information about alcohol polymer size through integration of vapor pressure data creates another avenue for model-independent comparison of vapor pressure data with the results of other experimental techniques. In particular, correlation of average polymer size with calorimetric heat of dilution data would be of interest. For example, if the assumption were made that all alcohol polymers were acyclic then the average enthalpy per hydrogen bond would be given by

$$\frac{f_A \phi_L}{(\text{pn} - 1)(e_A - C_A)} = \frac{f_A \phi_L}{f_A - e_A} = \text{Avg} \frac{\Delta H^\circ(\text{acyclic})}{(\text{bond})} \tag{14}$$

where ϕ_L is the heat of dilution to infinite dilution of a quantity of solution (with alcohol concentration f_A) containing 1 mol of alcohol. Similarly, if all alcohol polymers are assumed to be cyclic then the average enthalpy per H bond would be given by

$$\frac{f_A \phi_L}{(\text{pn})(e_A - C_A)} = \frac{f_A \phi_L}{f_A - C_A} = \text{Avg} \frac{\Delta H^\circ(\text{cyclic})}{\text{bond}} \tag{15}$$

Clearly, the above expressions correspond to two limiting descriptions neither of which may be strictly true for any given alcohol system. However, this approach does offer a means of model-independent characterization of the behavior of the average enthalpy per H bond as a function of concentration. We are not presently able to test the above correlations due to the lack of suitable calorimetric data.

Acknowledgment. Acknowledgment is made to the National Science Foundation (Grant No. GP-43307) for support of this work.

Supplementary Material Available: Vapor pressure data for ethanol–n-hexadecane solutions at 25, 35, 45 °C (7 pages). Ordering information is given on any current masthead page.

References and Notes

(1) E. E. Tucker and E. D. Becker, *J. Phys. Chem.*, **77**, 1783 (1973), Part 2.
(2) E. E. Tucker, S. B. Farnham, and S. D. Christian, *J. Phys. Chem.*, **73**, 3820 (1969), Part 1.
(3) E. E. Tucker, S. D. Christian, and L. N. Lin, *J. Phys. Chem.*, **78**, 1443 (1974).
(4) E. E. Tucker and E. Lippert in "The Hydrogen Bond: Recent Developments in Theory and Experiment", P. Schuster, G. Zundel, and C. Sandorfy, Ed., North-Holland, Amsterdam, 1976, Chapter 17.
(5) E. E. Tucker and S. D. Christian, *J. Phys. Chem.*, **79**, 2484 (1975).
(6) E. G. Hoffmann, *Z. Phys. Chem. B.*, **53**, 179 (1943).
(7) A simple trapezoidal method was used for the integration.
(8) P. Mukerjee and A. K. Ghosh, *J. Am. Chem. Soc.*, **92**, 6403 (1970).
(9) R. O. Inlow, M. D. Joesten, and J. R. Van Wazer, *J. Phys. Chem.*, **79**, 2307 (1975).
(10) B. D. Anderson, J. H. Rytting, S. Lindenbaum, and T. Higuchi, *J. Phys. Chem.*, **79**, 2340 (1975).
(11) A. N. Fletcher, *J. Phys. Chem.*, **76**, 2562 (1972).
(12) E. W. Lassettre, *J. Am. Chem. Soc.*, **59**, 1383 (1937).
(13) H. Kempter and R. Mecke, *Z. Phys. Chem. B*, **46**, 229 (1940).
(14) D. S. Abrams and J. M. Prausnitz, *J. Chem. Thermodyn.*, **7**, 61 (1975).
(15) F. Kohler, E. Liebermann, R. Schano, H. E. Affsprung, J. K. Morrow, K. Sosnkowska-Kehiaian, and H. Kehiaian, *J. Chem. Thermodyn.*, **7**, 241 (1975).
(16) H. Fujiwara and T. Ikenoue, *J. Chem. Soc., Faraday Trans. 1*, **72**, 2375 (1976).
(17) R. L. Scott and D. V. Fenby, *Annu. Rev. Phys. Chem.*, **20**, 111 (1969).
(18) N. D. Coggeshall and E. L. Saier, *J. Am. Chem. Soc.*, **73**, 5414 (1951).
(19) R. H. Stokes, *J. Solution Chem.*, **3**, 671 (1974).

"Iceberg" Formation and Solubility

Kōzō Shinoda

Department of Chemistry, Faculty of Engineering, Yokohama National University, Ooka-2, Minamiku, Yokohama, Japan *(Received October 29, 1976)*

Publication costs assisted by Yokohama National University

The solubility of paraffin chain alcohols, amines, hydrocarbons, rare gases, etc., in water is very small, so that a large entropy of solution is expected. Yet, the enthalpy and entropy of solution of these solutes at room temperature are small or negative. This abnormal solubility behavior has been explained coherently taking into account iceberg formation of water molecules surrounding the solute molecules. The enthalpy and entropy of solution of hydrocarbons in water determined from the temperature dependence of solubility were divided into contributions due to mixing and to iceberg formation of solvent. It is concluded that the enthalpy of mixing of solute with water is as large as expected from widely different intermolecular forces, but is largely cancelled by the enthalpy decrease due to iceberg formation of water. Thus, the apparent enthalpy of solution is slightly positive, zero, or negative around room temperature (0–80 °C). Unlike currently accepted views on so-called hydrophobic bonding, it is concluded that the slight solubility of these solutes in water is mainly the effect of a large positive enthalpy of mixing, which at lower temperature is diminished (and the solubility promoted) by a large negative enthalpy of iceberg formation in the surrounding water. The small temperature dependence of solubility of nonelectrolytes in water at room temperature occurs because in that temperature range the large negative enthalpy of iceberg formation cancels the large positive enthalpy of mixing. Enthalpy loss due to iceberg formation of water is larger than the corresponding entropy loss, so that iceberg formation is not the entropy effect. These conclusions are widely applicable to the solubility behavior of most substances in water, including biocolloids.

Introduction

The enthalpy, entropy, and Gibbs free energy of solution of a second component from a pure liquid state to a solute state are expressed as

$$\Delta\overline{H}_2 - T\Delta\overline{S}_2 = \Delta\overline{G}_2 = RT \ln a_2 = RT \ln (p_2/p_2^0) \qquad (1)$$

where a_2 is the activity relative to the pure liquid, and p_2 and p_2^0 are the vapor pressures of the second component in equilibrium with the solution and pure liquid 2, respectively.

The entropy of dissolution of a liquid (second component) in a liquid for regular solution is

$$\Delta\overline{S}_2 = -R \ln x_2 \qquad (\mathrm{L_2 \ in \ L_1}) \qquad (2)$$

where x_2 is the solubility of the second component expressed as mole fraction.[1]

If the mutual solubility of a liquid–liquid mixture is small, the vapor pressure of the solute is close to that of the pure liquid, i.e., $\ln a_2 \approx 0$ and we obtain

$$RT \ln (p_2/p_2^0) \approx 0 \approx \Delta\overline{H}_2 + RT \ln x_2 \qquad (3)$$

It is evident from eq 3 that the enthalpy of a solution is large if the solubility is small. However, the enthalpy of aqueous solutions of many substances, as determined from the temperature dependence of the solubility

$$\Delta\overline{H}_2 = -R\left(\frac{\partial \ln x_2}{\partial (1/T)}\right)_{\mathrm{satd}} \qquad (4)$$

is generally small or even negative at 10–25 °C. Two examples of alcohols in water are shown in Figure 1.[2-4]

In order to explain this important abnormality, i.e., a large entropy of dilution, $-R \ln x_2$, and a small or negative entropy of solution, $R(\partial \ln x_2/\partial \ln T)$, Frank and Evans postulated that water molecules surrounding solute molecules form frozen patches or microscopic icebergs.[5] The solute molecule brings about an increase in the total amount of "order" in the water.[6] In the present paper, the apparently abnormal solubility behavior of solutes in water is explained coherently by adoption of the concept of iceberg formation of water molecules. Several misinterpretations concerning hydrophobic bonding are elucidated.

Correlations among Solubility Curves

The logarithm of solubility vs. the reciprocal of temperature is linear in ordinary solutions just as is the logarithm of vapor pressure vs. the reciprocal of temperature. The slope multiplied by $-R$ is equal to the enthalpy of solution. Below the melting point of a solute, the solubility decreases more rapidly and the slope discontinuously increases in the amount ΔH_2^{f} and ΔS_2^{f}.

$$\Delta\overline{H}_2(\mathrm{S_2 \ in \ L_1}) = \Delta\overline{H}_2(\mathrm{L_2 \ in \ L_1}) + \Delta H_2^{\mathrm{f}} \qquad (5)$$

$$\Delta\overline{S}_2(\mathrm{S_2 \ in \ L_1}) = -R \ln x_2 + \Delta S_2^{\mathrm{f}} \qquad (6)$$

The solubility curve deviates downward as compared to that of a supercooled liquid in liquid.

Contrary to this, the solubility curve may deviate upward if solvent molecules surrounding the solute partially solidify or form icebergs, because the change in properties of the surrounding solvent molecules is reflected upon the partial molal quantity of a solute in dilute solution. The extent of partial solidification of solvent molecules surrounding the solute may increase with decreasing temperature and thereby provide an increasing negative enthalpy term. Thus, the slope of the solubility curve may also decrease progressively. The temperature dependence of these solubility phenomena are illustrated in Figure 2.

Enthalpy of Mixing of Hydrocarbons in Water

The surface tension, γ, of liquids is a direct measure of intermolecular forces. For saturated hydrocarbons, whose intermolecular forces are purely dispersion forces, $\gamma_2 = 20{\sim}26$ dyn/cm. For water, $\gamma_1 = 72.8$ dyn/cm, which is

TABLE I: Analysis of the Enthalpy and Entropy of Solution of Liquid Hydrocarbons in Water at 25 °C (First Approximation)[a]

Solute	$\Delta\overline{H}_2{}^b =$	$\Delta\overline{H}_2(\text{H bonds}) +$	$n\Delta\overline{H}_i$	$\Delta\overline{S}_2{}^c =$	$R \ln x_2 +$	$\Delta\overline{S}_2(\text{H bonds}) +$	$n\Delta\overline{S}_i$	$\overline{T}_i$,[d] K	V_2, cm^3
C_6H_6	+580 =	8100	− 7520	+1.9 =	15.4 +	7.2	− 20.7	363	89
$CH_3C_6H_5$	+640 =	9260	− 8620	+2.2 =	17.9 +	7.9	− 23.6	365	107
$C_2H_5C_6H_5$	+400 =	10500	− 10100	+1.4 =	20.4 +	8.4	− 27.4	370	123

[a] Numerical values in Table I are not accurate, but are indispensable to draw semiquantitative or qualitative conclusions. Enthalpy of solution = $\Delta\overline{H}_2 = -R[\partial \ln x_2/\partial(1/T)]_{\text{satd}}$; entropy of solution = $\Delta\overline{H}_2/T$; enthalpy [entropy] of mixing (H bonds interaction) = $\Delta\overline{H}_2$(H bonds) [$\Delta\overline{S}_2$(H bonds)]; entropy of dilution = $-R \ln x_2$; enthalpy of iceberg formation = $n\Delta\overline{S}_i$; mean temperature of iceberg formation = $\overline{T}_i = \Delta\overline{H}_i/\Delta\overline{S}_i$; Molar volume at 25 °C = V_2. [b] cal/mol. [c] cal/(deg mol). [d] $\overline{T}_i = \Delta\overline{H}_i/\Delta\overline{S}_i$.

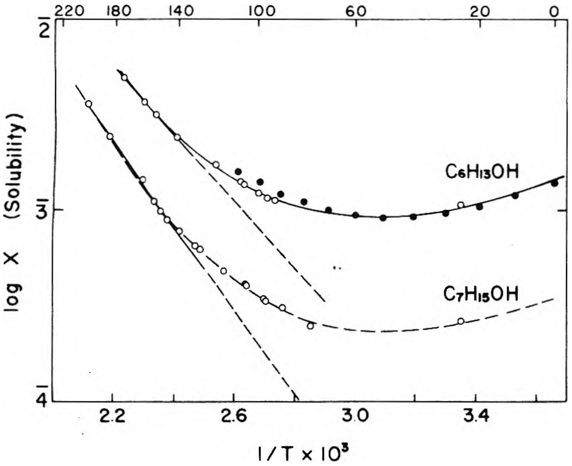

Figure 1. Solubility of hexanol and heptanol in water as a function of temperature.

the sum of the contributions of dispersion forces and hydrogen bonding interactions. The interfacial tension between water and saturated hydrocarbons, γ_{12}, is about 50~52 dyn/cm at 20 °C. Introducing these values into the Fowkes's equation, which relates the interfacial tension to surface tensions of respective components

$$\gamma_{12} = \gamma_1 + \gamma_2 - 2(\gamma_1{}^d\gamma_2)^{1/2} \tag{7}$$

Fowkes can evaluate the contribution of dispersion forces to the surface tension of water, which is $\gamma_1{}^d = 21.8 \pm 0.7$.[7] This value is close to that of saturated hydrocarbons, i.e., the dispersion energy per unit volume of water is close to that of the hydrocarbon. Hence, the enthalpy of mixing of hydrocarbons with water is mostly due to changes in the hydrogen bonding interaction in the water surrounding the solute.

In dissolution of saturated hydrocarbons in water, the destruction of hydrogen bonding interactions and the formation of "icebergs" in the water surrounding the solute molecules may be the dominating processes. The enthalpy and entropy of solution of sparingly soluble hydrocarbons in water is expressed as follows:

$$\Delta\overline{H}_2 = \Delta H_2(\text{H bonds}) + n\Delta\overline{H}_i \tag{8}$$

$$\Delta\overline{S}_2 = -R \ln x_2 + \Delta S_2(\text{H bonds}) + n\Delta\overline{S}_i \tag{9}$$

Where $n\Delta\overline{H}_i$ ($n\Delta\overline{S}_i$) is the change in the partial molal enthalpy (entropy) of the solute due to iceberg formation of n moles of solvent, ΔH_2(H bonds) [ΔS_2(H bonds)] is the partial molal enthalpy (entropy) of the solute due to the decrease in hydrogen bonding interactions, and $-R \ln x_2$ is the entropy of dilution.

The extent of iceberg formation of the solvent (as shown by the value of n) will diminish with a rise in temperature, and the enthalpy of solution, $-R[\partial \ln x_2/\partial(1/T)]$, should approach a more constant value. The enthalpy of solution at the temperature at which iceberg formation disappears (~160 °C) may be evaluated as follows:

$$-R\frac{\partial \ln x_2}{\partial(1/T)} = \Delta\overline{H}_2 = \Delta\overline{H}_2(\text{H bonds}) \quad \text{at } 160\ ^\circ\text{C} \tag{10}$$

$$\Delta\overline{H}_2/T = \Delta\overline{S}_2 = -R \ln x_2 + \Delta S_2(\text{H bonds}) \quad \text{at } 160\ ^\circ\text{C} \tag{11}$$

Once ΔH_2(H bonds) and ΔS_2(H bonds) are determined, $n\Delta\overline{H}_i$ or $n\Delta\overline{S}_i$ may be evaluated from the solubility and the temperature dependence of the solubility at any temperature with eq 8 and 9.

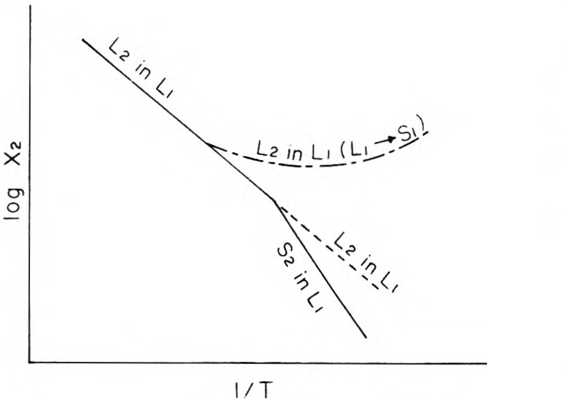

Figure 2. Schematic diagram of the correlations among the solubility vs. temperature curves of solid in liquid, liquid in liquid, and liquid in liquid accompanied with iceberg formation of solvent. The logarithm of solubility vs. $1/T$ is nearly straight, but the slope suddenly increases below the melting point of solute and the solubility of solid deviates downward compared that of the supercooled liquid. In the case when solvent molecules surrounding solute form icebergs with the consequent decrease in enthalpy of solution the solubility of solute will deviate upward. The slope, $\partial \ln x_2/\partial(1/T)$ will decrease gradually according to the increase in iceberg formation at lower temperature as shown in dashed curve.

Analysis of the Temperature Dependence of the Solubility of Hydrocarbons in Water

The solubilities of aromatic hydrocarbons in water are known up to 250 °C or so.[8,9] The logarithms of solubilities vs. the reciprocal of temperature are plotted in Figure 3.

The temperature dependence of solubility, $-\partial \ln x_2/\partial(1/T)$, increases at higher temperatures and it becomes almost constant at ~160 °C where iceberg formation of water seems mostly to disappear. If there is no iceberg formation, the enthalpy of solution, i.e., the slope, may be nearly constant. The straight lines in Figure 3 express the solubility of the respective liquid hydrocarbons in water assuming no iceberg formation.

The enthalpy and entropy of solution of liquid hydrocarbons in water at 25 °C are calculated from the temperature dependence of the solubility and shown in Table I.

The enthalpy of solution, ΔH_2(H bonds), is obtained from the slope of straight lines in Figure 3, then the en-

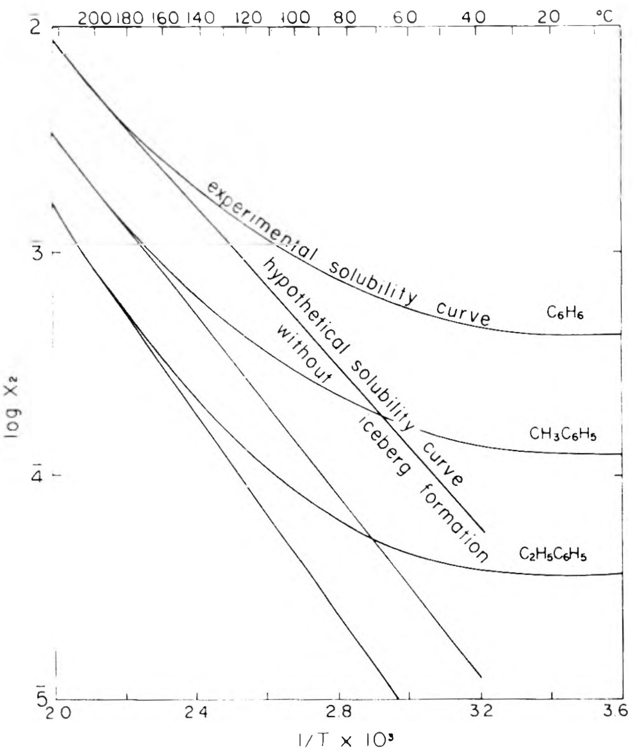

Figure 3. The solubility of aromatic hydrocarbons in water as a function of reciprocal temperature.

thalpy change due to iceberg formation, $n\Delta\bar{H}_i$, is readily obtained using eq 8. The entropy change due to hydrogen bonding interactions, ΔS_2(H bonds), is evaluated with eq 11, and $n\Delta\bar{S}_i$ is then obtained from eq 9. All these values are summarized in Table I. As the solubilities of water in these hydrocarbons are so small, $x \approx 10^{-3}$, the separated hydrocarbon phase can be assumed to be a pure phase.[10] The numerical values in Table I are not accurate because of the long extrapolation assuming a constant slope and somewhat arbitrary temperature at which the slope is drawn.

The enthalpy of mixing is approximately proportional to the molal volumes of respective alkanes, and the ratio of $\Delta\bar{H}_i/\Delta\bar{S}_i$ = 360~380 K, mean temperature of iceberg formation analyzed at 25 °C, is nearly constant for all hydrocarbons examined. As iceberg formation proceeds above room temperature, this is a reasonable value as a first approximation. Kauzmann obtained a very low temperature, because he used $\Delta\bar{H}_2$ for his calculation.[11] The amount of enthalpy and entropy loss due to iceberg formation decreases with temperature rise and the ratio of these value is enhanced as would be expected. These relations support the consistency of the present theory. Unlike currently accepted views,[11,12] it is evident from Figure 3 and Table I that the enthalpy of mixing is a large positive value as would be expected on the basis of intermolecular forces. A small negative enthalpy of solution, $\Delta\bar{H}_2$, results from a large positive enthalpy of mixing and a large negative enthalpy of iceberg formation. Table I and Figure 3 are useful to demonstrate that the small solubility of hydrocarbons in water results mainly from the large positive enthalpy of mixing, and the enthalpy of iceberg formation is largely cancelled by the accompanying entropy decrease at 25 °C, and that the solubility increase from the solid lines to the experimental curves in Figure 3 is due to the iceberg formation. This conclusion is opposite to that of Nemethy and Scheraga, who concluded iceberg formation depressed solubility.[12] Recent findings by Patterson and Barbe[13] are consistent with the present conclusions. Ideal entropy of mixing is used in the present systems, because the simplified Flory–Huggins entropy is certainly an overestimate in these systems.[14,15]

Conclusion

(1) The enthalpy of solution of hydrocarbons in water has a large positive value at temperatures above 160 °C, where iceberg formation of water molecules surrounding solute molecules becomes negligible.

(2) The enthalpy of solution of hydrocarbon in water gradually diminishes with decrease in temperature due to a negative enthalpy of iceberg formation of the surrounding water molecules.

(3) The small or negative enthalpy of solution of hydrocarbons at room temperature results from a large positive enthalpy of mixing (decrease in hydrogen bonding interaction of adjacent water) and a large negative enthalpy of iceberg formation.

(4) The large negative standard entropy of solution also results from iceberg formation.

(5) Iceberg formation is somewhat similar to a liquid–solid phase change. Such a phase change always involves both an enthalpy and an entropy changes. It is not an entropy process.

(6) Solubility increases due to the iceberg formation. Namely, the actual solubility curve is shifted to higher concentration than the hypothetical solubility curve in which no iceberg formation occurs.

References and Notes

(1) J. H. Hildebrand and R. L. Scott, "Regular Solutions", Prentice-Hall, Englewood Cliffs, N.J., 1962.
(2) F. Fontein, *Z. Phys. Chem.*, **73**, 212 (1910).
(3) H. Fühner, *Berichte*, **57**, 510 (1924).
(4) K. Kinoshita, H. Ishikawa, and K. Shinoda, *Bull. Chem. Soc. Jpn.*, **31**, 1081 (1958).
(5) H. S. Frank and M. W. Evans, *J. Chem. Phys.*, **13**, 507 (1945).
(6) A. Ben-Naim, *J. Phys. Chem.*, **69**, 3240 (1965).
(7) F. M. Fowkes, *J. Phys. Chem.*, **67**, 2538 (1963).
(8) "API Technical Data Book-Petroleum Refining", 2nd ed, American Petroleum Institute, 1970.
(9) A. N. Guseva and E. I. Parnov, *Vestn. Mosk. Univ., Khim.*, **18**, 76 (1963); *Chem. Abstr.*, **58** 9673*f*; R. L. Bohon and W. F. Claussen, *J. Am. Chem. Soc.*, **73**, 1751 (1951); D. M. Alexander, *J. Phys. Chem.*, **63**, 1021 (1959).
(10) C. Black, G. G. Joris, and H. S. Taylor, *J. Chem. Phys.*, **16**, 537 (1948).
(11) W. Kauzmann, *Adv. Protein Chem.*, **14**, 1 (1959).
(12) G. Nemethy and H. A. Scheraga, *J. Chem. Phys.*, **36**, 3401 (1962).
(13) D. Patterson and M. Barbe, *J. Phys. Chem.*, **80**, 2435 (1976).
(14) K. Shinoda and J. H. Hildebrand, *J. Phys. Chem.*, **61**, 789 (1957); **65**, 1885 (1961).
(15) Reference 1, pp 29–33 and 147–149.

Standards for Magnetic Measurements. A Comparison and a Proposal for the Use of Tetramethylethylenediammonium Tetrachlorocuprate(II)

David B. Brown,[1a] Van H. Crawford,[1b] James W. Hall,[1b] and William E. Hatfield*[1b]

Department of Chemistry, University of North Carolina, Chapel Hill, North Carolina 27514 and Department of Chemistry, University of Vermont, Burlington, Vermont 05401 *(Received January 14, 1976)*

The magnetic properties of three compounds which are appropriate as magnetic susceptibility standards have been studied in detail. A new value of -1.86 ± 0.01 K has been determined for the Weiss constant of HgCo(NCS)$_4$, and the zero-field splitting parameter, D, has been found to be $+19 \pm 3$ cm^{-1} with g being 2.22 ± 0.03. The magnetic data for bis(2,2′-bipyridine)thioureacopper(II) perchlorate may be reproduced accurately from the expression $M = Ng\beta JB_J(X)$ where $B_J(X) = [(2J+1)/2J] \coth \{[(2J+1)/2J]X\} - (1/2J) \coth (X/2J)$ and $X = g\beta JH/kT$ using $g = 2.1175$, the average of the single crystal EPR g values. The magnetic data for $[(CH_3)_2NHCH_2CH_2NH(CH_3)_2]CuCl_4$ may also be reproduced by these expressions using $g = 2.15$. This latter compound is suggested to be a convenient magnetic susceptibility standard.

Introduction

Magnetic susceptibilities are measured over wide ranges of temperature and magnetic fields, and these ranges have been expanding as technology has progressed. Precise measurements, which are necessary for adequate characterization of materials, require standards that have well-known values under the conditions that they are used. A number of materials have been used as magnetic susceptibility standards, including water, mercury, $Cu(SO_4)\cdot 5H_2O$, $Ni(en)_3(S_2O_3)$, nickel, and HgCo(NCS)$_4$. This last complex has enjoyed wide popularity in recent years with systems designed for the study of the susceptibilities of transition metal complexes.[2,3]

In view of the 4% discrepancy[2,3] in the reported values of the magnetic susceptibility of HgCo(NCS)$_4$ based on the Curie–Weiss law fits, it is clear that additional measurements are required. This compound as well as the previously reported bis(2,2′-bipyridine)thioureacopper(II) perchlorate, $[Cu(bpy)_2(tu)][ClO_4]_2$, were further investigated at low temperatures and high magnetic fields and the results of those studies are reported herein.

There are disadvantages to the use of both of these materials. We have found that tetramethylethylenediammonium tetrachlorocuprate satisfies all the requirements of a general susceptibility standard, and we report its preparation and properties here.

Experimental Section

The compounds HgCo(NCS)$_4$[2] and $Cu(bpy)_2tu(ClO_4)_2$[4] were prepared by literature methods.

$[(CH_3)_2NHCH_2CH_2NH(CH_3)_2]CuCl_4$. Four grams of tetramethylethylenediamine were neutralized and acidified by the careful addition of 12.0 mL of concentrated HCl. The resulting solution was added to a solution containing 12.0 g of $CuCl_2\cdot 2H_2O$ in 15 mL of 3 M HCl. After stirring for 0.5 h, this solution was added slowly to 300 mL of acetone with vigorous stirring. The resulting yellow precipitate was filtered, washed extensively with acetone, and dried under vacuum: yield, 8.4 g.

Anal. Calcd for $C_6N_2H_{18}CuCl_4$: C, 22.27; H, 5.61; Cu, 19.64. Found (two independent preparations): C, 22.23, 22.33; H, 5.61, 5.41; Cu, 19.09, 19.66. Analyses for carbon and hydrogen were performed by Integral Microanalytical Laboratories, Inc., Raleigh, N.C.

Magnetic susceptibilities were measured at room temperature by the Faraday method using a Cahn RG-100 electrobalance and a Varian V4004 magnet. In the temperature range 1.5–100 K, Princeton Applied Research Models 155/150A and 155/151 vibrating sample magnetometers (VSM) were used. Each VSM was calibrated with a sphere of very pure nickel metal.[5] Temperatures were measured using a Ga/As diode driven by a 100-μA constant current source; the voltage across the diode junction was monitored with a Dana Model 4700 digital multimeter. The working diode, located directly above the sample on the drive rod,[6] was calibrated vs. a calibrated diode supplied by Lake Shore Cryotronics, Inc. A continuous relationship between voltage and temperature was generated using a Chebyshev polynomial. The accuracy of the temperatures which can be measured with the diode in the field independent range is estimated to be better than 0.1%.

Results and Discussion

There are several factors which must be considered in the selection of a standard for susceptibility measurements. The material must be easily prepared (or obtained) in pure form, should be stable for long periods of time in all environments to which it will be subjected, and should have well-known magnetic properties as a function of temperature and magnetic fields. There may be other requirements which are dictated by the experimental method to be employed, and these requirements may limit the choice of a standard. Regarding the common calibrants for magnetic susceptibility, the two liquids, mercury and water, are diamagnetic with quite small values[3] of χ_g, and, consequently, they are only useful for work with diamagnetic materials. Hydrated salts, such as $Cu(SO_4)\cdot 5H_2O$, suffer the disadvantage of losing waters of hydration when finely ground or exposed to vacuum.

Although impractical for use with the Guoy or Faraday balance, pure nickel metal is quite satisfactory for calibration purposes when the required saturation field is easily obtained, and this material has the advantage that the susceptibility is not highly temperature dependent. This latter property is a disadvantage for use in determining temperatures from susceptibilities.

HgCo(NCS)$_4$. The compound HgCo(NCS)$_4$ has been used frequently as a magnetic susceptibility standard for Gouy and Faraday techniques because of its properties of being easily prepared in pure form, stable, and convenient to handle under the experimental conditions of these techniques, e.g., it easily packs in Gouy tubes. The results of Figgis and Nyholm[2] had been accepted for many years,

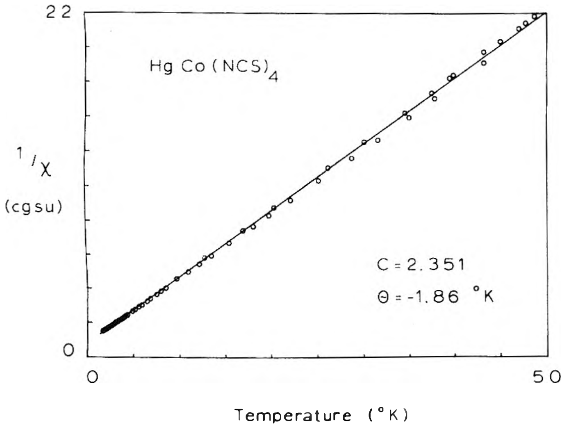

Figure 1. Inverse molar magnetic susceptibility data (O) for $HgCo(NCS)_4$. Curie-Weiss law line calculated with C = 2.351 and θ = −1.86 K.

but recently Räde[3] remeasured the magnetic properties of $HgCo(NCS)_4$ and obtained different results. The 4% difference between the values obtained by these workers is significantly greater than the precision which can be obtained in the magnetic susceptibility measurement using modern equipment. Thus, it was of real importance to reexamine the properties of this compound and to obtain reliable values for this commonly used standard.

The magnetic susceptibilities of five independently prepared samples were measured at room temperature on the Faraday balance. The ratios of sample weights to changes in weight due to the magnetic field gradient have the same ratio with an acceptable 1% experimental error. The data indicate that the results are reproducible for different preparations. The fact that one sample was over 8 years old, while three samples were prepared recently, certainly indicates good shelf-life stability.

Data were collected from 1.7 to 50 K on two samples, and the results are plotted as inverse susceptibility vs. temperature in Figure 1. Using the Curie–Weiss law in molar units, $\chi_M = C/(T - \theta)$, the best fit line is also shown in the figure, where the parameters are $C = 2.351 \pm 0.002$ and $\theta = -1.86 \pm 0.01$ K. It is important to note that these values are obtained using no corrections to the data to account for diamagnetism or temperature independent paramagnetism of the compound; therefore, they would be the appropriate values for calibrating an experimental magnetic susceptibility apparatus.

It is interesting to compare the results obtained here with those previously reported. For the gram susceptibility at 20 °C, we calculate $\chi_g = 16.20 \times 10^{-6}$ cgsu. Figgis and Nyholm[2,7] and Räde[3] both obtained 16.44×10^{-6} cgsu for χ_g at 20 °C, but Figgis and Nyholm[7] specify using a diamagnetic correction of 137×10^{-6} cgsu/mol. When this quantity is added to our value, the agreement is excellent. Räde does not specify the details of the calculation so this comparison cannot be made with his data. It is the low temperature region of the Curie–Weiss line which frequently attracts the most attention, and here we find some discrepancies, the three θ values being −10,[2,7] +2,[3] and −1.86 K (this work). The −10 K value was determined from an extrapolation of a data set collected only down to 80 K, and the +2 K value, although obtained from a data set in the region 5.8–293 K, was derived from a measurement using standards which have very small values for magnetic susceptibility. Also, the calibration apparently was carried out at a temperature almost 300 K away from the temperature axis intercept of the Curie–Weiss plot.

In order to more thoroughly investigate the magnetic properties of $HgCo(NCS)_4$, particularly in hopes of finding a convenient material to correlate high magnetic fields and low temperatures, a magnetization study was undertaken. The data collected at liquid helium temperature (4.2 K), where temperature measurement and control are not field dependent, are shown in Figure 2. The corrections applied to the data are as follows: diamagnetic correction of the atoms -190×10^{-6} cgsu/mol, and temperature independent paramagnetism of 400×10^{-6} cgsu/mol. These are very small numbers compared to the values of susceptibilities at this temperature. The best fit to the data shown as the broken line in Figure 2 was calculated from eq 1,[8] where J was taken to be 3/2 for Co^{2+} (the spin-only value) and g was found to be 1.90. The appropriate equations are

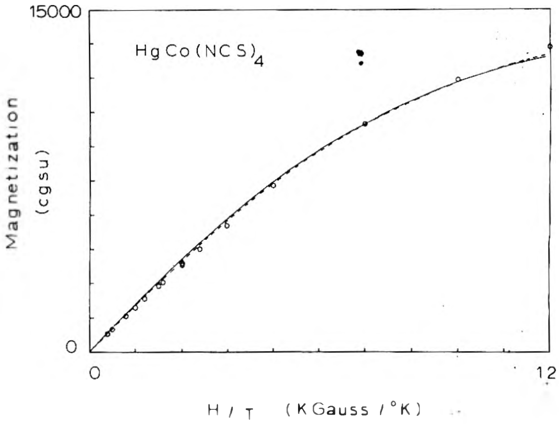

Figure 2. Magnetization data (O) at 4.2 K for $HgCo(NCS)_4$. Broken line calculated from eq 1 with J = 3/2 and g = 1.90; solid line calculated from eq 2 with J = 1.23 and g = 2.24.

$$M = Ng\beta J B_J(X) \tag{1}$$

where

$$B_J(X) = \frac{2J+1}{2J}\coth\left(\frac{2J+1}{2J}X\right) - \frac{1}{2J}\coth\frac{X}{2J}$$

and

$$X = g\beta JH/kT$$

The symbols in these equations have their usual meanings. This value of g, being less than g_e, is unreasonable for a d^7 ion. Another calculation of g, from the Curie constant, eq 2,[8] yields $g = 2.24$. The best fit for this value is shown

$$g = \left[\frac{C(3k/N\beta^2)}{S(S+1)}\right]^{1/2} \tag{2}$$

in Figure 2 as the solid line. Here J (or S') is 1.23, a value less than 3/2, which is consistent with the finite value for θ from the Curie–Weiss fit.

Since the environment of the cobalt ion is not exactly tetrahedral,[9,10] zero field splitting of the ^4A ground state is possible as a second-order effect arising from spin–orbit coupling. Figgis et al.[11,12] discuss zero-field splitting effects, but unfortunately the expressions given in their paper for the magnetic susceptibility[11] are incorrect. The correct expressions are

$$\chi_{\parallel} = \frac{N\beta^2 g^2}{4kT}\left[\frac{\dfrac{\sinh(y/2)}{y/2} + 9e^{-x}\dfrac{\sinh(3y/2)}{(3y/2)}}{\cosh(y/2) + e^{-x}\cosh(3y/2)}\right]$$

$$\chi_{\perp} = \frac{N\beta^2 g^2}{kT}\left[\frac{\dfrac{\sinh(y)}{y} + \dfrac{3}{2x}\cosh(y)e^{z} - \dfrac{3}{2x}e^{-z}e^{-x}}{e^{z}\cosh(y) + e^{-z}e^{-x}}\right]$$

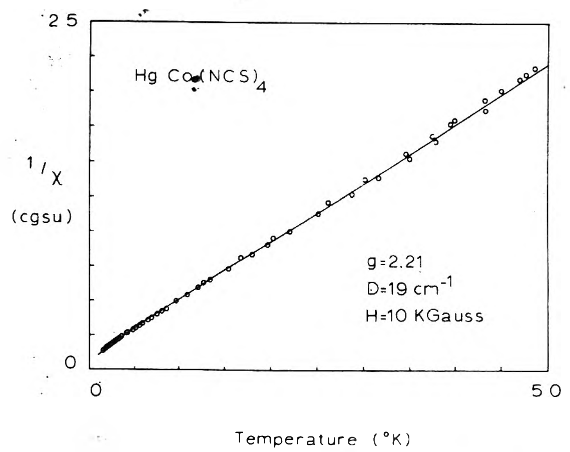

Figure 3. Inverse molar magnetic susceptibility data (O) for $HgCo(NCS)_4$. Solid line calculated from eq 3 with $g = 2.21$, $D = 19$ cm^{-1}, and $H = 10\,000$ G.

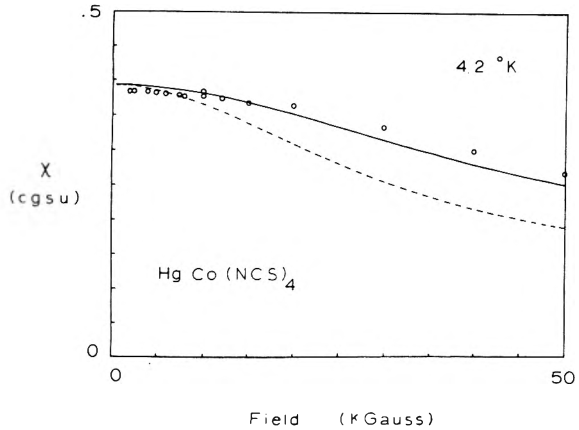

Figure 4. 4.2 K molar magnetic susceptibility data (O) for $HgCo(NCS)_4$. Solid line calculated from eq 3 with $D = 19$ cm^{-1}, dashed line calculated with $D = -19$ cm^{-1}, $g = 2.21$ for both lines.

where

$$x = D/kT$$

$$y = g\beta H/kT$$

$$z = \frac{3}{4}\frac{y^2}{x}$$

and

$$\bar{\chi} = (\chi_{\parallel} + 2\chi_{\perp})/3 \qquad (3)$$

The corrected data are plotted in Figure 3 as inverse susceptibility vs. temperature and the solid line was calculated from eq 3 with $g = 2.21$ and $D = 19$ cm^{-1}. This g value is slightly smaller than the 2.24 obtained from the Curie–Weiss law and D is quite large. It is not possible to compare the D value obtained here with the 10 cm^{-1} value reported earlier[11] because of the problem with the formulas. The magnetic susceptibilities in eq 3 are field dependent and at the lowest temperatures the susceptibilities are dependent on the sign of D. In Figure 4 the 4.2 K data are plotted as susceptibility vs. field along with the curves calculated for $D = \pm 19$ cm^{-1}. While the fit for $D = +19$ cm^{-1} is not perfect, it is clear that the negative sign is not appropriate. The calculated curves are sensitive to small changes in the parameters and the experimental error in the measured data, noticeable at 10 kG where data were obtained on different samples, does not provide the precision in the fit noted in earlier cases. However, the data convincingly show that there is a significant zero field splitting and that the sign of D may be determined from the magnetic susceptibility. For $HgCo(NCS)_4$, values of $D = 19 \pm 3$ cm^{-1} and $g = 2.22 \pm 0.03$ describe the magnetic properties very well. The negative θ value of the Curie–Weiss fit apparently arises from zero-field splitting, and there is no direct evidence of exchange interactions.

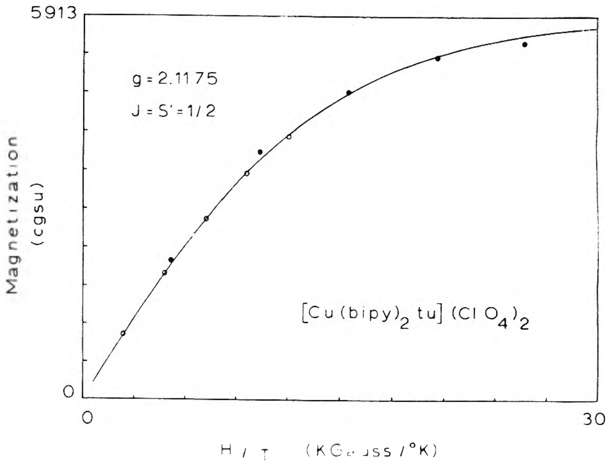

Figure 5. Magnetization data for $[Cu(bpy)_2(tu)](ClO_4)_2$ at 4.2 (O) and 1.95 K (●). Solid line calculated from eq 1 with $J = 1/2$ and $g = 2.1175$.

The existence of zero-field splitting implies that the temperature dependence of the susceptibility will not follow a Curie–Weiss law exactly, and the different values of the Weiss constant which have been reported are not surprising considering the different temperature intervals which have been examined.

$[Cu(bpy)_2(tu)][ClO_4]_2$. Long-range magnetic interactions are not desirable characteristics for magnetic susceptibility standards, rather magnetically dilute compounds are preferred. Previous magnetic susceptibility studies on the polycrystalline compound $[Cu(bpy)_2(tu)](ClO_4)_2$ ruled out the possibility of intermolecular exchange interactions. Also, the EPR data indicated that the value of the exchange constant was -0.002 cm^{-1}.[4] This compound was further investigated at low temperatures and high fields, and the magnetization data are shown in Figure 5 along with the solid line calculated from eq 1 with $J = 1/2$ and $g = 2.1175$. This value of g is the average of the principle g values obtained from the single crystal EPR data.[4] Thus, there is no parameter fitting involved and the agreement is excellent, especially for the 4.2 K data. The 1.95 K data were collected by monitoring the pressure in the sample zone and are subject to a somewhat greater error because of minor temperature fluctuations; nevertheless, the data convincingly follow the predicted behavior and this material is certainly well behaved. It is a good candidate for use in determining temperatures at high fields, via the measurement of magnetic susceptibility.

$[(CH_3)_2NHCH_2CH_2NH(CH_3)_2]CuCl_4$. In the course of our studies of the complexes formed between bifunctional bases and copper halides in acidic media, we prepared the complex tetramethylethylenediammonium tetrachlorocuprate. The observation that it appears to be a perfect Curie paramagnet attracted our attention to this material as a possible calibrant for magnetic measurements. Over the temperature range of 1.7–52 K, μ_{eff} is constant at 1.86 μ_B. The data may be fitted to a Curie–Weiss law with $\theta = -0.07$ K and $C = 0.433$. The g value obtained from the fit is 2.149. For comparison, the EPR spectrum, which is slightly asymmetric on the high-field side with a peak-to-peak width of 125 G, is centered at $g = 2.168$. Figure 6 shows the variation of the reciprocal susceptibility and effective magnetic moment for this compound with temperature, and the solid line represents the best Curie–Weiss law fit to this data. For the purpose of these calculations molar ligand diamagnetism of 217×10^{-6} cgsu

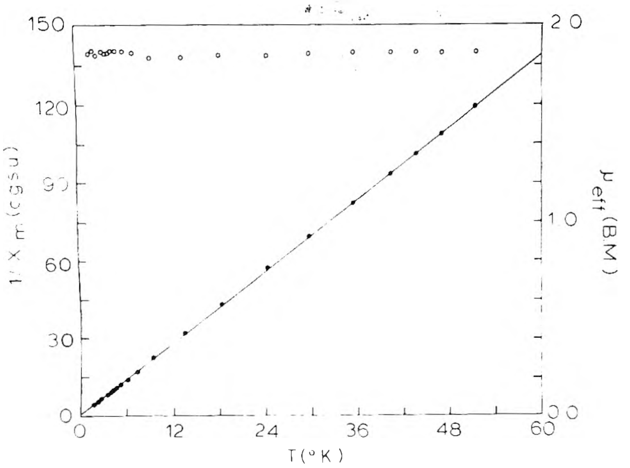

Figure 6. Magnetic data for $[(CH_3)_2NHCH_2CH_2NH(CH_3)_2]CuCl_4$; (O) magnetic moments, (●) inverse molar susceptibility; H = 10 000 G.

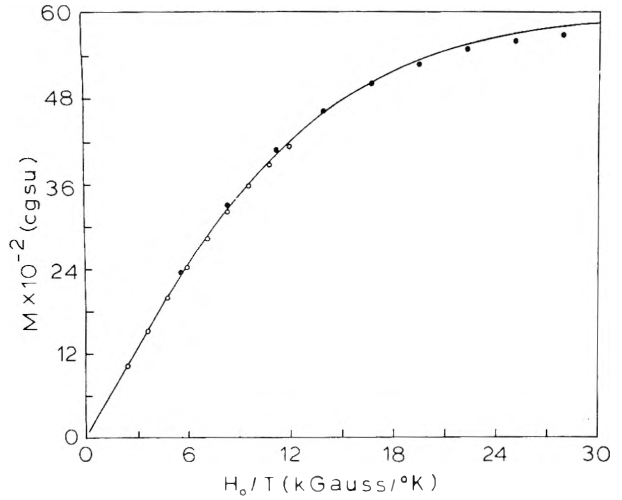

Figure 7. Magnetization data for $[(CH_3)_2NHCH_2CH_2NH(CH_3)_2]CuCl_4$ at 4.2 (O) and 1.79 K (●).

and temperature independent paramagnetism ($N\alpha$) of 60 × 10^{-6} cgsu were assumed.

Several features of this complex suggest it as a good candidate for a susceptibility standard. First, it is easily prepared in nearly quantitative yield and pure form from readily available starting materials, and it exists as a tractable powder. The complex appears to be quite stable, although it may be very slightly hygroscopic, and as a precaution it should be stored in a desiccator following initial drying. Most importantly, the nearly perfect Curie law behavior suggests that the complex contains effectively isolated tetrachlorocuprate ions, with all exchange interactions being negligible. Furthermore, since zero-field splitting is of no concern for monomeric copper(II) complexes, the field dependence of the magnetization should be readily predictable from the Brillouin function, eq 1. This is supported by the magnetization data at 4.16 and 1.79 K as shown in Figure 7. The solid line gives the calculated curve assuming a g value of 2.15 (the value derived from the Curie–Weiss law fit) and $J = 1/2$. The data at very high fields and low temperatures are subject to some error, since temperatures could be estimated only by monitoring the helium vapor pressure. Nonetheless, it is clear from these data that the complex is suitable for temperature calibration at high fields using magnetic measurements.

TABLE I: Recommended Values of Magnetic Parameters for Magnetic Susceptibility Standards

Compound	g	J	C	θ, K
$HgCo(NCS)_4$	2.22	3/2	2.35	−1.86
$[Cu(bpy)_2tu](ClO_4)_2$	2.1175	1/2	0.420	0
$[(CH_3)_2NHCH_2CH_2NH(CH_3)_2]CuCl_4$	2.149	1/2	0.433	−0.07

Conclusions

The present data allow the evaluation of these three materials as magnetic susceptibility standards. For the vibrating sample magnetometer, using a superconducting solenoid, calibration is most conveniently done at 4.2 K, and either of these standards is suitable. The magnitudes of the susceptibility values for $[Cu(bpy)_2(tu)](ClO_4)_2$ and $[(CH_3)_2NHCH_2CH_2NH(CH_3)_2]CuCl_4$ are substantially smaller than those of $HgCo(NCS)_4$ and nickel. For Faraday or Gouy systems at high temperatures where the saturation field of nickel metal may not be easily obtained, $HgCo(NCS)_4$ is clearly the best choice, since the magnitudes of the susceptibilities for the copper salts at room temperature are quite small. There is an additional disadvantage with $[Cu(bpy)_2(tu)](ClO_4)_2$; it is more difficult to prepare and must be obtained as good crystalline material to assure reproducible results. The recommended values for the magnetic parameters of the standards are collected in Table I.

Nickel is not satisfactory for determining temperatures owing to the small temperature coefficient, and $HgCo(NCS)_4$ has the disadvantage of requiring more complex expressions to evaluate the magnetic behavior at very low temperature and very high fields. Thus, $[(CH_3)_2NHCH_2CH_2NH(CH_3)_2]CuCl_4$ is the most promising material for this purpose.

Räde has recently informed us that he has determined a Weiss constant of −1.8 K using improved equipment.[13]

Acknowledgment. This research was supported by the National Science Foundation under Grant No. MPS74-11495 and by the Materials Research Center of the University of North Carolina under Grant No. DMR72-03024 from the National Science Foundation.

References and Notes

(1) (a) University of Vermont, Burlington, Vt. 05401. (b) University of North Carolina, Chapel Hill, N.C. 27514.
(2) B. N. Figgis and R. S. Nyholm, *J. Chem. Soc.*, 4190 (1958).
(3) H. St. Räde, *J. Phys. Chem.*, **77**, 424 (1973).
(4) K. T. McGregor and W. E. Hatfield, *J. Chem. Soc., Dalton Trans.*, 2448 (1974).
(5) Princeton Applied Research: Saturation moment (field) of nickel; 4.2 K, 58.19 emu/g (6 kG); 293 K, 55.01 emu/g (8 KG).
(6) R. F. Drake and W. E. Hatfield, *Rev. Sci. Instrum.*, **45**, 858 (1974).
(7) B. N. Figgis and R. S. Nyholm, *J. Chem. Soc.*, 338 (1959).
(8) J. S. Smart, "Effective Field Theories of Magnetism", Saunders, Philadelphia, Pa., 1966, Chapter 1.
(9) J. W. Jeffery, *Nature (London)*, **159**, 610 (1974).
(10) J. W. Jeffery, *Acta Crystallogr., Sect. A*, **16**, 66 (1963).
(11) B. N. Figgis, *Trans. Faraday Soc.*, **56**, 1553 (1960).
(12) B. N. Figgis, M. Gerloch, and R. Mason, *Proc. R. Soc. London*, **279**, 210 (1964).
(13) H. St. Räde, private communication.

Formation of Superoxide Ion during the Decomposition of Hydrogen Peroxide on Supported Metals

Yoshio Ono,* Tsuyoshi Matsumura, Nobumasa Kitajima, and Shun-ichi Fukuzumi

Department of Chemical Engineering, Tokyo Institute of Technology, Ookayama, Meguro-ku, Tokyo, Japan

(Received December 14, 1976)

Publication costs assisted by the Tokyo Institute of Technology

Presence of the superoxide ion (O_2^-) in the aqueous phase during the decomposition of hydrogen peroxide over supported metals has been revealed by quenching the reacting solution and measuring the ESR of the quenched ice. Observation of the superoxide ion in an aqueous phase gives direct evidence for the involvement of free-radical intermediates during peroxide decomposition by solid catalysts. The kinetics of hydrogen peroxide decomposition and of superoxide formation were studied. The rate of superoxide formation is expressed by $d[O_2^-]/d[W/F] = k_2[H_2O_2]_t - k_3[O_2^-]$, where $[H_2O_2]_t$ is the total analytical concentration of hydrogen peroxide, W is the amount of catalyst, and F is the flow rate of the solution. A reaction mechanism for the formation of the superoxide ion has been proposed based on the Haber–Weiss mechanism. It was also found that the superoxide ion trapped in ice decayed with second-order kinetics above −70 °C with an activation energy of 50 kJ/mol.

Introduction

Decomposition of hydrogen peroxide has been the subject of many investigations. The decomposition mechanism in aqueous solution with metal cations is well established based on the classical Haber–Weiss mechanism.[1-3] In some cases, free-radical intermediates have been evidenced by the ESR method.[4-8] However, the mechanism of decomposition over heterogeneous catalysts is by no means established.[9-12] As for the decomposition over metals, Weiss proposed the following radical mechanism:[10]

$$S + H_2O_2 \xrightarrow{k_{1S}} S^+ + OH^- + \cdot OH \tag{1}$$

$$H_2O_2 + \cdot OH \xrightarrow{k_{2S}} H_2O + \cdot HO_2 \tag{2}$$

$$S^+ + O_2^- \xrightarrow{k_{3S}} S + O_2 \tag{3}$$

$$S + \cdot HO_2 \xrightarrow{k_{4S}} S^+ + HO_2^- \tag{4}$$

$$S^+ + HO_2^- \xrightarrow{k_{5S}} S + \cdot HO_2 \tag{5}$$

Here, S and S^+ represent the uncharged and charged parts of the metal surface, respectively. The principal role of the metal surfaces is in the electron transfer processes, (1), (3), (4), and (5). This mechanism is based mainly on kinetic results and no direct evidence for free-radical formation has been obtained. It is not specified whether the free-radical species exist on the surface or in the aqueous phase. Thus, it is of interest to obtain direct evidence for the formation of free-radical intermediates during peroxide decomposition by solid catalysts. For this purpose, we have applied a flow technique to radical detection.[13-15] Hydrogen peroxide in an alkaline solution was passed through a column packed with the catalyst (metals supported on alumina) and was frozen at the outlet with liquid nitrogen. From the ice thus formed, a strong ESR signal due to the superoxide ion (O_2^-) was detected. This is the first direct evidence that the decomposition of hydrogen peroxide over heterogeneous catalysts involves free-radical processes and has the character of a heterogeneous–homogeneous reaction.

Formation of the O_2^- ion in the aqueous phase has been studied mainly from the viewpoint of the biological importance of the radical.[16-19] The way we adopted may provide a simple method to prepare this radical in aqueous solution.

In this work, the kinetics of superoxide ion formation by the decomposition of hydrogen peroxide over supported metals will be examined. The thermal stability of the radical trapped in ice will be also given.

Experimental Section

Catalysts. Platinum, palladium, and silver supported on alumina were obtained from Nippon Engelhard. The diameter of the pellets is 1.0–1.5 mm and the metal content is 0.5 wt %.

Gold supported on alumina was prepared as follows: Alumina from Sumitomo Chemicals was sieved into 15–24 mesh and heated in air at 550 °C for 5 h. The alumina was then immersed in an aqueous solution of $HAuCl_4$ (obtained from Wako Pure Chemical Industry) overnight, dried, and calcined in air at 400 °C for 1 h.

Reagent. An aqueous solution of hydrogen peroxide (30 wt %) was obtained from Mitsubishi Gas Chemical Industry. The concentration was determined by titration with potassium permanganate (0.1 N).

Procedure. The catalyst (0.15–1.5 g) was packed in 7-mm Pyrex tubing which was temperature controlled at 2 °C. The H_2O_2 solution was fed from a reservoir at a rate of 8 $cm^3\ min^{-1}$ with a roller pump. The concentration of hydrogen peroxide was determined by titration of the solution at the outlet with potassium permanganate under acidic condition. For determination of the superoxide ion concentration, the outflow was directly led into liquid nitrogen through a nozzle. The ice thus formed was picked up and the amount of the radical was determined by ESR at 77 K.

The ESR measurements were carried out with a JEOL X-band spectrometer (PE-1X). The radical content was determined by comparison of the area under the absorption curve for the anion and that for 1,1-diphenyl-2-picrylhydrazyl (DPPH) in benzene. The change in Q factor for the O_2^- and DPPH measurements was calibrated by use of an ESR marker included in the ESR cavity.

Results and Discussion

ESR Spectrum of O_2^-. Figure 1 shows a typical ESR spectrum of the solution frozen at the exit of the catalyst

TABLE I: Rate Constants for Hydrogen Peroxide Decomposition with Various Catalysts at 275 K

	10^3k_1, (g of catalyst)$^{-1}$ L min^{-1}	10^6k_2, (g of catalyst)$^{-1}$ L min^{-1}	10^2k_3,[a] (g of catalyst)$^{-1}$ L min^{-1}
Ag/Al_2O_3	4.0 ± 0.2	50 ± 3	1.3 ± 0.1
Pt/Al_2O_3	2.6 ± 0.3	$k_2/k_3 = (1.9 \pm 0.2) \times 10^{-4}$	
Pd/Al_2O_3	2.2 ± 0.2	4.5 ± 0.3	5.0 ± 0.3
Au/Al_2O_3	1.8 ± 0.2	2.7 ± 0.2	4.9 ± 0.4
Al_2O_3	0.26 ± 0.02	2.1 ± 0.2	4.1 ± 0.3
Charcoal	4.0 ± 0.3	8.4 ± 0.2	5.8 ± 0.3

[a] At a KOH concentration of 1.0 N.

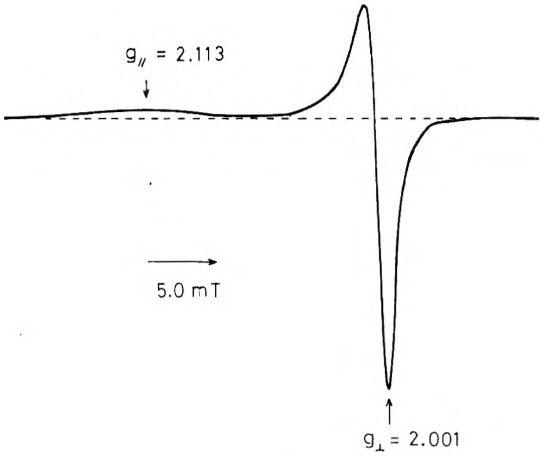

Figure 1. ESR spectrum of the O_2^- radical produced during the decomposition of H_2O_2 over Ag/Al_2O_3 in 1.0 N KOH aqueous solution.

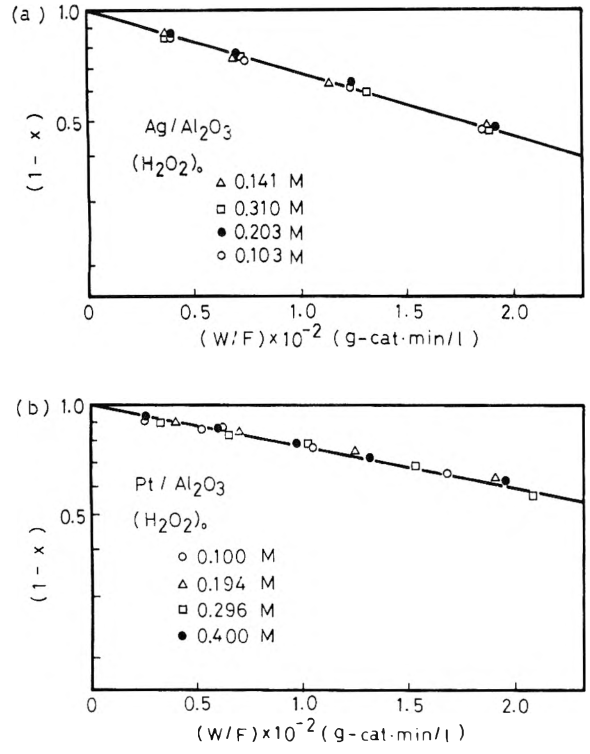

Figure 2. ln (1 − *x*) plotted against the contact time (*W*/*F*) for the H_2O_2 decomposition over (a) Ag/Al_2O_3 and (b) Pt/Al_2O_3 at various initial concentrations of H_2O_2 at 275 K; *x* is the conversion of H_2O_2, *W* is the amount of the catalyst, and *F* is the feed rate of the solution (8.0 cm^3 min^{-1}); the KOH concentration was 1.0 N.

column of silver supported on alumina. The spectrum shows a radical of axial symmetry and *g* values are $g_{\parallel} = 2.113$ and $g_{\perp} = 2.001$. From a comparison of the *g* values with those in literatures,[16-18] the paramagnetic species was assigned to the superoxide ion (O_2^-). No other paramagnetic species such as $\cdot OH$ or $\cdot HO_2$ were detected.

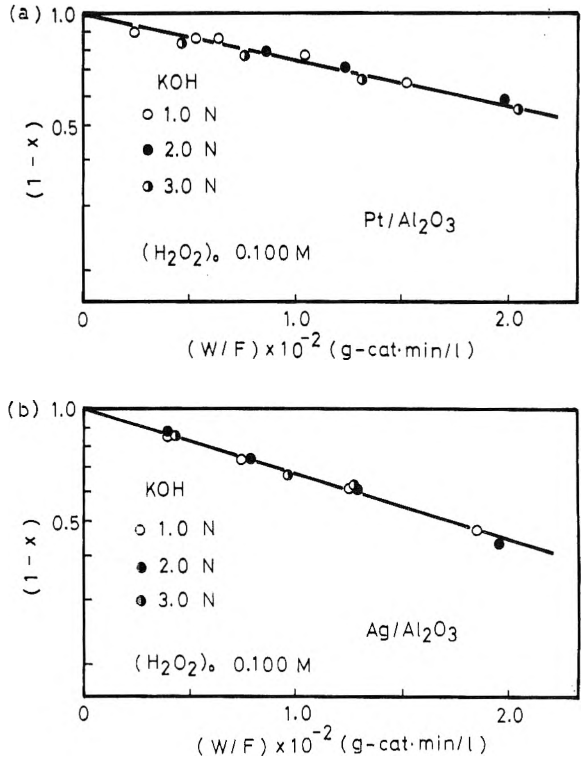

Figure 3. ln (1 − *x*) plotted against the contact time (*W*/*F*) for the H_2O_2 decomposition over (a) Pt/Al_2O_3 and (b) Ag/Al_2O_3 at various KOH concentrations at 275 K; the initial concentration of hydrogen peroxide was 0.100 M.

Kinetics of H_2O_2 Decomposition. The conversion (*x*) of H_2O_2 was measured as a function of catalyst amount (*W*) in the column. The feed rate (*F*) of the solution was kept constant at 8.0 cm^3 min^{-1}. Figure 2a,b shows a plot of ln (1 − *x*) against *W*/*F* for decomposition over Ag/Al_2O_3 and Pt/Al_2O_3, respectively. In each case, a straight line was obtained and the slope of the line was independent of the initial concentration of H_2O_2. Thus, the decomposition is the first order with respect to peroxide concentration:

$$-d[H_2O_2]_t/d[W/F] = k_1[H_2O_2]_t \qquad (6)$$

where $[H_2O_2]_t$ is the total analytical concentration of hydrogen peroxide.

First-order kinetics hold for H_2O_2 decomposition by all the catalyst used in this study. Figure 3a,b shows that the rate of decomposition both on silver and on platinum is almost independent of the concentration of potassium hydroxide. The values of the rate constant, k_1, for the various catalysts are summarized in Table I.

O_2^- Formation on Ag/Al_2O_3. The concentration of the superoxide ion at the column exit was calculated from the ESR intensity of the frozen solution. The concentration of the superoxide ion formed by decomposition on Ag/Al_2O_3 was plotted as a function of the contact time (*W*/*F*) in Figure 4. The radical concentration increases with the contact time and then, through a maximum, it decreases

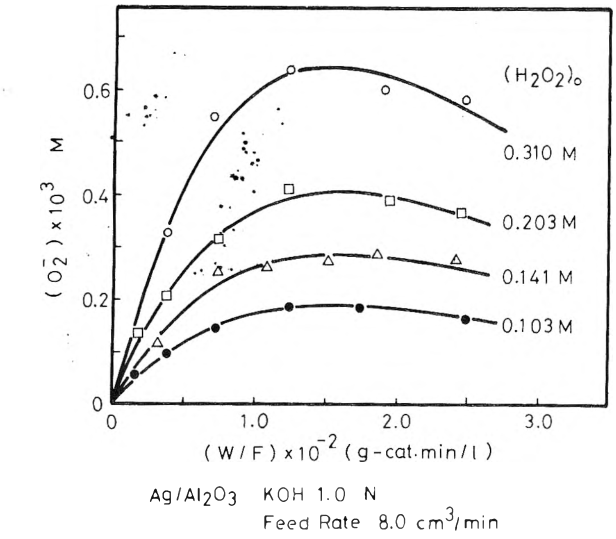

Figure 4. Concentration of O_2^- plotted against the contact time (W/F) during the H_2O_2 decomposition for different initial concentrations of H_2O_2 at 275 K; the catalyst was Ag/Al_2O_3; the KOH concentration was 1.0 N.

with further contact with the catalyst. At the maximum, an O_2^- yield of as high as 0.62 mM is obtained. The contact time which gives the maximum yield of O_2^- is independent of the initial concentration of hydrogen peroxide and is 140 (g of catalyst) min L^{-1}.

The rate of superoxide formation can be expressed by the following equation:

$$d[O_2^-]/d[W/F] = k_2[H_2O_2]_t - k_3[O_2^-] \qquad (7)$$

Rate eq 7 was confirmed in the following manner.

The initial rate of O_2^- formation is given by

$$d[O_2^-]/d[W/F] = k_2[H_2O_2]_{0t} \qquad (8)$$

where $[H_2O_2]_{0t}$ is the initial analytical concentration of hydrogen peroxide. The initial rate of O_2^- formation determined from the slope of Figure 4 in the low W/F region is proportional to the initial concentration of hydrogen peroxide and the value of k_2 is determined as 5.0 ± 0.3 × 10^{-5} L min^{-1} (g of catalyst)$^{-1}$.

Integration of eq 7 using eq 6 gives

$$[O_2^-] = \frac{k_2[H_2O_2]_{0t}}{k_1 - k_3}[\exp(-k_3W/F) - \exp(-k_1W/F)] \qquad (9)$$

The contact time which gives the maximum yield of superoxide is obtained by differentiating eq 9 and is expressed by

$$(W/F)_{max} = \ln (k_1/k_3)/(k_1 - k_3) \qquad (10)$$

This agrees with the experimental fact that the contact time which gives the maximum yield of superoxide ion is independent of the initial concentration of hydrogen peroxide. By setting $(W/F)_{max}$ = 130 (g of catalyst) min L^{-1} and k_1 = 4.0 ± 0.2 × 10^{-3} (g of catalyst)$^{-1}$ L min^{-1}, one obtains the k_3 value of 1.3 ± 0.1 × 10^{-2} L min^{-1} (g of catalyst)$^{-1}$.

Using the determined values of k_1, k_2, and k_3, the solid curves in Figure 4 were drawn. The agreement of the calculated lines with the experimental results is fairly good.

Effect of KOH Concentration. The effect of the concentration of potassium hydroxide on O_2^- formation is illustrated in Figure 5, which shows that the initial rate of O_2^- formation is independent of KOH concentration; the rate constant k_2 is independent of KOH concentration, but the maximum O_2^- concentration increases with increasing KOH concentration. As described earlier, the first-order rate constant k_1 for H_2O_2 decomposition does not depend on the KOH concentration, then the value of k_3, the decay rate constant of O_2^-, should decrease with increasing KOH concentration. From Figure 5, the values of k_3 are determined as 13 ± 1 × 10^{-3} (g of catalyst)$^{-1}$ L min^{-1} ([KOH] = 1.0 N), 6.8 ± 0.5 × 10^{-3} (g of catalyst)$^{-1}$ L min^{-1} ([KOH] = 2.0 N), 4.5 ± 0.2 × 10^{-3} (g of catalyst)$^{-1}$ L min^{-1} ([KOH] = 3.0 N).

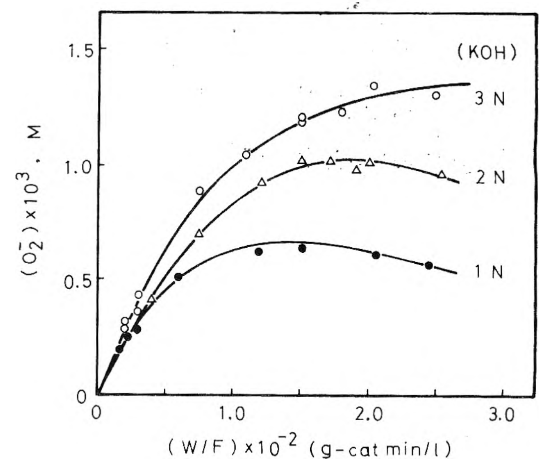

Figure 5. Concentration of O_2^- plotted against the contact time (W/F) during the H_2O_2 decomposition for different KOH concentrations at 275 K; the catalyst was Ag/Al_2O_3; the initial concentration of H_2O_2 was 0.300 M.

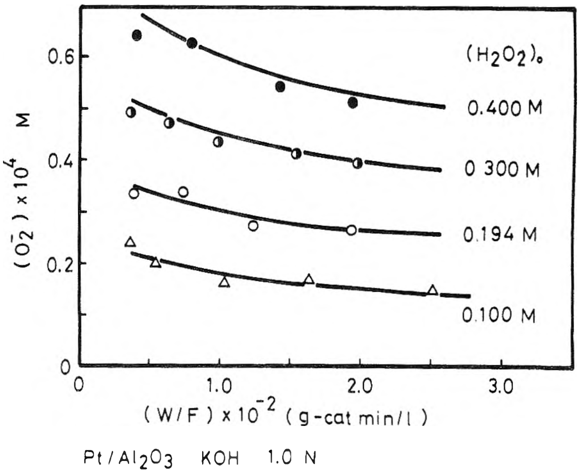

Figure 6. Concentration of O_2^- plotted against the contact time (W/F) during the H_2O_2 decomposition over Pt/Al_2O_3 at 275 K; the KOH concentration was 1.0 N.

O_2^- Formation on Pt/Al_2O_3. As stated earlier, the rate of decomposition of hydrogen peroxide over Pt/Al_2O_3 is first order. Figure 6 shows the dependence of the superoxide concentration on the contact time (W/F) in this system. The superoxide concentration is an order of magnitude smaller than that observed in the case of Ag/Al_2O_3. The superoxide concentration is proportional to the initial concentration of hydrogen peroxide. Under our experimental conditions, it decreases with increasing contact time (W/F). It was also found that the superoxide concentration increased with increasing KOH concentration. By assuming the same kinetics as in the case of Ag/Al_2O_3, the ratio of the rate constants k_2 and k_3 is estimated from the results in Figure 6 and is listed in Table I. Using the determined ratio, k_2/k_3, and the rate constant for decomposition, k_1, the solid curves in Figure 6 were drawn. The agreement between the calculated lines and the experimental points is good.

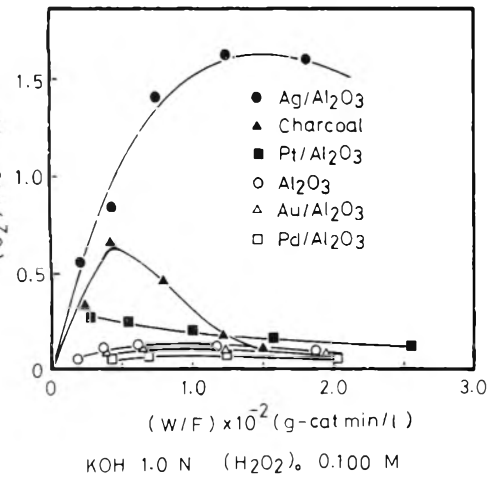

Figure 7. Comparison of O_2^- concentration plotted against the contact time (W/F) during the H_2O_2 decomposition over various catalysts at 275 K; the initial concentration of H_2O_2 was 0.100 M; the KOH concentration was 1.0 N.

Decomposition over Other Catalysts. The decomposition of hydrogen peroxide and the formation of the superoxide ion were studied also on Pd/Al_2O_3, Au/Al_2O_3, alumina, and charcoal. The decomposition is first order in every case and the rate constants are listed in Table I. The concentrations of superoxide ion were compared together with the cases of Ag/Al_2O_3 and Pt/Al_2O_3 in Figure 7. Applying the same kinetic equation (eq 7) as in the case of Ag/Al_2O_3, the kinetic parameters k_2 and k_3 are estimated and listed in Table I.

Mechanism of O_2^- Formation. Observation of the superoxide ion in the aqueous phase clearly indicates that the decomposition of hydrogen peroxide on heterogeneous catalysts involves free-radical processes at least partly and that the radical formed on the surfaces can desorb into the homogeneous phase as a superoxide ion. Thus, we assume that some of the superoxide ion formed on the surface desorbs without transferring an electron into the metal.

If one assumes the mechanism proposed by Weiss,[10] eq 1–6, and uses the steady-state approximation for ·OH, ·HO_2, and S^+, then the rate of H_2O_2 decomposition, r, is given by[10]

$$r = -\frac{d[H_2O_2]_t}{d[W/F]} = \frac{2k_{1s}\Gamma_s\sigma[H^+]}{(\Gamma_s + [H^+])(K_{H_2O_2(a)} + [H^+])} \times [H_2O_2]_t \qquad (11)$$

where $\sigma = [S] + [S^+]$, $\Gamma_s = (k_{3s}k_{5s}K_{HO_2(a)}K_{H_2O_2(a)}/k_{1s}k_{4s})^{1/2}$, and $K_{HO_2(a)}$ and $K_{H_2O_2(a)}$ are the dissociation constants of the perhydroxyl radical and hydrogen peroxide in the adsorbed states. The dissociation constant of H_2O_2 in aqueous solution, $K_{H_2O_2}$, is 1.7×10^{-12} M at 20 °C.[20] Under our experimental conditions, $K_{H_2O_2}$ is much greater than $[H^+]$; $K_{H_2O_2} >> [H^+]$. If $K_{H_2O_2(a)} >> [H^+]$ and $\Gamma_s << [H^+]$, rate eq 1 is reduced to

$$r = \frac{2k_{1s}\Gamma_s\sigma}{K_{H_2O_2(a)}}[H_2O_2]_t \qquad (12)$$

Equation 12 is in accord with the experimental facts that rate is the first order with respect to peroxide concentration and is independent of KOH concentration.

From the steady-state approximation, the concentration of the superoxide ion on the metal surface is expressed by eq 13 where $K_{H_2O_2} >> [H^+]$ is incorporated. The rate of

$$[O_2]_{\text{surface}} = \Gamma_s\frac{k_{1s}}{k_{5s}}\frac{[H_2O_2]_t}{K_{H_2O_2(a)}} \qquad (13)$$

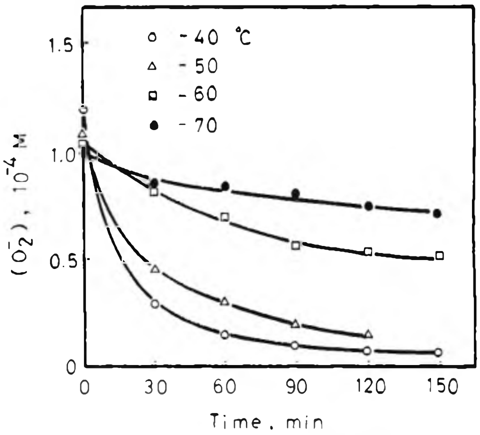

Figure 8. Decay curves of O_2^- trapped in ice at various temperatures.

superoxide formation in an aqueous solution may be proportional to the surface concentration of the ion. Thus

$$\frac{d[O_2]_{\text{solution}}}{d[W/F]} = \alpha\Gamma_s\frac{k_{1s}}{k_{5s}}\frac{[H_2O_2]_t}{K_{H_2O_2(a)}} \qquad (14)$$

where α is a proportionality constant. This is in accord with the fact that the initial rate of O_2^- formation in the aqueous phase is proportional to peroxide concentration and independent of KOH concentration.

Thus, the rate constants experimentally determined, k_1 and k_2, can be related to the rate constants of the elementary steps as follows:

$$k_1 = 2k_{1s}\Gamma_s\sigma/K_{H_2O_2(a)} \qquad (15)$$

$$k_2 = \alpha\Gamma_s k_{1s}/k_{5s}K_{H_2O_2(a)} \qquad (16)$$

Decay Constant k_3. The superoxide ion desorbed from the metal surface decays with first-order kinetics with a rate constant k_3, as in rate eq 7. It is known that the superoxide ion is quite stable in aqueous solution of high pH,[21-23] and its lifetime is about 1 min.[21] Under our experimental conditions, the contact time is at most 8 s. Therefore, the decay of the superoxide ion in the homogeneous phase is negligible. Thus, the decay of the superoxide ion signal is caused entirely by the readsorption of the superoxide ion onto the solid surface. Dependence of k_3 values on the nature of the catalysts substantiates the above discussion. The pH dependence of k_3 may indicate that the decay of O_2^- involves the decay of ·HO_2, which is in equilibrium with O_2^- in the aqueous solution, onto the solid surface.

Stability of O_2^- in Ice. The line shape and intensity of the ESR spectrum of the frozen solution containing the superoxide ion as a function of temperature did not change up to −120 °C. The signal broadens above −120 °C and disappears completely at −70 °C. However, the process is completely reversible; cooling the system back to −150 °C restores the original intensity. Thus, the change in this temperature region is entirely ascribed to the change in the relaxation time due to the tumbling motion of the superoxide ion. Above −70 °C, irreversible decay of the superoxide concentration was observed. The change in radical concentration with time was examined at various temperatures and is illustrated in Figure 8. A plot of the reciprocal of the radical concentration against time gives a straight line at each temperature. Thus, the decay follows second-order kinetics. An Arrhenius plot of the decay rate constant gives an activation energy of 50 kJ/mol. This value suggests that the decay process is diffusion controlled.

Acknowledgment. We wish to thank Professor T. Keii for helpful discussions.

References and Notes

(1) F. Haber and J. Weiss, *Proc. R. Soc. London, Ser. A*, **147**, 332 (1934).
(2) N. Uri, *Chem. Rev.*, **50**, 375 (1952).
(3) C. Walling, *Acc. Chem. Res.*, **8**, 125 (1975).
(4) W. T. Dixson and R. O. C. Norman, *J. Chem. Soc.*, 3119 (1963).
(5) E. Saito and B. H. Bielski, *J. Am. Chem. Soc.*, **83**, 4467 (1961).
(6) Y. S. Chiang, J. Craddook, D. Mickervich, and J. Turkevich, *J. Phys. Chem.*, **70**, 3509 (1966).
(7) F. Scillo, R. E. Florin, and L. A. Wall, *J. Phys. Chem.*, **70**, 47 (1966).
(8) M. Setaka, Y. Kirino, T. Ozawa, and T. Kwan, *J. Catal.*, **15**, 209 (1969).
(9) J. Weiss. *Trans. Faraday Soc.*, **31**, 1547 (1935).
(10) J. Weiss. *Adv. Catal.*, **4**, 343 (1952).
(11) D. W. Mckee, *J. Catal.*, **14**, 355 (1969).
(12) D. C. Bond, "Catalysis by Metals", Academic Press, London, 1962, p 432.
(13) S. Fukuzumi, Y. Ono, and T. Keii, *Bull. Chem. Soc. Jpn.*, **46**, 3353 (1973).
(14) S. Fukuzumi, Y. Ono, and T. Keii, *Int. J. Chem. Kinet.*, **7**, 535 (1975).
(15) S. Fukuzumi and Y. Ono, *J. Chem. Soc., Perkin Trans. 2*, in press.
(16) P. F. Knowles, J. F. Cibson, F. M. Pick, and R. C. Bray, *Biochem. J.*, **111**, 53 (1969).
(17) D. Ballon, G. Palmer, and V. Massey, *Biochem. Biophys. Res. Commun.*, **36**, 898 (1969).
(18) R. Nilson, F. M. Pick, and R. C. Brag, *Biochem. Biophys. Acta*, **192**, 145 (1969).
(19) J. M. McCord and I. Fridovich, *J. Biol. Chem.*, **244**, 6065 (1969).
(20) M. G. Evans and N. Uri, *Trans. Faraday Soc.*, **45**, 224 (1949).
(21) G. Czapski and L. M. Dorfman, *J. Phys. Chem.*, **68**, 1176 (1964).
(22) J. Rabani and S. O. Nielsen, *J. Phys. Chem.*, **73**, 3736 (1969).
(23) D. Behar, C. Czapski, J. Rabani, L. M. Dorfman, and H. A. Schwarz, *J. Phys. Chem.*, **74**, 3212 (1970).

Mean Spherical Model for Asymmetric Electrolytes. 2. Thermodynamic Properties and the Pair Correlation Function

L. Blum*

Physics Department, College of Natural Sciences, University of Puerto Rico, Rio Piedras, Puerto Rico 00931

and J. S. Høye

Institutt for Teoretisk Fysikk, University of Trondheim, 7034 Trondheim NTH, Norway

(Received December 28, 1976)

It is shown that the excess thermodynamic properties calculated from the mean spherical approximation (via the energy integrals) for the primitive model of ionic mixtures, that is, electrolytes and molten salts, can be expressed as functions of a single parameter Γ. The expressions are quite simple, and for what we call low concentrations (up to 1 N of a simple salt) reduce to the same relations that Debye found for the finite size ions, only that 2Γ takes the place of the Debye length. The interpretation that 2Γ is in fact the correct screening parameter for finite size ions is borne by the asymptotic form of the pair correlation function at small densities.

1. Introduction

In a recent paper we found the general solution of the mean spherical approximation (MSA)[1] for a neutral mixture of charged hard spheres.[2] The unrestricted general solution is possible because in the MSA the properties and structure functions of the individual ions are scaled by a single parameter Γ, which has the dimensions of an inverse length. In our previous work, we gave rather complicated expressions for the thermodynamic properties of the mixture, involving integrals that had to be found numerically. However, for equal sizes, and/or low concentrations we found that the osmotic coefficient[3] (and also the activity coefficient[4]) could be integrated explicitly to yield a strikingly simple formula (in complete agreement with the Waisman-Lebowitz result[1]), which looked just like the Debye-finite size expression, but just with 2Γ in the place of the inverse Debye screening length.[5] In the present work we give general expressions for the excess osmotic coefficient and excess activity coefficient of the general mixture. A formula for the excess free energy is also found, which is in agreement with an expression derived independently by Hiroike.[6,21] All of these expressions consist of the sum of two terms: The first term is of the Debye–Hückel form, involving the parameter Γ, while the second depends also on the size differences of the ions, and vanishes when all the ions have the same diameter. The size difference term is analogous to the one discussed by Stell and Lebowitz,[7] and reflects the different shielding capability of the ions according to their size. Larger ions are less effective in their shielding ability than the smaller ones for the simple reason that their sheer size prevents them from coming close to the center ion. Indeed, $(2\Gamma)^{-1}$ is always larger than the Debye shielding length

$$\varkappa_0 = \left[4\pi \frac{\beta e^2}{\epsilon_0} \sum_l \rho_l z_l^2\right]^{1/2} \tag{1.1}$$

The striking similarity of the MSA to the Debye–Hückel theory is also present in the binary correlation function. However here matters are more complex because the excluded volume effects should give charge oscillations in the ionic cloud, as predicted by the Stillinger–Lovett second moment condition[8]

$$4\pi\int_0^\infty \mathrm{d}r \sum_{i,j} z_i z_j \rho_i \rho_j g_{ij}(r) r^4 = -6\sum_l \rho_l z_l^2/\varkappa_0^2 \tag{1.2}$$

in a more classical language, the charge oscillation is reflecting the ion pair formation that Onsager discussed many years ago.[9] Indeed, the hard core version of the Debye theory, which has been popular among electrochemists in its original form and in many improved versions, does not satisfy the second moment condition, while Groeneveld has shown[10] that the MSA and the hypernetted chain (HNC) approximations are among the theories that satisfy (1.2) exactly. Indeed, the work of Friedman and collaborators[11] has shown that the HNC[12] equation is a very succesful one, since it does represent the results of computer experiments and real systems quite well. However it is not an easy theory to work with, and the calculations represent a substantial programming job. This explains why there is still so much interest in the improved versions of the Debye theory, which combines intuitive interpretation with simplicity in the calculation. We should mention in this connection the recent work of Olivares and McQuarrie,[13] Outhwaite,[14] and Pitzer[15] in which different but ad hoc modifications of this theory are presented. However in the Debye theory, the ions of the ionic cloud are point charges, and this makes the theory inconsistent from the statistical point of view. Even worse, the thermodynamic limit does not exist for a system of point charges, without repulsion core. We believe that the new results presented here show that the MSA is the Debye–Hückel theory with the correct treatment of the exclusion core, not only by its formulation (Percus[1]), but also since it has a similar structure, that is the equations are formally the same, with the only difference that the ionic cloud is not calculated for point objects, but rather finite size charges. So we believe that the MSA represents the "middle of the road" alternative, and has simplicity and intuitive appeal, if perhaps not as accurate as the HNC.

A short summary of the pertinent results of ref 2 are given in the next section, where we also discuss convenient ways to calculate the parameter Γ. In section 3 we give the main results of this work: quite simple formulas for the thermodynamic properties for arbitrary mixtures of hard ions in the MSA. Section 4 is devoted to the discussion of the pair correlation function. For the restricted primitive model, Hirata and Arakawa[16] obtained the Laplace transform of this function and also a series for the function itself. We will get the general form of the Laplace transform of the pair correlation function for the arbitrary ionic mixture. This function is shown to be symmetric in a nontrivial calculation. Furthermore for the restricted primitive model the expression is in agreement with the previous work. In the low concentration regime, much of the complicated charge-hard core cross contribution vanishes and one recovers a simple formula which again has two terms: a hard core term, which is the Percus–Yevick pair correlation function for hard spheres, and a purely ionic term, which on Laplace inversion will yield the charge oscillation predicted by Stillinger and Lovett. For dilute solutions we give a more convenient expansion that starts with

$$g_{ij}(r) = -\frac{\beta e^2}{\epsilon_0 r} z_i z_j e^{-2\Gamma r} \tag{1.3}$$

which again is of the Debye–Hückel form, with 2Γ as the shielding parameter. This result lends support to the interpretation of 2Γ as the shielding parameter in the calculation of the thermodynamic properties.

2. Summary of Previous Results

We will represent the actual electrolytic solution (or molten salt) by the primitive model, which consists of a mixture of charged hard spheres of species $1, \ldots i, \ldots, n$, with number density ρ_i, diameter σ_i, and charge (actually electrovalence) z_i. The mixture is embedded in a continuum of dielectric constant ϵ_0, and is electroneutral. In other words we require that

$$\sum_{i=1}^{n} \rho_i z_i = 0 \tag{2.1}$$

We recall, furthermore, the MSA boundary conditions for the pair correlation function

$$h_{ij}(r) = g_{ij}(r) - 1 \tag{2.2}$$

The hard core exclusion requires that for $r \leq \sigma_{ij}$

$$h_{ij}(r) = -1 \tag{2.3}$$

while for the direct correlation function the MSA condition is

$$c_{ij}(r) = -\beta u_{ij}(r) \tag{2.4}$$

for $r > \sigma_{ij}$ here

$$\sigma_{ij} = (1/2)(\sigma_i + \sigma_j) \tag{2.5}$$

is the distance of closest approach. Furthermore, the electrostatic potential is

$$u_{ij}(r) = e^2 z_i z_j / \epsilon_0 r \tag{2.6}$$

The solution of the Ornstein–Zernike equation of ref 2 was given in terms of the factor correlation function[17] matrix $\mathbf{Q}(r)$. For the general ionic mixture in the MSA has the following form

$$Q_{ij}(r) = \lim_{\mu \to 0} \{(r - \sigma_{ij})Q_{ij}' + (1/2)(r - \sigma_{ij})^2 Q_j'' - z_i a_j e^{-\mu r}\}$$
$$\lambda_{ji} < r \leqslant \sigma_{ij} \tag{2.7}$$

$$Q_{ij}(r) = \lim_{\mu \to 0} \{-z_i a_j e^{-\mu r}\} \quad r > \sigma_{ij};\ \lambda_{ji} = (1/2)(\sigma_j - \sigma_i) \tag{2.8}$$

where Q_{ij}', Q_j'', and a_j are numeric coefficients that were found by solving a set of algebraic equations derived from the conditions (2.3) and (2.4),[2] and also by considering the integral equation that defines the pair correlation function in terms of the matrix elements of $Q_{ij}(r)$

$$J_{ij}(r) = Q_{ij}(r) + \sum_k \rho_k \int_{\lambda_{jk}}^{\infty} \mathrm{d}r_1\, J_{ik}(|r - r_1|)Q_{kj}(r_1) \tag{2.9}$$

where

$$J_{ij}(r) = 2\pi \int_r^{\infty} \mathrm{d}r_1\, r_1 h_{ij}(r_1) \tag{2.10}$$

The coefficients of the factor correlation function are found to be

$$Q_{ij}' = \frac{2\pi}{\Delta}\left(\sigma_{ij} + \frac{\pi}{4\Delta}\sigma_i \sigma_j \zeta_2\right) - \frac{2\Gamma^2}{\alpha^2} a_i a_j \tag{2.11}$$

$$Q_j'' = \frac{2\pi}{\Delta}[1 + \zeta_2 \sigma_j(\pi/2\Delta) + (1/2)a_j P_n] \tag{2.12}$$

$$a_j = \frac{\alpha^2}{2\Gamma(1 + \Gamma\sigma_j)}\left(z_j - P_n \sigma_j^2 \frac{\pi}{2\Delta}\right) \tag{2.13}$$

with

$$P_n = \frac{1}{\Omega} \sum \rho_k \sigma_k z_k / (1 + \Gamma\sigma_k) \tag{2.14}$$

$$\Omega = 1 + \frac{\pi}{2\Delta} \sum \rho_k \sigma_k^3 / (1 + \Gamma\sigma_k) \tag{2.15}$$

$$\zeta_n = \sum \rho_k (\sigma_k)^n \qquad n = 0, 1, 2, 3 \tag{2.16}$$

$$\Delta = 1 - \pi\zeta_3/6 \tag{2.17}$$

$$\alpha^2 = 4\pi\beta e^2/\epsilon_0 \tag{2.18}$$

finally the parameter Γ is determined by solving the algebraic equation[3]

$$2\Gamma = \alpha \left\{ \sum_{i=1}^{n} \rho_i \left[\left(z_i - \frac{\pi}{2\Delta}\sigma_i^2 P_n\right) \Big/ (1 + \Gamma\sigma_i) \right]^2 \right\}^{1/2} \tag{2.19}$$

the degree of this equation depends on the number of ions involved: for a binary salt it is of the 6th degree and has to be solved numerically. From all the six solutions we have to select the physically acceptable, which is positive and tends to the Debye inverse length κ_0 from below for infinite dilution

$$2\Gamma \xrightarrow{<} \kappa_0 \tag{2.20}$$

The numerical solution can be obtained from either the Newton–Raphson formula or even by simple iteration of some guessed initial value of Γ. For 1–1 electrolytes a very good initial value is obtained from the inverse screening length obtained from the Waisman–Lebowitz solution but using the average diameter

$$\bar{\sigma} = \zeta_1/\zeta_0 \tag{2.21}$$

as the hard core diameter. That is, the initial value is

$$2\Gamma_0 = [-1 + (1 + 2\kappa_0\bar{\sigma})^{1/2}]/\bar{\sigma} \tag{2.22}$$

to conclude this section we should mention that the coefficients Q_{ij}' and Q_j'' are simply related to physically interesting quantities. It is easy to see from (2.9) that the contact value of the pair correlation function is given by

$$g_{ij}^{+}(\sigma_{ij}) = Q_{ij}'/(2\pi\sigma_{ij}) \tag{2.23}$$

while, differentiating (2.9) twice we also obtain

$$Q_j''/2\pi = 1 - \sum_{h=1}^{n}\rho_k \int_{\lambda_{jk}}^{\infty} \mathrm{d}r\, Q_{kj}(r) \tag{2.24}$$

which together with

$$\chi^{-1} \equiv \frac{\partial\beta P}{\partial\zeta_0} = 1 - \frac{1}{\zeta_0}\sum_{k,j}\rho_k\rho_j \int_0^{\infty} \mathrm{d}\vec{r}\; c_{k,j}(\vec{r}) \tag{2.25}$$

where[2] (see also ref 2 for notation)

$$\delta_{ij} - (\rho_i\rho_j)^{1/2}\tilde{C}_{ij}(0) = \sum_k \tilde{Q}_{ik}(0)\tilde{Q}_{jk}(0) \tag{2.26}$$

yields the simple formula for the inverse compressibility χ^{-1}

$$\chi^{-1} = \frac{1}{4\zeta_0\pi^2}\sum_{j=1}^{n}\rho_j(Q_j'')^2 \tag{2.27}$$

3. Thermodynamic Properties

One of the convenient features of the MSA is that it gives explicit, yet general relations for the thermodynamic properties, such as the osmotic and activity coefficients, derived via the internal energy. We recall first that since the MSA is not the exact solution of the statistical mechanical problem of the neutral mixture of hard spheres, it will be inconsistent, in the sense that the same quantity, for example, the pressure, when computed in different ways, say, the virial, compressibility, or energy formulas, will yield different numerical answers. From past experience and comparison to computer experiments it is expected that the best results will be those of the internal energy path. It has been recently shown by Høye and Stell[18] that the virial pressure equals the energy pressure when the second-order corrections from the graphical expansion to the MSA are taken into account. This result, general for the MSA, is also the basis for the calculations of the thermodynamic properties of this section.

Let us first recall that the excess internal energy is given by[2,3]

$$\Delta E = -\frac{e^2}{\epsilon_0}\left\{\Gamma\sum_{i=1}^{n}\rho_i z_i^2/(1 + \Gamma\sigma_i) + \frac{\pi}{2\Delta}\Omega P_n^2\right\} \tag{3.1}$$

where, as in the previous section, e is the electron charge, ϵ_0 is the dielectric constant. ΔE is calculated in (3.1) from the MSA pair correlation function using the standard formula. To obtain the free energy we notice that the thermodynamic relation

$$\partial\beta\Delta A/\partial\beta = \Delta E \tag{3.2}$$

where ΔA is the excess free energy, can be integrated, after minor changes, to yield[18]

$$-\beta\Delta A = -(^2/_3)\beta\Delta E + \frac{1}{12\pi}\sum_{i,j}\rho_i\rho_j\sigma_{ij}[(Q_{ij}')^2 - (Q_{ij}^{0\prime})^2] - \frac{1}{8\pi^2}\sum_j\rho_j[(Q_l'')^2 - (Q_l^{0\prime\prime})^2] \tag{3.3}$$

this result is obtained from ref 18 together with eq 2.23 and 2.25. The superscript zero means that we are taking the values for the discharged case. Some algebra shows that (3.3), together with (2.11), (2.12), and (2.13) yields the surprisingly simple formula

$$\beta\Delta A = \beta\Delta E + \Gamma^3/3\pi \tag{3.4}$$

This same relation was obtained recently in an independent investigation by Hiroike.[6]

Next we compute the excess osmotic coefficient from the thermodynamic relation

$$\Delta\phi \doteq \frac{\beta\Delta P}{\zeta_0} = \zeta_0\frac{\partial(\beta\Delta A/\zeta_0)}{\partial\zeta_0} \tag{3.5}$$

where ΔP is the excess pressure, and β is the Boltzmann thermal factor $(1/k_BT)$. For this quantity we have from ref 18

$$\Delta\phi = \frac{1}{3}\beta\frac{\Delta E}{\zeta_0} + \frac{1}{12\pi\zeta_0}\sum_{i,j}\rho_i\rho_j\sigma_{ij}[(Q_{ij}')^2 - (Q_{ij}^{0\prime})^2] \tag{3.6}$$

which, after some algebra, leads to

$$\Delta\phi = -\frac{\Gamma^3}{3\pi\zeta_0} - \frac{\alpha^2}{8\zeta_0}\left(\frac{P_n}{\Delta}\right)^2 \tag{3.7}$$

Finally, we get the activity coefficient from the thermodynamic formula

$$\beta\frac{\Delta A}{\zeta_0} = -\Delta\phi + \Delta\ln\gamma_\pm \tag{3.8}$$

and the previous results (3.4) and (3.7). The activity coefficient is then

$$\Delta\ln\gamma_\pm = \left[\beta\Delta E - \frac{\alpha^2}{8}\left(\frac{P_n}{\Delta}\right)^2\right]\Big/\zeta_0 \tag{3.9}$$

where ΔE is given by (3.1).

We observe that all of the above expressions for the excess thermodynamic properties in the MSA consist of the sum of two terms, one of which is exactly of the Debye–Hückel form, but with 2Γ as the shielding parameter, while the other contains the parameter P_n defined by eq 2.14. For low numerical densities (still a respectable 1 N of a 1–1 electrolyte) this parameter is quite small and can be neglected. In this case, we obtain

$$\Delta\phi = -\Gamma^3/3\pi\zeta_0 \tag{3.10}$$

$$\Delta\ln\gamma_\pm = -\frac{\alpha^2\Gamma}{4\pi\zeta_0}\sum_i\frac{\rho_i z_i^2}{1 + \Gamma\sigma_i} \tag{3.11}$$

Both of these relations were derived previously from approximate relations that neglected P_n from the start.[3,4]

In this case the integration of (3.2) is especially simple, since all the thermodynamic quantities depend on the single parameter $\alpha^2\rho$, instead of α^2 and ρ separately. As was already mentioned in the Introduction (3.10) and (3.11) are very similar to the Debye–Hückel formulas (for the primitive model in which the ion has a finite size)

$$\Delta\phi = -\varkappa_0{}^3/24\pi\zeta_0 \tag{3.12}$$

$$\Delta \ln \gamma_{\pm} = -\frac{1}{8\pi\zeta_0}\frac{\varkappa_0{}^3}{1+\sigma\varkappa_0} \tag{3.13}$$

with the only difference that the inverse screening length is now 2Γ. In the next section we will show that this is due to the fact that in the MSA and for relatively low concentrations, 2Γ is the inverse shielding length in the Debye sense, that is, the decay rate of the correlation function, and therefore it is only natural that all the thermodynamic quantities are scaled by this length.

The surprising simplicity of the above results is in sharp contrast with the rather involved manipulations that are necessary to derive them. There is also no *rigorous* proof that the scaling relation is correct as conjectured in ref 2. Therefore it is quite important to have independent tests of the solution: One of these tests is the fact that the pair correlation function $g_{ij}(r)$ is symmetric, as will be shown in the next section. This result is nontrivial and depends quite heavily on all the details of the analytic solution. A further, perhaps more reliable, check is possible using the general results of ref 18, in which relations that do not depend on the details of the solution were derived. The only relations needed were the Ornstein-Zernike equation and eq 2.3 and 2.4. The first of these relations is

$$\left(\frac{\partial(\beta\Delta A)}{\partial\beta}\right)_{\zeta_0} \mathrm{d}\beta + \left(\frac{\partial(\beta\Delta A)}{\partial\zeta_0}\right)_{\beta} \mathrm{d}\zeta_0 = \Delta E\ \mathrm{d}\beta + \Delta \ln\gamma_{\pm}\ \mathrm{d}\zeta_0 \tag{3.14}$$

Here, we have checked the numerical derivatives against the analytical expressions of ΔE (3.1) and $\Delta \ln \gamma_{\pm}$ (3.11). We found agreement within the precision of the computer. Another check can be obtained from the relation

$$(\partial\Delta A/\partial\rho_i)_{\beta,\rho_{j\neq i}} = \mu_i \tag{3.15}$$

in which the right-hand side is calculated by numerical differentiation of (3.3)[18] while the left-hand side is obtained from the analytic solution of the MSA. This test also shows perfect agreement. A further test of the solution was to obtain the dense point limit of Waisman and Lebowitz.[1] Again here, there was complete agreement.

As an interesting mathematical sideline, we note that in the cases were the temperature β or the interaction strength α (which is dependent on the dielectric constant ϵ_0) are not the fixed quantities, it will be unnecessary to solve (2.19) to obtain Γ. All we need to do is to compute α, and therefore β as a function of Γ. In fact, everything else depends only on Γ (and of course on the individual z_i, σ_i, and ρ_i). Thus, Γ plays the crucial role of the universal scaling parameter.

4. The Pair Correlation Function

A quantity of major interest in the study of ionic solutions and molten salts is the pair correlation function $g_{ij}(r)$. In this section we will derive a general formula for the Laplace transform

$$\tilde{G}_{ij}(s) = \int_0^\infty \mathrm{d}r\, e^{-sr} r g_{ij}(r) \tag{4.1}$$

As is known, in fluid theory, even for the simple models, the analytic structure of $\tilde{G}_{ij}(s)$ in the complex plane is not all that simple[19] and an explicit, closed formula for $g_{ij}(r)$ cannot be obtained. Numerically, however, the Laplace inversion of (4.1) should be rather simple, since the Laplace transform can be converted to a Fourier transform, for which very efficient and fast programs for calculating the inverse exist.

To compute $\tilde{G}_{ij}(s)$ we first take the derivative of (2.9) with respect to r, and the take the Laplace transform. A simple calculation leads to

$$\sum_k \tilde{G}_{ik}(s)[\delta_{kj} - \rho_k\tilde{Q}_{kj}(s)] = \frac{e^{-s\sigma_{ij}}}{2\pi s^2}[Q_j{}'' + sQ_{ij}{}'] \tag{4.2}$$

where

$$\tilde{Q}_{kj}(s) = \int_{\lambda_{jk}}^\infty \mathrm{d}r\, e^{-sr} Q_{kj}(r) \tag{4.3}$$

and using (2.7)

$$\tilde{Q}_{kj}(s) = e^{-s\lambda_{jk}}[\varphi_1(\sigma_k)Q_{kj}{}' + \varphi_2(\sigma_k)Q_j{}'' - z_k a_j/s] \tag{4.4}$$

where $\phi_n(\sigma)$ are slightly modified incomplete gamma functions

$$\varphi_1(\sigma_k) = (1 - s\sigma_k - e^{-s\sigma_k})/s^2 \tag{4.5}$$

$$\varphi_2(\sigma_k) = (1 - s\sigma_k + s^2\sigma_k{}^2/2 - e^{-s\sigma_k})/s^3 \tag{4.6}$$

From (2.11), (2.12), and (2.13) we readily obtain

$$\delta_{kj} - \rho_k\tilde{Q}_{kj}(s) = e^{-s\lambda_{jk}}[\delta_{kj} - \rho_k(\alpha_k + \sigma_j\beta_k + a_j\gamma_k)] \tag{4.7}$$

where

$$\alpha_k = \frac{2\pi}{s\Delta}[(1/2)\sigma_k\varphi_0(\sigma_k) + \varphi_1(\sigma_k)] \tag{4.8}$$

$$\beta_k = \frac{\pi}{\Delta}[\varphi_1(\sigma_k) + (1/2)\zeta_2\alpha_k] \tag{4.9}$$

$$\gamma_k = \frac{1}{S}\left[P_n\frac{\pi}{\Delta}\varphi_1(\sigma_k) - \frac{2\Gamma a_k}{\alpha^2}(1 + \Gamma\varphi_0(\sigma_k))\right] \tag{4.10}$$

where $\varphi_0(\sigma)$ is the Laplace transform of the square wave pulse

$$\varphi_0(\sigma) = \int_0^\sigma \mathrm{d}r\, e^{-sr} = (1 - e^{-s\sigma})/s \tag{4.11}$$

The matrix defined by (4.7) is of the so-called Jacobi type, and has an inverse that can be found explicitly for any size of the matrix. When this inverse is replaced into eq 4.2, we obtain after some rather laborious algebra (see Appendix A for details)

$$\tilde{G}_{ij}(s) = \frac{D_0D_{\pm}}{D_{\mathrm{T}}}\tilde{G}_{ij}{}^0(s) - \frac{D_0\Gamma^2}{s\alpha^2\pi D_{\mathrm{T}}}e^{-s\sigma_{ij}}a_ia_j + \Delta\tilde{G}_{ij}(s) \tag{4.12}$$

here, the first term gives essentially the Percus–Yevick, pure hard sphere pair distribution, the second gives the MSA pure excess electrostatic contribution, and the third one, the cross interactions of the hard core and the charges. The terms in (4.12) are defined as follows:

$$D_{\mathrm{T}} = D_0 D_{\pm} + \Delta D_{\mathrm{T}} \tag{4.13}$$

$$\begin{aligned} D_0 = {} & 1 - \frac{2\pi}{\Delta}\sum_l \rho_l \varphi_2(\sigma_l)\left(1 + \frac{\pi}{2\Delta}\zeta_3\right) \\ & - \frac{2\pi}{\Delta}\left\{\sum_l \rho_l \varphi_1(\sigma_l)\left[\sigma_l\left(1 + \frac{\pi}{4\Delta}\zeta_2 \sigma_l\right)\right.\right. \\ & \left.\left. + \frac{\pi}{4\Delta}\sum_k \rho_k \varphi_1(\sigma_k)(\sigma_k - \sigma_l)^2\right]\right\} \end{aligned} \tag{4.14}$$

$$\begin{aligned} D_{\pm} \doteq {} & 1 + \frac{2\Gamma}{s}\left[1 + \frac{\Gamma}{\alpha^2}\sum_k \rho_k a_k^2 \varphi_0(\sigma_k)\right] \\ & - \frac{\pi}{s\Delta} P_n P_{\varphi_1} \end{aligned} \tag{4.15}$$

$$\begin{aligned} \Delta D_{\mathrm{T}} = {} & \frac{\pi}{s\Delta}\left\{P_n P_{\varphi_1}\left[\delta_1{}^2 - \frac{2\pi}{\Delta}\delta_2 \sum_l \rho_l \varphi_2(\sigma_l)\right]\right. \\ & + 4\frac{\Gamma^2}{\alpha^2}\left[P_{\varphi_1}(\delta_2 P_{\varphi_1} + \delta_1 P_{\varphi_0})\right. \\ & \left.\left. + \frac{\pi}{2\Delta}P_{\varphi_0}{}^2 \sum_l \rho_l \varphi_2(\sigma_l)\right]\right\} \end{aligned} \tag{4.16}$$

where

$$P_{\varphi_1} = \sum_l \rho_l a_l \varphi_1(\sigma_l) \tag{4.17}$$

$$P_{\varphi_0} = \sum_l \rho_l \sigma_l a_l \varphi_0(\sigma_l) \tag{4.18}$$

$$P_n = \frac{2\Gamma}{\alpha^2}\sum_l \rho_l \sigma_l a_l \tag{4.19}$$

$$\delta_1 = 1 - (\pi/\Delta)\sum_l \rho_l \sigma_l \varphi_1(\sigma_l) \tag{4.20}$$

$$\delta_2 = 1 + (\pi/2\Delta)\sum_l \rho_l \sigma_l{}^2 \varphi_0(\sigma_l) \tag{4.21}$$

With these definitions, we write first the "discharged" pair correlation function

$$\begin{aligned} \tilde{G}_{ij}{}^0(s) = {} & \frac{e^{-s\sigma_{ij}}}{s^2 \Delta D_0}\left\{s\left[\sigma_{ij} + \sigma_i \sigma_j \frac{\pi}{4\Delta}\zeta_2\right]\right. \\ & + 1 + \frac{\pi}{2\Delta}\zeta_3 + \frac{\pi s}{2\Delta}\sum_l \rho_l \varphi_1(\sigma_l)(\sigma_l - \sigma_i)(\sigma_l \\ & \left. - \sigma_j)\right\} \end{aligned} \tag{4.22}$$

while the cross contribution to the pair correlation function is

$$\begin{aligned} \Delta\tilde{G}_{ij}(s) = {} & \frac{e^{-s\sigma_{ij}}}{2\Delta s^2 D_t}\left\{\frac{\pi}{s\Delta}\left(2\delta_2 P_n P_{\varphi_1}\right.\right. \\ & \left. - \frac{2\Gamma^2}{\alpha^2}P_{\varphi_0}{}^2\right) + \frac{2\pi}{\Delta}\sigma_{ij}P_{\varphi_1}\left(\frac{2\Gamma^2}{\alpha^2}P_{\varphi_0} + \delta_1 P_n\right) \\ & - \frac{s\pi}{\Delta}P_{\varphi_1}\sigma_i\sigma_j\left(\frac{2\Gamma^2}{\alpha^2}P_{\varphi_1} - P_n\delta_3\right) - \frac{2\Gamma^2}{\alpha^2}[(a_i \\ & + a_j)(\delta_1 P_{\varphi_0} + 2\delta_2 P_{\varphi_1}) + s(a_i\sigma_j \\ & \left. + a_j\sigma_i)(\delta_1 P_{\varphi_1} + \delta_3 P_{\varphi_0})]\right\} \end{aligned} \tag{4.23}$$

with

$$\delta_3 = \frac{\pi}{\Delta}\sum_l \rho_l \varphi_2(\sigma_l) \tag{4.24}$$

It is easy to see that all the P's vanish for equal size ions, and that they are quite small for low ionic concentration ($\rho\sigma^3 \sim 0.1$). Therefore for not too concentrated ionic solutions, they can be neglected. We obtain

$$\tilde{G}_{ij}(s) = \tilde{G}_{ij}{}^0(s) - \frac{\Gamma^2 e^{-s\sigma_{ij}}}{\pi s \alpha^2 D_{\pm}}a_i a_j \tag{4.25}$$

and, using (2.13) and (4.15), we obtain in this regime

$$\begin{aligned} \tilde{G}_{ij}(s) = {} & \tilde{G}_{ij}{}^0(s) \\ & - \frac{A_{ij}e^{-s\sigma_{ij}}}{s + 2\Gamma\left[1 + \frac{\Gamma}{\alpha^2}\sum_l \rho_l a_l{}^2 \varphi_0(\sigma_l)\right]} \end{aligned} \tag{4.26}$$

$$A_{ij} = z_i z_j \alpha^2/[4\pi(1 + \Gamma\sigma_j)(1 + \Gamma\sigma_j)] \tag{4.27}$$

The Laplace inverse of the excess electrostatic part can be obtained either by expanding the denominator of (4.26)

$$\begin{aligned} & 1/\left\{s + 2\Gamma(1 + \Gamma/s) - \frac{2\Gamma^2}{\alpha^2 s}\sum_l \rho_l a_l{}^2 e^{-s\sigma_l}\right\} \\ & = s\sum_{m=0}^{\infty}\left\{[2\Gamma^2 \sum_{l=1}^{\infty}\rho_l{}^2 a_l{}^2 e^{-s\sigma_l}/\alpha^2]^m\right. \\ & \left. /[s^2 + 2\Gamma s + 2\Gamma^2]^{m+1}\right\} \end{aligned} \tag{4.28}$$

and obtain the zone expansion of the pair distribution function[16]

$$\begin{aligned} & \Delta g_{ij}(r) = \sum_{m=0}^{\infty}\Delta g_{ij}{}^{(m)} \\ & \Delta g_{ij}{}^{(1)}(r) = -A_{ij}\frac{2\Gamma^2}{r}[\sin\Gamma(r - \sigma_{ij}) \\ & \quad - \cos\Gamma(r - \sigma_{ij})]e^{-\Gamma(r - \sigma_{ij})} \\ & \quad \sigma_{ij} < r < \min(\sigma_{ij} + \sigma_l) \end{aligned} \tag{4.29}$$

This expansion is rather inconvenient for low concentrations, because then the shielding length is much larger than the hard core diameter, and very many terms of (4.29) are needed. These terms become increasingly complicated, as can be appreciated. A more sensible expansion for the low concentration regime is obtained using the fact that for this case it is true that

$$\frac{2\Gamma^2}{\alpha^2}\frac{1}{s + 2\Gamma}\sum_l \rho_l a_l{}^2 \varphi_0(\sigma_l) < 1 \tag{4.30}$$

and therefore we expand

$$\frac{1}{sD_{\pm}} = \frac{1}{s + 2\Gamma}\sum_{m=0}^{\infty}\left[-\frac{2\Gamma^2}{\alpha^2(s + 2\Gamma)}\sum_k \rho_k a_k{}^2 \varphi_0(\sigma_k)\right]^m \tag{4.31}$$

The Laplace inversion of this series is quite straightforward, since, apart from some discontinuities, it has only one pole at $s = -2\Gamma$. Using (4.11) we have for the first few terms

$$\begin{aligned} g_{ij}(r) = {} & g_{ij}{}^0(r) - (A_{ij}/r)\left\{\eta(r - \sigma_{ij})e^{-2\Gamma(r - \sigma_{ij})}\right. \\ & - \frac{2\Gamma^2}{\alpha^2}\sum_l \rho_l a_l{}^2 \int_0^{r - \sigma_{ij}} \mathrm{d}r_1\, r_1 e^{-2\Gamma r_1}\,\eta(\sigma_l + \sigma_{ij} - r \\ & \left. + r_1) + \cdots\right\} \end{aligned} \tag{4.32}$$

where $g_{ij}{}^0(r)$ is the Percus–Yevick, hard core pair correlation function, and $\eta(x)$ is the Heaviside function.

This approximation for the pair correlation function is quite appealing. Due to its simplicity, it can be used to compute higher order graph contributions beyond the ring diagrams which yield the Debye–Hückel approximation, with relatively little effort,[5] and indeed, we plan to do such a calculation in the near future, and expect to get results considerably more accurate than the classic ones because of the optimization of the MSA.[20] Finally, we should remark that to the first approximation in the ionic strength (4.32) is just of the same form as the classical Debye result

$$\delta g_{ij}(r) = A_{ij}e^{-2\Gamma(r-\sigma_{ij})}/r \qquad r > \sigma_{ij} \tag{4.33}$$

but with the different shielding length 2Γ.

Acknowledgment. We are indebted to Professor K. Hiroike for sending us a copy of his work prior to publication.

Appendix A. Derivation of the Pair Correlation Function

The solution of the system of linear equations (4.2) requires the inversion of a matrix with elements

$$M_{ij} = e^{s\lambda_{ij}}[\delta_{ij} - \rho_i\tilde{Q}_{ij}(s)] \tag{A.1}$$

We first observe that **M** is a matrix of the form

$$M_{ij} = \delta_{ij} - \hat{a}_i\hat{b}_j - \hat{c}_i\hat{d}_j - \hat{e}_i\hat{f}_j \tag{A.2}$$

where we are using the notation

$$\begin{aligned} \hat{a}_i &= \rho_i\alpha_i & \hat{b}_j &= 1 \\ \hat{c}_i &= \rho_i\beta_i & \hat{d}_j &= \sigma_j \\ \hat{e}_i &= \rho_i\gamma_i & \hat{f}_j &= a_j \end{aligned} \tag{A.3}$$

By simple substitution we can check that the inverse of this matrix, $\mathbf{M}^{-1}$, has elements

$$\begin{aligned} M_{ij}^{-1} = \delta_{ij} + \frac{1}{D_T}\{&\hat{a}_i\hat{b}_j[(1 - \hat{c}\hat{d})(1 - \hat{e}\hat{f}) - (\hat{c}\hat{f})(\hat{e}\hat{d})] \\ &+ \hat{a}_i\hat{d}_j[(\hat{c}\hat{b})(1 - \hat{e}\hat{f}) + (\hat{b}\hat{e})(\hat{c}\hat{f})] \\ &+ \hat{a}_i\hat{f}_j[(\hat{b}\hat{e})(1 - \hat{c}\hat{d}) + (\hat{b}\hat{c})(\hat{d}\hat{e})] + \hat{c}_i\hat{d}_j[(1. \\ &- \hat{a}\hat{b})(1 - \hat{c}\hat{f}) - (\hat{a}\hat{f})(\hat{b}\hat{e})] + \hat{c}_i\hat{b}_j[(\hat{a}\hat{d})(1 - \hat{e}\hat{f}) \\ &+ (\hat{a}\hat{f})(\hat{d}\hat{e})] + \hat{c}_i\hat{f}_j[(\hat{d}\hat{e})(1 - \hat{a}\hat{b}) + (\hat{a}\hat{d})(\hat{b}\hat{e})] \\ &+ \hat{e}_i\hat{f}_j[(1 - \hat{a}\hat{b})(1 - \hat{c}\hat{d}) - (\hat{a}\hat{d})(\hat{b}\hat{c})] \\ &+ \hat{e}_i\hat{b}_j[(\hat{a}\hat{f})(1 - \hat{c}\hat{d}) + (\hat{a}\hat{d})(\hat{c}\hat{f}) + \hat{e}_i\hat{d}_j[(\hat{c}\hat{f})(1 - \hat{a}\hat{b}) \\ &+ (\hat{a}\hat{f})(\hat{b}\hat{c})]\} \end{aligned} \tag{A.4}$$

where

$$\begin{aligned} D_T = {}&(1 - \hat{a}\hat{b})(1 - \hat{c}\hat{d})(1 - \hat{e}\hat{f}) - (\hat{a}\hat{d})(\hat{b}\hat{c})(1 - \hat{e}\hat{f}) \\ &- (\hat{c}\hat{f})(\hat{e}\hat{d})(1 - \hat{a}\hat{b}) - (\hat{a}\hat{f})(\hat{b}\hat{e})(1 - \hat{c}\hat{d}) \\ &- (\hat{a}\hat{d})(\hat{b}\hat{e})(\hat{c}\hat{f}) - (\hat{a}\hat{f})(\hat{b}\hat{c})(\hat{d}\hat{e}) \end{aligned} \tag{A.5}$$

and we used the notation

$$(\hat{a}\hat{b}) = \sum_{l=4}^{n} \hat{a}_l\hat{b}_l \tag{A.6}$$

throughout. Replacing this result into (4.2), and making use of (A.3), (A.4), (4.8), (4.9), and (4.10) yields an explicit, but quite complex expression for $\tilde{G}_{ij}(s)$. This expression is not symmetric as required by simple reciprocity. The fact that after a nontrivial algebraic calculation, which makes full use of the solution of ref 2, $\tilde{G}_{ij}(s)$ turns out to be symmetric constitutes an argument for the correctness of the symmetrization conjecture used in this work. One of the crucial relations used derives from (2.13), and reads

$$\begin{aligned} \frac{-2s\Gamma^2}{\alpha^2}(\hat{a}\hat{f}) = \frac{\pi}{\Delta}[&2(\hat{b}\hat{e}) + s(\hat{d}\hat{e}) \\ &+ P_n(1 - \hat{a}\hat{b})] \end{aligned} \tag{A.7}$$

similarly, we also need

$$\begin{aligned} \frac{-2s\Gamma^2}{\alpha^2}(\hat{c}\hat{f}) = \frac{\pi}{\Delta}\Big[&\left(s + \zeta_2\frac{\pi}{\Delta}\right)(\hat{b}\hat{e}) + s\zeta_2\left(\frac{\pi}{2\Delta}\right)(\hat{d}\hat{e}) \\ &- P_n(\hat{b}\hat{c})\Big] \end{aligned} \tag{A.8}$$

where the symbols are defined above and in section 2. Repeated used of these relations shows that the pair correlation function is indeed symmetric:

$$\begin{aligned} \tilde{G}_{ij}(s) = {}&\frac{D_0}{D_T}(1 - \hat{e}\hat{f})\tilde{G}_{ij}{}^0(s) \\ &+ \frac{e^{-s\sigma_{ij}}}{2\pi s^2 D_T}\left\{\frac{2\pi}{\Delta}(\hat{e}\hat{d})\left[-(\hat{c}\hat{f}) + (1/2)(\hat{a}\hat{f})\left(s + \frac{\pi}{\Delta}\zeta_2\right)\right]\right. \\ &+ \frac{\pi s}{\Delta}\left[(\hat{c}\hat{f}) - (\hat{a}\hat{f})\frac{\pi}{2\Delta}\zeta_2\right][(\hat{b}\hat{e})\sigma_i\sigma_j - 2(\hat{d}\hat{e})\sigma_{ij}] \\ &+ \left[\frac{\pi}{\Delta}P_n - \frac{2\Gamma^2 s}{\alpha^2}(a_i + a_j)\right][(\hat{a}\hat{f})(1 - \hat{c}\hat{d}) \\ &+ (\hat{c}\hat{f})(\hat{a}\hat{d})] - \frac{2\Gamma^2 s}{\alpha^2}[\sigma_i a_j + \sigma_j a_i][(\hat{c}\hat{f})(1 - \hat{a}\hat{b}) \\ &\left.+ (\hat{a}\hat{f})(\hat{b}\hat{c})] - \frac{2\Gamma^2 D_0}{\alpha^2}a_i a_j\right\} \end{aligned} \tag{A.9}$$

and replacing (A.3), (4.8–10), and (2.13) into this yields after some more algebra, eq 4.12.

References and Notes

(1) J. K. Percus and G. Yevick, *Phys. Rev.*, **136**, B290 (1964); J. L. Lebowitz and J. K. Percus, *ibid.*, **144**, 251 (1966); E. Waisman and J. L. Lebowitz, *J. Chem. Phys.*, **56**, 3086, 3093 (1972).

(2) L. Blum, *Mol. Phys.*, **30**, 1529 (1975).

(3) R. Triolo, J. R. Grigera, and L. Blum, *J. Phys. Chem.*, **80**, 1858 (1976).

(4) J. C. Rasaiah, D. N. Card, and J. P. Valleau, *J. Chem. Phys.*, **56**, 248 (1972).

(5) J. E. Mayer, *J. Chem. Phys.*, **18**, 1426 (1950).

(6) K. Hiroike, *Mol. Phys.*, in press.

(7) G. Stell and J. L. Lebowitz, *J. Chem. Phys.*, **49**, 3706 (1968).

(8) F. H. Stillinger and R. Lovett, *J. Chem. Phys.*, **48**, 3858 (1968).

(9) L. Onsager, *Chem. Rev.*, **13**, 73 (1933).

(10) J. Groeneveld, unpublished.

(11) J. C. Rasaiah and H. L. Friedman, *J. Chem. Phys.*, **48**, 2742 (1968); **50**, 3965 (1969).

(12) A. R. Allnatt, *Mol. Phys.*, **8**, 533 (1964).

(13) W. Olivares and D. McQuarrie, *Biophys. J.*, **15**, 143 (1975).

(14) C. W. Outhwaite, "Equilibrium Theory of Electrolyte Solutions" in "Statistical Mechanics", Vol. II, The Chemical Society, London, 1975.

(15) K. S. Pitzer, *J. Chem. Phys.*, **77**, 268 (1973).

(16) F. Hirata and K. Harakawa, *Bull. Chem. Soc. Jpn.*, **48**, 2139 (1975).

(17) R. J. Baxter, *J. Chem. Phys.*, 52, 4559 (1970).

(18) J. S. Høye and G. Stell, "Thermodynamics of the MSA for Simple Fluids", SUSB Report No. 287, Stony Brook, 1976.

(19) M. S. Wertheim, *J. Math. Phys.*, **5**, 643 (1964).

(20) H. C. Andersen and D. Chandler, *J. Chem. Phys.*, **57**, 1818 (1972); D. Chandler and H. C. Andersen, *ibid.*, **57**, 1930 (1972).

(21) While this work was in preparation we received a preprint from Professor K. Hiroike in which, among other results, an expression for the free energy was given.

Infrared Study of Oxidized and Reduced Palladium Loaded Zeolites

M. Primet* and Younès Ben Taarit

Institut de Recherches sur la Catalyse, 79, boulevard du 11 novembre 1918, 69626 Villeurbanne, Cedex, France

(Received May 13, 1976; Revised Manuscript Received March 9, 1977)

Publication costs assisted by Institut de Recherches sur la Catalyse

The acidic properties of a NaPd(II)–Y zeolite were investigated using pyridine adsorption as studied by infrared spectroscopy. Palladium ions were shown to be able to move in the zeolite framework and coordinate pyridine molecules. Hydrogen reduction resulted in two distinct effects: (i) the lattice acquired hydroxyl groups having very similar properties to those of decationated zeolites; and (ii) palladium ions were reduced into metal whose dispersion was studied by volumetric methods and appeared to be strongly temperature dependent. Under mild reduction conditions (below 300 °C), isolated metal atoms were formed. They exhibited a strong electron-deficient character. Metal–pyridine complexes were detected. Under more drastic reduction conditions, metal particles were formed at the expense of isolated atoms. Pyridine adsorption appeared as a decisive and convenient method to characterize this evolution.

Introduction

In recent years, a number of papers were devoted to the examination of structural modifications caused by the presence of the first row transition metal ions in zeolites.[1] Acid–base properties of the host lattice as well as the structure of various complexes formed upon adsorption of various reagents and/or probes were thoroughly investigated.[2-6] However, with the exception of an early paper devoted to the modifications of the structural and acidic properties of Cu(II)–Y zeolite upon reduction by hydrogen or carbon monoxide,[7] no infrared studies were reported on the changes in the acidic properties of the zeolite lattice resulting from the reduction of noble metal cations into small clusters or slightly larger metal particles. In this respect zeolite hosts provide outstanding matrices for both cation or reduced metal crystallites. Zeolite indeed appeared as a unique support for particularly tiny metal particles[8] (as small as 10-Å diameter clusters). In some instances isolated atoms could seemingly be formed.[4,8] These findings and the major role of small noble metal particles in many catalytic processes prompted us to examine the modifications of the lattice acidic properties caused by the hydrogen reduction of Pd(II) loaded zeolites and to investigate the properties of the resulting metal as a function of the conditions of reduction.

In this work, we shall be concerned mainly with the state of palladium following reduction under mild conditions. The properties of this zeolite reduced form will be investigated using essentially pyridine adsorption as studied by infrared spectroscopy. In the course of this study, we shall also resort to volumetric measurements as well as poisoning experiments. Dispersion measurements, in particular, are not meant as dispersion studies as such, but rather as complementary and useful data regarding the investigated samples.

Experimental Section

Materials. The NH_4– and NH_4Na–Y Forms. The starting material was the Linde Na–Y form (SK 40). The NH_4–Y form was prepared by the conventional exchange procedure using an excess of dilute NH_4NO_3 solution at room temperature. The exchange was repeated 20 times in order to reach a residual sodium content of about 0.8%. The NH_4Na–Y form was prepared in the same fashion. However the ammonium nitrate solution volume was adjusted to obtain a residual sodium content of 6.4%.

In both cases, flame spectrometry was used in order to determine the zeolite sodium content. The overall formulae for the exchanged materials are respectively $Na_4(NH_4)_{52}Al_{56}Si_{136}O_{384}$ and $Na_{34}(NH_4)_{22}Al_{56}Si_{136}O_{384}$.

The NaPd–Y Form. Tetraamminepalladium chloride was prepared by refluxing $PdCl_2$ in ammonia solution with final removal of excess ammonia at 80 °C. The sodium ions were exchanged for tetraamminepalladium ions using an aqueous solution of tetraamminepalladium chloride for 12 h at 25 °C. The resulting sample was then washed until free of chloride ions and dried at 80 °C in air. The flame photometry technique was used to determine the actual sodium content. The palladium content was determined by a spectrophotometric method using the formation of a Pd(II)–nitroso R–salt complex[9] in the pH range 2–2.6. The absorbance of the red organo–palladium complex is measured at 510 nm. Chemical analysis gave the following overall formula for the exchanged material: $Pd_{11}H_4Na_{30}Al_{56}Si_{136}O_{384}$. The number of protons per unit cell was calculated to ensure charge balance and is therefore rather uncertain.

Hydrogen was purified using a Deoxo catalyst and stored over 5A molecular sieves after activation at 350 °C. High purity pyridine was dried by trapping over activated molecular sieves prior to each use.

Techniques. Sample wafers of about 20 mg and 18 mm in diameter were compressed at a pressure of 10^5 kPa. The pellet was then introduced in a quartz sample holder fitting into a grease-free infrared cell otherwise similar to that described previously.[10]

Spectra were recorded at room temperature on a Perkin-Elmer Model 125 grating spectrophotometer. Slit widths were programmed so as to obtain a resolution better than 3 cm^{-1} in the 4000–1200-cm^{-1} range. The reference beam was attenuated and the instrument continuously purged with H_2O and CO_2 free air.

Volumetric measurements were carried out in a conventional pyrex constant volume cell. Gas pressure was monitored by a Texas Instruments quartz spiral Bourdon gauge. The samples were heated in flowing oxygen using a flow-through design cell allowing the determination of hydrogen consumption during the reduction process as well.

Sample Treatments. The first step of the thermal treatment of palladium zeolites was the removal of ammonia generated by the decomposition of the tetra-

TABLE I: Volumetric Measurements[a]

H_2 treatment temp T, °C	H_2 final press P_f, Torr	n_R, µmol g^{-1}	n_A, µmol g^{-1}	n_D, µmol g^{-1}	Reduction level	n_A/n_R	n_D/n_R
16	76.3	392	15.5	2.24	0.62	0.04	0.006
17	62.58	324	16.5	0	0.516	0.051	0
74	48.48	517.3	44.9	0	0.824	0.087	0
91	41.52	626	46.5	0	1.0	0.07	0
117	101.6	624	33.7	11.6	1.0	0.05	0.018
135	71.2	628	77.2	21.6	1.0	0.123	0.034
250	68.67	630	86.1	78.5	1.0	0.137	0.124
300	42.97	630	76.15	68.2	1.0	0.121	0.108
400	53.56	628	83.2	75.9	1.0	0.132	0.121
500	60.8	627	81.0	81.8	1.0	0.129	0.130
500	54.47	623	78.6	131	1.0	0.126	0.21

[a] The NaPd-Y sample contains 628 µmol of Pd^{2+} ion per gram of exchanged material n_R, n_A, and n_D referred to 1 g of sample. n_R is the number of µmol of H_2 consumed by the reduction of Pd(II) into Pd(0). n_A is the number of µmol of H_2 adsorbed on the metal particles. n_D is the number of µmol of H_2 dissolved into the bulk for an hydrogen pressure set to the final pressure (P_f).

amminepalladium complex. In this purpose, the samples were slowly heated at a rate of 0.5 °C min^{-1} in flowing oxygen to 500 °C. They were then evacuated at the same temperature at a pressure of 2×10^{-6} Torr. These samples were labeled oxidized samples and contain palladium mainly as Pd(II).

The reduction step was achieved by contacting the oxidized samples with 200 Torr of hydrogen at temperatures ranging from 25 to 500 °C for at least 8 h. All samples were subsequently evacuated at 200 °C for 6 h. The residual pressure was less than 2×10^{-6} Torr.

Results

(1) *Volumetric Data.* A known amount of hydrogen was admitted at room temperature (RT) onto the oxidized sample. The temperature was then raised to the desired value in the range 16–500 °C. The system was maintained at this temperature (T) for 12 h. Afterwards, the sample was cooled to room temperature and the final hydrogen pressure (P_f) was measured. Knowledge of the dead volume, and the initial and the final pressures allowed the determination of the total amount (n_T in micromoles per gram of catalyst) of H_2 consumed during the entire process.

In this process, hydrogen was consumed in four different ways: (i) reduction of Pd(II) ions into Pd(0) metal, n_R; (ii) adsorption of H_2 on metal particles, n_A; (iii) dissolution of H_2 in the bulk of the metal, n_D; and (iv) physisorption of H_2 on the support, n_p.

n_D is the amount of H_2 dissolved in the bulk and was shown[11] to be strongly pressure dependent. Further, this dissolved hydrogen could be removed by prolonged evacuation at room temperature. This evacuation does not alter the amount of adsorbed hydrogen (n_A), while physisorbed hydrogen was removed. The amount of dissolved hydrogen was determined by the back-sorption method described by Boudart and Hwang.[11]

n_p was determined using the room temperature adsorption isotherm on a blank sample $Na_{34}(NH_4)_{22}Al_{56}Si_{136}O_{384}$ activated at the corresponding temperature T.

n_A is the amount of chemisorbed hydrogen; it could be determined by titration with oxygen according to the scheme proposed by Boudart et al.[12]

$$Pd_s\text{-}H + {}^3/_4O_2 \rightarrow Pd_s\text{-}O + {}^1/_2H_2O \text{ (adsorbed on the support)}$$

After the final pressure P_f has been measured, the sample was evacuated for 20 min at room temperature. Hydrogen adsorption isotherm was performed on this sample. The hydrogen uptake at P_f represents the sum of n_D and n_p. Taking into account n_p from blank experiments, n_D could be determined. Again the sample was evacuated for 20 min at room temperature and successive increments of oxygen were admitted at 25 °C. The oxygen uptake allowed the determination of the number of dissociated hydrogen molecules and hence n_A using the stoichiometry of the titration reaction. After all these different quantities have been determined, n_R was deduced.

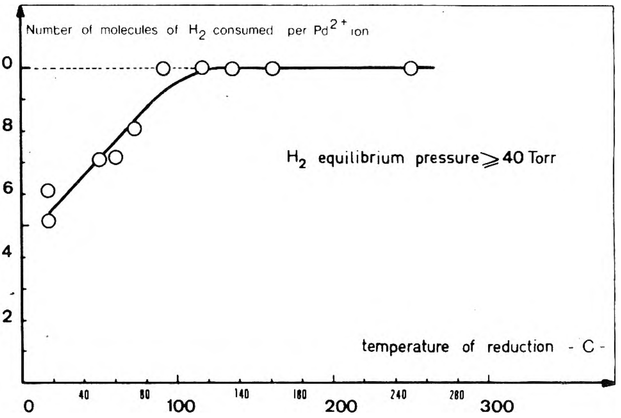

Figure 1. Degree of reduction of Pd^{2+} ions in NaPb-Y zeolite vs. the temperature of reduction under hydrogen for an equilibrium pressure above 40 Torr.

Table I gives the different values of n_R, n_A, and n_D at various reduction temperatures T. The reduction level is defined as the number of hydrogen molecules consumed per Pd^{2+} ion by the sole reduction process. Figure 1 shows the variation of the reduction level as a function of temperature. It is clear that beyond 100 °C all palladium ions were reduced to metal.

(2) *Infrared Studies.* Following Parry's pioneer work,[13] pyridine has been extensively used to investigate the nature of the acid sites on surfaces.[13-15] Owing to the extreme sensitivity of many of its vibration modes to the nature of the bond in which the N atom is involved, pyridine provided a most suitable probe to characterize surface centers.

Earlier workers, as indicated in Table II, showed that the infrared bands relative to some of the vibration modes that occur in the 1700–1400-cm^{-1} range were markedly shifted from those of liquid pyridine when the organic base was combined with various species. In this respect the 19b and 8a modes appeared to be singled out from other modes and gave rise to specific bands when pyridine was allowed to react with protons to form pyridinium ions (1540 cm^{-1}, 19b; 1620 cm^{-1}, 8a) or coordinated to metals or metal ions (1450 cm^{-1}, 19b; ~1610 cm^{-1}, 8a).

In our description of the experimental spectra, we shall be exclusively concerned with those most meaningful modes. The experimental optical densities were determined by substracting the zeolite background. They all refer to a constant mass of sample, namely 100 mg. Pyridine was introduced at room temperature, then the sample was evacuated at 150 °C for 10 h to remove excess and physisorbed pyridine, and a residual pressure of 5 × 10^{-6} Torr was measured.

(a) *NaY Zeolite.* The infrared spectrum of a Na-Y sample treated at 400 °C under oxygen, then in vacuo, only showed at weak ν(OH) band at 3745 cm^{-1}. Upon the addition of pyridine new bands developed in the 1800–1200-cm^{-1} region. In particular, sharp bands at 1595 (8a), 1485 (19b), and 1440 cm^{-1} (19b) appeared and resisted evacuation of excess pyridine at 150 °C. These bands are indicative of pyridine interacting with Na^+ ions.[21] When small increments of water vapor were admitted onto the sample, the general features of the spectrum were not altered and, particularly, no band could be observed at 1540 cm^{-1}. Indeed the $\delta(H_2O)$ band at 1640 cm^{-1} appeared in the spectrum, nevertheless pyridine coordinated to sodium ions was not converted into pyridinium ions.

(b) *$NaNH_4$-Y and NH_4-Y Zeolites.* Upon activation at 400 °C under oxygen, then in vacuo, both $NaNH_4$-Y and NH_4-Y forms exhibited OH groups which absorb at 3740, 3635, and 3540 cm^{-1}. The intensity of the latter two decreased as the activation temperature was raised. At 500 °C, these ν(OH) bands were rather weak and their intensity varied with the desorption duration. When small increments of pyridine were allowed to react at 25 °C with NH_4-Y samples treated at 400 °C, both bands at 3635 and 3540 cm^{-1} decreased regularly and eventually vanished. Simultaneously, bands at 1630–1540 cm^{-1} and weak ones at 1620–1452 cm^{-1} appeared in the spectrum as shown in Figure 2. Desorption of pyridine at 150 °C did not affect the bands at 1630 and 1540 cm^{-1} due to pyridinium ions, although the ν(OH) band at 3540 cm^{-1} was totally restored (Figure 2e).

Evacuation of the obtained samples at higher temperatures led to the disappearance of the bands due to chemisorbed pyridine: the 1630–1540-cm^{-1} bands disappeared between 400 and 500 °C whereas the 1620–1452-cm^{-1} bands were no longer observed by vacuum treatment above 500 °C.

Samples treated at 600 °C did not show ν(OH) bands, with the exception of that at 3740 cm^{-1}. Addition of pyridine resulted in the appearance of strong bands at 1620 (8a) and 1452 cm^{-1} (19b) indicative of pyridine coordinated to Lewis centers, i.e., trigonal aluminum atoms. Addition of increments of water vapor progressively and quantitatively converted the coordinated pyridine into pyridinium ions. Pyridine coordinated to trigonal aluminum atoms could only be removed by evacuation at temperatures above 500 °C.

(c) *Pyridine Interaction with Palladium Exchanged Zeolite. The Oxidized Pd(II)-Y Form.* The fresh Pd(II)-Y samples exhibited bands at 1343 and 1314 cm^{-1} due to the bending vibrations of NH_3 in the $[Pd(NH_3)_4]^{2+}$ complex.[22] Upon heating the fresh samples in flowing oxygen at increasingly higher temperatures, the bands at 1343 and 1314 cm^{-1} decreased in intensity and ultimately vanished when the temperature was raised beyond 350 °C. It is noteworthy that neither the fresh samples nor the partially decomposed ones showed, at any stage, bands attributable to NH_4^+ ions. Therefore these ions were never formed either during the exchange process or the subsequent decomposition of the tetraammine complex.

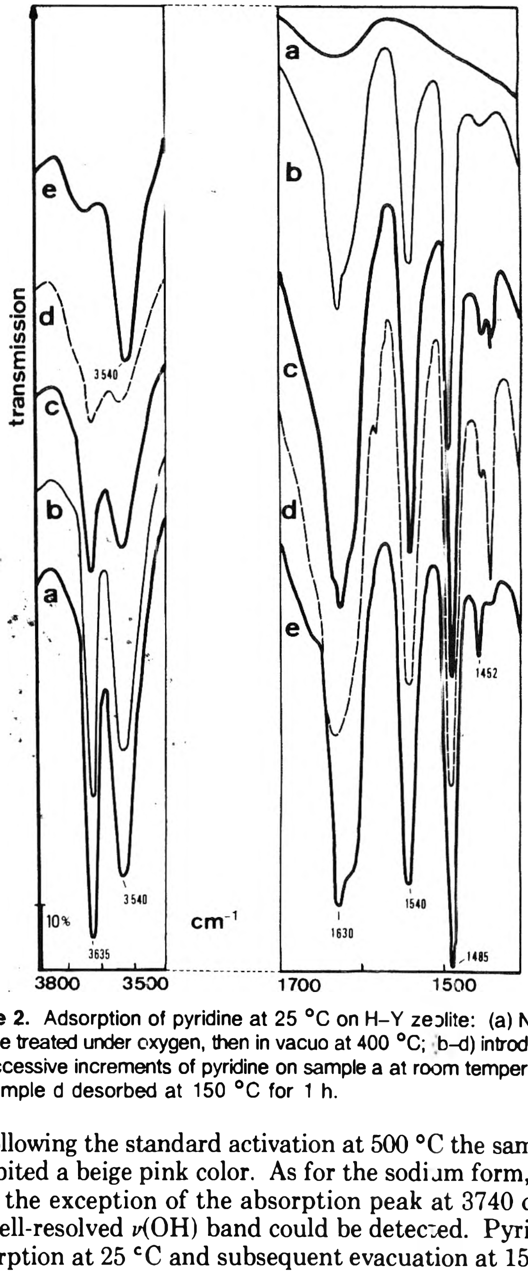

Figure 2. Adsorption of pyridine at 25 °C on H-Y zeolite: (a) NH_4-Y sample treated under oxygen, then in vacuo at 400 °C; (b–d) introduction of successive increments of pyridine on sample a at room temperature; (e) sample d desorbed at 150 °C for 1 h.

Following the standard activation at 500 °C the samples exhibited a beige pink color. As for the sodium form, and with the exception of the absorption peak at 3740 cm^{-1}, no well-resolved ν(OH) band could be detected. Pyridine adsorption at 25 °C and subsequent evacuation at 150 °C gave rise to a very weak band at 1540 cm^{-1} (19b) indicative of trace amounts of pyridinium ions and strong peaks at 1605 (8a) and 1452 cm^{-1} (19b) (Figure 3b). Contrary to the 1452-cm^{-1} (19b) band encountered for the dehydroxylated Y form, *this band was not affected by addition of water increments.* The corresponding coordinated pyridine was not converted into pyridinium ions by simple addition of water vapor. The band at 1605 cm^{-1} was not affected either.

On evacuation at 300 °C, the samples turned black, the 1452- (19b) and 1605-cm^{-1} (8a) bands decreased sharply in intensity, while the bands at 1630 (8a) and 1540 cm^{-1} (19b) due to $(C_5H_5NH^+)$ strongly developed. Readdition of pyridine, following evacuation at 300 °C, failed to restore the bands which previously appeared at 1452 and 1605 cm^{-1}, while it emphasized the Brönsted acidity enhancement. Evacuation of pyridine at even higher temperatures generated ν(OH) bands at 3635 and 3545 cm^{-1} which could not be traced prior to pyridine adsorption.

The Hydrogen Reduced Pd-Y Forms. When oxidized samples were reduced at temperatures ranging from 25 to 500 °C in 200 Torr of hydrogen and cooled to room temperature, their infrared spectra showed the presence of both water and hydrogen bonded hydroxyl groups.

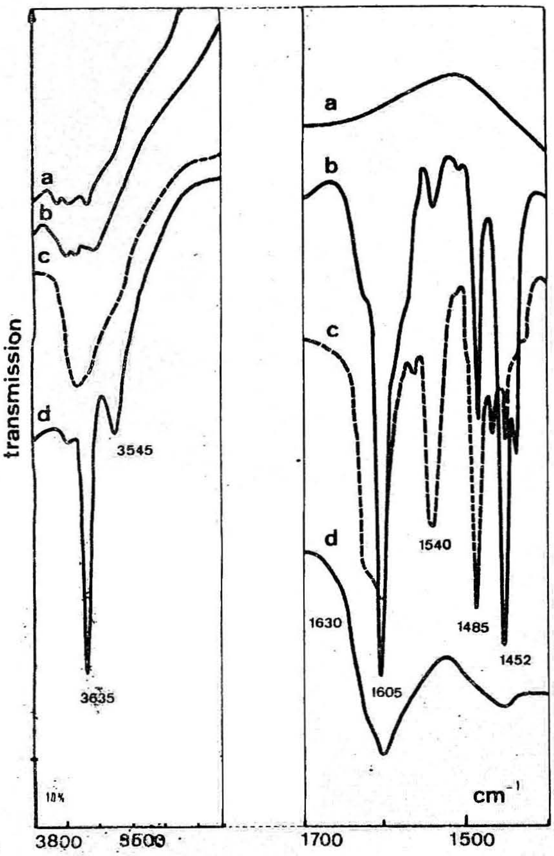

Figure 3. Adsorption of pyridine on NaPd–Y oxidized form: (a) NaPd–Y sample treated under oxygen, then in vacuo at 500 °C; (b) pyridine irreversibly adsorbed at 150 °C on sample a; (c) sample b desorbed at 300 °C for 3 h; (d) sample c desorbed at 500 °C for 3 h.

Upon room temperature reductions, the intensity of the ν(OH) bands increased by increasing the hydrogen pressure (7–60–200 Torr) for a given reduction time (Figure 7).

On evacuation of the reduced samples at 150 °C the $\delta(H_2O)$ band disappeared, while two intense ν(OH) bands at 3635 and 3545 cm^{-1} showed clearly (Figure 4). The intensity of the main one (3635 cm^{-1}) remained constant as the reduction temperature was raised beyond 200 °C (Figure 7).

Pyridine adsorption at 25 °C on reduced samples led to the disappearance of both bands assigned to hydroxyl groups. Removal of excess or weakly held pyridine at 150 °C resulted in the typical IR spectrum shown in Figure 4 where bands at 1630 and 1540 cm^{-1} (pyridinium ions) together with bands at 1605 (8a) and 1452 cm^{-1} (19b) (coordinated pyridine) could be seen. While the 1540-cm^{-1} band (pyridinium ions) increased in intensity with H_2 pressure (7–60–200 Torr) for reductions at 25 °C, by contrast the band at 1452 cm^{-1} decreased in intensity under the same experimental conditions (Figure 7). By vacuum treatment at increasing temperatures, chemisorbed pyridine was progressively eliminated from the sample: coordinated pyridine was removed above 300 °C and pyridinium ions disappeared at about 400 °C. When the reduction temperature increased from 200 to 500 °C, the intensity of the band at 1540 cm^{-1} did not change significantly whereas those at 1605 and 1452 cm^{-1} decreased continuously (Figure 7). In particular, following reduction at 500 °C and subsequent evacuation at 150 °C, pyridine addition did not lead to coordinated pyridine (Figure 5). It is significant that, for all reduced samples, coordinated pyridine, whenever observed, could not be converted into pyridinium ions by equilibration with water vapor (Figure 4d).

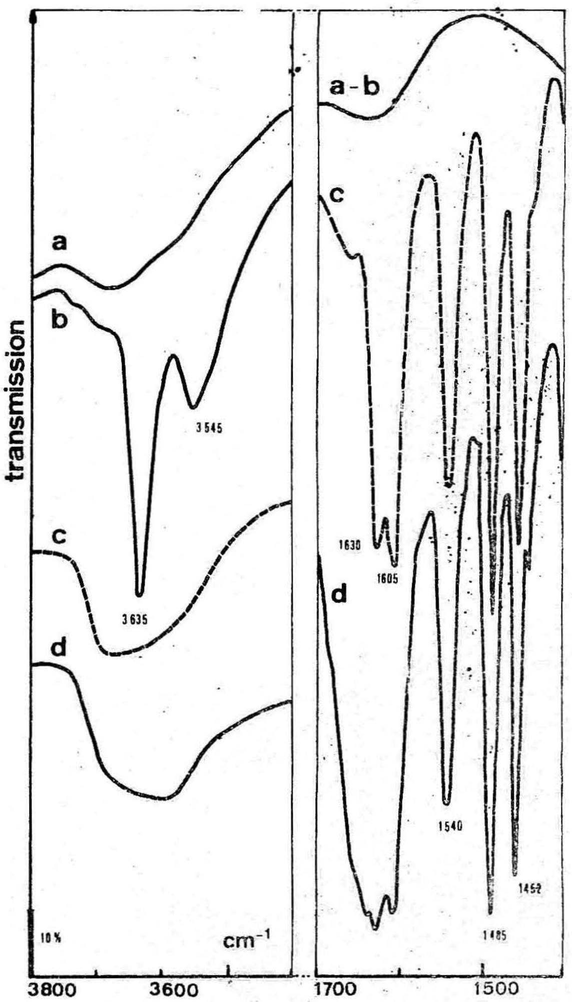

Figure 4. Adsorption of pyridine on reduced NaPd–Y form: (a) NaPd–Y oxidized form (oxygen and vacuum treatments at 500 °C); (b) sample a treated with 200 Torr of hydrogen at 150 °C for 4 h, then desorbed at 200 °C for 12 h; (c) sample b equilibrated with pyridine at 25 °C, then desorbed at 150 °C for 3 h; (d) introduction of water vapor at room temperature on sample c.

By contrast, samples reduced at 500 °C and further evacuated at 600 °C exhibited medium bands at 1620 (8a) and 1452 cm^{-1} (19b) upon pyridine admission. The corresponding species could be totally converted into pyridinium ions by water vapor.

H_2S Poisoning. In a typical experiment the oxidized sample was reduced at 200 °C and further evacuated at the same temperature. It was then equilibrated with H_2S at 200 °C and given final evacuation also at 200 °C. Under these conditions, as apparent from Figure 6, addition of pyridine gave rise essentially to bands at 1630 and 1540 cm^{-1} indicative of pyridinium ions while no band could be detected at 1452 or 1605 cm^{-1} suggesting that pyridine coordination centers were poisoned by H_2S.

Discussion

While the 19b vibration mode of pyridine appeared, through the literature, to be a particularly convenient way to discriminate Brönsted and Lewis centers, it failed to differentiate true Lewis acid sites such as $AlCl_3$, trigonal aluminum ions on surfaces, etc., and pyridine combined with transition metal ions or atoms in coordination compounds. By contrast the 8a mode, as obvious from Table II, appeared to be very sensitive to the nature of the bonding site and even to the type of solvent.[23] While pyridine coordinated to trigonal aluminum sites (Lewis sites) of alumina and/or silica–alumina was characterized

TABLE II: Dependence of the Frequencies of Some Vibrations Modes of Pyridine on Bonding[a]

State of pyridine	Vibration modes, cm^{-1} 19b	19a	8b	8a
Liquid pyridine[b]	1439 (vs)	1478 (s)	1572 (m)	1583 (vs)
Complex pyridine $AlCl_3$[c] or BF_3[d]	1455			1620
Pyridine adsorbed on alumina[d-f]	1444 (vs)	1487 (m)	1576 (s)	1620 (s)
Complex $PtCl_2Py_2$[g]	1452 (trans) 1450 (cis)	1477 (trans) 1484 (cis)	1570 (trans) 1567 (cis)	1608 (trans) 1608 (cis)
Pyridinium ion[h]	1525 (s) 1542 (vs)	1478 (s) 1490 (vs)	1600 (s) 1613 (vs)	1631 (m) 1640 (vs)
Pyridinium ion adsorbed on a silica-alumina catalyst[d,e]	1544	1490	1575 (w) 1620 (vs)	1638
Pyridinium ion adsorbed on a HY zeolite[i]	1540	1489.5 1487.5	1620	1632-1630

[a] Intensities of the infrared bands are designated by w = weak, m = medium, s = strong, vs = very strong. [b] Reference 16. [c] Reference 17. [d] Reference 13. [e] Reference 15. [f] Reference 35. [g] Reference 18. [h] Reference 19. [i] Reference 20.

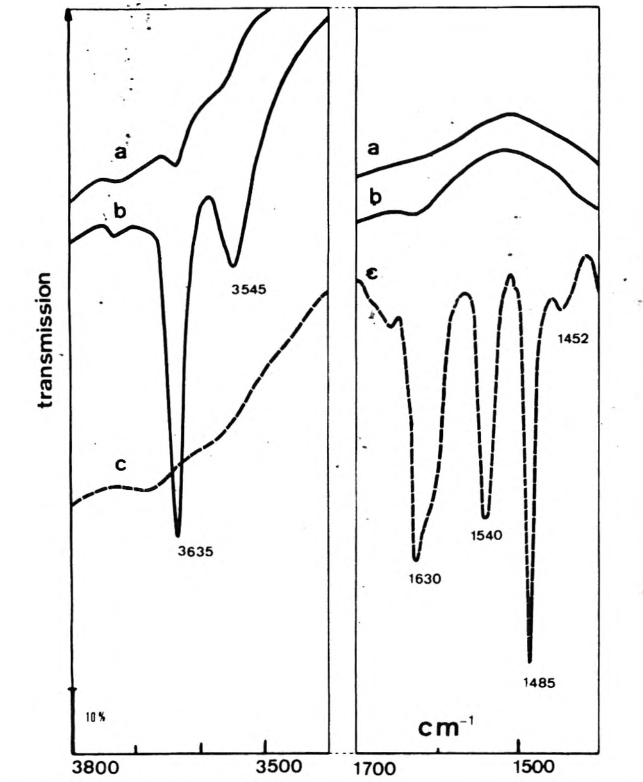

Figure 5. Adsorption of pyridine on reduced NaPd-Y zeolite: (a) NaPd-Y oxidized form (oxygen and vacuum treatments at 500 °C); (b) sample a treated with 200 Torr of hydrogen at 500 °C for 6 h, then desorbed at 200 °C for 12 h; (c) sample b equilibrated with pyridine at 25 °C, then desorbed for 6 h at 150 °C.

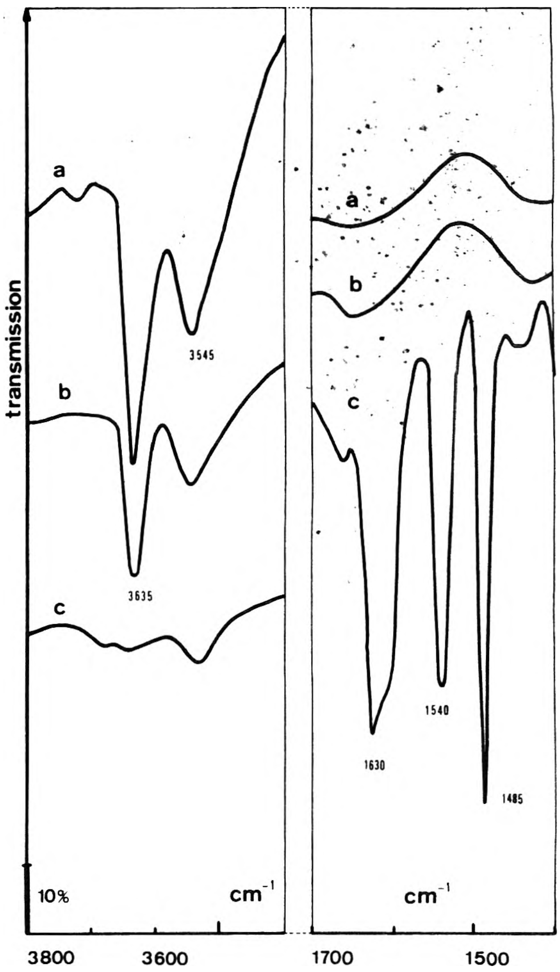

Figure 6. Poisoning effect of H_2S: (a) NaPd-Y oxidized form reduced at 150 °C and evacuated at 200 °C; (b) sample a heated in 30 Torr of H_2S at 200 °C for 3 h, then evacuated for 4 h at 200 °C; (c) pyridine irreversibly adsorbed at 150 °C on the previous sample.

by absorption at 1620-1630 cm^{-1} for this 8a mode, for pyridine complexed to cations or transition metals, the 8a mode absorption occurred around 1595-1610 cm^{-1}. Hence this absorption mode should enable one to discriminate pyridine bonded to aluminum Lewis centers and organometallic complexes of pyridine.

(1) *The Oxidized Pt(II) Form.* In agreement with earlier reports[21] in pure Na-Y zeolite, sodium ions were shown to coordinate pyridine whose 19b vibration mode absorbed at 1440 cm^{-1}; the 8a mode absorption occurred at 1595 cm^{-1} reflecting a weaker interaction between sodium ions and pyridine than between trigonal aluminum ions and pyridine (8a mode absorbed at 1620-1630 cm^{-1}). Similarly Pd(II) ions of the Pd-Y form are thought to coordinate pyridine. These ions are expected to bind more tightly to pyridine than alkaline-earth metal ions; this is in agreement with the shift of the 19b vibration mode to higher frequencies (1452 cm^{-1} instead of 1440 cm^{-1}). The same relative shift is observed for the 8a mode (1595 cm^{-1} for Na^+ ions vs. 1605 cm^{-1} for Pd^{2+} ions).

In a infrared study of pyridine adsorption on cation exchanged Y zeolite, Hall and co-workers[21] first showed that the frequencies of the 8a and 19b absorption modes of adsorbed pyridine vary with the nature of the coordinating cation. These frequencies were shown to increase with the electron affinity of the exchanged cation.[21] We also showed that copper ions in Y zeolite[2] do coordinate pyridine and give rise to bands at 1612 and 1455 cm^{-1}

corresponding to the 8a and 19b modes, respectively. X ray studies[25] as well as EPR[24] measurements confirmed the nature of the coordination site. In the case of copper(II) as well as in the present case, pyridine coordinated to the cation *was not affected* by water adsorption and indeed not converted into pyridinium ions. By contrast pyridine coordinated to trigonal aluminum atoms either belonging to alumina, silica-alumina, or zeolites exhibits an 8a mode vibration at 1620–1630 cm^{-1} and certainly not at lower frequency. On the other hand, in the latter two cases, it is readily converted to pyridinium ions whereas in the case of alumina, which never showed a strong Brönsted acidity pyridine although not converted to pyridinium ions, it was *displaced* by water and just exhibited the bands due to *physisorbed pyridine* or weakly interacting with OH groups.[35] Therefore we rule out the trigonal aluminum atoms as the centers responsible for pyridine adsorbed in the case of Pd(II)–Y and assign these bands to pyridine coordinated by Pd(II) ions. This is also in agreement with the increase in the intensity of these bands upon increase of palladium(II) content. Although most Pd(II) ions were located at $S_{I'}$ sites as was the case for Cu(II) ions following activation at 500 °C, Pd(II) ions are very likely to migrate to the sugercages to coordinate pyridine in the same way as Cu(II) ions were shown to behave. Such cation migration is not unlikely and has already been reported[24-26] and is now fully accepted if not always understood or predictable.

On the other hand, while few pyridinium ions were formed upon pyridine reaction with freshly oxidized samples, removal of the organic base at increasingly higher temperatures appeared to favor the formation of more pyridinium ions. This could be explained in terms of palladium reduction during the decomposition of the Pd(II)–pyridine complex, by the evolving pyridine. This reduction would form protons which in turn would react with released pyridine. This is probably the most sensible interpretation of the Brönsted acidity enhancement at the expense of pyridine coordinated to palladium ions. This interpretation was further substantiated by the appearance of ν(OH) bands following total removal of pyridine.

(2) *The Reduced Pd*(0)*–Y Form.* (a) *Metal Dispersion.* Under mild reduction conditions (100–200 °C), where all palladium ions were reduced, the quasi zero solubility of hydrogen tends to indicate a 100% dispersion. Therefore, the number of adsorbed hydrogen atoms per Pd atom ($2n_A/n_R$) should rigourously equal 1. In fact, the experimental ratios $2n_A/n_R$ over this temperature range vary slightly from 0.1 to 0.2. The ratios are indicative of a mean particle size of 50 to 100 Å which indeed is in sharp contrast with the quasi zero solubility of H_2 in the reduced palladium. This reduced particle size is also inconsistent with the x-ray data which failed to detect metal particles in this case. It is therefore obvious that the chemisorption pattern of results as a whole cannot fit in a simple model as yet described in the literature for metals supported on silica or alumina surfaces.

The apparent discrepancies between hydrogen dissociation and dissolution data could be rationalized assuming that isolated metal atoms or at most small clusters generated during the reduction process are encaged in the sodalite units[27] and therefore inaccessible to molecular oxygen. In this case, n_A determined by the oxygen titration method should be appreciably lower than the expected value for 100% dispersion. As the useful diameter of the sodalite cavities is around 6.6 Å, the number of Pd atoms per encaged particle should not exceed 6 and hydrogen dissolution should be, as actually is the case, negligible. It therefore appears that only a model assuming the formation of isolated atoms or at most small encaged clusters of 6.6 Å would account for the volumetric data and the x-ray results.

At higher reduction temperatures, which are not of primary interest to us in this paper, the experimental results seem to better fit in a more classical model; x-ray scattering showed the formation of metal particles of a *predominant size* of 18 Å. However, the formation of a limited number of much larger particles at the external surface of the zeolite cannot be excluded. These metal particles necessarily grow at the expense of isolated atoms and/or small clusters originally trapped in the sodalite units. Indeed chemisorption data indicate a dispersion of about 25–30% while the ratio of dissolved hydrogen atoms to the total Pd atoms as defined by Boudart and Hwang[11] ($2n_D/n_R$) was 0.25–0.30 suggesting a dispersion of ca. 50–30% and a *mean particle size* of 20–30 Å. Hence chemisorption data for samples reduced at high temperatures show some disagreements with x-ray scattering measurements which indicate a *predominant particle size* of 18 Å. However, the formation of much larger particles, limited in their number, would easily reconcile both types of data although we do not claim a correlation of dispersion measurements and particles size determinations by x-ray scattering. This is not the main concern to us since we are primarily interested in the species formed under mild reduction conditions.

However, palladium reduction by H_2 was reported to lead to the Pd(I) (d^9) species.[28] This seems to contradict our claim, but these were formed in very small amounts (4% of the total Pd content) and disappeared beyond 150 °C. Therefore, Pd(I) species formation cannot account for our experimental data.

(b) *Origin and Acidity of the Hydroxyl Groups.* The hydroxyl groups generated on reduced Pd–Y zeolite absorb at the same frequency as those encountered for decationated (H–Y) zeolites. Similarly they react with pyridine to form pyridinium ions which demonstrates their acidic character. Hence it is tempting to claim that they also originate from the reaction of protons with lattice oxygen ions. These protons are presumably formed during the reduction of palladium ions by hydrogen according to the overall redox equation

$$Pd^{2+} + H_2 \rightarrow 2H^+ + Pd(0)$$

In previous studies,[29,30] the hydroxyl groups associated with the high-frequency band (3635 cm^{-1}) were noticed to react readily with pyridine and were identified with $O_{(1)}$–H sticking out of the hexagonal ring surrounding S_I sites.[31] Therefore, they were thought to be readily accessible hence extremely reactive. The hydroxyl groups associated with the low-frequency band (3540 cm^{-1}), on the basis of their observed lack of reactivity toward pyridine and on the basis of T–$O_{(3)}$ lengthening,[32] were identified as $O_{(3)}$–H groups located in the sodalite cages thus accounting for their reported behavior toward pyridine. This latter consideration might be questioned since mobile enough protons need not be initially located at accessible positions to react with strong enough bases. Indeed both the high-frequency and low-frequency hydroxyl groups do react readily with pyridine in the case of Pd(0)–Y as well as decationated zeolites (Figure 2). This is in disagreement with most reports in the literature. However, the hydroxyl groups associated with the low-frequency band were observed to be more tightly bound to pyridine in the Pd(0)–Y form than in the H–Y form. This might be due to an acidity enhancement in their character which could presumably be due to electronic interactions between the

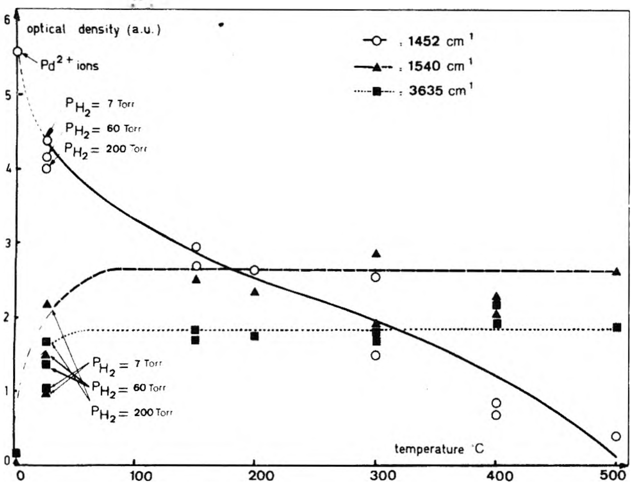

Figure 7. Hydrogen reduction temperature dependence of (○) OH groups (high-frequency band), (▲) pyridinium ions (1540-cm^{-1} band), and (■) coordinated pyridine (1452-cm^{-1} band).

lattice and small metal particles. These small particles are known to be electron deficient[33] and therefore likely to deplete the lattice of part of its negative charge density thus resulting in more mobile protons of the $O_{(3)}$–H groups that are in the sodalite units.

(c) *The Nature of Surface Sites.* As we already discussed earlier, all Pd(II) ions were reduced at 100 °C. Therefore, these ions could no more be involved in pyridine chemisorption. Again, it was inconsistent to ascribe the bands that appeared at 1452 (19b) and 1605 cm^{-1} (8a) to pyridine interacting with a strong Lewis acid center such as trigonal aluminum atoms. Furthermore, the failure to convert this chemisorbed pyridine into pyridinium ions confirms our belief that trigonal aluminum atoms presence should be ruled out. These two absorption peaks should better be assigned to pyridine coordinated to isolated palladium atoms which fit in the model that we have put forward in order to account for the chemisorption data. These isolated palladium atoms may form coordination complexes where pyridine would less tightly bind than when combined with a trigonal aluminum center. This hypothesis is in agreement with the observation that, under more severe reduction conditions, few centers were still available to coordinate pyridine. An opposite behavior was expected should the trigonal aluminum centers be involved, whereas isolated palladium atoms are expected to form clusters and increasingly larger size particles under more drastic conditions, hence few of them would yet coordinate pyridine molecules. Indexed x-ray diffraction analysis showed the formation of large size particles (20 Å) upon reduction at temperatures ranging from 300 to 500 °C. Under these conditions pyridine adsorption revealed that fewer and fewer metal sites were available to coordinate pyridine thus proving that the formation of metal particles at the expense of isolated atoms dramatically decreases the number and the strength of the metal coordination centers, as evidenced by the drastic decrease of the bands at 1452 and 1605 cm^{-1} as the reduction conditions got more severe (Figure 7). It is not surprising that the intensity of the 1452- and 1605-cm^{-1} bands for samples reduced under mild conditions was less than that observed for unreduced samples. Indeed, if small clusters were trapped in the sodalite units, they should not be able to move to the supercages in order to bind to pyridine. Strong evidence for the involvement of isolated atoms was provided by the poisoning experiments with H_2S. It appeared that pyridine coordination was inhibited while pyridinium ions were again formed.

Again the state of the metal dispersion was confirmed to be the dominant factor which governs the interaction between the metal and pyridine; the reduction of Pd(II)–Y by adsorbed pyridine was accompanied by a severe loss of intensity of the bands at 1452 (19b) and 1605 cm^{-1} (8a). Even readmission of pyridine failed to restore these two bands, strongly suggesting that reduction by pyridine does yield acidic hydroxyl groups but rather poorly dispersed metal thus precluding any further interaction with pyridine.

By contrast, part of the band at 1452 cm^{-1} which appeared for moderate reduction conditions followed by evacuation at high temperatures, well beyond 500 °C, is presumably due to pyridine coordinated by trigonal aluminum centers especially that the observed dehydroxylation certainly leads to the formation of such centers. Furthermore a small shoulder at 1620 cm^{-1} (8a), associated with this species, easily converted into pyridinium ions following water addition which is characteristic of pyridine combined with true Lewis acids.

(d) *Reduction Mechanisms.* Several reaction schemes could possibly be anticipated in order to describe the reduction of the exchanged zeolite: (i) removal of an extra framework oxygen part or a

$$[\mathrm{Pd}\overset{\mathrm{O}}{\diagup\ \diagdown}\mathrm{Pd}]^{2+}$$

pair which might lead to a Pd^+ intermediate and water formation; (ii) reduction of Pd^{2+} and Pd^+ ions by hydrogen leading to palladium metal and protons:

$$Pd^{2+} + H_2 \rightarrow 2H^+ + Pd(0)$$

or

$$2Pd^+ + H_2 \rightarrow 2H^+ + Pd(0)$$

the protons would then readily combine with lattice oxygen ions to form the observed hydroxyl groups; (iii) hydrogen might also extract framework oxygen ions leading to water and possibly trigonal aluminum centers but no involvement of Pd^{2+} ions could then be conceivable.

The first scheme would imply two vicinal Pd^{2+} ions in a nonlinear $[PdOPd]^{2+}$ pair. Such pairs should be formed upon removal of water from two vicinal $(PdOH)^+$ species. $(MOH)^+$ species were reported or postulated for a number of cation-exchanged zeolites. Similar nonlinear pairs were detected by EPR in the case of Cu(II)–Y zeolites.[34] In the present study, flowing oxygen at moderate temperatures showed the formation of hydroxyl groups attached to Pd^{2+} ions absorbing at 3605 cm^{-1}. Since most Pd^{2+} ions were located in the sodalite unit $S_{I'}$ sites the exchange level reached here suggests that approximately three pairs and five isolated ions should result from the activation procedure. Hence a reasonable quantity of water is expected to form upon simple hydrogen addition. This is in agreement with the experimental data. It is however unlikely that this is a unique mechanism since it does not account for the formation of hydroxyl groups.

The second scheme seems more attractive since it accounts for the presence of hydroxyl groups generated by the combination of the protons with lattice oxygen ions. This reduction process seems to take place at fairly low temperatures, since the ν(OH) bands associated with these OH groups reached their maximum intensity below 150 °C and did not significantly change in the 150–500 °C interval (Figure 7). These hydroxyl groups could later condense releasing water and forming tricoordinated aluminum acidic centers.

The last scheme would not result in the reduction of the metal ions and seems unlikely to occur at least under mild conditions since the energy required to remove the oxygen from the Si–Al bridge is reasonably high and only provided by heating at high temperatures. It is more reasonable to focus on reduction of impurities such as iron prior to considering such an extreme reaction.

Conclusions

Palladium exchange appeared to alter drastically the properties of the parent material.

The oxidized samples showed their ability to strongly coordinate pyridine molecules to Pd^{2+} ions. Almost in the same fashion as in solution Pd^{2+} could move freely from the sodalite cavities to the larger supercages.

The coordinated pyridine may not be displaced or transformed by water and seems to be strongly held. The thermal decomposition of the Pd(II) pyridine complex leads to the reduction of the cation while the zeolite matrix acquires Brönsted sites. The failure of the resulting metal to coordinate readded pyridine might be due to a rather ill-dispersed state or poisoning by carbonaceous residues.

The ability to stabilize atoms and small particles is probably specific to zeolite matrices since isolated atoms and small clusters were also reported to be formed for platinum and other metals in zeolite host lattices.

On the other hand, the zeolite matrix gains structural hydroxyl groups upon reduction of palladium ions. These silanol groups behave in a much similar way as those of decationated zeolites. However the $O_{(3)}H$ groups (low-frequency band) seem to have a more pronounced acidic character as compared to those of H–Y zeolites. The possibility of electronic interactions between the small metal particles or atoms with the lattice may tentatively explain the enhancement of the mobility of the relevant hydrogen.

This method appears therefore to be a convenient one to obtain highly dispersed metals on Brönsted acid carriers. It is also possible to induce true Lewis acidity by dehydroxylation at temperatures above 500 °C following reduction under mild conditions.

An interesting development of pyridine adsorption was witnessed in this study for the first time. Not only did pyridine prove to be a powerful and specific method to characterize accurately the nature of surface acidity, but it, above all, appeared as a convenient technique to characterize isolated atoms when trapped in solid matrices. Up to now every physical method failed to characterize them or observe them directly and the only proof of their existence was negative evidence: lack of reactivity toward hydrogen and/or oxygen, failure to observe metal particles by electron microscopy.

This is the first instance where isolated atoms could be characterized directly. We feel it is even possible, provided extreme care is taken in dealing with calibration problems, to obtain quantitative informations regarding these atoms.

Acknowledgment. The authors are very grateful to Mr. Marc Dufaux for his technical assistance with the infrared experiments and to Dr. P. Gallezot for x-ray determinations. We are happy to acknowledge many fruitful discussions with Dr. P. Gallezot, Dr. M. V. Mathieu, and Dr. B. Imelik.

References and Notes

(1) See, for example, "Molecular Sieves", *Adv. Chem. Ser.*, **No. 101** (1971); "Molecular Sieves", *Adv. Chem. Ser.*, **No. 121** (1973).
(2) Y. Ben Taarit, M. Primet, and C. Naccache, *J. Chim. Phys.*, **67**, 1434 (1970).
(3) C. Naccache, M. Primet, and M. V. Mathieu, *Adv. Chem. Ser.*, **No. 121**, 266 (1973).
(4) P. Gallezot and B. Imelik, *Adv. Chem. Ser.*, **No. 121**, 66 (1973).
(5) M. Che, J. F. Dutel, P. Gallezot, and M. Primet, *J. Phys. Chem.*, submitted for publication.
(6) C. Naccache, J. F. Dutel, and M. Che, *J. Catal.*, **29**, 179 (1973).
(7) C. Naccache and Y. Ben Taarit, *J. Catal.*, **22**, 171 (1971).
(8) P. Gallezot, A. Alarcon-Diaz, J. A. Dalmon, A. J. Renouprez, and B. Imelik, *J. Catal.*, **39**, 334 (1975).
(9) J. S. Shamir and A. Schwartz, *Talanta*, **8**, 330 (1961).
(10) M. V. Mathieu and P. Pichat, "La Catalyse au Laboratoire et dans l'Industrie", Masson et Cie, Paris, 1966, p 319.
(11) M. Boudart and H. S. Hwang, *J. Catal.*, **39**, 44 (1975).
(12) J. E. Benson, H. S. Hwang, and M. Boudart, *J. Catal.*, **30**, 146 (1973).
(13) E. P. Parry, *J. Catal.*, **2**, 371 (1963).
(14) M. R. Basilia and T. R. Kantner, *J. Phys. Chem.*, **70**, 1681 (1966).
(15) P. Pichat, M. V. Mathieu, and B. Imelik, *Bull. Soc. Chim. Fr.*, **1**, 2611 (1969).
(16) D. A. Long and E. L. Thomas, *Trans. Faraday* Soc., **59**, 783 (1963).
(17) A. Terenin, W. Filimonow, and D. Bystrom, *Z. Elektrochem.*, 62, 180 (1958).
(18) N. S. Gill, R. H. Nuttall, D. E. Scaife, and D. W. A. Sharp, *J. Inorg. Nucl. Chem.*, **18**, 79 (1961).
(19) D. Cook, *Can. J. Chem.*, **39**, 2009 (1961).
(20) J. W. Ward, *J. Catal.*, **9**, 225 (1967).
(21) L. G. Christner, B. V. Liengme, and W. K. Hall, *Trans. Faraday Soc.*, **64**, 1679 (1968).
(22) D. B. Powell and N. Sheppard, *J. Chem. Soc.*, **1**, 3108 (1956).
(23) H. Takahashi, K. Mamola, and E. K. Plyler, *J. Mol. Spectrosc.*, **21**, 217 (1966).
(24) C. Naccache and Y. Ben Taarit, *Chem. Phys. Lett.*, **11**, 11 (1971).
(25) P. Gallezot, Y. Ben Taarit, and B. Imelik, *J. Catal.*, **26**, 295 (1972).
(26) P. Gallezot, Y. Ben Taarit, and B. Imelik, *J. Phys. Chem.*, **77**, 2556 (1973).
(27) P. Gallezot, unpublished results.
(28) M. Che, J. F. Dutel, and C. Naccache, to be submitted for publication.
(29) A. Bielanski and J. Datka, *J. Catal.*, **32**, 183 (1974); **37**, 383 (1975).
(30) T. R. Hughes and H. M. White, *J. Phys. Chem.*, **71**, 2192 (1967).
(31) D. H. Olson and E. Dempsey, *J. Catal.*, **13**, 221 (1969).
(32) P. Gallezot and B. Imelik, *J. Chim. Phys.*, **68**, 816 (1971).
(33) P. Gallezot, J. Datka, J. Massardier, M. Primet, and B. Imelik, Proceedings of the VIth International Congress on Catalysis, London, 1976, paper A11.
(34) C. C. Chao and J. H. Lunsford, *J. Chem. Phys.*, **57**, 2890 (1972).
(35) H. Knözinger and H. Stolz, *Fortschr. Kolloid. Polym.*, **55**, 16 (1971).

Bonding in Silver Complexes of Carboxylic Acid Substituted Thionamides Examined by Infrared, Laser-Raman, and X-Ray Photoelectron Spectroscopy

P. J. Trotter,* M. G. Mason, and L. J. Gerenser

Research Laboratories, Eastman Kodak Company, Rochester, New York 14650
(Received January 17, 1977)

Publication costs assisted by the Eastman Kodak Company

Silver complexes of acid-substituted thionamides have been investigated by means of infrared, laser-Raman, and x-ray photoelectron (ESCA) spectroscopies. The 1:1, 2:1, and 3:1 complexes of 3-carboxymethyl-4-methyl-4-thiazoline-2-thione (CMMTT) and 1:1 and 2:1 complexes of 3-(2-carboxyethyl)-4-hydroxymethyl-4-thiazoline-2-thione (CEHTT) were studied. Complexing of thione sulfur with silver, $C{=}S{-}Ag^+$, was established for all complexes. The 1:1 complexes contain carboxylate ion groups, while the 2:1 complexes contain carboxyl groups connected by either symmetrical (CMMTT) or asymmetrical (CEHTT) O–H–O hydrogen bridges. The 3:1 complex of CMMTT gave spectra indicative of carboxylate ion, as in the 1:1 complex, plus a hydrogen bonded acid dimer. Hydrogen bonding of the hydroxymethyl and carboxyl groups of CEHTT was readily observed in the infrared.

Introduction

We have examined bonding characteristics in several silver complexes of carboxylic acid substituted thionamides. Structures of the ligands studied are shown in 1 and 2. The combination of infrared, laser-Raman, and photoelectron spectroscopies for structural characterization of silver complexes has been demonstrated previously.[1] This work represents an extension of the previous study to more complex systems. Again, the analysis is aided by molecular orbital calculations. Atomic charges were determined from CNDO (complete neglect of differential overlap) calculations. ESCA binding energies were correlated with the calculated charges by use of the "potential model" equation:[2,3]

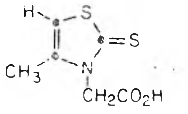

3-carboxymethyl-4-methyl-4-thiazoline-2-thione

1 CMMTT

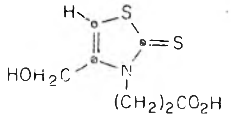

3-(2-carboxyethyl)-4-hydroxymethyl-4-thiazoline-2-thione

2 CEHTT

$$E_B{}^i = kq_i + V_i + l \qquad (1)$$

$E_B{}^i$ is the binding energy of a core level on atom i, relative to a chosen reference energy, q is the calculated charge on atom i, and k and l are empirical parameters determined by a least-squares fit of experimental data to eq 1. The term V_i is referred to as the molecular potential and accounts for the electrostatic potential produced by the other charged atoms in the molecule. This potential has most commonly been calculated by a simple point-charge model in which

$$V_i = \sum_{j \neq i} q_j / R_{ij} \qquad (2)$$

where R_{ij} is the interatomic distance between atoms i and j and q_j is the calculated charge on atom j.

Experimental Section

The photoelectron spectra were recorded on a Hewlett-Packard 5950A ESCA spectrometer at about 100 K. The method of calibration was described previously.[1] The samples were prepared by dispersing the insoluble powders in CCl_4 and allowing the dispersion to dry down on a glass substrate. Spectra from all samples prepared in this manner were stable with time and showed no indications of photolytic decomposition due to x-ray exposure. The samples were prepared and mounted in the spectrometer in an atmosphere of dry nitrogen; this was found to reduce contamination of the samples by adsorbed oxygen-containing species. Binding energies for overlapping lines were determined on the DuPont 310 curve resolver.

Raman spectra from 15 to 4000 cm^{-1} were excited at 6471 Å (270 mW) with a Spectra-Physics Model 164 krypton laser and were recorded on a Cary Model 82 Raman spectrometer.[1] A Beckman IR-12 infrared spectrophotometer was used to obtain IR scans from 200 to 4000 cm^{-1}. Spectra were obtained from KBr pressings, Nujol mulls, and Fluorolube mulls for all samples. It was found that some silver complexes reacted with KBr, yielding altered IR spectra; in these cases Nujol and Fluorolube mulls were used.

Complexes were prepared by addition of stoichiometric amounts of silver nitrate to the acid ligands (LH) in aqueous solution. These complexes precipitate immediately. To allow complete equilibration, the solution was stirred for 4 h to 4 days depending on the complex being prepared. After equilibration, the complex was collected by vacuum filtration, washed with water and methanol, and vacuum dried at 70 °C for 4 h. The compounds were formed in ligand-to-silver ratios of 1:1 ($Ag^+ L^-$), 2:1 ($Ag^+ LHL^-$), and 3:1 ($Ag^+ (LH)_2L^-$). All complexes were verified as to correct anhydrous stoichiometry by titration of the acidic protons and by elemental analyses of Ag, C, H, N, and S.

Results and Discussion

A. *Silver–Thione Interactions.* As shown previously, silver–thione interactions were most readily investigated by ESCA.[1] Typical ESCA S 2p spectra for CMMTT and its 1:1 silver complex are shown in Figure 1. Photoelectron peaks from two chemically distinct sulfurs are observed in each case. The doublet of higher binding energy corresponds to the ring sulfur and that of lower binding energy to the thione sulfur.[4]

Table I gives the ESCA results for CMMTT, CEHTT, and their silver complexes. In all cases, the binding energies of the ring sulfur and nitrogen are relatively unchanged in the silver complex relative to those of the pure ligand. However, complex formation causes the thione

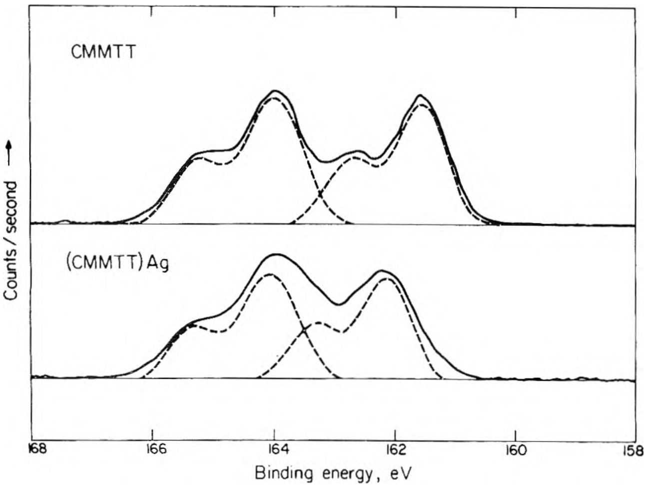

Figure 1. S 2p spectra for CMMTT and its 1:1 silver complex.

TABLE I: ESCA Binding Energies for Ligands and Their Silver Complexes

Compound	Binding Energy, eV		
	S / \	=S	\ / N |
CMMTT	163.9	161.6	400.6
(1:1) $Ag^{+}L^{-}$	163.9	162.1	400.4
(2:1) $Ag^{+}(LHL)^{-}$	163.9	162.1	400.4
(3:1) $Ag^{+}L^{-}(LH)_2$	164.0	162.0	400.5
CEHTT	164.0	161.6	400.4
(1:1) $Ag^{+}L^{-}$	164.0	162.1	400.4
(2:1) $Ag^{+}(LHL)^{-}$	163.9	162.1	400.4

sulfur to shift to higher binding energies in all cases by about 0.5 eV. The shift to higher binding energy is consistent with an increased positive charge due to coordination with the silver cation and is in agreement with previous results for thionamide silver nitrate complexes.[1]

Since the sulfur and nitrogen ESCA spectra were nearly identical for all complexes, the following discussions will concentrate on the interactions of the carboxylic acid group.

B. *Carboxylic Acid Interactions.* Carboxylic acid interactions and hydrogen bonding could readily be investigated utilizing infrared spectra as illustrated in Figures 2 and 3. The carbonyl frequencies are indicative of hydrogen-bonded species or carboxylate ion groups as shown in Table II. The ESCA O 1s binding energies for the pure ligands and their silver complexes are given in Table III. Figure 4 shows the O 1s spectra and resolved curves for the CMMTT ligand and its three silver complexes.

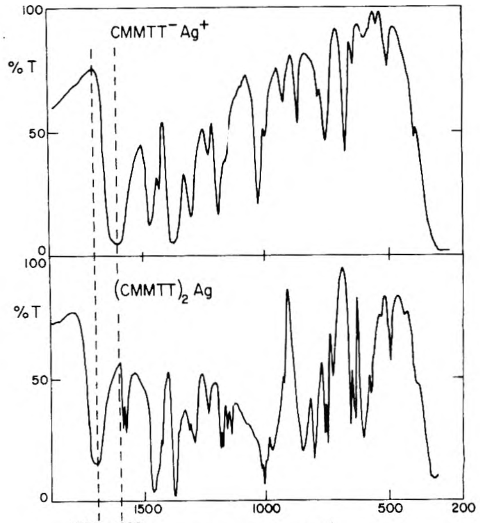

Figure 2. Infrared spectra (Nujol mull) of 1:1 CMMTT–Ag^{+} and 2:1 $(CMMTT)_2Ag$, (LHL)–Ag^{+}. The carbonyl band is shifted from 1590 cm^{-1} in the 1:1 carboxylate compound to 1700 cm^{-1} in the O---H---O bridged 2:1 species.

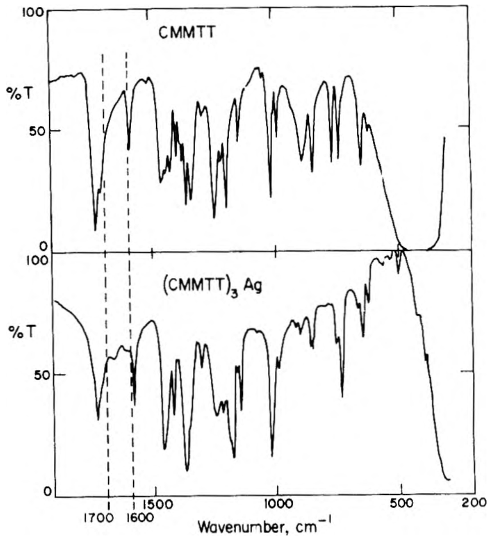

Figure 3. Infrared spectra (Nujol mull) of CMMTT ligand compared with the $(CMMTT)_3Ag$ complex. The H-bonded carboxylic acid groups are characterized by carbonyl bands near 1735 cm^{-1} in both the ligand and the 3:1 complex.

TABLE II: Carbonyl Frequencies (cm^{-1}) of Structural Groups and Complexes Measured by Infrared Spectroscopy

Parent Compound	Monomer[b] -COOH (vapor)	Dimer[b] 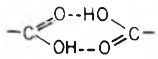	Symmetrical[c] hydrogen bridge 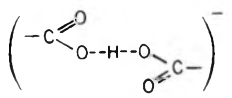	Carboxylate $-COO^{-}$
CF_3COOH	1826	1787	1790	1687[a]
CCl_3COOH	1784	1750	1750	1680[a]
CH_3COOH	1799	1730	1710	1580[a]
CMMTT (LH)		1733		
(1:1) $Ag^{+}L^{-}$				1590
(2:1) $Ag^{+}(LHL)^{-}$			1700	
(3:1) $Ag^{+}L^{-}(LH)_2$		1735		1600
CEHTT (LH)		1712		
(1:1) $Ag^{+}L^{-}$				1550
(2:1) $Ag^{+}(LHL)^{-}$		(———— 1687 ————)		1605

[a] Sodium salts. [b] References 5-7. [c] References 12, 13, and 17.

TABLE III: Oxygen 1s Binding Energies and Line Widths for Ligands and Their Silver Complexes

Compound	Binding energy, eV	Line width, eV	Binding energies of resolved components, eV[a]				
			Acid dimer		Hydrogen bridge		Carboxylate
			(C-OH)	(C=O)	(CO--H)	(C=O)	(COO^-)
CMMTT	532.4	2.6	533.0	531.9			
(1:1) Ag^+L^-	530.5	2.0					530.5
(2:1) $Ag^+(LHL)^-$	531.6	2.7			532.2	531.1	
(3:1) $Ag^+L^-(LH)_2$	532.3	3.2	533.1	532.0			530.6
CEHTT	532.5	2.8		*b*			
(1:1) Ag^+L^-	532.2, 530.5	2.8		532.2			530.5
(2:1) $Ag^+(LHL)^-$	531.5	2.6		*b*			

[a] Determined using the DuPont 310 curve resolver with a 1.8-eV fwhm Gaussian for individual components. This line width is based on that observed in ionic carboxylates. [b] Too complex to resolve.

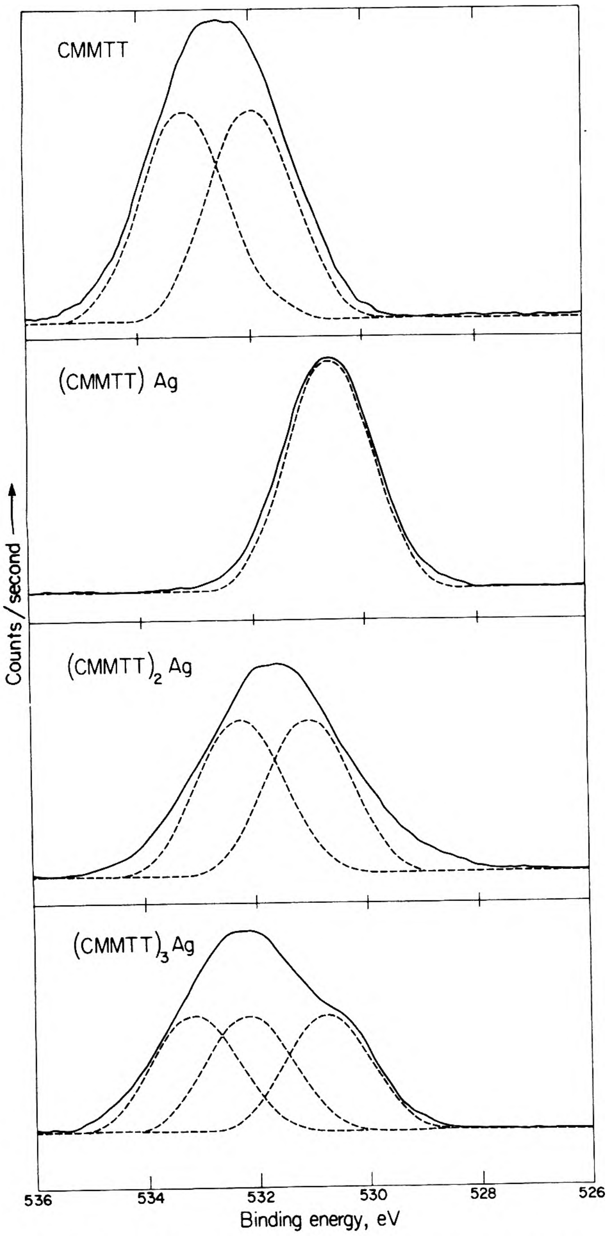

Figure 4. O 1s spectra for CMMTT and its silver complexes.

CMMTT Ligand. The IR carbonyl frequency for the pure ligand is at 1733 cm^{-1}, indicative of an asymmetric hydrogen-bonded acid dimer of the type:[5]

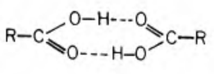

3

This type of hydrogen bonding is commonly found in carboxylic acids.[5-7]

In this ligand, the ESCA O 1s spectrum consists of a single broad line (2.6 eV fwhm) with a binding energy of 532.4 eV. This broad line can be resolved to give two components of equal intensity at 533.0 and 531.9 eV corresponding respectively to the hydroxyl and hydrogen bonded carbonyl oxygens.[8] The formation of intermolecular hydrogen bonds between carboxyl groups has shifted these binding energies relative to the literature values of 533.2 and 531.4 eV for free molecules of carboxylic acids.[9] This is shown by CNDO calculations on a free acid and a cyclic dimer using the bond distances given by Pimentel and McClellan.[5] In the free acid the charges are −0.37 and −0.26 for the carbonyl and hydroxyl oxygens respectively, compared to −0.38 and −0.33 in the cyclic dimer. Using the *k* value determined by Stucky and co-workers,[3] these charges correspond to an O 1s splitting of 3.8 eV in the free acid and 1.4 eV in the cyclic dimer. The calculated value of 1.4 eV is close to our experimental splitting of 1.1 eV; however, the 3.8-eV splitting calculated for the free acid is much larger than that observed experimentally for gas phase acetic[2] and formic acids.[10] Davis and Shirley also calculated a similar large splitting for a free molecule of formic acid in both the ground state potential model (GPM) and the relaxation potential model (RPM).[10] The work of Davis et al.[11] suggests that this large variation is due to a final state effect which is not sufficiently accounted for in the relaxation potential model.

CMMTT (1:1) Ag^+L^-. The IR spectrum of the 1:1 CMMTT-Ag complex shown in Figure 2 indicates a carboxylate group with the $-COO^-$ band at 1590 cm^{-1} identical with carboxylate in the model Na^+L^- salt.

The ESCA O 1s spectrum for the 1:1 complex gives a single peak at 530.5 eV. This is a shift of about 2 eV to lower binding energy relative to the pure ligand. Such a shift indicates a large negative charge or an unusually large spatial separation of the anion and cation centers. The decrease in line width to about 2.0 eV (fwhm) suggests a nearly equivalent charge distribution between the two carboxyl oxygens.

CMMTT (2:1) $Ag^+(LHL)^-$. A strong IR band centered at 1700 cm^{-1}, a C=O frequency lying between those of the ligand $(-COOH)_2$ and 1:1 $-COO^-$, was observed in the 2:1 complex, Figure 2. This observation suggests the presence of a bridging hydrogen bond between carboxyl groups of the type:

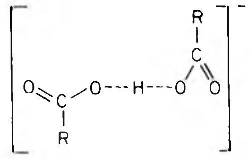

4

Our vibrational evidence supports a symmetrical structure as shown in **4**. This support rests on the correlation between our data and recent fundamental infrared and Raman studies of O–H–O bonding in compounds such as $[Cs^+(CF_3COO^-)(CF_3COOH)]$[12] and $[Rb^+(CCl_3COO^-)(CCl_3COOH)]$.[13] Basic investigations of O–H–O hydrogen bonded structures in crystals have been carried out previously by Speakman and co-workers,[14-17] and several other examples of this O–H–O bridging have been reported.[18-22] Carbonyl frequencies of these symmetrical hydrogen-bridged structures,[12-18] along with those of other carboxylic species,[5-7] are shown in Table II.

Other vibrational modes characteristic of the hydrogen-bridged structure **4** have also been analyzed[12,13] but are difficult to assign for the compounds reported here due to mixing with a number of thiazoline–thione ligand vibrations.[23,24] The strong IR band at 798 cm^{-1}, which appears only in the 2:1 complex, may possibly be due to the O–H–O asymmetric stretching mode.[13]

Although the dimeric **3** and hydrogen-bridged ionic **4** structures cannot be readily distinguished on the basis of carbonyl shifts alone, it has been shown by elemental analysis and acid proton titration that the elemental and hydrogen ion composition of the 2:1 complex is correct for the hydrogen-bridged ion. This fact, combined with the appearance of a strong IR band in the hydrogen-bridged carbonyl region and the absence of a $-COO^-$ band, leads us to conclude that a structure of type **4** is present in the 2:1 complex.

The ESCA O 1s binding energy for the 2:1 complex shifts about 1 eV to lower binding energy compared to the pure ligand, Table III. The spectrum is again quite broad (2.7 eV fwhm) indicating that the oxygens have nonequivalent charges. The shift to lower binding energy is consistent with a partial negative charge due to the loss of one proton. The resolved spectrum shown in Figure 4 gives two components of equal intensity at 532.2 and 531.1 eV corresponding respectively to the hydrogen-bridged and carbonyl oxygens. CNDO calculations on a symmetrical hydrogen-bridged dimer with bond distances and angles taken from Speakman and Manojlovic[25] predict the splitting between the two oxygens to be 1.2 eV with the carbonyl oxygen at lower binding energy.

CMMTT (3:1) $Ag^+L^-(LH)_2$. The 3:1 complex shows a characteristic IR pattern with a strong sharp band centered at the hydrogen bonded $(-COOH)_2$ dimer position of 1735 cm^{-1} and a broad, weaker carboxylate band near 1600 cm^{-1} (cf. Figure 3). This indicates that the 3:1 complex consists of a hydrogen-bonded CMMTT (cf. structure **3**) plus the basic 1:1 carboxylate unit.

The ESCA O 1s spectrum for the 3:1 complex peaks at 532.3 eV, which is identical with that of the pure ligand, and exhibits a definite shoulder at lower binding energy. This spectrum could be resolved into three components, each with equal intensity, as shown in Figure 4. The two components of higher binding energy are equivalent to those in the resolved spectrum of the pure ligand, indicating a dimerized hydrogen-bonded species. The lowest binding energy component is equivalent to that of the 1:1 complex, thus indicating the presence of carboxylate ions.

CEHTT (1:1) Ag^+L^-. The IR spectrum of the 1:1 complex of CEHTT indicates a carboxylate group as was found in the 1:1 complex of CMMTT in Table II. The most significant structural difference between CEHTT and CMMTT is the hydroxymethyl group in the 4 position of the thiazoline ring. The CEHTT pure ligand shows this O–H vibration at 3360 cm^{-1}, consistent with hydrogen bonding in the solid ligand, whereas the 1:1 complex shows the O–H vibration shifted to 3620 cm^{-1} in the "free" O–H region.[5]

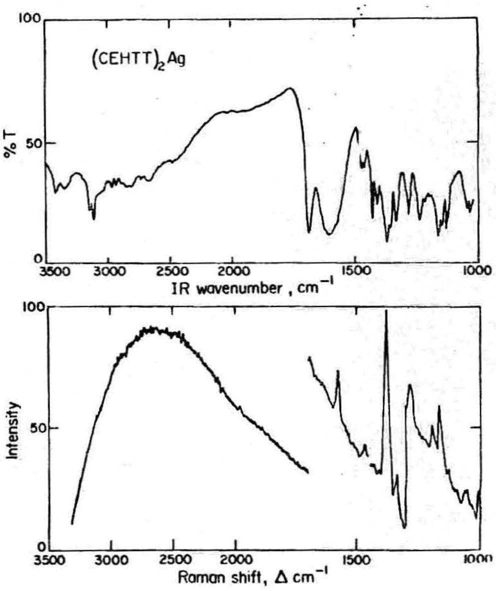

Figure 5. Infrared and Raman spectra of $(CEHTT)_2Ag$ from 1000 to 3500 cm^{-1}. The IR is from a KBr pressing and Raman was run at 5-cm^{-1} resolution and 6471-Å (200 mW) excitation. The measured sample fluorescence peaks near 2650 cm^{-1} in the Raman.

The ESCA O 1s spectrum for the 1:1 complex shows two peaks; one at 530.5 eV corresponding to a carboxylate ion, and one at 532.2 eV which is consistent with the "free" OH group seen by IR.

CEHTT (2:1) $Ag^+(LHL)^-$. The infrared pattern of this 2:1 complex exhibits structural characteristics markedly different from those found for $(CMMTT)_2Ag$. Infrared and Raman spectra of $(CEHTT)_2Ag$ are shown in Figure 5 and carbonyl frequencies are listed in Table II. The IR spectrum shows a strong band at 1687 cm^{-1} which lies between the acid dimer carbonyl (1733 cm^{-1}) and carboxylate regions; an equally strong band from a carboxylate, $-COO^-$, species is also observed at 1605 cm^{-1}. This additional $-COO^-$ vibration is at a frequency 55 cm^{-1} higher than that observed in the 1:1 complex of CEHTT listed in Table II. A band shift of this type is consistent with strong hydrogen bonding to the COO^- group. This hydrogen-bonding shift is similar to that shown in salicylate ionic salts.[26,27] For example, in potassium benzoate the $-COO^-$ asymmetric stretching band appears at 1552 cm^{-1} and is shifted to 1605 cm^{-1} in potassium salicylate, where the ortho –OH group is strongly hydrogen bonded to carboxylate.[26,27] These shifts appear to be due to a shortening of the carbonyl C–O bond in the hydrogen-bonded species.

Hydrogen-bonding interactions are also apparent in the fundamental O–H vibrations of the hydroxymethyl groups. At least two types of H-bonded RO–H groups are present in this 2:1 structure, as shown by the two O–H frequencies observed in Figure 5. Table IV shows these variations compared to the pure ligand and the 1:1 complex, along with shifts involving the olefinic group.

The IR data may be explained by invoking a hydrogen-bridged structure similar to **4**, with the requirement of highly asymmetric bonding[14-16] as shown in **5**.

The asymmetry in structure **5** may result from secondary hydrogen bonding to neighboring $-CH_2OH$ groups on the thiazoline ring to form RO–H---O bonds. Although most hydrogen-bridged acid salts[14-21] form symmetrical O---H---O bonds, examples involving asymmetric structures[14,16] have also been identified. In these asymmetric groups the acidic radicals in the formula $[M^+(COO^-)(COOH)]$ become

TABLE IV: Vibrational Frequencies (cm^{-1}) in CEHTT and Its Silver Complexes

Compound	$-CH_2O-H$ (IR)	$=C-H$ (olefinic C-H, IR)	C=C (IR)	C=C (Raman)
CEHTT (LH)	3360	3090	1575 (w)	1583
(1:1) Ag^+L^-	3620	3088 (w)	[a]	1580 (w)
(2:1) $Ag^+(LHL)^-$	3415, 3345	3145, 3110	[a]	1573

[a] Masking by $-COO^-$ obscures C=C in the IR.

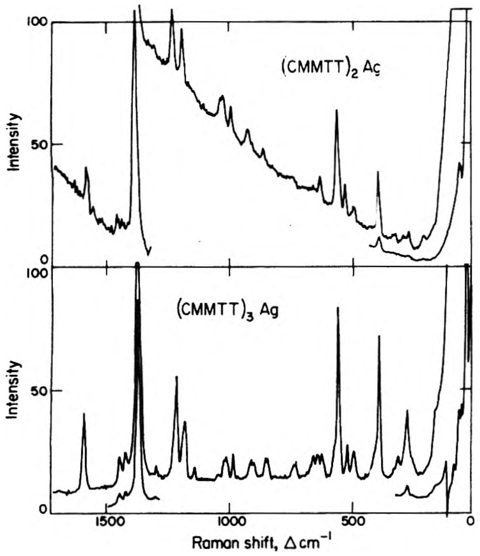

Figure 6. Raman spectra of 2:1 and 3:1 CMMTT–Ag complexes. The 3:1 complex shows low frequency lattice "fingerprint" bands. A rising background in the 2:1 spectrum is due to trace fluorescent impurities. Spectra were run at 5-cm^{-1} resolution and 6471-Å (200 mW) excitation with various attenuations.

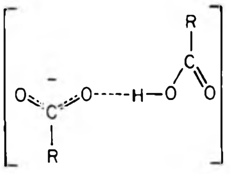

5

crystallographically distinct. The IR spectra thus approach a superposition of separate acid ligand plus carboxylate salt.[16] This type of behavior was found in $(CEHTT)_2Ag$ with COO^----H at 1605 cm^{-1} and COOH at 1687 cm^{-1} in the IR.

Silver–Olefin Interactions. Laser-Raman spectra of the 2:1 and 3:1 CMMTT–Ag complexes are shown in Figure 6. Raman spectra of the 1:1 complex were nearly identical with that of the 2:1 complex. The C=C vibration is located at 1583, 1584, and 1588 cm^{-1} in the 1:1, 2:1, and 3:1 complexes, respectively; these frequencies represent small shifts from the uncomplexed ligand C=C at 1596 cm^{-1}. Since a C=C shift of about 35–40 cm^{-1} to lower frequency is expected in specific silver–olefin complexes,[28] these smaller shifts do not indicate any strong silver–π interactions. An effect on complexing was also observed in the IR spectra by shifts in the olefinic C–H vibration from 3095 cm^{-1} in the pure ligand to a pair of sharp bands at 3120 and 3050 cm^{-1} in the 2:1 complex. The strong carboxyl bands in the IR are not observed by Raman, which allows the measurement of the C=C vibration without interference. One also notes some "fingerprint" differences between the 2:1 and 3:1 complexes in the low-frequency Raman region (280 cm^{-1} and below) in Figure 6. Table IV shows shifts involving the olefinic group in the thiazoline ring of CEHTT. Laser-Raman spectra show the C=C group at 1583 cm^{-1} in the pure ligand shifted to 1573 cm^{-1} in the 2:1 complex. These shifts are similar to those observed for CMMTT complexes.

TABLE V: Oxygen 1s Binding Energies and Line Widths for Model Compounds and Silver Complexes

Compound	Binding energy, eV	Fwhm, eV	Type of bonding
Ag behenate	531.5	1.9	Covalent
Na behenate	531.0	1.8	Ionic
Ag acetate	531.4	1.8	Covalent
Na acetate	530.9	1.9	Ionic
Ag cyclohexanebutyrate	531.6	1.8	Covalent
Na cyclohexanebutyrate	530.9	1.9	Ionic
K cyclohexanebutyrate	530.7	1.6	Ionic
1:1 CMMTT	530.5	2.0	Ionic
1:1 CEHTT	530.5	1.9[a]	Ionic

[a] Resolved on DuPont 310 curve resolver.

Structural Considerations

The evidence presented so far has established the primary bonding sites of Ag^+ to the thione sulfur of the acid-substituted thionamides and has determined the types of hydrogen bonding in the ligands and silver complexes. This information in itself is not sufficient to determine the spatial arrangement of these molecules in the complete crystal structure. Any attempt to do so without x-ray diffraction data is, of course, speculative; but there exist sufficient x-ray data of structurally similar compounds to justify such speculation. In this section we will propose a limited number of structural possibilities based on crystal structures of closely related compounds and our own spectral determinations.

A. *1:1 Complexes.* The covalent $S-M^{n+}-S$ bond is almost universally observed in thiourea type complexes with Ag^+,[29,30] and with a large number of other metallic ions (M^{n+}) such as Mn^{2+}, Cu^{2+}, Ni^{2+}, Pb^{2+}, and Cu^+.[31] In many cases this bonding produces polymeric structures via bridging sulfur.[29–31] For the 1:1 complexes this would suggest a structure of the type **6** where the carboxylate groups are coordinated to Ag^+ only in an ionic sense.

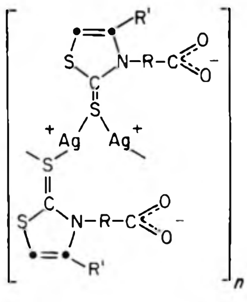

6

The purely ionic nature of the Ag^+-O^- interaction is evidenced by the ESCA binding energies in these complexes. The normal covalent Ag–O bond found in simple carboxylate salts has an O 1s binding energy of about 531.6 eV (Table V). The binding energy for an ionic M^+-O^- structure depends upon the internuclear distance and will decrease in going to larger cations as a result of decreasing Madelung energy.[32] Among the alkali metal ions, K^+ has an ionic radius (1.33 Å) most closely approaching that of

Ag^+ (1.26 Å). Therefore, potassium carboxylate salts should be excellent models for predicting the O 1s binding energy of an ionic Ag^+-O^- salt. As seen in Table V there is excellent agreement between the O 1s binding energy in potassium cyclohexanebutyrate and the 1:1 silver complexes.

B. *3:1 and 2:1 Complexes.* Smith and Luss have recently determined the structure of the closely related 3:1 complex of silver-4-methyl-4-thiazoline-2-thione (MTT).[33] This structure is based on a ring system consisting of two 3:1 units with two bridging thione sulfurs and four terminal thione sulfurs as shown in **7**. These individual dimeric units are then hydrogen bonded to adjacent units via N-H---N bonds. A similar structure is proposed for the 3:1 acid-substituted thionamides with the carboxylic acid group producing the intermolecular hydrogen bonds as shown in structure **3**. The single unprotonated carboxylate would then ionically coordinate with silver in a manner similar to that of the 1:1 complexes discussed previously. Another 3:1 complex of this ring-bridging type is found in the tris(thiourea)silver perchlorate structure.[34] The fact that 3:1 is the highest obtainable stoichiometric ratio[35] also implies strongly that a bridging sulfur exists. This type of bridging is found in almost all silver–sulfur complexes.[29,30,34,36-39]

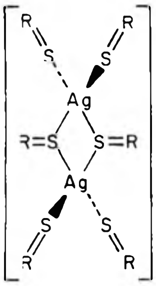

7

The 2:1 complexes are expected to have a similar tetrahedral ring structure[33,34] which may be formed as part of a polymer chain as shown in **8**. The intermolecular hydrogen-bonding would be as shown in structure **4** for $(CMMTT)_2Ag$ and in structure **5** for $(CEHTT)_2Ag$.

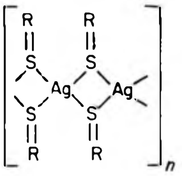

8

Acknowledgment. The authors are grateful to A. H. Herz, D. D. F. Shiao, and T. J. Davis for valuable discussions concerning silver–thione complexes, and we thank J. W. Boettcher for the original suggestion of a hydrogen-bonded bridge structure in 2:1 CMMTT–Ag. We are also grateful to D. L. Smith and H. R. Luss for x-ray information on analogous compounds. The CMMTT–Ag complexes were prepared by R. A. Guistina. Titrimetric and elemental analyses were performed by J. T. Alessi and G. N. Meyer. Infrared spectra were run by T. F. Hall and R. Riley.

References and Notes

(1) L. J. Gerenser, M. G. Mason, and P. J. Trotter, *J. Phys. Chem.*, **80**, 2384 (1976).
(2) K. Siegbahn, C. Nordling, G. Johansson, J. Hedman, P. F. Heden, K. Hamrin, U. Gelius, T. Bergmark, L. O Werme, R. Manne, and Y. Baer, "ESCA Applied to Free Molecules", Elsevier, New York, N.Y., 1969, pp 126–127.
(3) G. D. Stucky, D. A. Matthews, J. Hedman, M. Klasson, and C. Nordling, *J. Am. Chem. Soc.*, **94**, 8009 (1972).
(4) B. J. Lindberg, K. Hamrin G. Johansson, U. Gelius, A. Fahlman, C. Nordling, and K. Siegbahn, *Phys. Scr.*, **1**, 286 (1970).
(5) G. C. Pimentel and A. L. McClellan, "The Hydrogen Bond", W. H. Freeman, San Francisco, Calif., **1960**, and references therein.
(6) N. Fuson, M. L. Josien, E. A. Jones, and J. R. Lawson, *J. Chem. Phys.*, **20**, 1627 (1952).
(7) D. Hadzi, "Hydrogen Bonding", Pergamon Press, New York, N.Y., 1959.
(8) M. E. Schwartz and J. D. Switalski, *J. Am. Chem. Soc.*, **94**, 6298 (1972).
(9) The values of 533.2 and 531.4 eV are from ref 2 with the C 1s binding energy taken as 284.6 eV.
(10) D. W. Davis and D. A. Shirley, *J. Electron Spectrosc.*, **3**, 137 (1974).
(11) D. W. Davis, M. S. Banna, and D. A. Shirley, *J. Chem. Phys.*, **60**, 237 (1974).
(12) P. J. Miller, R. H. Butler, and E. R. Lippincott, *J. Chem. Phys.*, **57**, 545 (1972).
(13) D. Hadzi, M. Obradovic, B. Orel, and T. Solmajer, *J. Mol. Struct.*, **14**, 439 (1972).
(14) J. C. Speakman, *MTP, Int. Rev. Sci., Phys. Chem., Ser. One*, **11**, 1–31 (1972), and references therein.
(15) J. C. Speakman, *J. Chem. Soc.*, 3357 (1949).
(16) H. N. Shrivastava and J. C. Speakman, *J. Chem. Soc.*, 1151 (1961).
(17) J. C. Speakman and H. H. Mills, *J. Chem. Soc.*, 1164 (1961).
(18) N. Albert and R. M. Badger, *J. Chem. Phys.*, **29**, 1193 (1958).
(19) W. C. Hamilton and J. A. Ibers, "Hydrogen Bonding in Solids", W. A. Benjamin, New York, N.Y., 1968, p 182.
(20) S. N. Vinogradov and R. H. Linnell, "Hydrogen Bonding", Van Nostrand, New York, N.Y., 1971, Chapter 7.
(21) D. P. C. Thackeray and B. C. Stace, *Spectrochim. Acta, Part A*, **30**, 1961 (1974).
(22) B. Orel, D. Hadzi, and F. Cabassi, *Spectrochim. Acta, Part A*, **31**, 169 (1975).
(23) R. Mecke et al., *Chem. Ber.*, **90**, 957 (1957).
(24) C. N. R. Rao and R. Venkataraghavan, *Spectrochim. Acta*, **18**, 541 (1962).
(25) L. Manojlovic and J. C. Speakman, *Acta Crystallogr., Sect. B*, **24**, 323 (1968).
(26) H. Musso, *Chem. Ber.*, **88**, 1915 (1955).
(27) J. H. S. Green, W. Kynaston, and A. S. Lindsey, *Spectrochim. Acta*, **17**, 486 (1961).
(28) J. L. Carter, D. J. Yates, P. J. Lucchesi, J. J. Elliott, and V. Kevorkian, *J. Phys. Chem.*, **70**, 1126 (1966).
(29) E. A. Vizzini, I. F. Taylor, and E. L. Amma, *Inorg. Chem.*, **7**, 1351 (1968).
(30) M. Nardelli, G. F. Gasparri, G. G. Battistini, and A. Musatti, *Chem. Commun.*, **10**, 187 (1965).
(31) M. Nardelli, G. Favo, and P. Boldrini, *Gazzetta*, **92**, 1392 (1962), and references therein.
(32) L. Pauling, "The Nature of the Chemical Bond", Cornell University Press, Ithaca, N.Y., 1972, p 507.
(33) D. L. Smith and H. R. Luss, private communication.
(34) M. R. Udupa and B. Krebs, *Inorg. Chim. Acta*, **7**, 271 (1973).
(35) D. D. F. Shiao, A. H. Herz, and R. A. Guistina, private communication.
(36) I. Lindquist and B. Strandberg, *Acta Crystallogr.*, **10**, 173 (1957).
(37) C. Panattoni and E. Frasson, *Acta Crystallogr.*, **16**, 1258 (1960).
(38) D. Coucovanis, N. C. Baenziger, and S. M. Johnson, *Inorg. Chem.*, **13**, 5, 1191 (1974).
(39) F. J. Hollander and D. Coucouvanis, *Inorg. Chem.*, **13**, 10, 2381 (1974).

Spectroscopy of Pyridoxal Analogues. 2. *N*-Ethylsalicylaldimines

Carl J. Seliskar

Chemistry Department, University of Cincinnati, Cincinnati, Ohio 45221 *(Received January 12, 1977)*

The intense electronic transitions found at $\lambda > 1900$ Å in four chemical variants of *N*-ethylsalicylaldimine (and by analogy all *N*-alkyl derived molecules) are presented and transition assignments are made. The $^1A'' \leftarrow 1^1A'$ ($\pi^* \leftarrow \sigma(n)$) transitions calculated to lie at $\lambda > 1900$ Å have not been located experimentally but tentative conclusions based on previous work are made. The major effect of the solvent medium on the neutral/dipolar ion–molecule equilibrium appears to be quite specific to proton-donating alcohol solvents. A reasonable model for solvent alcohol interaction suggests intermolecular hydrogen bonding with the oxygen atom of the aldimine.

Introduction

Salicylaldehydes (o-hydroxybenzaldehydes) and their *N*-alkyl Schiff's bases (o-hydroxybenzaldimines) are chemical prototypes of pyridoxal and, in general, the B_6 vitamins. In a previous paper[1] the electronic absorption spectroscopy of the parent molecule salicylaldehyde was presented. In this communication we report on the spectroscopy of *N*-ethylsalicylaldimines. In subsequent papers we shall present the luminescence spectroscopy of these molecules and their trivalent metal chelates.

The basic structure of *N*-alkylsalicylaldimines is (R = methyl, ethyl, etc.)

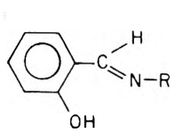

and embodies several key molecular features common to pyridoxal mediated biocatalytic reactions. First, exocyclic groups OH and (-CH=N-) are able to intramolecularly hydrogen bond and this is similar to salicylaldehyde itself.[1] Second, the strength of the intramolecular hydrogen bond in salicylaldimines is of sufficient magnitude to permit proton tautomerism to occur in the planar structure.[2] The end result of proton tautomerism is, thus, formation of an internal dipolar ion. Third, salicylaldimines are capable of forming bis chelates with a series of trivalent metals and the properties of such chelates relate directly to extensive studies[3] on model vitamin B_6 reactions.

Proton tautomerism and chemical protonation of *N*-alkylsalicylaldimines constitute a set of isoelectronic processes and these are shown in Scheme I. As the now extensive literature[2,3] on pyridoxal analogues indicates, these structural and chemical processes are fundamental to the observed spectral behavior of the B_6 vitamins. Apart from relatively subtle differences, the electronic spectra of *N*-derived salicylaldimines is represented by *N*-ethylsalicylaldimine whose chemical stability allows detailed examinations to be made. Thus, the spectroscopy of this molecule assumes a significant role in elucidation of the spectroscopy of vitamin B_6.

Neglecting quite small $\sigma\pi$ mixing effected by nonplanar exocyclic chemical groups (e.g., R = C_2H_5), the electronic states of *N*-alkylsalicylaldimines (and, indeed, most pyridoxal analogues) may be described within the C_s point group. The ground and all monoexcited $\pi\pi^*$ states are of orbital symmetry A′; all $\sigma(n)\pi^*$ states of species A″. Beginning with the ground electronic singlet state (= $1^1A'$) excited states are designated as follows: $1^3A'$, $2^{1,3}A'$, ...; $1^{1,3}A''$, $2^{1,3}A''$, ... In the singlet manifold, all $\pi^* \leftarrow \sigma(n)$ transitions (i.e., $^1A'' \leftarrow 1^1A'$) are out-of-plane (z) polarized; all $\pi^* \leftarrow \pi$ transitions (i.e., $^1A' \leftarrow 1^1A'$) are in-plane (x,y) polarized.

Scheme I

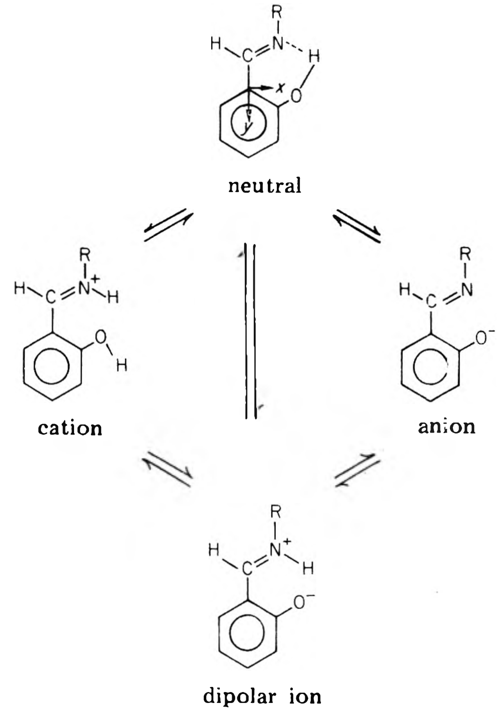

Experimental Section

N-Ethylsalicylaldimine was prepared by allowing 100 mL of salicylaldehyde (Fisher) to react with 150 mL of anhydrous ethylamine (Eastman) in 150 mL of methanol. The formation of the aldimine was driven to completion by final refluxing of the reaction mixture for 2 h. After evaporation of residual ethylamine and methanol solvent, the yellow liquid product was dried over anhydrous sodium sulfate and vacuum distilled. *N*-Ethylsalicylaldimine was collected at 87–88 °C and 5 mm of pressure. Comparison of the spectra of the product with those of salicylaldehyde showed the aldimine to be more than 99% pure. Acids, bases, and solvents were used as commercially available spectroscopic or analytical grade without further purification. Electronic survey spectra were taken on a Cary 14 spectrophotometer using either a 10 cm gas cell or 1 cm liquid cell at 300 K.

Concentration ratio measurements (cf. Figure 2) were made from deconvoluted spectra of dipolar ion/neutral molecule mixtures in various solvents. The estimated

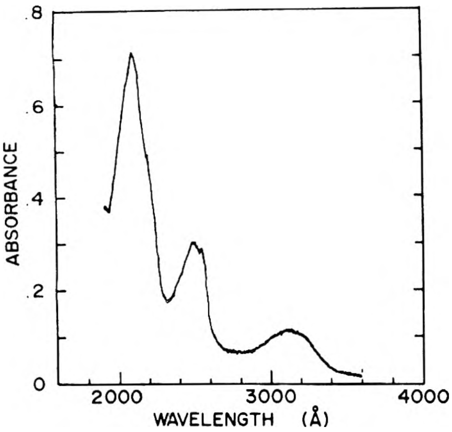

Figure 1. The low resolution survey spectrum of *N*-ethylsalicylaldimine vapor at 300 K. The absorption due to the vapor cell alone is negligible in the wavelength region shown.

accuracy for this procedure is ±10%.

Results and Discussion

N-Ethylsalicylaldimine Vapor. *N*-Ethylsalicylaldimine vapor exhibits three intense broad absorptions at $\lambda \geq 1900$ Å as shown in Figure 1. On the basis of intensity alone, these electronic absorption bands must be attributed to $^1A' \leftarrow 1^1A'$ ($\pi^* \leftarrow \pi$) transitions of the planar aromatic portion of the molecule. Comparison of solution- and gas-phase molecule spectra shows that the structure of the exocylic hydrogen-bonded atoms must be that of an internally neutral species (cf. Scheme I). The three absorption bands of the gas-phase molecule are discussed in more detail below.

3100-Å Absorption Band. The 3100-Å absorption band is featureless and corresponds to the 3200-Å band of salicylaldehyde.[1] Measurement of its oscillator strength gives a value of $f = 0.093$ in cyclohexane solvent (vide infra). On the bases of intensity and analogy with salicylaldehyde,[1] the 3100-Å absorption of *N*-ethylsalicylaldimine is assigned as $2^1A' \leftarrow 1^1A'$.

2500-Å Absorption Band. The 2500-Å absorption band of *N*-ethylsalicylaldimine carries high oscillator strength ($f = 0.18$ in cyclohexane solvent) and a suggestion of vibrational definition. The lack of extensive vibrational structure in the 2500-Å transition is to be contrasted with the structured 2525-Å salicylaldehyde band system which is its electronic counterpart. In every other way, however, the aldimine 2500-Å absorption is analogous to that in salicylaldehyde and may be straightforwardly designated $3^1A' \leftarrow 1^1A'$.

2100-Å Absorption Band. The 2100-Å absorption band has high oscillator strength ($f = 0.73$ in cyclohexane solvent), shows no vibrational definition, and corresponds to the 2100-Å absorption in salicylaldehyde.[1] As in the latter case, the aldimine 2100-Å band may contain intensity from more than one $\pi^* \leftarrow \pi$ transition (vide infra).

N-Ethylsalicylaldimines in Solution. The electronic absorption spectroscopy of solution-phase salicylaldimines differs significantly from that of salicylaldehydes.[1] These differences are marked and ultimately attributable to differences between isoelectronic exocyclic groups (–CH=N–) and –CHO.

Neutral and Dipolar Ion Molecules. It is well known[2-4] that uncharged aldimines of pyridoxal analogues in polar solvents can exist as equilibria between internally neutral and dipolar-ion forms. However, little is known about the role of the solvent medium in the formation of these species, albeit speculation does exist in the literature.[4] We have measured the effects of the solvent medium (16 solvents) on the neutral/dipolar ion–molecule equilibrium and find several interesting results:

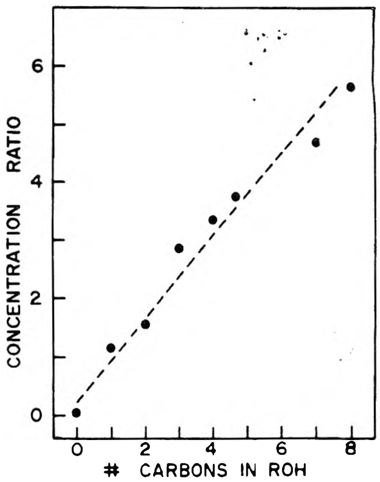

Figure 2. The internally neutral to dipolar-ion–molecule concentration ratio as a function of the number of aliphatic carbon atoms in a series of straight chain alcohols, ROH (R = H, CH_3, etc.). The dashed line represents the approximate linear relationship.

(1) The role of solvent polarity, per se (e.g., bulk solvent dielectric constant), is slight in determining the ratio of the concentration of the two chemical forms. For example, the ratios of concentrations of the neutral to dipolar-ion form at 300 K are as follows: chloroform, 15; methylene chloride, 18; acetonitrile, 17. However, the polarity of the solvent medium does appear to limit the presence of the dipolar ion in cases of totally nonpolar media: carbon tetrachloride, >350; *n*-hexane, >60; 1,4-dioxane, >90.

(2) Wide variation in the concentrations of the neutral and dipolar-ion forms is found specifically for proton-donating alcohol solvents. This behavior is shown in Figure 2 for a series of straight chain alcohol solvents. That the variation of the neutral to dipolar-ion concentration ratio is roughly linear with number of solvent carbon atoms is puzzling but suggests formation of intermolecular hydrogen-bonded complexes between solvent molecules and the oxygen atom of the aldimine. This sort of intermolecular interaction would tend to reduce internal aldimine –OH bond strength and, thus, favor proton transfer to the nitrogen center. The variation in concentration ratios with size of aliphatic carbon chain in ROH may then be attributed to proton-donating ability of the hydroxyl group of the alcohol.[5]

(3) The absorption maxima of the $2^1A' \leftarrow 1^1A'$ ($\pi^* \leftarrow \pi$) transitions in the neutral and dipolar-ion forms shift little over a wide range of solvent polarity. For example, wavelength shifts of ~50 Å for the neutral and ~100 Å for the dipolar ion are found in comparing the absorption maxima in carbon tetrachloride and acetonitrile solvents, respectively. The smallness of these wavelength shifts for both chemical forms argues strongly for little intramolecular charge-transfer character in their $2^1A' \leftarrow 1^1A'$ transitions.

Anionic and Cationic Molecules. Cation. The electronic absorption spectrum of the monoprotonated cation (i.e., protonation at the nitrogen atom) of *N*-ethylsalicylaldimine is shown in Figure 3. The integrated intensities of the 3550-Å ($f = 0.12$) and the 2750-Å ($f = 0.26$) bands require that these transitions be assigned as $2,3^1A' \leftarrow 1^1A'$ analogous with those found in the neutral molecule. In the case of the cation the $2,3^1A' \leftarrow 1^1A'$ transitions are red-shifted relative to the dipolar-ion molecule. This behavior appears to be typical of most, if not all, vitamin B_6 related molecules in solution.[1-4]

TABLE I

	CNDO/S-CI(60)			Experiment	
Transition	Energy, eV	Oscillator strength	Polarization[a]	Energy (fwhm), eV	Oscillator strength
Neutral molecule					
$1^1A'' \leftarrow 1^1A'$	3.66	0.005	z		
$2^1A' \leftarrow 1^1A'$	4.32	0.105	xy	3.69-4.48	0.09
$3^1A' \leftarrow 1^1A'$	5.06	0.349	y	4.71-5.12	0.18
$4^1A' \leftarrow 1^1A'$	5.95	0.602	xy	5.39-6.14	0.73
Dipolar ion molecule					
$1^1A'' \leftarrow 1^1A'$	2.70	0.000	z		
$2^1A' \leftarrow 1^1A'$	3.21	0.235	xy	2.89-3.42	$\epsilon_{max}{}^b$ 7.2 × 10^3
$3^1A' \leftarrow 1^1A'$	4.80	0.164	y	4.36-4.68	
$2^1A'' \leftarrow 1^1A'$	4.96	0.000	z		
$4^1A' \leftarrow 1^1A'$	5.04	0.041	xy	5.16(max)	
$5^1A' \leftarrow 1^1A'$	5.48	0.766	y		
Anionic molecule					
$1^1A'' \leftarrow 1^1A'$	3.22	0.001	z		
$2^1A' \leftarrow 1^1A'$	3.44	0.246	xy	3.34-3.84[b]	$\epsilon_{max}{}^b$ 6.7 × 10^3
$2^1A'' \leftarrow 1^1A'$	4.15	0.002	z		
$3^1A'' \leftarrow 1^1A'$	4.76	0.008	z		
$3^1A' \leftarrow 1^1A'$	4.81	0.062	xy	4.82(max)[b]	
$4^1A' \leftarrow 1^1A'$	5.11	0.083	xy		
$5^1A' \leftarrow 1^1A'$	5.77	1.24	xy		
Cationic molecule					
$2^1A' \leftarrow 1^1A'$	3.80	0.106	x	3.29-3.85	0.12
$3^1A' \leftarrow 1^1A'$	4.68	0.575	y	4.30-4.79	0.26
$1^1A'' \leftarrow 1^1A$	4.93	0.001	z		
$4^1A' \leftarrow 1^1A'$	5.57	0.010	xy	5.51(max)	

[a] For definition of axes see Scheme I. Axial specification of in-plane polarization is given according to dominant orientation (x or y) or heavily mixed orientation (xy). [b] Reference 4.

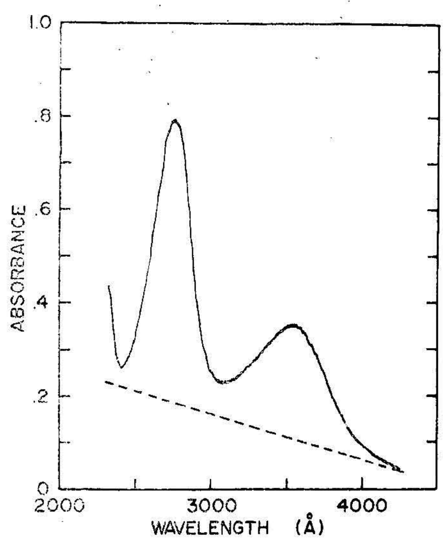

Figure 3. The electronic absorption spectrum of monoprotonated N-ethylsalicylaldimine in diethyl ether saturated with HCl(g) at 300 K. The dashed line represents an extrapolated baseline absorbance for the solvent/HCl(g) mixture. It is to be noted that the sample mixture is very slightly turbid at HCl(g) saturation.

Anion. The monoanion (i.e., proton released by the phenolic hydroxyl group) is not chemically stable in aqueous or alcoholic solvents except in the presence of a huge excess of ethylamine.[4] However, the anion has a half-life of the order of 5 min in ethanol/base after initial deprotonation and measurement of the spectrum of the monoanion can be made. Our results are in agreement with those of Alexander and Sleet[4] who measured the spectrum in aqueous ethylamine. (We refer the reader to Table I for a catalogue of transition assignments.) It is important to note that the absorption spectrum of the anion is very similar to those of trivalent metal chelates of N-alkylsalicylaldimines. The latter point is amplified in detail in a forthcoming paper.

Quantum Chemical Results

All valence-electron molecular orbital calculations, i.e., CNDO/S–CI,[6,7] were done on four chemical variants of salicylaldimine (cf. Scheme I; R = H). Configuration interaction was limited to the first 60 singly excited configurations and two-center electron repulsion integrals were taken according to the Mataga approximation.[6,7] In all cases phenyl C–C and C–H bond distances were taken as 1.390 and 1.085 Å, respectively. Associated phenyl angles ∠CCC and ∠CCH were assumed to be 120°. Exocyclic hydroxyl group atom coordinates were taken as those in salicylaldehydes.[1] Imine group (–CH=NH) geometry was assumed as follows: r(CH) = 1.071 Å; r(CN) = 1.300 Å; r(NH) = 1.014 Å; all angles, 120°.

Comparison of calculations for salicylaldimines (R = H) with our experimental results for N-ethylsalicylaldimine (R = C_2H_5) is given in Table I. As our previous work[8] and the literature specifically on pyridoxaldimines[2,3] shows, alkylation results in small systematic spectral shifts which do not confuse assignments by such a comparison of calculation and experiment. Examination of Table I and allied computational results (which may be obtained from the author on request) result in several principal conclusions:

(1) Excepting the case of the cationic molecule, the lowest energy transition is calculated as $1^1A'' \leftarrow 1^1A'$. We are not yet able to give positive location of these $\pi^* \leftarrow n(\sigma)$ transitions. However, we have found that the lowest energy emitting level in the anion (which we presume is the lowest singlet) is the $2^1A'$ $(\pi\pi^*)$ state. This result is consistent with our experience[1,8] that CNDO/S–CI computations place the $1^1A''$ $(\sigma(n)\pi^*)$ state too low in energy by 0.5–1.0 eV. Using this energy discrepancy as a diagnostic, we tentatively conclude that the neutral and dipolar ion may have $1^1A''$ lowest energy singlets. Our

continuing luminescence measurements on these compounds should test this hypothesis.

(2) Agreement between calculated and experimental energies for $2,3,4\,^1A' \leftarrow 1\,^1A'$ ($\pi^* \leftarrow \pi$) transitions is excellent and corresponding assignments are straightforward. Comparison of measured and calculated oscillator strengths where spectral deconvolution is reliable (i.e., ±10%) shows that computation is within a factor of 2 of experiment. It is important to note that trends in calculated oscillator strengths between and within molecular species are borne out by experiment. In this regard, these results are consistent with our previous experience.[1,8]

(3) Several $^1A'' \leftarrow 1\,^1A'$ ($\pi^* \leftarrow \sigma$) transitions are predicted to lie at energies where their low intensity ($f < 0.01$) would be overwhelmed by surrounding $^1A' \leftarrow 1\,^1A'$ intensity ($f \geq 0.1$). We have no experimental information regarding location of these $\pi^* \leftarrow \sigma$ transitions and it is unlikely that they will be locatable by conventional absorption spectroscopy.

(4) Of the transitions which lie at $\Delta E \leq 6$ eV, only the $1\,^1A'' \leftarrow 1\,^1A'$ transitions are calculated to have significant intramolecular charge transfer character. Even in the case of the $2,3\,^1A' \leftarrow 1\,^1A'$ transitions of the anion, where charge transfer character might be anticipated, only slight amounts are calculated. Our computational results are, thus, in complete accord with measured solvent polarity insensitivity of the transitions of these molecules (vide supra).

Conclusions

The intense electronic transitions found at $\lambda > 1900$ Å in four chemical variants of *N*-ethylsalicylaldimine (and by analogy all *N*-alkyl derived molecules) are presented and transition assignments are made. The $^1A'' \leftarrow 1\,^1A'$ ($\pi^* \leftarrow \sigma(n)$) transitions calculated to lie at $\lambda > 1900$ Å have not been located experimentally but tentative conclusions based on previous work[1,8] are made. The major effect of the solvent medium on the neutral/dipolar ion–molecule equilibrium appears to be quite specific to proton-donating alcohol solvents. A reasonable model for solvent alcohol interaction suggests intermolecular hydrogen bonding with the oxygen atom of the aldimine.

References and Notes

(1) C. J. Seliskar, *J. Mol. Spectrosc.*, **53**, 140 (1974).
(2) See, for example, D. Heinert and A. E. Martell, *J. Am. Chem. Soc.*, **84**, 3257 (1962).
(3) See, for example, S. Matsumoto and Y. Matsushima, *J. Am. Chem. Soc.*, **96**, 5228 (1974).
(4) P. W. Alexander and R. J. Sleet, *Aust. J. Chem.*, **23**, 1183 (1970).
(5) G. C. Pimentel and A. L. McClellan, "The Hydrogen Bond", W. H. Freeman, San Francisco, Calif., 1960, Chapter 3.
(6) J. Del Bene and H. H. Jaffé, *J. Chem. Phys.*, **48**, 1807 (1968).
(7) R. L. Ellis, Ph.D. Dissertation, University of Cincinnati, 1971.
(8) C. J. Seliskar and S. P. McGlynn, *J. Chem. Phys.*, **56**, 1417 (1972).

Temperature-Dependent Cation Distribution in Dehydrated Calcium-Exchanged Mordenite

W. J. Mortier

Centrum voor Oppervlakteschelkunde en Colloïdale Scheikunde, Katholieke Universiteit Leuven, De Croylaan 42, B-3030 Heverlee, Belgium

(Received December 1, 1976)

Publication costs assisted by the Katholieke Universiteit Leuven

An equilibrium distribution of exchangeable cations in zeolites might reflect the Boltzmann distribution law, the occupancy ratios of the cation sites being related to the energy level differences and the absolute temperature. Dehydrated calcium mordenite ($Ca_{3.33}Al_{7.82}Si_{40.2}O_{96}$) was chosen to follow the variation of the Ca ion localization with temperature. Two crystals were studied: A at 25 and 350 °C (accidentally rehydrated) and B at 345 and 635 °C with single crystal x-ray diffraction methods. The Ca ions are distributed among four nonequivalent sites. A shift of the population parameters with temperature is observed, the sites yielding a better coordination to the cations becoming more and more stable. This indicates a change in the energy level of the sites. At all temperatures, site I is the most stable site, located in the center of a highly twisted eight-ring and coordinated to six framework oxygens. Sites III and VI have a one-sided coordination to four framework oxygens and site IV is located off-center on the eight-ring, coordinated to only two oxygens. The stability sequence of these sites, as calculated from the energy level differences is I > VI > IV > III at temperatures below 345 °C, site IV showing considerable destabilization at 635 °C. The presence of water molecules at 350 °C resulted in stabilization of sites I and IV by increasing the coordination of the cations.

Introduction

In the past two decades, zeolites became the subject of intensive research and have found numerous industrial applications as, e.g., heterogeneous catalysts or drying agents. Possible differing cation loadings by ion exchange, reversible dehydration, and their uniform but limited pore size allows the variation of specific physicochemical properties. Catalytic properties result from cation–framework interactions allowing the formation of surface complexes as reactive intermediates. In most zeolites, cation sites can be distinguished, depending on framework coordination and adsorption capability. The cations are mobile to a large extent as shown by ion exchange and electric conductivity. Interactions of the cations with the framework, with other cations, and with sorbed molecules determine the difference in energy level of the cation sites. Assuming a Boltzmann distribution of the cations over these sites, it is possible to calculate the differences in energy level as described earlier.[1] According to this formalism (logarithm of the site occupancy ratio being proportional to the energy level difference and the reciprocal absolute temperature), the temperature may influence the cation distribution either directly or indirectly by change of the energy level differences. Interpretations of catalytic phenomena (mostly at elevated temperatures) based on structural data obtained at room

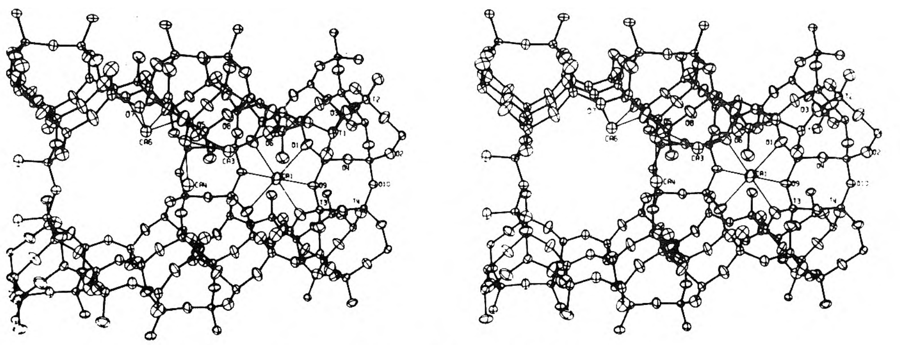

Figure 1. Stereo plot of the B635 structure. Displacement ellipsoids shown at 30% probability level.

Chart I

A025	a 18.009(5)	b 20.248(5)	c 7.461(3)
A350	a 18.061(7)	b 20.331(7)	c 7.490(4)
B345	a 18.048(10)	b 20.284(13)	c 7.483(4)
B635	a 17.881(7)	b 20.189(8)	c 7.479(3)

temperature may therefore be biased. The present work tries to elucidate the extent of structural changes with the study of the influence of temperature on dehydrated Ca-exchanged mordenite.

Experimental Section and Results

Two crystals (A, 0.07 × 0.07 × 0.5 mm; B, 0.08 × 0.08 × 0.5 mm) of Ca-exchanged ptilolite, a natural mordenite variety, from the same batch as studied previously,[2] $Ca_{3.33}Al_{7.82}Si_{40.2}O_{96}$, were mounted in a silica capillary, evacuated at 10^{-5} Torr as follows: A 2 h, 100 °C; 16 h, 250 °C; 3 h, 500 °C; B 12 h, 100 °C; 24 h, 250 °C; 4.5 h, 470 °C and sealed at that temperature. A slightly modified single crystal furnace as described by Brown et al.[3] was used for data collection on a Picker FACS-1 automated single crystal diffractometer. Temperature calibration was made against the melting points of $NaNO_3$, $Ba(NO_3)_2$, and NaCl. Intensities were collected at 25 (±2) and 350 (±10) °C (crystal A) and 345 (±10) and 635 (±15) °C (crystal B) with $\theta - 2\theta$ scans (2°/min) up to $\sin \theta/\lambda = 0.6$, Mo K_α radiation. The data sets will be identified as A025, A350, B345, and B635, respectively. One equivalent data set was collected (about 1390 reflections) yielding 874, 876, 994, and 1168 reflections with $F \geq 3\sigma_F$ respectively. Before data collection started, the crystal was equilibrated for 1 day at each temperature. It was observed, for B635, that the peak shape varied with time, reaching about one-fourth of its original width after 4 days of data collection. This might result from the gradual release of the strain in the crystal since small pieces were expelled at one side of the needle. Due to this loss, the intensity of the three standard reflections, collected every 100 reflections, decreased. Recollection of the first half of the reflections and rescaling indicated that there was no relative change in the intensities. The unit cell parameters (in Å) in *Cmcm*, obtained from a least-squares refinement using 15 Friedel pairs, are shown in Chart I. Details of the data reduction procedure are the same as described by Rinaldi, Pluth, and Smith.[4] Lorentz and polarization but not absorption corrections ($\mu = 7.9$ cm^{-1}) were applied. The structures were refined using full-matrix least-squares and Fourier methods (X RAY system[5]). Stacking faults identical with those described for dehydrated hydrogen mordenite[6] were detected and refined on the occupancy of the T(3) and T(4) atoms. A mean percentage for both temperatures was taken for every crystal (A, 2.4%; B, 1.7%). Final R_F (= $\sum||F_o| - |F_c||/\sum|F_o|$) and wR_F (= $\sum w||F_o| - |F_c||/\sum w|F_o|$) values of 0.079, 0.046; 0.071, 0.058; 0.063, 0.055; and 0.058, 0.046 were obtained, respectively.

TABLE I: Statistical Comparison of the Structures A025, A350, B345, and B635 Relative to the B635 Structure (Calculation of Q)

	B635	B345	A350[a]	A025	q
Framework + cations	0.011	5.325	5.734	5.998	112
Framework	0.012	5.534	5.835	6.518	94
Cations	0.007	3.087	5.150	3.244	18

α	$F_{112,120}$	$F_{94,120}$	$F_{18,120}$
0.100	1.27	1.29	1.50
0.050	1.36	1.38	1.70
0.025	1.44	1.47	1.87
0.010	1.55	1.59	2.09
0.005	1.63	1.67	2.26

[a] O(II) not included in the comparison.

A statistical comparison was made using the B635 structure as a reference following a method described earlier.[7] A subset ($\hat{\beta}_i$) of a given structure is compared with the same set of parameters ($\hat{\beta}_o$) of a reference structure using

$$Q = \frac{(\hat{\beta}_i - \hat{\beta}_o)'S_1(\hat{\beta}_i - \hat{\beta}_o)}{2qs^2} = F_{q,n-p}(\alpha)$$

where S_1 is the $q \times q$ matrix of the coefficients of normal equations, $s^2 = \sum(w_i^{1/2}\Delta_i)^2/(n-p)$, n being the number of observations and p the number of parameters. If $Q > F_{q,n-p}(\alpha)$, the equality of the parameter vectors can be rejected with a probability α of being in error. The test is performed on a conditional basis since the remaining ($p - q$) parameters are not considered. The variance–covariance matrix S was taken from a second refinement cycle with the least-squares program NUCLS (see also ref 4), using the X RAY parameters as starting values. A final R index of 0.059 was obtained. The results are given in Table I. Since $n - p = 869$ is closer to 120 than ∞ (usually given in F tables), the Q values are compared with $F_{q,120}(\alpha)$, also given in Table I. It is clear that structures B345, A350, and A025 do significantly differ from the B635 structure, when either cations, framework, or both are considered.

The tables listing structure factors, population and positional parameters, anisotropic thermal parameters and interatomic distances, and bond angles for the framework are available as supplementary material (see paragraph at end of text regarding supplementary material). Tables II and III list the population parameters of the cations and their coordination distances.

Discussion

A stereoscopic drawing of the framework, including the cation positions, is given in Figure 1 for the B635 structure. The framework structure consists of distorted six-ring sheets parallel to the bc plane, interconnected in the a direction with each other through single four-membered rings, whereby five-rings are generated.[8] Large and small

TABLE II: Population Parameters for the Cations (No./Unit Cell)

Site type	d Ca mordenite (2)	A025	A350	B345	B635
Ca(I) (4b)	1.66(2)	1.89(4)	1.97(5)	1.75(4)	2.12(3)
Ca(III) (16h)	0.62(4)[a]	0.58(6)	0.37(8)	0.48(6)	0.41(5)
Ca(IV) (8f)	0.45(4)	0.40(6)	0.73(10)	0.52(6)	0.14(4)
Ca(VI) (8g)	0.63(3)	0.46(4)	0.52(6)	0.56(4)	0.56(3)
O(II) (4c)			2.61(15)		

[a] This site was described in an 8g-type position.

TABLE III: Interatomic Distances for the Cations

	d Ca mordenite (2)	A025	A350	B345	B635
Ca(I)-4O(1)	2.849(5)	2.832(6)	2.849(6)	2.850(5)	2.839(4)
-2O(9)	2.569(5)	2.554(8)	2.604(8)	2.580(6)	2.541(5)
-2O(II)			2.358(17)		
Ca(III)-O(1)	3.27(2)	2.78(5)	2.79(9)	2.86(5)	2.80(5)
-O(2)	3.29(2)	2.94(5)	2.95(9)	2.83(5)	2.89(5)
-O(5)	2.40(3)	2.58(5)	2.68(9)	2.46(5)	2.59(5)
-O(6)	2.46(3)	2.46(5)	2.62(9)	2.56(5)	2.66(5)
-O(8)	3.10(2)	2.84(5)	3.08(8)	2.72(4)	3.01(5)
Ca(IV)-2O(2)	2.81(3)	2.89(4)	2.72(4)	2.83(3)	2.89(6)
-2O(5)	3.19(1)	3.16(2)	3.25(2)	3.19(1)	3.12(2)
-O(10)	2.99(5)	3.13(6)	2.86(6)	3.04(5)	3.15(9)
Ca(VI)-2O(3)	2.57(2)	2.55(3)	2.69(4)	2.57(2)	2.32(2)
-2O(7)	2.55(1)	2.61(3)	2.70(4)	2.58(2)	2.32(2)
O(II)-2Ca(I)			2.358 (17)		
-4Ca(III)			3.19(9)		
-4O(I)			3.274(6)		
-2O(6)			3.169(9)		
-2O(9)			3.24(3)		

channels are created parallel to the *c* axis. A projection on the *bc* plane of the "accessible" tetrahedra, represented by their T atoms, is given in Figure 2. The framework oxygens are represented by straight lines, the interconnecting four-rings by double lines. The site nomenclature is the same as adopted for the rehydrated Ca variety.[9] They are progressively numbered by Roman numerals from the center of the small channel (site I) through the interconnecting channels (sites II, III, and IV) to the large channel (site VI). The oxygens available for coordination are also indicated in Figure 2.

The framework changes are only limited and comparable to previously described mordenite structures. An extensive comparison may be found in ref 10. There is not always an increase of the thermal parameters with temperature but they are merely related to the crystal itself and might be an effect of disorder. Indeed, symmetry lowering was already observed for the dehyrated potassium form.[10] The changes of the interatomic distances follow the change in cation site population, especially the increase at site I and the decrease at site IV, affecting the T–O distances for the T(3) and T(4) tetrahedra (four rings of the mordenite framework). It is only for B635 that there is an appreciable change. The mean T–O distances for this structure are 1.599, 1.583, 1.659, and 1.595 Å for T(1) to T(4), respectively, showing an increase of T(3)–O and a decrease of T(4)–O to an extent of about 0.02 Å. Two effects are involved: bond lengthening upon cation coordination and a concomitant narrowing of the T–O–T angle. A strong correlation between the T–O–T angles and the T–O distances exists for all mordenites and was most accurately described for the dehydrated hydrogen form.[6] Site I being coordinated to O(1) and O(9) oxygens, bond lengthening occurs at T(3) as a result of the site I population increase, and the narrowing of the T–O(1)–T angle from 146.5^2 to 144.8°. The change of the T–O(9)–T angle is minor (136.5 to 136.2°). These interactions are probably the main reason for the change in the unit cell parameters. However, the irregular variation of these indicates that this system is a complicated one. The mean T–O distances in B635 would also suggest that the Al content of the T(3) tetrahedra would be higher than already assumed for the previously described mordenites.[10] The higher Al content of T(3) and T(4) is in agreement with the hypothesis of Meier[8] considering the frequent occurrence of six-ring sheets of SiO_4 tetrahedra in zeolite frameworks.

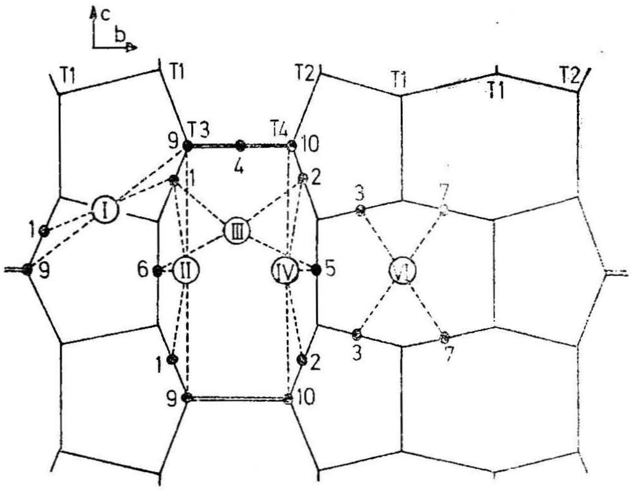

Figure 2. Projections on the *bc* plane of the "accessible" tetrahedra, represented by their T atoms. The framework oxygens are represented by straight lines, and the interconnecting four-rings by double lines. Cation sites I, II, III, IV, and VI are indicated together with the coordination possibilities.

Details of the cation coordination are shown in the Figure 3 for B365, and are representative for all structures considering the limited variation from structure to structure. Site I, in the center of a puckered eight-ring (2/*m* point symmetry) blocking the small channels parallel

TABLE IV: Differences in Energy Level Relative to Site I (in 10^{-23} J)[a]

Sample Temp, K	d Ca mordenite (2) 298	A025 298	A350 623	B345 618	B635 908
Site III	975(27)	1053(43)	2632(187)	2338(108)	3798(154)
Site IV	823(37)	922(62)	1445(120)	1631(100)	4287(359)
Site VI	683(20)	864(37)	1743(102)	1570(64)	2532(69)

[a] Standard deviations in parentheses estimated as $\sigma_{\Delta\epsilon_{ij}} = kT[(\sigma_{n_i}/n_i)^2 + (\sigma_{n_j}/n_j)^2]^{1/2}$.

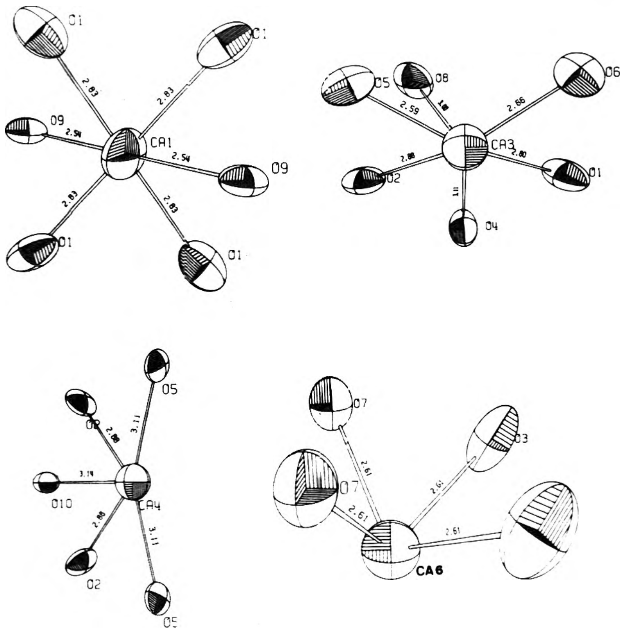

Figure 3. Environment and displacement ellipsoids (50% level) for sites I, III, IV, and VI (B635 structure).

to the c axis, is coordinated to six near-planar oxygens: four O(1) and two O(9). Site III has a one-sided coordination to four framework oxygens (O(1), O(2), O(5), and O(6)) of the "boat" shaped walls of the channel connecting the large and small channels. In the first structure published, this site was located at the symmetry plane bisecting the interconnecting channels. However, thermal ellipsoids suggested the present and obviously correct position. Refinement with isotropic thermal parameters allowed the shift of the cation sites from the symmetry plane. Site IV has a poor coordination at the slightly elongated eight-rings of the large channel (point symmetry *m*), displaced from the center. Site VI has a one-sided coordination against four oxygens of the walls of the large channel (two O(3) and two O(7), point symmetry *m*). Sample A350 which has accidentally been rehydrated shows a water molecule adsorbed to site I, i.e., in the center of the near-circular eight-ring (site II) of the small channel (point symmetry *mm*) with possible contact with all surrounding oxygens, i.e., four O(1), two O(6), and two O(9).

The population of the cation sites changes with temperature (see Table II). We shall consider dehydrated calcium mordenite (see ref 2) together with the B crystal first, for reasons given below. Site I becomes more and more populated with increasing temperature (42% at 25 °C to 53% at 635 °C). We also observe a slight decrease of site III and VI population and a dramatic depopulation of site IV. At high temperatures, the best coordinated site (site I) seems to become increasingly stable while the very poorly coordinated site IV undergoes a rapid depopulation at temperatures above 350 °C. A change in energy level may cause the new equilibrium distribution. Considering the occupancy figure (n), the site multiplicity (ω), and the absolute temperature, the energy level differences ($\Delta\epsilon_{ij}$) between site i and j may be calculated[1] as

$$\Delta\epsilon_{ij} = \epsilon_i - \epsilon_j = -kT \ln (n_i\omega_j/n_j\omega_i)$$

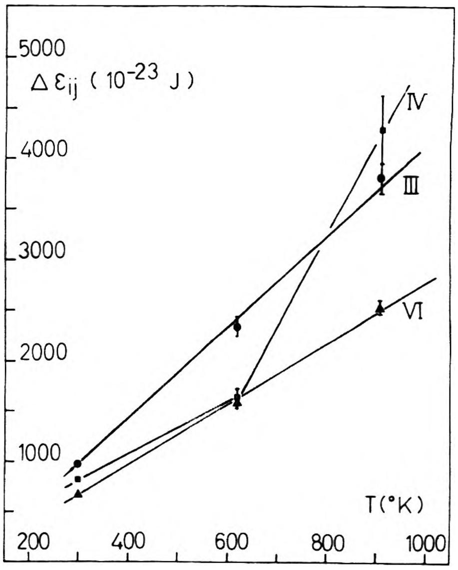

Figure 4. Energy level differences relative to site I (●, ■, ▲: sites III, IV, and VI for d Ca mordenite (2), B345, and B635, respectively).

No change in energy level means a more equal distribution of the cations at higher temperatures. The increased population of site I is an inverse effect. The energy level differences, calculated relative to site I, are given in Table IV. A plot (Figure 4) against the temperature reveals that, within the standard deviations, these energy level differences vary linearly with the temperature for sites III and VI. The dramatic increase of site IV energy level is obvious.

The change in energy level with temperature is surprising. Indeed, for orthopyroxenes, the theoretical variation of the Mg^{2+}/Fe^{2+} distribution among the M(1) and M(2) sites revealed that the energy level differences remained constant.[1] Obviously, the full coordination sphere of the M(1) and M(2) sites differs markedly from the situation in zeolites where planar or one-sided coordinations prevail. In this way, thermal vibrations may seriously affect the stability of similar configurations. A second crystal (A025) studied at 25 °C (see Table II) showed a different cation distribution, such that the question arises whether the equilibrium has been reached at this temperature. The population is intermediate between B345 and B635 for sites I and IV, but higher for III and lower for VI. The intensities of the A crystal were collected immediately following the pretreatment, and finished within 3 days. The previously described crystal was allowed to stand for at least 14 days before data collection, the data collection itself taking 10 days (four data sets); Weissenberg films were also taken before (Cu radiation). The longer equilibration time and irradiation with x-rays (more energy is absorbed with Cu radiation) might have brought the cation distribution of the first crystal closer to equilibrium. It was indeed observed for Ca–Y and La–Y zeolites, dehydrated at elevated temperatures, that irradiation (Cu) at 25 °C resulted in a considerable shift of the cation positions.[11] The present distribution of A025 still reflects the distribution at 500 °C (highest pretreatment temperature), site I and IV population being in accordance, and site III population having a temporarily higher population due to diffusion effects (site I → other sites). Further experiments are needed.

The A crystal at 350 °C will have reached equilibrium. This crystal has obviously been hydrated and shows the adsorption site for water molecules at 350 °C, together with the influence on the energy levels. Only one adsorption site has been detected, i.e., at site II, completing the coordination sphere at site I, analogous to hydrated Ca mordenite.[9] The water population at site II is such that some sites I may have two water molecules adsorbed, i.e., at both sides of the plane formed by the framework oxygens. A stabilization of site I is shown by the population increase as compared to B345. A significant increase of site IV population is also observed which may indicate that unobserved water molecules might be involved. It is probable that some of the cation sites are also partly occupied by water molecules for the A350 case. Indeed, the number of cations from chemical analysis being 3.33, the number of cations located at sites I, III, IV, and VI is, in the same sequence as Table I, 3.36(7), 3.33(10), 3.59(15), 3.31(10), and 3.23(8), respectively. A comparison of the energy level differences is not allowed since another reference (site I hydrated) has been taken. The preference of the Ca ions for fully coordinated sites was also reflected in the hydrated Ca mordenite structure,[9] where half of the cations were located at site I, the other half being located in the center of the large channels in a full coordination of water.

In conclusion we can state that the stability sequence for dehydrated Ca mordenite is I > VI > IV > III at temperatures below 350 °C, the stability of sites IV and III being reversed at elevated temperatures. Care should be taken not to extrapolate to other cation-exchanged forms as, e.g., no potassium ions are located at site I in dehydrated potassium mordenite.[10] Room temperature data may not show an equilibrium distribution nor may they be extrapolated to higher temperatures. Interpretations of the physicochemical properties based on the cation distribution must consider the influence of the temperature as well as the presence of sorbed molecules, both changing the energy level of the exchange sites.

Acknowledgment. The author thanks Professor J. V. Smith and Dr. J. J. Pluth of the University of Chicago for their continuous interest and suggestions during a stay at the Department of Geophysical Sciences. The invaluable assistance of Dr. J. J. Pluth with the performance of this experiment is gratefully acknowledged. The author also thanks the "Belgisch Nationaal Fonds voor Wetenschappelijk Onderzoek" for a research grant as "aangesteld navorser" and the Belgian Government (Dienst voor Programmatie van het Wetenschapsbeleid) for financial aid.

Supplementary Material Available: Positional parameters, occupancy factors, anisotropic thermal parameters, interatomic distances and bond angles of the framework, and a list of $|F_o|$ and F_c for all structures (44 pages). Ordering information is given on any current masthead page.

References and Notes

(1) W. J. Mortier, *J. Phys. Chem.*, **79**, 1447 (1975).
(2) W. J. Mortier, J. J. Pluth, and J. V. Smith, *Mat. Res. Bull.*, **10**, 1037 (1975).
(3) G. E. Brown, S. Sueno, and C. T. Prewitt, *Am. Mineral.*, **58**, 698 (1973).
(4) R. Rinaldi, J. J. Pluth, and J. V. Smith, *Acta Crystallogr., Sect. B*, **30**, 2426 (1974).
(5) J. M. Stewart, G. J. Kruger, H. L. Ammon, C. Dickinson, and S. R. Hall, Ed., "The X-ray System", Technical report TR-192, University of Maryland, 1972.
(6) W. J. Mortier, J. J. Pluth, and J. V. Smith, *Mat. Res. Bull.*, **10**, 1319 (1975).
(7) W. J. Mortier, *Acta Crystallogr., Sect. A*, **29**, 473 (1973).
(8) W. M. Meier, Proceedings of the Conference on Natural Zeolites at Tucson, Pergamon Press, New York, N.Y., in press.
(9) W. J. Mortier, J. J. Pluth, and J. V. Smith, *Mat. Res. Bull.*, **11**, 15 (1976).
(10) W. J. Mortier, J. J. Pluth, and J. V. Smith, Proceedings of the Conference on Natural Zeolites at Tucson, Pergamon Press, New York, N.Y., in press.
(11) M. L. Costenoble, W. J. Mortier, and J. B. Uytterhoeven, manuscript in preparation.

Frictional Coefficient Formalism and Mechanical Equilibrium in Membranes

Adrien Schmitt and James B. Craig*

Centre de Recherches sur les Macromolecules, C.N.R.S., 6 rue Boussingault, 67083 Strasbourg, Cedex, France and Department of Chemistry, University of Aberdeen, Meston Walk, Old Aberdeen AB9 2UE, Scotland, United Kingdom

(Received October 6, 1976; Revised Manuscript Received March 28, 1977)

The frictional coefficient formalism is now widely applied to express coupling between diffusional fluxes in solutions at mechanical equilibrium. It is shown that, by defining proper diffusional forces, this formalism may be applied unchanged to isotropic systems in which the conditions of mechanical equilibrium need not prevail. The question of whether a membrane system should be considered as a one-phase or two-phase system is discussed and it is shown that, for the former case, the steady-state transport processes are truly diffusional if analyzed at the correct molecular level. It is emphasized that the distinction between diffusional and viscous flows can only be made if the molecular scale of the transport parameters is defined unambiguously.

I. Introduction

The application of nonequilibrium thermodynamics to transport across homogeneous and isotropic membranes has been the subject of much theoretical and experimental work.[1,2] In "discontinuous" systems, where a membrane separates two homogeneous outer phases, it has been shown that, under steady-state conditions and in the absence of temperature gradients or of chemical reactions, a set of ν linear phenomenological equations describes the unidirectional fluxes of the ν mobile species:

$$J_i^0 = -\sum_{j=1}^{\upsilon} L_{ij}\Delta(\tilde{\mu}_j) \qquad (i = 1,\ldots,\upsilon) \tag{1}$$

J_i^0 is the flux of species i relative to the membrane as the reference frame; $\Delta(\tilde{\mu}_j)$ is the difference in electrochemical potential of species j in the two outer phases, and L_{ij} is a conductance coefficient whose value depends on the nature of the membrane and of the outer phases. To establish eq 1, one can either integrate a set of "local" equations, or consider the membrane as a "black box" separating two solutions between which irreversible exchanges occur. The L_{ij} coefficients are very complicated terms in that each may reflect the combined effects of several different molecular interactions. Alternative sets of linear flux-force equations have also been used for practical purposes.

Spiegler[3] was the first to apply the formalism of friction coefficients to transport processes in membranes. This formalism implies that locally within a membrane, the thermodynamic force acting on 1 mol of i is balanced by the sum of all the frictional forces, i.e.

$$-\nabla\tilde{\mu}_i = \sum_{\substack{j=0\\ j\neq i}}^{\upsilon} c_j\xi_{ij}(\mathrm{v}_i{}^0 - \mathrm{v}_j{}^0) \qquad (i = 1,\ldots,\upsilon) \tag{2}$$

$\nabla\tilde{\mu}_i$ is the electrochemical potential gradient of i, c_j is the molar concentration of j, ξ_{ij} is a resistance coefficient, and $\mathrm{v}_i{}^0$ and $\mathrm{v}_j{}^0$ the velocities of i and j relative to species 0, the membrane. Equation 2 can be derived from a set of local equations analogous to eq 1 by inverting the matrix of local conductance coefficients (L_{ij}) to obtain a matrix of resistance coefficients, if linear dependencies have been allowed for (see ref 8). Identification with the friction-coefficient formalism ($c_j\xi_{ij} = f_{ij}$) is then straightforward.[2,4]

The formalism has also been widely applied to ordinary solutions to express the coupling between diffusional fluxes in a medium at mechanical equilibrium. As this condition does not necessarily prevail in membranes, the significance of the friction coefficients used to describe transport in membranes has recently been questioned.[4,5] The purpose of this paper is to discuss this problem.

II. Diffusional Fluxes at Mechanical Equilibrium

In a solution containing $\nu + 1$ species (ions or molecules), the local rate of entropy production per unit volume, σ_{D}, resulting from a mass-transfer process is given by

$$\sigma_{\mathrm{D}} = \frac{1}{T}\sum_{i=0}^{\upsilon} \mathbf{J}_i\cdot(-\nabla\tilde{\mu}_i + \mathbf{F}_i) > 0 \tag{3}$$

$\mathbf{J}_i$ is the diffusional flux of i relative to the centre of mass as the reference frame, i.e.

$$\mathbf{J}_i = c_i(\mathbf{v}_i - \mathbf{v}) \tag{4}$$

$\mathbf{v}_i$ and $\mathbf{v}$ being the species and center-of-mass velocities, respectively, relative to the cell, where transport occurs, as the reference frame. $\mathbf{F}_i$ is an external force acting on 1 mol of i, and T is the thermodynamic temperature.

At mechanical equilibrium, the total force per unit volume is zero, i.e.

$$\sum_{i=0}^{\upsilon} c_i(-\nabla\tilde{\mu}_i + \mathbf{F}_i) = -\nabla p + \sum_{i=0}^{\upsilon} c_i\mathbf{F}_i = \mathbf{0} \tag{5}$$

where ∇p is the pressure gradient. Furthermore, the following relation among the diffusional fluxes holds:

$$\sum_{i=0}^{\upsilon} M_i\mathbf{J}_i = \mathbf{0} \tag{6}$$

where M_i is the molar mass of i.

Equations 5 and 6 show that one can write a set of ν *independent* linear equations relating forces and fluxes. Such a set enables one to describe all the mass-transfer processes occurring under the stated conditions.

In addition, it has been shown by Prigogine[7] that eq 3 is invariant if the barycentric velocity $\mathbf{v}$ in the definition of $\mathbf{J}_i$ (eq 4), is replaced by any arbitrary velocity $\mathbf{v}^{\mathrm{a}}$; this really shows the *diffusional* character of the flows describing mass transfer (in comparison to viscous flow).

Using the above conditions, Laity[8] was able to derive for a multicomponent system a diffusion equation of the general form:

$$c_i(-\nabla\tilde{\mu}_i + \mathbf{F}_i) = \sum_{\substack{j=0\\ j\neq i}}^{\upsilon} c_ic_j\xi_{ij}(\mathbf{v}_i - \mathbf{v}_j) \qquad (i = 1,\ldots,\upsilon) \tag{7}$$

This equation indeed remains unchanged if the mean velocities $\mathbf{v}_i$ are expressed with respect to different reference frames. The summation of both sides of eq 7 over all species is zero, according to the symmetry relation:

$$\xi_{ij} = \xi_{ji} \tag{8}$$

Equation 7 has also been derived on a statistical mechanical basis.[9]

III. Diffusional Fluxes in the Presence of Viscous Flow

In an isothermal medium which is not at mechanical equilibrium, the total rate of entropy production per unit volume, σ, is[10]

$$\sigma = \sigma_{\mathrm{D}} - \frac{1}{T}\,\mathrm{grad}\ \mathbf{v}:\ \Pi \tag{9}$$

σ_{D} is still that given by eq 3, and Π is the viscous stress tensor, assumed here to be symmetric.[11] If one considers an isotropic system, then it can be shown[12] that fluxes and thermodynamic forces whose tensorial order differ by an odd number do not couple. Consequently, the entropy production equation and the related phenomenological equations can each be separated into their constituent parts, which means that the inequality in eq 3 remains valid. Nevertheless the total force per unit volume is now nonzero, so that eq 5 is no longer valid.

A generalized diffusional force $\mathfrak{F}$[12,13] can be introduced such that

$$\mathfrak{F}_i = -\nabla\tilde{\mu}_i + \mathfrak{F}_i - \frac{M_i}{\rho}\left(-\nabla p + \sum_{i=0}^{\upsilon} c_i\mathbf{F}_i\right) \tag{10}$$

where ρ is the density of the solution

$$\rho = \sum_{i=0}^{\upsilon} c_iM_i \tag{11}$$

Equation 3 now reads

$$\sigma_{\mathrm{D}} = \frac{1}{T}\sum_{i=0}^{\upsilon} \mathbf{J}_i\cdot\mathfrak{F}_i > 0 \tag{12}$$

and, as expected, the *total diffusional force* per unit volume is zero

$$\sum_{i=0}^{\upsilon} c_i\mathfrak{F}_i = \mathbf{0} \tag{13}$$

It follows directly that Prigogine's theorem[7] can be generalized, so that eq 12 can be expressed in the form

$$\sigma_{\mathrm{D}} = \frac{1}{T}\sum_{i=0}^{\upsilon} \mathbf{J}_i{}^{\mathrm{a}}\cdot\mathfrak{F}_i \tag{14}$$

where

$$\mathbf{J}_i{}^{\mathrm{a}} = c_i(\mathbf{v}_i - \mathbf{v}^{\mathrm{a}}) = c_i\mathbf{v}_i{}^{\mathrm{a}} \tag{15}$$

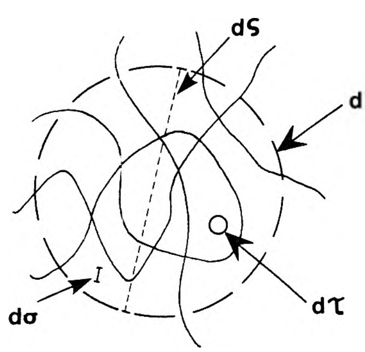

Figure 1. Volume elements dV and $d\tau$ in a polyelectrolyte solution.

For example, if $\mathbf{v}^a$ is chosen to be the velocity of species 0, eq 14 reads

$$\sigma_D = \frac{1}{T}\sum_{i=1}^{\nu} \mathbf{J}_i^0\cdot\mathfrak{F}_i \tag{16}$$

so that only ν diffusional fluxes are independent. Accordingly, it is also possible to derive a generalized, multicomponent, diffusion equation of the form:

$$c_i\mathfrak{F}_i = \sum_{\substack{j=0\\ j\neq i}}^{\nu} c_i c_j \xi_{ij}(\mathbf{v}_i^a - \mathbf{v}_j^a) \qquad (i = 1, \ldots, \nu) \tag{17}$$

Comments made about eq 7 remain valid. Moreover, eq 17 shows for example that pressure gradients can contribute to diffusional flows, contrary to what Newman[13] says.

Now in addition to the set of ν independent local diffusion equations, one has to solve a Navier–Stokes equation, with the appropriate boundary conditions, which provides $\mathbf{v}$, the local velocity of the center of mass expressed, as is $\mathbf{v}_i$, in the reference frame of the laboratory.

To distinguish between diffusional and convectional contributions, the choice $\mathbf{v}^a = \mathbf{v}$ is then imposed, and the relationship between the *macroscopic* (or average) diffusional ($\overline{J_i^d}$), absolute ($\overline{J_i^a}$), and convectional ($\overline{J_i^c}$) fluxes is, for the $\nu + 1$ species:

$$\overline{\mathbf{J}_i^d} = \overline{\mathbf{J}_i^a} - \overline{\mathbf{J}_i^c} \tag{18a}$$

or

$$\overline{c_i(\mathbf{v}_i - \mathbf{v})} = \overline{c_i\mathbf{v}_i} - \overline{c_i\mathbf{v}} \qquad (i = 0, \ldots, \nu) \tag{18b}$$

Barred terms are space averaged. For specific examples of averaging processes, see ref 10 or 11.

IV. Mass Transfer in Membranes

At this point, we may enquire whether or not a multicomponent diffusion equation of the form expressed by eq 7 or 17 should be used to describe isothermal, irreversible processes in membranes. This question has been raised[4,5] and an answer will be attempted here.

(1) *Membrane as a Species.* In some models the membrane is considered to be a macroscopic body with macroscopic pores (>1 μm) which impose some boundary conditions[10] on the solution within the pores. This class of membranes can be described as heterogeneous and inert.

Whenever the membrane modifies the physiochemical properties of the solution within its pores, it should be considered as a chemical species. Consider a volume element, dV (Figure 1), large enough with respect to the pore dimensions so that the average properties inside dV are independent of its location in the membrane. We can then apply a local Gibbs–Duhem relationship, including the membrane species 0, such that

$$\sum_{i=0}^{\nu} c_i\nabla\mu_i^c = \mathbf{0} \tag{19}$$

where μ_i^c is the concentration-dependent part of the chemical potential of i. Actually in most cases, the intermixing of the membrane and mobile species is so intimate, that a two-phase model is unrealistic.

(2) *The Condition of Mechanical Equilibrium.* This condition implies that acceleration of dV, as defined above, whose center-of-gravity velocity is $\mathbf{v}$, is zero, i.e.

$$d\mathbf{v}/dt = \mathbf{0} \tag{20}$$

This further implies that in the steady state, $\mathbf{v}$ should be constant with position (**grad** $\mathbf{v} = 0$), and thus independent of the location of dV. Such a condition is a consequence of choosing dV to be large enough to obtain mean, macroscopic properties. However, it we consider a *local* volume element, $d\tau$ ($d\tau \ll dV$, Figure 1), there will probably be velocity gradients and hence no mechanical equilibrium at this local level.[11] Moreover, the interactions between fluxes within this volume element are then unlikely to be representative of the global interactions in the membrane.

(3) *From a Polyelectrolyte Solution to a Polyelectrolyte Membrane.* A. *Transport in an Electric Field.* To illustrate the consequence of the above assertions, consider a common solution of a polyelectrolyte and a low-molecular-weight salt, the polyion concentration being sufficiently large for overlapping of chains to occur. There are at least four mobile species: solvent, counterions, coions, and polyions. If an electrical field is applied to such a chemically homogeneous solution confined in a closed vessel, there will be four different particle fluxes, of which only three will be independent. Indeed, if the volume element dV is sufficiently large so that electroneutrality prevails on a time average, the total mean electrical force applied to the ionic species inside dV is zero. Thus, mechanical equilibrium exists, friction-coefficient formalism, as expressed by eq 7, can be applied, and one usually expresses velocities relative to the solvent as the reference frame.[1,14] Within $d\tau$ electroneutrality does not subsist, but the equations of motion appertaining to $d\tau$ have to be averaged over a larger volume element, such as, dV, to obtain representative values.

Let us suppose that it is possible to fix, with respect to the cell, the center of gravity of each polyion without perturbing the chain statistics (for example, by smooth cross linking). If an electrical field is again applied, will the relative mean velocities of the different species be modified? We propose that the answer to this question is "no", and claim that the friction-coefficient formalism still applies, with the same values of the coefficients, under steady-state conditions. Whereas in the first experiment we were interested in the electrophoretic Hittorf mobilities with the solvent as the reference frame, we will now express the small-ion fluxes and the solvent flux (electroosmosis) relative to the polyion (or gel, or membrane) as the reference frame. One restriction has to be made however: the above assertions are true if the solution cell can be considered as infinite, or, in other words, if there are no boundary conditions perturbing the flow at a given point in the cell.

To be more explicit about this latter point, let us consider the cell as being of macroscopic dimensions (Figure 2). If the concentration of polyions is sufficiently low, and the tube diameter small, the boundary conditions might play a significant role giving rise to a nonlinear velocity profile. However, if the polyion concentration is sufficiently high (which means that dV is now smaller) as

Figure 2. Flow regime of a polyelectrolyte solution in a tube.

in membranes or gels, then the boundary conditions will only perturb the velocity profile very near to the cell wall because of the better "hydrodynamic screening effect" (see Appendix). Consequently, we can consider the membrane as being infinite, and reach the foregoing conclusions about the validity of eq 7. Indeed, if the polyions are included in the balance of forces, it can be seen that the total force acting on dV is still zero.

Finally, the foregoing assertions can be understood if one refers to the way molecular theories are worked out. Consider a solution of a model polymer in an electrical field in the absence of pressure and concentration gradients. It would be necessary to express the following differential coupled equations which are valid for the volume element $d\tau << dV$: Poisson equation (one equation), transport of small ions (two equations), Navier–Stokes vectorial equations (three equations), and an incompressibility equation (one equation). These would have to be solved for the appropriate boundary conditions and then averaged over a large enough volume, such as dV. In a membrane model the polymer would be the reference frame: in the solution model the solvent, for example, could be the reference frame. However, for both models the relative local and average velocities would be the same.

B. *Transport in a "Chemical" Field.* The situation appears to be more complicated when a membrane is separating two solutions of differing concentration but at the same pressure in open-circuit conditions. Inside the membrane there exists a diffusion potential but, as already seen, this does not give rise to a volume force within dV because of electroneutrality. Does a pressure gradient exist? The answer is no, as long as the membrane is considered to be a single-phase system in the sense of Gibbsian thermodynamics. It has been pointed out by several authors that if the membrane bears fixed charges,[15] or if it has exclusion properties with respect to a given solute, then the pressure cannot be uniform at the membrane–solution interface.[16,17] Nevertheless, if the solution and membrane are considered as separate phases, exchanging volume and matter under isothermal conditions, the thermodynamic equilibrium condition indicates that the pressure *is* the same on both sides of the membrane–solution interface.[18,19] How does this contradiction arise? It arises because, quite often, the existence of an osmotic volume or solvent flow is attributed to a pressure gradient in the membrane.[16,17] This is indeed so if the pressure force experienced by a probe surface dσ, $d\sigma \sim d\tau^{2/3}$, is defined *in the liquid* (Figure 1).

If a probe surface, dS, has dimensions comparable with $dV^{2/3}$ (Figure 1), then it would be necessary to separate many polymer segments and attach them to the probe surface. For the resulting force on dS there is, as in the case of the liquid, an excess of force resulting from the momentum exchange with particles of the liquid, and also a *negative* contribution due to the traction exerted by the polymer segments. When both contributions are added, one obtains the same value as that for the external solution, a value defined thermodynamically by

$$p = \frac{\partial F}{\partial V}\bigg|_{T,n_i} \qquad (21)$$

where F is the free energy of volume V, $V > dV$. (Note that the overpressure could only be defined locally, i.e., for $d\tau$.)

Finally, in the situation where there is only a chemical potential gradient in the membrane, then by the Gibbs–Duhem equation, eq 19, there will be a zero volume force and, consequently, a true diffusional transport process.

C. *Transport in a Pressure Field.* The analysis of the above steady-state diffusional processes concerned only those in a membrane which was not, strictly speaking, mechanically held.

Where a membrane separates two identical solutions at different pressures, the problem is somewhat different because an external mechanical force is needed to restrain the membrane from moving. From an analysis of the forces per unit volume inside a volume element, such as dV, one obtains

$$-\nabla p + c_0\mathbf{F}_0 = 0 \qquad (22)$$

Here, $c_0\mathbf{F}_0$ is the sum of the surface forces per unit volume exerted by the polymer segments outside dV on the polymer segments inside dV. This situation is similar to that in a viscosity experiment with a polymer solution, but in the membrane experiment there is no velocity gradient so that $\mathbf{F}_0$ adjusts itself to counterbalance the applied pressure force, and appears formally as an externally applied mechanical force. We therefore see that eq 22 is a specific example of the general eq 5, so that, under the stated conditions, the formalism of friction coefficients can be applied:

$$c_i\overline{V}_i(-\nabla p) = \sum_{\substack{j=0\\ j\neq i}}^{\nu} c_i c_j \xi_{ij}(\mathrm{v}_i - \mathrm{v}_j) \qquad (i = 1, \ldots, \nu) \quad (23)$$

This set of ν independent equations is sufficient to describe properly the flow processes inside the membrane.

V. Conclusion

In the first part of this paper we recalled that, if proper diffusional forces are defined, the friction coefficient formalism is not limited to mechanical equilibrium conditions. However, in a chemically homogeneous medium ($\nabla\mu_i^c = 0$ at the appropriate scale), the diffusional contribution to the fluxes will be generally negligible compared to the convective contribution ($\overline{c_i|\mathbf{v}_i - \mathbf{v}|} << \overline{c_i|\mathbf{v}|}$), unless the conditions are designed specifically for separation processes. In this respect, one wonders whether all of the consequences of eq 10 have been fully examined.

The analysis of transport processes in membranes raised the question of whether the membrane could be considered as a one-phase or as a two-phase system. In a two-phase system, the "membrane" phase imposes definite boundary conditions (i.e., pore dimensions, fixed-charge densities, etc.) on the equilibrium and transport processes occurring in the "liquid" phase, and in such a system, transport parameters can in theory be calculated from a solution of a set of local equations which have been averaged over macroscopic dimensions. This type of approach has been worked out by different authors.[10,11,15]

If the membrane is considered as a one-phase system, then all the steady-state transport processes, if analyzed at the correct molecular level, are truly diffusional, as we have shown. Thermodynamic criteria which will enable the choice between a one-phase and a two-phase system to be made are discussed in ref 19.

We therefore conclude that if one wishes to distinguish between a diffusional and viscous flux, then it is essential to define the molecular *scale* of the transport parameters. When, in theoretical calculations, one chooses a given

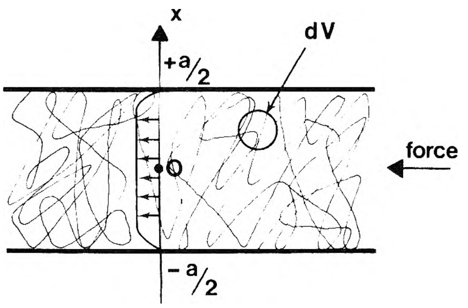

Figure 3. Flow regime in a gel restrained between two parallel plates.

microscopic friction coefficient, it is already related, at the local level, to a viscous dissipation. Such friction coefficients are then used in a set of local transport and equilibrium-perturbed equations, a Navier–Stokes equation being part of this set. However when, finally, one averages these local fluxes over a region characteristic of the macroscopic properties of the system, then one might conclude that the flow properties are truly diffusional if the system is considered to be a single phase, in the Gibbsian sense.

To distinguish clearly between a diffusion and a viscous process, it is obvious that the molecular scale chosen for the analysis will be different for a gas, a liquid, a macromolecular solution, a homogeneous membrane, and a heterogeneous membrane. It is our belief that controversies and ambiguities can be avoided if authors would explicitly define the terms "phase" and "elementary volume" representative of the properties of the phase.

Acknowledgment. We wish to thank Professor Patrick Meares of the University of Aberdeen for his helpful comments, and one of us (J.B.C.) is grateful to the Carnegie Trust for the Universities of Scotland for a research grant.

Appendix

The planar problem: Consider a neutral polymer gel, of segment concentration c_m and with each segment having a coefficient of friction f_{mw} with solvent w, placed between two parallel plates separated by a distance a (Figure 3). We solve the one-dimensional Navier–Stokes equation for a local volume element dV when a uniform pressure gradient, grad p, is applied:[20]

$$\eta\nabla^2 v - c_m f_{mw} v = \text{grad } p \tag{A1}$$

where v is the velocity of the solvent relative to the fixed center-of-mass of polymer segments. η is the viscosity. Introducing the Debye hydrodynamic shielding length λ[20]

$$\lambda = (\eta/c_m f_{mw})^{1/2} \tag{A2}$$

the general solution for $v(x)$ is

$$v(x) = -\frac{\text{grad } p}{c_m f_{mw}}\left[1 - \frac{\cosh(x/\lambda)}{\cosh(a/2\lambda)}\right] \tag{A3}$$

Let us estimate the order of magnitude of λ by choosing the worst situation such as a dilute gel where $c_m = 0.01$ M, and take typical values of $\eta = 10^{-2}$ g cm^{-1} s^{-1}, $f_{mw} = 10^{+15}$ g s^{-1} mol^{-1}. Then $\lambda = 0.01$ μm. In a membrane we will always have $\lambda << 0.01$ μm so that for all values x, a, $a - x << \lambda$, we have the limiting form

$$v = -\frac{\text{grad } p}{c_m f_{mw}} \tag{A4}$$

It is only at distances of the order of λ from the edges that there will be velocity gradients. This enables us to claim that elsewhere in the membrane

$$\nabla^2 v = 0 \tag{A5}$$

a relation expressing the condition of mechanical equilibrium inside dV, the pressure force being counterbalanced by the friction force.

At distances greater than a few λ from the edges, the presence of the polymer creates a hydrodynamic screening effect, the screening length being λ, so that the boundary condition $v = 0$ at $x \pm a/2$ is ignored. This result is, of course, independent of the vessel shape.

References and Notes

(1) A. Katchalsky and P. F. Curran in "Nonequilibrium Thermodynamics in Biophysics", Harvard University Press, Cambridge, Mass., 1967.
(2) P. Meares, J. F. Thain, and D. G. Dawson in "Membranes", Vol. 1, Marcel Dekker, New York, N.Y., 1972, Chapter 2.
(3) K. S. Speigler, *Trans. Faraday Soc.*, **54**, 1409 (1958).
(4) J. A. M. Smit, J. C. Eijsermans, and A. J. Staverman, *J. Phys. Chem.*, **79**, 2168 (1975).
(5) G. S. Manning, *J. Phys. Chem.*, **76**, 393 (1972).
(6) D. C. Mikulecky, *Biophys. J.*, **12**, 1642 (1972).
(7) I. Prigogine in "Etude thermodynamique des phénomenès irrêversibles", Desoer, Liège, 1947.
(8) R. W. Laity, *J. Phys. Chem.*, **63**, 80 (1959); *J. Chem. Phys.*, **30**, 682 (1959).
(9) R. J. Bearman and J. G. Kirkwood, *J. Chem. Phys.*, **28**, 136 (1958); R. J. Bearman, *ibid.*, **31**, 751 (1959).
(10) S. R. de Groot and P. Mazur in "Non-Equilibrium Thermodynamics", North-Holland Publishing Co., Amsterdam, 1969, p 405.
(11) D. C. Mikulecky and S. R. Caplan, *J. Phys. Chem.*, **70**, 3049 (1966).
(12) J. O. Hirshfelder, C. F. Curtiss, and R. B. Bird in "Molecular Theory of Gases and Liquids", Wiley, New York, N.Y., 1954, p 718.
(13) J. S. Newman in "Electrochemical Systems", Prentice-Hall, Englewood Cliffs, N.J., 1973, p 254.
(14) A. Schmitt and R. Varoqui, *J. Chem. Soc., Faraday Trans. 2*, **69**, 1087 (1973).
(15) R. Schlogl in "Stofftransport durch Membranen", Steinkopf Verlag, Darmstadt, 1964.
(16) G. S. Manning, *J. Chem. Phys.*, **49**, 2668 (1968).
(17) P. Meares, *Eur. Polym. J.*, **2**, 241 (1964).
(18) H. B. Callen in "Thermodynamics", Wiley, New York, N.Y., 1966.
(19) J. J. Hermans in "Flow Properties of Disperse Systems", J. J. Hermans, Ed., North-Holland Pulbishing Co., Amsterdam, 1953, Chapter 3.
(20) P. Debye and A. M. Bueche, *J. Chem. Phys.*, **16**, 573 (1948).

A new concept in scientific publishing:

Journal of Chemical Research

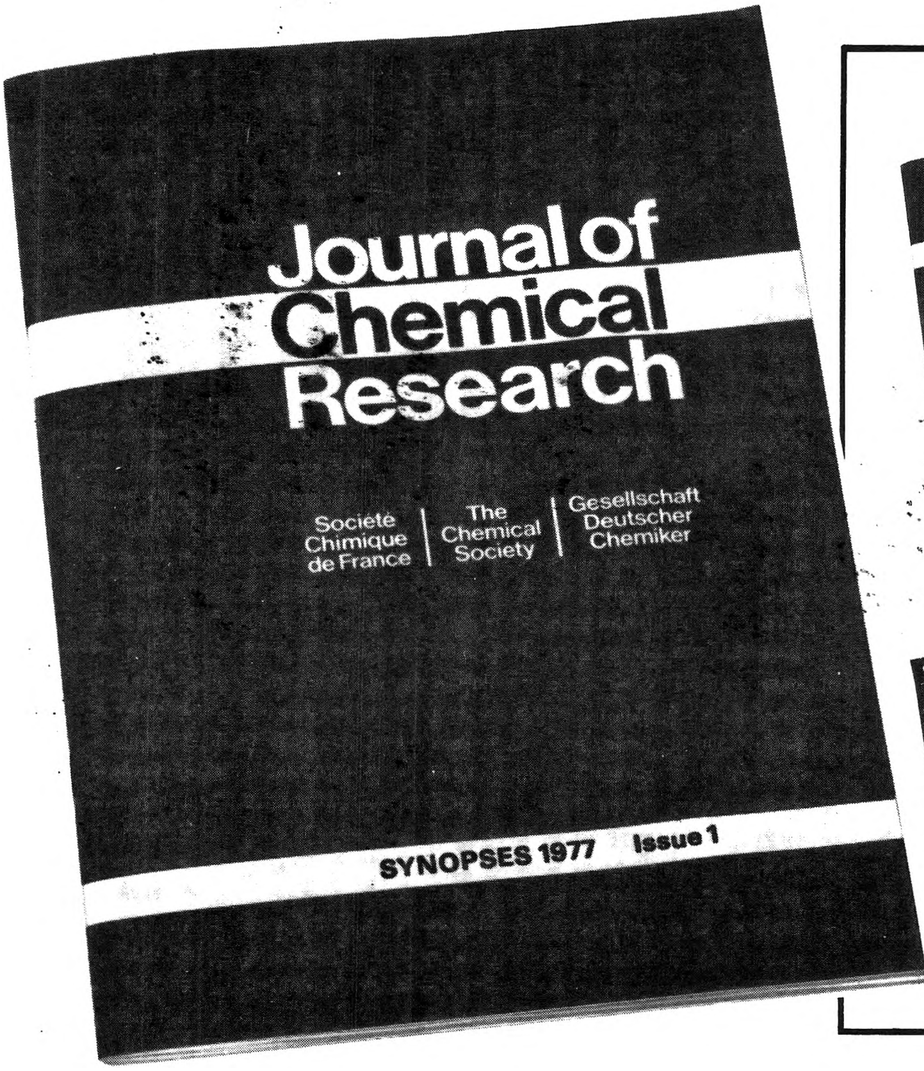

Miniprint

Microfiche

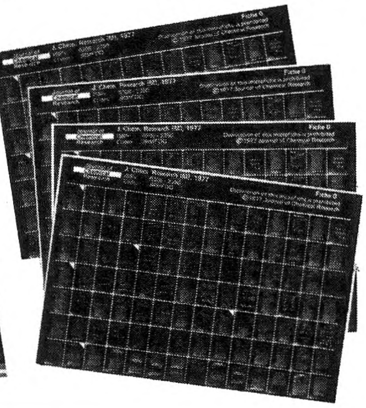

Journal of Chemical Research is a new multi-national journal which is being published in synopsis format backed up simultaneously with full texts in two forms – microfiche and miniprint. It was launched in January 1977 by The Chemical Society, Gesellschaft Deutscher Chemiker and Société Chimique de France as the first step towards the development of a more logical system of chemical primary publications.

It covers all kinds of chemistry and appears in two parts: Part S caters for current awareness needs and contains short synopses of papers in an easily browsable form; Part M fulfils the archival role of the journal and contains the full texts of the papers appearing in Part S in two alternative forms – microfiche and miniprint.

For sample copies and subscription details please complete and return the coupon:

To: The Marketing Officer, The Chemical Society,
Burlington House, London W1V 0BN, England.
Please send me a sample copy and subscription details of JOURNAL OF CHEMICAL RESEARCH.

Name ……………………………………………………

Address ……………………………………………………

……………………………………………………

……………………………………………………

……………………………………………………

Founding Sponsors:

The Chemical Society
Gesellschaft Deutscher Chemiker
Société Chimique de France

Supporting Societies:

Norsk Kjemisk Selskap Société Chimique de Belgique
Verein Österreichischer Chemiker Vlaamse Chemische Vereniging
Deutsche Gesellschaft für Chemisches Apparatewesen

BETTER BET ON THE RABBIT

In the fable, the tortoise wins.
Of course, everybody knows it didn't really happen that way.
That's why they call it a fable.
No two ways about it...
THE RACE IS TO THE SWIFT.

To keep current on developments in the fast-moving discipline of physical chemistry, you need a journal that publishes up-to-date articles, communications, and symposia. Biweekly—now *that's* up to date. And you'll get biweekly information in...

THE JOURNAL OF PHYSICAL CHEMISTRY.

Swift is fine, but it's not nearly enough for an authoritative publication of ACS. You'll find more than 20 papers in every issue, covering spectroscopy, thermodynamics, reaction kinetics, and other areas of experimental and theoretical physical chemistry.
Would you like to be a little bit ahead of the rest of your field—the people who *don't* use the Journal? Then, just...
Complete, clip, and mail the coupon below. Now?

- **new concepts**
- **new techniques**
- **new interpretations**
  ... plus reports on classical areas

The editors of the Journal of Physical Chemistry strive to select material that is useful in the classical areas of chemistry as well as in modern structural quantum mechanical areas. Start your subscription now. We'll do the rest.

Another service of ACS

The Journal of Physical Chemistry
American Chemical Society **1977**
1155 Sixteenth Street, N.W.
Washington, D.C. 20036

Yes, I would like to receive the JOURNAL OF PHYSICAL CHEMISTRY at the one-year rate checked below:

	U.S.	Foreign and Canada	Latin America
ACS Member *	☐ $24.00	☐ $ 34.00	☐ $ 33.00
Nonmember	☐ $96.00	☐ $106.00	☐ $105.00

Bill me ☐ Bill company ☐ Payment enclosed ☐

Air freight rates are available on request.

Name

Street Home ☐ Business ☐

City State Zip

Journal subscriptions start in January '77.
Allow 60 days for your first copy to be mailed.
* NOTE: Subscriptions at ACS member rates are for personal use only.

24.ส.ค. 2520